Neutrino physics with SuperNEMO and SoLid experiments

M. Bongrand

université
PARIS-SACLAY

Physique des neutrinos avec les expériences SuperNEMO et SoLid

Neutrino physics with SuperNEMO and SoLid experiments

Habilitation à diriger des recherches de l'Université Paris-Saclay

Spécialité : physique des neutrinos
Unité de recherche: Subatech UMR 6457
Référent: Pr. Bruno Espagnon

présentée et soutenue à Orsay,
le 9/02/2024, par

Mathieu BONGRAND

Composition du jury

Marie-Hélène SCHUNE Directrice de recherche au CNRS, IJCLab Orsay	Présidente
Corinne AUGIER Professeure à l'Université Claude Bernard, IP2I Lyon	Rapportrice
Andrea GIULIANI Directeur de Recherche CNRS, IJCLab Orsay	Rapporteur
Jacob LAMBLIN Maître de Conférences HDR à l'Université Grenoble Alpes, LPSC Grenoble	Rapporteur
Pascal PAGANINI Directeur de recherche au CNRS, LLR Palaiseau	Examinateur

Habilitation à diriger des recherches

NNT: 2020UPASA000

Contents

Introduction

The Standard Model is the actual theory of particle physics describing the elementary particles and the three fundamental interactions they are sensitive to. It is an extremely successful theory able to explain almost all the experimental observations with an incredible precision. As an example, we can give the extraordinary calculation of the anomalous magnetic moment of the electron with a theoretical precision at the 10^{-9} level, in agreement with the experiment. To my knowledge, this is the most accurate prediction in physics. The discovery of the Higgs boson at the LHC in 2012 provided the missing piece of the Standard Model, which was needed to provide masses to the elementary particles. The study of the Standard Model fascinated me as a student at University. It represented to me the synthesis between special relativity and quantum mechanics, which both motivated me to become physicist. Gravitation, which is the fourth interaction of nature, is described by general relativity. Despite being negligible at the particle level, these two infinites are connected. The discovery of the gravitational waves in 2015, thanks to km-scale interferometers on Earth, is another fantastic achievement of mankind.

Despite all its great successes, the Standard Model still leaves some unexplained phenomena. For example, it is unable to explain the smallness of neutrino masses compared to the other fermions, the neutrino mixing and flavour oscillations, the nature of dark matter, the matter-antimatter asymmetry observed in the Universe, the primordial inflation nor the accelerated expansion of the Universe. Improving our knowledge of neutrino physics might be a key to complete this theory or even go beyond the Standard Model, and better understand the Universe we are leaving in. In this regards, several anomalies in the neutrino oscillation experiments might indicate the existence of a new sterile neutrino state. Always fascinated by this enigmatic particle and its properties, I wanted to contribute to this field of research. Neutrinos are unique in the Standard Model since they are neutral fermions only sensitive to the weak interaction. They also certainly played a decisive role in the evolution of the Universe, as they do during the explosion of stars. Studying the history of the neutrino is very instructive. From its theoretical birth to explain the continuous energy spectrum in β-decay to the discovery of flavour oscillations to explain the deficit of Solar neutrinos, the repercussions were always unexpected. For all these reasons, I believe that neutrinos have still a lot to teach to us.

I have started my scientific career with my first internships at the *Laboratoire de l'Accélérateur Linéaire* (LAL) in Orsay, where I also performed my PhD thesis from 2005 to 2008, under the supervision of Corinne Augier. I was involved in the data analysis of the NEMO-3 double beta decay experiment. I was studying the ^{130}Te isotope which is a good candidate to search for neutrinoless double beta decay since its two neutrino decay is extremely rare, producing thus less background. The purpose of my thesis was precisely to measure this decay rate with the NEMO-3 data and to search for the neutrinoless double beta decay as well. It was also time to prepare the successor experiment, called SuperNEMO. In order to improve the sensitivity compared to NEMO-3 the radiopurity of the isotopic sources had to be reduced significantly. Unfortunately, the HPGe detectors were at the sensitivity limit for this kind of measurements. Therefore we started at LAL an R&D on a BiPo detector to improve the search of the main

background isotopes in the SuperNEMO sources. I was in charge of developing, constructing and exploiting a first prototype that demonstrated the feasibility of the BiPo detection technique and demonstrated that the sensitivity was achievable for the SuperNEMO requirements.

After my thesis, I continued to work on neutrino physics, but I changed of topic to work on neutrino flavour oscillations. I joined the Double Chooz experiment searching for the small θ_{13} mixing angle, which was the last unknown angle in the PMNS matrix in 2008. I was hired by prof. Fumihiko Suekane at the *Research Center for Neutrino Science* (RCNS) at Sendai, in Japan. I was in charge of leading the PMT integration of the Double Chooz far detector, at the nuclear reactor site in the Ardennes, in France. I also took part in several aspects of the detector construction and integration onsite. I left the Double Chooz experiment after a year of postdoc, when I obtained a position at CNRS, before the data taking could start.

As *Chargé de recherche* CNRS in the end of 2009, I resumed activities at LAL to work on the BiPo detector and the SuperNEMO experiment. After some more studies and characterization on the BiPo prototypes it was time to validate the improvements foreseen and to build the final BiPo-3 detector. The installation of this detector took place in Summer 2012 in the *Laboratorio Subterráneo de Canfranc* (LSC) in Spain. The background measurements showed a real improvement and a good sensitivity for the SuperNEMO sources characterization. The source materials, the selenium purification and the production methods were first tested with the BiPo-3 detector. The first SuperNEMO ^{82}Se foils were measured in 2016. After the installation of the BiPo-3 detector, I started to work more directly on the SuperNEMO experiment itself. First, by working with LAL mechanical staff on the design and integration of the detector, specially the calorimeter. I also participated to the first developments of the SuperNEMO software tools leaded by LPC Caen and to magnetic field studies. In 2015, we started the integration of the SuperNEMO demonstrator at the *Laboratoire Souterrain de Modane* (LSM), for which I was involved in many operations onsite. I was during four years the scientific responsible for the underground integration. The detector core has been successfully closed at the end of 2018. I was also in charge of the cabling of the full calorimeter, mostly prepared at LAL. The installation of the electronics, also developed at LAL, quickly followed the cabling and the early calorimeter commissioning could start in 2019. I was leading this effort with a small group of researchers and PhD students. We obtained very good performances of the detector despite the absence of shielding and without the tracker being operational. In the mean time, the tracker cabling and sealing finished, and its commissioning could start. Since 2022, the SuperNEMO demonstrator can take data with both the calorimeter and the tracker. The magnetic coil and the anti-radon tent integration have latter been installed. The iron shielding has been produced in 2023 and should be installed in 2024. The double beta decay data taking is about to start.

In parallel to the SuperNEMO detector construction, the LAL prospective meeting end of 2014 motivated the neutrino group to extend its implication in another field of neutrino physics. Many projects were considered, but as a first step it was decided to join the SoLid experiment, to search for a possible eV-scale sterile neutrino, at very short baseline from a nuclear reactor. The collaboration was about to start a real scale prototype, called SM1 for SoLid Module 1, at the BR2 reactor in Belgium. We decided to join the data analysis of this prototype and to develop a scintillator test-bench to investigate improvements in the light-yield and collection for the coming full scale detector. Unfortunately, the prototype results were limited by a very small anti-neutrino detection efficiency due to issues with the electronics and the very limited time of exposure to reactor neutrinos. This happened because of the planed long-term reactor shut down at the end of February 2015 and a delay in the commissioning of SM1. The following light-yield optimization studies as well as the search for funding were successful and permitted to build the full scale detector in 2017. After few months of commissioning and

detector tuning, stable and good quality data for physics were taken from May 2018. At LAL, we were then involved in the calibration of the detector, in collaboration with Subatech group, and in the data analysis of the backgrounds and the anti-neutrino signal. Unfortunately, the experiment was quickly facing a very high background because of low overburden and higher radioactivity background than expected, in the neutron screens. It took thus several years to improve the understanding of the detector and to reach a sufficient background rejection thanks to multi-variates analyses. This work is still ongoing. In the mean time, the hypothesis of the sterile neutrino to explain the reactor anti-neutrino anomaly had been ruled out, by a new ^{235}U β-spectrum measurement and other sterile neutrino search experiments.

During these years at LAL as CNRS researcher, I had the chance to supervise three PhD thesis. The first one was the theses of Guillaume EURIN, from *Université Paris-Sud* and University College London, from 2011 to 2015. The research subject was the complete analysis of the ^{96}Zr isotope double beta decays and its backgrounds in the NEMO-3 data. He was able to measure or put limits on many double beta decay processes of the ^{96}Zr isotope. The second aspect of his thesis was the development of the BiPo-3 detector for the measurement of the double beta sources for the SuperNEMO experiment. Guillaume took a major role in setting the BiPo-3 detector, developed the calibration methods, performed the first background measurements and did the analysis of samples for the SuperNEMO sources. After a postdoc at MPIK Heidelberg, Guillaume recently obtained a permanent position at Irfu in CEA Saclay.

The second thesis I supervised was the one of Delphine BOURSETTE, from ENS Cachan and *Université Paris-Saclay*, on both SuperNEMO and SoLid experiments from 2015 to 2018. Concerning SuperNEMO, the thesis consisted on evaluating the interest of using some copper foils (instead of ^{82}Se) to study the external background of the experiment. This analysis convinced the collaboration and copper foils were introduced in the detector. About the SoLid experiment the work of the thesis consisted on one hand in optimizing the light-collection with test-bench studies at LAL for the SoLid final detector, and on a second hand in the analysis of the first anti-neutrino data taken at the BR2 reactor in 2017. Delphine is now working on reactor simulations at EDF.

The third thesis I have been supervising is the thesis of Noë ROY, from *Université Paris-Saclay*, on the data analysis of the SoLid experiment from 2018 to 2021. In collaboration with Subatech group, we were in charge of the calibration of the detector and we developed several methods to calibrate more than 20 000 detector parameters and check the detector performances. After this work, Noë started to look for anti-neutrino interactions in the detector and performed background studies. The background revealed to be extremely important in SoLid and Noë had to develop multivariate analysis to reject as much as possible the background. He has investigated the background subtraction method and showed the limitations of the method by comparing different reactor off data periods. As a side subject, Noë was also involved with me on the LiquidO R&D by testing SiPMs and electronics. The LiquidO project consists on the development of an innovative technology of scintillator with particle identification capabilities for future possible anti-neutrino detectors with very low background. Our experience gained in SoLid is well suited to participate to the development of LiquidO's technology. Noë is now postdoc at York University in Canada working on long baseline neutrino oscillations.

At the end of 2019, for personal reasons, I have asked to IN2P3 a mobility to join Subatech Laboratory in Nantes to continue my activities with the group on SoLid experiment, increase my implication on LiquidO and start to contribute to JUNO reactor anti-neutrino experiment, under construction in China. I can keep an eye on SuperNEMO progress and results, but it is harder to contribute directly since the laboratory is not involved in this experiment. I joined Subatech in August 2020.

Part I

Neutrinoless double beta decay search

Chapter 1

Neutrinoless double beta decay

The first part of this *habilitation à diriger des recherches* focusses on the fundamental question of the nature of the neutrino: is it a Dirac particle, like any fermion of the Standard Model, or a Majorana particle, identical to its anti-particle? This question re-gained in importance in the last twenty years, after the discovery of neutrino oscillations, which proved that neutrinos are massive particles, a necessary condition to be a Majorana particle. Neutrino oscillations, and more specifically nuclear reactor experiments will be the subject of the second part of this document. Neutrino oscillation experiments revealed fundamental properties about neutrinos, but cannot provide any information on Dirac or Majorana nature of the neutrino. Despite these two subjects seems not related, we will try to show the interplay between them.

The Majorana nature of the neutrino could bring fundamental consequences in our understanding of the Universe. This property would allow violation of the lepton number conservation and the existence of matter creation processes, which could have played a role in the matter-antimatter asymmetry observed in the Universe. The Majorana neutrino mass term can be included in the simpliest extension of the Standard Model and explain the smallness of active neutrino masses, through the see-saw mechanism. To investigate the Majorana nature of the neutrino, the only experimental way is the search for neutrinoless double beta decay $0\nu\beta\beta$, which is the subject of this chapter. I've been involved in this field of research even before my PhD thesis. In addition to the nature of the neutrino, the discovery of $0\nu\beta\beta$ could bring another mean to constrain the absolute neutrino masses, maybe in the most sensitive way, through an effective neutrino mass for double beta decay $m_{\beta\beta}$. Unfortunately, this is today limited by the theoretical difficulties to predict the $0\nu\beta\beta$ rates, because of extremely complex many-body calculations of the nuclear matrix elements. The effective neutrino mass $m_{\beta\beta}$ also depends on the number of neutrinos (active or sterile), the PMNS mixing parameters, the Majorana CP-violation phases and the neutrino mass ordering.

In this chapter, we will present the two processes of the double beta decay, the computation of the nuclear matrix elements and give an overview of the current best experimental results.

Chapter contents

Introduction

The cosmological models, describing the evolution of the observed Universe, make us believe our Universe was initiated in a Big-Bang. In these very early times, the Universe consisted in an extremely hot and dense state, where energy and matter-antimatter were reciprocally converted into each other. Yet, our Universe seems to contain only matter today. This asymmetry indicates that processes which create matter or destroy anti-matter must exist. *CP-violation* has been observed from the quark sector, in the weak decays of mesons. But it seems not sufficient to explain the matter-antimatter asymmetry of the Universe [PDG, 2022]. Looking at ν_e appearance from ν_μ beams, neutrino oscillation experiments have started to constrain the CP-violation phase of the PMNS matrix ($\delta_{CP} = (1.23 \pm 0.21)\pi$ rad - PDG average 2023). But linked to the small θ_{13} mixing angle, this effect might again not be sufficient.

We must then look for other processes to explain the matter-antimatter asymmetry. In the Standard Model (SM) of particle physics, there is no necessity for an *a priori* principle of baryon and lepton conservation [Weinberg, 1979]. These conservations are accidental in the SM, since they are simply a consequence of the SU(2)×U(1) and SU(3) gauge symmetries. Violations of the baryon and lepton numbers conservations are likely to occur in grand unified theories aiming to combine the gauge theories of the weak, electromagnetic and strong interactions. One of the most promising violation process beyond SM is the proton decay, for example $p \to e^+ + \pi^0$, but it has never been observed yet, $\tau_p(p \to e^+ + \pi^0) > 2.4 \times 10^{34}$ y [Takenaka et al., 2020] or $\tau_p(p \to inv.) > 9.6 \times 10^{29}$ y [Allega et al., 2022].

The rarest process measured so far is the two neutrinos double beta decay $2\nu\beta\beta$, $T^{2\nu}_{1/2} \sim 10^{18-21}$ y [Agostini et al., 2023]. Related to it, the neutrinoless double beta decay $0\nu\beta\beta$ is intensively researched, with the best half-life limit being $T^{0\nu}_{1/2} > 2.3 \times 10^{26}$ y [Abe et al., 2023]. Such process would represent a direct creation of two electrons, thus a violation of the conservation of the lepton number. The $0\nu\beta\beta$ decay would be possible if the anti-neutrino could be changed into a neutrino, between the two decaying neutrons. In 1937, E. Majorana proposed an alternative to Dirac's theory, where electrically neutral particles could be identical to their anti-particles [Majorana, 1937]. Since the neutrino is the only neutral fermion of the SM, the theory of Majorana could be well describing neutrinos. The change from neutrino to anti-neutrino can occur through the Majorana mass mechanism, but not through the Dirac mass term (see figure 1.1). For Dirac particles, the mass term m_D couples the chirality projections of the field ψ, in a Lorentz invariant term:

$$\mathcal{L}_D = -m_D \, (\overline{\psi_L}\psi_R + \overline{\psi_R}\psi_L), \tag{1.1}$$

where ψ_L and ψ_R are respectively the left-handed and right-handed projections composing $\psi = \psi_L + \psi_R$, which are obtained from the transformation $\psi_{L,R} = 1/2(1 \mp \gamma_5)\psi$. Since we know from oscillations that neutrinos have masses, we have to include the right-handed field for the neutrino to the SM, despite it has never been observed. From the Yukawa interaction with the Higgs boson, the mass of the active neutrinos can be generated in this way, but we cannot explain why their masses are so small compared to the other fermions. Such small Yukawa coupling constants for the neutrinos make theorists believe other contributions to the neutrino mass could intervene [Balantekin and Kayser, 2018].

If charge conservation is not required, one can build a Lorentz scalar by combining the field ψ with its charge conjugate ψ^c, which has an opposite chirality. We can then construct the left-handed m_L and the right-handed m_R Majorana mass terms in the Lagrangian:

$$\mathcal{L}_M = -\frac{m_L}{2} \, (\overline{(\psi_L)^c}\psi_L + h.c.) - \frac{m_R}{2} \, (\overline{(\psi_R)^c}\psi_R + h.c.) \tag{1.2}$$

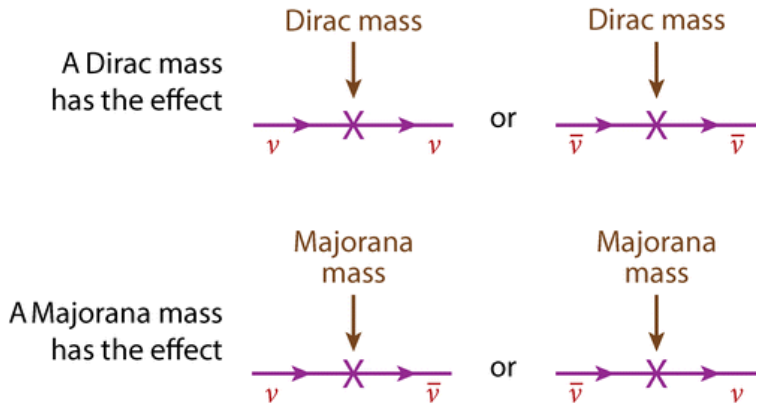

Figure 1.1: Effects of the Dirac and Majorana mass terms on the neutrino field in the Lagrangian [Balantekin and Kayser, 2018]

Complete details of the Dirac and Majorana neutrinos masses formalism can be found in [Bilenky and Petcov, 1987]. It is not necessary that both Majorana mass terms exists. In fact, the Majorana mass term m_L for the left-handed neutrino is forbidden by SM symmetries[1] [Giunti and Kim, 2007] and would need BSM physics to be generated through interaction with a weak isospin triplet [Balantekin and Kayser, 2018]. Combining Dirac and Majorana mass terms may provide an explanation to the small masses of the neutrinos, through the *see-saw* mechanism [Minkowski, 1977]. In the most straightforward see-saw model (called type-I), we write the following neutrino mass term of the Lagrangian:

$$\mathcal{L}_{D+M} = -\frac{1}{2}\left[\overline{(\nu_L)^c}, \overline{\nu_R}\right]\begin{bmatrix} 0 & m_D \\ m_D & m_R \end{bmatrix}\begin{bmatrix} \nu_L \\ (\nu_R)^c \end{bmatrix} + h.c. \tag{1.3}$$

The right-handed Majorana mass term does not violate any known conservation law and thus could be extremely large [Balantekin and Kayser, 2018]. On the other hand, the Dirac neutrino mass m_D can be on the same order than the leptons or quark masses. Diagonalizing the neutrino mass matrix of equation 1.3, we end-up with two mass eigenstates with values m_D^2/m_R and m_R, respectively associated to the two Majorana neutrinos ν and N, as defined in [Balantekin and Kayser, 2018]. This is the see-saw relation showing the heavier is N, the lighter is ν. For example, if m_D is of the order of the muon mass ($m_\mu = 106$ MeV), then $m_\nu \approx 0.1$ eV and $m_R \approx 10^8$ GeV, which is out of reach of near-future accelerators.

We have tried to illustrate the major importance to investigate the violation of the lepton number conservation and the role of the Majorana mechanism for the neutrinos. Neutrino masses might be a window to physics beyond the SM and the understanding of our Universe. Our best chance to demonstrate the Majorana nature of the neutrino, would be the discovery of the $0\nu\beta\beta$ decay. This is for all these reasons that this research field fascinated me. In the following of this chapter, we will concentrate on double beta decay.

1.1 Double beta decay theory

1.1.1 Two-neutrinos double beta decay

The two-neutrinos double beta decay ($2\nu\beta^-\beta^-$) is a rare nuclear process in which two neutrons are simultaneously transformed into two protons in a nucleus, with the emission of two electrons and two anti-neutrinos. For a nucleus with Z protons and A nucleons, the reaction is:

[1] the neutrino term $\overline{(\psi_L)^c}\psi_L$ has third component isospin $I_3 = 1$ and hypercharge $Y = -2$ but the SM does not contain any weak isospin triplet with $Y = 2$ to generate the Majorana mass.

$$(A, Z) \rightarrow (A, Z+2) + 2e^- + 2\bar{\nu}_e \tag{1.4}$$

This process allowed in the Standard Model, conserves the total L and the electron L_e lepton numbers. The $2\nu\beta\beta$ decay has been first proposed by M. Goeppert-Mayer [Goeppert-Mayer, 1935], one year after the Fermi weak interaction theory. She calculated the probability of the decay putting a lower limit on the decay half-life $T_{1/2} > 10^{17}$ y, from the second order of the perturbation theory. Isobar nuclei, having the same mass number A, are alternately distributed on two smooth mass curves against the atomic number Z because of nucleons pairing energy. These curves are approximately constantly separated, having thus the same minima, as shown on figure 1.2. Even-even nuclei lie in the lower curve since they are more stable, thanks to the pairing of their nucleons. In the neighbourhood of the minimum, it may happen that even-even nuclei cannot decay through single β-decay because of energy conservation, but have to decay through $2\nu\beta\beta$[2]. The ground states of even-even nuclei have spin 0 and positive parity +, so double beta decays to ground states are $0^+ \rightarrow 0^+$ transitions. The energy release in the decay, called $Q_{\beta\beta}$, corresponds to the mass difference of the two nuclei for $\beta^-\beta^-$. It is mostly shared between the leptons, since the nuclear recoil can be neglected. Detecting the two electrons produces a continuous energy spectrum, with $Q_{\beta\beta}$ as end-point, peaked around $1/3 \times Q_{\beta\beta}$, as illustrated on figure 1.11.

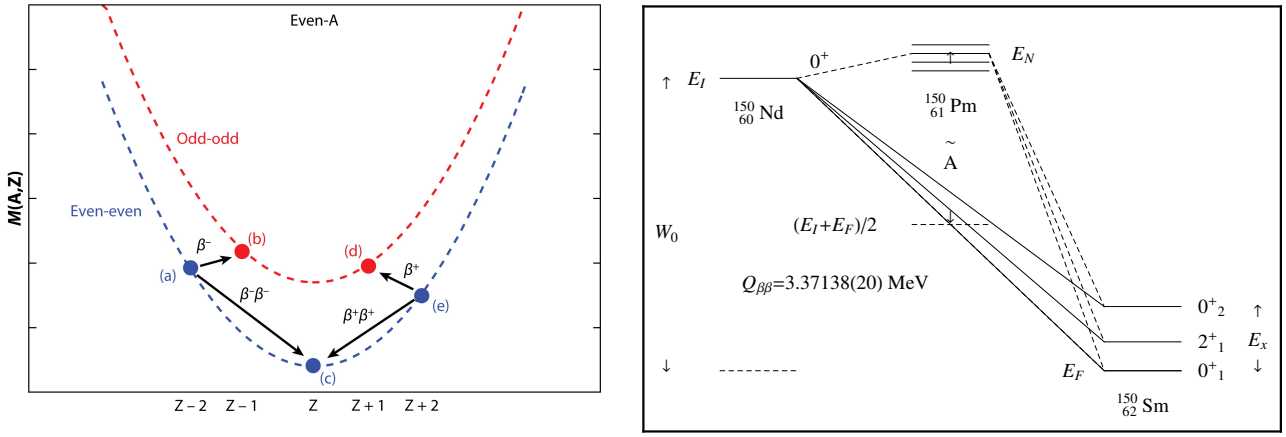

Figure 1.2: (left) Mass parabolas for isobar nuclei with even mass number A in the neighbourhood of the minimum showing the need for double beta decay [Saakyan, 2013]. (right) Example of double beta decay scheme of ^{150}Nd, to the ground state or the excited states of ^{150}Sm, illustrating the energy levels of the intermediate nuclei, used in theoretical calculations [Kotila and Iachello, 2012]

The rate of the $2\nu\beta\beta$ decay can be factorized by the product of a kinematic part, $G^{2\nu}(Q_{\beta\beta}, Z)$ corresponding to the phase space of the emitted leptons, and a nuclear part, $M^{2\nu}$ corresponding to the transition probability between the initial and final nuclei:

$$\Gamma^{2\nu}/\ln 2 = [T^{2\nu}_{1/2}]^{-1} = G^{2\nu}(Q_{\beta\beta}, Z)\ |M^{2\nu}|^2 \tag{1.5}$$

The *phase space factors* can be computed to a good precision [Kotila and Iachello, 2012, Mirea et al., 2015], at a level of about 5% for $\beta^-\beta^-$ decays. The phase space factors calculations use the Fermi functions computed from exact relativistic electron wave functions, obtained as solutions of a Dirac equation with Coulomb potential built from a realistic proton density distribution in nucleus, with the inclusion of nuclear finite size and screening effects. From the phase space calculations, we can also extract the single electron energy spectra, the summed energy spectra of the electrons and the electrons angular distribution. On the other hand, the

[2]The isotope ^{48}Ca is an exception since single-β decay is energetically possible ($Q_\beta = 278$ keV) but strongly suppressed because of large angular momentum difference ΔL with the first states of ^{48}Sc which are 6^+ or 5^+.

nuclear matrix elements $M^{2\nu}$ are much more difficult to calculate. This will be the subject of section 1.1.3.

The two neutrino $\beta^-\beta^-$ decay can occur in 35 isotopes and it has been measured for 11 of them, which were the most practical ones for experiments (section 1.2.2). Some details of the nine major isotopes considered today are presented on table 1.1. The $\beta^-\beta^-$ decay can also occur to excited states (2_1^+ or 0_1^+) of the daughter nucleus, where one or two γ-rays are respectively emitted, see figure 1.2 (right). The transition energy is reduced by the energy of the level, which results in a lower decay rate compared to $0^+ \to 0^+$ decays. Nevertheless, this decay can provide important additional informations on the double beta decay to nuclear calculations. The $2\nu\beta\beta$ decay to the 0_1^+ excited states has been detected for ^{100}Mo [Arnold et al., 2014a] and ^{150}Nd [Arnold et al., 2023], with half-lives $T_{1/2} > 10^{20}$ y. This decay is also being searched for ^{82}Se [Arnold et al., 2020].

Isotope	Abundance [%]	$Q_{\beta\beta}$ [MeV]	$G_{2\nu}$ [10^{-18} y^{-1}]	$T_{1/2}^{2\nu}$ [y]	$G_{0\nu}$ [10^{-15} y^{-1}]
^{48}Ca	**0.187**	**4.272**	15.6	$4.39 \pm 0.58 \times 10^{19}$	**24.8**
^{76}Ge	7.83	**2.039**	**0.0482**	$\mathbf{1.43 \pm 0.53 \times 10^{21}}$	**2.36**
^{82}Se	8.73	2.995	1.60	$9.19 \pm 0.76 \times 10^{19}$	10.2
^{96}Zr	2.80	**3.350**	6.82	$2.16 \pm 0.26 \times 10^{19}$	20.6
^{100}Mo	9.63	3.034	3.31	$\mathbf{6.98 \pm 0.44 \times 10^{18}}$	15.9
^{116}Cd	7.49	2.814	2.76	$2.89 \pm 0.25 \times 10^{19}$	16.7
^{130}Te	**34.1**	2.527	1.53	$7.14 \pm 1.04 \times 10^{20}$	14.2
^{136}Xe	8.86	2.458	1.43	$\mathbf{2.34 \pm 0.13 \times 10^{21}}$	14.6
^{150}Nd	5.6	**3.371**	**36.4**	$\mathbf{8.37 \pm 0.45 \times 10^{18}}$	**63.0**

Table 1.1: Key features of the most considered $\beta^-\beta^-$ isotopes for experiments. The values for $Q_{\beta\beta}$, $G_{2\nu}$ and $G_{0\nu}$ are taken from [Kotila and Iachello, 2012]. The natural abundance and the half-life $T_{1/2}^{2\nu}$ are taken from the BNL database (https://www.nndc.bnl.gov/bbdecay/). The extreme parameter values are highlighted in bold, the most favourable parameters in **black** and the others in **gray**.

The other possible 2ν decay processes ($\beta^+\beta^+$, single $\epsilon\beta^+$ or double $\epsilon\epsilon$ electron captures) get even lower decay rates because of lower $Q_{\beta\beta}$ energy transitions, producing smaller phase spaces. The half-life of the decays are expected to be $T_{1/2} > 10^{20}$ y. So far, only indications of the double electron capture $2\nu\epsilon\epsilon$ of ^{78}Kr [Gavrilyuk et al., 2013], ^{124}Xe [Aprile et al., 2019] and ^{130}Ba [Pujol et al., 2009] isotopes have been reported. These processes can only be detected through atomic X-rays or Auger electrons, in the keV range. In the following of this document, only $\beta^-\beta^-$ will be considered, since it is the most promising channel to test the nature of the neutrino.

1.1.2 Neutrinoless double beta decay

Two years after the publication of Goeppert-Mayer [Goeppert-Mayer, 1935], E. Majorana formulated the famous theory where the neutrino and the antineutrino would be indistinguishable [Majorana, 1937]. In 1939, W. Furry realized that the decay could then occur without the emission of neutrinos [Furry, 1939], this is the *neutrinoless double beta decay* $0\nu\beta\beta$:

$$(A, Z) \to (A, Z + 2) + 2e^- \tag{1.6}$$

In the reference [Agostini et al., 2023], one can find a discussion about the proper name for this decay. Since the underlying mechanism might be different from usual weak decays, other names

are proposed by the authors: creation of two electrons, creation of leptons without antileptons or creation of matter without antimatter. This is interesting to highlight the fundamental importance of such a unique decay, if it were detected. In the mechanism of light neutrino exchange, the Feynman graph of this process can be compared to the one of $2\nu\beta\beta$ on figure 1.3. The $0\nu\beta\beta$ decay process violates the lepton number conservation ($\Delta L = 2$) and is forbidden in the SM. Since only two electrons are emitted in the decay, Furry expected the transition probability to be much larger than the $2\nu\beta\beta$ transition. But the decay rate is in fact suppressed by the energy scale (Λ) of the Beyond Standard Model (BSM) process. The two double beta decay mechanisms, $2\nu\beta\beta$ and $0\nu\beta\beta$, enter in competition. The $2\nu\beta\beta$ is thus the irreducible background for $0\nu\beta\beta$ search. As we will see in section 1.2, the only way to distinguish them is by measuring the total energy of the two electrons, which would differ in the case of the emission of two anti-neutrinos.

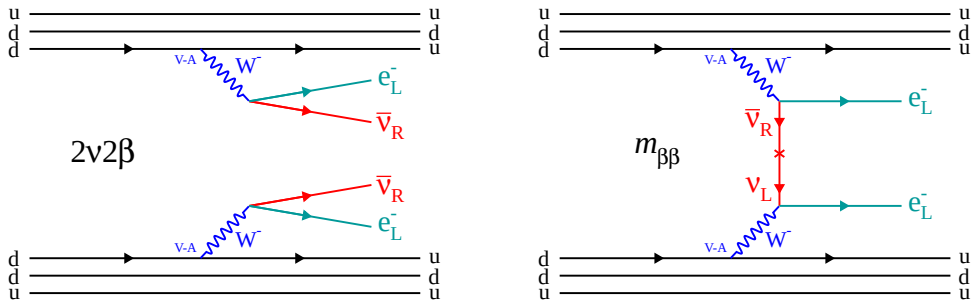

Figure 1.3: Feynman diagrams of $2\nu\beta\beta$ and $0\nu\beta\beta$ (in the case of light-neutrino exchange mechanism) decays at the quark level.

The evidence for neutrino mass and the lowest dimension operators (dimension-5) required to generate the lepton number violating BSM physics, might suggest that the light Majorana neutrino exchange mechanism could be the leading contribution to $0\nu\beta\beta$. In this Majorana neutrino model, the decay rate of the $0\nu\beta\beta$ can be written as:

$$\Gamma^{0\nu} / \ln 2 = [T^{0\nu}_{1/2}]^{-1} = G^{0\nu}(Q_{\beta\beta}, Z) \; |M^{0\nu}|^2 \; \langle m_{\beta\beta} \rangle^2 \tag{1.7}$$

where the phase space factor $G^{0\nu}(Q_{\beta\beta}, Z)$ describes the kinematics of the decay, the nuclear matrix element $M^{0\nu}$ represents the amplitude of the nuclear transition from the initial to the final nuclei and $\langle m_{\beta\beta} \rangle$ is the effective neutrino mass for neutrinoless double beta decay. The phase space factor $G^{0\nu}$ can here also be computed to a good precision. Compared to the two neutrinos decay where a factor $\sim$750 is observed between the $G^{2\nu}$'s of the different isotopes, the $G^{0\nu}$'s are much less dispersed with a factor $\sim$27, as can be seen on table 1.1. This can be partly explained by the strong dependence of $2\nu\beta\beta$ on $Q_{\beta\beta}$, since $G^{2\nu} \propto Q^{11}_{\beta\beta}$, while the $0\nu\beta\beta$ has a weaker one with $G^{0\nu} \propto Q^{5}_{\beta\beta}$ [Saakyan, 2013]. The nuclear matrix elements $M^{0\nu}$ are also very complicated to calculate, but are mandatory to access the effective neutrino mass $\langle m_{\beta\beta} \rangle$. This would be the ultimate goal for discovering the $0\nu\beta\beta$, measure the effective neutrino mass after proving that the neutrino is a Majorana particle and the lepton number conservation is violated. The effective neutrino mass $\langle m_{\beta\beta} \rangle$ is proportional to the inverse of the BSM ($1/\Lambda$) energy scale of the lepton number violating BSM process. It is related to the individual neutrino masses m_i and the parameters of the PMNS matrix U_{PMNS} (see section 5.1) but the Majorana phases φ_i need to be added:

$$\langle m_{\beta\beta} \rangle = | \sum_{i=1}^{3} \; |U^2_{ei}| \; e^{i\varphi_i} \; m_i \; | \tag{1.8}$$

where the U_{ei} elements of the PMNS matrix only depend on θ_{12}, θ_{13}, δ_{CP} and the two Majorana phases which are not degenerate. These Majorana phases cannot be probed by oscillation

experiments. Since the neutrino masses m_i are tiny, the decay rate of $0\nu\beta\beta$ is finally much lower than $2\nu\beta\beta$ decay rate. The possible existence of a sterile neutrino with a mass of the order of 1 eV, which is the subject of the part II of this document, could however boost the value of $\langle m_{\beta\beta} \rangle$ and significantly increase the $0\nu\beta\beta$ decay rate.

Prediction on the effective neutrino mass $m_{\beta\beta}$

Given the results already obtained by oscillation experiments on the mixing of neutrinos, see section 5.1, we can start to put predictions on the effective neutrino mass $\langle m_{\beta\beta} \rangle$ as a function of the lightest neutrino mass m_{light} (m_1 for normal ordering or m_3 for inverted ordering). Adding constraints from direct neutrino mass measurements in β-decays and cosmology creates an exciting interplay among different types of experiments. These constraints are illustrated on figure 1.4.

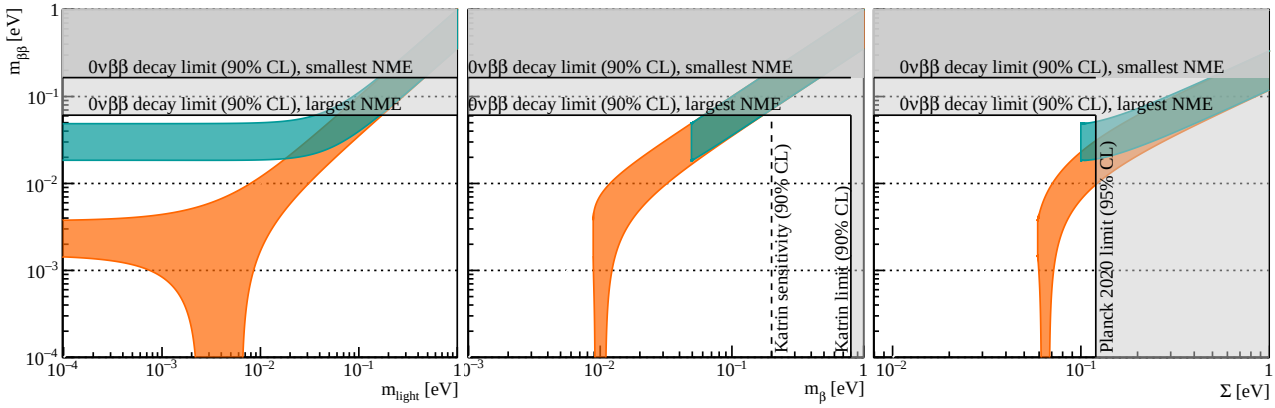

Figure 1.4: Maximal allowed parameter space for $\langle m_{\beta\beta} \rangle$ [Vissani, 1999] as a function of m_{light}, m_β and $\sum$ [Agostini et al., 2023], assuming the central values of the neutrino mixing parameters from PDG 2020. The orange and green regions correspond to normal or inverted neutrino mass ordering. The gray shaded areas are already excluded by experiments.

Direct mass measurement experiments can directly probe the effective neutrino mass m_β for β-decay, which like $\langle m_{\beta\beta} \rangle$ is related to neutrino mixing parameters[3]. The direct mass search is less model-dependent since it is not restricted to the Majorana neutrino theory, but it provides the weakest limits for now. Indeed, KATRIN, which is the most sensitive experiment investigating tritium β-decay, has put an upper limit of $m_\beta < 0.8$ eV (90% CL) in 2021 and is designed to reach 0.2 eV [Aker et al., 2022a]. This region is already being investigated by DBD experiments, but large uncertainties on the nuclear matrix elements prevent to exclude this region. Any positive measurement from KATRIN would be incompatible with $0\nu\beta\beta$ decay, unless neutrinos are only Dirac particles. Thanks to the Δm^2 measurements by oscillations experiments, we can already put lower limits on m_β around $m_\beta > 9$ meV in the case of normal ordering (NO) and around $m_\beta > 50$ meV for inverted ordering (IO).

Cosmology is strongly sensitive to the radiation density of neutrinos in the Universe (ρ_ν), which can be accessed through the relativistic degrees of freedom usually parametrized by (N_{eff}), and the sum of the neutrino masses ($\sum = \sum_i m_i$). This is described by the standard model of cosmology, called ΛCDM. These parameters depend on the initial conditions of the Big-Bang and the subsequent physics processes. Nowadays, this can be probed by the Big-Bang nucleosynthesis of the light elements, the large-scale structure formation and the possible existence of a cosmic neutrino background. The number of neutrino species $N_{eff} = 2.99 \pm 0.17$ is rather well determined in the fit of the temperature power spectrum of Planck data,

[3]The effective neutrino mass for β-decay is given by: $m_\beta^2 = \sum_{i=1}^{3} |U_{ei}^2| \, m_i^2$.

in combination with baryon acoustic oscillation (BAO) measurements [Aghanim et al., 2020]. But the sum of the neutrino masses is still unknown. Cosmology is setting the strongest limits on neutrinos masses but they rely on the ΛCDM model. The degeneracies between the large number of parameters are broken by combining different datasets, which also impact the limits setting. These limits also become weaker when considering other frameworks with more parameters. The current best limit has been set by Planck combined to other observations to an upper limit of $\sum < 120$ meV (95% CL). Future projects aim to measure $\sum$ with a precision of 20 meV. Like the other mass parameters, the sum of the neutrino masses $\sum$ is linked to the mass splitting Δm^2_{ij} measurements from oscillations. The lower values can be $\sum > 59$ meV for the NO case and $\sum > 100$ meV for the IO case. As suggested by these numbers and can be seen on figure 1.4, the inverted neutrino mass ordering region is close to be excluded by cosmological data.

The tightening experimental constraints which are put to the IO regions seems to be not favourable to the search for neutrinoless double beta decay. Figure 1.4 might even suggest it would be impossible to detect $0\nu\beta\beta$ decay in the case of NO. This feeling is accentuated by the bi-logarithmic scale of the $\langle m_{\beta\beta}\rangle$ as a function of m_{light} plot. We will discuss further the experimental sensitivity to $\langle m_{\beta\beta}\rangle$ in section 1.3 and we will see that linear scale starts to be used to report results. Even in the case of NO, we could be in a situation where m_{light} is still high enough to provide good sensitivity to $\langle m_{\beta\beta}\rangle$. The light Majorana neutrino exchange is favoured but there is always the possibility that another mechanism is responsible for the decay, which would produce a result outside the allowed $\langle m_{\beta\beta}\rangle$ regions.

We have presented here the mechanism of light neutrino exchange for which the half-life is proportional to the square of the scale of neutrino mass generation [Dolinski et al., 2019]. But other mechanisms could be responsible for the $0\nu\beta\beta$ decay. If heavy-physics is involved in the decay, the half-life would be proportional to the power 10 of the mass of the heavy particles [Dolinski et al., 2019]. As demonstrated by J. Schechter and J. W. F. Valle [Schechter and Valle, 1982], independently of the process, the discovery of neutrinoless double beta decay would prove the Majorana nature of the neutrino. Indeed, they demonstrated by moving the particle lines around the four vertices of the $0\nu\beta\beta$ decay, that a Majorana mass term between $\bar{\nu}_e$ and ν_e occurs. A nonzero Majorana mass term for the neutrino should thus be included in the Standard Model.

1.1.3 Nuclear matrix elements

Two neutrinos double beta decay NME

The nuclear matrix elements of the two neutrinos double beta decay are not related to the determination of the effective neutrino mass $\langle m_{\beta\beta}\rangle$. However, it is an important theoretical subject for nuclear physics by itself. It is also a precious test for the nuclear models trying to determine the NMEs for the neutrinoless double beta decay, this time needed for neutrino mass determination. Since the $2\nu\beta\beta$ has been detected for several isotopes, the NMEs can be measured to a good precision thanks to the half-life measurements, see equation 1.5. The results of the NME measurements for several isotopes can be seen on figure 1.5. The pattern between the different isotopes is explained by the nuclear shells. Due to the better stability of the filled shells, a factor ten difference is seen between $^{100}_{42}$Mo and $^{136}_{54}$Xe, which has a magic number of neutrons. Single β-decay rate measurements can be also precious inputs to the theoretical models.

It has been demonstrated that the $2\nu\beta\beta$ decay amplitude is dominated by the pseudo-vector Gamow-Teller operator [Haxton and Stephenson, 1984], in which the nucleon spin is flipped and

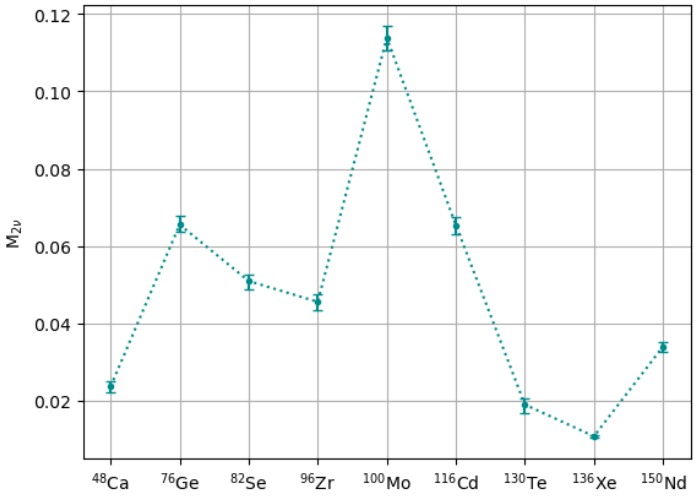

Figure 1.5: Nuclear matrix elements $M^{2\nu}$ for the $2\nu\beta\beta$ decay computed from the half-life measurements of several isotopes, reproduced from the values compiled in [Saakyan, 2013]. The $M^{2\nu}$ are often reported in [MeV^{-1}], after division by the electron mass.

the spins of the emitted electron and neutrino are aligned. The vector Fermi operator[4], where the electron and neutrino spins are anti-parallel and the nucleon spin is preserved, is strongly suppressed by isospin conservation rules for the 2ν transition. But this is not the case for $0\nu\beta\beta$ decay. Consequently, the NME for the $2\nu\beta\beta$ decay transition from the initial to the final state nuclei ($0_i^+ \rightarrow 0_f^+$), as illustrated on figure 1.2, with respective masses M_i and M_f, can be written as:

$$M^{2\nu} \approx M^{2\nu}_{GT} = \sum_m \frac{\langle 0_f^+ | \sum_n^A \vec{\sigma}_n \tau_n^+ | 1_m^+ \rangle \langle 1_m^+ | \sum_n^A \vec{\sigma}_n \tau_n^+ | 0_i^+ \rangle}{E_m - (M_i + M_f)/2} \tag{1.9}$$

where $\vec{\sigma}$ are the Pauli spin matrices, τ^+ is the isospin ladder operator changing the quark flavour ($d \rightarrow u$). The intermediate nuclear states 1_m^+ have an energy level E_m. The right term of the numerator represents the amplitude of the β^- decay of the initial nucleus, while the left term corresponds to a β^+ decay of the final nucleus. The denominator of this equation shows that the low energy intermediate states 1_m^+ contribute significantly more than the high energy states. In earlier times, the intermediate states were not explicitly treated. An average energy was replacing the intermediate energies E_m which were summed up, this was called the *closure approximation* [Haxton and Stephenson, 1984]. Nowadays, interference between the individual terms of the matrix elements are considered and the closure approximation is no longer appropriate for $2\nu\beta\beta$.

In certain nuclei, the lowest 1^+ state may dominate the decay single-state dominance SSD while others could be dominated by higher-state dominance HSD. This has been demonstrated thanks to single energy electron spectra in NEMO-3 for ^{100}Mo [Arnold et al., 2019] and on the total energy spectra for ^{82}Se with CUPID-0 [Azzolini et al., 2019c].

The different theoretical models will be presented in the following sections, after the case for $0\nu\beta\beta$ calculations.

Neutrinoless double beta decay NME

As shown in equation 1.7, good knowledge of the nuclear matrix elements (NME) is absolutely needed to extract the effective neutrino mass $\langle m_{\beta\beta} \rangle$, or the new physics parameters involved in the $0\nu\beta\beta$ decay. Unfortunately, there is no experimental way to measure the NMEs for

[4]The Fermi term would take the form: $M_F^{2\nu} = \sum_m \frac{\langle 0_f^+ | \sum_n^A \tau_n^+ | 1_m^+ \rangle \langle 1_m^+ | \sum_n^A \tau_n^+ | 0_i^+ \rangle}{E_m - (M_i + M_f)/2}$

$0\nu\beta\beta$ independently. There is also no correspondence between the $M^{2\nu}$ and $M^{0\nu}$ NMEs, since they represent different decay processes. Indeed, there is a significant difference of momentum transfer between the nucleons ($\sim Q_{\beta\beta}$ for $2\nu\beta\beta$ and $\sim$100 MeV for $0\nu\beta\beta$). We have thus to rely on nuclear models to compute the NMEs. The challenge is to compute how the decay occur in a many-body system with high correlation between the nucleons. Despite recent progress, the calculations suffer from large variations from a model to another. This is a very delicate subject that cannot be fully covered here. Recent reviews can be found in [Engel and Menéndez, 2017, Agostini et al., 2023]. In this document, we will modestly try to highlight the key parameters of the calculations and the main aspects of the two main models used.

The weak current at the quark level has a simple $V-A$ structure, but the weak nucleon current contains additional terms because it is a composite object [Šimkovic et al., 1999]:

$$J^{\mu+} = \bar{\Psi}\tau^{+}\left[\, g_V(q^2)\gamma^{\mu} - ig_M(q^2)\frac{\sigma^{\mu\nu}}{2m_p}q_{\nu} - g_A(q^2)\gamma^{\mu}\gamma_5 + g_P(q^2)q^{\mu}\gamma_5 \,\right]\Psi \tag{1.10}$$

where the form factors g's encode the coupling of the weak interaction to nucleons with the vector, weak-magnetism, axial-vector and induced pseudoscalar coupling constants, $q_\mu = (p-p')_\mu$ is the momentum transferred from hadrons to leptons, p and p' are the four momenta of neutron and proton and $\sigma^{\mu\nu} = (i/2)[\gamma^{\mu},\gamma^{\nu}]$. The weak magnetism form factor is simply proportional to g_V: $g_M(q^2) = (\mu_p - \mu_n)g_V(q^2)$. The induced pseudoscalar form factor is usually evaluated using the partially conserved axial-vector current hypothesis $g_P(q^2) = (2m_p \times g_A(q^2))/(q^2 + m_\pi^2))$ [Vogel, 2012].

Taking into account these higher order terms and reducing the nucleon current to the non-relativistic form [Šimkovic et al., 1999], compared to previous descriptions, the nuclear matrix element for $0\nu\beta\beta$ becomes:

$$M^{0\nu} = M^{0\nu}_{GT} - \frac{g_V^2}{g_A^2}M^{0\nu}_{F} + M^{0\nu}_{T} \tag{1.11}$$

where the three terms correspond to Fermi (F), Gamow-Teller (GT) and tensor (T) operators. The formulation of the individual terms can be found in [Engel and Menéndez, 2017]. The Fermi component is unchanged, the Gamow-Teller is modified and the tensor component appeared due to the new terms introduced. A reduction of about 20-30% (depending on the nucleus) of the NME is expected from these new calculations [Šimkovic et al., 1999], in the case of light neutrino exchange.

The goal is now the computation of the nuclear structure of the initial and final nuclear states, which are complex multi-body systems. The transition to the daughter nucleus goes through virtual intermediate states of energy E_n (figure 1.2 (right)), which need to be summed up since the combinations in which the electron-neutrino system appears in the intermediate steps is unknown. These intermediate energy states can expand up to the order of 100 MeV for the $0\nu\beta\beta$, because of Heisenberg's uncertainty principle applied to the volume of the nucleus. On the other hand, for the $2\nu\beta\beta$ only the 1^+ intermediate states are to consider, because two anti-neutrinos are emitted, and the energy is limited to few MeV, the $Q_{\beta\beta}$ value. Because of the large momentum transfer of the virtual neutrino compared to the nuclear excitation energies, the *closure approximation*, i.e. without explicit treatment of the virtual states in the intermediate odd-odd nucleus, is better justified than in the case for $2\nu\beta\beta$ decay. As already said, the hadronic currents are treated in the non-relativistic *impulse approximation*.

First, it is necessary to define the mean field in which the nucleons involved in the decay are bound. This allows then to determine the set of single particles states and to decide the fully occupied and the empty states of both the initial and final nuclei. The remaining states, either partially occupied or with different occupancy between initial and final nuclei, form the valence space. The residual interaction between the nucleons of the valence space needs to be taken

into account. The single particle wave functions are typically taken to be the eigenfunctions of the harmonic oscillator potential, or superpositions of such functions.

Historically, two methods have been used from the 1980s to compute the nuclear matrix elements for double beta decay: the nuclear shell model (NSM) [Sinatkas et al., 1992] and the quasiparticle random phase approximation (QRPA) [Vogel and Zirnbauer, 1986]. They have very different treatment of the problem, in their choice of the valence space, the interaction hamiltonian and in solving the equations of motion. Both methods can be used for single β-decay, $2\nu\beta\beta$ in addition to the $0\nu\beta\beta$ calculations. This provides good possibilities to test and tune these models.

The nuclear shell model

The nuclear shell model (NSM) describes the structure of the nucleus in energy levels, shells of protons and neutrons. It started to be investigated in the thirties, but it was finally correctly formulated in 1949, with the major contributions of M. Goeppert-Mayer and J.H.D Jensen. It takes its origin from the experimental evidence of an independent behaviour of the nucleons in the nuclei, such as extra binding produced by the *magic numbers* of protons and neutrons. The Pauli exclusion principle combined with short-range nucleon-nucleon repulsion lead to a nearly independent particle motion. The nucleons are confined by an isotropic harmonic oscillator mean field, corrected for surface effects, forming different energy levels. A strong attractive spin-orbit term is also added to split the principal shells in different energy subshells, or orbits, of different total angular momentum. The protons and neutrons shells are then populated from the lowest orbits. In case the number of protons or neutrons doesn't correspond to filled shells, a residual two-body interaction must be added to break the degeneracies between configurations.

The NSM is very well suited for low mass nuclei but the increasing number of configurations, with the increasing number of nucleons, makes it computationally impracticable. This can be reduced considering that the nucleons near the Fermi level, in the *valence space*, are the most important for nuclear properties at low energy. The calculations are thus simplified by using a restricted number of nucleons and an effective Hamiltonian adapted to the configuration space. The other nucleons, considered as a frozen core on the lowest energy orbitals, are not included in the calculations. On the other hand, the NSM tries to consider all the correlations between the valence nucleons. Due to computation limitations, only one main shell of nucleons is usually considered. Nowadays, two shells computation are emerging and provides a $\sim$20% enhancement of the NME [Agostini et al., 2023]. A complete description of the NSM, the computation method and results can be found in [Caurier et al., 2005]. The NSM describes well the nuclei masses, separation energies, charge radii as well as the spectroscopy of the low-lying energy states.

Concerning the double beta decay, another main success of the NSM was the accurate calculation of the $2\nu\beta\beta$ of ^{48}Ca in the 90's [Caurier et al., 1990], before it was experimentally measured [Balysh et al., 1996]. Even at higher masses, the NSM is describing reasonably well the NMEs of the main DBD isotopes [Caurier et al., 2012], but the quenching factor q of axial vector coupling constant g_A (seen in equation 1.11 and discussed in section 1.1.3) needs to be reduced for heavier nuclei from 0.74 for ^{48}Ca to 0.45 for ^{136}Xe.

The quasiparticle random phase approximation

The other major theoretical model for NME calculations is the quasiparticle random phase approximation (QRPA). It was the first many-body method to reliably address double beta decay [Vogel and Zirnbauer, 1986, Engel et al., 1988]. In some sense, QRPA and NSM represent two opposite approaches. Indeed, the QRPA includes an unlimited set of single-particle states, but only a limited subset of configurations.

The QRPA model takes its origin in the pioneer work of [Brown and Bolsterli, 1959], who introduced the particle-hole interactions (RPA), to explain the high cross-section of (γ, p) in heavy nuclei ; and the work of [Baranger, 1960] who introduced the two quasi-particles approximation (QRPA) to compute the properties of all low-lying levels of heavy spherical even-even nuclei. In spherical nuclei with partially filled shells, the most important effect of the two-body force is to produce pairing correlations. Those correlations are treated in the Bardeen-Cooper-Schrieffer (BCS) theory, which is used to explain superconductivity. In the work of [Baranger, 1960], transformations on a general shell-model Hamiltonian are performed and the result can be interpreted in terms of a Hamiltonian of *quasi-particles* and an interaction between these quasi-particles. Using linearized equations of motion and treating states which are weakly collective only, it ends-up with equations similar to two-body shell model calculation, which are easier to solve.

To deal with double beta decay, the QRPA must be modified to become *charge-changing*, or *proton-neutron*, in order to guarantee that the phonon excited state has one more proton and one neutron less than the initial nucleus. Two separate QRPA calculations, one based on the initial nucleus and one on the final nucleus, are needed to compute double beta decay. The closure approximation is not required in QRPA.

The interaction strength of the particle-particle and particle-hole pairs are respectively given by the coupling parameters g_{pp} and g_{ph}. Usually, g_{ph} is determined to reproduce the excitation energy of the Gamow-Teller giant resonance and g_{pp} is left as a free parameter of the theory. Since QRPA has to use a limited set of correlations, the parameter g_{pp} serves to modify the effective nucleon-nucleon interaction. The modification of this effective interaction depends on the size of the single-particle basis used in the QRPA calculation. The orbitals within one or two oscillator shells of the Fermi surface are usually treated explicitly. A method to suppress the dependence on the size of the single-particle basis has been proposed by [Rodin et al., 2003] and is illustrated on figure 1.6. We can see tuning the g_{pp} value with the measured value of $M^{2\nu}$ can indeed cancel the dependence on the number of levels for $M^{0\nu}$.

Other models and comparison

Recently, other nuclear models entered the field: projected Hartree-Fock-Bogoliubov (PHFB) model [Rath et al., 2010], the microscopic interacting boson (IBM) model [Barea et al., 2015], the energy density functional (EDF) method [Rodriguez and Martinez-Pinedo, 2010] and the relativistic EDF (REDF) model [Yao et al., 2015]. A list of publications about these models and their results can be found in [Vergados et al., 2016, Saakyan, 2013, Dolinski et al., 2019]. So far these methods concentrate on calculating $M_{0\nu}$ and have not been used to compute $M^{2\nu}$.

The result of different $0\nu\beta\beta$ NMEs calculation methods is presented on figure 1.7. As already said, we observe a large dispersion between the different models. This would be the main limitation to determine the effective Majorana neutrino mass, in the case of $0\nu\beta\beta$ discovery. The NSM tends to underestimate the NMEs, thus predicts longer half-lives, maybe because the pairing correlations are not all accounted for. On the other hand, the QRPA calculations lack of correlations and tends to overestimates the NMEs. The other models are in agreement with NSM and QRPA. Considering a given model we observe very little variations of the NMEs between different nuclei. This is not the case for the $2\nu\beta\beta$ NMEs, see figure 1.5.

A recent promising line of development has emerged from *ab initio* calculations [Gysbers et al., 2019], which will be presented in the following section. This method is not setting approximations and uses all the nucleons of the system and fits experimental data on small nucleonic systems, to set the interactions. Recent *ab initio* calculations of double beta decay are encouraging for light-nuclei [Pastore et al., 2018] or ^{48}Ca [Yao et al., 2018].

The computation of NME is a very active theoretical field, and we can expect the cal-

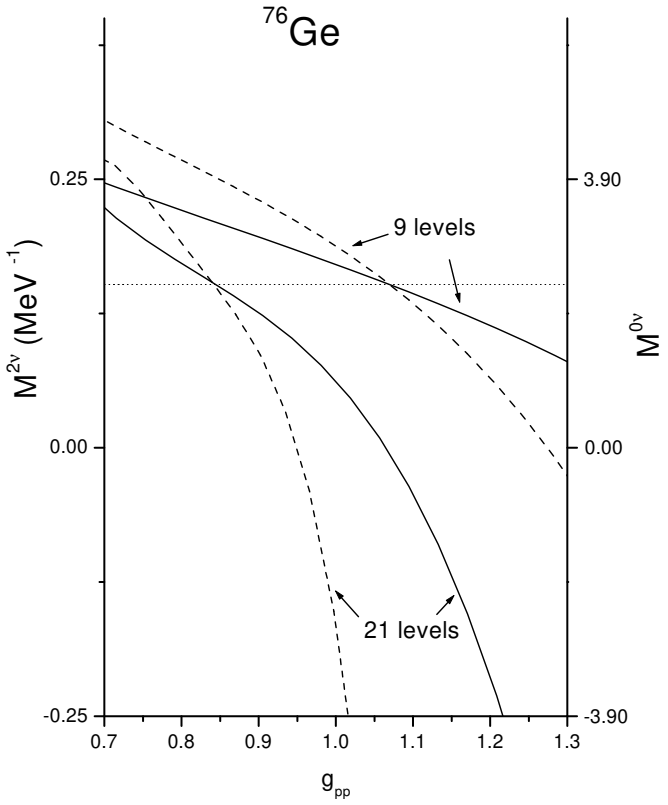

Figure 1.6: Nuclear matrix elements $M^{2\nu}$ (left scale, dashed lines) and $M^{0\nu}$ (right scale, solid lines) for the double beta decays of ^{76}Ge as a function of the strength of the proton-neutron interaction g_{pp} in the QRPA calculation, in the case of 9 and 21 single-particle orbitals [Rodin et al., 2003]. The dotted horizontal line represents the measured value of $M^{2\nu}$.

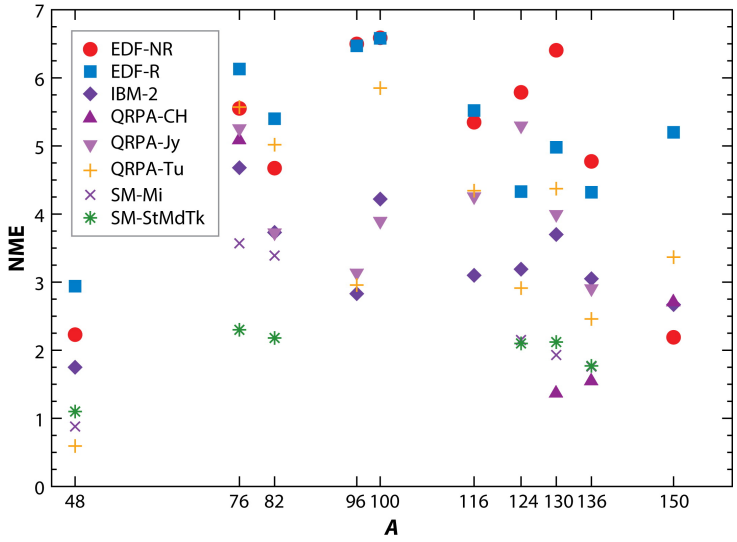

Figure 1.7: Compilation of $0\nu\beta\beta$ nuclear matrix elements calculations for several isotopes [Dolinski et al., 2019].

culations to converge in the future. From the experimental point of view, there are also attempts to provide inputs to the nuclear models [Dolinski et al., 2019]: β decays in the β^-

and β^+ directions, two-nucleon transfers or muon-capture reactions. The NUMEN collaboration, standing for NUclear Matrix Elements for Neutrinoless double beta decay, has engaged a new approach by the mean of the heavy-ion induced double charge exchange (DCE) reactions [Cappuzzello et al., 2018]. The principle of NUMEN consist of sending ions beams (^{18}O or ^{20}Ne) on targets containing the DBD candidate (A, Z) or its daughter nucleus $(A, Z+2)$. The measured cross-sections of the produced nuclei with a spectrometer can be then compared to theoretical predictions. Despite the DBD and DCE are triggered by weak or strong interaction respectively, there are important analogies between the nuclear operators. Complementary reactions are also investigated, thanks to the various products of the interactions.

Quenching of g_A

For decades, it has been observed that the measured β-decay rates of nuclei were systematically smaller than theoretical predictions. This is attributed to the calculation of the Gamow-Teller transitions, which turns out to be overestimated. An attempt to fix this problem was to introduce a *quenching* to the fundamental axial-vector coupling constant $g_A = 1.2754 \pm 0.0013$[5], by an effective factor of about $g_A^{eff} \approx 0.75$. This would reduce the strength of the GT operator compared to the β-decay of a free neutron. Since the double beta decay rates depend on the square of the nuclear matrix element, which are proportional to the square of the coupling constant g_A (see equations 1.7 and 1.11), the impact of $(g_A^{eff})^4$ might be considerable. If the $0\nu\beta\beta$ decay rates are smaller than expected, the sensitivity of the future experiments with respect to the neutrino mass ordering might be significantly lower.

The origin of this quenching is controversial and has been debated extensively. It is now believed to be attributed to the coupling of the weak force to two nucleons (contributions from meson exchanges) and from missing nuclear correlations in the nucleus [Gysbers et al., 2019]. In this publication, we can find a comprehensive study of Gamow-Teller decays through many-body computations of nuclei based on effective field theories (EFT) of quantum chromodynamics (QCD). EFT enables a consistent description of the coupling of weak interactions to two nucleons, via two-body currents (2BC). The 2BC enters as sub-leading corrections to the one-body standard GT operator. An unprecedented amount of correlations in the nuclear wave functions is also included. The authors find out a good agreement between their prediction and the experimental values for a large number of light and medium-mass nuclei up to ^{100}Sn. This work paves the way for nuclear calculations without quenching of the axial-vector coupling g_A, including in the search for neutrino-less double-beta decay.

As we have seen in section 1.1.1, the two-neutrino double-beta decay is dominated by GT transitions and the NME can be directly measured from the decay rate, thanks to equation 1.5. The $2\nu\beta\beta$ is thus a good mean to study the quenching of g_A problem. In that objective, an improved formalism of the two-neutrino double-beta decay has been presented in [Šimkovic et al., 2018]. It takes into account the dependence of energy denominators on lepton energies via a Taylor expansion, whereas only the leading term in this expansion were considered before. Considering the two first orders of the Taylor expansion, the new formulation of the $2\nu\beta\beta$ half-life is obtained:

$$[T_{1/2}^{2\nu}]^{-1} = (g_A^{eff})^4 \; |M_{GT-3}^{2\nu}|^2 \; \frac{1}{|\xi_{31}^{2\nu}|^2}(G_0^{2\nu} + \xi_{31}^{2\nu} G_2^{2\nu}) \tag{1.12}$$

which depends on the effective axial-vector coupling constant g_A^{eff}, the nuclear matrix element $M_{GT-3}^{2\nu}$, a ratio of two NMEs $\xi_{31}^{2\nu} = M_{GT-3}^{2\nu}/M_{GT-1}^{2\nu}$, two phase space factors ($G_0^{2\nu}$, $G_2^{2\nu}$), which can be computed with good accuracy. The calculation of $M_{GT-3}^{2\nu}$ should be more reliable than

[5] Averaged value from PDG-2023, using free neutrons decay measurements. At the quark level, the axial-vector constant is exactly equal to unity: $g_A^{quark} = 1$.

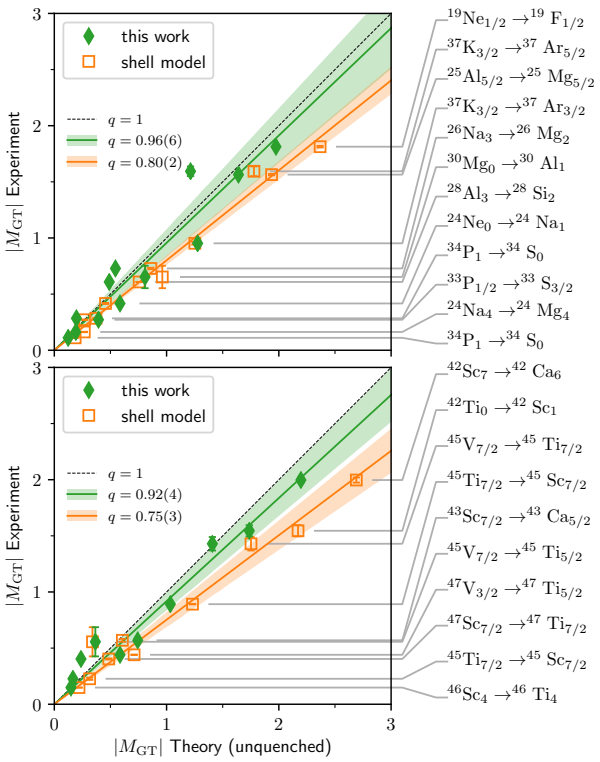

Figure 1.8: Comparison of experimental and theoretical Gamow-Teller matrix elements for medium-mass nuclei for NSM and the work of [Gysbers et al., 2019]. The solid lines represent the fit and the bands the 1σ standard deviation. The green results are in agreement with no quenching of g_A ($q = 1$).

$M^{2\nu}_{GT-1}$, because the contribution of the low energy states of the intermediate nucleus dominates, since:

$$M^{2\nu}_{GT-1} = \sum_n M_n \frac{m_e}{E_n - (E_i + E_f)/2} \quad \text{and} \quad M^{2\nu}_{GT-3} = \sum_n M_n \frac{4m_e^3}{[E_n - (E_i + E_f)/2]^3} \tag{1.13}$$

where M_n carries the GT operator. The NME ratio $\xi^{2\nu}_{31}$ becomes a new parameter which can be determined phenomenologically from the shape of the energy distribution of the electrons. As can be seen on figure 1.9, the individual energy of the electrons is the most sensitive way to access $\xi^{2\nu}_{31}$, but high precision and statistics would be needed. This new method offers an opportunity to determine the effective axial-vector coupling constant g_A^{eff} for the double-beta decay.

This new formalism has been investigated for the first time by the KamLAND-Zen experiment on the total energy spectra of ^{136}Xe [Gando et al., 2019]. This energy spectra is presented on figure 1.10 (left) with different values of $\xi^{2\nu}_{31}$ illustrated. A best-fit value with too large uncertainties is found. Thus an upper exclusion limit has been set to $\xi^{2\nu}_{31} < 0.26$ (90% CL). This exclusion is reported on the g_A^{eff} versus $M^{2\nu}_{GT-3}$ plane, see figure 1.10 (right). This limit is in agreement with the NSM and QRPA calculations. Part of the $\xi^{2\nu}_{31}$ allowed range is however excluded in the QRPA model by KamLAND-Zen.

The problem of quenching of the NMEs remains one of the main sources of uncertainty to determine the NME values. An experiment like SuperNEMO, which would be able to measure the single electron energy, should improve the sensitivity to determine $\xi^{2\nu}_{31}$ [Hoballah, 2022].

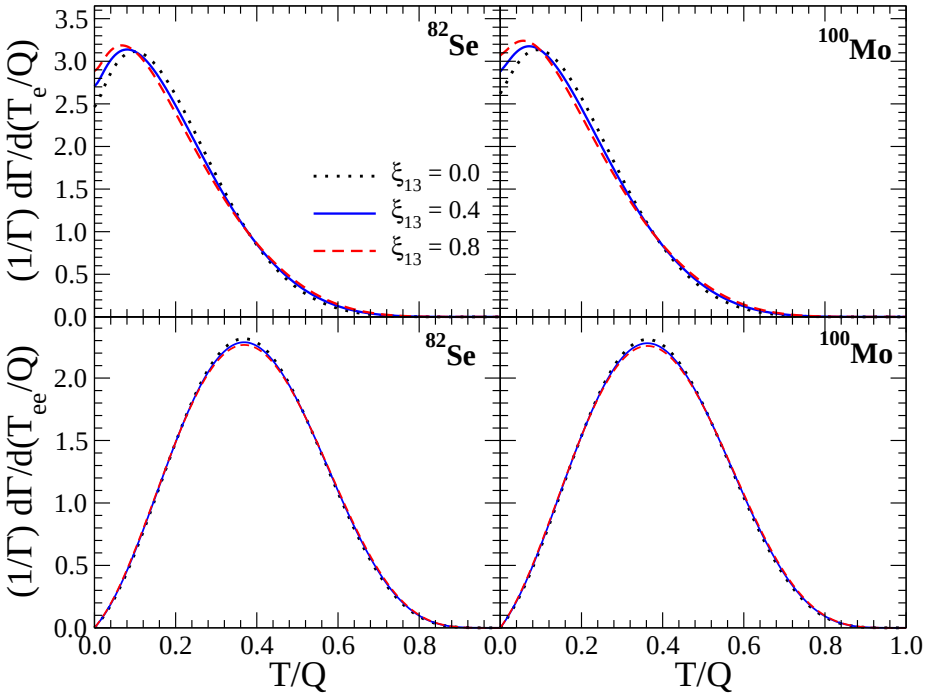

Figure 1.9: Individual electrons energy (top) and the sum of the two electrons energies (bottom) distributions for ^{82}Se and ^{100}Mo for different values of the $\xi^{2\nu}_{31}$ NME ratio [Šimkovic et al., 2018].

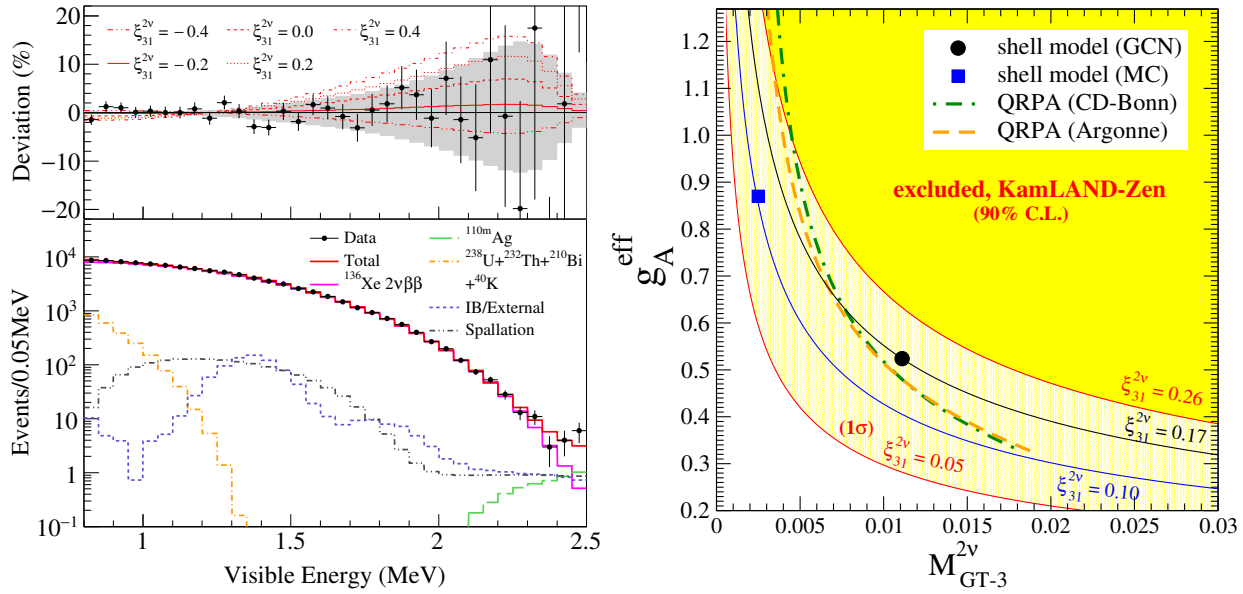

Figure 1.10: (left) Total energy spectrum measured in KamLAND-Zen with the best background fit and the $2\nu\beta\beta$ decay from ^{136}Xe floating in $\xi^{2\nu}_{31}$ [Gando et al., 2019]. (right) Corresponding excluded region in the g_A^{eff} versus $M^{2\nu}_{GT-3}$ plane compared to NSM and QRPA calculations [Gando et al., 2019].

1.2 Experimental criteria

The experimental study of double beta decay (DBD) focusses on the detection of the two emitted electrons. Using different calorimetric techniques, the detectors aim to measure the total energy of the two electrons. This is the main objective since this parameter is the only way to discriminate between the $2\nu\beta\beta$ and $0\nu\beta\beta$ decays. Indeed, the two anti-neutrinos emitted in the $2\nu\beta\beta$ are taking away part of the transition energy, so a continuous energy spectrum

is observed, with a maximum around 1/3 of $Q_{\beta\beta}$. In contrast, the $0\nu\beta\beta$ electrons are taking all the transition energy and a peak is expected at $Q_{\beta\beta}$, see figure 1.11. An excellent energy resolution is then a key feature for all the DBD experiments.

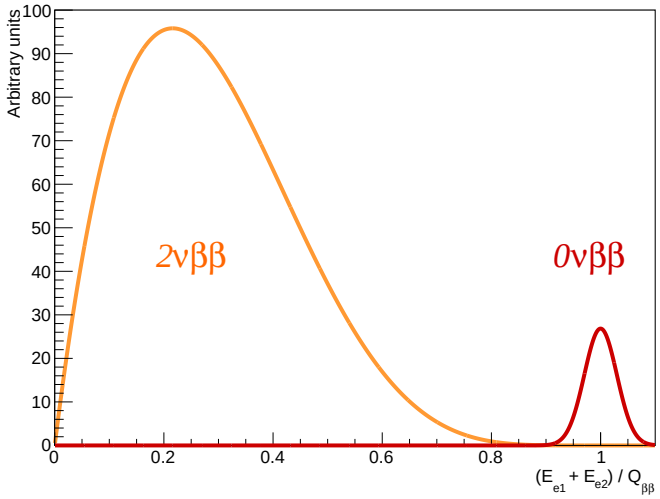

Figure 1.11: Illustration of the expected energy spectra of the two electrons for $2\nu\beta\beta$ and $0\nu\beta\beta$ decays with an energy resolution of 7% at 1 MeV full width at half-maximum (FWHM).

Some experiments are also trying to measure the electron tracks to fully sign the DBD events and reject the backgrounds. Measuring individually the energy of each electron would also be decisive to reveal the underlying mechanism of the decay [Arnold et al., 2010]. These individual electron energy spectra are an help for the NME calculations in order to determine if the $2\nu\beta\beta$ of a given isotope is dominated by single-state dominance (SSD), where the lowest 1^+ intermediate nuclei state dominates the decay rate, or by higher-state dominance (HSD), where higher levels also contribute [Saakyan, 2013]. As just discussed the single electron energy spectra is also the most sensitive to investigate the quenching of the axial-vector coupling constant g_A. If the two electrons can be tracked individually, it is also possible to access the angular distribution of the emitted electrons, which is also an important parameter to understand the $0\nu\beta\beta$ decay process.

Since the energy transition $Q_{\beta\beta}$ is very well know, the neutrinoless double beta decay search are counting experiments in the region of interest (ROI), determined by the energy resolution ΔE of the detector. In the case of observation, the number of events detected $N_{0\nu}$ in the ROI would be converted into the half-life of the decaying isotope by:

$$T_{1/2}^{0\nu} = \ln(2)\,\frac{N_A}{M}\,\frac{\epsilon_{0\nu}\,m\,t}{N_{0\nu}} \tag{1.14}$$

where $N_A = 6.022 \times 10^{23}$ mol^{-1} is the Avogadro number, M is the molar mass of the DBD isotope in kg mol^{-1}, $\epsilon_{0\nu}$ is the $0\nu\beta\beta$ detection efficiency in the ROI, m is the total mass in kg of the isotope corrected by its natural abundance or the enrichment factor and t the measurement time in years. The Avogadro number obviously helps to compensate the extremely long half-lives of the process researched.

If the neutrinoless double beta decay is not discovered, the experiment needs to set a lower limit on the half-life, for which the number of excluded events depends on the background. If no background is expected the half-life sensitivity grows linearly with time. On the other hand, in the presence of background the sensitivity would be proportional to the square root of time divided by the number of events in the ROI (in Gaussian regime):

$$(T_{1/2}^{0\nu})_{lim} \propto \begin{cases} \epsilon_{0\nu}\,m\,t & \text{background free} \\ \epsilon_{0\nu}\sqrt{\frac{m\,t}{b\,\Delta E}} & \text{with background} \end{cases} \tag{1.15}$$

where b is the *background index* in units of counts $keV^{-1}kg^{-1}y^{-1}$. After energy resolution consideration discussed earlier, the background reduction is the main challenge for neutrinoless double beta decay experiments. Both are however entangled because equation 1.15 shows that better energy resolution means less background in the ROI. An example of the evolution of exclusion and discovery sensitivity as a function of the isotope mass *exposure* over time (in kg y or t y), in the context of the future ^{76}Ge LEGEND experiment (see section 1.3) is presented on figure 1.12, with different background indexes. These figures show the linear grow of the sensitivity in the absence of background and the deviation from it, when the background increases. The figures also reveal that the exclusion sensitivity is less impacted by the background than the discovery potential, which can be drastically delayed if background is too important (note the logarithmic scale of the x-axis).

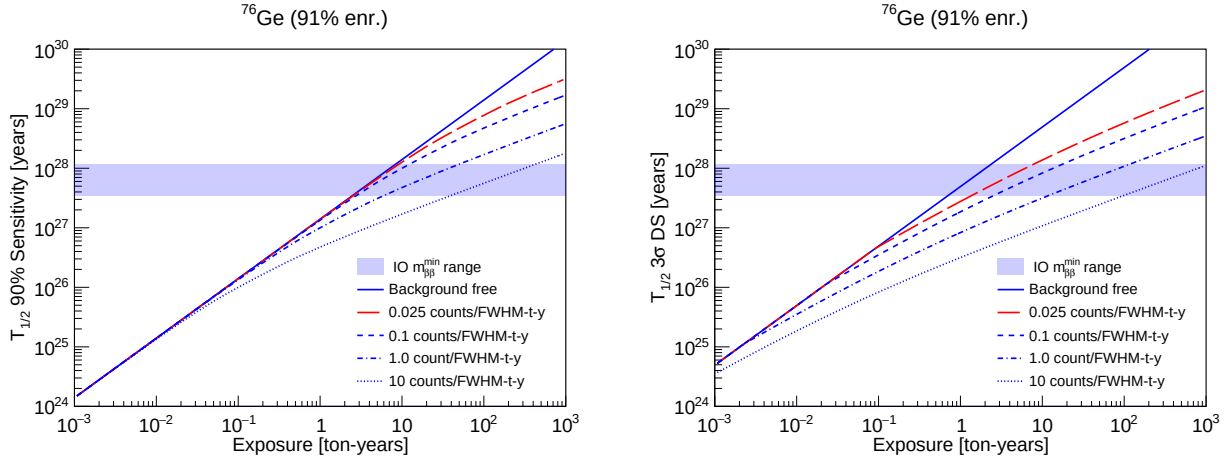

Figure 1.12: Sensitivity to a $0\nu\beta\beta$ decay signal in ^{76}Ge as a function of exposure and background for a (left) 90% CL exclusion sensitivity and (right) 3σ (99.7% CL) discovery sensitivity (DS) for a 2.5 keV FWHM energy resolution [Abgrall et al., 2021]. The inverted ordering mass range of the effective neutrino mass $\langle m_{\beta\beta}\rangle$ is indicated by the violet band as a target for the future experiments.

In the following subsections we will discuss some general key aspects of a double beta decay experiment.

1.2.1 Type of experiments

The historical experiments looking for double beta decay were geochemical, that is measuring the isotopic abundance of the daughter nuclei in old geological ores to determine the decay rates. Nowadays, the goal of DBD experiments is to directly detect the decays and measure the energy of the electrons, to search for the $0\nu\beta\beta$ decay separately from $2\nu\beta\beta$. Looking at the equations 1.14 and 1.15, we can point the key parameters to design DBD experiments with the best sensitivity possible:

- **high signal detection efficiency $\epsilon_{0\nu}$:** this is a key parameter since the sensitivity is directly proportional to the efficiency. We will show in the following that active source detectors have very high efficiencies (∼90%) compared to non-active source detectors (∼10-20%), which however can compensate by background rejection.
- **low energy resolution ΔE:** this helps to discriminate between $2\nu\beta\beta$ and $0\nu\beta\beta$ but also to reduce backgrounds. Most of the time, the background appears like a continuum in the ROI where a $0\nu\beta\beta$ peak is expected. The only exception comes for ^{136}Xe for which $Q_{\beta\beta}$ (2.458 MeV) is very close to the energy of a γ-ray of ^{214}Bi (2.448 MeV).

- **low background index *b*:** ultimately having no background in the ROI would allow the sensitivity to grow linearly with time. This can be achieved by careful low radioactivity materials selection and by active techniques for background mitigation.
- **identify the daughter nuclei:** this would be an undeniable proof that a double beta decay occurred instead of radioactivity background. This is currently being investigated in gaseous xenon detectors looking for online barium tagging techniques.

Fulfil all these items in a single experiment is not possible, so it is a matter of compromise to be found by the experimental technique. Basically, the DBD experiments can be classified among two techniques.

Active source experiments

The active source experiments are mostly calorimetric experiments for which the isotopic source is the detector itself. Most of the DBD experiments enter this category. We can mention, for example, semiconductor detectors: high-purity germanium (HPGe) or cadmium-zinc-telluride (CdZnTe), low-temperature bolometers, isotope loaded liquid scintillators and liquid-noble gas detectors.

Since the decays from the isotopes happen directly in the active volume, the $0\nu\beta\beta$ detection efficiency is very high in these experiments. These techniques can also be extended to large masses of isotopes, up to the ton scale is considered for the future experiments. Except for the scintillator experiments, all these techniques also offer excellent energy resolutions, down to few keV for HPGe. Liquid-noble gas detectors exploit the two detection channels: ionisation and scintillation, and their anti-correlation to improve the energy resolution.

All the active source detectors consist of an extremely radiopure active volume. The radioactive contaminations are thus mostly originating from the supporting materials of the detectors, the detector mechanical structure or its surrounding. Large volume detectors can accommodate this by self-shielding and fiducialization cuts, thanks to good determination of the decay positions. This comes at a cost of lower isotope mass studied, sometimes down to 50%. Time analysis also allows to reject cascades of decays at the same location, like ^{214}Bi$\rightarrow^{214}$Po for example. The background induced by γ-rays can be identified by multi-sites events, since the γ can proceed to several Compton interactions in the active volume. The semi-conductor or bolometer detectors are segmented detectors (size $\sim$10 cm) and can reject these types of background by anti-coincidences between the different crystals or by immersing them in an instrumented veto medium, like liquid argon for example. The HPGe detectors have developed pulse-shape analysis on the collected signals to discriminate surface events, dominated by background, with respect to bulk events, where $0\nu\beta\beta$ decays are mostly expected. The bolometers are now developing complementary scintillation detectors, to combine heat and scintillation signals to get rid of α background interacting on the surface of the crystals.

Tracking experiments

Tracking experiments aim to reconstruct the topological informations of the DBD by detecting the electron tracks and measure, at the same time, the energy released by the decay. In most of the tracking experiments, the isotopic source and the active detector are separated. The exception are the high-pressure gaseous time-projection chambers (TPC), in which the isotope is the noble gas itself. The other types of tracking experiments can be combination of tracking and calorimeter, *à la NEMO*, tracking only with intense magnetic field or pixelated detectors (CdZnTe or CdTe combined with Si-Timepix). For these types of detectors, the isotopic sources needs to be as thin as possible to let the electrons escape to the tracking volume.

In general, the tracking experiments possess relatively larger sizes, lower detection efficiencies and poorer energy resolutions. Their main target is really to show a full signature of the double beta decay events, by showing the image of the two electrons. This would be a real asset to convince for a discovery of the $0\nu\beta\beta$ decay. In terms of experimental sensitivity, these problems are very well compensated by the event-by-event background rejection capabilities offered in these techniques. Indeed, single-β, α and γ particles can be identified and rejected, unless they accomplish more complicated processes than creating two electrons.

For now, only the NEMO experiments can really measure the angular distribution or the single energies of the two electrons. As already said, this would an asset to reveal the underlying mechanism of the decay and to precise the NMEs calculations.

1.2.2 Choice of isotope

The actual candidates for the search for $0\nu\beta\beta$ have already been presented in table 1.1. In some experiments the choice of the isotope is imposed by the technology, for example germanium semi-conductor experiments, but others are free to study most of the isotopes or even several isotopes at the same time. There is no single best isotope, the choice is more based on the detector technology and on the isotope production capabilities. There is also interest for the community to investigate several isotopes with different experimental techniques, to improve the robustness of a possible discovery. Ideally, the choice of an isotope for a DBD experiment should try to satisfy most of the following criteria that impact equations 1.14 and 1.15. We can list them as follow:

- **high energy transition $Q_{\beta\beta}$:** higher values allow to reduce the natural radioactivity background, caused single β-decay isotopes with high Q_β (mostly ^{214}Bi and ^{208}Tl) or by α-decays. The isotopes having $Q_{\beta\beta}$ under 2 MeV (^{76}Ge) are not considered nowadays. The best candidates for this criteria are ^{48}Ca, ^{150}Nd and ^{96}Zr.
- **high isotope mass m:** is possible with high natural abundance or good enrichment capabilities, in order to collect the highest number of DBD nuclei. This is where the best three isotopes in terms of $Q_{\beta\beta}$ fail. In contrast, ^{130}Te can even be used in experiments without enrichment. The molar mass M should also favour lighter isotopes at similar masses.
- **high $2\nu\beta\beta$ half-life $T^{2\nu}_{1/2}$:** corresponds to lower $2\nu\beta\beta$ decay rate $\Gamma_{2\nu}$ (low $G^{2\nu}$ or $M^{2\nu}$) and less $2\nu\beta\beta$ events in the ROI, which is the ultimate irreducible background for $0\nu\beta\beta$.
- **high $0\nu\beta\beta$ decay rate $\Gamma_{0\nu}$:** this would be the case for isotopes having high phase space factor $G^{0\nu}$ or high nuclear matrix element $M^{0\nu}$. Unfortunately, the large uncertainties on the NMEs calculations prevents to use them as a criteria for choosing an isotope. We have also shown the little dependence of the NMEs to the DBD nuclei. Concerning the phase space, ^{150}Nd is the most favoured while ^{76}Ge would have to compensate by other means.

1.2.3 Backgrounds

The most challenging aspect in all the experiments looking for the $0\nu\beta\beta$-decay rare events is certainly the background mitigation. Like for any low energy neutrino experiment, the background comes from two origins: cosmic-rays and natural radioactivity.

The cosmic-ray muons can cause several types of backgrounds in the DBD experiments. To reduce drastically the muon flux, the detectors are located in deep underground laboratories, as presented on figure 1.13. We observe an exponential decrease of the muon flux as function of the laboratory depth, converted in *meter water equivalent* (mwe) to account for the shape and

the material of the overburden. This is the main strategy to reduce the cosmic background. Muons are not directly a concern since they can usually be identified in the detector or in a muon veto. But the cosmic background is produced by secondary events caused in the detector or its surrounding by the primary muon interactions. One contribution, is due to the secondary neutrons, which can deeply penetrate the detector and produce elastic or inelastic scattering or radiative capture. If the path of the muon in the detector can be reconstructed, an active region of the detector can be vetoed for a given time. The second contribution comes from the production of long-lived cosmogenic isotopes, specially on the DBD isotopes. The decay of these products could occur long time after the muon interaction, when the correlation between the two events can be lost. Depending on the studied isotopes, the experiments are not equal in facing this cosmogenic background. In some experiments, the cosmic-rays exposure of the detector materials and the isotopic sources are carefully monitored and minimized.

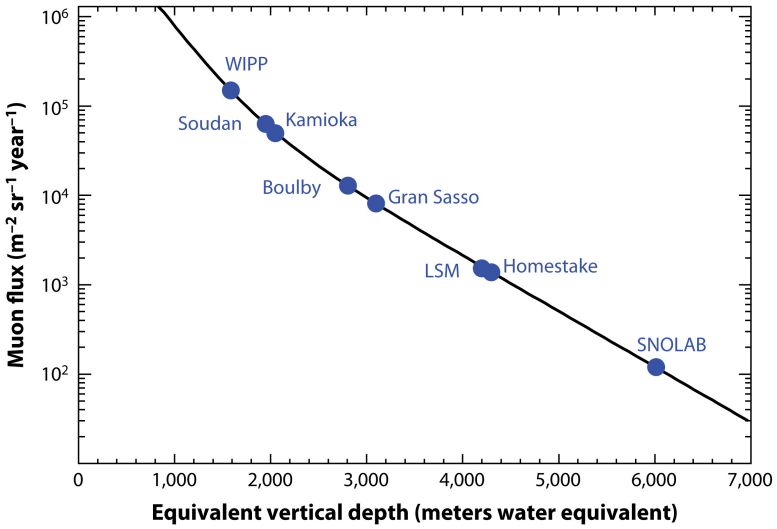

Figure 1.13: Muon flux as a function of the depth of deep underground laboratories [Saakyan, 2013].

Given the energy transitions of the $0\nu\beta\beta$ decays (few MeV), the main background in the experiments comes from the natural radioactivity, which is present in any material on Earth. The origin of this background lie on the existence of very long lived isotopes: ^{238}U ($t_{1/2} = 4.5 \times 10^9$ y), ^{232}Th ($t_{1/2} = 1.4 \times 10^{10}$ y), ^{235}U ($t_{1/2} = 7.0 \times 10^8$ y) and ^{40}K ($t_{1/2} = 1.3 \times 10^9$ y). These isotopes are not always directly the source of background, but they can create radioactive decay chains (two examples on figure 1.14), in which dangerous isotopes for the $0\nu\beta\beta$ decay search can be found. For instance, ^{214}Bi and ^{208}Tl which have high-energy β-decays are troublesome. ^{40}K decays directly into stable isotopes with too low energies to be a concern. All the β-decays of the ^{235}U daughters are low energies emitters as well, but an experiment could be sensitive to the α-decays in this chain. In the ^{238}U decay chain, we can find ^{226}Ra and ^{222}Rn. The long-lived radium-226 can have a different contamination level than ^{238}U, since it can be off from the secular equilibrium with uranium. The radon-222, simply called *radon* because it is the most stable isotope of radon, is a noble gas with a sufficiently long half-life to penetrate the detectors and produce background. This is one of the most difficult background to fight for the DBD experiments. The radon-220, called *thoron*, is less a concern because its short half-life prevents it to penetrate the detectors or emanate from materials. Confronting this natural radioactivity background can be very different from an experiment to another, depending on its detection technique. The common strategy is the careful selection of all the materials through HPGe γ-spectroscopy, to achieve the lowest contamination levels possible. Extreme cleaning procedures and construction in clean environment are also mandatory.

Finally, the detectors needs to be surrounded by massive shielding with dedicated parts

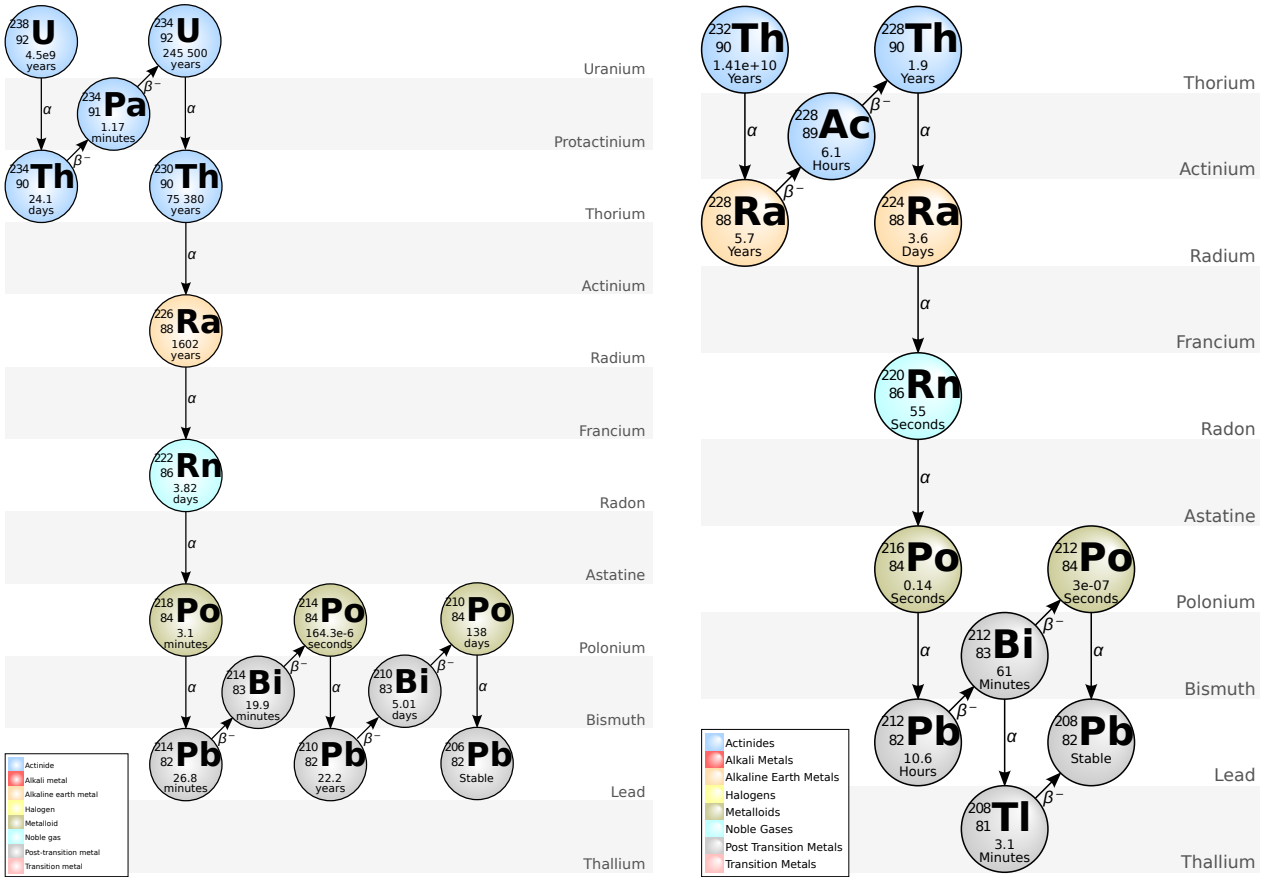

Figure 1.14: Natural radioactivity decay chains of ^{238}U on the left, where ^{222}Rn and ^{214}Bi can be found and of ^{232}Th on the right, where ^{208}Tl and its parent ^{212}Bi can be found, from Wikimedia Commons.

for γ-particles and neutrons, which are both very present in the underground laboratories. As just said, they could be produced by cosmic muons or by natural radioactivity in the rocks. Depending on the laboratory depth, one contribution could dominate the other.

Historically, the first search for double beta decay was realized by E. L. Fireman in 1948, on ^{124}Sn isotope [Fireman, 1948]. No signal was observed, hence an upper limit was set to $T_{1/2} > 3 \times 10^{15}$ y. A year latter, Fireman thought he obtained the first measurement by comparing the count rates between an enriched and a depleted sample, corresponding to an half-life of $\sim 10^{16}$ y [Fireman, 1949]. In fact this excess was certainly due to a radioactive contamination of the enriched sample. The first DBD measurement occurred in 1950 by M. H. Inghram and J. H. Reynolds with a geochemical measurement (by xenon extraction) of old tellurium ores, leading to an half-life of $\sim 1.4 \times 10^{21}$ y for ^{130}Te. Another geochemical measurement happened for ^{82}Se in 1967 ($T_{1/2} \sim 1.4 \times 10^{20}$ y) [Kirsten and Müller, 1969]. Given the importance of the germanium detectors technology today, we can note the first germanium experiment performed by E. Fiorini et al., with Ge(Li) crystals also in 1967 [Fiorini et al., 1967]. The two electrons emitted in the double beta decay where only observed for the first time in 1987 by S. R. Elliott, A. A. Hahn, and M. K. Moe, using a time projection chamber (TPC) studying ^{82}Se [Elliott et al., 1987].

The false observation of Fireman was not the only one in the history of DBD, for a detailed review see the publication of V.I. Tretyak [Tretyak, 2011]. Among them, we can to cite the work of H. V. Klapdor-Kleingrothaus et al., who believed in an *evidence for neutrinoless double beta decay* [Klapdor-Kleingrothaus et al., 2001] and even a 6σ *discovery* [Klapdor-Kleingrothaus and Krivosheina, 2006], till the final contradiction by GERDA experiment.

After all these pioneer experiments, the technologies became more and more mature. The $2\nu\beta\beta$ studies reached high level of precision and the sensitivity to $0\nu\beta\beta$ are always pushed forward, as we will show in the following.

1.3 Review of recent results

The search for neutrinoless double beta decay is a very active experimental field, we will not thus be able to cover all the experiments in this document. We will focus on the most recent results obtained with the major experimental techniques. The NEMO-3 and SuperNEMO experiments, to which I participated, will be the subject of chapter 2. Nowadays, the half-life sensitivities for the neutrinoless search have reached sensitivities of about $T_{1/2} > 10^{26}$ y, which corresponds to looking at less than four events per year in 100 kg of double beta isotope.

KamLAND-Zen - ^{136}Xe

Today, the most sensitive result in the search for $0\nu\beta\beta$ decay has been produced by the KamLAND-Zen experiment. This experiment emerged rather recently (first publication in 2012), with a sort of countercurrent strategy compared to historical technology developments in the DBD field. The historical techniques where continuously improving their energy resolution and background reduction, but using rather small masses of isotopes (<100 kg). The KamLAND-Zen experiment directly started with a huge mass of ^{136}Xe (more than 300 kg) in a detector with a modest energy resolution of 6.7% at 1 MeV. However, the KamLAND detector had already achieved a very low level of background for neutrino oscillation studies. This is due to the radio-pure materials used and the design of the detector comprising several shells: a water muon veto, an inactive buffer oil in the PMT region and 1000 tons of very pure liquid scintillator (LS) at the center, inside a 6.5 m radius nylon balloon. The enriched xenon (∼91% of ^{136}Xe) was dissolved in the LS (∼3% by weight) of a smaller central nylon balloon, which was specially deployed inside the KamLAND detector, for the $0\nu\beta\beta$ decay search. The surrounding LS is thus an important self-shielding of the detector. The first phase of the experiment, with almost 400 kg of xenon was using a balloon of 1.54 m radius, which turned-out to be contaminated in the β^- emitter ^{110m}Ag, coming from the Fukushima accident fallout. Despite this background and thanks to strong fiducial cuts, KamLAND-Zen provided quickly the most stringent limit on the 0ν half-life [Gando et al., 2016].

A second phase of the experiment started in 2019, with a new balloon of 1.90 m radius, containing almost 800 kg of xenon. A factor ten background reduction has been obtained by changing the inner balloon. The radioactive isotopes produced through cosmic muon spallation on carbon or xenon represent now the dominant background, as presented on figure 1.15. This is already a remarkable fact, the natural radioactivity background in KamLAND-Zen has been pushed to lower levels than the cosmogenic background, which is usually the main contribution in DBD experiments. A triple coincidence analysis has been specifically developed to reduce this cosmogenic background. It is efficient against the spallation on carbon and the ^{137}Xe production, but it is not sufficient for long-lived xenon spallation products. Because of the modest energy resolution, the $2\nu\beta\beta$ background is the second most important contribution in the [2.35,2.70] MeV ROI for $0\nu\beta\beta$.

The result published in 2022 [Abe et al., 2023], combining the two phases of the experiment, with a total exposure of 970 kg y, provides the actual best sensitivity on the search for $0\nu\beta\beta$ decay. Since no evidence of the decay has been found, a lower limit on the half-life has been set to $T^{0\nu}_{1/2} > 2.3 \times 10^{26}$ y at 90% CL. It corresponds to upper limits on the effective Majorana neutrino mass of $\langle m_{\beta\beta} \rangle <$ 36-156 meV, depending on the NMEs used, in the model of light-neutrino exchange. This limit plotted on figure 1.16, illustrates that the inverted ordering (IO)

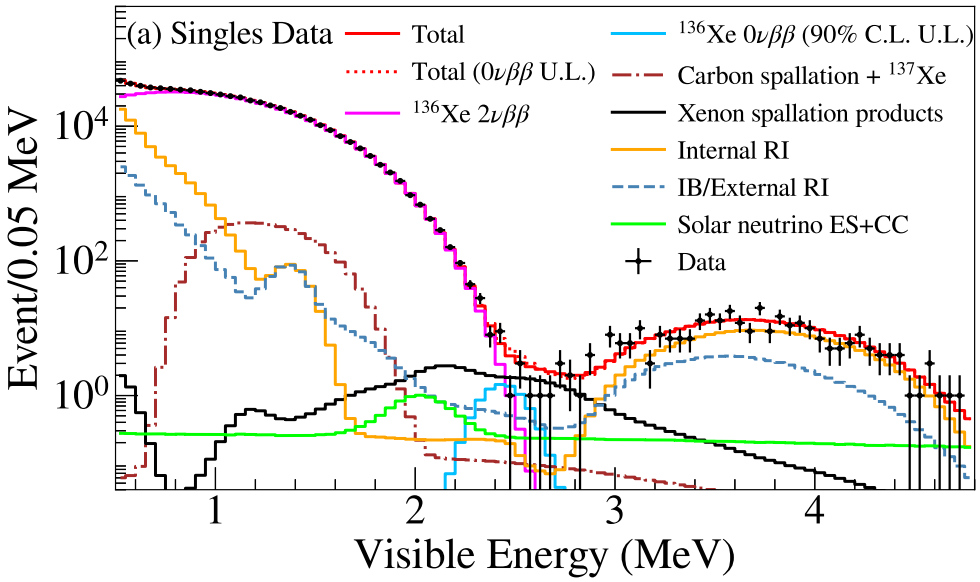

Figure 1.15: Energy spectra of the selected $\beta\beta$ candidates of KamLAND-Zen phase 2, within the 1.57 m radius fiducial volume. The best fit on the backgrounds with the individual contributions are also displayed: carbon and xenon spallation, ^{136}Xe $2\nu\beta\beta$, internal and external radioactive impurities (RI) in the LS and on the inner balloon (IB) and the solar neutrinos elastic scattering (ES) and charged current (CC) interactions. The upper limit on the $0\nu\beta\beta$ of ^{136}Xe is also presented [Abe et al., 2023].

of the three flavours neutrino masses starts to be investigated.

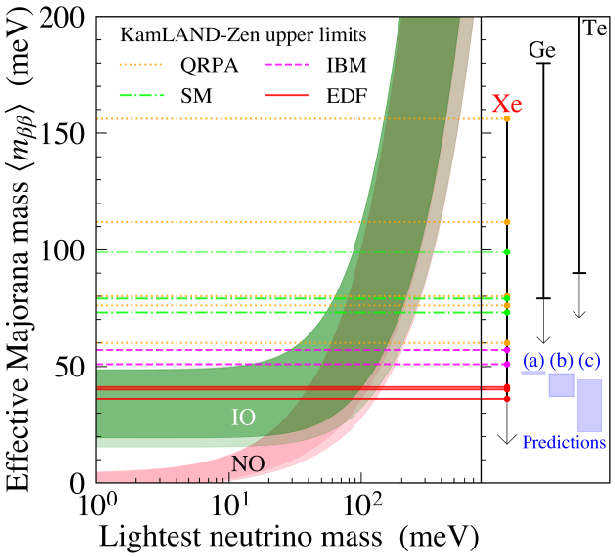

Figure 1.16: Effective Majorana neutrino mass $\langle m_{\beta\beta}\rangle$ as a function of the lightest neutrino mass compared to the the best-fit values of neutrino oscillation for inverted (IO) or normal (NO) ordering neutrino masses. Different nuclear matrix elements calculations are presented on horizontal lines. The side panel shows the corresponding limits for the most sensitive results on three isotopes with some theoretical predictions on $\langle m_{\beta\beta}\rangle$ [Abe et al., 2023].

An upgrade to KamLAND2-Zen is being considered with improved electronics for rejection of the xenon spallation products, one ton of ^{136}Xe, improved light collection and photo-coverage (by using Winston cones and high quantum efficiency PMTs) coupled to higher light-yield liquid scintillator (changing from decane+pseudocumene to LAB). The objective is to reach the ∼20 meV region of $\langle m_{\beta\beta}\rangle$ in 5 years of data taking.

Xenon TPCs - ^{136}Xe

An other competitive type of xenon experiments are liquid xenon time projection chambers (TPC). The EXO-200 experiment has demonstrated the interest for this technology, with large detector mass, three-dimensional event vertex reconstruction and good energy resolution. Combining the light and charge signals, to build a *rotated energy* estimator, an energy resolution of $\sigma/E = 1.15\%$ (2.7% FWHM) has been achieved. The vertex reconstruction allows to discriminate between single-site events (SS - like $\beta\beta$) and multi-site events (MS - like γ interactions). This is powerful to constrain the backgrounds in the MS channel and reject them for the $0\nu\beta\beta$ decay search in the SS channel, as can be seen on figure 1.17. Two phases of data were collected over 1181 days at the Waste Isolation Pilot Plant (WIPP - 1620 mwe), New Mexico. The second phase of data taking occurred after an accident at the WIPP facility, which was also the opportunity for detector upgrade and an increase of the electric field. Of the 200 kg of enriched xenon at 80.6% available, 175 kg are in liquid phase, and 110 kg are in the active volume of the detector. Fiducial cuts are imposed to reject the background on the boundaries of the active volume, reducing the ^{136}Xe mass to 74.7 kg. After an exposure of 234 kg y, EXO-200 has reached a sensitivity of $T^{0\nu}_{1/2} > 3.5 \times 10^{25}$ y at 90% CL [Anton and others", 2019]. As we can see on the energy spectra 1.17, EXO-200 suffers from ^{214}Bi background, progeny of radon and ^{238}U, which have a γ-line (2448 keV) very close to the $Q_{\beta\beta}$ value (2458 keV).

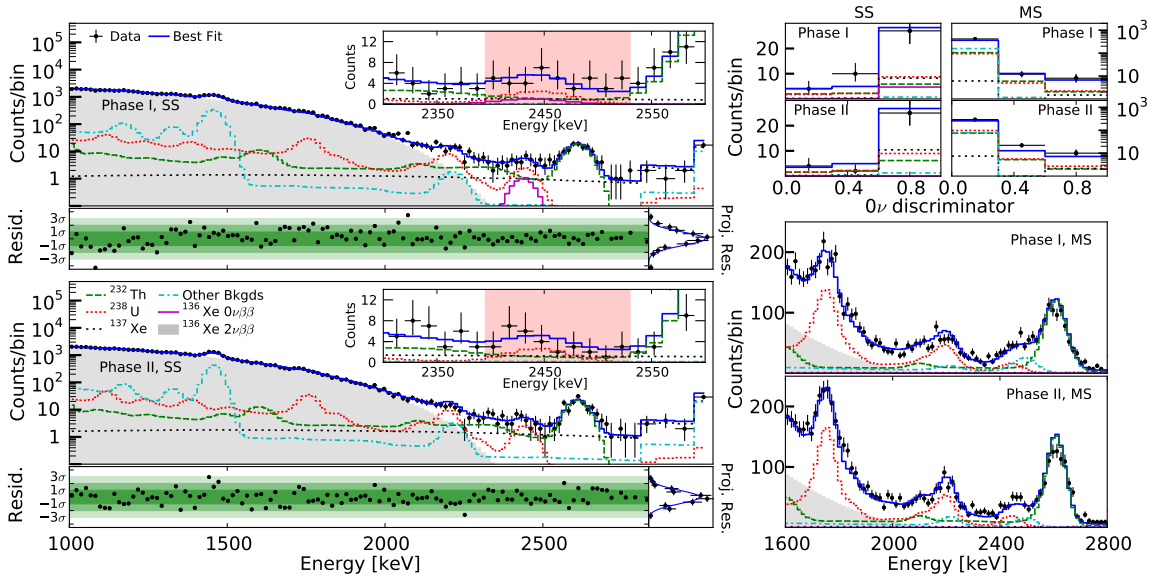

Figure 1.17: Best fits to the low background data SS energy spectrum for Phase I (top left) and Phase II (bottom left) of EXO-200 [Anton and others", 2019]. The energy bins are 15 keV below 2800 keV and 30 keV above. The inset shows an enlarged view around the best-fit value for $Q_{\beta\beta}$. (Top right) Projection of events in the range of 2395 to 2530 keV on the deep neural network fit dimension for SS and MS events. (Bottom right) MS energy spectra.

The successor of EXO-200, nEXO is being designed [Adhikari et al., 2022] to reach a sensitivity beyond 10^{28} y in 10 years of data taking, with 5 tons of enriched xenon. The DARWIN experiment looking for dark-matter with natural liquid xenon could also play a role in $0\nu\beta\beta$ decay search, with an expected sensitivity beyond 10^{27} y [Aalbers et al., 2023].

Another interesting technique consist of high-pressure xenon gas TPC investigated by the NEXT collaboration. To the good performances of liquid xenon TPCs, this technology provides better energy resolution and the topological identification of the two electrons, from the tracks and the two final Bragg's peaks [Simón et al., 2021]. Online tagging of the ^{136}Ba^{2+} ions in

coincidence with energy deposit around $Q_{\beta\beta}$ is under R&D [Herrero-Gómez et al., 2022]. This tagging would fully sign a double beta decay event in the TPC and strongly reject backgrounds.

GERDA - ^{76}Ge

At first look, the ^{76}Ge isotope seems not to be the best isotope to search for neutrino-less double beta decay, see section 1.2.2. Indeed, the energy of the transition $Q_{\beta\beta}$ is rather low and the phase space factor $G_{0\nu}$ is the lowest of the candidate isotopes, see table 1.1. But this is largely overwhelmed by the fantastic performances of the high-purity germanium (HPGe) detectors.

Firstly, the crystal growth process for germanium detectors provides several purification steps resulting in extremely low levels of internal contaminations from natural radioactivity (high radiopurity). Secondly, the germanium detectors achieve an outstanding energy resolution of few keV, which is the best compared to any DBD experiments. Finally, decades of germanium detectors developments (and the associated electronics) offers excellent background rejection capabilities. The detectors innovation followed a sequence from semi-coaxial, p-type point-contact (PPC), broad-energy Ge (BEGe) and finally inverted-coaxial point-contact (ICPC) detectors. Through pulse shape discrimination (PSD) techniques, the germanium detectors can now reject multi-sites and surface interaction events, which are not DBD events. The anti-coincidence between several crystals is also used to complete the background rejection. The crystals are produced several years in advance and stored underground, to allow for cosmogenic isotopes cool-down (mostly ^{60}Co and ^{68}Ge).

The most sensitive germanium experiment to date is the GERmanium Detector Array (GERDA). In several phases, the experiment used 15.6 kg of coaxial detectors, 20 kg of BEGes detectors and 9.6 kg of ICPC detectors. The ^{76}Ge enrichment is about 87% for all the crystals. The energy resolution at $Q_{\beta\beta}$ ranges from 2.6 to 3.6 keV FWHM, depending on the germanium detector technology, BEGes being the best. The crystals are assembled in strings, placed inside a nylon mini-shrouds to limit radioactive ions collection (^{222}Rn progenies and ^{42}Ar), are immersed in 64 m^3 of liquid argon (LAr) for shielding and cooling ($\sim$70 K). The LAr volume is also instrumented with cryogenic PMTs and a curtain of wavelength-shifting fibers connected to silicon photomultipliers (SiPMs), to serve as active veto around the germanium detectors. The cryostat is finally surrounded by a water tank with 590 m^3 of purified water equipped with PMTs to detect the residual cosmic muons in the *Laboratori Nazionali del Gran Sasso* (LNGS) in Italy.

The best result in the search for $0\nu\beta\beta$ decay has been obtained in GERDA Phase II [Agostini et al., 2020], for which the total exposure is 103.7 kg y in ^{76}Ge. The full energy distribution is shown on figure 1.18 (left), before and after applying the analysis cuts, which reduces the background by a factor $\sim$10 at $Q_{\beta\beta}$. At low energy, the counting rate is mostly dominated by the $2\nu\beta\beta$ decay. At higher energies, it is dominated by α decays (like ^{210}Po), ^{42}Ar/K β-decays or γ-rays from ^{238}U and ^{232}Th decay chains. The $0\nu\beta\beta$ search is performed in the [1930-2190] keV ROI, where 13 events have been observed (after exclusion of two known γ-lines) as shown on figure 1.18 (right). The statistical analysis of these events, fitted by a flat background and a Gaussian peak at $Q_{\beta\beta}$, conducted to no indication for a signal. A lower limit on the half-life has been set to $T^{0\nu}_{1/2} > 1.5 \times 10^{26}$ y at 90% CL. The remarkable background index of $5.2^{+1.6}_{-1.3} \times 10^{-4}$ counts keV^{-1}kg^{-1}y^{-1} surpasses the design goal of the experiment.

Combining with the phase I data, slightly enhances the sensitivity to $T^{0\nu}_{1/2} > 1.8 \times 10^{26}$ y at 90% CL. It corresponds to upper limits on the effective Majorana neutrino mass of $\langle m_{\beta\beta} \rangle <$ 79-180 meV. This result is included on the sensitivity limits on figure 1.16.

In parallel to the GERDA experiment, the Majorana experiment was carried out in the USA. Using similar types of germanium detectors, without LAr veto, very good results were

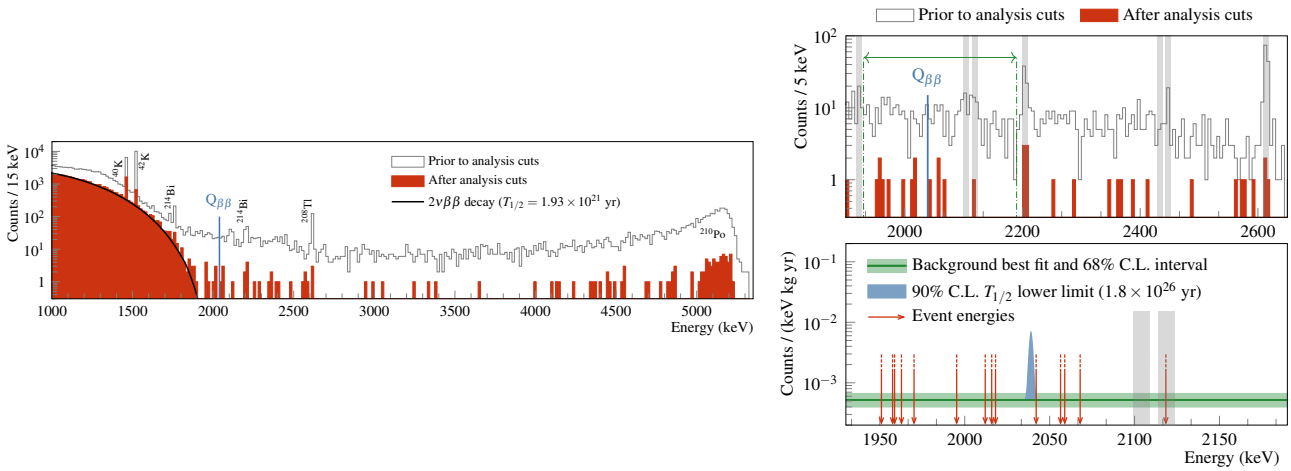

Figure 1.18: (left) Full energy spectra of GERDA phase II with an exposure of 103.7 kg y in ^{76}Ge, with the events before (white filling) and after cut (red filling), [Agostini et al., 2020]. (right) Two energy distribution windows of the $0\nu\beta\beta$ analysis of the GERDA phase II, showing the excluded γ-lines (in grey), the fitted background (in green) and the lower half-life limit (in blue).

also obtained [Alvis et al., 2019]. We can highlight the successful developments of the Majorana experiment: underground electro-formed copper production (0.1 µBq kg^{-1} for both U and Th chains), improved lower mass front-end electronics for PSD and energy resolution, lower background cabling and the invention of the ICPC detectors. The improved PSD allows to better reject the surface α events. The ICPC crystals allows to increase the isotope mass (2-3 kg instead of ∼1 kg for BEGes) for a lower number of detectors, which reduces the cables, connectors and support materials, and offers a better surface to volume ratio. These are assets to further reduce the backgrounds in the experiment. This technology is the baseline for the fusion of GERDA and Majorana collaborations for the construction of the LEGEND experiment [Abgrall et al., 2021], aiming for 10^{28} y half-life sensitivity. The first step of this experiment, LEGEND-200, is already taking data taking the advantage of both experiments, in the LAr cryostat at LNGS.

CUORE - ^{130}Te

Another very sensitive experiment in the search for $0\nu\beta\beta$ is CUORE, the Cryogenic Underground Observatory for Rare Events, located at LNGS in Italy, at a depth of 3600 mwe. It is a cryogenic calorimeter made of natural tellurium ($^{\text{nat}}$Te) oxide. This is the main advantage of the ^{130}Te isotope, which can be used without enrichment thanks to the highest natural abundance of the candidates (34%). These bolometers offer very good energy resolution and radiopurity levels, however slightly lower than germanium detectors. But they require to be operated at much lower temperature, approximately 10 mK.

A great achievement of the experiment relies on the development of a multistage cryogen-free cryostat, based on dilution refrigerator technology, reaching an experimental volume of approximately 1 m^3 and a cold mass of 1.5 t (detectors, holders, shields). The detector comprises 988 crystals of $^{\text{nat}}TeO_2$ with 5×5×5 cm^3 size, distributed in 19 towers (13 floors of 4 crystals). The total mass of crystals is 742 kg, corresponding to 206 kg of ^{130}Te. The crystals are operated as bolometers, meaning they measure the energy deposited by the DBD through heat increase (∼100 µK MeV^{-1}). Each CUORE crystal is instrumented with a neutron-transmutation-doped germanium thermistor (NTD) that converts thermal pulses into electric signals (∼400 µV MeV^{-1}). On the crystals are also installed heaters to inject reference heat pulses for thermal gain stabilization over time. The CUORE experiment achieve an energy

resolution of 7.8±0.5 keV FWHM at $Q_{\beta\beta}$ (extrapolated from the 2.615 MeV γ peak of ^{208}Tl) and an energy bias lower than 0.7 keV.

The full energy spectrum of CUORE, as presented in 2022, can be seen on figure 1.19. At low energy, we observe a continuum of background from natural radioactivity as well as several very sharp γ-lines and the $2\nu\beta\beta$ energy spectra. At higher energy, the spectrum is dominated by α background revealing peaks and degraded α's. The [2.490, 2.575] MeV ROI of CUORE for the $0\nu\beta\beta$ search contains a peak at 2.506 MeV, corresponding to the simultaneous absorption of the two γ's of ^{60}Co and a background continuum. About 90% of this continuum consists of degraded α's from the support structure and the remaining 10% consists of the multi-Compton of the 2.615 MeV γ from ^{208}Tl. The background index at $Q_{\beta\beta}$ is 1.49 ± 0.04 counts keV^{-1}kg^{-1}y^{-1}, which is quite high.

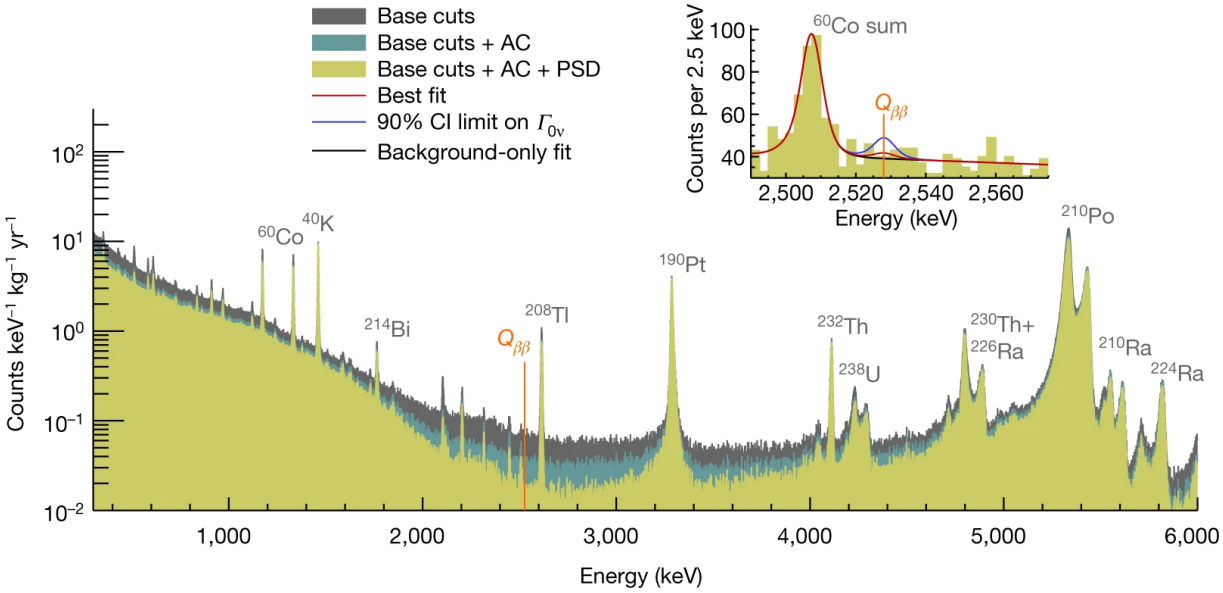

Figure 1.19: Full energy spectra of the CUORE experiment showing the effects of the anti-coincidence (AC) cut and the pulse shape discrimination (PSD). The upper right panel details the [2.490, 2.575] MeV ROI for the $0\nu\beta\beta$ search, displaying the best signal plus background fit (in red) corresponding to a rate of $\Gamma_{0\nu} = (0.9 \pm 1.4) \times 10^{-26}$ y^{-1} and the half-life limit $T^{0\nu}_{1/2} > 2.2 \times 10^{25}$ y 90% CL (in blue) [Collaboration, 2022].

In the analysis, events with coincidences between crystals or with pulse shape indicating more than one energy deposit in the crystal are discarded. No evidence for $0\nu\beta\beta$ decay has been found in the ROI after an exposure of 288.8 kg y in ^{130}Te. A lower limit on the half-life has thus been set to $T^{0\nu}_{1/2} > 2.2 \times 10^{25}$ y at 90% CL. In the model of light-neutrino exchange, this exclusion translates in upper limits on the effective neutrino mass of $\langle m_{\beta\beta} \rangle <$ 90-305 meV, depending on the NMEs used. This result is also included on the sensitivity limits on figure 1.16. The CUORE experiment is still taking data and the exposure will increase up to 1 ton y of ^{130}Te in the coming years.

The SNO experiment is also about to search for neutrinoless double beta decay with natural tellurium loading in the liquid scintillator [Albanese et al., 2021]. A first filling with 0.5% loading, corresponding to 1.3 tons of ^{130}Te, is expected in 2024. After 5 years, this would push the sensitivity for ^{130}Te above 2×10^{26} y. R&D is also ongoing to increase the loading up to 3%. After the investigation of the neutrino mass ordering around 2030, the JUNO experiment is also considering $^{\text{nat}}$Te (or ^{136}Xe) loading to search for $0\nu\beta\beta$ decay.

CUPID - ^{82}Se/^{100}Mo

The successor of CUORE, named CUPID (CUORE Upgrade with Particle IDentification), is already scaling up with several ongoing R&D's. The principle of the new detectors is to use scintillating bolometers to combine heat and light signals, in order to discriminate β/γ's from α's. A thin light detector is added close to the DBD bolometer to collect the scintillation light, as illustrated on figure 1.20 (left). For a same energy deposit measured in the heat channel the scintillation light differs between β/γ's and α's, see figure 1.20 (right). This will reject the main background observed in CUORE. The energy transition of the ^{130}Te $0\nu\beta\beta$ decay is lower than the 2.615 MeV γ-line of the ^{208}Tl background. CUPID is thus investigating isotopes with higher energy transitions, like ^{82}Se or ^{100}Mo.

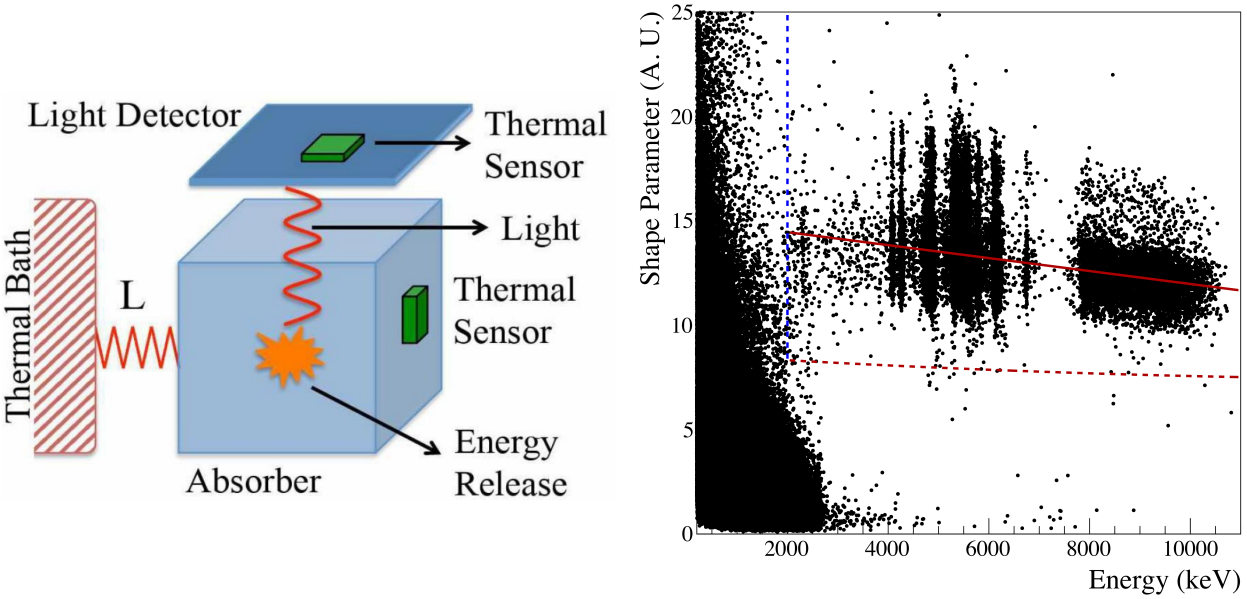

Figure 1.20: (left) Principle of a scintillating bolometer coupled to a thin light detector [Alfonso et al., 2023]. (right) Particle identification in the CUPID-0, Zn^{82}Se scintillating bolometers [Azzolini et al., 2019a]. The x-axis represents the heat channel measuring the energy while the y-axis represents the pulse shape discriminating parameter on the light signal. The α-particles lie on the top right of the plot (average mean value in red) and the β/γ-particles lie on the left.

The first pilot experiment using scintillating bolometers is CUPID-0 with Zn^{82}Se crystals in the CUORE-0 cryostat at LNGS. The experiment comprises 24 enriched crystals at 95% in ^{82}Se (plus two natural ones), interleaved with thin germanium bolometric light detectors. Both types of crystals are equipped with NTD thermal sensors. The achieved energy resolution of about 20 keV FWHM at $Q_{\beta\beta}$ would require further R&D. The background index at $Q_{\beta\beta}$ is greatly improved compared to CUORE: $(3.5 \pm 1.0) \times 10^{-3}$ counts keV^{-1}kg^{-1}y^{-1} [Azzolini et al., 2019b]. After an exposure of 5.29 kg y, CUPID-0 reached the current best limit on the search for $0\nu\beta\beta$ decay of ^{82}Se, which has been set to $T^{0\nu}_{1/2} > 3.5 \times 10^{24}$ y (90% CL), corresponding to $\langle m_{\beta\beta}\rangle$ < 311-638 meV [Azzolini et al., 2019d]. Newest preliminary result were presented at Neutrino 2022 conference with 16.6 kg y exposure leading to the limits $T^{0\nu}_{1/2} > 4.7 \times 10^{24}$ y (90% CL) and $\langle m_{\beta\beta}\rangle$ < 276-570 meV.

In the prospect of larger mass scale experiments, the CUPID collaboration concentrated the efforts on a second technology: $Li_2{}^{100}MoO_4$ crystals, named CUPID-Mo. The choice was driven by better energy resolution, better radiopurity and easier crystal growth. CUPID-Mo consists of an array of 20 crystals arranged in five towers, operated at the *Laboratoire souterrain de Modane* (LSM) in Edelweiss cryostat. Each bolometer and its germanium light detector is encapsulated in a copper housing. The total mass of ^{100}Mo is 2.264 kg, coming from the

NEMO-3 experiment. Due to cryostat failure, the first physics data taking was limited but sufficient to reveal the good performances of the technology: energy resolution of (6.5 ± 1.4) keV FWHM at 2.615 MeV, light-yield for β/γ events of 0.6-0.9 keV/MeV, full separation of β/γ to α (see figure 1.21 (left)) thanks to the 20% quenching of the scintillation for α-particles and excellent radiopurity levels have been demonstrated [Armengaud et al., 2020]. After more than one year of running (1.17 kg y of ^{100}Mo exposure), no event has been observed in the ROI around $Q_{\beta\beta}$, see figure 1.21 (right). CUPID-Mo already reached the best sensitivity in the search for $0\nu\beta\beta$ decay with ^{100}Mo: $T^{0\nu}_{1/2} > 1.5 \times 10^{24}$ y (90% CL) and $\langle m_{\beta\beta}\rangle <$ 310-540 meV [Armengaud et al., 2021]. Depending on the fit conditions, the background index has been determined to $2 - 6 \times 10^{-3}$ counts keV^{-1}kg^{-1}y^{-1} in a 10 keV window around $Q_{\beta\beta}$.

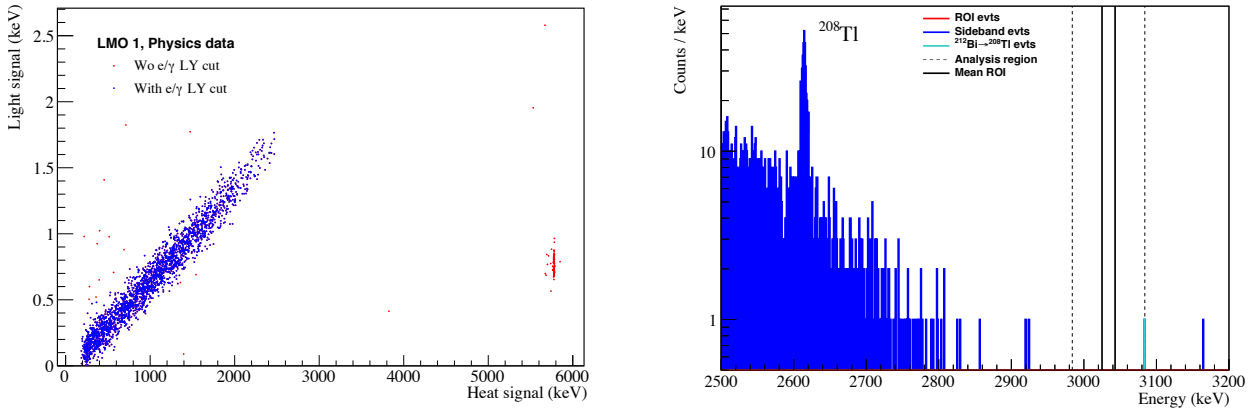

Figure 1.21: (left) Light yield versus heat signal scatter-plot, using 11 days of physics data from the highest contaminated $Li_2{}^{100}MoO_4$ crystal of CUPID-Mo [Armengaud et al., 2020]. The mono-energetic ^{210}Po α events appear in red on the right while the β/γ events appear in blue on the left. (right) Energy spectrum for 1.17 kg y of ^{100}Mo exposure after un-blinding where no event is observed in the 17.9 keV wide ROI. A single event, highlighted in cyan, attributed to the natural decay cascade of ^{212}Bi$\rightarrow{}^{208}$Tl$\rightarrow{}^{208}$Pb has been observed in the analysis region [Armengaud et al., 2021]

A full tower of 28 $Li_2{}^{100}MoO_4$ crystals is now taking data in the cryostat at LNGS. Moving to naked crystals should help to further reduce the background and get closer to the target background index of CUPID-Mo, being 10^{-4} counts keV^{-1}kg^{-1}y^{-1}. The full scale experiment aims to replace the CUORE detectors in the LNGS cryostat, with CUPID-Mo technology and 240 kg of ^{100}Mo. The experiment should allow to test the inverted ordering of neutrino masses, down to $\langle m_{\beta\beta}\rangle <$ 12-20 meV. Improvements on the light detectors are however needed to reduce the $2\nu\beta\beta$ pile-up background.

Future experiments sensitivity

The $0\nu\beta\beta$ process could be soon discovered by the ton-scale experiments. To draw an overview of the recent results in the search for $0\nu\beta\beta$ decay and compare the sensitivity of the future projects, we can use the exhaustive review compiled in [Agostini et al., 2023]. As already said, different strategies have been adopted by the experiments and half-life comparison between different isotopes is not possible. In addition, the calculation of the nuclear matrix elements gives large variations. Thus the comparison of experiments is not an easy task. The work of this review is trying to define some relevant parameters to quantify the assets of each technique, as illustrated on figure 1.22. The isotope mass (expressed here in mole to account for the different atomic weight of several nuclei), detection efficiency and energy resolution are the key parameters for sensitivity comparisons, as used in equation 1.15. Then follows the *sensitive exposure* (in mol y), which is the product of the number of moles of isotope in the active fiducial

volume, the live-time, and the signal detection efficiency. It reflects the probability for a $0\nu\beta\beta$ decay to occur in the sensitive volume of the detector to be detected. Finally, the *sensitive background* (in events / mol y) is the number of background events in the sensitive volume after analysis cuts, divided by the sensitive exposure.

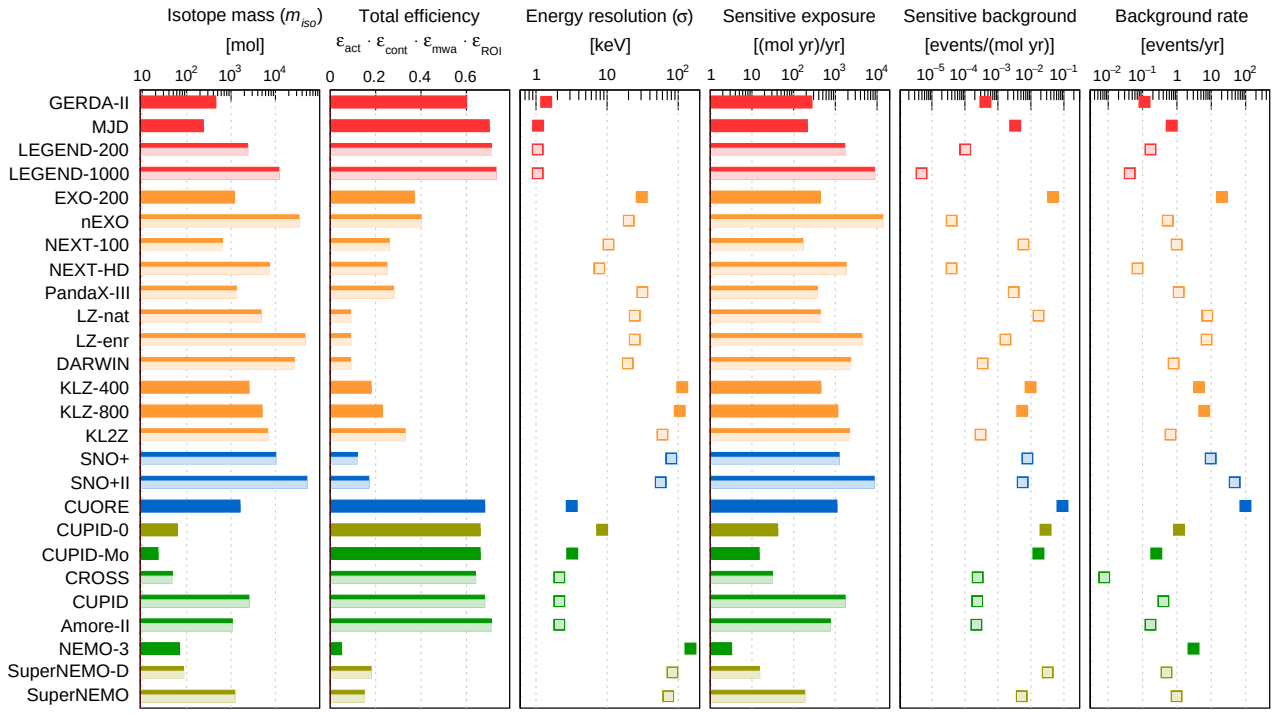

Figure 1.22: Parameters driving the sensitive background and exposure, and consequently the sensitivity, of recent and future phases of existing experiments [Agostini et al., 2023]. Red is used for ^{76}Ge experiments, orange for ^{136}Xe, blue for ^{130}Te, green for ^{100}Mo, and sepia for ^{82}Se. The sensitive exposure is computed for one year of live-time. Lighter shades indicate experiments which are under construction or proposed.

The figure 1.22 illustrates similar exposures can be achieved with high mass but poorer energy resolution and poorer efficiency by gas or liquid detectors, or with small mass but high resolution and efficiency by solid state detectors. The gas and liquid detectors suffer from non-uniform background from the boundaries and require substantial fiducial cuts, which strongly reduces the efficiency. The solid state detectors have kilogram-scale which limits the total isotope mass reachable, but this can be compensated by excellent efficiency and energy resolution.

In the end, the DBD experiments will be compared in terms of effective neutrino mass $\langle m_{\beta\beta} \rangle$ with equation 1.7. The goal for the future experiments is to cover the inverted mass ordering region. Using the global results of neutrino oscillations (PMNS matrix elements), the minimal value of the effective neutrino mass, in the case of inverted ordering, has been computed to $(m^{min}_{\beta\beta})_{IO} = 18.4 \pm 1.3$ eV in the review [Agostini et al., 2021]. The uncertainty is dominated by the uncertainty on the solar mixing angle θ_{12}, which should be soon better measured by JUNO [An et al., 2016a]. This value of $(m^{min}_{\beta\beta})_{IO}$ is thus the target for future experiments. It corresponds to half-life sensitivities up to $10^{27\text{-}28}$ y depending on the isotopes. All the experiments have been placed on a sensitive background versus sensitive exposure scatter plot in [Agostini et al., 2023]. This is presented on figure 1.23. The current experiments lie on the top left, and improving them push the experiments to the bottom right. The objective is to be below the 18.4 ± 1.3 eV line for each DBD isotope. CUPID, LEGEND-1000 and nEXO should be in very good situation to test the inverted neutrino mass ordering minimal value. The

tellurium experiments lie more on the top of the scatter plot because they use natural tellurium. For them increasing the exposure should be more efficient than reducing the background.

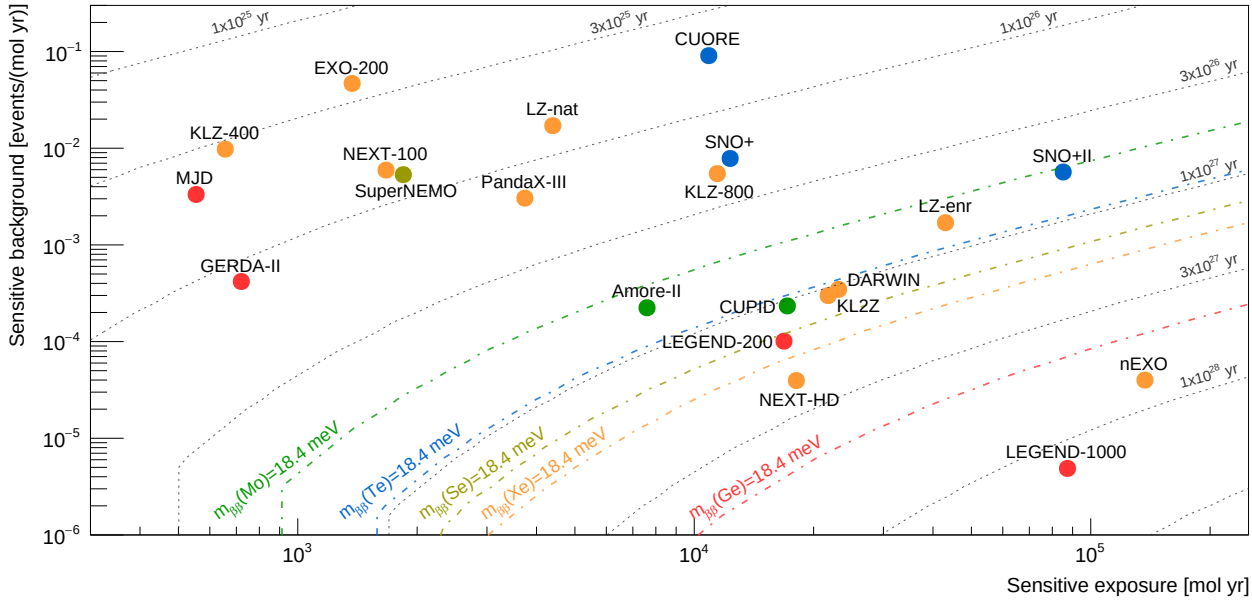

Figure 1.23: Sensitive background and exposure for recent and future experiments. The grey dashed lines indicate specific discovery sensitivity values on the $0\nu\beta\beta$-decay half-life. The colored dashed lines indicate the half-life sensitivities required to test the bottom of the inverted ordering scenario for ^{76}Ge, ^{136}Xe, ^{130}Te ^{100}Mo, and ^{82}Se, assuming for each isotope the largest NME value among the QRPA calculations listed in [Agostini et al., 2023]. A livetime of 10 years is assumed except for completed experiments, for which the final reported exposure is used.

The three most sensitive future experiments at the ton-scale level are thus: LEGEND-1000 studying ^{76}Ge, CUPID for ^{100}Mo and nEXO for ^{136}Xe. These experiments should be able to fully cover the inverted neutrino mass ordering, in the light-neutrino exchange mechanism. But the previous plots have not taken into account the NME calculations. This was done in another review [Agostini et al., 2021]. The different NME calculations can differ up to a factor three for a single isotope and make the comparison between different isotopes difficult. We are used to compare experiments in terms of exclusion sensitivity, using the median 90% CL upper limit on $\langle m_{\beta\beta}\rangle$, supposing the $0\nu\beta\beta$ has not been observed. Instead, the authors of this review recommend to compare the discovery sensitivity, which is defined as the smallest value of $\langle m_{\beta\beta}\rangle$ at which an experiment has 50% chance of observing the $0\nu\beta\beta$ at 99.73% CL. For the three isotopes, these two sensitivities are presented on figure 1.24. The differences between the NME calculations, which cannot be taken as an uncertainty, prevent to rank the experiments. The inclusion of the different NMEs might also prevent the full coverage of the inverted ordering region. The right figure illustrates however a good chance to discover the neutrinoless double beta decay in the inverted mass ordering region in a near future. This is a strong motivation to maintain several ton-scale experiments with different isotopes, for the $0\nu\beta\beta$ decay search. In the case of normal mass ordering, Bayesian analyses also suggest a 50% probability to discover a signal around 20 meV with these experiments [Agostini et al., 2017].

Conclusion

The lepton number conservation is accidental in the Standard Model of particle physics. The violation of this conservation seems necessary to explain matter-antimatter asymmetry observed in the Universe. The symmetrical theory of Majorana applied to the neutrino, which would be

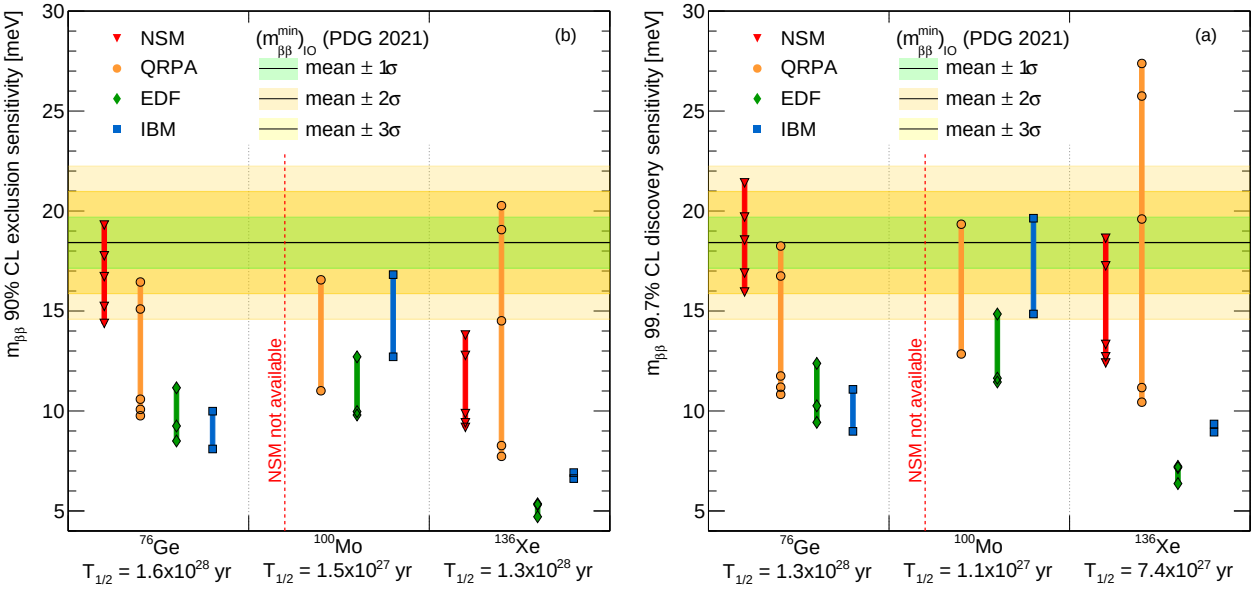

Figure 1.24: Comparison of the 90% CL exclusion sensitivity (left) and the 99.7% CL discovery sensitivity (right) for the three isotopes considered for ton-scale experiments, considering recent NME calculations and the claimed half-life sensitivities [Agostini et al., 2021]. The vertical bands illustrates the uncertainty on the neutrino mixing parameters.

identical to the anti-neutrino, provides a path to lepton number violation. One process of major interest is the neutrinoless double beta decay, which violates the total and the electron numbers. The Majorana mass generation mechanism for neutrino could also explain the smallness of neutrino masses, through the see-saw mechanism. In case of discovery, the effective neutrino mass for double beta decay could bring constrains to the global picture of the neutrino masses, in interplay with cosmology, direct mass measurements and oscillation experiments. The latter can only provide informations about the mass splittings (Δm^2's) but not about the absolute mass scale of neutrinos. Direct mass measurements are lead by KATRIN experiment, which has put an upper limit of $m_\beta < 0.8$ eV. Concerning cosmology, the current best upper limit on the sum of neutrino masses has been set by Planck to $\sum < 0.12$ eV.

The only practical way to test the Majorana nature of the neutrino is to search for neutrinoless double beta decay. We have first presented the two neutrinos double beta decay, which is an important step to improve the nuclear calculations and constrain the coupling constants of the theoretical models (g_{pp} or g_A). We have tried to illustrate the principle of the very complex many-body calculations of the nuclear matrix elements. We have introduced the two main models: the nuclear shell model (NSM) and the quasiparticle random phase approximation (QRPA). The large differences between the models would be the largest uncertainty in determining the effective neutrino mass for double beta decay $m_{\beta\beta}$, in case of discovery. The $2\nu\beta\beta$ decay is also the irreducible background for the $0\nu\beta\beta$ decay. Careful measurements of this process are thus necessary.

In the second part of this chapter, we have tried to explain how difficult are the double beta decay experiments, in reaching very high half-life sensitivities and in mitigating the backgrounds. We have listed the main criteria experiments have to optimize as best as possible. We have illustrated the major types of experiments and tried to explain their assets and limitations.

This chapter ends by a review of the recent experimental results. No evidence of the $0\nu\beta\beta$ decay has been found yet. The most sensitive lower limit on the half-life has been set to $T^{0\nu}_{1/2} > 2.3 \times 10^{26}$ y at 90% CL by KamLAND-Zen experiment with ^{136}Xe isotope. This limit corresponds to an upper limits on the effective Majorana neutrino mass of $\langle m_{\beta\beta} \rangle <$ 36-156 meV, depending on the NMEs used, in the model of light-neutrino exchange.

The perspective for the future ton-scale experiments have finally been highlighted. The discovery of neutrino-less double beta decay might just be behind the corner, in the case of inverted neutrino mass ordering ($(m_{\beta\beta}^{min})_{IO} = 18.4 \pm 1.3$ meV) or if the lightest neutrino mass is high enough ($m_{light} \gtrsim 20$ meV). Three different experimental techniques using, three different isotopes (^{76}Ge, ^{100}Mo and ^{136}Xe), are on the way to be constructed or to scale-up in mass. Given the experimental challenges, having three experiments is a real necessity for an irrefutable discovery of the $0\nu\beta\beta$.

Chapter 2

From NEMO-3 to SuperNEMO

Already at the time of my PhD thesis, I was involved in the search of neutrinoless double beta decay with the NEMO experiments. I defended my thesis in 2008 at *Université Paris-Sud* [Bongrand, 2008]. Firstly, I was working on the data analysis of the NEMO-3 experiment, specifically on the ^{130}Te isotope. Secondly, I was taking part to the preparation of the SuperNEMO experiment, by the development of the BiPo detector to measure the internal contamination of the ^{82}Se isotopic sources. After a post-doc on the Double Chooz experiment, I resumed these activities on SuperNEMO as CNRS researcher in LAL Orsay in 2009. I've been co-supervising the PhD thesis of Guillaume Eurin from 2011 to 2015 [Eurin, 2015], also on NEMO-3 data analysis and the development of the BiPo detector.

The major interest of the NEMO experiments lies in their unique feature of combining a tracker to a segmented calorimeter. The two electrons emitted during the double beta decay can be fully detected, which would be a *smoking gun* in the case of neutrino-less double beta decay discovery. In addition this technique allows to measure the individual electron energies and the relative angular distribution, which could help understanding the underlying mechanism of the neutrinoless double beta decay.

Chapter contents

2.1 From NEMO-3 to SuperNEMO

2.1.1 The NEMO-3 experiment

The NEMO-3 experiment was carried out by an international collaboration gathering 25 institutes from nine countries. The detector was located at the *Laboratoire Souterrain de Modane* (LSM), situated in the middle of the Fréjus tunnel, between France and Italy. This site offers an overburden of 4800 meter-water-equivalent (mwe), among the deepest in the world. The experiment took data from 2003 to 2011, separated in two phases in 2004, after the installation of an anti-radon tent around the detector flushed with de-radonised air in order to reduce the corresponding background by a factor six. A picture of the detector at the end of its construction can be seen on figure 2.1 (left). The detector is further shielded by 19 cm of steel and 30 cm of borated water, as can be seen under the anti-radon tent on figure 2.1 (right). The complete description of the NEMO-3 detector can be found in [Arnold et al., 2005, Augier, 2005].

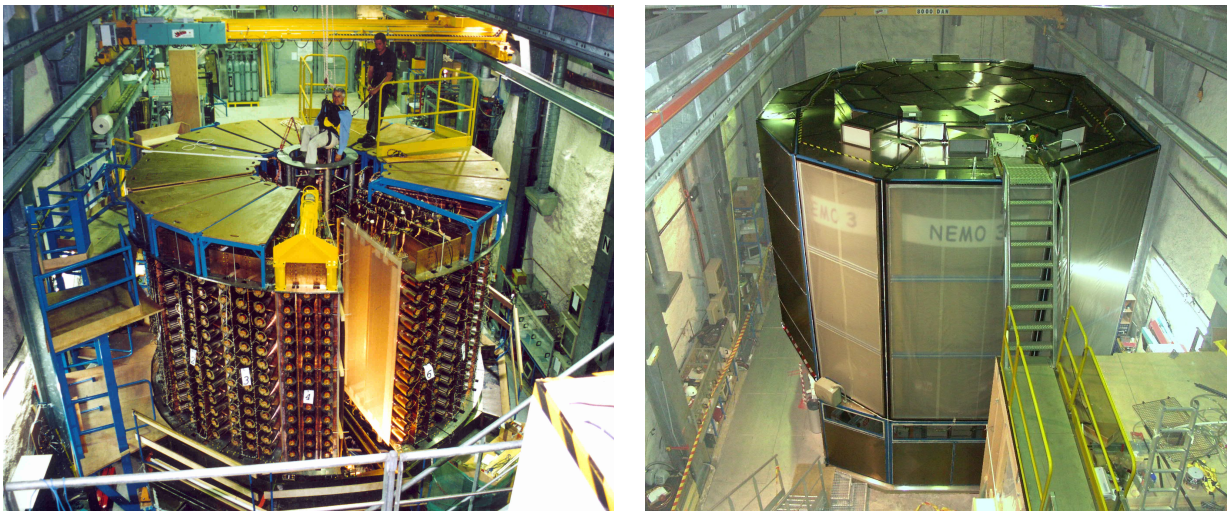

Figure 2.1: Pictures of the NEMO-3 detector at the end of the detector construction with one missing sector (left) and after the installation of the shielding and the anti-radon tent (right).

The NEMO-3 detector comprises almost 10 kg of DBD isotopes in the form of thin vertical source foils of around 2.5 m high, as can be seen on figure 2.2. The main isotope for the search of $0\nu\beta\beta$ is ^{100}Mo because it represents the higher mass with 6.9 kg in the detector. It is followed by 0.93 kg of ^{82}Se, which also allows an interesting search for $0\nu\beta\beta$. Other interesting isotopes with smaller masses have been added to the NEMO-3 experiment: 454 g of ^{130}Te, 405 g of ^{116}Cd, 37 g of ^{150}Nd, 9.4 g of ^{96}Zr and 7.0 g of ^{48}Ca. They are devoted to the precise measurements of the two-neutrinos double beta decay ($2\nu\beta\beta$) and the investigation of the internal backgrounds for future experiments. This variety of isotopes is possible because the NEMO technology allows to separate the detection volume from the isotopic sources. The sources are either metallic or composite, that is a mixture of glue with the metallic powder sandwiched in two mylar films.

The tracking detector of NEMO-3 consists of 6180 vertical drift cells, 2.7 m long, operating in Geiger mode at both sides of the isotopic sources. The tracking gas is a mixture helium, argon and ethyl alcohol. This device allows for a three-dimensional reconstruction of the charged particles tracks with few millimetres precision. A magnetic field of 25 G allows to curve the electron tracks and determine their electric charge (e^-/e^+ discrimination) and the direction of motion (crossing electrons rejection). The magnetic field is produced by a copper solenoid surrounding the detector. An example of a DBD candidate from the NEMO-3 data is presented on figure 2.3. A delayed electronics allows to detect retarded α-tracks produced by the delayed decays of ^{214}Po, in the BiPo background events.

The segmented calorimeter of NEMO-3 is made of 1940 large blocks of plastic scintillators coupled to very low radioactivity 3- and 5-inches PMTs. The calorimeter measures the individual particles energies with a resolution of 15% at 1 MeV. This resolution is crucial to discriminate $2\nu\beta\beta$ and $0\nu\beta\beta$ candidates. The PMTs also permits time-of-flight measurements with 250 ps resolution at 1 MeV. This offers a rejection of external events that or not originating from the isotopic sources.

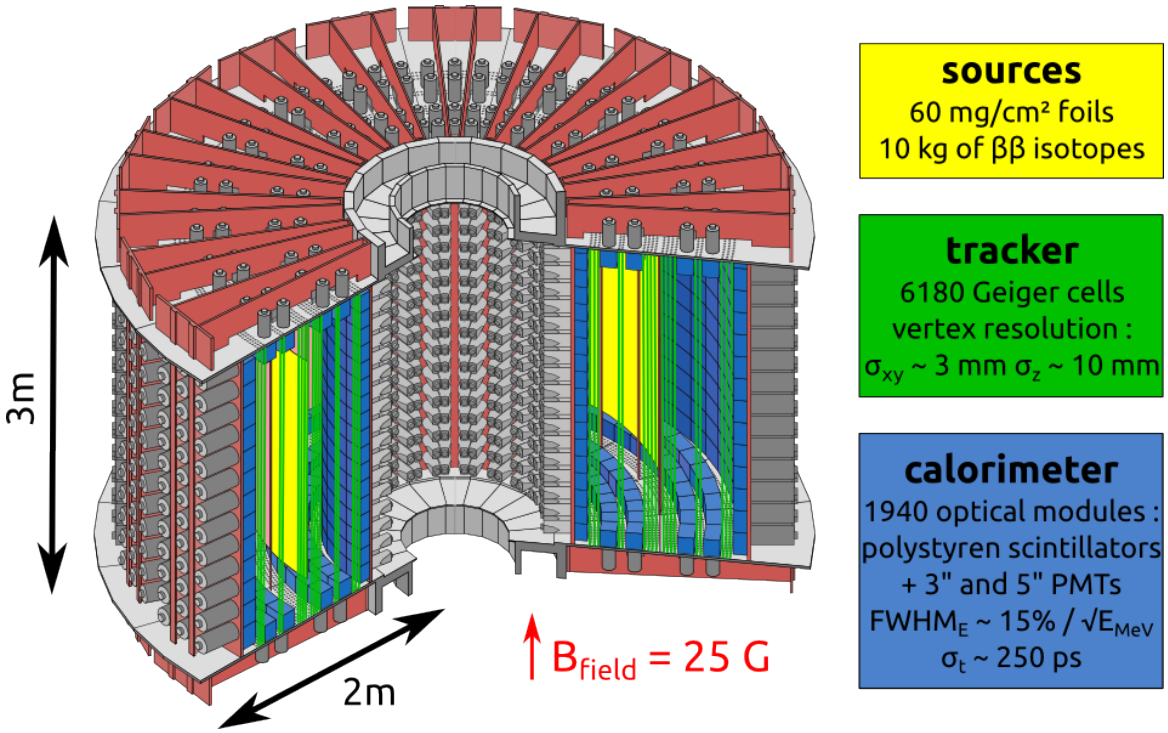

Figure 2.2: Details of the NEMO-3 detector (courtesy of Emmanuel Chauveau).

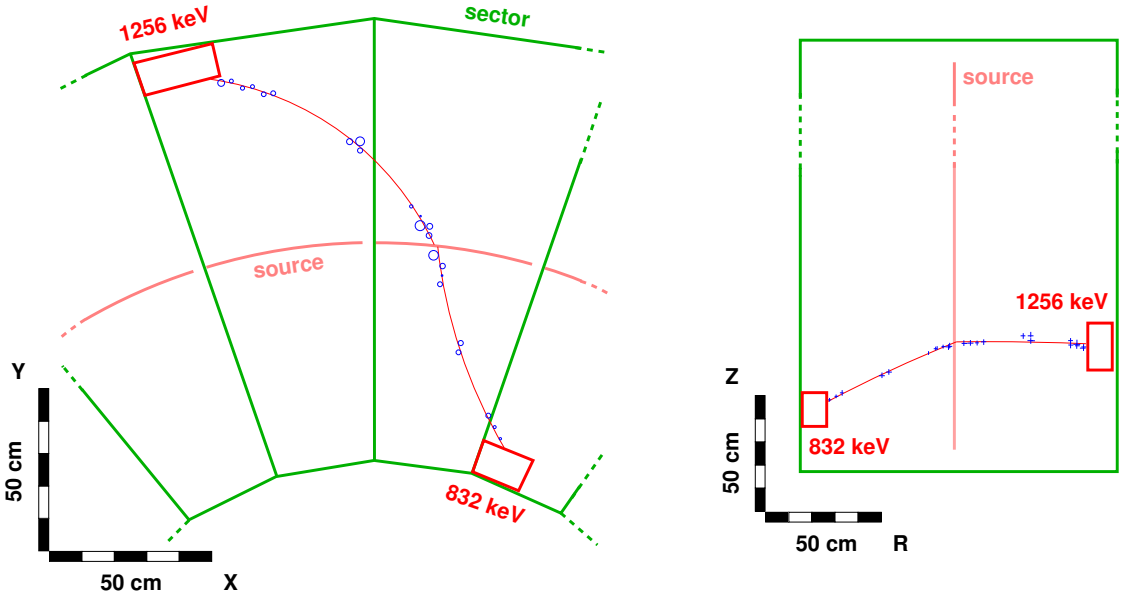

Figure 2.3: Example of a DBD candidate from the NEMO-3 data viewed from the top (left) and the side (right) [Arnold et al., 2014b]. The blue circles represents the diameters measured from the drift times in the tracking cells, the red lines are the ellipsoidal fitted tracks of the two electrons and the red rectangles the scintillators triggered with the measured energies indicated.

The excellent performances of the NEMO-3 detector can be demonstrated with the analysis of the $2\nu\beta\beta$ of ^{100}Mo, which has been extensively studied in [Arnold et al., 2019]. This is illustrated on figure 2.4, where the two-electrons energy sum, single electron energy spectra and distribution of the angle between the electrons are presented with an unprecedented statistics of $5{\times}10^5$ events and a signal-to-background ratio of about 80. These performances are obtained thanks to the relatively low two-neutrinos half-life of the ^{100}Mo isotope: $T_{1/2} = 6.81 \pm 0.01\,(stat) \pm 0.40\,(syst) \times 10^{18}$ y, the radiopurity control in the construction and the excellent background rejection capabilities of the NEMO-3 detector. The data to Monte-Carlo agreement is also excellent.

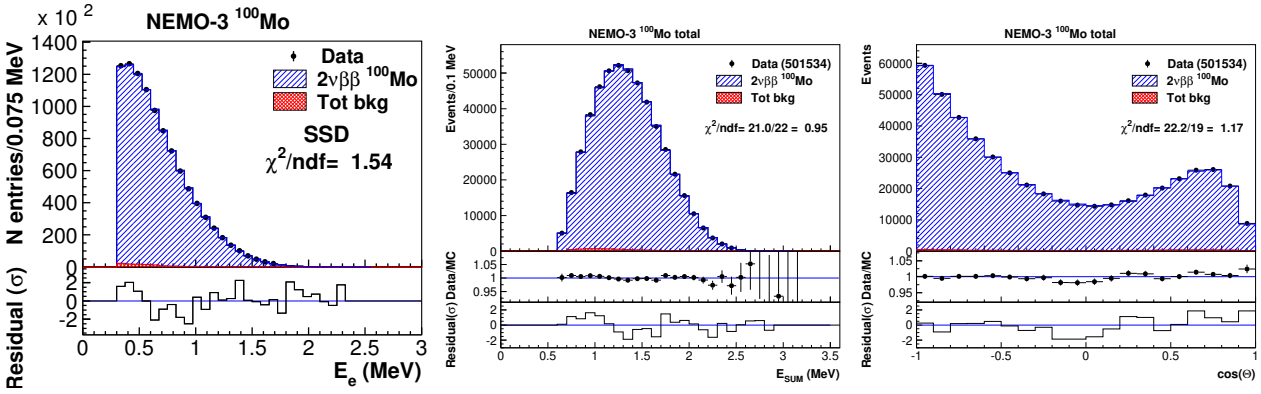

Figure 2.4: Distributions of the two-electrons events with the MC spectra in the NEMO-3 experiment [Arnold et al., 2019]. From left to right: single electron energy, energy sum of the two electrons and angular distribution between the two tracks.

2.1.2 Backgrounds in the NEMO experiments

Like for any DBD experiment, the backgrounds in NEMO-3 are dominated by the natural radioactivity. All the construction materials and processes have been selected thanks to γ-spectroscopy assays with underground *high-purity germanium* (HPGe) detectors. The remaining traces of radioactive isotopes can occasionally produce two-electrons events and thus mimic $\beta\beta$-decay events, as illustrated on figure 2.5. The largest contributions come from isotopes that are progenies of ^{238}U (^{234m}Pa, ^{214}Pb, ^{214}Bi, ^{210}Bi) and of ^{232}Th (^{228}Ac, ^{212}Bi, ^{208}Tl), as well as ^{40}K.

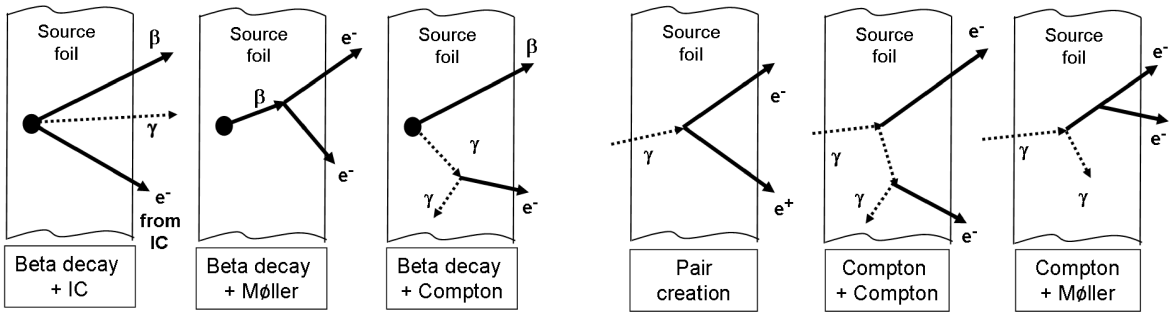

Figure 2.5: Illustration of two electrons production mechanisms from internal (right) and external (left) backgrounds in the NEMO experiments [Arnold et al., 2019].

The background is categorised as internal if it originates from radioactive decays inside the $\beta\beta$ source foils, see figure 2.5 (left). Two electrons can be produced via β-decay followed by a

Møller scattering, β-decay to an excited state with the subsequent internal conversion or due to Compton scattering of the de-excitation gamma.

Decays inside the tracking detector volume form a separate background category. The main source of this background is radon, ^{222}Rn and its progeny ^{214}Bi. The decay of radon progenies near the source foil can produce signal-like events in an analogous manner to internal background decays.

The third background category is due to the external γ-ray flux, see figure 2.5 (right), produced by the decays of radioactive isotopes in the detector components or in the surrounding area or could be due to neutron interactions in the shield and materials of the detector. Despite its low activity, the PMT glass is the main source of these γ-rays inside the detector. They can produce two-electrons events due to e^+e^- pair creation in the source foil with a subsequent charge misidentification, double Compton scattering or Compton scattering followed by Møller scattering.

Finally, the last background to consider in the NEMO-3 experiment, is the allowed $2\nu\beta\beta$ decay. This is the drawback of the NEMO technology, since the calorimeter is separated from the isotopic source, the energy resolution is degraded and the $0\nu\beta\beta$ energy peak at $Q_{\beta\beta}$ is smeared and the $2\nu\beta\beta$ tail is elongated in this region. In general, the pure calorimetric experiments offer better energy resolutions, see section 1.2.

A detailed discussion of the NEMO-3 background model is presented in [Argyriades et al., 2009]. In this article, the analysis of all the event channels used to measure each specific background are presented in depth. These analyses with the Monte-Carlo simulations allow to extrapolate the backgrounds in the two-electrons channel for the search of neutrino-less double beta decay. Given the calorimeter resolution and the energy losses, the region of interest (ROI) of the energy sum of the two electrons for the $0\nu\beta\beta$ search is [2.8-3.2] MeV, given $Q_{\beta\beta}(^{100}\text{Mo}) = 3.035$ MeV. The breakdown of the backgrounds in this window is presented, in decreasing order, in table 2.1. The total level of observed background in this $0\nu\beta\beta$ signal region is only 0.44 ± 0.13 counts/kg/yr. We can also note that no events are observed in the interval [3.2-10] MeV, proving the efficient shielding and external background rejection.

	Expected background in [2.8 - 3.2] MeV
^{100}Mo $2\nu\beta\beta$	8.45 ± 0.05
^{214}Bi from radon	5.2 ± 0.5
^{208}Tl internal	3.3 ± 0.3
^{214}Bi internal	1.0 ± 0.1
External	< 0.2
Total	18.0 ± 0.6
Data	15

Table 2.1: Breakdown of the NEMO-3 backgrounds, with the total and the measured number of events for comparison, in the region of interest for the $0\nu\beta\beta$ search.

2.1.3 Final result of the NEMO-3 experiment

Once the total expected background of 18.0 ± 0.6 events has been determined, it can be compared to the data (see table 2.1) where 15 events have been detected in the [2.8-3.2] MeV window. The energy sum of the two electrons with the expected backgrounds is presented on figure 2.6. A slight deficit, which could be attributed to a negative statistical fluctuation, is thus observed. This is supported by the very good agreement of the energy spectrum on a wider

energy range, starting at 2 MeV, as illustrated on figure 2.6 where the residuals lie within $\pm 1\sigma$. Further thorough tests on dedicated background channels ($e^-e^-N\gamma$, $e^-e^-\alpha$, e^+e^-) or on blank tellurium and copper foils have been performed to consolidate the reliability of the background model. This is detailed in [Arnold et al., 2014b].

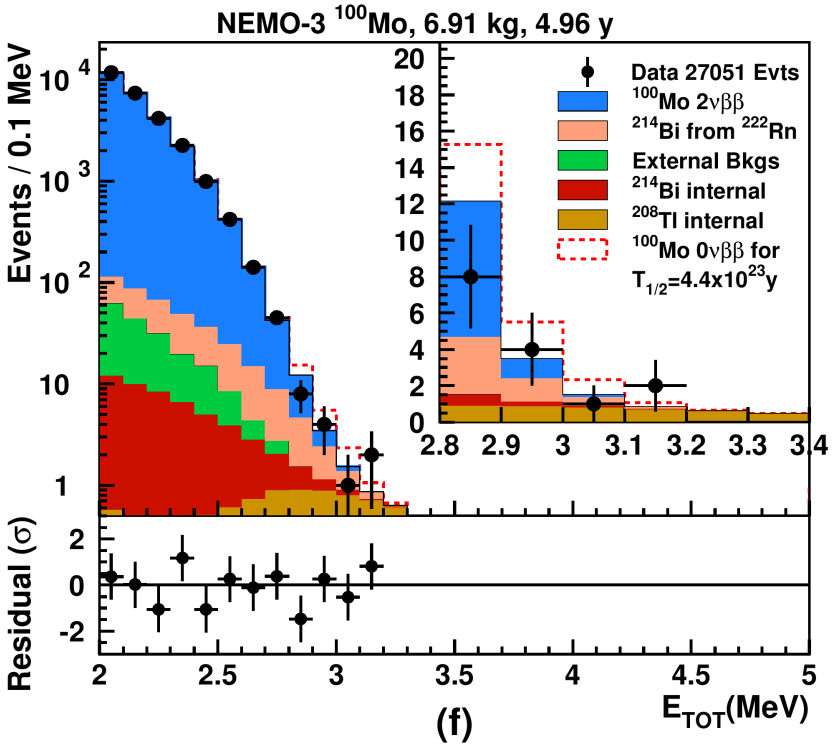

Figure 2.6: Distribution of sum energy E_{TOT} for two-electrons events above 2 MeV from the ^{100}Mo source foils for the total exposure 34.3 kg·y of the NEMO-3 experiment [Arnold et al., 2014b].

Since no event excess above the background has been detected at the $Q_{\beta\beta}$, a limit on the $0\nu\beta\beta$ decay of ^{100}Mo has been derived. Accounting for 6.914 kg of ^{100}Mo using the entire NEMO-3 data set with a detector live time of 4.96 y, the total exposure of the experiment is 34.3 kg·y. The limit is computed with a frequentist analysis using the full information of the binned energy sum distribution in the [2.0-3.2] MeV energy range for signal and background. The lower limit on the half-life of $0\nu\beta\beta$ decays in ^{100}Mo is:

$$T_{1/2}^{0\nu\beta\beta}(^{100}Mo) > 1.1 \times 10^{24} \text{ y at the 90\% CL}, \tag{2.1}$$

under the hypothesis of decay kinematics similar to that for light Majorana neutrino exchange. Depending on the model used for calculating nuclear matrix elements, the limit for the effective Majorana neutrino mass lies in the range:

$$\langle m_{\beta\beta} \rangle < 0.33 - 0.62 \text{ eV}. \tag{2.2}$$

This result, published in 2015, was comparable to the leading results from other experiments on different isotopes at that time. Constraints on other lepton-number violating mechanisms for $0\nu\beta\beta$ decays were also reported in [Arnold et al., 2014b].

2.1.4 Improvements for SuperNEMO

The excellent results of the NEMO-3 experiment motivated the collaboration to improve the technology and to build a more sensitive experiment: SuperNEMO. The NEMO collaboration increased at that time with major contributions from USA and UK compared to NEMO-3.

The figure 2.6 is a good tool to illustrate the major improvements decided by the SuperNEMO collaboration compared to NEMO-3:

- **double beta decay isotope:** changing from ^{100}Mo to ^{82}Se allows to reduce the $2\nu\beta\beta$ background because of the longer half-life of ^{82}Se, $T_{1/2} = 9.39 \pm 0.17\,(stat) \pm 0.58\,(syst) \times 10^{19}$ y [Arnold et al., 2018], compared to $T_{1/2} = 6.81 \pm 0.01\,(stat) \pm 0.40\,(syst) \times 10^{18}$ y. This is almost a factor 14 reduction of the $2\nu\beta\beta$ event rate. The transition energy of ^{82}Se, $Q_{\beta\beta} = 2.995$ MeV, is almost unchanged compared to 3.035 MeV for ^{100}Mo. With our current knowledge of DBD, there is no correlation between the $2\nu\beta\beta$ and $0\nu\beta\beta$ decay rates that could disfavour ^{82}Se because of the longer $2\nu\beta\beta$ half-life. The phase space factor of ^{82}Se is a bit lower but the impact on sensitivity is moderate.
- **energy resolution:** the NEMO-3 energy resolution was about 15% at 1 MeV for the scintillators coupled to 5-inches PMTs. A dedicated R&D conducted in France allowed to reach an energy resolution of 7% with improved plastic scintillator blocks, larger 8-inches PMTs and an improved HV divider on the PMT basis [Marquet et al., 2015]. Reducing the energy resolution would further reduce the $2\nu\beta\beta$ and the internal backgrounds, by reducing the number of events in the $0\nu\beta\beta$ region of interest. A better energy resolution also allows to reduce the width of this ROI, further reducing the backgrounds.
- **increasing the DBD source isotopic mass:** the sensitivity of a double beta decay experiment scales with the isotopic mass (linearly for a background-free experiment or as the square root of the mass in the presence of background, see section 1.2). In the NEMO experiments, the source foils need to remain thin in order to limit energy losses and conserve the detection efficiency. Increase the size and the number of detectors is thus mandatory. The objective of the collaboration was to reach 100 kg of isotope compared to almost 7 kg in NEMO-3. In the presence of background, this would induce almost a factor four improvement on the sensitivity or a factor 14 if the background can be completely rejected.
- **investigate higher transition energy isotopes:** several double beta decay isotopes have transition energies above the main backgrounds from natural radioactivity such as ^{214}Bi with $Q_\beta = 3.27$ MeV and ^{208}Tl with $Q_\beta = 5.0$ MeV, including a γ-ray at 2.6 MeV. These isotopes are ^{96}Zr with $Q_{\beta\beta} = 3.35$ MeV, ^{150}Nd with $Q_{\beta\beta} = 3.37$ MeV and ^{48}Ca with $Q_{\beta\beta} = 4.27$ MeV. The SuperNEMO collaboration has initiated R&D towards the enrichment of these isotopes which have lower natural abundance or technical challenges to be enriched.
- **radon in the tracking detector:** the initial level of the radon background in the NEMO-3 detector was much higher than expected and justified the construction of the anti-radon tent and a de-radonised air factory at the LSM. Taking this into account in the SuperNEMO design and using well known protections against radon, conducted the collaboration to envisage a radon level in the tracking gas of 0.15 mBq m^{-3}, compared to 5 mBq m^{-3} in NEMO-3.
- **internal contamination of the isotopic sources:** the production of the enriched isotope and the manufacture of isotopic sources should be improved in order to decrease the internal backgrounds. This involves improving the selection of the constituting materials and manufacturing processes as well as implementing purification processes. Compared to the NEMO-3 ^{100}Mo composite sources[1] [Argyriades et al., 2009], the SuperNEMO requirements have been set to:

[1]The metallic molybdenum sources have a better radio-purity in NEMO-3 but the production of metallic selenium foils for SuperNEMO resulted in too fragile sources to be used.

- 10 µBq kg^{-1} in **^{214}Bi** instead of 300 ± 70 µBq kg^{-1} in NEMO-3
- 2 µBq kg^{-1} in **^{208}Tl** instead of 120 ± 10 µBq kg^{-1} in NEMO-3

Combining all these improvements should result in an almost negligible background ($2\nu\beta\beta$ and internal) of 5×10^{-5} counts/keV/kg/y in the SuperNEMO experiment, compared to 1.3×10^{-3} counts/keV/kg/y in NEMO-3. Investigating 100 kg of ^{82}Se over 5 years should lead to an half-life sensitivity of $T_{1/2}(0\nu\beta\beta) > 1 \times 10^{26}$ y. This could be translated into a sensitivity in the effective neutrino mass $\langle m_{\beta\beta}\rangle < 0.04 - 0.10$ eV, using the same nuclear matrix element than the final result of NEMO-3 (section 2.1.3).

2.2 The BiPo detector

The measurement of an activity of 2 µBq kg^{-1} in ^{208}Tl in the SuperNEMO source foils is extremely challenging. It represents only 63 decays per kilogram of material in a year. The radio-purity assays, generally preformed with HPGe detectors underground, are not sensitive to such levels and the detectors are extremely occupied. Measuring from several kg's to 100 kg over months or years would be impossible. In addition, the ^{208}Tl has a lower detection efficiency in the HPGe's because it is characterized by a high-energy γ-ray of 2.6 MeV. The shape of the SuperNEMO source foils is finally not well suited to be rolled into the limited space of HPGe detectors. Measuring the activity of the sources in their final shape is nevertheless the goal for the preparation of the SuperNEMO detector.

For all these reasons, the SuperNEMO collaboration started an R&D programme to develop a BiPo detector dedicated to the measurements of extremely low levels of ^{214}Bi and ^{208}Tl in thin source foils. These two isotopes, produced in the natural radioactivity decay chains of ^{238}U and ^{232}Th as illustrated on figure 1.14, are the most dangerous for the neutrinoless double beta decay search. The principle of the BiPo detector relies on detecting the coincidences between the β-decay of bismuth and the delayed α-decay of polonium. The ^{214}Bi activity can be directly measured this way in coincidence with ^{214}Po, while the ^{208}Tl activity can be measured through its parent, the ^{212}Bi decaying into ^{212}Po, after taking into account the branching ratios. The two isotopes can thus be assayed with the same detection technique and the time delay difference would allow to identify each isotope. Indeed the ^{214}Po half-life is 164 µs while the ^{212}Po half-life is 300 ns.

The BiPo detector is based on calorimetry technique with fast plastic scintillators readout by PMTs. The principle is to place the isotopic source foils between thin plastic scintillators and to detect the β and α-delayed coincidences at both sides of the source, as illustrated on figure 2.7 (left block). The decays can also be detected on the same side of the source but the contribution of the surface background should increase. Indeed the thickness of the SuperNEMO sources prevents α-particles to cross the full source, thus shielding half of the surface background. The detector efficiency has been determined by GEANT4 simulations to be 5.5% in the case of back-to-back events and 8.3% including the same-side events [Argyriades et al., 2010]. These efficiencies are reduced by the auto-absorption of the α-particles inside the source foils.

The backgrounds of the BiPo detector, presented on the three right blocks of figure 2.7, can be listed as:

- BiPo contamination on the surface of the scintillator
- BiPo contamination in the volume of the scintillator
- random coincidences of two independent particles

The first background type could be due to contaminations in the sputtered aluminium on the surface of the scintillators, serving as light reflector, or radon from the air penetrating between

the foil and the scintillator. The second type of background is negligible thanks to the excellent radiopurity of the scintillator material, demonstrated with the BiPo-1 prototype to be lower than 0.13 µBq kg^{-1} [Argyriades et al., 2010]. In addition, it can be further reduced thanks to the low threshold of the detector, because the β-particle would also deposit some energy in the contaminated scintillator where the decay occurred. The final background is due to random coincidences of two independent particles which are dominated by the γ-particles from the radioactivity of the PMTs or the detector materials. This background can be reduced thanks to the e/α pulse shape discrimination that was implemented in the BiPo detector [Bongrand, 2008], thanks to its excellent digitization electronics.

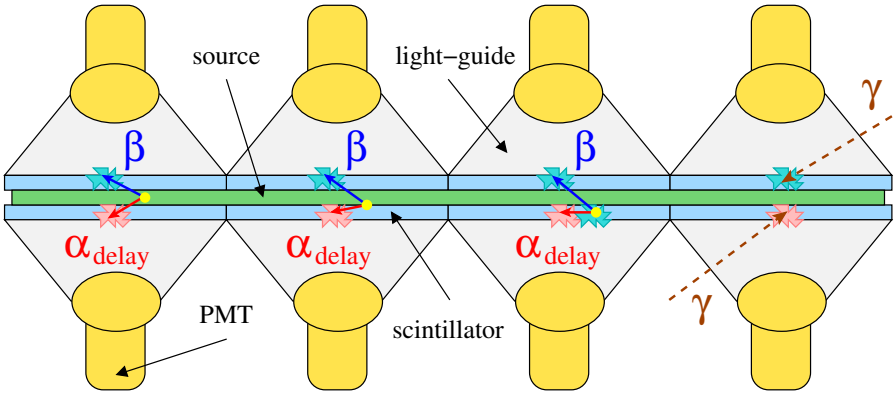

Figure 2.7: Illustration of the BiPo detection principle with, from left to right, contamination in the source foil, on the surface or in the volume of the BiPo scintillators and random coincidences.

The thickness of the scintillators has been optimized to 2 mm for the BiPo-3 detector in order to reduce the random coincidences rate. The scintillation light is collected through UV-transparent PMMA light-guides to 5-inch low radioactivity PMTs (Hamamatsu R6594-MOD). The design of the BiPo-3 light-guides has been optimized to improve the uniformity of the surface response, thanks to optical simulations from colleagues at CENBG Bordeaux. To enhance the light collection, the light-guides are covered with Tyvek masks preformed to the corresponding shape. The scintillators entrance faces are also aluminised to improve light collection and to reduce light-leaks. For the BiPo-3 detector, a brand new sputtering device has been used with improved cleaning procedures before the process. All the other passive detector components are mostly made of pure iron or polyethylene which have been selected through radiopurity assays. Massive shielding of lead and iron finally surrounds the BiPo-3 detector.

The PMT signals of the BiPo-3 detector are sampled with the 4 channesl MATACQ VME digitizer boards [Breton et al., 2005] during 2.5 ms time window with a high sampling rate of 1 GS/s, a 12-bit resolution, a high dynamic range of 1 V and an electronic noise of 250 µV. This time window has been divided in two in order to be sensitive to both ^{212}BiPo and ^{214}BiPo decay times. A dedicated acquisition has been developed by colleagues of LPC Caen to operate the BiPo-3 detector, register the data and process them for events reconstruction. An example of the digitized pulses of two BiPo candidates is presented on figure 2.8.

2.2.1 The BiPo prototypes

The BiPo R&D started during my PhD thesis and I was in charge of developing the first BiPo prototype, called BiPo-1 [Bongrand, 2008]. It was installed at LSM with an active surface of 0.8 m^2 divided in 20 modules with two face-to-face polystyrene-based scintillators of 200×200×3 mm^3 volume. This prototype, not comprising any source, was dedicated to the qualification of the intrinsic backgrounds. A ^{208}Tl surface activity of 1.5 ± 0.4 µBq m^{-2} has

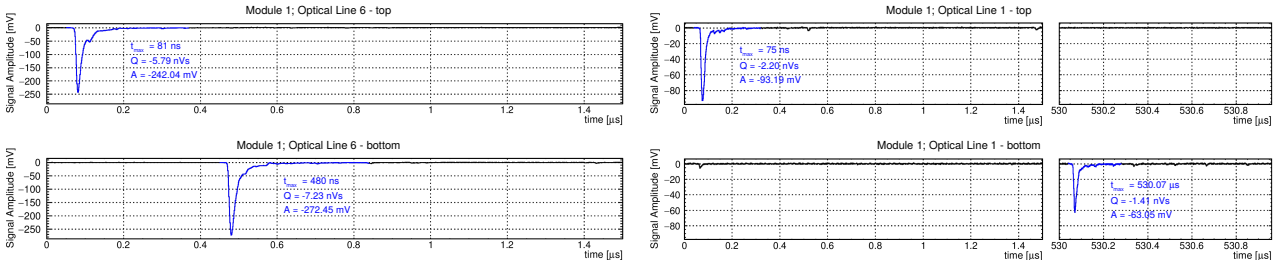

Figure 2.8: Example of the digitized pulses of two facing PMTs for ^{212}BiPo (left) and ^{214}BiPo (right) candidates. The short delayed decays can be found in the first sampling window, while the longer ones require a second trigger to use the remaining sampling window. Event display of Xavier Garrido.

been measured [Argyriades et al., 2010]. Extrapolating to a 12 m^2 BiPo detector, corresponding to the surface of the isotopic sources of a SuperNEMO detector, would allow to put a limit of <2 µBq kg^{-1} (90 % CL) in ^{208}Tl in 6 months, if no contamination were observed. The measurement of an aluminium foil, with a known contamination in ^{208}Tl, was also performed with BiPo-1 and demonstrated its capability to measure a thin source and recover the correct activity. The ^{214}Bi could not be measured during my thesis because an upgrade of the electronics was needed to pause the sampling window of the MATACQ boards to register a delayed signal up to few ms (corresponding to several half-lives of ^{214}Po), see figure 2.8 (right). Nevertheless, the random coincidences rate was measured and revealed not to be an issue to measure 10 µBq kg^{-1} in ^{214}Bi. The electronics upgrade was operated for the thesis of Arnaud Chapon, who took over the analyses of the BiPo-1 prototype, at LPC Caen [Chapon, 2011]. The ^{214}Bi studies revealed more complicated because of radon penetration in the detector, despite the anti-radon air flushing system already implemented in BiPo-1. A ^{214}Bi surface contamination of 150 ± 20 µBq m^{-2} was also measured, which was too high compared to the requirements. Improvements were thus needed to reach the ^{214}Bi sensitivity for the final BiPo-3 detector.

The first results of the BiPo-1 prototype were very encouraging and demonstrated the excellent capabilities of the BiPo technique. A second prototype, called BiPo-2, with a more sophisticated detection technique, with large polished scintillator plates readout by several PMTs for precise position reconstruction was also tested. The scintillators were not sputtered with aluminium which was suspected to be the major source of surface background. This prototype revealed not mature enough because of several problems like: high optical cross-talk between the two scintillator plates, high counting rate and no possible e/α discrimination because of the lower light collection level.

2.2.2 BiPo-3 detector construction

At the time of my recruitment at CNRS in 2009, the SuperNEMO collaboration decided to build the BiPo-3 detector dedicated to the qualification of the SuperNEMO sources. It inherited from the BiPo-1 prototype and improvements were identified to reach the ^{214}Bi sensitivity. For space constraints in underground laboratory and funding considerations, the active surface of the BiPo-3 detector was limited to 3.6 m^2. This would still offer an unprecedented sensitivity of 3-4 µBq kg^{-1} in ^{208}Tl in 6 months, according to BiPo-1 results.

The PhD thesis of Guillaume Eurin that I supervised consisted in building, commission, calibrate and operate the BiPo-3 detector [Eurin, 2015]. The work started in 2011 at the *Laboratorio Subterráneo de Canfranc* (LSC) in Spain with the tests of a small prototype, called the *pre-production module*, which is presented on figure 2.9. The goal of this pre-production module was to validate the final design of the detection cells (with scintillators of 300×300×2 mm^3) and to test the external shielding. Dedicated radon studies were also performed to determine

the optimal flushing of the detector with pure nitrogen gas, obtained by the evaporation in a liquid nitrogen tank. To fight against this background, several volumes with dedicated flushing were implemented and tested in the detector design, as can be seen of figure 2.9. This module was also used to qualify the surface background. After 29 days measuring the 0.09 m^2 surface, the improvements made for the construction of BiPo-3 were confirmed. For the ^{208}Tl, an upper limit of <8 µBq m^{-2} (90% CL) has been set. This is limited by the small surface compared to BiPo-1 but no sign of extra contamination was seen. For ^{214}Bi, which was the main objective of this test, only one event has been detected. This corresponds to a range of $[0.6, 24.5]$ µBq m^{-2} (90% CL) which is at least 6 times better than the BiPo-1 background.

This prototype was also the opportunity to build precise GEANT4 simulations of the BiPo detector, benefiting from the ongoing developments of the simulations for SuperNEMO. This was a major step to get the energy spectra of all the β and α decays and allowed to understand the corresponding shapes, which will provide better control of the background during source measurements. Given the small thickness of the scintillators, the calibration spectra from ^{54}Mn mono-energetic γ sources were not easy to fit and GEANT4 simulations were mandatory. This is why we developed the numerical method to adjust the calibration data with convoluted GEANT4 spectra, selected with a Kolmogorov-Smirnov test [Eurin, 2015]. This method is explained in section 8.2 where it was reused and improved for the calibration of SoLid detector.

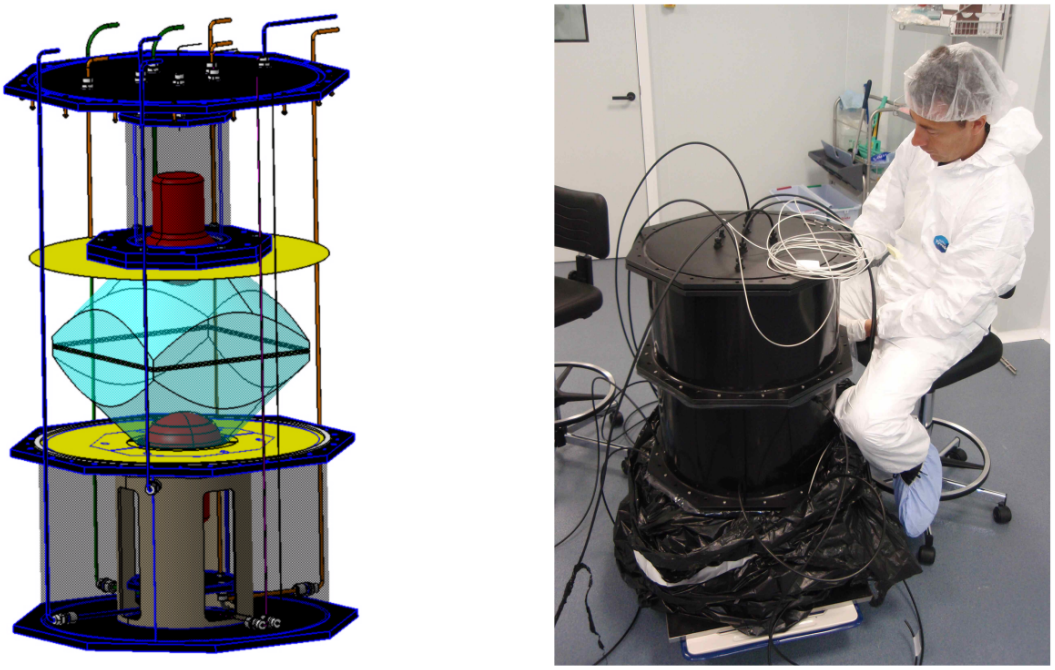

Figure 2.9: Illustration of the BiPo-3 pre-production module (left) which was tested at the LSC in Spain with a picture of its assembly in the LSC clean room (right).

After the validation with the pre-production module, the BiPo-3 detector construction stared in 2011 at LAL Orsay in a dedicated clean room. The BiPo-3 detector is illustrated on figure 2.10 and described in detail in the publication [Barabash et al., 2017b], with its first results. The two BiPo-3 detector modules, comprising 20 detection cells each, were transported underground and fully integrated inside the shielding tank (see figure 2.11) at the LSC in 2013. The thesis of Guillaume Eurin [Eurin, 2015] continued with the commissioning and the calibration of the BiPo-3 detector with the ^{54}Mn mono-energetic gamma source. A precise GEANT4 simulation study was necessary to determine the optimal source positions and the energy spectra collected by each scintillator, which depends on its position with respect to the calibration source. Details can be found in the thesis.

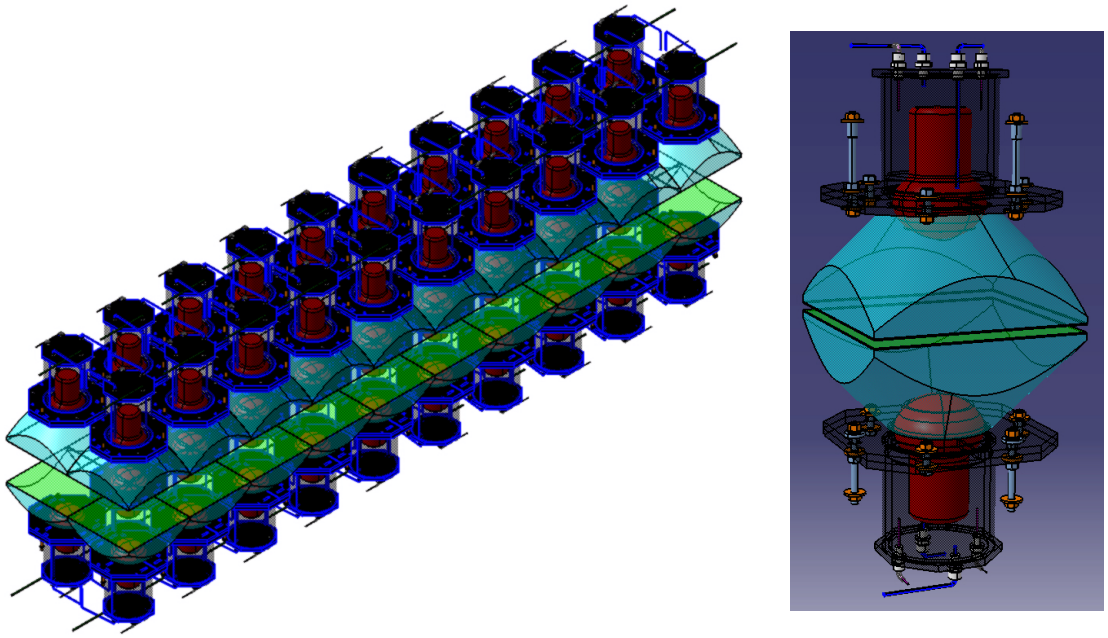

Figure 2.10: Illustration of the design of one module of the BiPo-3 detector (left) and the detail of one detection cell (right). The scintillators are represented in green, the light-guides in cyan, the PMTs in red which are all supported by a black polyethylene hat.

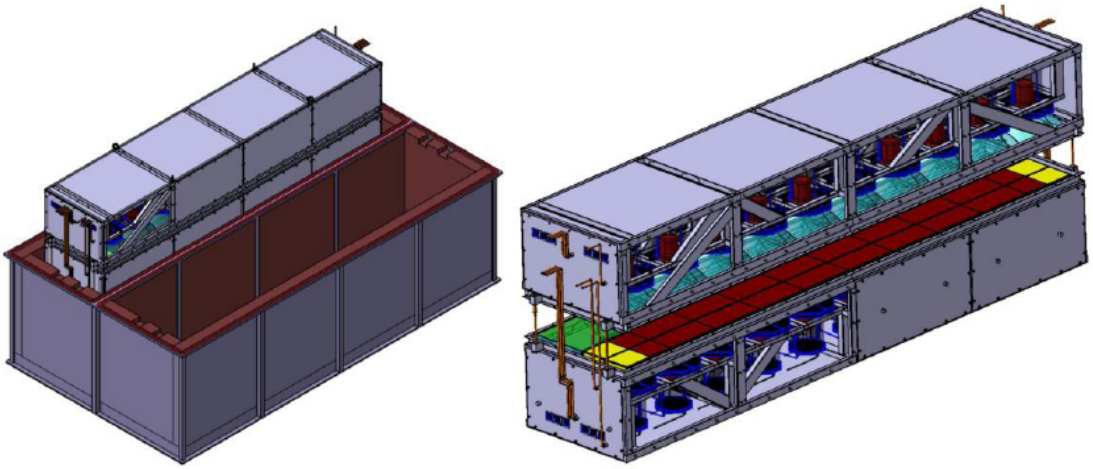

Figure 2.11: Illustration of the BiPo-3 shielding tank (left) with $3.9\times2.1\times1.4$ m^3 dimensions and the extraction of one module (right) to be opened in the clean room to introduce the SuperNEMO source foils, represented in yellow (mylar) and red (isotopic ^{82}Se source).

2.2.3 BiPo-3 results

The BiPo-3 detector was quickly operational after commissioning and calibrations. The first objective was again to determine the backgrounds. The ^{208}Tl background has been studied through the ^{212}BiPo channel over 200.4 days measurements with a scintillator surface area of 3.1 m^2, because of cabling defects. The surface contamination is dominating this background since the random coincidences rate is almost negligible in the 1 ms time window. The result was very uniform in space and time and in perfect agreement between the two modules. The prompt and delayed energy distributions of the 29 detected events are presented on figure 2.12. These

energy distributions correspond well to the simulated ones, which are adjusted by a likelihood fits. They also correspond well to β and α decay spectra. Compared to the theoretical one, the β-spectrum is pushed to the lower energy because of the small thickness of the scintillators, not fully containing the electrons tracks. The α-spectrum is peaked around 1 MeV, instead of 8.95 MeV, because of the quenching of the scintillation for α-particles. A thorough study of the quenching effect in the BiPo scintillators was also presented in [Barabash et al., 2017b]. From this result, the background surface activity has been determined to:

$$\mathcal{A}(^{208}\mathrm{Tl}) = 0.9 \pm 0.2 \ \mu\mathrm{Bq\,m^{-2}} \tag{2.3}$$

which is almost a factor two better than the BiPo-1 result cited before.

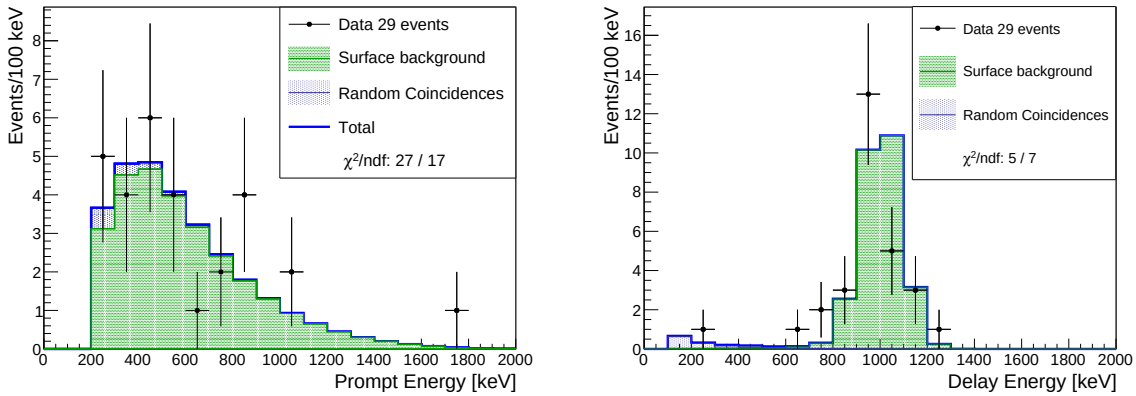

Figure 2.12: Distributions of the prompt energy (left), the delayed energy (right) for the ^{212}BiPo background measurements corresponding to 200.4 days of data collection and an effective scintillator surface area of 3.10 m^2. The data are fitted by the expected background from the ^{212}Bi contamination on the surface of the scintillators (green histogram) and from the random coincidences (blue histogram) [Barabash et al., 2017b].

In the ^{214}BiPo channel, the random coincidences rate becomes much higher because of the longer half-life of ^{214}Po, but it is well controlled by its flat delay time distribution. Since the shielding was not complete at the start of data taking, only 111.9 days have been used for the ^{214}Bi background measurement with a scintillator surface area of 3.24 m^2, because of a dead PMT. In addition to the random coincidences, an unexpected background appeared with a delay time distribution corresponding to ^{214}Po but with a degraded α energy, instead of the expected energy peak produced by the surface events. This means that the α-decays occurred further away from the scintillators and some energy was lost on the way to the scintillator. This background could be produced by radon surrounding the scintillators, which might not be fully covered on the lateral sides by the Tyvek mask. This was not seen in BiPo-1 detector for which the sides were tightly wrapped with Teflon, but it was no longer used for BiPo-3. This background was rejected by increasing the threshold of the delayed signal to 300 keV, with a counterpart of 60% efficiency reduction when measuring a source foil. The α peak of the surface background events can be extracted since it appears around 0.8 MeV instead of 7.83 MeV, because of the scintillation quenching. The ^{214}Bi surface contamination has been determined with the likelihood fit of the delayed energy spectrum to:

$$\mathcal{A}(^{214}\mathrm{Bi}) = 1.0 \pm 0.4 \ \mu\mathrm{Bq\,m^{-2}} \tag{2.4}$$

This level of contamination is a major improvement compared to the BiPo-1 prototype. It is also well distributed in space and time and compatible between both modules. However, an higher random coincidence rate has been observed compared to BiPo-1. This is certainly due

to a less efficient shielding. Indeed, at LSM the BiPo-1 prototype was shielded by 15 cm of very old lead, thus having a lower activity compared to the 10 cm of recent lead for BiPo-3. The radon level in the air at LSM (20 $\mathrm{Bq\,m^{-3}}$ [Hodák et al., 2019]) was also lower compared to LSC (50-80 $\mathrm{Bq\,m^{-3}}$ [Ianni, 2016]).

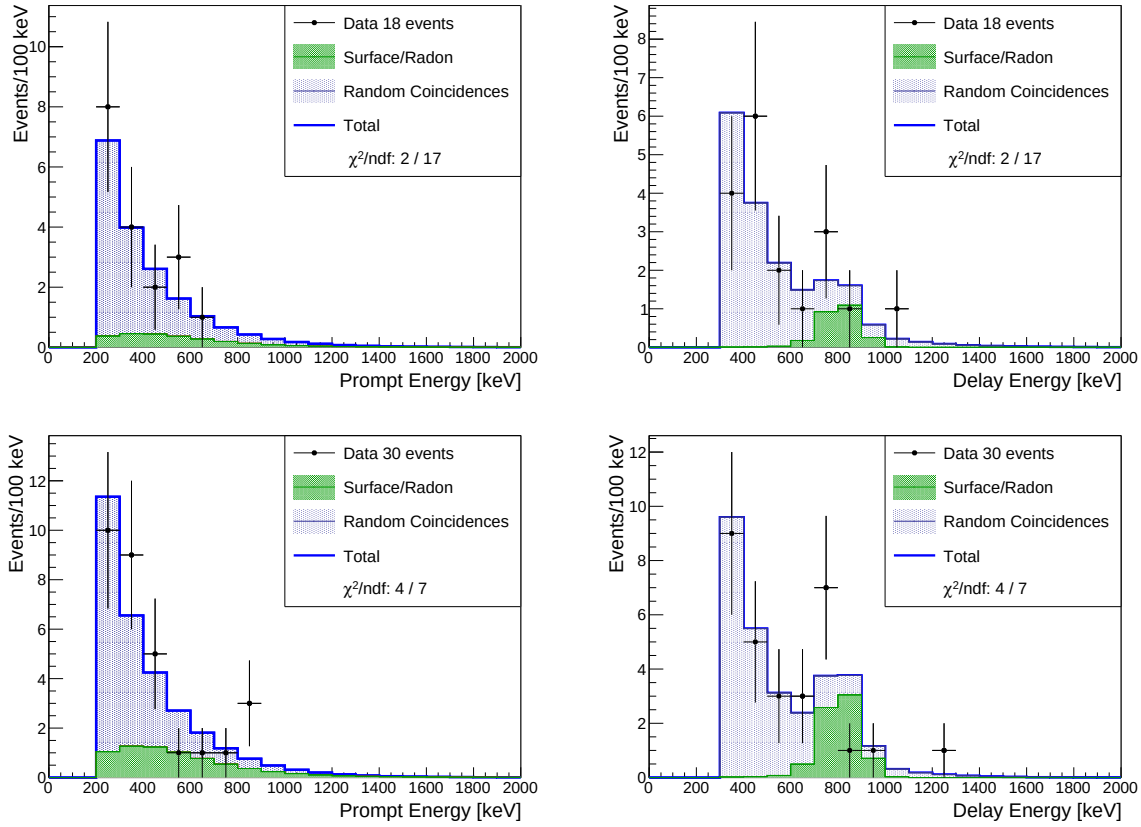

Figure 2.13: Distributions of the prompt energy (left), the delayed energy (right) for the ^{214}BiPo background measurements in the BiPo-3 module 1 (top) and 2 (bottom). The results for Module 1 corresponds to 36.2 days of measurement and an active scintillator surface area of 3.06 $\mathrm{m^2}$. The results for Module 2 corresponds to 75.7 days of measurement and an active scintillator surface area of 3.42 $\mathrm{m^2}$. The data are fitted by the expected background from the ^{214}Bi contamination on the surface of the scintillators (green histogram) and from the random coincidences (blue histogram) [Barabash et al., 2017b].

The BiPo-3 detector development has been very successful over one decade and has demonstrated sensitivities of 2 $\mu\mathrm{Bq\,kg^{-1}}$ (90% CL) for ^{208}Tl and 140 $\mu\mathrm{Bq\,kg^{-1}}$ (90% CL) for ^{214}Bi in 6 months measurements of the isotopic SuperNEMO sources. The BiPo-3 detector has also been decisive to select the materials to use for the source foil production like raw mylar, perforated mylar by irradiation, PVA glue, Se powder... All the SuperNEMO source foils have been qualified in the BiPo-3 detector before integration in the SuperNEMO demonstrator and LSM. The results are reported in section 3.3. For illustration purpose, the energy distributions of the four first SuperNEMO strips measured from August 2014 to June 2015 are presented on figures 2.14 and 2.15. Thanks to the strong energy losses of the α-particles, the origin of the contamination can be identified: surface background, irradiated Mylar, internal mixture of ^{82}Se and glue or random coincidences. The relative level of each background is determined through a likelihood fit on the delayed energy spectra.

After the SuperNEMO sources campaign, the BiPo-3 detector has measured some materials for other experiments. After some years, the DAQ and the electronics started to show weaknesses and an upgrade would have been necessary to maintain the detector. It has been

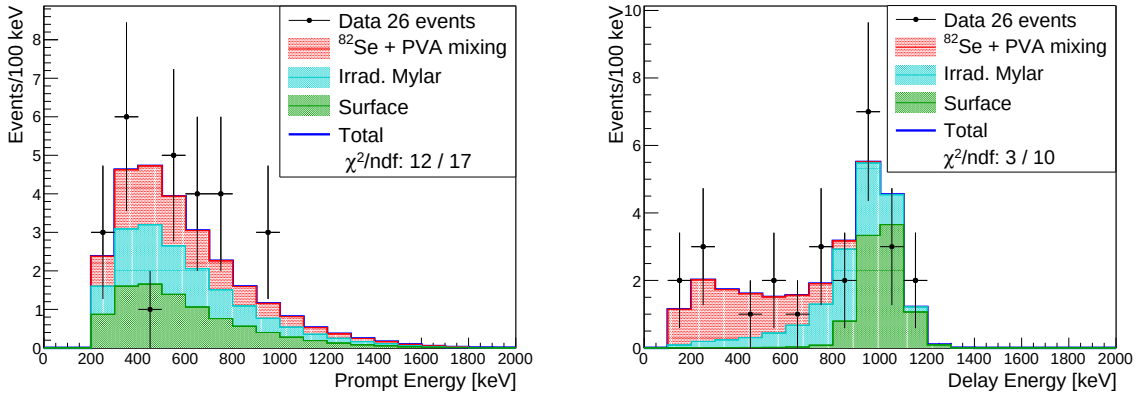

Figure 2.14: Distributions of the prompt and delayed energy for the ^{212}BiPo measurement of the four first enriched ^{82}Se SuperNEMO foils, with 262 days of data collection, an effective mass of ^{82}Se+PVA mixture of 359 g and a surface area of measurement of 2.13 m^2. The data are compared to the expected background from the ^{212}Bi contamination on the surface of the scintillators (green histogram) and in the irradiated Mylar (light blue histogram). The excess of observed events with a low delayed energy corresponds to a ^{212}Bi contamination inside the Se+PVA mixture (red histogram) of $17.8^{+16.4}_{-11.5}$ µBq kg^{-1} (90% CL) [Barabash et al., 2017b].

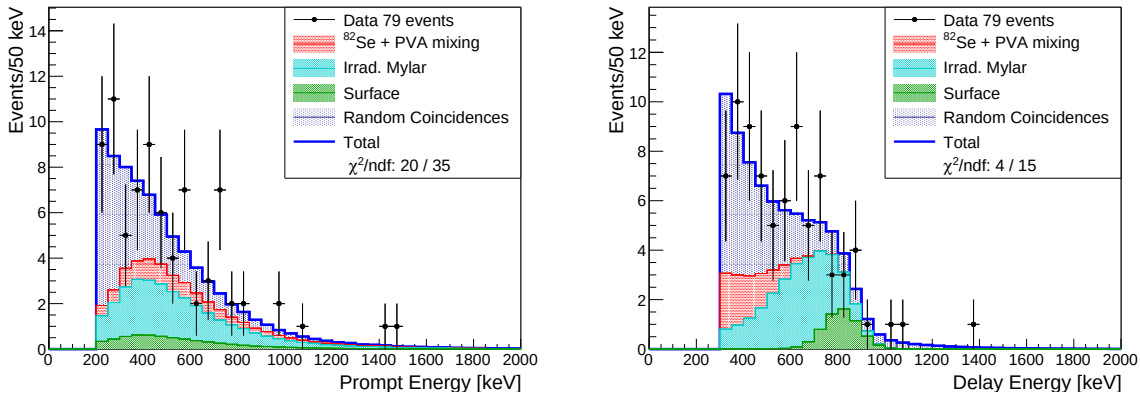

Figure 2.15: Distributions of the prompt and delayed energy for the ^{214}BiPo measurement of the four first enriched ^{82}Se SuperNEMO foils, with 241.1 days of data collection, an effective mass of ^{82}Se+PVA mixture of 352 g and a surface area of measurement of 1.97 m^2. The data are compared to the expected background from the random coincidences (dark blue) and from the fitted ^{214}Bi contamination on the surface of the scintillators (green histogram) and in the irradiated Mylar (light blue histogram). A slight excess of data events (1.35σ) can be attributed to a contamination of the ^{82}Se+PVA mixture. The significance of this excess is too low to extract a value, thus an upper limit of the ^{214}Bi activity of $\mathcal{A}(^{214}\text{Bi}) < 300$ µBq kg^{-1} (90% CL) has been set (red histogram) [Barabash et al., 2017b].

switched off in 2018 and dismantled afterwards.

Conclusion

This chapter presented the details of the NEMO-3 experiment and its final result in the search for $0\nu\beta\beta$: $T^{0\nu\beta\beta}_{1/2}(^{100}Mo) > 1.1\times10^{24}$ y at the 90% CL corresponding to $\langle m_{\beta\beta}\rangle < 0.33-0.62$ eV. This result has been driving the preparation of the successor SuperNEMO experiment and the possible improvements achievable thanks to several R&D efforts performed in the collaboration. Among them, we have presented the development of the BiPo detector dedicated to the measurement of extremely low contamination levels of ^{214}Bi and ^{208}Tl for the preparation and the

final qualification of the SuperNEMO source foils. The objectives for the 100 kg SuperNEMO experiment have not been achieved yet, but the levels correspond to a major improvement compared to NEMO-3 and offers still a very good sensitivity to the SuperNEMO demonstrator. If the background levels can be controled for the 100 kg experiment, the SuperNEMO sensitivity could reach $T_{1/2}^{0\nu\beta\beta} > 1 \times 10^{26}$ y, corresponding to $\langle m_{\beta\beta} \rangle < 0.04 - 0.10$ eV.

Chapter 3

The SuperNEMO demonstrator

This chapter is dedicated to the SuperNEMO demonstrator and its integration at LSM. From the beginning of the underground integration in 2015 and up to the closure of the internal detector in 2018, I was the *scientific responsible* for the demonstrator integration. I was closely working with the technical coordinator, Cedric Cerna from CENBG, and Christian Bourgeois from LAL, the mechanical coordinator. The integration at LSM is foreseen to finish in 2024, by the massive shielding integration.

All along the detector integration, I have encouraged the involvement of the PhD students of France in the integration tasks. Guillaume Eurin [Eurin, 2015] has been involved in the tracker construction in UK, Steven Calvez [Calvez, 2017] and Delphine Boursette [Boursette, 2018] participated to the calorimeter integration and tests underground. In addition, the PhD thesis of Delphine, that I supervised, comported a work on the simulation of the external background and its measurement on copper foils, which will be presented here. Cloé Girard-Carillo [Girard-Carillo, 2020] participated to the calorimeter cabling with the construction of the cables and their routing on the detector at LSM, along with the electronics installation.

Chapter contents

Introduction

To study an isotopic mass of 100 kg with a surface density of 40 mg cm^{-2}, the SuperNEMO experiment would need to build about 20 detectors with 12.5 m^2 surface of sources. The thickness of the foils, which has been minimised to reduce the energy losses of the DBD electrons, imply to increase the source surface compared to calorimetric experiments. This represents the major difficulty of the NEMO technology, to reach a sufficient isotope mass for a high sensitivity in terms of $0\nu\beta\beta$ half-life. Having 20 detectors underground was under consideration at the time of building the second gallery of the Fréjus road tunnel, between France and Italy. This major civil work represented an opportunity to build an extension of the LSM, with a new experimental hall up to 100 m long. Unfortunately, this project did not materialized.

Nevertheless, the SuperNEMO experiment started with the construction of a first detector, called the *demonstrator* comprising almost 7 kg of ^{82}Se. It is similar to the NEMO-3 detector in size and technology but includes many improvements of the detector performances, which were obtained after intensive R&D phases. The goal of the SuperNEMO demonstrator is to confirm the R&D improvements and to prove the feasibility of a larger scale experiment, in terms of detector performances and background reduction. The objective is to reach a background free experiment at 100 kg mass scale, where the sensitivity would increase linearly with the exposure time, see chapter 1.

3.1 Principle of the SuperNEMO experiment

The SuperNEMO experiment is unique compared to the actual DBD experiments in using a combination of a tracking detector and a segmented calorimeter, enclosing the passive isotopic source. This technique allows to detect directly the two electrons emitted from the same location of the source, measure their trajectories, individual energies and times of flight. Thus, it offers a complete signature of the DBD events with the full kinematics reconstruction, which would be a "smoking gun" in case of $0\nu\beta\beta$ discovery. It would also offer the chance to study the underlying mechanism of the decay and possibly probe new physics, which is only possible with SuperNEMO [Arnold et al., 2010] for now. The isotopic source being independent of the detector, almost all the metallic isotopes could be investigated in SuperNEMO, in the case of discovery in another experiment. This techniques has also tremendous advantages to study and reject the backgrounds thanks to particles identification of e^-, e^+, γ, α and $\mu^\pm$. However, these features come at the cost of a lower detection efficiency and a poorer energy resolution, compared to pure calorimetric experiments, as presented in section 1.2.

The figure 3.1 illustrates the detection principle of a DBD event, top view, in the SuperNEMO detector. The two electrons are emitted from a vertical thin source foil enriched with a specific isotope, their trajectories are reconstructed in three dimensions, in the magnetised tracking chamber composed of vertical drift cells to end up in the plastic scintillators and measure the arrival times and energies. The curvature of the electron tracks in the magnetic field and the time of flight analysis ensure that the two electrons are emitted from the source and the event does not correspond to a crossing electron. This complete signature is very powerful to reject the backgrounds.

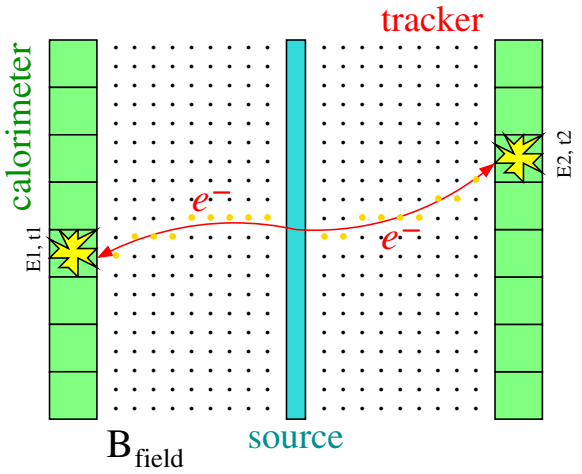

Figure 3.1: Two dimensional top view of the detection principle of two electrons from a double beta decay in the source of the SuperNEMO experiment.

3.2 Design of the demonstrator

The SuperNEMO demonstrator has adopted a planar geometry in order to be divided in subdetectors with specific functions: isotopic source and calibration frame, tracker sections, calorimeter walls, magnetic coil and shielding. This permitted the construction in parallel in the different institutes of the collaboration. It was also a way to facilitate the integration of such a big detector at LSM with important space constraints. The objective was also to keep the possibility

to reopen the detector after the study of ^{82}Se to investigate another isotope, like ^{150}Nd if the enrichment R&D turns out to be successful.

The design of the SuperNEMO demonstrator is presented in figure 3.2. In the center of the detector we can find the source frame, holding the vertical strips of the selenium sources but also the deployment system of the calibration sources. This frame is surrounded by two tracking detectors of 44 cm depth with the vertical drift cells. These trackers also integrate calorimeter modules on the sides (X-walls) to detect electrons from the sources and other modules on top and bottom (G-vetos), to detect γ's since the extremities of the drift cells will cover these modules for electrons. These modules help to maximise the calorimetric coverage of the detector. The tracking volumes are then closed by two main calorimeter walls (M-walls) with optimised performances in timing and energy resolution. A copper magnetic coil embraces all these sub-detectors, to impose a curvature to the electron tracks. To protect the detector from the radon present in the air of the laboratory, a gas tight anti-radon tent is enclosing the demonstrator. This tent includes several gas tight patch-panels for the cabling of the detector elements. The internal volume of the tent is flushed with de-radonised air produced by a dedicated factory at LSM [Hodák et al., 2019]. The detector is finally surrounded by a gamma shielding made of steal and a neutron shielding made of water tanks and polyethylene.

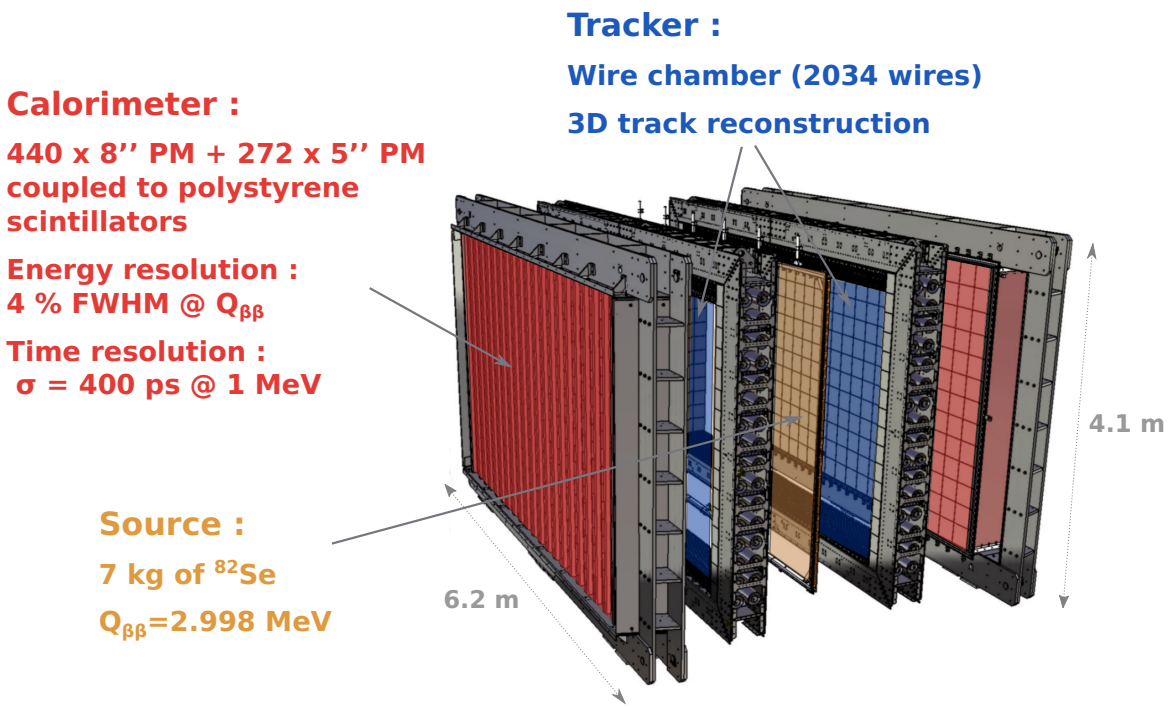

Figure 3.2: Overview of the SuperNEMO demonstrator detector in a splitted view.

As already mentioned, the SuperNEMO demonstrator replaces the NEMO-3 experiment at LSM. The planar sub-detectors are assembled onsite thanks to an integration clean room and a support structure that will support each sub-detector from the top, as presented on figure 3.3. The clean tent is made of aluminium profiles and polycarbonate panels. The panels can be easily removed to introduce sub-detectors or large pieces. Flushed by 12 fanjets HEPA filters on the top and exhausts at the bottom, an ISO7 cleanliness level has been reached. Temporary curtains can also be installed to separate volumes inside the tent to introduce sub-detectors or to work in different conditions. The support structure is made of three massive iron I-beam frames connected to each other. The sub-detectors are hanging on these beams with travelling

crane trolleys. Thanks to this, the sub-detectors can be easily moved when needed and latter brought together at the final position for sealing, see figure 3.4.

Figure 3.3: (left) Picture of the integration iron support structure at the location of the former NEMO-3 experiment at LSM. (right) Picture of the inside of the clean tent (before general cleaning) installed on the support structure with the top fanjets blowing clean air (right).

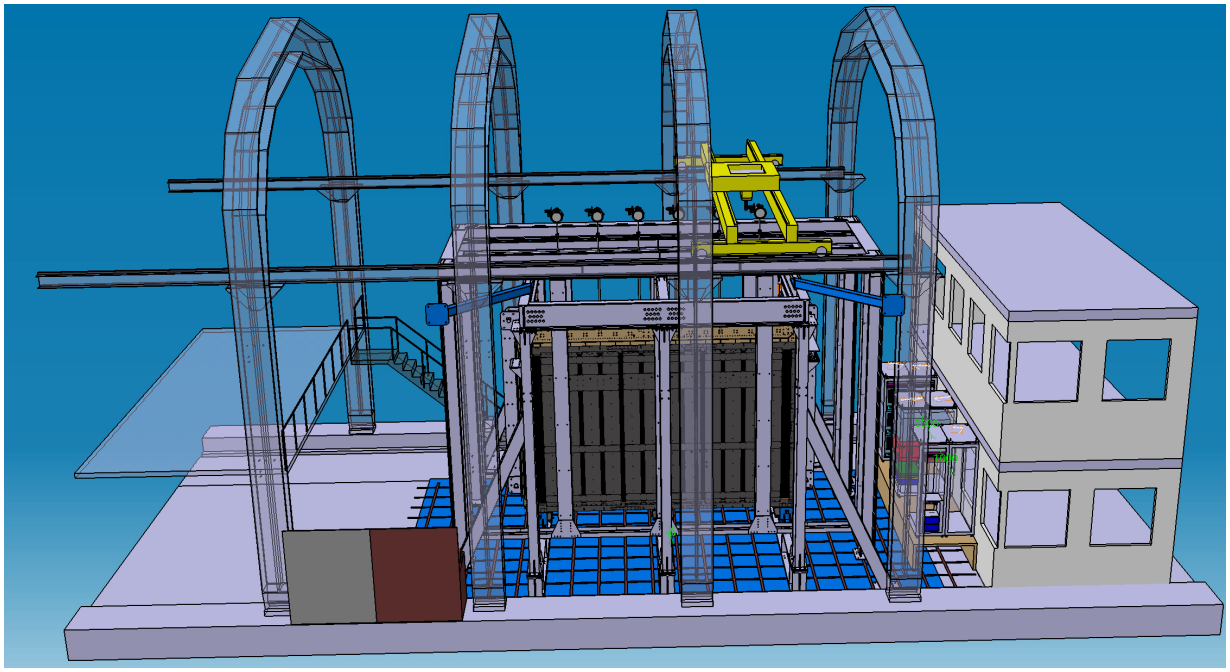

Figure 3.4: Illustration of the SuperNEMO demonstrator installed at LSM on its support structure before the installation of the anti-radon tent and shielding. The entrance mezzanine on the left, the LSM crane and the former Edelweiss hut on the right are also represented (dismantled in 2023).

3.3 The isotopic source

The isotopic source represent the heart of the SuperNEMO experiment. In consequence, extreme care needs to be taken in order to avoid radioactive contaminations all along the fabrication process of the sources. The sources of the SuperNEMO demonstrator consist of 36 vertical strips of 135.5 mm wide and 2.7 m high. The source strips are supported in a pure copper frame, thanks to delrin rolls attached to the mylar extensions of the foils which are hooked to the frame.

3.3.1 ^{82}Se sources

The choice of ^{82}Se, as the main isotope for SuperNEMO, has been already motivated by physics considerations in section 2.1.4. A general discussion about the choice of the isotopes for double beta decay experiment has been presented in section 1.2.2. To maximise the physics reach of the demonstrator, the thickness of the foils has been set to around 50 mg cm^{-2} (290 µm on average). In total, the demonstrator sources contains 6.25 kg of ^{82}Se.

The ^{82}Se for the SuperNEMO demonstrator has been enriched by gaseous centrifugation in Russia. A SeF_6 gas is formed from natural selenium which is then centrifuged to isolate the heavier almost stable isotope, which is ^{82}Se. An enrichment factor above 96% has been obtained. After centrifugation, the gas is exposed to electrical discharges to produce an enriched selenium powder. Radioactivity measurements of this enriched powder have shown that the enrichment process must be complemented with a purification process. Several purification techniques have been tested for the demonstrator: double distillation, chemical purification or reverse chromatography [Rakhimov et al., 2020]. These techniques have been successfully tested in the NEMO-3 experiment [Arnold et al., 2005]. The purified selenium produced with these processes comes in a form of powder or metallic blocks. To built the SuperNEMO sources, the selenium must be grinded into fine powder with grains smaller than 45 µm. The selenium powder is then mixed with a radiopure polyvinyl alcohol glue (PVA) with the proportions 92% and 8% respectively. To support the mixture, it is necessary to incorporate it between two films of 12 µm thick mylar. For this encapsulation, two techniques have been used in the SuperNEMO demonstrator:

- **the NEMO-3 method** uses a perforated mylar, called *backing film*, produced by ion beam irradiation followed by chemical etching with NaOH at 70°C and acetic acid rinsing. Inside a clean room, the Se+PVA mixture is spread on one layer of this backing film into a mold with the shape of the SuperNEMO strips. A delrin roller is used to spread uniformly the mixture and control the thickness of the foils. A second layer of backing film is added on top of the mixture and is left as it is, for drying over 10 h. This drying would be impossible without perforating the mylar. In total, 19 foils have been produced with this NEMO-3 method for the SuperNEMO demonstrator.

- **the LAPP method** was developed to get rid of the perforated mylar and improve the radiopurity of the sources after a dedicated R&D [Jeremie et al., 2022]. The method consists in first preparing stand-alone selenium pads and then wrapping them in the 12 µm raw mylar. Intermediate welding of the mylar between pads are then realized. Addition of 10% of iso-propanol to the mixture just before spreading it in the mold improved the uniformity in selenium and the flatness of the pads. The geometry with the stand-alone pads and the raw Mylar film with eight pads was chosen. This number of pads and soldering lines was also optimized to ease the handling of the sources. In total, 15 foils have been produced with the LAPP method for the SuperNEMO demonstrator.

The BiPo-3 detector has been used to measure the materials of the SuperNEMO sources, the results are presented in the table 3.1. The mylar before irradiation and the PVA are very pure in ^{208}Tl. On the other hand, the irradiated mylar is contaminated. For ^{214}Bi, no excess of events has been observed for the bulk contamination. Limits have been set but they are relatively high because of the important background and the higher threshold used in the ^{214}BiPo channel, see section 2.2.3. However, an excess of surface contamination in ^{214}Bi has been observed on the irradiated mylar and the PVA, which doesn't appear from these total activity numbers.

Sample	$\mathcal{A}(^{208}\mathrm{Tl})$ [µBq kg^{-1}]	$\mathcal{A}(^{214}\mathrm{Bi})$ [µBq kg^{-1}]
Raw mylar	< 49	< 195
Irradiated mylar	90^{+63}_{-42}	< 690
PVA	< 12	< 505

Table 3.1: Results of the BiPo-3 measurements of the components of the SuperNEMO source foils [Loaiza et al., 2017, Jeremie et al., 2022]. Limits are given at 90% CL.

As already mentioned, almost all the SuperNEMO source foils have been measured in the BiPo-3 detector. In order to compare the different purification methods and the production methods, five batches of selenium have been virtually gathered for comparison purpose [Jeremie et al., 2022]. Batch 1 is the selenium that was recovered from NEMO-3 and reused. Batches 2 and 6 were purified recently with the novel and robust reverse chromatographic method. They differ by the time of preparation. The three other batches (3, 4 and 5) were purified with more classical methods (chemical or double distillation) in different laboratories. The results of these radiopurity measurements from the BiPo-3 detector are summarized in table 3.2. These results show that we have not yet reached the radiopurity levels targeted for the 100 kg SuperNEMO experiment. Large statistical uncertainties are still to consider because of the low mass of the samples and since none of the foils were measured for the six months required for the maximum sensitivity of BiPo-3, but closer to half that time. Batches 1 and 2 give the best radiopurity results, the first being the double distilled ^{82}Se used in NEMO-3 and the second one has been purified with the novel reverse chromatographic method. In ^{208}Tl, the central value is a least a factor five better than NEMO-3. These two batches also have the highest enrichment factor. Batches 3 and 4 could not be measured because of time pressure to close the SuperNEMO demonstrator. In the 2.5 years of data taking, the activities will be very well measured but the levels reported here are already very good for $0\nu\beta\beta$ search with the demonstrator.

Batch	Se mass [kg]	Purification	Production	$\mathcal{A}(^{208}\mathrm{Tl})$ [µBq kg^{-1}]	$\mathcal{A}(^{214}\mathrm{Bi})$ [µBq kg^{-1}]
1	1.95	double distillation	NEMO-3	24^{+14}_{-11}	< 290
2	1.5	reverse chromatography	LAPP	22^{+32}_{-14}	< 595
5	1.4	double distillation	LAPP	131^{+112}_{-68}	< 525
6	0.97	reverse chromatography	LAPP	< 106	< 1374

Table 3.2: Results of the BiPo-3 measurements of all the SuperNEMO source foils gathered in five batches to compare purification and production methods [Jeremie et al., 2022]. Limits are given at 90% CL.

3.3.2 Copper sources

In the PhD thesis of Delphine Boursette [Boursette, 2018], we have investigated the interest to add copper foils in the demonstrator to study and measure the backgrounds produced in non-active foils. This strategy was already used in NEMO-3 [Argyriades et al., 2009], but was not considered at first for SuperNEMO. As the copper is not a double beta emitter and is among the best radiopure metals, most of the events detected from these foils would be produced by external backgrounds or radon in the tracking chamber. Delphine simulated the copper foils at the edge of the detector with the SuperNEMO source foils dimensions[1]. Taking the internal background activities determined from the one electron channel analysis in NEMO-3 [Argyriades et al., 2009], Delphine simulated the expected energy spectra of the two electron events in SuperNEMO produced by internal background in 2.5 years, see figure 3.5 (left). The external background should be dominated by the radioactivity of the PMTs, thanks to the massive shielding that will be placed around the SuperNEMO detector. Delphine simulated also this external background to build the expected energy spectra of the two electron events, as shown on figure 3.5 (right). About 90 events with two electrons are expected for both internal and external backgrounds.

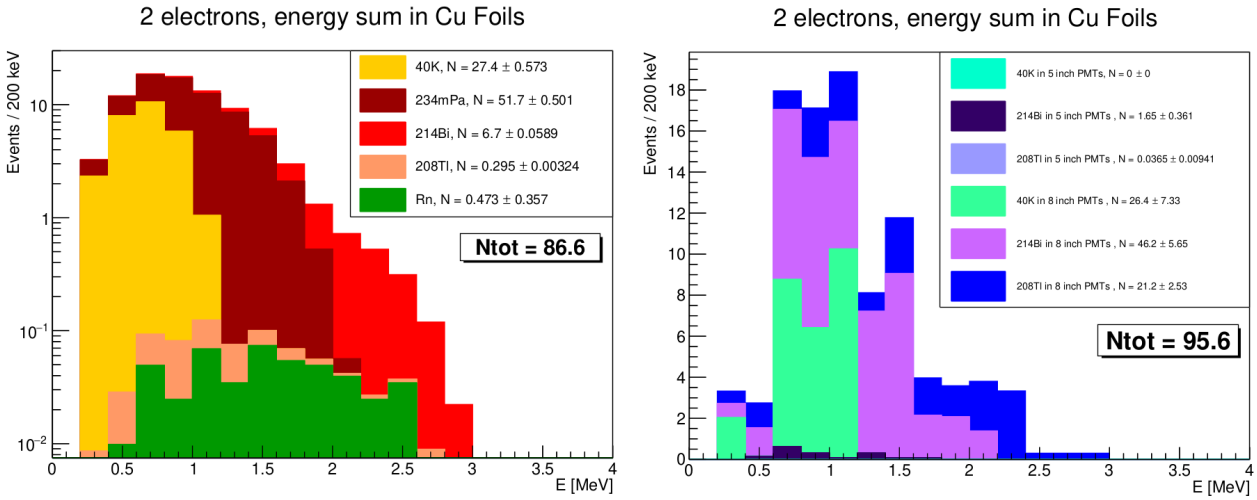

Figure 3.5: Simulated energy sum of the two electrons produced by internal (left) or external (right) backgrounds from the copper SuperNEMO sources in 2.5 years [Boursette, 2018].

In conclusion, the study has shown that in 2.5 years, the two copper foils would be sensitive enough to control the external background in the two electrons channel with an accuracy around 10% [Boursette, 2018], independently from the ^{82}Se internal background. This result encouraged the SuperNEMO collaboration to install copper foils in the demonstrator. Two radiopure copper foils, 125 mm wide[2] and 2500 mm long, from the 57.5 µm thick radiopure copper used in NEMO-3, have thus been produced at LAPP in the same conditions than the selenium sources. The copper foils were glued with stycast to raw mylar foils on top and bottom to be supported in the source frame. They were installed at the two edges of the source frame (strips 1 and 36). The total mass of copper is about 0.32 kg.

3.3.3 Source frame and foils integration at LSM

The source frame is made of pure copper profiles for radiopurity reasons. The four beams have a U-shape of 60 mm high and 58 mm depth. This frame has been assembled at LSM directly

[1] with a thickness of 63 µm as first expected, but more precise measurements conducted to 57.5 µm.
[2] the width available for the two edge strips is reduced compared to the middle ones of 135.5 mm.

on one tracker frame (figure 3.6), because it is not self-supporting. The source foils dimensions and positions have been optimized relatively to the ^{207}Bi calibration sources positions, to ensure a good uniformity of the calorimeter blocks coverage. There are six slots for the calibration deployment system, placed every six source foils, starting three foils from the edges. This sub-detector was in charge of our colleagues from University of Texas (UT) at Austin.

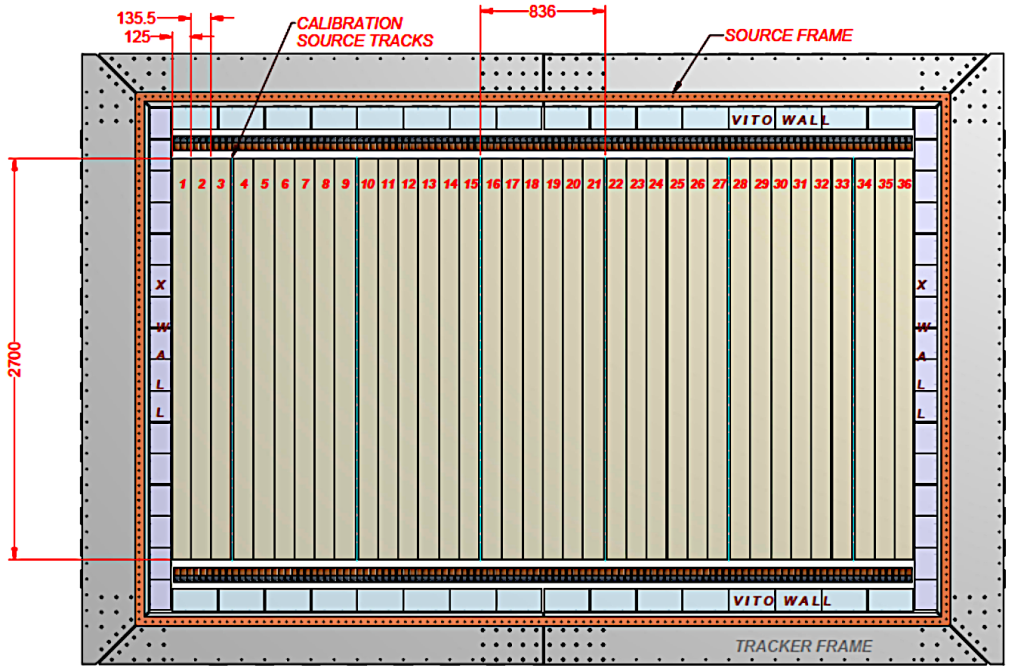

Figure 3.6: Illustration of the SuperNEMO copper source frame integrated on one tracker frame. The dimension and positions of the two edge copper foils and of the 34 ^{82}Se source foils, as well as the 18 mm space for the calibration sources deployment, are also presented.

All the source foils have mylar ends with holes to be attached to radiopure delrin rolls, which can be hooked into place on top and bottom of the source frame. The installation of the foils has been done by UT and LAPP teams, while the demonstrator was opened, between the two tracker halves. For the installation process, a pulley was attached to the top of the demonstrator with a wire and a foil attachment system. The foil was then slowly pulled up. The top end was then hooked into place, and the bottom one was tensioned into place. The foil tension can be adjusted at the bottom by rolling more or less the mylar on the delrin roll, thanks to attachment holes 1 mm apart. To ensure maximum surface coverage, without space between the foils, the fixation systems are alternatively facing opposite directions. All the foils after installation at LSM can be seen on figure 3.7.

The foils in place in the demonstrator have been measured by laser tracking with a Leica T-Scan 5, which spatial resolution is a fraction of millimetre. Figure 3.8 shows the result of this global survey of all the foils. Both types of foils can be distinguished as well as the ^{207}Bi calibration sources that where deployed between the foils for the survey. The two shorter copper foils at each extremity are also visible. This survey has become necessary because we have observed that the foils were unfortunately not completely flat. This can be seen on the top panel of the figure where the effect has been slightly enhanced to have a better view of the shapes. This curvature occurred because of shrinking during the drying process. The classical foils have a more or less pronounced inward curve. The extremities are less curved than the centre. The foils made with the novel method are globally flatter thanks the mechanical constraint added by the regularly spaced transverse soldering, in addition to the fact that the pads were soldered with alternate positions regarding the surface that was on top during the drying process.

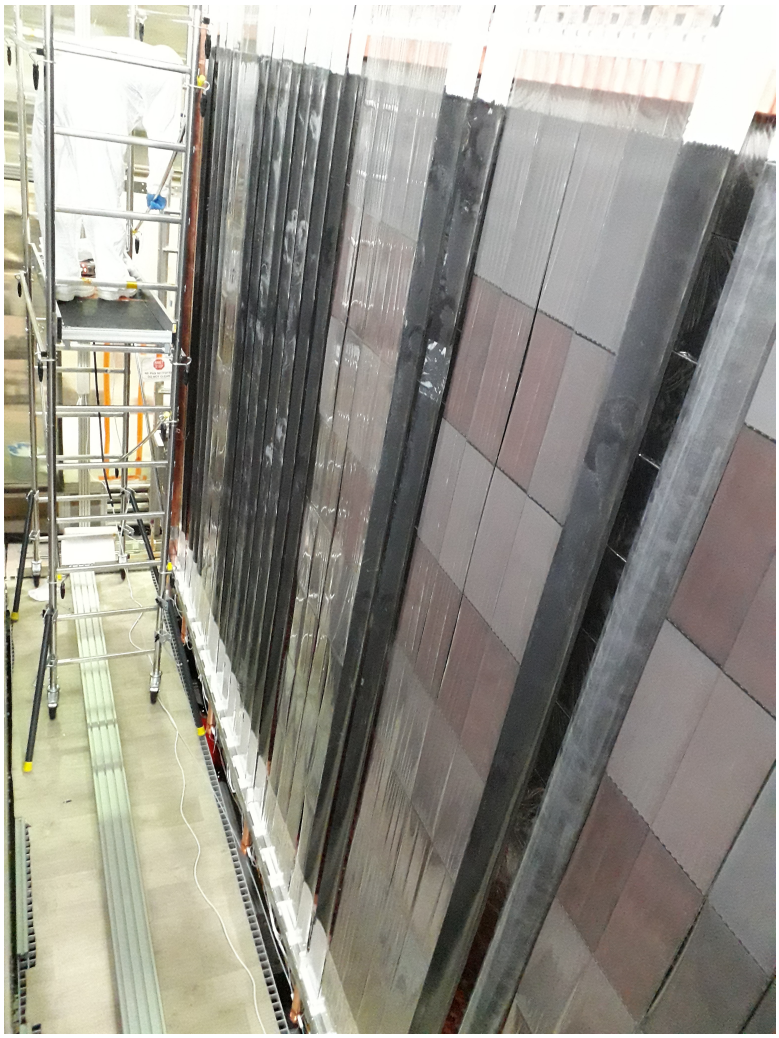

Figure 3.7: Picture of all the SuperNEMO source foils installed on the source frame at LSM. We can observe the classical foils produced with the NEMO-3 method in one piece and the foils made with the novel LAPP method with its eight pads.

The exact source foils shapes have been implemented in the SuperNEMO simulation and its impact on the DBD detection is being investigated.

3.4 The tracker

The double beta decay electrons escape the source foils to enter the tracking chamber. The goal of SuperNEMO tracker is to determine precisely the location of this escape point from the sources, called the vertex. This is of major importance to make sure the two electrons come from the same decay and to reduce the backgrounds. The curvature of the electrons, under magnetic field deviation, also needs to be measured over the depth of the tracker. A major requirement for the tracking detector is to minimize the energy losses of the electrons travelling in the tracker. Finally, the tracker needs to determine in which calorimeter block the electron ended. The determination of the precise location on the entrance face of the scintillator is an asset to improve the energy measurement. Indeed, the geometrical light collection in the scintillator towards the PMT can induce percent level differences, depending on the location of the interaction on the surface of the scintillator.

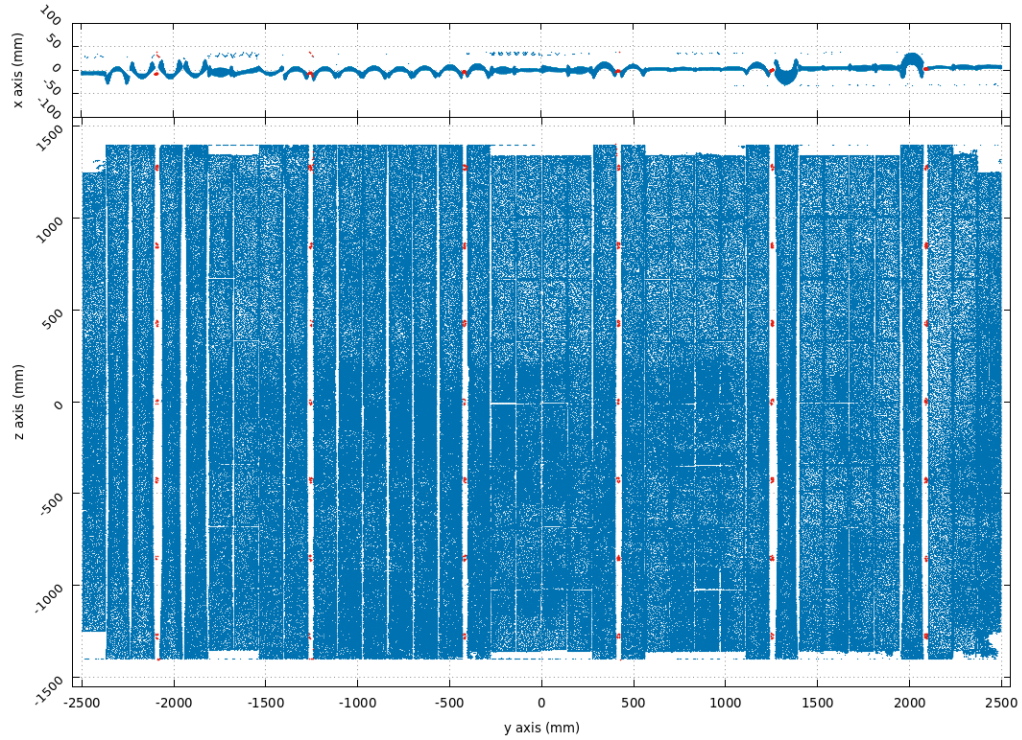

Figure 3.8: Result of the laser survey of the SuperNEMO source foils for top and front views. The two copper foils, the 19 NEMO-3 like foils and the 15 LAPP foils can be seen. The ^{207}Bi calibration sources that were deployed for the survey, can also be seen in red.

3.4.1 Tracker design

The SuperNEMO tracker was the responsibility of the UK colleagues in several institutes. It inherits from the NEMO-3 technology: vertical drift cells immersed in a mixture of helium, ethanol and argon tracking gas. The electrons, or any electrically charged particle, ionise the tracking gas and the drift cells provide horizontal and vertical location of the passing through electrons. In order to release space in the gas chamber, the diameter of the cells has been increased to 44 mm compared to NEMO-3, where it was 30 mm. Since the height of the SuperNEMO sources has also increased compared to NEMO-3, the cells needed to reach 3 m.

The SuperNEMO tracking cells consist of a central anode wire set to high-voltage (∼1800 V) and 12 field shaping wires set to ground. When a charged particle ionise the gas in the cell, the electrons are accelerated to the anode wire and produces more ionisation and create an avalanche. The collection of the charges on the anode wire provides the drift time, which compared to the arrival time in the calorimeter can provide the radius at which the electron passed through the cell. The cells are operated in Geiger mode, meaning that the avalanche going to the anode wire is saturated and the process would stop. However, the UV photons produced by de-excitation or recombination can produce new avalanches along the cell length. A plasma is then propagated to both ends of the cells. Measuring the arrival time thanks to two copper rings at ends of the cells allows to determine the vertical position of the electrons in the tracking chamber. Combining these signals in all the cells provides a three-dimensional reconstruction of the particle tracks. The cell wires are made of stainless steel with thicknesses of 40 µm for the anode wire and 50 µm for the ground wires. These diameter have been minimised to reduce the amount of material in the tracking chamber, for radiopurity reasons and to reduce energy losses of the DBD electrons.

Increasing the cell length and diameter, while preserving the signal quality and the vertical drift efficiency, has been a major improvement for the SuperNEMO tracker. This has been

possible thanks to the construction processes of the tracking cells which has been developed by our UK colleagues. The cells production has been automated with a wiring robot functioning in a clean room at Manchester. Prior to the automated wiring, a very efficient cleaning procedure of the wires has also been developed. The cells were produced by cassettes of 2×9 cells, as can be seen on figure 3.9 (left). Each cassette was tested before being sent to London for integration in the tracker. This automated wiring process allowed to build the 2034 tracking cells in relatively short time. This demonstrated the capability of producing enough cells for a possible 100 kg isotope SuperNEMO experiment.

The tracking detector has been designed to be built in four parts, called C-sections. This division allowed to build the C-sections horizontally one by one, inside a clean room in the MSSL laboratory in London, to be latter delivered fully equipped to LSM for integration. A temporary support structure is first built horizontally in the clean room. The tracker C-sections are made of two pure iron beams on top and bottom and one non-magnetic stainless steel (SS 304) on the side. These beams are assembled on the support structure with bottom stainless steal sealing plates. The calorimeter blocks included in the tracker are directly attached to these beams and the PMTs are passing through. Special sealing strategy has been implemented to prevent radon penetration through this channel. The cassettes of tracking cells are inserted vertically to the dedicated copper rails, which are installed in front of the G-veto blocks as shown on figure 3.9 (right). At the end of the construction process an extra cleaning is performed on the whole C-section with UV light inspection, to spot residual dust.

Finally, the C-section is closed with a top sealing plate and tested for radon emanation. Given the extremely low levels requested (0.15 mBq m^{-3}), UCL has built a radon concentration line to measure the radon emanation of the C-sections after construction. In order to be protected from external radon, a plastic cover, flushed with nitrogen for the measurement, has been installed around the C-section. On the first C-section (called C0), the radon level was measured to be 0.3±0.1 mBq m^{-3}. This is a factor two higher than the target, but a contamination of the carrier gas is suspected to tarnish the real emanation value. This result is thus very promising.

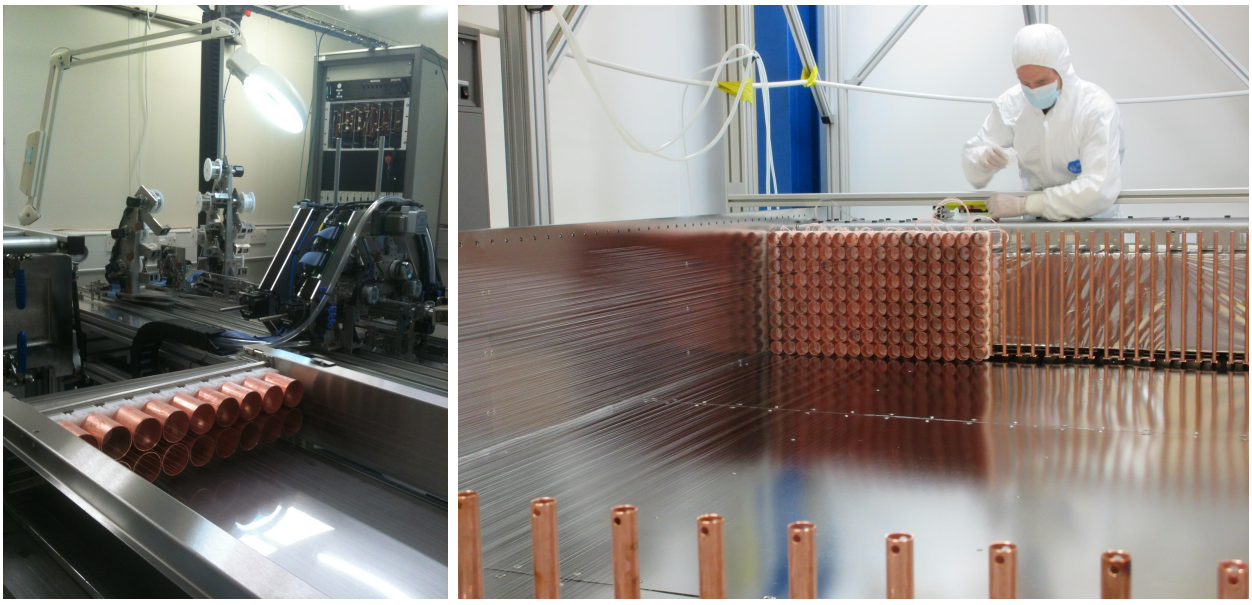

Figure 3.9: (left) Picture on 2×9 cells being wired in a cassette by the wiring robot. (right) Picture of one C-section during the insertion of the tracking cells.

3.4.2 Tracker integration at LSM

Once a C-section has been fully constructed and tested at MSSL, a secondary support structure is installed on top. The C-section is then covered with plastic film and the whole setup is installed in a clean protection bag. The C-section is then extracted from the laboratory on wheels, rotated vertically and installed in a transport box, which is installed on a lorry with another cover bag to be transported to Modane. Once in Modane, the C-section is removed from the vertical transport box and rotated again and installed in an horizontal box in order to enter the road tunnel. The delivery to the LSM is made at night with a special closure of the tunnel traffic. The transport box is dismantled around the C-section in front of the laboratory entrance. After several operations and rotations in the LSM, one support structure is removed and the C-section can enter vertically the integration clean tent with the external crane. Once inside the clean tent, the C-section is supported by the internal support structure and placed in position.

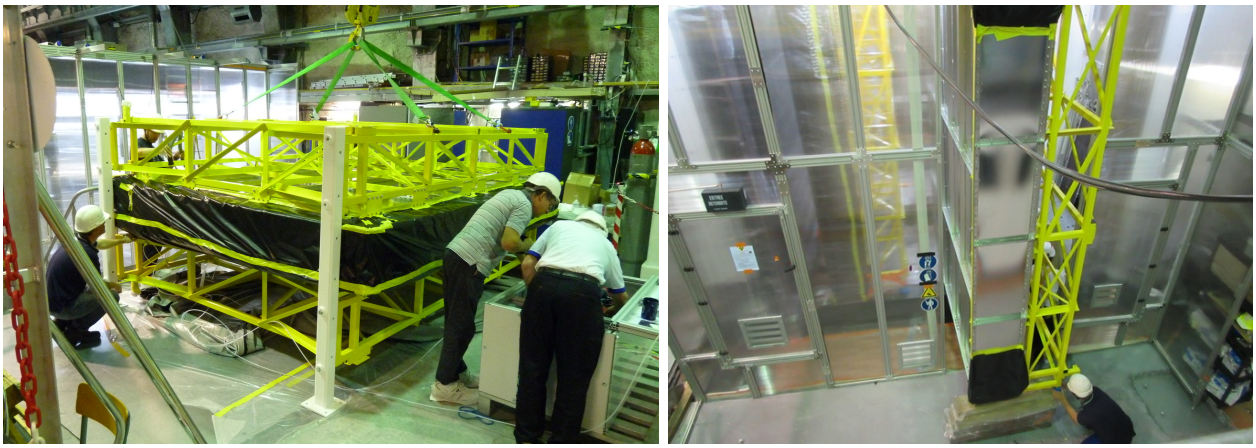

Figure 3.10: (left) Picture of the C0 section on the LSM mezzanine with its two support structures, before lowering to the SuperNEMO integration clean tent. (right) Insertion of the C1 section in the clean tent with C0 already inside.

After the delivery of a second C-section at LSM, it is necessary to couple it with the previous one to form one half tracker. After assembly of the two C-sections, a final row of 9 cells needs to be inserted in the middle of the two C-sections, see figure 3.11. Halves trackers, at both sides of the sources, finally comport each 113 rows of 9 cells (1017 cells). Both trackers have been assembled before the source frame and its foils in order to preserve the latter as much as possible. A picture of the last tracker integrated on the source frame is visible on figure 3.12.

In order to prevent radon penetration into the tracker from the calorimeter main wall, a radon barrier needs to be added between the tracker and the calorimeter. An OPA film from mf-folien company[3] has been selected for being the widest (2 m) and the thinnest (25 µm) radon-tight film available. Its structure of co-extruded and biaxially-oriented multi-layer nylon film provides an excellent radon barrier. A radon diffusion measurement of this film has been performed at CTU in Prague, using two vessels separated by the material to test. In the first vessel a radon source is emanating and the radon concentrations are measured in both vessels. The comparison of the two concentrations provided a factor better than 16000 between the radon concentrations for this OPA nylon film. Two strategies have been tested to install the two nylon films between the trackers and the calorimeters and will be presented in the following section.

[3] http://www.mf-folien.de/EN/produkte.html

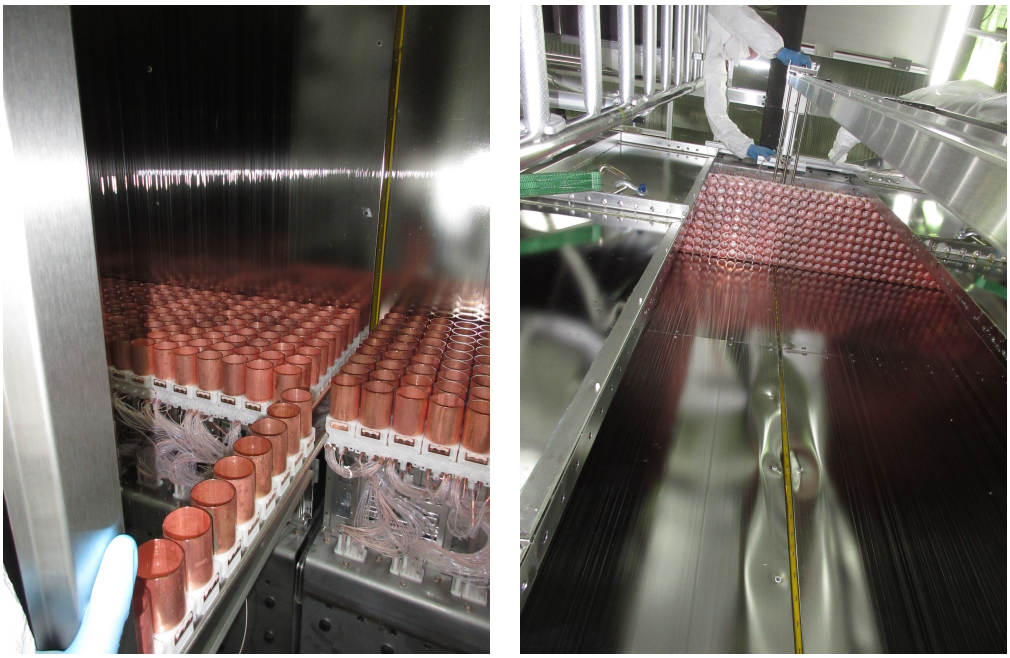

Figure 3.11: (left) Insertion of the last row of 9 cells between C0 and C1 assembled. (right) View of the full half tracker joined. We can observe the tracking wires from the flash light reflection, the copper end-caps of the cells and the G-veto scintillator blocks.

3.5 The calorimeter

Once the double beta decay electrons have been detected in the tracking chamber, it is necessary to measure precisely their energies. Plastic scintillators have been chosen for their excellent radiopurity, high light-yield and low retro-diffusion probability of the electrons. To investigate the DBD to excited states or reject and study the backgrounds, the SuperNEMO calorimeter has also been designed to detect γ-particles. The depth of the scintillators has thus been increased to almost 20 cm, while few cm would be enough for electrons. To reach the best energy resolution and light collection uniformity possible, large photocathode area PMTs are directly glued to the scintillators, without interface light-guides.

In total, the SuperNEMO calorimeter is segmented into 712 optical modules to detect individually the β and γ particles. This is a unique feature for double beta decay experiments, to be able to measure the energy of each particle separately. The two calorimeter main walls, *M-wall*, are segmented in $20 \times 13 = 260$ optical modules each. Each tracker detector has $2 \times 16 = 32$ *X-wall* optical modules on both edges and 16 *G-veto* optical modules on top and bottom. These three categories of optical modules are presented on figure 3.13, with the labelling convention.

3.5.1 The optical modules

An optical module (OM) consists of an assembly of an organic scintillator and a photomultiplier tube (PMT) glued with RTV-615 optical glue. The scintillator is a polystyrene based organic scintillator doped with 0.05 % of POPOP (1.4-bis(5-phenyloxazol-2-yl)benzene) and 1.5 % of p-Terphenyl (pTP) wavelength shifters. The scintillator is wrapped with Teflon on the sides and two layers of 6 µm aluminised mylar all around to improve the light collection towards the PMT. The thickness of the front face of the scintillator wrapping is minimized to reduce energy losses for the entering β-particles. Two type of PMTs have been used with the scintillators: new 8 inches Hamamatsu R5912-MOD and 5 inches R6594 Hamamatsu refurbished from the previous NEMO-3 experiment [Arnold et al., 2005, Augier, 2005].

Figure 3.12: Final view of the SuperNEMO tracker closed on the source frame with foils installed, before closure of the main calorimeter wall. A flash light allows to reveal the pattern of the wires in the tracking cells.

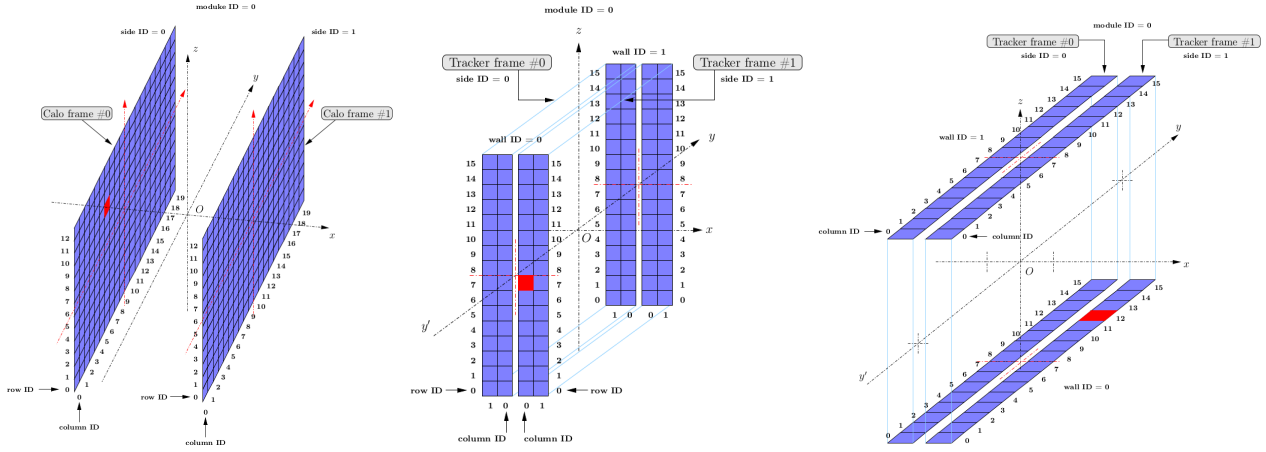

Figure 3.13: Illustration of the SuperNEMO calorimeter segmentation with M-wall (left), X-wall (middle) and G-veto (right) optical modules with the labelling convention example for three modules in red: `MCALO:S0.C6.R9`, `XCALO:S1.W0.C0.R7` and `GVETO:S1.W0.C12` [Lemiere et al., 2014].

As can be seen on figure 3.14, four types of optical modules have been used for the SuperNEMO calorimeter. Firstly, to fit with the mechanical design of the tracker or the main wall sub-detectors. Secondly, to get the best energy resolution for the detection of the double beta decay electrons, which would be mostly detected on the calorimeter main walls. The MW

OMs are made of the best plastic scintillators with 8 inches PMTs to achieve 8 % FWHM energy resolution at 1 MeV. Except for the top and bottom rows, where 5 inches PMTs have been used since the end-caps of the tracking cells prevent the β-particles emitted from the sources to be detected there. These MW scintillators have a larger front face to maximize the detection surface and to leave space for the magnetic-shield. Indeed, 3 mm thick magnetic shields of squared section are surrounding all the MW OMs. This is to prevent the penetration of the magnetic field, used to curve the electrons tracks, into the PMTs. Parallel to the tracking cells, the X-walls are made of smaller scintillators coupled to 5 inches PMTs with a PMMA light guide. A cylindrical mu-metal magnetic shield is covering the PMT and its light guide but not the scintillator. These X-wall OMs also permit to detect the double beta decay particles from the source foils but with a poorer energy resolution of 12 % FWHM at 1 MeV. A similar design is used for the G-veto OMs but with larger scintillator blocks. Like for the top and bottom OMs of the MW, these OMs will not detect the β-particles of the sources because they come on top (or bottom) of the end-cap of the tracking cells. The constraint on the energy resolution can be relaxed and they achieve 16 % at 1 MeV. More details about the development of these optical modules and the radiopurity budget can be found in [Barabash et al., 2017a].

Figure 3.14: Picture of the four types of optical modules used for the SuperNEMO calorimeter during assembly at CENBG. From left to right: M-wall OMs with 8 and 5 inches PMTs, X-wall and G-veto OMs with 5 inches PMTs and PMMA light-guide.

3.5.2 The magnetic shields of the PMTs

The presence of the magnetic field in the tracking chamber of SuperNEMO is necessary to sign the electric charge of the electrons, but it is a major disturbance for the functioning of the PMTs. A magnetic coil has been built in Orsay to study the magnetic shields for the protection of the PMTs, see figure 3.15 (left). Using a Hall probe we could mesure the field inside the coil and the magnetic shields. It represented a part of the PhD work of Steven Calvez [Calvez, 2017], directed by Xavier Garrido. I collaborated with them to this work. The SuperNEMO experiment plans to run with a 25 G (10^{-4} T) magnetic field but we have measured that the signal is lost in the 8-inch PMTs at only 1 G, unless a magnetic shield is used, as presented on figure 3.15 (right).

The magnetic shields of the 5-inch PMTs (X-wall and G-veto) directly reuse the mu-metal cylinders of the NEMO-3 experiment (1.5 mm thick, 150 mm diameter and 250 mm long) [Augier, 2005]. For the 8-inch PMTs it was necessary to build new magnetic shields. The mu-metal was rejected for cost and radiopurity considerations. In addition, our studies in Orsay demonstrated that covering the PMT at a distance of about the radius of the PMT, in front of the photocathode is necessary (see figure 3.16 (left)). The shape of the magnetic shields has

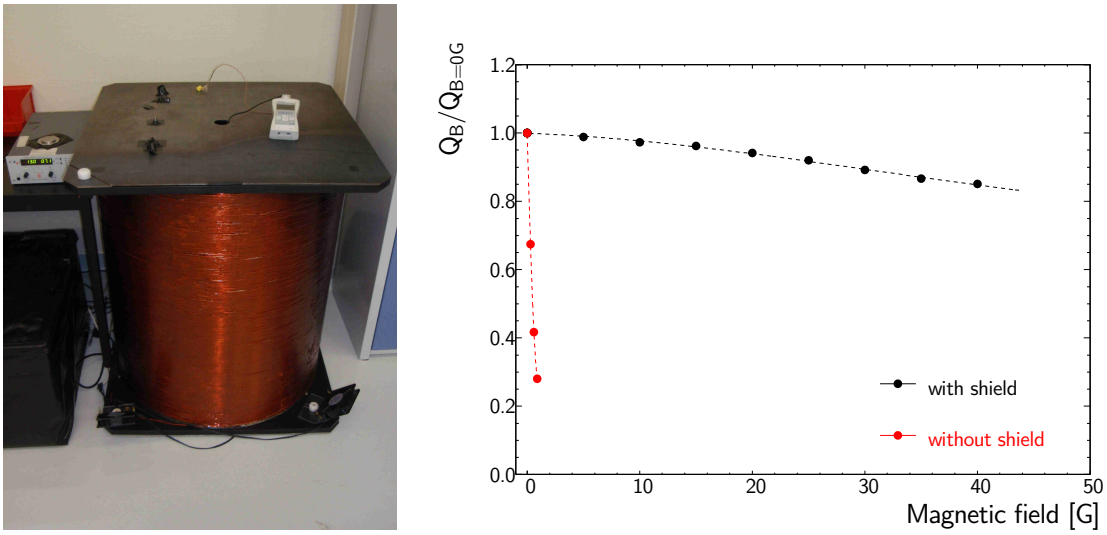

Figure 3.15: (left) Picture of the magnetic coil built at LAL to test the SuperNEMO magnetic shields. (right) Effect of a vertical magnetic field, applied to an horizontal 8-inch SuperNEMO PMT, on the charge Q_B collected by the PMT compared to the no-field case $Q_{B=0G}$.

thus to be adapted to the PMT and the scintillator shapes, in order to cover the scintillator. The design of the SuperNEMO calorimeter took advantage of this, to also use the magnetic shields as mechanical structure to support the OMs into the calorimeter frame. The shape of the magnetic shields for the 5-inch and 8-inch PMTs is presented on figure 3.17. They adopt a square section of 249 mm side and a length of 420 mm. Such magnetic shields built from 3 mm thick pure iron ARMCO[4] plates have demonstrated very good performances, almost similar to mu-metal shields, see figure 3.16 (left). The residual field penetrating the shields can be easily compensated by increasing the high-voltage (HV) applied to the PMT, as presented on figure 3.16 (right). Special care about the first dynode orientation, with respect to the magnetic field, has also been demonstrated. The first dynode must be facing the magnetic field direction to reduce the negative impact of the field [Calvez, 2017].

A special process to build the SuperNEMO magnetic shields has been developed with an aeronautic manufacturing company. The pure iron plates were completely cut and welded with laser to build the shields from three pieces at an industrial cadence. No additional materials, which could be an important source of radio-contamination, are needed in the process. To recover the optimal magnetic protection after machining, a thermal treatment has to be applied to the manufactured pieces, the *annealing*. This was performed in Bodycote company using the recommended heat treatments from AK Steel, producer of the pure iron. The magnetic shields production was performed from two different batches of pure iron. For an unknown reason, two different annealing processes were needed for these two batches. Thanks the traceability followed in our processes, this was easy to handle. The steps of these two processes are presented below:

- Recrystallization annealing: standard magnetic treatment (Batch 868021)
  - Heating: 2-4°C min^{-1}
  - Holding temperature: 820°C ($\pm$ 20°C)
  - Holding time: 240 min minimum

[4]The pure iron ARMCO, for American Rolling Mill Company, is a product of AK Steel International that has been developed for many applications including magnetic shielding. It has also demonstrated excellent radiopurity levels for a steel, thanks to its highest purity level in iron of 99.85% minimum. https://www.aksteel.eu/products/armco-pure-iron/

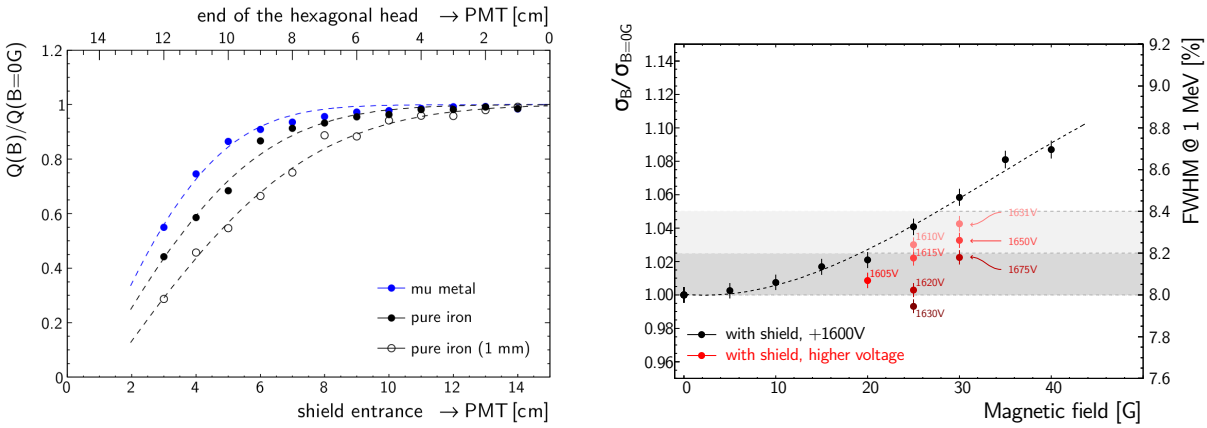

Figure 3.16: (left) Relative effect on the charge Q(B) collected by the 8-inch PMT as a function of its position with respect to the distance to the shield entrance face, for three types of shields 1 mm mu-metal, 3 and 1 mm thick pure iron. (right) Relative effect on the energy resolution (σ_B) of the 8-inch PMT inside a magnetic shield as a function of the external field applied. In red are presented different HV corrections, with respect to the nominal HV, to recover the loss of light-collection affecting the energy resolution.

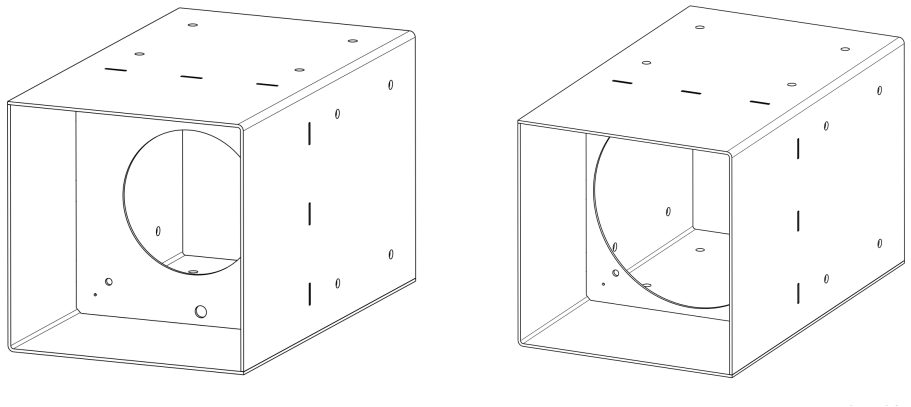

Figure 3.17: Mechanical design of the SuperNEMO magnetic shields for the 5-inch (left) and 8-inch (right) PMTs with a square section of 249 mm side and a length of 420 mm. The vertical scintillator support plate is at 160 mm of the shield entrance face and has a hole corresponding to the PMT diameter. The shields are built from three pieces in 3 mm thick pure iron after laser cutting and welding.

  - N_2 cooling: 1°C min^{-1} until 400 °C
  - Protected atmosphere until 300°C

- Normalization annealing: optimized magnetic treatment (Batch 402591)
  - Heating: 2-4°C min^{-1}
  - Holding temperature: 950°C (+ 20°C / - 10°C)
  - Holding time: 90 min minimum
  - N_2 cooling: 1°C min^{-1} until 400°C
  - Protected atmosphere until 300°C

After all these processes, the magnetic shields were cleaned with in ultrasonic bath with 10% acetic acid solution and rinsed with pure water and iso-propanol at LAL Orsay. During our tests of the magnetic shields, it was realized another opportunity to compensate the remaining

magnetic field inside the shield. Indeed, the pure iron uses magnetisation to compensate the external field and a magnetic hysteresis cycle could be applied to cancel the internal field. This was demonstrated on a single shield in Orsay, as shown on figure 3.18, and on a 3×3 array of shields in LPC Caen, which built a prototype coil in the preparation of the full SuperNEMO magnetic coil. This is to be investigated on the full SuperNEMO demonstrator, once turning on the magnetic field.

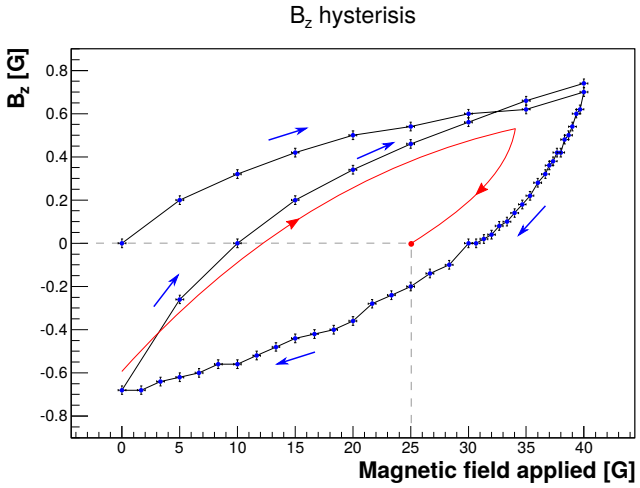

Figure 3.18: Example of an hysteresis cycle applied to a SuperNEMO magnetic shield to cancel the internal field seen by the PMT [Calvez, 2017].

3.5.3 The main wall calorimeter frame

The dimensions of the calorimeter frame have been driven by the source surface to offer an active area of about 5×3 m^2. Building such detector in one piece would be difficult to transport to Modane. In addition, these dimensions could not fit through the LSM entrance from the tunnel. The frame has thus been designed as an assembly of four beams to be assembled underground and to be populated with the optical modules onsite. The structure of the calorimeter frame has to support the important weight of about 6.5 tons of the 260 OMs (around 25 kg each). The four beams consist of reinforced structures made from 30 mm thick pure iron plates from ARMCO. This material has been selected for mechanical considerations and its very good radiopurity. A picture of the calorimeter frame assembly test in Orsay can be seen on figure 3.19. On the inner side of top and bottom beams, 3 mm thick pure iron plates have been installed to maintain the OMs, support the gasket and ensure the return of the magnetic field.

3.5.4 The main wall calorimeter bricks

The X-wall and G-veto OMs have been integrated directly on the tracker frames in UK before the insertion of the tracking cells. As already said, the MW OMs had to be installed directly onsite at LSM on the calorimeter frame, after reassembly of this frame. Because of the fragility of the scintillator wrapping and to speed-up the integration underground, the OMs were packed in *calobricks*. These calobricks were horizontal assemblies of 4×2 or 4×1 OMs (because there is 13 rows of OMs per MW). Mechanical drawings of a calobrick are presented on figure 3.20. The support structure of the calobricks rely on the magnetic shields which are screwed together with radiopure brass bolts, separated by PMMA spacers. A back-plate of black PMMA is also added to the calobricks, which can be closed for gas flushing or light tightness. But this option was not implemented in the end. All the pieces are maintained by the same radiopure brass screws and nuts.

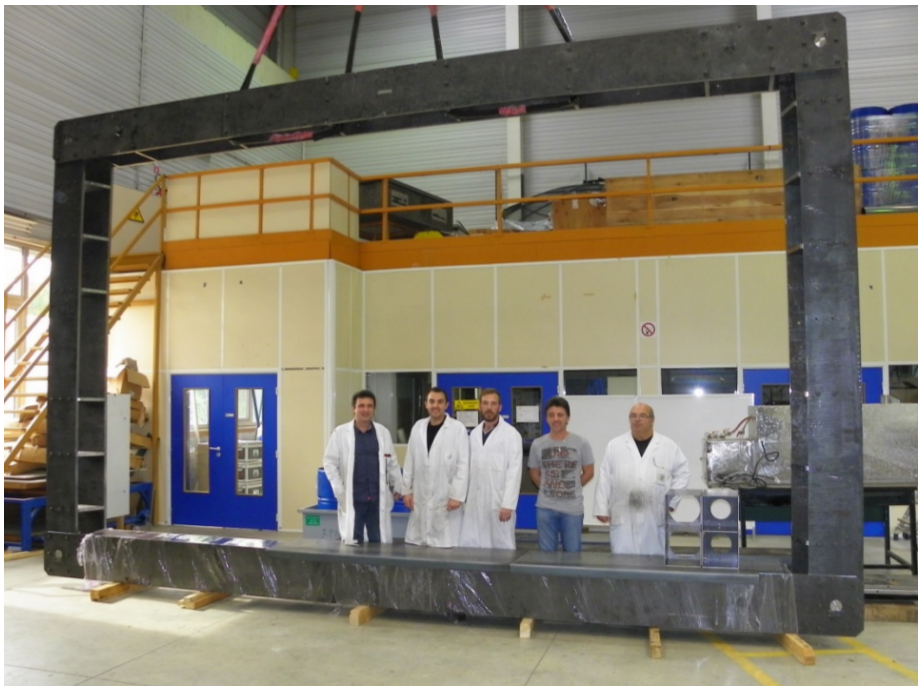

Figure 3.19: Picture of the calorimeter frame assembly test in Orsay before dismantling and delivery to LSM.

The mechanical structures of the calobricks were assembled at Orsay in a clean room. The gas tightness of the pieces were ensured by gluing with stycast, which is an efficient radon barrier. The calobricks structure were then sent to Bordeaux, for the integration of the OMs that were assembled and qualified on the electron spectrometer beam, see figure 3.21. After test of the OMs, the calobricks, with the scintillators facing down, were wrapped with two layers of plastic protection. Finally, the calobricks were sent to Modane in special transport and rotation boxes.

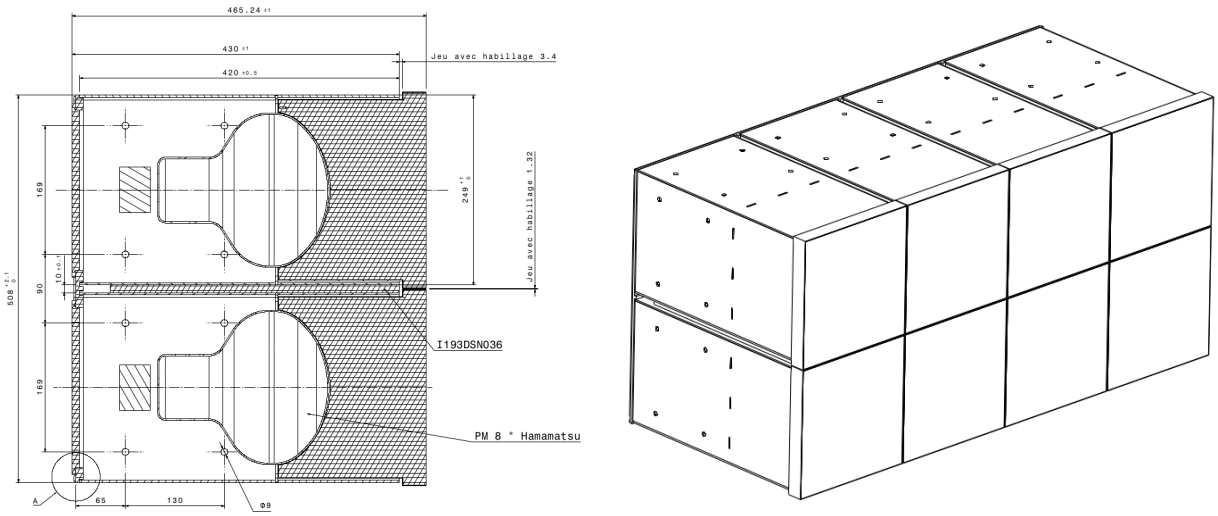

Figure 3.20: Mechanical drawings of a 4×2 calobricks with 8 inches PMTs with a cut (left) and a view of the entrance face of the scintillators (right).

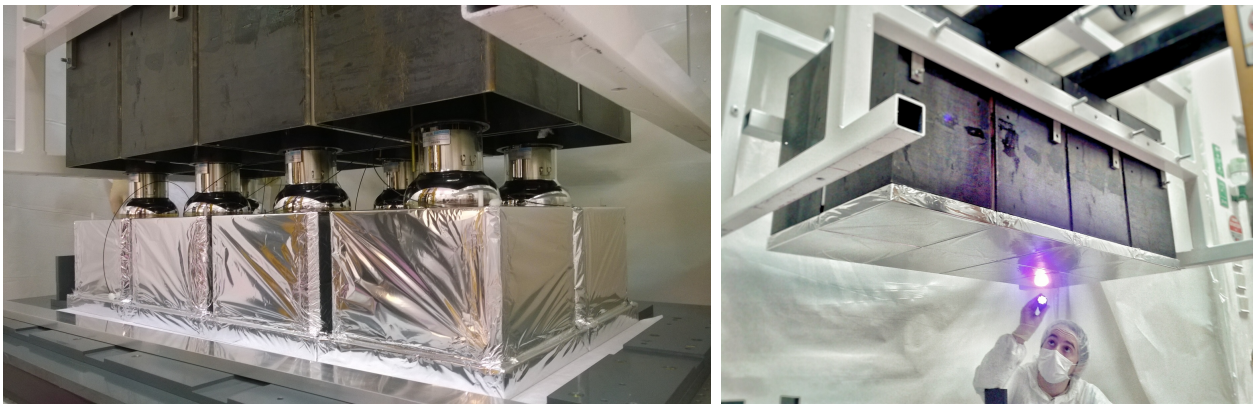

Figure 3.21: Pictures of the assembly of a 4×2 calobrick during in the clean-room at Bordeaux. (left) Insertion of the mechanical structure on the OMs. (right) UV light inspection of the entrance face of the scintillators.

3.5.5 Integration at LSM

As already explained, the calorimeter frames where pre-assembled in Orsay and transported in four beams to LSM. The integration of the frames in the clean tent where rather straightforward operations, despite the weights and the sizes of the beams. Most of the work consisted then in populating the frames with the calobricks.

The calobricks prepared in Bordeaux were delivered at LSM for a full wall at once and stored on the mezzanine underground. On each transport box, shock and rotation visual sensors have been glued to ensure the calobrick arrived safely at LSM. The transport boxes were then taken one by one and deposited on the entrance platform of the clean room airlock. After rotation of the box to place the scintillators front faces vertical, the transport box was deposited on a rolling cart. The top and two sides of the box were removed and the others were covered with plastic before entering the clean room. A storyboard of the introduction of a calobrick in the clean tent is presented on figure 3.22.

Once in the clean room, we performed fast tests to ensure that all the OMs to be installed in the calorimeter main wall would be properly functioning. For these tests, a ^{22}Na γ source has been used with a separate OM to make coincidences and avoid background in the energy spectra. The calobrick was cabled with temporary HV and signal bundles and a black polyethylene dark box was placed over it. The PMT signals were acquired with a WaveCatcher system [Breton et al., 2011] and the amplitude of the 511 keV and 1.27 MeV peaks were checked online. A storyboard of this test is also presented on figure 3.23. The PhD students greatly contributed to these tests.

After validation of a calobrick, it was fixed to a special hook system to be transported on the calorimeter frame, see figure 3.24 (left). PMMA spacers, like the ones used between the magnetic shields in the calobrick, are installed on top of the calorimeter beam or on top of the previous row of calobrick, see figure 3.24 (right). The calobricks were installed one by one in rows of five before going up to the next row. The alignment of the bricks was done by hand with rulers relatively to the calorimeter frame gasket, which will be the interface with the tracker. The calobricks are finally fixed together with radiopure brass bolts. Because of space constraints on the top, the final row of OMs of the M-wall has been installed OM per OM.

To complete the gas tightness of the calorimeter main walls, it was first thought to wrap each individual calobrick in the nylon film (section 3.4.2), but the number of interfaces would be to hard to tighten. The first main wall was thus wrapped by rows of calobrick but several issues and possible gas leaks occurred on the edges. The two films between two rows of calobricks were glued with stycast contained in a cord of silicone type glue, see figure 3.25 (left). The second

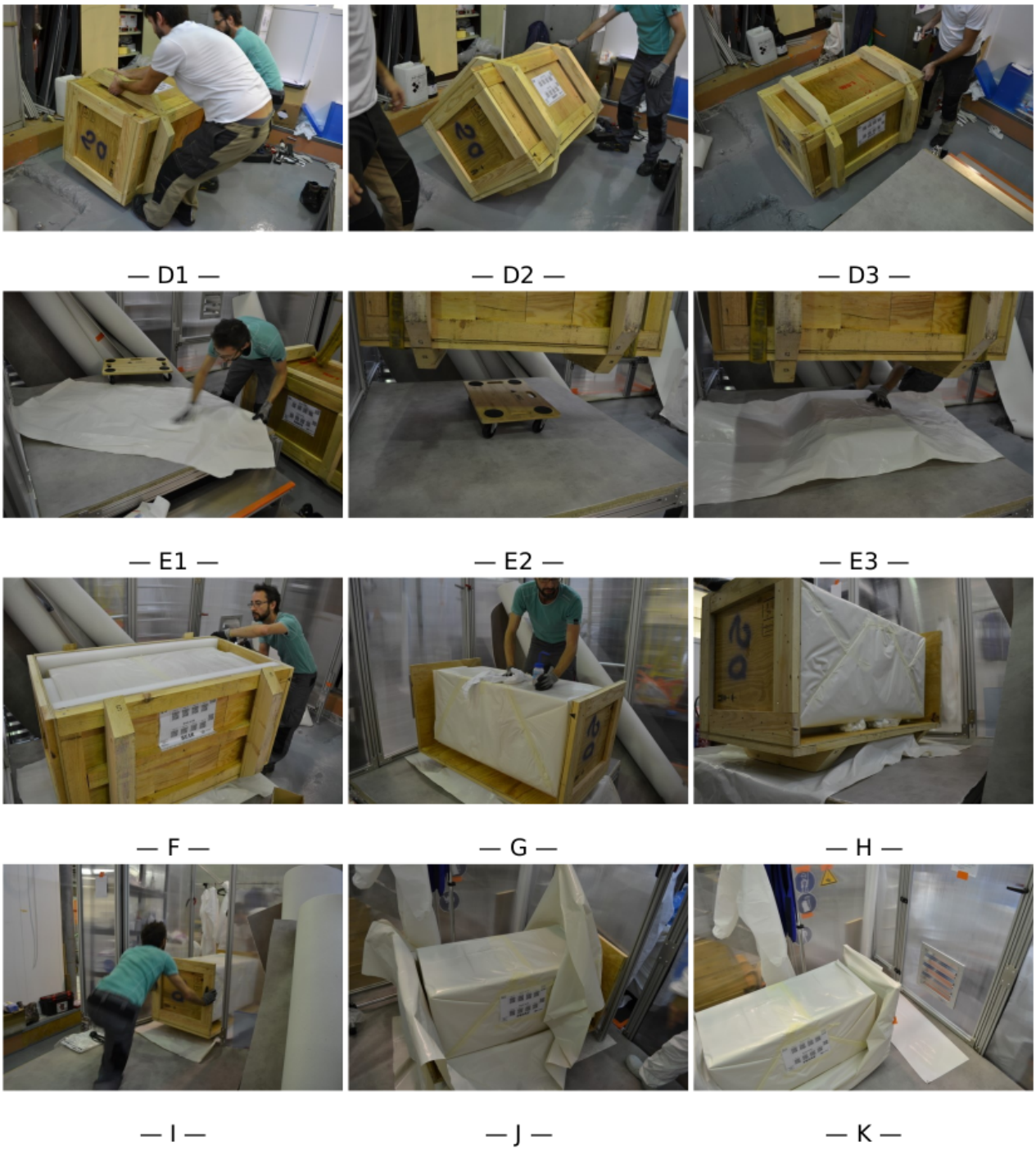

Figure 3.22: Storyboard of the opening of a transport box of a calobrick and entrance in the integration clean room.

main wall was tighten with two vertical nylon foils glued together, see figure 3.25 (right), and to the gasket on the calorimeter frame. This efficiently improved the gas tightness on this side of the detector. On the back of the calorimeter walls, nylon strips and cords of stycast glue were used to ensure the gas tightness. All the heads of screws and nuts were also glued with stycast and polyethylene caps. After the inner detector closure, argon and helium leak tests were intensively used to fix the numerous leak points.

Like for the isotopic sources and each sub-detectors mechanical frames, a laser survey of the main calorimeter walls has been performed before the closure of the SuperNEMO demonstrator. For the first calorimeter, situated at the French side of the laboratory, the positions of the front faces of all the calobricks have been registered with four points on the corners. As expected,

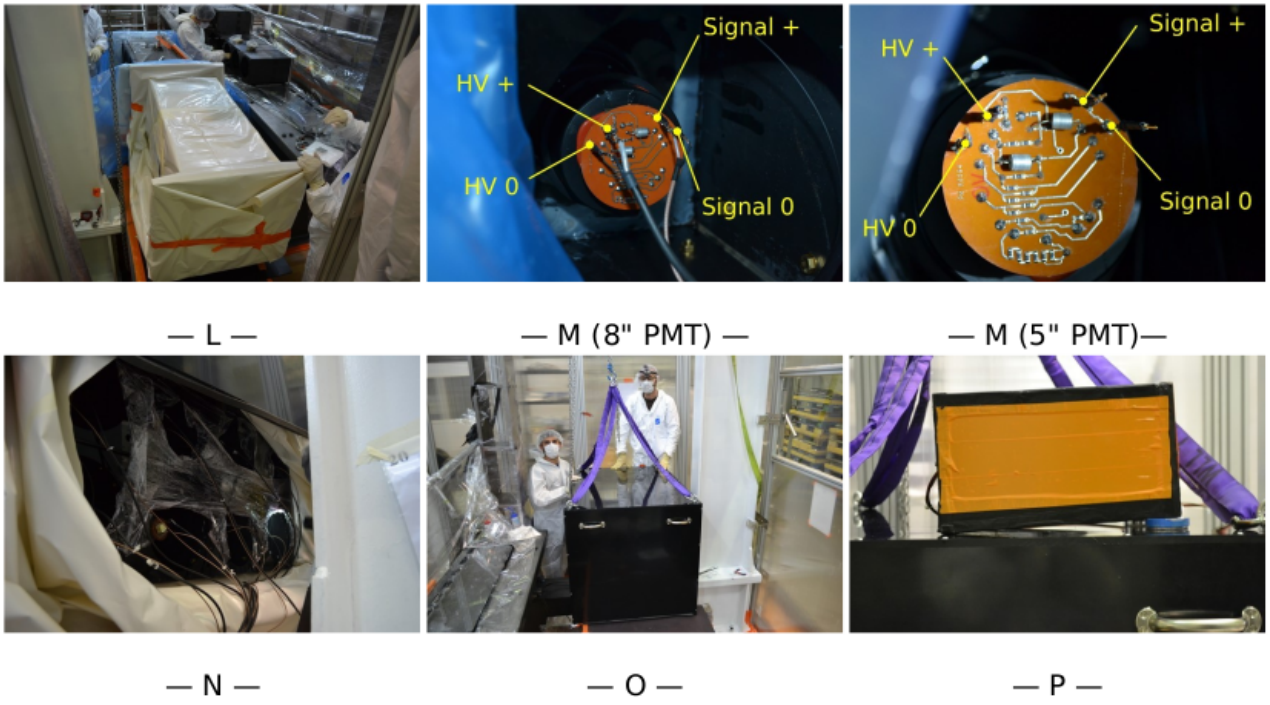

Figure 3.23: Storyboard of the test of a calobrick inside the clean tent before integration on the calorimeter main wall. The separate OM for coincidence, in the orange box, is placed on top of the black box covering the calobrick and the ^{22}Na source can be seen in blue.

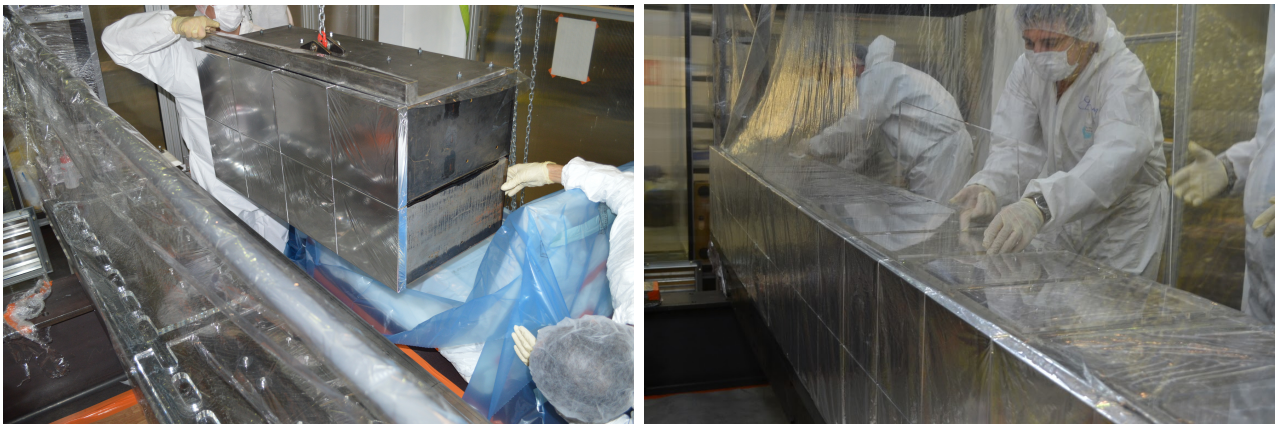

Figure 3.24: (left) Installation of the first calobrick on the calorimeter frame. (right) Completion of the first row of calobricks on the first calorimeter frame and installation of the PMMA spacers for the next row.

the calorimeter wall presents a belly in the middle, toward the tracker of about +7 mm, and a retract in the middle of the two lateral edges of about -6 mm. These values are acceptable since it preserves enough distance to the tracking wires, thanks to the gasket support. The top and bottom edges lie within few millimetres. For the second calorimeter wall, situated at the Italian side of the laboratory, the laser survey was improved and the positions of the front faces of each scintillator have been registered. The deformation numbers are very similar to the first wall, but the belly is at a lower vertical position, while the retract is at higher vertical position with respect to the middle of the calorimeter wall.

Figure 3.25: (left) Pouring of stycast glue on top on a nylon film after completion of a row of calobrick of the first calorimeter main wall, before placing the next film already hanging in the back. (right) Gas tightness of the second calorimeter main wall ensured by the gluing of two nylon films together directly in front of the calorimeter wall, populated with all its calobricks.

3.5.6 The calorimeter cabling

The SuperNEMO detector will be protected by a tight anti-radon tent flushed with deradonised air. The calorimeter electronics is outside of this tent and the HV and signal cables, connecting the PMTs to the electronics, have to go through the tent while keeping gas tightness. For this reason, different set of cables are used inside and outside of the anti-radon tent. Internal and external cables are connected together at the patch-panels on the anti-radon tent with dedicated connectors, as shown on figure 3.26. The patch-panels are made of drilled pure iron plates to accept from inside fixed female connectors and from outside removable cables with their male connectors. These calorimeter signal and HV cables with their respective connectors will be described in the following sections.

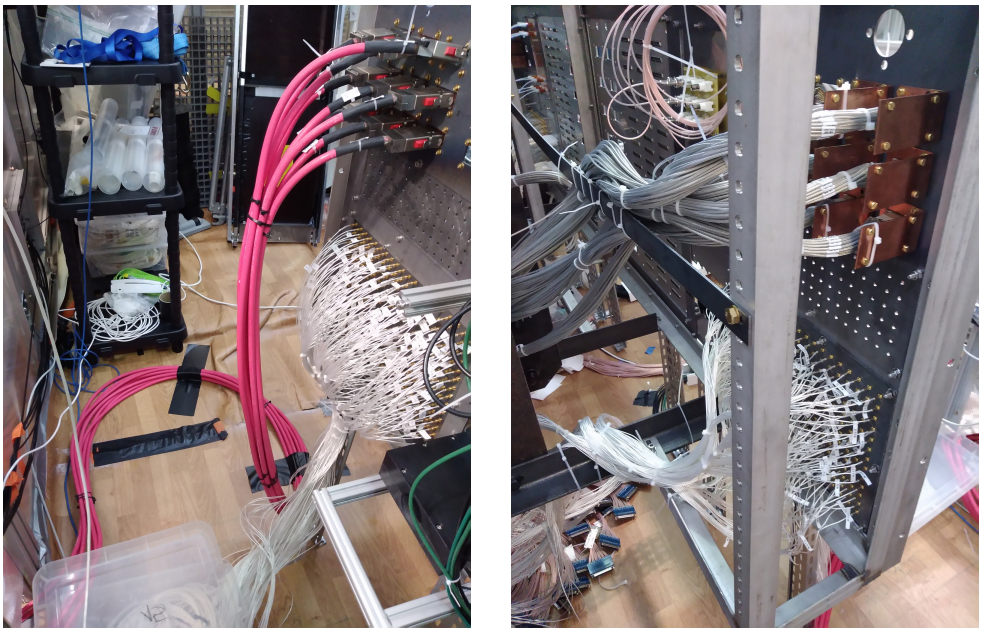

Figure 3.26: Pictures of one patch panel during cabling operations from outside (left) and inside (right). On top the HV cables can be seen, while the signal cables are at the bottom.

Signal cabling

The signal cable of the SuperNEMO calorimeter has been selected for its radiopurity and compatibility with the front-end electronics. It is a coaxial cable with the reference M17/93 RG-178 from Axon Company, with a transparent sheath since it has a better radiopurity. In order to reduce the amount of cable inside the anti-radon tent, the cables have been cut at the needed lengths to reach each PMT by first a vertical routing to the OM row and then an horizontal routing to the PMT location. The cables are attached to vertical copper bars attached to the calorimeter pure iron frame. This scheme allows to reflect the mapping of the OMs in the detector at the patch-panel and at the front-end electronics boards (see section 3.10). The steps are 25 cm between OMs in both directions. It results in internal signal cable lengths going from 3.25 m to 11 m. The difference in cable lengths will be compensated offline by time alignment of all the channels, see section 4.3. The cables are connected to the PMT dividers using two Souriau pins for the inner connector, see figure 3.27 (left). The other extremity of the internal signal cable has a female MCX coaxial connector straight bulkhead jack to be fixed on the patch-panel plate, as shown on figure 3.27 (right).

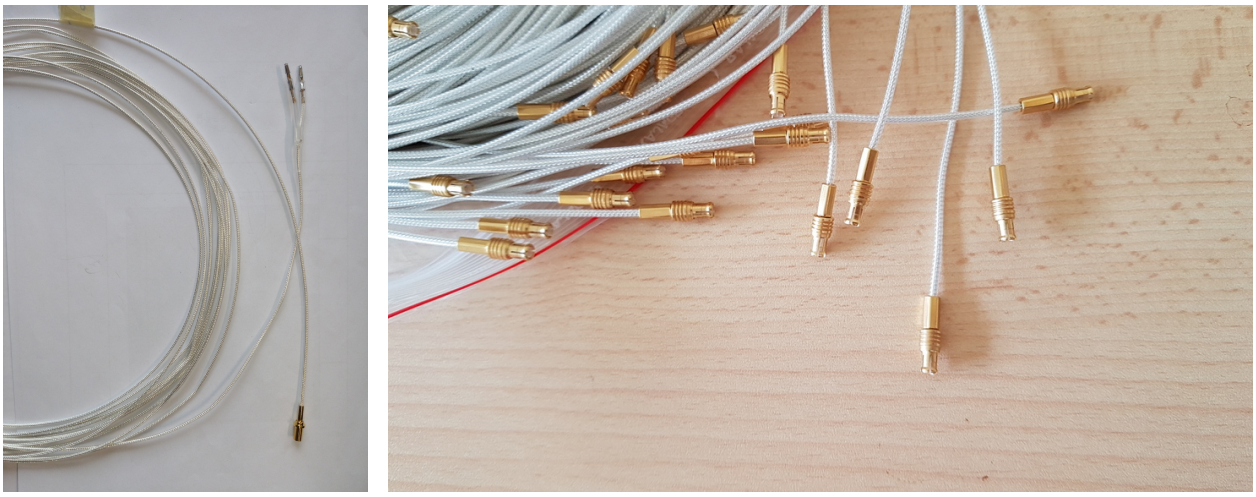

Figure 3.27: Picture of the PMT signal cables of the SuperNEMO calorimeter one internal with two Souriau pins at the PMT divider side and an MCX at the patch-panel side (left) and a bundle of external cables with MCX connectors at both ends (right).

Given the relatively small dimension of the patch-panel and the compactness of the front-end electronics all the external cables have been cut at the same length of 7 m. For simplicity the same Axon cable has been used as for the internal cables. On the SuperNEMO front-end boards (section 3.10) a female MCX 50 Ohms coaxial connector is used similar to what is used at the patch panel for the internal cable. The signal external cables have thus two male coaxial MCX connectors from Radial on both ends.

HV cabling

For the same reasons as for the signal cables, the HV cables are separated in internal and external cables to the anti-radon tent. The power supplies of the SuperNEMO calorimeter is provided by three CAEN SY4527 units. The crates are populated with 32 channels A1536 HV boards. These boards come with 52 pins connectors from Radial. To fit with this connector a HV cable produced by CERN has been selected for the external part. It consists of a 37 multi-cables bounding in a red jacket. In this cable, 32 channels are used to supply individual HV to the PMTs and 5 channels are used to provide grounding. The connectors on this external

HV cable are a female Radial connector at the electronics side and Redel LEMO 51 pins at the patch-panel side. A picture of a full external HV cable can be seen on figure 3.28 (left).

Inside the anti-radon tent, the HV cables become individual. The connector at the patch panel is a male Redel LEMO corresponding to the female external one. An home-made circuit has been designed to merge the grounds at this level and distribute all the HV in the dedicated pins of the connector to the individual internal cables, see figure 3.28 (middle). The internal cable is an Axon AK4902A coaxial HV cable also selected for its good radiopurity. Like for the signal cable, the external HV cable can be disconnected from the outside while the internal one is fixed to the patch-panel. The internal cables are connected to the PMT dividers using two Souriau pins SM20WL3S26 (one male for the core and one female for the ground mesh to prevent mis-connection), see figure 3.28 (right). A small copper braid has also been added to connect the PMT divider to the mechanical grounding of the calorimeter wall.

The routing scheme of the internal cables on the calorimeter is similar to the signal cables but with a different pattern to fit the mapping between OMs and the channels on the HV boards, see section 3.10. We have also avoided to route together signal and HV cables to reduce possible catch-up of noise.

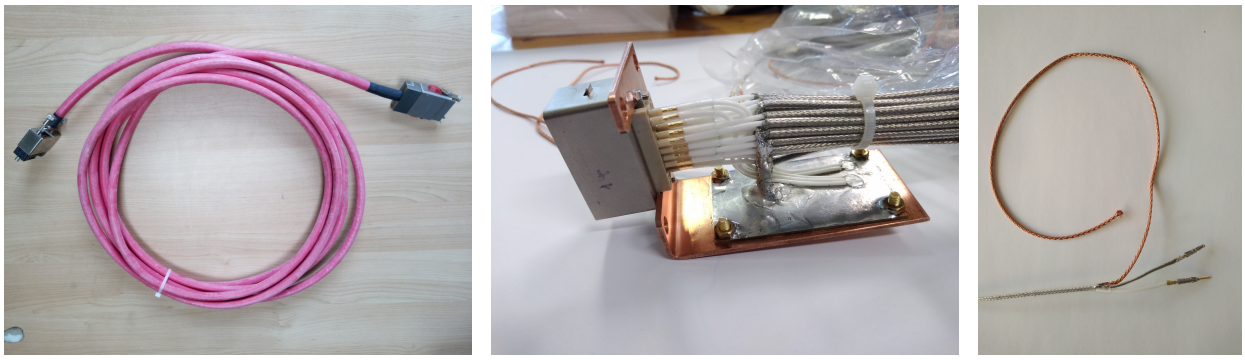

Figure 3.28: Pictures of the SuperNEMO calorimeter HV cables, from left to right: external 37 multi-cables bounding HV cable with the Radial and Redel connectors, home maid connection of 32 HV internal cables to the Redel connector and PMT divider side of an HV cable with its grounding copper braid.

Electrical grounding

In order to prevent to collect noise on the signal channels and electric charge accumulation in the detector, special care has been taken to ground the SuperNEMO calorimeter. Two types of copper braids have been deployed to ensure this grounding. Firstly a large copper braid (10 mm^2) is routed all along the calorimeter walls, with a snake shape, and connected to the vertical copper bars also used to support the PMT cables. The connection is made by pinching the copper braid with a copper plate on the vertical bars. To connect each PMT divider to the ground, a second copper braid has been added (1.5 mm^2). It is soldered to the naked ground mesh of each HV cable and then pinched to the large copper braid with small copper plates.

The whole detector and its electronics are installed on brass plates that ensure the overhaul grounding of the experiment. These brass plates are connected to the general grounding of the LSM. All the apparatus and sub-detectors are grounded to these plates trough copper plates or braids.

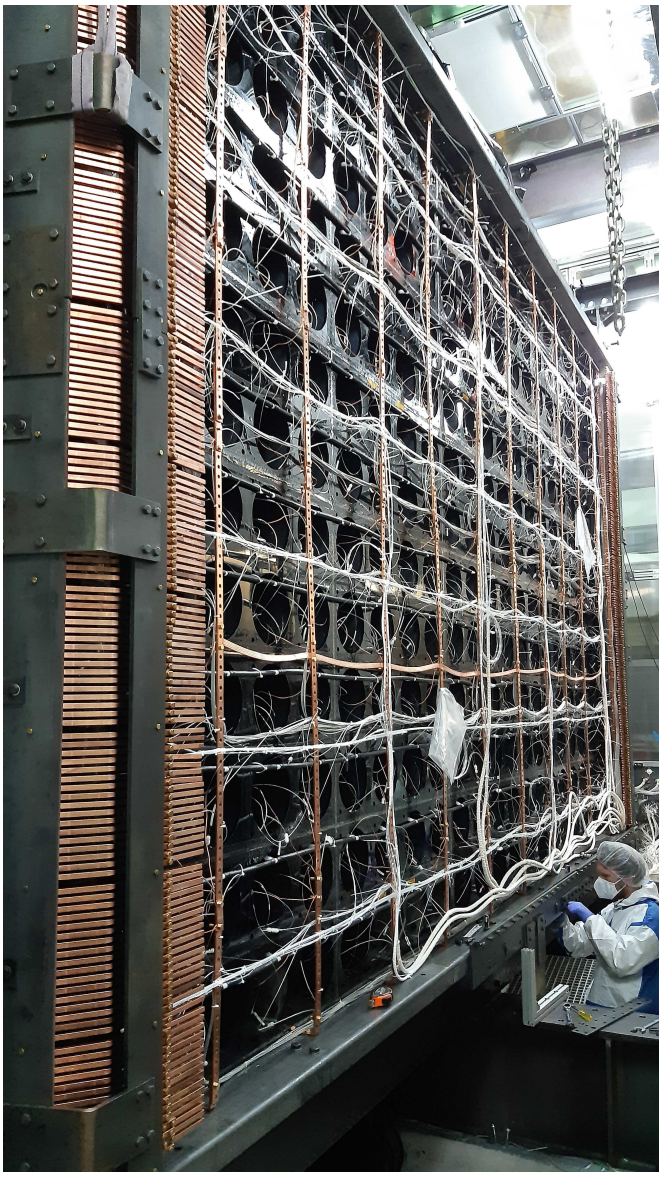

Figure 3.29: Picture of the back of one calorimeter main wall showing the horizontal routing of the signal and HV cables to the PMT dividers in the alcoves, the vertical grounding copper bars, the large and small copper braids and the optical fibers of the light injection system in their white jackets.

3.6 The magnetic coil

3.6.1 The coil design

The copper bars of the NEMO-3 experiment have been reused for the construction of the SuperNEMO magnetic coil. The copper bars have a squared section of 1×1 cm^2 and a length of about 1.7 m. To cope with the bigger size of the SuperNEMO detector, the space between the rings has been increase to 16 mm (compared to 3 and 10 mm in NEMO-3). The total number of rings in the coil is 200. The connection between the individual bars are insured by brass screws pushers in a copper ring. For the construction and onsite integration, the coil has been divided into 12 panels. The copper bars are supported by delrin insulating pieces. The structure is supported by vertical 10 mm thick Armco pure iron plates, which also ensure the magnetic field return to improve the uniformity of the internal field. On top and bottom of the demonstrator this is also ensured by pure iron beams of each sub-detectors. The coil panels are supported by the calorimeter frame. The side coil panels penetrates the calorimeter wall

because the vertical iron beam would catch the magnetic field. The vertical tracker beams are made of a-magnetic stainless steel to prevent this issue.

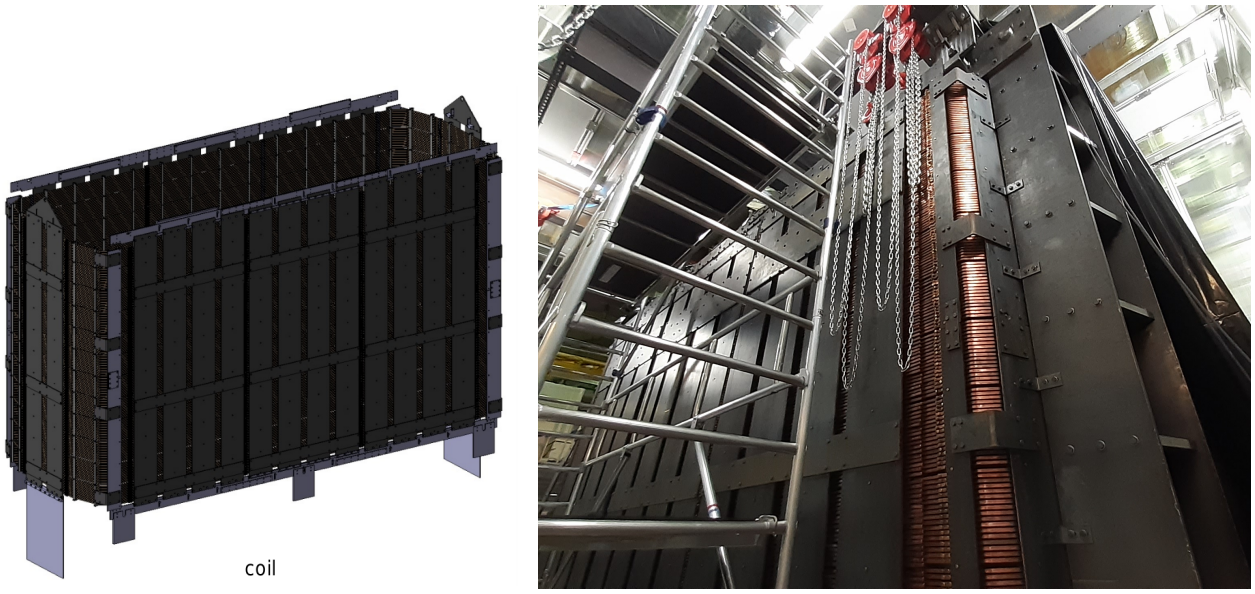

Figure 3.30: (left) CAD view of the SuperNEMO magnetic coil with horizontal copper rings and vertical pure iron plates. (right) Picture of the magnetic coil after integration at LSM in 2021.

3.6.2 Tracker internal magnetic field

A second study we conducted with the LPC Caen prototype coil, in the context of Steven Calvez PhD thesis [Calvez, 2017], was to investigate the effect of the magnetic shields on the applied magnetic field in the tracker. Using one or three shields vertically stacked, we have been measuring the magnetic field as a function of the distance to the shields, this is presented on figure 3.31. This test revealed that the magnetic field in the tracker of the SuperNEMO demonstrator will not be uniform in the direction perpendicular to the sources, which is the propagation direction of the DBD electrons. The magnetic field will be 25 G at the source foil position but it will be reduced to about 10 G at the entrance of the scintillators. This is a different situation compared to NEMO-3 and the curvature of the electrons tracks will be impacted. This situation conducted to the realisation of complete magnetic simulations of the SuperNEMO demonstrator. A realistic 3-dimensional field map in the tracker has been produced and is now used in the GEANT4 simulation software.

The behaviour of the magnetic field in the SuperNEMO demonstrator and its impact on the particle tracking or the PMTs response will require thorough tests. The strategy of switching on the magnetic field needs to be defined. It is considered to start the data taking of the SuperNEMO demonstrator without switching on the magnetic coil.

3.7 The anti-radon tent

The air of the LSM laboratory contains about 20 $\mathrm{Bq\,m^{-3}}$ [Hodák et al., 2019], mostly emanated from the laboratory rocks. The SuperNEMO detector needs to be protected by a tight anti-radon tent (ART) flushed with deradonised air, which is produced by the factory at LSM, reaching a residual contamination of about 10 $\mathrm{mBq\,m^{-3}}$. The objective is to reach about 20 $\mathrm{mBq\,m^{-3}}$ in the ART and 150 $\mathrm{\mu Bq\,m^{-3}}$ in the tracking chamber. From the radon diffusion model, the radon-free air flushing has been estimated to 120 $\mathrm{m^3\,h^{-1}}$, to reach these objectives [Perrot et al., 2020].

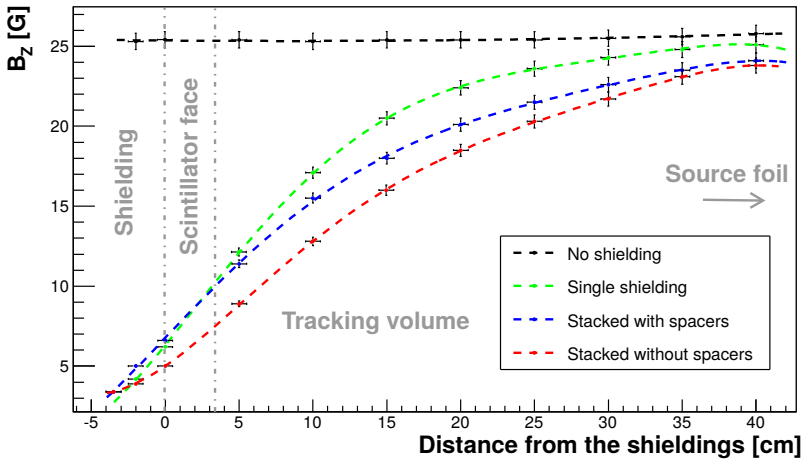

Figure 3.31: Evolution of the magnetic field as a function of the distance from the magnetic shielding measured in the LPC Caen coil, with one shield (green) or three shields stacked vertically with (blue) or without spacers (red) [Calvez, 2017].

The skeleton of the ART is made of stainless steel profiles and the panels are made of black high density polyethylene (HDPE), as shown on figure 3.32. Samples of the HDPE panels have been measured with HPGe detectors and no contamination has been observed, down to levels better than the requirements. The gas sealing is ensured by RTV-382 glue. The remaining holes in the patch-panels have also been tighten thanks to this RTV. The assembly of the sides of the ART has been finished in 2022. The top and bottom pieces remained opened longer for the tracker commissioning, which is finished now. The completed tent has been connected to the anti-radon gas factory at the patch-panels, with bubblers to ensure an overpressure in the tracker and in the ART.

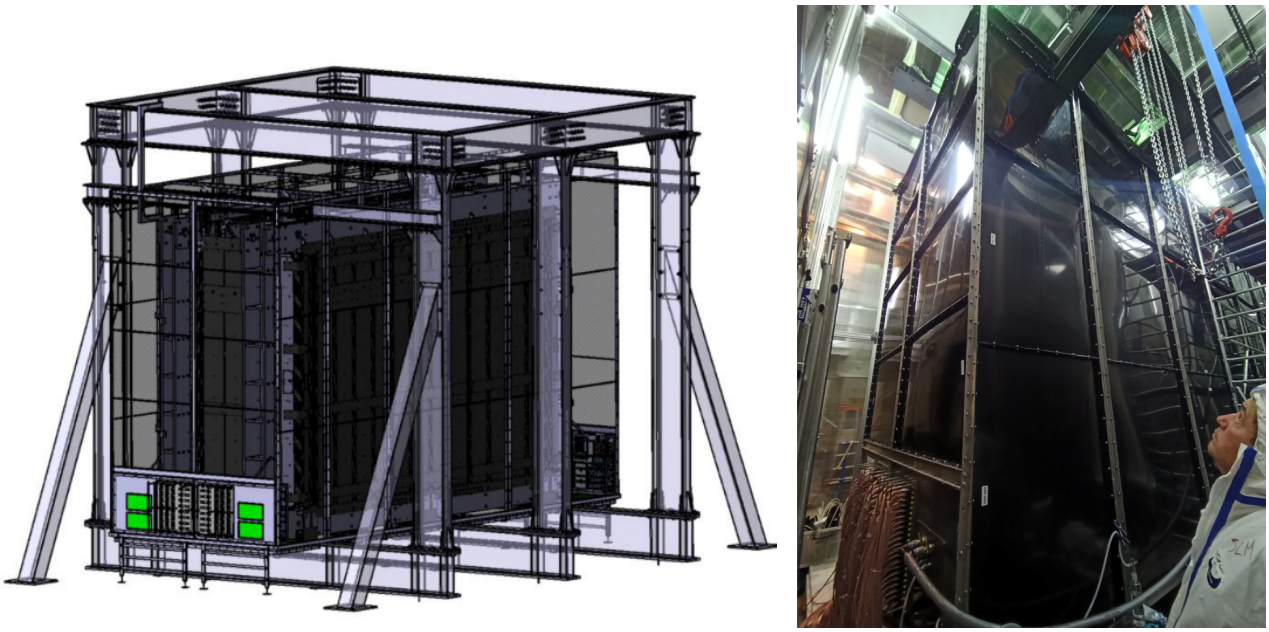

Figure 3.32: (left) CAD view of the anti-radon tent and its cabling patch-panels towards the electronics with the SuperNEMO demonstrator inside and the support structure outside. (right) Picture of the ART during integration at LSM. Tracker patch panels can be seen on bottom left.

3.8 Calibration systems

The survey of the energy scale and of the detector stability over time is of major importance for SuperNEMO, like for any DBD experiment. To perform regular energy calibrations, an automated deployment system of radioactive sources has be developed in Texas. As used in the NEMO-3 experiment, the ^{207}Bi isotope is a good candidate since it emits mono-energetic conversion electrons, with three KLM conversion peaks at two main energies: [482-554-565] keV and [976-1048-1060] keV [Bé et al., 2010]. These electrons are easily reconstructed in the tracking chamber and their energy measured in the scintillator blocks. The Gaussian energy peaks measured in the OMs can be easily fitted to determine the energy scale and to follow possible gain variations over time. Taking data with several ^{207}Bi, well distributed in the detector (see section 3.3.3), on a weekly basis, allows to survey each OM at better than 1% precision. The deployment system consists of six vessels comprising a wheel connected to the source frame with stainless-steel pipes, as presented on figure 3.33. The vessels are located outside the detector shielding to ensure low radioactivity of the detector. The radioactive sources are attached to two stainless steel (SS) wires rolled onto the wheels. They can be deployed into the detector thanks to gravity with a copper plumb bob. The sources are precisely guided by two other SS wires, in dedicated gaps between the double beta source foils, as can be seen on figure 3.34 before the closure of the second calorimeter main wall. An LED system ensures the correct positioning of the plumb bob in the bottom of the source frame at the end of deployment. Motors allow to retrieve the sources after calibration and gas tight valves prevent radon to penetrate the detector through this channel.

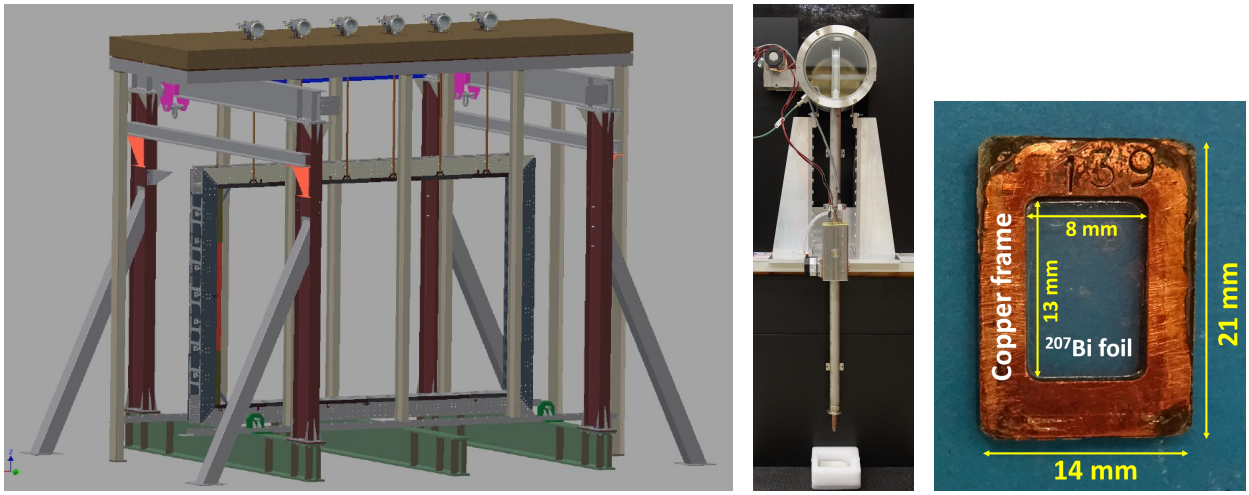

Figure 3.33: (left) CAD view of the source deployment system with the six vessels on top of the shielding and the six guide tubes to the source frame attached to one tracker frme for illustration. (middle) View of a calibration vessel with the wheel, guide tube, gas tight valve and copper plumb bob on a mock-up. (right) View of a ^{207}Bi calibration source from the NEMO-3 experiment with its copper frame and the isotope deposition on mylar foil [Arnold et al., 2021].

The reconstruction of the electrons from the ^{207}Bi sources will also help to estimate the tracking detector performances, vertex resolution, detection efficiency... To achieve a good precision on the analyses with these sources, a dedicated measurement campaign has been realized [Arnold et al., 2021]. The radioactive sources, refurbished from the NEMO-3 experiment, consist a ^{207}Bi solution droplet between two thin mylar foils (12 µm thick), enclosed by a copper frame. This allows to minimise the amount of material to be crossed by the electrons and thus, the energy losses. The publication of the qualification of the sources presents a novel method for precisely measuring the exact geometry of the deposition of ^{207}Bi droplets within the frames, using Timepix pixel detectors. This method has been developed in CTU Prague.

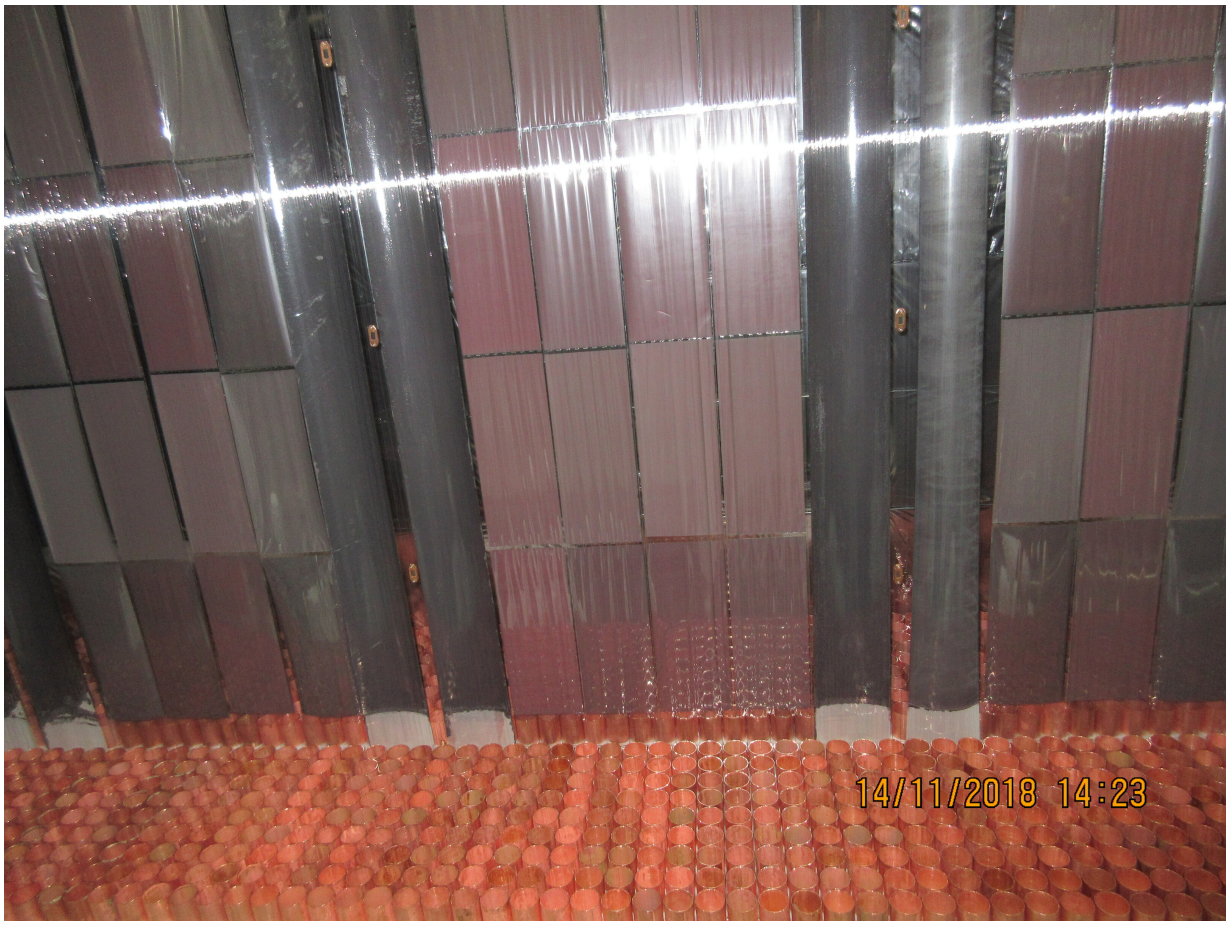

Figure 3.34: Picture of the inside of the SuperNEMO demonstrator before closure of the second calorimeter main wall. The ^{207}Bi calibration sources are visible between the isotopic sources.

49 different sources have been tested and 42 high-quality sources were selected, with the most central source positioning.

To perform more regular gain surveys, from hour to daily basis, a light-injection system has also been implemented in SuperNEMO. It relies on UV pulses from LEDs (BIVAR model UV5TZ-400-30) injected in the back of the scintillators through optical fibers (SH-4001 1.3 fibers produced by ESKA). In case of damages and for systematic studies, two optical fibers were implemented to each OM. Twenty LEDs, placed in a black electronic box outside the detector, distribute the light to bundles of fibers to illuminate the whole detector. This system can also be used to study the linearity of the PMT response. To test the stability of the light injection system, five reference OMs have been installed outside the detector, in one of the electronics racks. They are coupled to ^{207}Bi calibration sources, which emits mono-energetic γ-rays. In addition to the natural radioactivity γ's from the laboratory, the high-statistics energy spectra are fitted to precisely measure the reference OMs gains from the position of the γ energy peaks. Comparing these spectra to the peaks of the light injection system allows to follow the drifts of the 20 LEDs. The target of monitoring the reference OMs at 0.1% level has been demonstrated with the commissioning data [Aguerre, 2023].

3.9 The shielding

The shielding of SuperNEMO consists of two parts: an iron shield and a polyethylene or water shield. The iron shielding aims to stop the external γ's which could produce external background (section 2.1.2). These γ's are mostly produced by natural radioactivity in the

rocks of the LSM. To be efficient to shield high-energy γ's, it is 18 cm thick. Part of the iron shielding comes from the NEMO-3 shielding. For the rest, a new production of iron pieces has been realised in China and smaller pieces of stainless steel (SS-304) in France. The total weight of the iron shielding is about 250 tons. It is represented on figure 3.35 (left).

The neutron shielding is needed to slow down and absorb the neutrons, for which radiative captures in the detector could produce high-energy mis-identified e^+e^- pairs. Since the laboratory is deep underground, these neutrons are mostly produced by natural radioactivity through (α, n) reactions. For the top, bottom and the two smallest walls, the neutron shielding will be made of 20 cm thick HDPE plates. For the two biggest walls, 50 cm thick HDPE blocks filled with water will be used. These self-supporting blocks, developed by MRP Systems in UK, have also been used to shield the SoLid detector, see section 6.5.

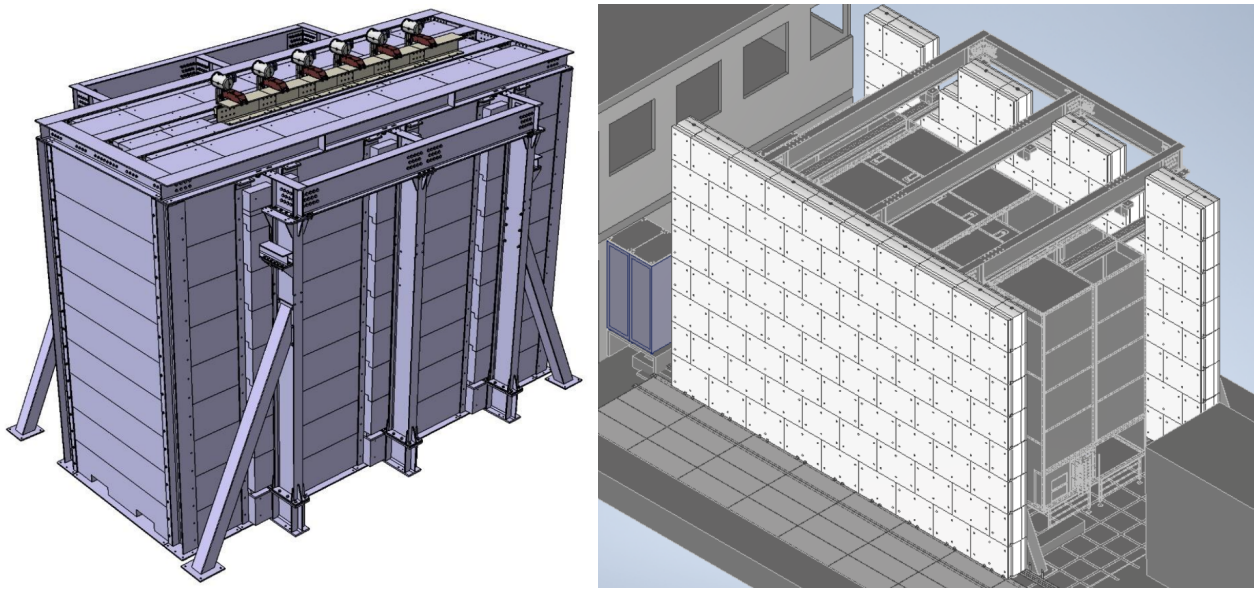

Figure 3.35: CAD view of the 18 cm thick iron shielding on its support structure (left) and of the two main shielding walls made of self-supporting HDPE blocks filled with water (right).

At the time of year 2023, the detector commissioning has been achieved and the ART has been completed. The dismantling of the integration clean tent also occurred and the SuperNEMO detector shielding assembly has started. The construction should be completed by the end of 2023 and the $0\nu\beta\beta$ search should start in 2024.

3.10 Electronics

As already explained in the calorimeter section 3.5, the SuperNEMO electronics is completely outside the detector and its shielding. All the electronics is grouped inside six electronic racks, as displayed on figure 3.36. They are located on the side of the SuperNEMO demonstrator close to the former Edelweiss experiment, see figure 3.4. Two racks are dedicated to the calibration systems, two others for the calorimeter and two more for the tracker. For these two sub-detectors, there are CAEN systems to provide the high-voltages (HV) to the PMTs or to the tracking cells and custom made front-end boards (FEB) to collect the signals. These boards are inserted inside *versa module eurocard* (VME) crates with a custom backplane developed in Orsay. The FEBs are handled by a control board (CB) in each VME crate. The CBs ensure the synchronisation of the FEBs, exchange the trigger decisions, concentrate and transmit the signals registered by the FEBs. Both calorimeter and tracker electronics are managed by a single trigger board (TB) connected to all the CBs and the DAQ. The TB distributes the 40

MHz clock and takes the triggering decision, which is configurable. A complete description of the SuperNEMO electronics can be found in the thesis of Guillaume Oliviero [Oliviero, 2018]. The rack number 4 also includes the computers for DAQ, data storage and a switch for network distribution. The collected data are daily transferred to CC-IN2P3 for storage, processing and analysis.

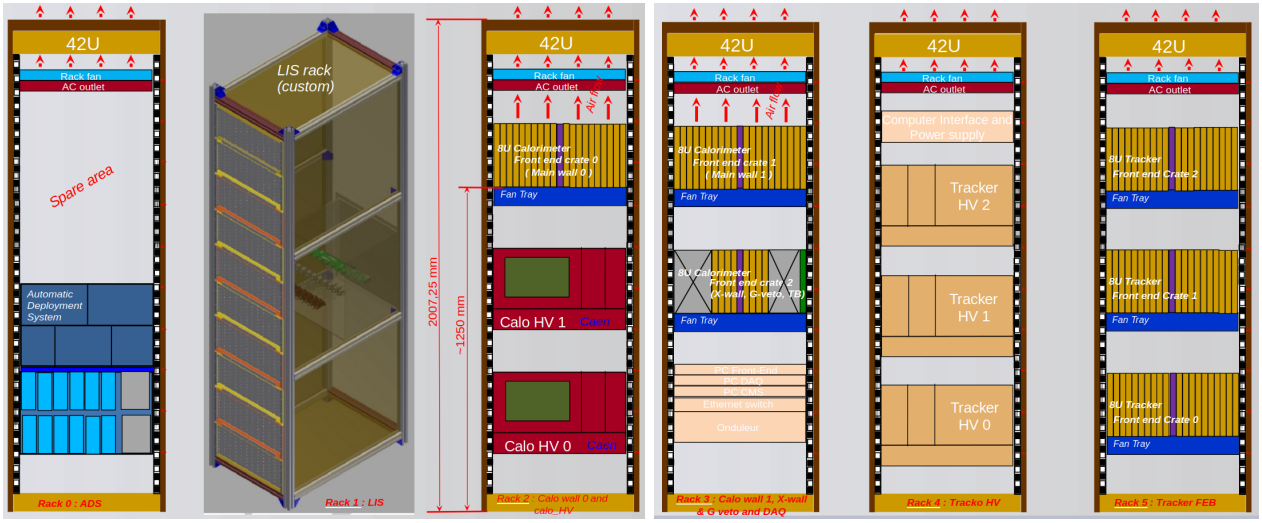

Figure 3.36: Illustration of the six electronics racks of the SuperNEMO demonstrator. From left to right these racks are dedicated to: source deployment, light-injection, calorimeter HV and FEB and tracker HV and FEB. The computing is also included in rack number 4.

The CBs and TB were developed at LAL Orsay with the calorimeter FEBs, while the tracker FEBs were developed in the UK. The calorimeter front-end electronics has been a major contribution of the French institutes and will be further presented in chapter 4 concerning the commissioning of the calorimeter.

3.11 The SuperNEMO demonstrator sensitivity

The objective of the SuperNEMO demonstrator is to improve the current best limit on the search for neutrino-less double beta decay for the ^{82}Se isotope, which has been set to $T_{1/2}(0\nu\beta\beta) > 3.5\times10^{24}$ y (90% CL) after an exposure of 5.29 kg×y by the CUPID-0 experiment [Azzolini et al., 2019d].

The PhD thesis of Steven Calvez at LAL [Calvez, 2017] was the first dedicated to the sensitivity studies of the SuperNEMO demonstrator, with the full simulation software. Using the requirements values for the background levels (section 2.1.4), Steven has demonstrated the capability of SuperNEMO to study each of the backgrounds with several analysis channels and to measure their activities, despite the extremely low levels, with a good precision (dominated by systematics) in 2.5 years of data taking with the expected 7 kg ^{82}Se source at that time. Since the detector finally contains 6.25 kg of ^{82}Se, this exposure of 17.5 kg×y could be reached in 2.8 years instead. The simulation of the main backgrounds, normalized to the requirements for SuperNEMO, performed by Steven are presented on figure 3.37 (left). This first work consisted in a standard cut analysis and simple optimization of the region of interest. Using a semi-frequentist approach to set a corresponding limit, the expected sensitivity of the SuperNEMO demonstrator would be $T_{1/2}(0\nu\beta\beta) > 5.35 \times 10^{24}$ y at 90% CL. Steven Calvez completed this study by using a multi-variates analysis (MVA) and a boosted decision tree (BDT) as presented on figure 3.37 (right). We can see a very good discrimination of almost all the backgrounds, excepts for the internal ^{208}Tl, which is harder to discriminate. Given the low levels of background expected, the multi-variates analysis only produces a moderate increase

(∼9%) in sensitivity compared to simple cuts:

$$T_{1/2}(0\nu\beta\beta) > 5.85 \times 10^{24} \text{ y at } 90\% \text{ CL.} \tag{3.1}$$

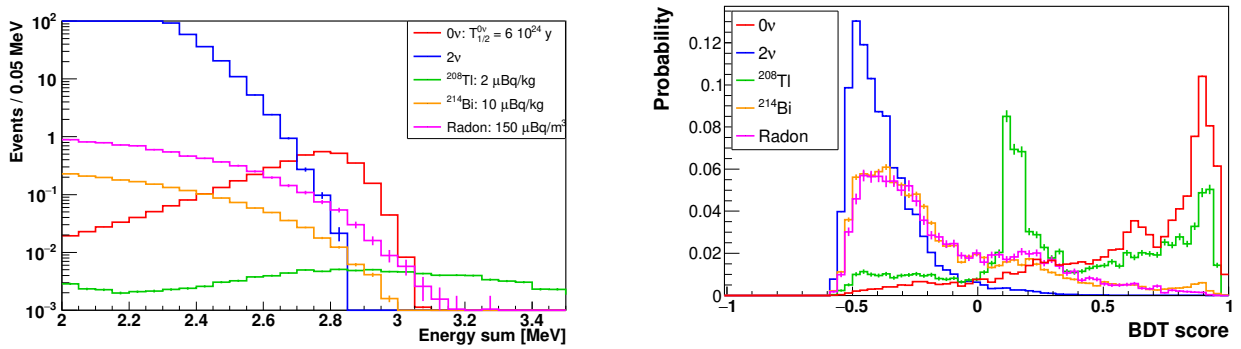

Figure 3.37: (left) Expected energy sum of the two electrons events from the main backgrounds in the simple analysis normalized to the SuperNEMO requirements, with an exposure of 17.5 kg×y. The $0\nu\beta\beta$ is normalized to unity for illustration purpose. (right) Distribution of the BDT scores of the multi-variates analysis for the simulated backgrounds and $0\nu\beta\beta$. [Calvez, 2017]

Unfortunately, the BiPo-3 measurements (section 3.3) have demonstrated that the background levels will be higher than the requirements in the SuperNEMO demonstrator. The MVA and the BDT might be mitigating this effect because these tools will be more efficient facing more background. This was already investigated in the thesis of Steven Calvez, when he compared the half-life sensitivity of the SuperNEMO demonstrator, as a function of the three main backgrounds levels. This is illustrated on figure 3.38.

For the internal ^{214}Bi, only an upper limit has been set around 300 µBq kg^{-1} by BiPo-3. In this worst case, the sensitivity would decrease to around 4.5×10^{24} y, but the MVA helps to preserve the sensitivity by 15%.

For the internal ^{208}Tl, a mean contamination of around 20 µBq kg^{-1} has been measured. This value is still a very small level and the sensitivity would only decrease to 5.5×10^{24} y, with 10% sensitivity gain from the MVA.

For the radon contamination, the MVA is much more efficient because the events are not originating from the sources. For example, even with the NEMO-3 radon level, the sensitivity would remain higher than 5×10^{24} y, with almost 150% improvement from the BDT. However, the radon measurements of the tracker commissioning have not pointed to higher radon contamination levels. But the situation might be different underground with the full detector assembled.

Conclusion

This chapter was dedicated to the description of the SuperNEMO demonstrator and its integration at LSM. The total construction of the detector is about to end in 2024, after tremendous efforts of the international collaboration. The NEMO technology offers many physics variables measured at each DBD event: individual energies, angular distribution, time-of-flight, vertex, interaction point... The first results of SuperNEMO will concentrate on thorough study of the $2\nu\beta\beta$ decay and all these variables, to improve the inputs to the theoretical nuclear models (HSD vs SSD, quenching of g_A). The numerous variables can be exploited in a multi-variates analysis to maintain a good sensitivity in the search for neutrinoless double beta decay, even in the case of higher backgrounds than expected. The BiPo-3 measurement have shown that

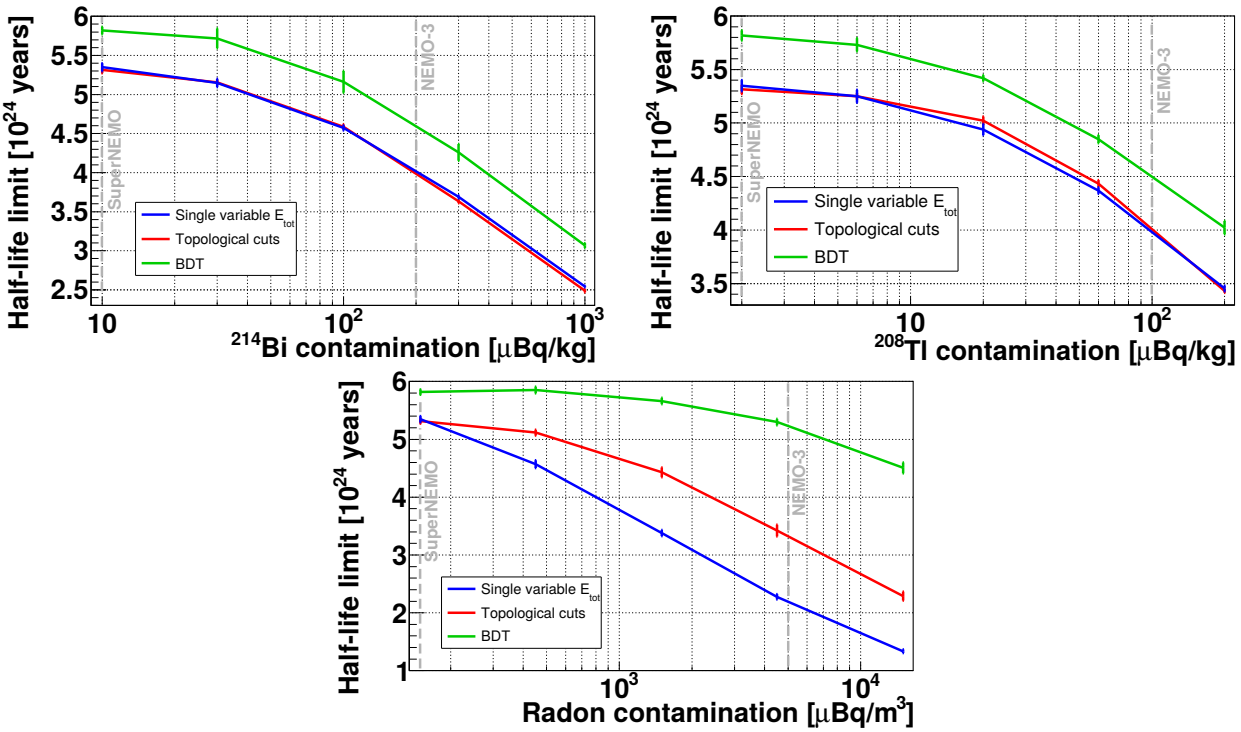

Figure 3.38: Half-life sensitivity of the SuperNEMO demonstrator with a 17.5 kg×y exposure as a function of the background levels in ^{214}Bi, ^{208}Tl and radon [Calvez, 2017].

internal contamination of the sources are higher than the requirements for the 100 kg experiment, but the impact at the demonstrator level is moderate. The limit on the $0\nu\beta\beta$ half-life of the ^{82}Se isotope should be improved by a factor two compared to the current best limit, in less than three years data taking with the SuperNEMO demonstrator.

Chapter 4

Commissioning of the SuperNEMO calorimeter

I would like to finish the SuperNEMO part of this document by a very exciting work I contributed to: the commissioning of the calorimeter of SuperNEMO demonstrator. After years of constructions underground, it was a real pleasure to switch on all these PMTs and to detect the first particles in the detector. At LAL Orsay (now IJCLab), we were on the front line on this subject because we had in charge the mechanics and the construction of the calorimeter, its cabling with the grounding of the detector, as well as the development of the front-end electronics. We had a strong support of the electronics team, Jihane Maalmi and Dominique Breton, to start collecting the first data. We will see in this chapter the quality of the PMT pulses digitizing electronics. We got also the precious involvement of our colleagues from LPC Caen, who worked with the electronics team on the data formats and trigger strategies, but also on the data processing, storage and analysis tools. Finally, our colleagues from CENBG Bordeaux (now LP2I) were also very much involved on this commissioning, since they built all the optical modules and characterised them after assembly, with the spectrometer electron beam.

All along the calorimeter commissioning, several PhD students contributed to this work, which was really motivating to me. In this chapter, I will take contributions from the work of Cloé Girard-Carillo [Girard-Carillo, 2020], Hichem Tedjidi [Tedjditi, 2021], Axel Pin [Pin, 2020], Malak Hoballah [Hoballah, 2022]. Cloé and Malak being students at IJCLab, I participated to the supervision of their work on the detector commissioning, Laurent Simard was their supervisor. Concerning the energy calibration of the optical modules with γ-particles, we reused the method firstly developed for the BiPo detectors. In the mean time, this method was improved in SoLid within the thesis of Noë Roy [Roy, 2021], that I supervised. The calibration of the optical modules was initiated in the thesis of Axel Pin and pursued in the thesis of Xalbat Aguerre [Aguerre, 2023].

Chapter contents

Introduction

After the detector closure and the cabling operations of the calorimeter, and since the front-end electronics was ready, we had everything in hand to start taking data with the calorimeter at the end of 2018. The only limitation was the integration of the trigger board to orchestrate the communication between all the control boards, which was not though to be needed yet. The tracker cabling was unfortunately delayed after the discovery of cracks on the tracking cells cabling feed-through connectors. The tracker commissioning was then further delayed because a deformation of the tracker was observed in 2019, from the top at the joining of the C-sections. This was first identified by testing the cells, where many short-cuts on the cells at the center of the trackers had been identified. After fixing all these issues, the tracker commissioning could resume in 2021. After I moved to Subatech during Summer 2020, I had to progressively reduce my activities on SuperNEMO, thus my contributions stopped on the commissioning of the calorimeter, which is the subject of this chapter.

4.1 Calorimeter preliminary tests

We have presented in section 3.5.6 the cabling of the SuperNEMO calorimeter with two networks, one for signal cables and one for HV cables. We remind that both are separated in two corresponding to internal or external cables separated by patch-panels on the anti-radon tent. Most of the cabling work, from cutting the cable, soldering of the connectors to the routing and the connection to the PMTs or the electronics boards, have been done manually. Some continuity tests were performed with multimeter by the cabling team, but no more precise tests of the cables were realised before integration. Damages could have also been made to the cables during transportation, cleaning or integration on the detector. The first stage of the calorimeter commissioning consisted thus in testing the whole cabling network. Different kind of tests have been deployed to check the signal or the HV cabling networks.

4.1.1 HV cabling tests

Concerning the HV cables, the tests were rather simple. We have switched on the PMT HVs per power supply board, each of them corresponding to different sectors of the calorimeter. We started by setting low voltages, of the order of 100 V, with different values for each of the 32 channels of the board. With a voltmeter, we could check directly on the calorimeter the voltages of the PMT dividers. Reading the correct voltage value allowed first to validate (or correct) the mapping between the PMT position on the calorimeter and the HV channel at the electronics side. This secondly allowed to check the correct delivery of the HV up to the PMT divider. This was further tested by increasing progressively the HV to 500 V, 1000 V, 1200 V and finally to nominal HV value of the PMT. This required to cover the detector with black plastic protections and to switch off the light in the LSM, since the detector was not light tight at this stage of integration. Increasing to higher voltages allowed to reveal tripping channels, meaning a shortcut was arising somewhere. This occurred if a cable had been pinched at some place along the cable, if a connector was broken, if a pin was disconnected at the PMT divider or if the copper braid was touching the PMT circuit. These minor issues were fixed when needed. At the nominal HV, we have finally checked that the delivered currents per channel were of the same order for all the channels (with different values for 5-inch and 8-inch PMTs). After these operations, the HV system of the SuperNEMO calorimeter was fully operational.

All these operations seem rather simple, but it is worth to mention that even basic tests, in an underground laboratory of hot and dry atmosphere, in a noisy and low light environment, inside a clean room with clean suits and gloves, creeping under the detector or at 5 m high on a scaffolding, are never easy tasks.

4.1.2 Signal cabling tests

Reflectometry measurements

The first quality tests performed on the signal cabling were possible without switching on the PMTs, and thus avoided covering the whole detector for light tightness or work in the dark. For the very first tests, a very powerful feature of the SuperNEMO front-end electronics has been used. In each board there is the possibility to generate an electronic signal, with a gate shape, which is injected into each signal channel. These pulses are then transmitted through the coaxial signal cables to the PMT dividers, where it is then reflected by the RC circuit back to the electronics. This feature allows to test the whole chain of signal transmission and its quality. We called these measurements *reflectometry*.

Thanks to the 400 ns length of the sampling window (see section 4.2) and the maximal cable length of about 18 m, both the generated and the reflected pulses can be digitized and stored in the same waveform. An example of such waveform for one SNFEE board with 13 channels is shown on figure 4.1. We can see the first generated pulses around 100 ns and the reflected pulses starting from around 200 ns. As expected, the generated gate is exactly the same for all the channels. Concerning the reflected pulses, we can observe three features:

- there is a few nanoseconds time shift in the return of the pulses, which is due to the increasing cable lengths. The routing of the signal cables is made by rows of two, one above and one below the cable, and the rows are separated by approximately 50 cm. This is why the reflected pulses come grouped by two, except for the 13^{th} which is alone.
- the reflected pulse shapes are varying with the increasing cable length. We observe an attenuation in amplitude, which is partly compensated by a broadening of the pulses.
- two different shapes of reflected pulses can be seen between the 5 and 8 inches PMTs. The first and the last pulses, corresponding to the 5-inch PMTs, present a wavy shape. The others, corresponding to the 8-inch PMTs, are closer to a gate signal. This can be explained by the difference in the decoupling resistance on the PMT dividers, which are 1 MΩ and 10 kΩ for the 5-inch and 8-inch PMTs respectively.

The analysis of the reflectometry data allowed to perform the visual inspection of the reflected pulses. Firstly, we needed to check if the time position of the reflected pulse was correct. For example, we detected issues at the patch-panel where the pulses were reflected at a shorter time, see figure 4.2 (top). We could also spot wrong cable lengths in this way. Secondly, the shape of the reflected pulses allowed to investigate connection defects or damages on the connectors or the PMT dividers, see figure 4.2 (bottom). All these defects were minor and were easily corrected. The reflectometry measurements really provided an efficient quality checking of the signal calorimeter cabling.

PMT signals verification

To go further in testing the calorimeter signal cabling, we have used the PMT signals. First, we switched on the PMTs one by one and checked on the acquisition if the correct channel was triggering and showing PMT pulses. For this test, we used the online software inherited from the WaveCatcher software, which was also used to test the calobricks before integration

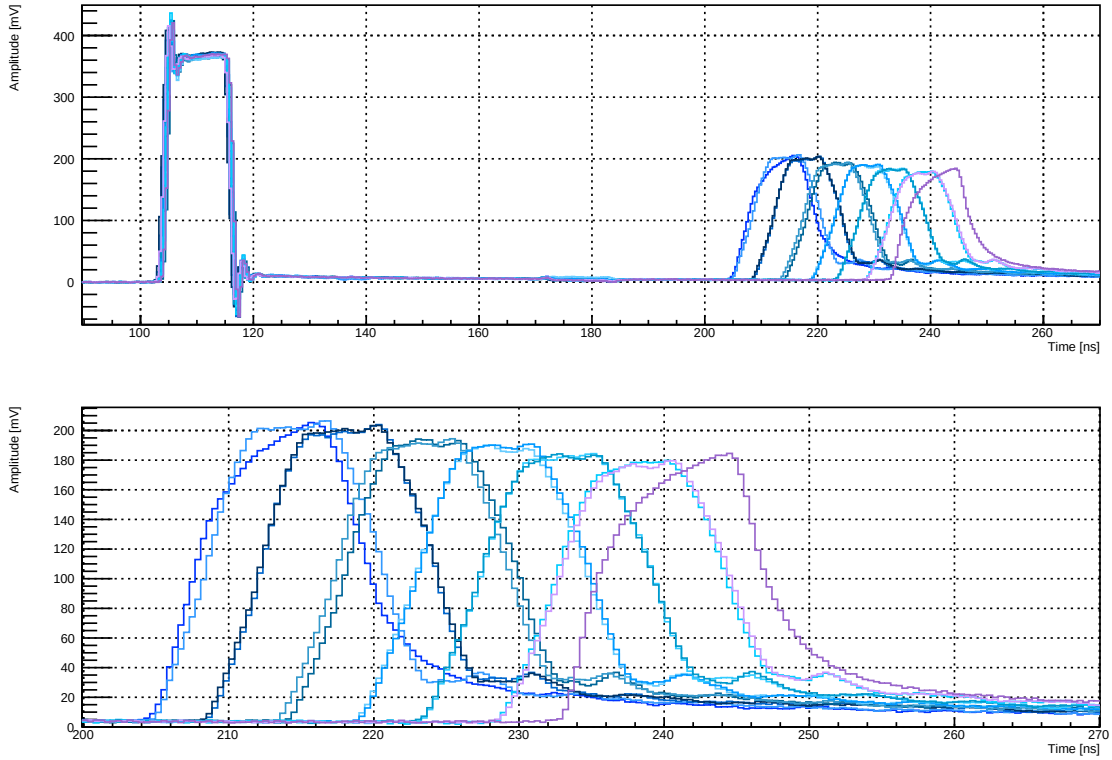

Figure 4.1: (top) Reflectormetry example of the averaged waveforms of the 13 channels of one SNFEE board. The generated pulses can be seen around 105 ns and the reflected pulses starting from 205 ns. The time shift and the attenuation are explained by increasing cable lengths. (bottom) Zoom on the reflected pulses. The two wavy shapes correspond to the top and bottom 5-inch PMTs.

on the calorimeter wall, see section 3.5.5. This test also allowed to validate the correspondence between HV and FEB channels. Secondly, a visual inspection of the PMT pulses helped to find more problematic channels. When it was a connection issue or a defect on the PMT divider, this was solved on the detector. On the other hand, few problematic channels revealed some broken PMTs. This was confirmed by looking from the back of the PMT, where the normal yellowish color of the PMT was gone. This means the photocathode was sublimated because of broken vacuum. These damages might have been caused by a shock on the PMT or too much stress on the pins exiting the glass. Since the PMTs were tested at LSM just before integration on the wall, damages certainly occurred during the screwing of the calobricks together. A summary of the non-functioning PMTs can be seen on figure 4.3. In total, 16 PMTs are not operating over 712 PMTs, which represents around 2% of defects.

Reflectometry time measurements

As already said, we have decided to minimise the amount of cable inside the anti-radon tent, in order to reduce the radioactivity background. Thus the PMT cables have been cut to the exact lengths to reach the PMTs. This will produce time delays between the different channels of the segmented calorimeter, which needs to be calibrated. In SuperNEMO, the timing performances are of major importance. Indeed, coincidences are needed between the two DBD electrons, but also to reject crossing electrons, which are external background events produced by γ-rays, see section 2.1.2. This is done thanks to the time-of-flight analysis [Boursette, 2018].

The reflectometry measurements are a nice way to produce a first measurement of the time difference between all the channels. This was a mandatory step before trying to produce any physics data. We have performed this study in the thesis of Cloé Girard-Carillo

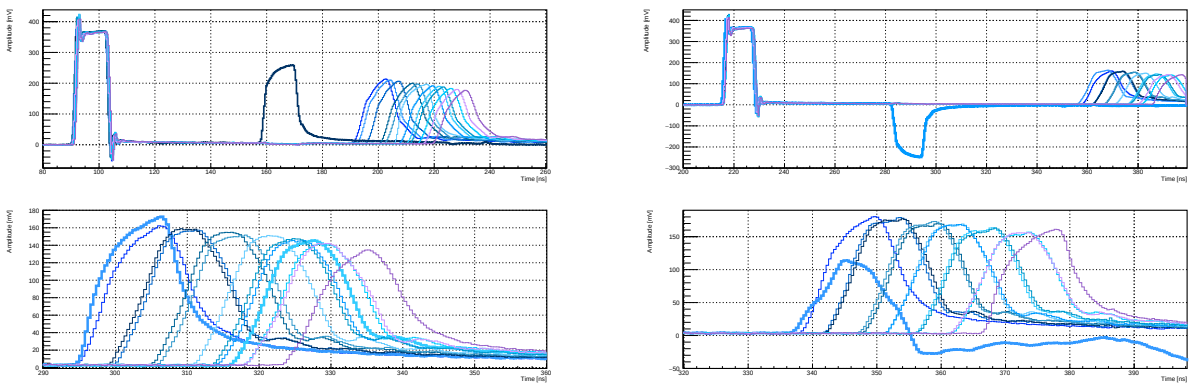

Figure 4.2: Examples of bad reflected pulses, highlighted by the thicker line: (top) at the patch-panel level corresponding to a disconnected cable (left) and a shortcut in the connector (right) ; (bottom) at the PMT divider level with a disconnected pin and a too long cable (left) and a swap of the two pins of the signal cable at the PMT divider (right).

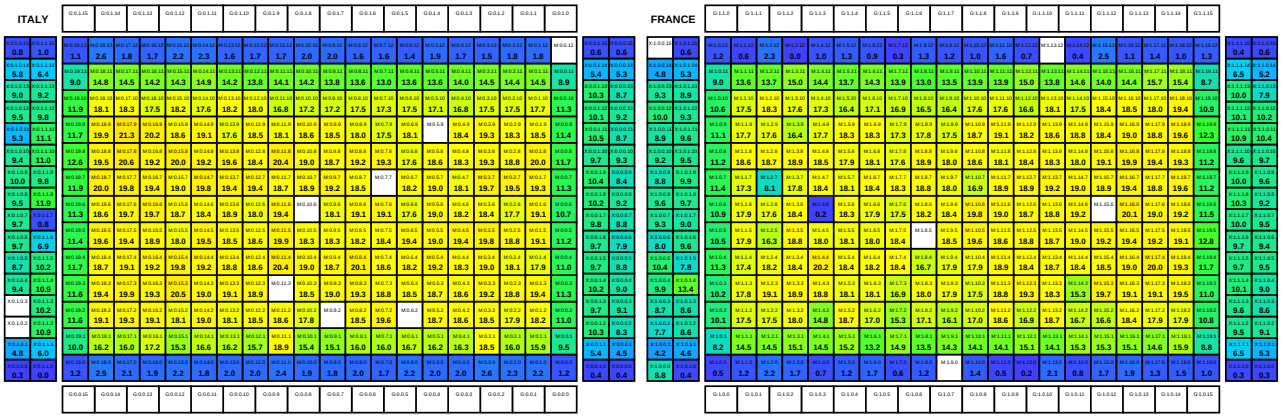

Figure 4.3: Most recent illustration of the functioning PMTs of the SuperNEMO calorimeter, as of Summer 2023, without detector shielding. The picture represents the counting rate per minute of electron-like events, for the two sides of the detector (France or Italy), having a coincidence between the scintillator block and at least one tracking cell, in the three layers in front of the block. The blocks dedicated to γ-particles detection (G-veto and top/bottom rows of the MW) remain white since they are not detecting these electron-like events. Courtesy of Emmanuel Chauveau.

[Girard-Carillo, 2020]. The analysis of the waveforms was exploited to measure the time difference between the generated and reflected pulses for each channel. We expect a small bias from this measurement because the shape of the generated and reflected pulses are different, as well as their rise times. But this should represent only a minor correction. To be independent on the amplitude of the signals, the time of the pulses has been defined by its *constant fraction discriminator* (CFD) time, which has been found to be optimal around 50% of the pulse amplitude for this type of pulses [Girard-Carillo, 2020]. With a dedicated test, such analysis have first confirmed the propagation speed in the coaxial cable at $v_p = 0.69 \times c$. A second test, which consisted in splitting the same signal into two channels, provided the precision of the time measurement with this method, which revealed to be $\sigma_t \approx 70$ ps. Finally, all the time differences were measured for the 712 channels, see figure 4.4 for the M-Walls. A resulting time calibration file has been produced and shared with the whole collaboration, for the first commissioning analyses.

For the anecdote, this analysis showed that few cables were longer than expected. One cable had also to be swapped on the French-side calorimeter main wall, because it was too short to reach the foreseen PMT. These defects have no impact on the performances, since the delays

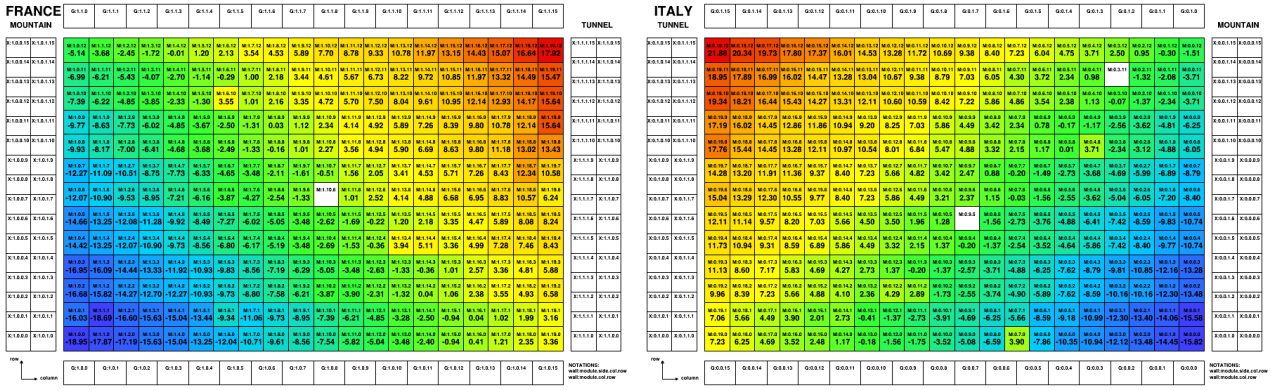

Figure 4.4: Result of half the time difference measurements between the generated and reflected pulses in reflectometry runs, for the two calorimeter main walls [Hoballah, 2022].

are corrected by the time calibration. Despite a small systematic drift of 10 cm, all the other cables were cut at the correct lengths with a dispersion of about 5 cm [Girard-Carillo, 2020].

Calorimeter FEBs synchronisation

The previous work allowed to compensate the time differences between channels due to different cable lengths. Another source of time delay has been identified between the calorimeter FEBs. These boards are managed by the control boards in the middle of the frame, which communicates to ten boards on each side through the backplane, see section 3.10. Depending on the position of the board in the frame, different communication times have been observed. This has been characterized with another dedicated campaign using a split signal sent to two different boards. The time difference has been measured for all the channels in the three crates. The effect is of second order compared to cable lengths since a spread of ± 1 ns, correlated to the distance to the control board, has been measured [Girard-Carillo, 2020].

4.2 PMT pulses reconstruction

All the informations about particles interactions in the SuperNEMO calorimeter need to be extracted from the PMT pulses. The PMT pulses are digitized in the SNFEBs at 2.56 GS/s overs 1024 samples, providing a total time window of 400 ns. An example of 8-inch PMT pulse is presented on figure 4.5. In order to reconstruct the best possible parameters for the determination of the physics variables of interest in each event, pulse shape analysis algorithms have been developed on the SuperNEMO PMT signals.

A complete description of the data format produced by the acquisition is detailed in the thesis of Guillaume Oliviero [Oliviero, 2018]. The events are a collection of hits described by a header followed by metadata which are computed by the SAMLONG chip and the digitized samples. For the calorimeter hits, these samples are 1024 values of ADC encoded in 12 bits, corresponding to the 1 V input range of the chip (0.25 mV steps). The timestamp of the trigger is encoded by the 40 bits TDC counter provided with a 160 MHz clock by the SAMLONG chip (6.25 ns steps) and corresponds to the end of the sampling window. The measured time of the pulse must then be reconstructed by the following equation:

$$t_{meas}\ [ns] = TDC \times 6.25\ [ns] - 400\ [ns] + t_{CFD}\ [ns] \tag{4.1}$$

where t_{CFD} corresponds to the time of the pulse in the sampling window, as described below.

We have defined four parameters of major interest that are computed for each PMT pulses:

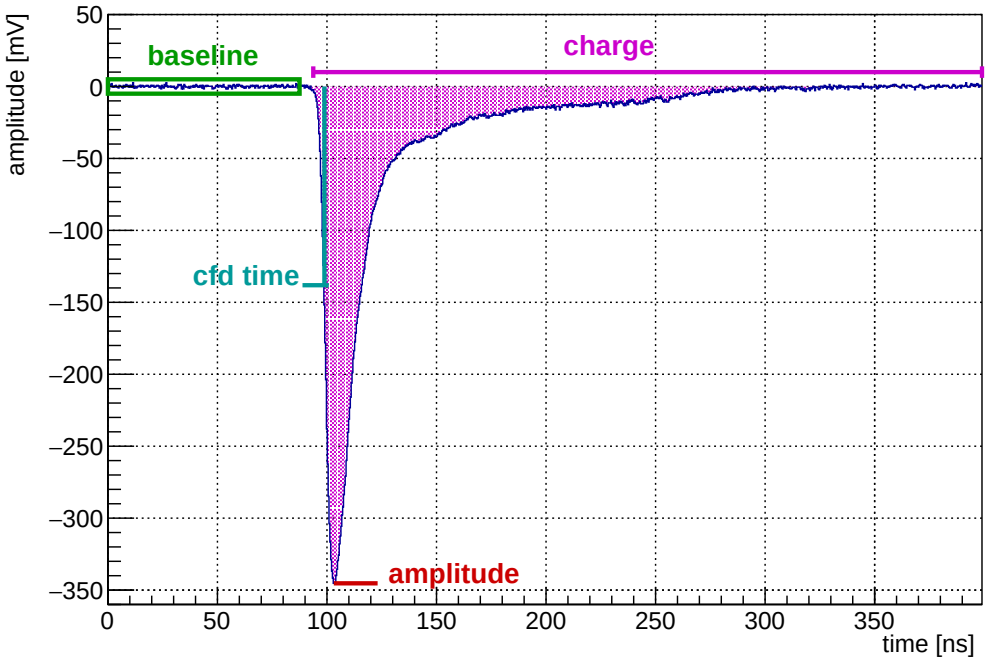

Figure 4.5: Example of one of the first 8-inch PMT signal recorded at LSM. The four main parameters used in the analysis have been illustrated as reconstructed on the PMT pulse.

- **baseline:** a space of 93.75 ns is left before the PMT pulse in order to compute the baseline mean amplitude and its standard deviation for the channel, both expressed in mV. This is very important for a precise energy determination in each event and the survey of the calorimeter stability over time. Sometimes, noise or PMT pre-pulses can occur in this region. For this reason, the algorithm is investigating the samples per block of 16 samples (6.25 ns) and would stop at the previous block if a deviation of 5σ is found. The baseline algorithm and the stability of the baseline for the whole calorimeter has been studied in great detail in the PhD thesis of Hichem Tedjiditi [Tedjditi, 2021]. Most of the baselines are within [-0.25,0.25] mV with a mean standard deviation of about 0.09 mV. An excellent stability over the duration of a run (about one hour) has been demonstrated.

- **amplitude:** once the raw ADC values of the samples have been converted to mV, the amplitude of the pulse is simply its minimal value. This position can also give the time of the peak but this is not the best region for precise time determination, because of the cancellation of the derivative. The amplitude was used as a first estimator for the energy but we have seen that attenuation with increasing cable length changes the amplitudes for a same input signal. However, it is still the estimator used for the trigger decision on channels, which is set on the amplitude passing a certain threshold.

- **CFD time:** the time measurement on a pulse is the most precise in the sharp rising of the pulse (high derivative). If we were using a fixed threshold value of the amplitude to determine the time, we would be dependant of the total amplitude of the pulse. For example, this phenomena required to determine time-energy corrections in the NEMO-3 experiment, which can bring uncertainties. Using a constant fraction discriminator (CFD) time removes the dependence on the total signal amplitude. Once the pulse amplitude has been determined, the algorithm simply look back in the samples the closest to the fraction of amplitude. The optimal value has been found to 40% of the pulse amplitude for PMT signals [Girard-Carillo, 2020]. A linear fit between the samples around this amplitude is

performed to get the interpolated time crossing the relative threshold.

- **charge:** the charge of the pulse is simply the rectangular integration of the area under the pulse, right after the baseline till the end of the time window, multiplied by the 390.625 ps (2.56 GS/s sampling frequency) time gap between the samples. It is expressed in nVs. This is the estimator we use to reconstruct the deposited energy in the scintillator by the particles, which needs to be calibrated [Aguerre, 2023].

An attempt to fit the 8-inch PMT pulses from a template with a matched-filter analysis, has been developed in the thesis of William Quinn at UCL [Quinn, 5 28].

4.3 Time calibration of the calorimeter

4.3.1 Sources of time dispersion

We have seen the sources of time difference on the electronics side between the channels of the SuperNEMO calorimeter. These differences are constant shift which can be corrected thanks to calibration. Now we will focus on the instrumental timing response. A major aspect for the time-of-flight analysis is the existence of variations (or jitter) in the individual time measurements with the different OMs. In SuperNEMO calorimeter, these spreads could originate from the scintillator or the PMT. These sources listed below are also illustrated on figure 4.6 (left):

- **particle type:** the calorimeter of SuperNEMO is dedicated to the detection of electrons and γ-particles. The electrons will enter from the tracking chamber into the front face of the scintillator, to leave energy in the first few millimetres. The γ-particles could interact at any location in the scintillator volume. They travel at the speed of light c like in vacuum, while the scintillation photons travel at lower speed c/n_{PS} ($n_{PS} = 1.59$ being the refractive index of polystyrene scintillator). For an 19 cm deep scintillator, it could represent 1 ns time difference.
- **scintillator interaction point:** the light collection in the scintillator towards the PMT depends on the position of the scintillation light emission. This effect will have a small impact for electrons since the distance between the front face and the PMT is not very different [Huber, 2017]. In addition, thanks to the tracking which provides the location of the impact point on the scintillator, it could be calibrated. On the other hand, γ-particles could interact anywhere in the volume of the scintillator and the effect should be very dependent on the position. We also expect more sharing between the direct and reflected light collections for γ's than for electron, where the direct light should dominate.
- **scintillator time response:** the timing measurement is dominated by the fast component of the scintillation light, which has an exponential decay slope. The decay time constant of 2.5 ns for the plastic scintillators of SuperNEMO, can produce fluctuating shift and spread in the light emission.
- **PMT transit time:** the transit time spread (TTS) of the PMT is a fluctuation of the transit time (TT) of the PMT pulses. They both depend on the size and location of the illuminated part of the photo-cathode, since the photo-electrons could have a different pathways to the focussing dynode. The mean values of these parameters also depend on the number of photo-electrons detected, in $1/\sqrt{N_{pe}}$.
- **PMT HV:** the voltage applied to the PMT and more specifically to the electron-optical input system. The higher is the PMT voltage, the lower are the transit-time (TT) and the transit time spread (TTS). In order to optimize the uniformity of the energy measurement of the calorimeter, the PMT HV have been adapted to the response of the fully assembled

OM. This produces a wide range of voltages applied to the PMTs, from 1200 V to almost 1700 V. These voltage differences can have an important impact on the timing response of the PMT, as can be seen on figure 4.6 (right). Between these two extreme values, we could expect the TT to vary from 70 ns to 50 ns, and the TTS to vary from 3 ns to 2 ns. The rise time is also depending on the HV applied to the PMT.

- **PMT signal dynamics:** finally the shape of the PMT signals could differ from one PMT to another. In addition, we use a mix of 5 and 8 inches PMTs, which should show different pulse shapes. The use of CFD time should account for the difference in the amplitude of the pulses, and should not be a source of dispersion.

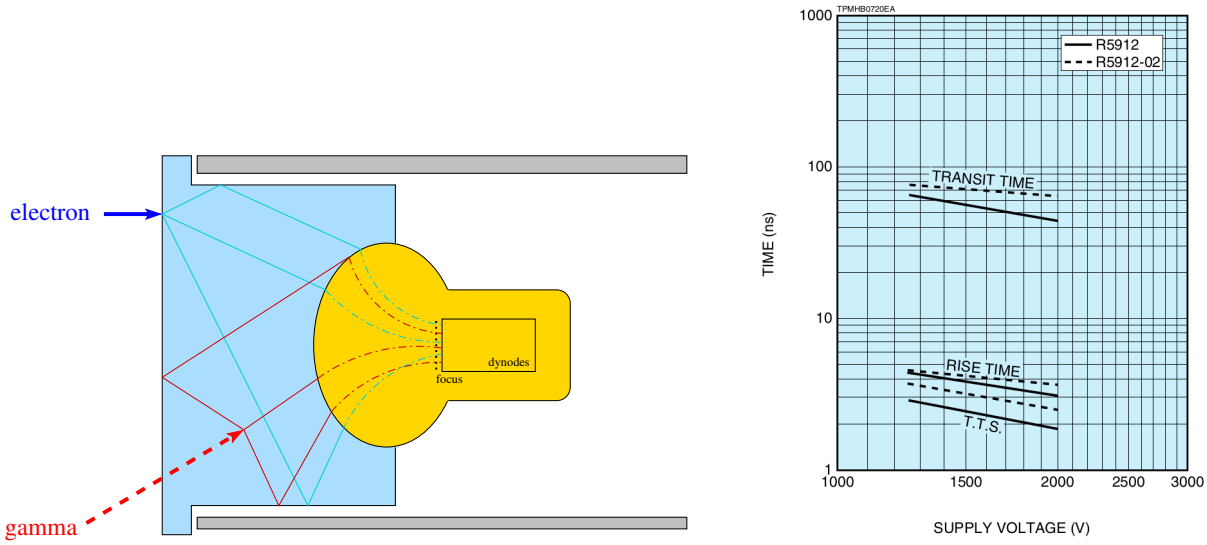

Figure 4.6: (left) Illustration of the different sources of timing difference or dispersion: particle type, interaction point, transit-time and transit time spread in the PMT. (right) Timing response of the Hamamatsu R5912 PMTs used for SuperNEMO calorimeter, as a function of the HV applied.

4.3.2 Time calibration with the ^{60}Co source

The ^{60}Co source

The ^{60}Co source is very well suited to perform time alignment of several detectors, because it emits two γ-rays in time coincidence, with 1.17 and 1.33 MeV energies, as illustrated on figure 4.7. Comparing the time measurements of two particles detected in the scintillators would integrate all the processes (electronics, instrumental and physics) that could produce time delay or jitter. It was thus the method used to go further in the time calibration of the SuperNEMO calorimeter and latter study its time resolution.

The ^{60}Co source, with an activity of about 200 kBq, was loaned from Orsay and twice transported to LSM, for the dedicated campaigns. It was one of the very first measurements performed in the context of the PhD thesis of Cloé. Unfortunately, we were in the same time working on the energy calibration of the calorimeter and the alignment was not good enough to provide accurate results for the whole detector. Nevertheless, this allowed to develop the methodology and the work was pursued and improved in the thesis of Malak [Hoballah, 2022].

After coverage of the SuperNEMO detector with black plastic sheet, the measurements were taken in the dark with the ^{60}Co source. Without detector shielding, this measurement was facing an important external background. In addition, the source had to be placed 1 m away from the detector, in order to increase the coverage of the calorimeter sections. But this

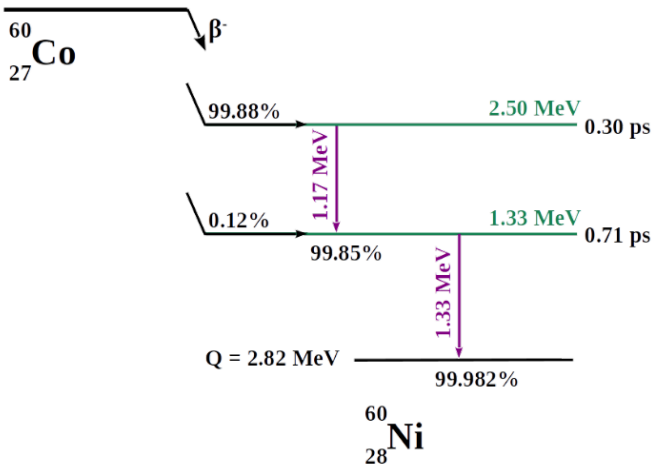

Figure 4.7: Simplified decay scheme of ^{60}Co [Girard-Carillo, 2020], reproduced from [Bé et al., 2006].

reduces the signal to background ratio. To qualify the whole detector, the source was placed in nine positions for each M-wall and one position for each of the X-wall and G-veto (26 positions in total). At this early stage of detector commissioning, it was not possible to take a global acquisition using the full detector. Hence, acquisitions were performed separately for each calorimeter part, M-wall and X-wall and G-veto.

Working only with γ-particles provides very little information on the event topologies, which is also increasing the background. The background could come from natural radioactivity of the detector materials or from the laboratory rocks. We could have accidental coincidences of two γ-particles or a double Compton effect of the same γ, in two different scintillators. Among the γ-ray lines, the 2.6 MeV line of ^{208}Tl would be very close to the total energy of the two γ's of ^{60}Co. In addition to runs with the source, several runs were taken without source in order to register this external background. At lower energy, the double Compton coincidences could also be produced by the γ's from the ^{60}Co source. Despite all these difficulties, basics cuts allowed to reach sufficient background rejection to produce performant time analyses. Firstly at the trigger level, where two hits above 300 keV within 62.5 ns were required. Secondly offline, by asking for spatial coincidences and removing the direct neighbours of a given OM. This was completed with energy cuts on the two deposits in the scintillators. As presented on figure 4.8 (left), the double Compton of the same γ from ^{60}Co produces two energy peaks around 0.3 and 0.8 MeV (Y-axis). Using only energy deposits larger than 0.7 MeV and lower than 1.4 MeV would ensure the detection of the two γ's emitted by the source. Finally, a minimum of 50 coincidences for a couple of OMs was requested to get a minimal statistics. An example of coincidence rate map after these cuts is presented on figure 4.8 (right).

Time calibration

Thanks to the ^{60}Co calibration data, we aim to compensate all the timing differences between two channels of the SuperNEMO calorimeter, as presented in section 4.3.1. Starting from the measured time of a calorimeter hit given by equation 4.1, we want to build the absolute time of the hit considering the time-of-flight of the γ-particle emitted from the source, supposing the γ interacted in the middle of the scintillator. The absolute detection time of the OM i can thus be written as:

$$t^i_{abs} = t^i_{meas} - ToF_i - \kappa_i \tag{4.2}$$

where κ_i is the total time calibration constant we want to determine. The time difference between two OMs, $\Delta t_{ij} = t^i_{abs} - t^j_{abs} = \kappa_j - \kappa_i$, will provide the relative delay between the calibration constants κ. The delay time distributions present a Gaussian shape easy to fit.

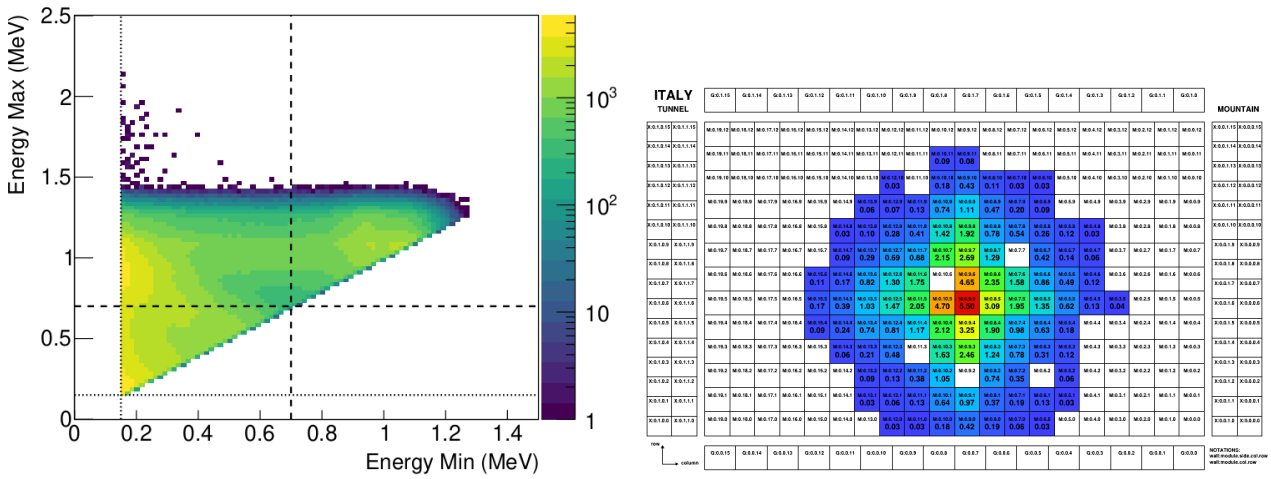

Figure 4.8: (left) Simulated maximal versus minimal energies distribution for ^{60}Co events in coincidence, with the minimal energy cut of 0.7 MeV illustrated by the dashed line [Girard-Carillo, 2020]. (right) Coincidence rate per OM in Hz for a ^{60}Co run with the source at the center of the Italian-side M-wall, after application of the cuts presented in the text [Hoballah, 2022].

The fitted mean value is used to determine the calibration constants, and the fitted standard deviation to determine the uncertainty. We have to define a reference OM, for which $\kappa_{ref} = 0$ ns, respective to which all the OMs will be relatively calibrated. Since these calibration runs could only be acquired by calorimeter crate, three reference OMs have been used, one for each M-Wall and one G-veto block. The result of this process for all the M-Wall OMs is presented on figure 4.9. The values have also been computed for the X-wall and G-veto blocks.

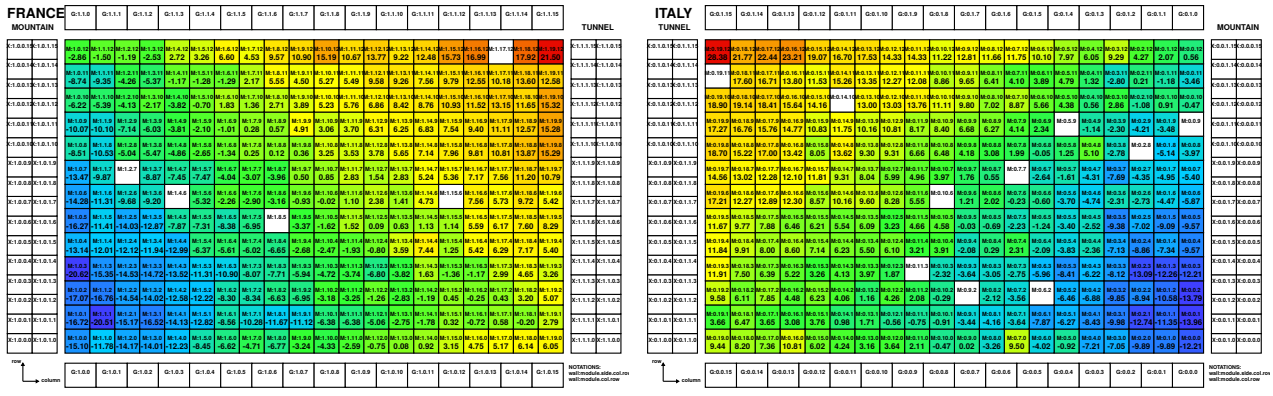

Figure 4.9: Result of the time difference measurements with the ^{60}Co data, determining the relative calibration constants κ_i for the two calorimeter main walls [Hoballah, 2022].

We recognize the pattern dominated by the cable lengths, as in figure 4.4. It confirms that the other effects are smaller order corrections to the time delay. The statistical uncertainties on these calibration constants present a peaked distribution around 30 ps for each of the M-walls, with a standard deviation around 20 ps. However, there are several uncertainty values extending up to ∼100 ps in a tail, which might require further studies or data. For the X-wall and G-veto, this uncertainty distribution is peaked around 80 ps and show a wider spread around 40 ps. Some systematic studies have been performed to test the validity of the results looking at several points of the method, but the results were found stable [Hoballah, 2022].

In order to verify these results, a comparison with the reflectometry measurements has been performed. A good correlation has been observed and the difference between the calibration constants is below one nanosecond. The dispersion is however larger since a standard deviation

of about 2 ns has been found. The reasons for these differences are known and further studies could be realized if necessary. For example investigating the dependence as a function of the cable length (for signal shape attenuation), of the PMT HV, 5 or 8 inches PMTs or other parameters.

After applying the calibration constant to the time measurements, the final check performed in Malak's thesis consisted in checking the time-of-flight alignment of the two γ's of ^{60}Co. The distribution of the ToF difference between the two OMs are well centred at zero. The standard deviations are about 120 ps for the M-wall and around 300 ps for X-wall and G-veto OMs. These OMs have poorer light collection and thus poorer time resolution. The choice of a better reference OM, in the M-wall might have improved the precision of the calibration for these OMs. Nevertheless, these results are quite impressive given the status of the detector in this early commissioning, without shielding installed around the detector. This result is very promising regarding the performances of the SuperNEMO calorimeter and its electronics.

4.3.3 Calorimeter time resolution determination with the ^{60}Co source

Now that the calorimeter OMs have been aligned thanks to the time calibration, we want to measure the time resolution of each OM. This will be decisive for the quality of the time-of-flight analysis, which is based on a χ^2 comparison with a formula of the type $\chi^2 = (\Delta t)^2/\sigma_t^2$, see for example [Boursette, 2018]. The objective is to be at least as good as NEMO-3, for which $\sigma_t =$ 250 ps at 1 MeV, or even better. However, the SuperNEMO scintillators blocks have a larger volume and the PMTs have also a larger diameter. This is not going in the right direction to improve the timing performances. The SuperNEMO digitizing electronics might be able to mitigate this effect.

In order to determine the individual time resolution of each OM, a new method has been developed. The uncertainties on the time difference measurements, noted σ_{ij}, presented in the previous section represent a combination of the time resolution σ_i for each of the two OMs:

$$\sigma_{ij}^2 = \frac{\sigma_i^2}{E_{ij}} + \frac{\sigma_j^2}{E_{ji}} \tag{4.3}$$

where E_{ij} corresponds to the energy measured by the OM i in the events in coincidence with the OM j, and E_{ji} the opposite. The energies must be taken into account since the time precision depends on the number of photons detected, thus on the energy. In order to determine the individual time resolutions σ_i, we can triangulate between three OMs and use the measurements for the couples ij, jk and ik. Solving the system of three equations allows to determine the three resolutions of interest. Repeating these calculations allows to get the individual resolutions for all the OMs of the SuperNEMO calorimeter. The result is presented in form of maps on figure 4.10. The result is quite uniform except for the top and bottom rows, which show poorer time resolution since the OMs consist of 5-inch PMTs.

To determine the precision on the computed time resolutions, similar maps have been realized with the uncertainty for each OM on figure 4.11. We can directly see on these figures the pattern of the nine positions of the ^{60}Co source for each M-wall. When the OMs are further away from the source we observe an increase of the resolution, which is responsible for this pattern. This is certainly due from one hand to a lower statistics for the farther away OMs. On the second hand, this might also be due to the method which associates the OMs from the position of the source to the edges. We can thus suspect accumulation of the uncertainties during the process. This could be improved by taking more data with more source positions. Having a shielding to reduce the laboratory background would also be an improvement.

In order to provide a number on the SuperNEMO calorimeter time resolution, weighted averages have been computed for the 5 and 8 inches PMTs. Systematic studies varying the

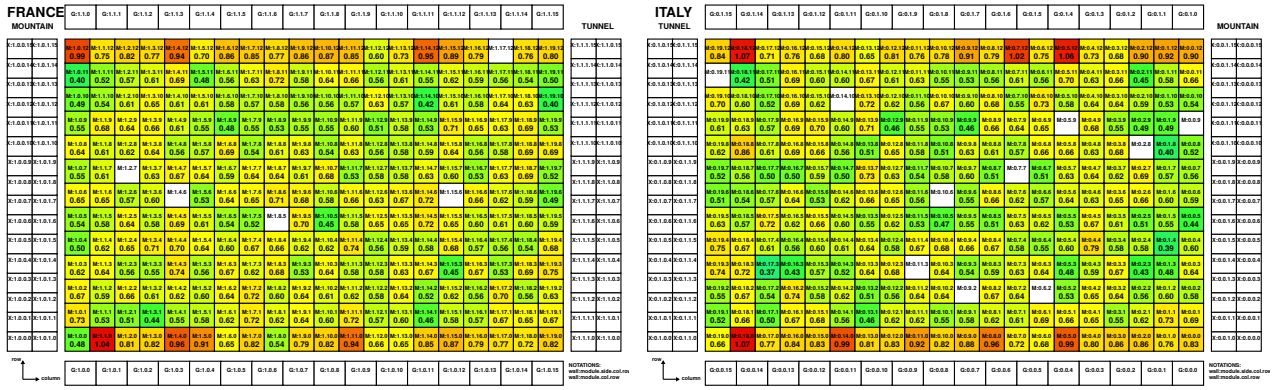

Figure 4.10: Time resolution measurements of each OM of the two calorimeter main walls with the ^{60}Co data [Hoballah, 2022].

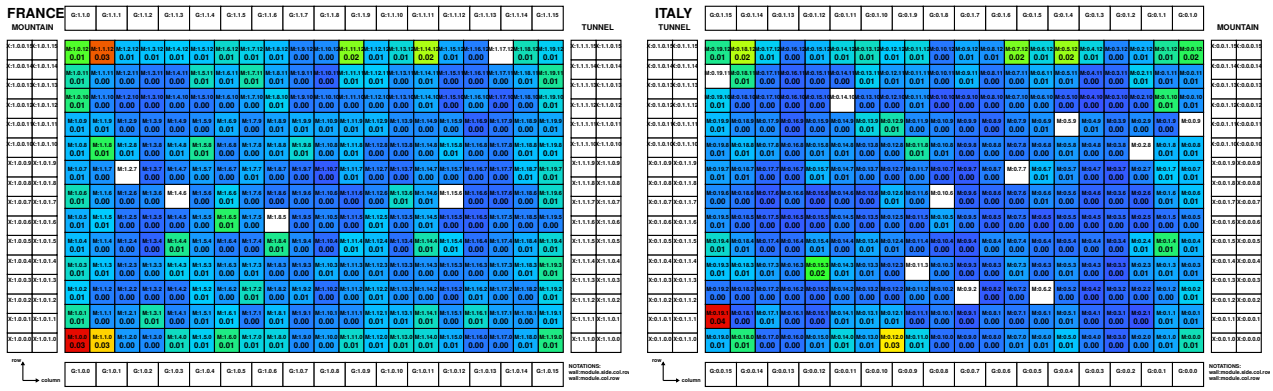

Figure 4.11: Uncertainty on the time resolution measurements of each OM of the two calorimeter main walls with the ^{60}Co data [Hoballah, 2022].

analysis cuts have been performed to estimate the systematics uncertainty on these averaged resolutions. The final result of the time resolution of the M-walls of the SuperNEMO calorimeter, extracted from the ^{60}Co data, is presented on table 4.1.

	8-inch PMTs	5-inch PMTs
French-side M-wall	619 ± 2 (stat) $^{+49}_{-4}$ (syst) ps	814 ± 6 (stat) $^{+73}_{-1}$ (syst) ps
Italian-side M-wall	614 ± 2 (stat) $^{+64}_{-1}$ (syst) ps	828 ± 5 (stat) $^{+101}_{-1}$ (syst) ps

Table 4.1: Results of the time resolution of the SuperNEMO calorimeter M-walls extracted from the ^{60}Co data [Hoballah, 2022].

This work has not been performed yet for the X-wall and G-veto because we have seen already in the previous section worse time alignment of the ToF of the ^{60}Co coincidences for these blocks. The time resolution of the calorimeter has also been investigated by the matched-filter technic in the PhD thesis of Will Quinn, but the results are about 20% higher [Quinn, 5 28].

The final time resolution of about 600 ps seems far from the 250 ps of NEMO-3, but this result for SuperNEMO has been obtained with γ-particles and we expect an higher dispersion because of the unknown interaction point in the volume of the scintillator block. Indeed, the NEMO-3 time resolution has been determined with 1 MeV electrons. We expect to improve a lot this value for electrons also in SuperNEMO. In addition, this work was done at an early stage of the detector commissioning with a limited statistics and without shielding to remove

the ambient background. We expect better results in a near future with the conversion electrons of the ^{207}Bi calibration sources, which require the tracking detector. Secondly, the installation of the detector shielding will be necessary to provide the final precision.

As already said, the timing performances are important to reject the external background producing crossing electrons. We would like to mention here that there is also an attempt to better reject the internal background of ^{208}Tl in SuperNEMO. We are particularly interested in the case of decay through the 5^- second excited state (almost 87% branching ratio), 583 keV above the 3^- level at 2.615 MeV, see figure 4.12. Despite a good coverage of the calorimeter some of these γ's can escape detection and the decay would only produce two electrons events. The 5^- level has an half-life of 294 ps, which could be long enough to detect a time delay between the initial β-decay and the conversion electron of the 3^- level. It has been studied that a 250 ps time resolution could allow to reject 50% of the ^{208}Tl events, while preserving 85% of the $0\nu\beta\beta$ efficiency [Girard-Carillo, 2020].

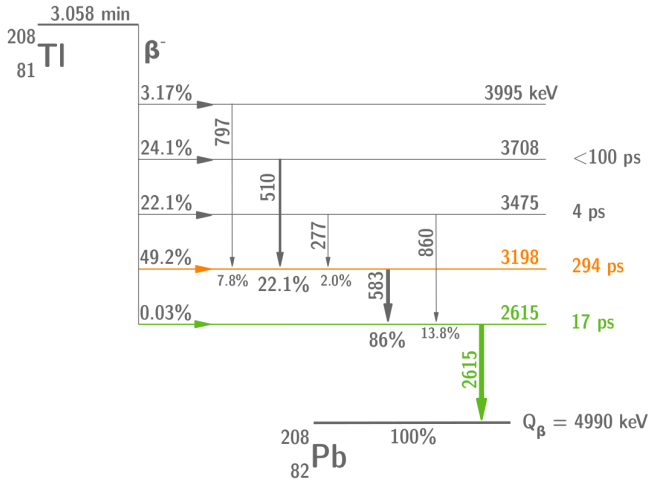

Figure 4.12: Simplified β-decay scheme of ^{208}Tl to ^{208}Pb [Girard-Carillo, 2020], reproduced from [Bé et al., 2010].

4.4 Energy calibration of the calorimeter

Measuring precisely the energy of the two electrons from a double beta decay is of major importance for SuperNEMO. The energy calibration and its stability over time as well as the energy resolution is one of the most important work for the experiment. The energy calibration of the SuperNEMO calorimeter will be mostly performed by regular deployment of the ^{207}Bi sources, in the source frame (see section 3.3.3). The deployment system was already active at the time of the commissioning of the calorimeter, but unfortunately the activity of the sources is very low ($A < 150$ Bq [Arnold et al., 2021]) and there is no chance to detect the conversion electrons without the tracking detector.

Given the importance of this work, we wanted anyway to start studying the energy response of the SuperNEMO calorimeter. Since the shielding was not installed, we got the opportunity to use the high rate of external γ's emitted by the rock of the laboratory, to attempt the first energy calibration of SuperNEMO calorimeter. This γ flux at LSM is dominated by ^{40}K, ^{214}Bi and ^{208}Tl isotopes. Since they have different energies, it is possible to detect several Compton edges on the total energy spectrum in each calorimeter block, providing several energy calibration points at a time. There are almost ten γ-rays to consider in the ^{214}Bi decays, which are thus too difficult to be identified individually. But the total spectrum can be used. The 1460 keV of ^{40}K and the 2615 keV of ^{208}Tl are on the other hand easily identified. An example of PMT

amplitude spectra showing these two γ-rays is presented in figure 4.13. For the 5-inch PMTs of X-wall or G-veto, the poorer energy resolution makes the spectrum much smoother and the Compton edge positions are harder to distinguish, as it was for the BiPo-3 detector (section 2.2).

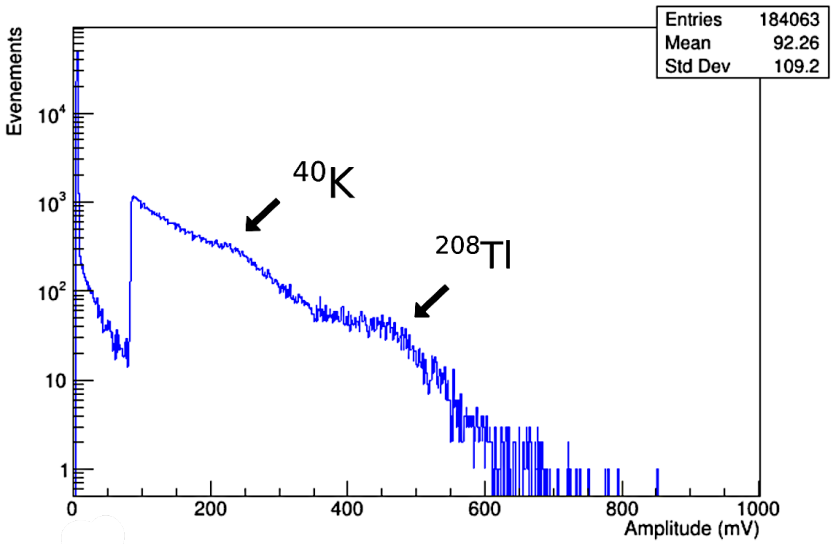

Figure 4.13: Example of spectra of the amplitude of a 8-inch PMTs showing the ambiant γ spectrum at LSM, where the two main Compton edges can be seen [Aguerre, 2023].

A first attempt to fit the energy spectrum with an analytical function was not sufficient to reach the best precision, but was already a good way to equalize the energy response of the calorimeter [Pin, 2020]. In addition, this first method helped to produce the starting step of energy calibrations for the second method. The second method was taken from the one developed for the BiPo-3 detector (see section 2.2), which was improved for SoLid detector (see section 8.1.6). The charge of the PMT pulses was used to obtain the calibration constants, in order to avoid issues with the amplitude attenuation already discussed in section 4.1.2. In the SuperNEMO case, several γ-rays, which need to be fitted in position and rate, appear in the energy spectrum. For this, it was necessary to produce simulations of the three isotopes on the walls of the LSM and to build *probability density functions* (PDF). This work was realized in the PhD thesis of Xalbat Aguerre [Aguerre, 2023]. Since the spectra were more complex and more parameters needed to be extracted, the simple likelihood of the original method was replaced by a more sophisticated procedure with the RooFit library provided by ROOT.

Having several energies tested at the same time is also very important for SuperNEMO because several non-linearity effects have to be taken into account. These effects have been studied for years in Bordeaux, with the electron spectrometer beam and with precise optical simulations [Huber, 2017]. Three main effects can produce non-linearities in the scintillator blocks: inhomogeneities in the light collection towards the PMT, Birks quenching of the scintillation light and the production of Cherenkov light by the high energy particles. The geometrical light collection effect is the dominant one, because of the important volume of scintillator blocks. It can reach 50% increase for light produced just in front of the photocathode and 10% loss in the dead angles. The Birks' law provoke few percents increase above 1 MeV[1] and a loss of 10% at 200 keV. Finally, the Cherenkov effect can produce $\pm$2% difference in the energy spectra, increasing with the energy detected. These effects have been applied to the simulations before fitting the measured energy spectra of the OMs. An example of the effect of optical corrections for ^{208}Tl is presented on figure 4.14, for all the types of scintillators of the SuperNEMO calorimeter. The peaks are shifted depending on the OM type and long tails appear in the

[1] 1 MeV has been chosen as the reference for the normalisation of the relative effects.

spectra at high energy. These corrections have thus an important impact on the results of the energy calibration.

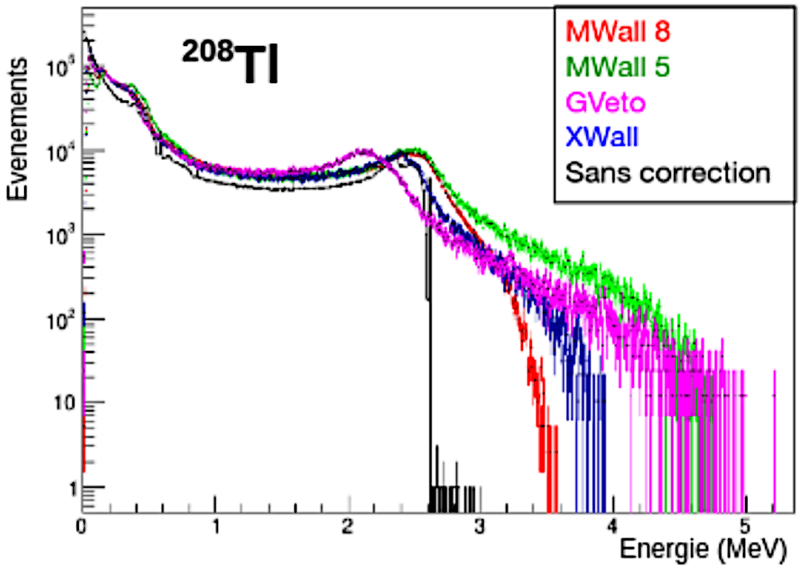

Figure 4.14: Simulated energy spectra of ^{208}Tl in the diffrent type of SuperNEMO optical modules, compared to the simulated spectra without optical corrections [Aguerre, 2023].

The energy spectra of the OMs can then be fitted to determine the five needed parameters: one calibration constant, one relative energy resolution and one activity for each of the three isotopes. The two first parameters are scanned in a defined range and the activities are adjusted by the fit. A statistical χ^2 test is computed at each step of the scans and the best calibration parameter is determined by fitting the $\Delta\chi^2$ curve, to find the minimum. Examples of calibration results for the three types of optical modules are presented on figure 4.15.

Almost all the optical modules have been calibrated thanks to this new method. Only few G-veto OMs need an increase of the PMT HV to be calibrated in future campaign. Figure 4.16 presents the current status of the energy calibration. We can see another equalization of the calorimeter might be needed to totally align all the optical modules, according to this new calibration method. Specifically for the X-wall OMs which show a lower calibration constant, thus higher gain, than the other OMs.

This method revealed to be very powerful to determine the calibration constants of the OMs. Unfortunately, this method was not able to provide the energy resolution for each OMs because the χ^2 distributions are fluctuating too much between the scanned values and no real minimum could be determined. More work will be needed to determine this very important parameter for SuperNEMO.

This work has finally been used to measure the total γ flux background at LSM. It appeared in good agreement compared to previous measurements. It will give a reference spectrum for the simulation of the external background in the experiment.

The global results of the energy calibration will certainly be improved with the ^{207}Bi calibrations, specifically for electrons, after the tracking detector commissioning and shielding installation. Nevertheless, these results with γ-particles will certainly be useful for the study of background events containing γ's or for the search for double beta decays to excited states.

Conclusion

In this chapter, we have presented the very first data obtained with the SuperNEMO calorimeter completely installed at LSM. Waiting for the end of the construction of the detector, this

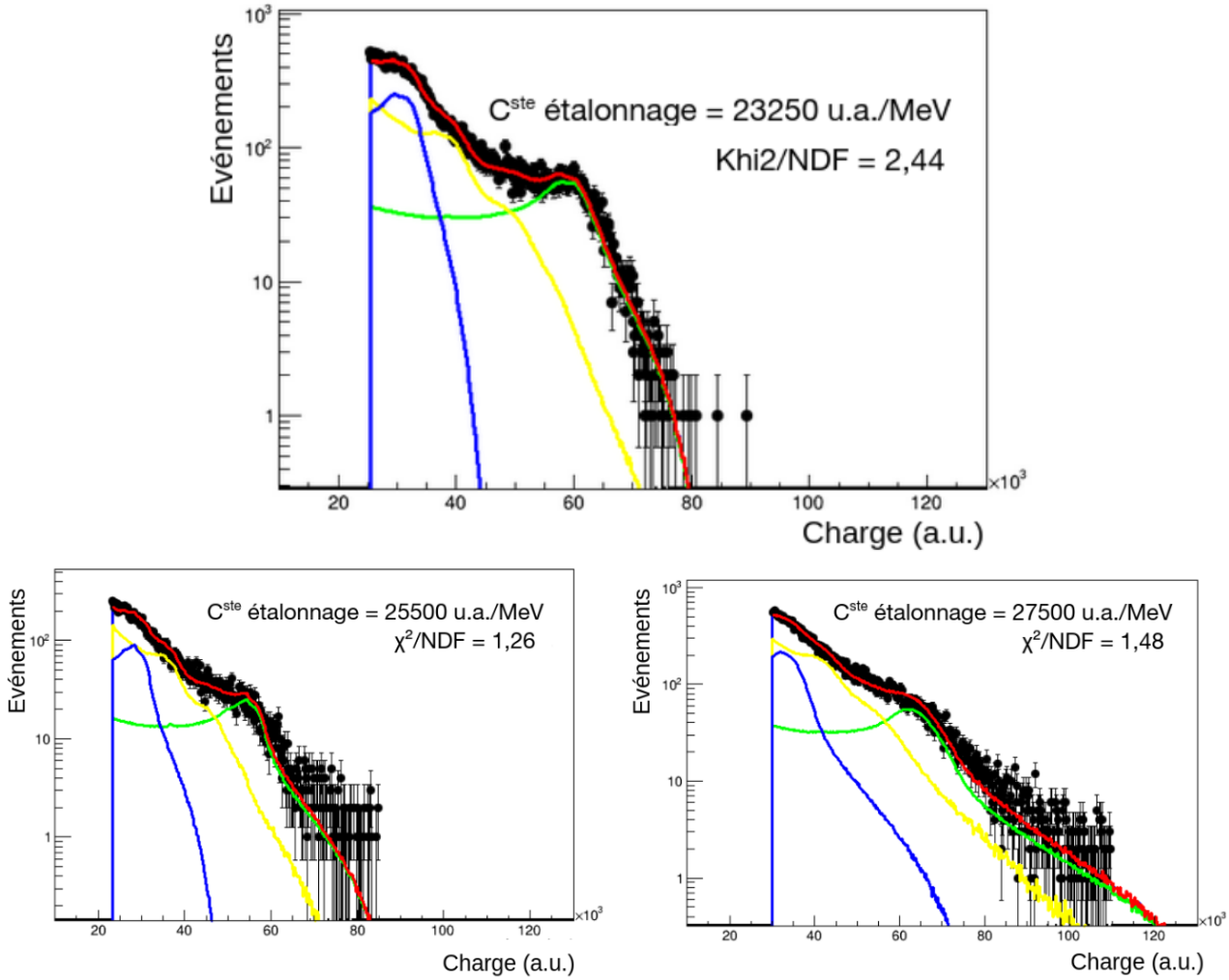

Figure 4.15: Results of the calibration of three OMs of the SuperNEMO calorimeter: M-Wall on top, X-wall bottom left and G-veto on bottom right. The contribution or the three isoptopes are represented in blue for ^{40}K, in yellow for ^{214}Bi and in green for ^{208}Tl. In red is represented the total reconstructed spectrum which give the best agreement to the data in black [Aguerre, 2023].

work allowed to test all the elements of the detector and fix the issues, except for some dead PMTs which can not be replaced. Good performances of the cabling and of the electronics have been demonstrated. Thanks to the precious work of many PhD students, we have been able to align in time and energy the optical modules of the calorimeter. The detection of the first real events with ^{60}Co calibration source and the ambient γ-flux of the LSM, which is dominated ^{40}K, ^{214}Bi and ^{208}Tl, allowed to determine key parameters for the calorimeter performances. The precision of the results is limited because the detection of γ-particles comprise more systematic uncertainties. The absence of shielding also adds background to these measurements and reduces the statistics we could obtain for the relevant events. These good results need to be confirmed by the detection of electrons from the ^{207}Bi sources or from background events. This will require the operation of the tracking detector which started in 2023. The installation of the detector shielding has also started and should be done in 2024.

I actively participated to the commissioning of the SuperNEMO calorimeter while I was in Orsay. I was able continue for some time after moving to Subatech, but since the laboratory is not participating to the SuperNEMO experiment, I could not continue to contribute sufficiently to SuperNEMO. In the mean time the tracker cabling ended and started another exciting phase of the commissioning of the experiment. Thanks to the combination of the tracker and the calorimeter, the topological reconstruction of events have started in SuperNEMO. First

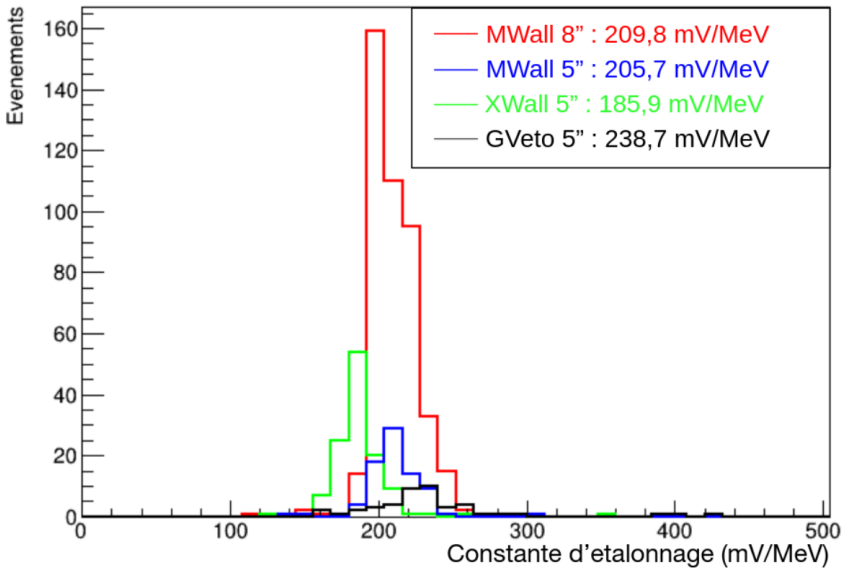

Figure 4.16: Distributions of the calibration constants of the different type of OMs of the SuperNEMO calorimeter [Aguerre, 2023]. The calibration constants are presented here relatively to the PMT pulse amplitude, because this is the variable of interest for the trigger.

backgrounds measurements, like the internal radon level, have also started. Some interesting event displays are presented on figure 4.17 to conclude this chapter.

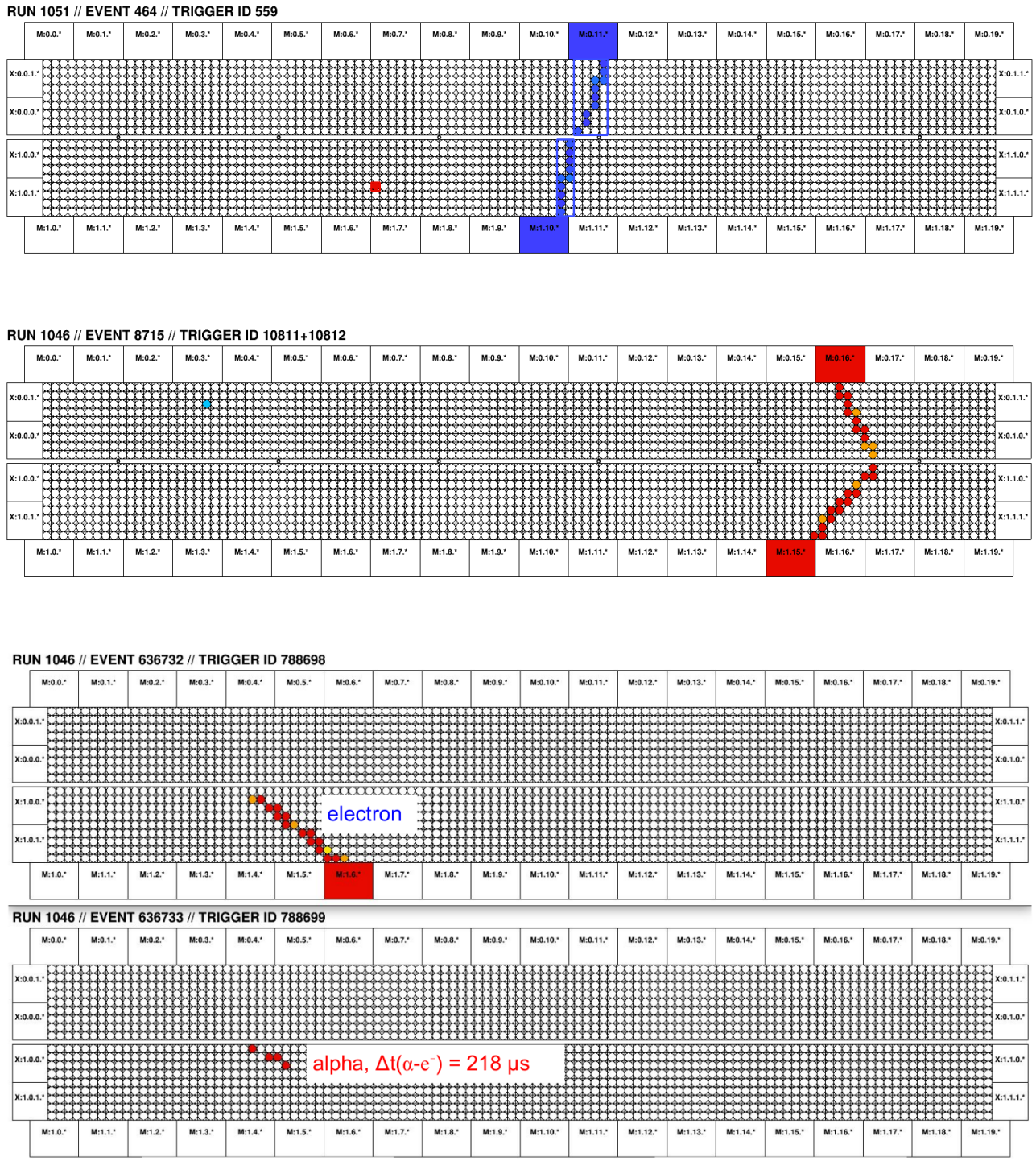

Figure 4.17: Few examples of recent interesting events (top view) detected in SuperNEMO with the tracker and the calorimeter. From top to bottom: crossing electron, double beta decay candidate, BiPo β-α delayed decays from radon in the tracking chamber.

Part II

Reactor anti-neutrino oscillations and search for sterile neutrino

Chapter 5

Reactor electron anti-neutrino oscillations

The discovery of neutrino oscillations proved that neutrino are massive particles, this fundamental discovery was rewarded by the Noble Prize in 2015. The study of these oscillations is a major field of research in neutrino physics. In the first part of this *habilitation à diriger des recherches*, we have discussed the search for neutrinoless double beta decay and the interest of Majorana neutrinos to explain the smallness of the neutrino masses. We have also discussed the question of the matter-antimatter asymmetry observed in the Universe, and matter creation processes. Despite the absolute neutrino masses and the nature of the neutrino cannot be tested with flavour oscillation experiments, these experiments provide very important measurements related to these questions, like the relative neutrino mass splitting Δm^2's or the CP-violating phase δ_{CP}. The double beta decay rates depend a lot on these input parameters to build predictions on the effective neutrino mass $\langle m_{\beta\beta} \rangle$. Among them, the mixing angles θ_{12} and θ_{13} are particularly well measured by the electron anti-neutrino experiments at nuclear reactors. The recent measurement of the θ_{13} mixing angle opened the way to the measurement of the CP-violating phase δ_{CP}, since they are linked in the PMNS mixing matrix. Finally, the neutrino mass ordering is the main objective for the next generation neutrino oscillation experiment.

Neutrino oscillations at nuclear reactors is the subject of this new chapter. After an overview of neutrino oscillations and a focus on the reactor experiments with their current results, we will present several oscillation anomalies which could be the sign of a new type of neutrino: the *sterile neutrino*. The existence of this sterile neutrino, which has to be a right-handed field since it does not participate to weak interactions, is mandatory to provide a mass to the neutrinos, as explained in the previous part of this document. The existence of the sterile neutrino could also completely change the predictions on the effective neutrino mass for double beta decay $\langle m_{\beta\beta} \rangle$. The search for this new particle was very exciting in the last decade and motivated me to join the quest.

Chapter contents

5.1 Overview of neutrino oscillations

The possibility of mixing between massive neutrinos was first introduced in the context of two neutrinos by Z. Maki, M. Nakagawa and S. Sakata in 1962 [Maki et al., 1962]. The possibility of two mixed massless neutrino (ν_e and ν_μ) had been previously considered Y. Katayama et al. [Katayama et al., 1962], in the process of building a unified model of elementary particles with neutrinos. The possibility of vacuum oscillations between neutrino and anti-neutrino $\nu \rightleftharpoons \bar{\nu}$, as well as $\nu_e \rightleftharpoons \nu_\mu$ transitions, had also been considered by B. Pontecorvo in a publication of 1967 [Pontecorvo, 1967].

The phenomenon of neutrino oscillations occurs through an interference between states in quantum mechanics [PDG, 2022]. The neutrino interaction, or flavour, eigenstates ν_α, $\alpha \in \{e, \mu, \tau\}$, are a linear combination of mass eigenstates ν_i, $i \in \{1, 2, 3\}$, determined by the mixing matrix U. In the case of three flavours of neutrinos, this translates into:

$$|\nu_\alpha\rangle = \sum_{i=1}^{3} U^*_{\alpha i} \, |\nu_i\rangle \tag{5.1}$$

Due to unitarity requirements $U^\dagger U = 1$, the mixing matrix can be written in terms of rotations of the orthogonal mass eigenstates into orthogonal flavour eigenstates with three mixing angles θ_{12}, θ_{13}, θ_{23} and a CP violating phase δ_{CP}. The mixing matrix, often called the PMNS[1] matrix, can be parametrized in three oscillation sectors as:

$$\begin{pmatrix} \nu_e \\ \nu_\mu \\ \nu_\tau \end{pmatrix} = \begin{pmatrix} 1 & 0 & 0 \\ 0 & c_{23} & s_{23} \\ 0 & -s_{23} & c_{23} \end{pmatrix} \begin{pmatrix} c_{13} & 0 & s_{13}\, e^{-i\delta_{CP}} \\ 0 & 1 & 0 \\ -s_{13}\, e^{i\delta_{CP}} & 0 & c_{13} \end{pmatrix} \begin{pmatrix} c_{12} & s_{12} & 0 \\ -s_{12} & c_{12} & 0 \\ 0 & 0 & 1 \end{pmatrix} \begin{pmatrix} \nu_1 \\ \nu_2 \\ \nu_3 \end{pmatrix} \tag{5.2}$$

where $s_{ij} = \sin\theta_{ij}$ and $c_{ij} = \cos\theta_{ij}$.

Due to their different masses, the mass states propagates with different phase velocities and the remaining neutrino $|\nu_\alpha(t)\rangle$ is no longer aligned with the initial flavour state $|\nu_\alpha\rangle$. If

[1] PMNS for Pontecorvo, Maki, Nakagawa and Sakata

this neutrino has enough energy, it can produce a charged lepton l_β with a new flavour $\beta \neq \alpha$ with the amplitude $\langle \nu_\beta | \nu_\alpha(t) \rangle$. This is the case of appearance experiments. Otherwise, the neutrino oscillation will manifest through a deficit of neutrinos, or disappearance ($\beta = \alpha$). In the neutrino oscillation experiments, the transition probability is generally dominated by one mass-splitting $\Delta m^2_{ij} = m^2_i - m^2_j$ and one mixing angle θ_{ij} (two flavours case). The oscillation probability for a neutrino of flavour α, with an energy E travelling a distance L, from the source to the detector, to become a neutrino of flavour β is:

$$P(\nu_\alpha \rightarrow \nu_\beta) = \delta_{\alpha\beta} - \sin^2 2\theta_{ij} \ \sin^2 \left(1.267 \ \frac{\Delta m^2_{ij} \ [eV^2] \ L \ [m]}{E \ [MeV]} \right) \tag{5.3}$$

Therefore, neutrino oscillations are possible if neutrinos have different masses ($\Delta m^2_{ij} \neq 0$) and non vanishing mixing terms. To measure these parameters, experiments need to adapt baselines and neutrino energies, or sources, to the oscillation frequencies driven by Δm^2_{ij} and their sensitivity to the oscillation amplitudes driven by $\sin^2 2\theta_{ij}$. Unfortunately, there is no way to access to the individual values of the neutrino masses m_i through oscillation experiments.

Historically the three parts of PMNS matrix, as presented in equation 5.2, have been addressed by:

- **atmospheric** and neutrino beam experiments for Δm^2_{23} and θ_{23}
- nuclear **reactor** and neutrino beam experiments for Δm^2_{13}, θ_{13} and δ_{CP}
- **solar** neutrino or long baseline reactor experiments for Δm^2_{12} and θ_{12}

Over three decades, many experiments tested the phenomenon of neutrino oscillations and measured the parameters of the mixing matrix. Two of them, Super-Kamiokande (SK) in Japan and SNO in Canada, were rewarded by the Nobel Prize of Physics in 2015 attributed to T. Kajita and A. B. MacDonald for *"the discovery of neutrino oscillations, which shows that neutrinos have mass"*. Today, few percent precision has been reached for many of the mixing parameters. Despite some strengthening hints, the octant of θ_{23}, δ_{CP} and the neutrino mass ordering ($m_1 < m_2 \ll m_3$ or $m_3 \ll m_1 < m_2$) are still to be measured. The current best results are illustrated with the example of the three neutrino flavours analysis of the NuFIT[2] group on figure 5.1.

5.2 Reactor anti-neutrino detection

Nuclear reactor are very powerful and pure sources of low energy (< 10 MeV) electron anti-neutrinos $\overline{\nu}_e$. Those anti-neutrinos are emitted by the β^- decays of the neutron rich fission fragments produced by the four fissile isotopes: ^{235}U, ^{239}Pu, ^{238}U and ^{241}Pu. On average six $\overline{\nu}_e$ are produced per fission and about $1{\times}10^{20}$ $\overline{\nu}_e$/s are emitted by $\mathrm{GW_{th}}$ of reactor thermal power [Vogel, 2019]. At the experimental site, the electron anti-neutrinos are detected through inverse beta decay (IBD) on the free protons of the detector and produce positrons and neutrons:

$$\overline{\nu}_e + p \rightarrow e^+ + n \tag{5.4}$$

This reaction has the highest cross-section ($\sigma > 10^{-43}$ cm^2) for anti-neutrinos at these energies but the detection threshold of 1.8 MeV is quite high. The combination of reactor flux and IBD cross-section allows to draw a detected anti-neutrino energy spectrum as presented in figure 5.2. The anti-neutrino energy can be measured by the positron energy deposit in the detector since the neutron has a very low recoil energy, $\mathcal{O}(10$ keV). The neutron is later captured on neutron

[2] http://www.nu-fit.org/

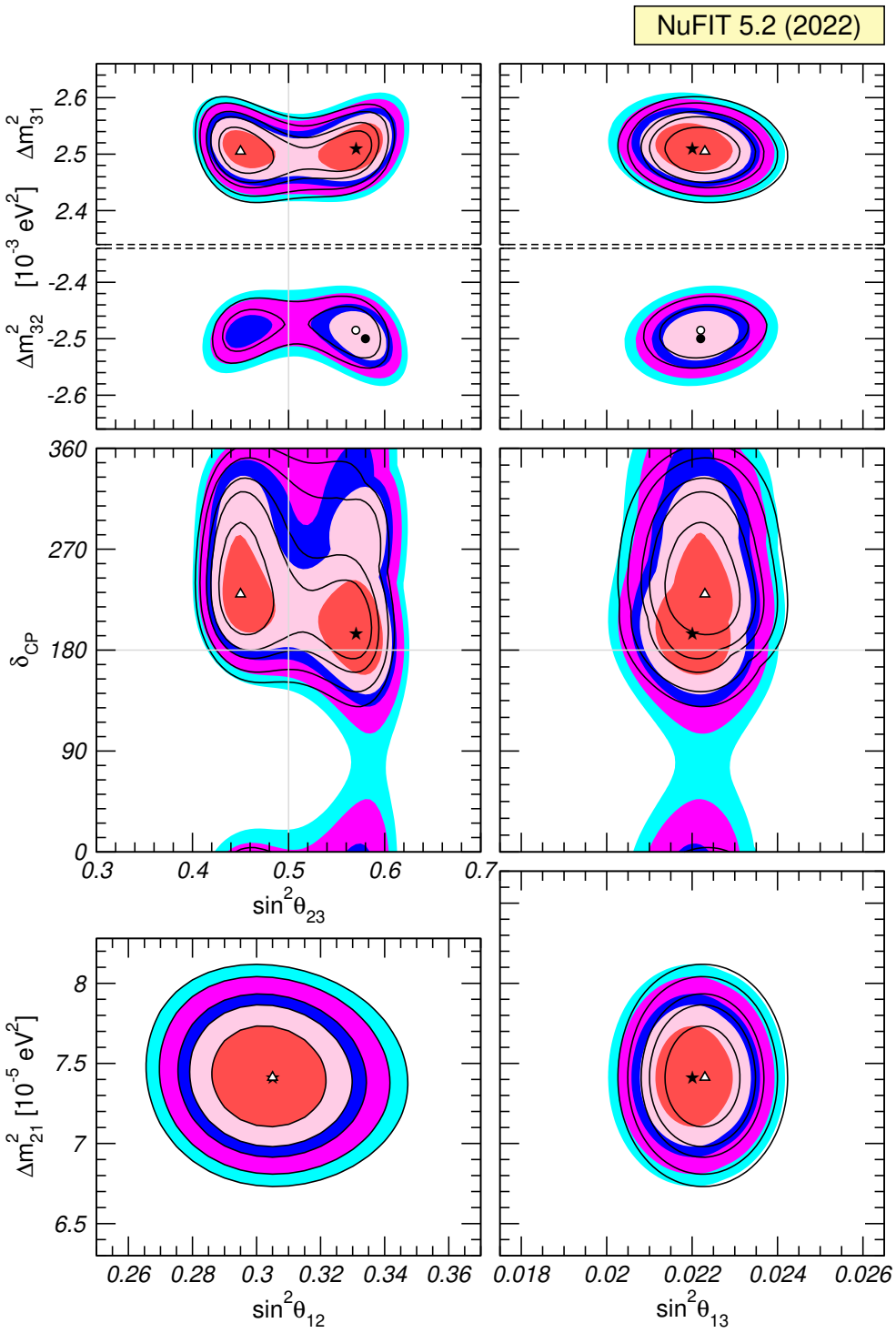

Figure 5.1: Global analysis of the three flavours neutrino oscillations from the NuFIT group at the date of November 2022 [Esteban et al., 2020]. Each panel shows the two-dimensional projection of the allowed six-dimensional region after marginalization with respect to the undisplayed parameters. Colored regions (black contour curves) are obtained without (with) the inclusion of the tabulated SK-atmospheric χ^2 data. The different contours correspond to the two-dimensional allowed regions at 1σ, 90%, 2σ, 99 %, 3σ confidence level. Note that as atmospheric mass-squared splitting we use Δm^2_{31} for normal ordering (NO) and Δm^2_{32} for inverted ordering (IO). The regions in the lower 4 panels are based on a $\Delta\chi^2$ minimized with respect to the mass ordering.

absorber nuclei like hydrogen, lithium, cadmium or gadolinium. The resulting nuclei will either break-up or emit de-excitation gamma particles. The space (tens of cm) and time (tens of µs) coincidences between the positron and the neutron signals are the key signatures of a $\overline{\nu}_e$ detection at nuclear reactors.

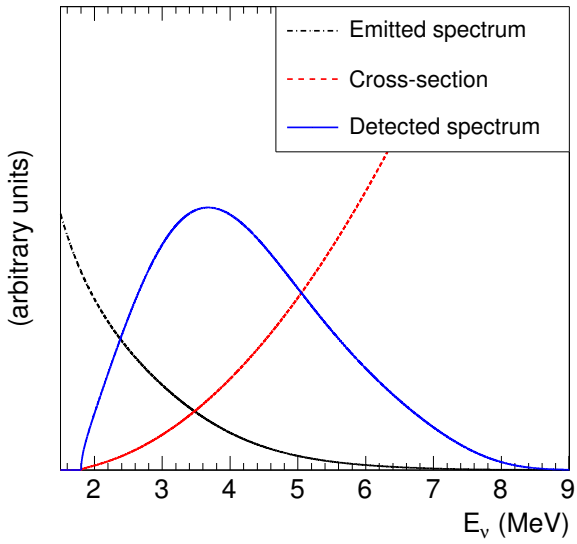

Figure 5.2: Reactor $\overline{\nu}_e$ flux, IBD cross-section and resulting $\overline{\nu}_e$ energy spectrum for ^{235}U [Mueller et al., 2011].

Because of the low interaction rate of electron anti-neutrinos, the main challenge for the detection in the MeV range at nuclear reactors, is to overcome the background. In the case of very short baseline experiments, generally located in the reactor building, the background can be produced by the core itself through the emission of γ and n. It can be *accidental* because of a random coincidence between a positron-like signal, produced by a γ or a neutron induced proton-recoil, and an uncorrelated neutron capture. The *correlated* background is due to the coincidence of two signals produced by the same cause, for example a proton-recoil from a n followed by its capture. At longer baselines, the background is caused by natural radioactivity of the detector materials, direct cosmic background from atmospheric showers or cosmogenic isotope production. Generally, longer is the baseline of the oscillation experiment, deeper is the detector site. Therefore, the detector overburden can range from almost zero to thousands meters water equivalent *(mwe)*. The direct cosmic background (n, μ) for short baseline experiments is then extremely high. At longer baselines, the cosmogenic activation by the deep penetrating muons and spallation neutrons dominates. The cosmogenic long-lived nuclei contribute to the backgrounds for example with $\beta - n$ decays.

It is close to the Savannah River Nuclear reactor in the USA that C. Cowan and F. Reines detected for the first time the neutrino in 1956 [Alamos, 1997]. The anti-neutrinos were interacting in water tanks loaded with $CdCl_2$. The two water tanks were surrounded by three liquid scintillator tanks readout by photomultipliers (PMTs). These calorimeter tanks were used in coincidence to detect the two annihilation γ from the positron, later followed by the de-excitation γ from neutron capture on cadmium. The detector design and the coincidences helped to sufficiently reduce the background.

The following experiments in the 60's and 70's were exploring the different detection processes of reactor electron anti-neutrinos [Vogel, 2019]. For example interactions with deuterium or elastic scattering on electrons have been detected. These experiments also demonstrated that the detection of neutrinos was possible almost on surface and that reactor backgrounds could be overcome. Since the first detection, the reactor anti-neutrino experiments have been using

the same principle for 70 years. The first observation of coherent elastic scattering of neutrinos on nuclei with CsI scintillator, exposed to neutrinos from the spallation neutron source at Oak Ridge in 2017 [Akimov et al., 2017], might open a new channel to study neutrinos. This process has the largest cross-section for low-energy neutrinos and anti-neutrinos interaction through neutral current (NC). There are ongoing efforts on the detector developments and experiments are being designed. Neutrino experiments in the 80's an 90's came back with the idea of detecting neutrino oscillations since it became a hot subject in the community, for example after the physics report of S. Bilenki and B. Pontecorvo in 1978 [Bilenky and Pontecorvo, 1978]. The mixing parameters were completely unknown at that time, hence these experiments were realised where it was feasible, with baselines lower than 100 m, and detectors of few hundreds of kilograms. Some those experiments and results will be presented in section 5.4. As they were all single site experiments, they relied on the prediction of the reactor anti-neutrino flux and energy spectra. This will be discussed in section 5.3.

To investigate neutrino oscillations, reactor experiments can only test the $\overline{\nu}_e$ disappearance since the MeV range neutrino energy cannot produce μ or τ by charged-current (CC) interaction. Most of the time a two flavour neutrino oscillation is a good description for reactor experiments and the mixing angle and the mass splitting can be determined with the disappearance probability, already presented in equation 5.3 (with $\beta = \alpha$). The figure 5.3 illustrates the disappearance probability as a function of L/E in the case of high values of the parameters for illustration (mass splitting corresponding to sterile neutrino search). Depending on the distance from the source to the detector, the oscillation can be seen either by *shape* or by *rate* analysis. The shape analysis can reveal the oscillation pattern as a function of energy or distance: the mixing angle is determined by the amplitude of the oscillation ($\sin^2 2\theta$) and the mass splitting by the oscillation frequency (Δm^2). At higher distances, the oscillation becomes extremely rapid and the detector energy resolution is no longer sufficient. The oscillation is observed by a deficit, thus related to the rate, of the anti-neutrino flux, averaged out to $|1 - \frac{1}{2}\sin^2 2\theta|$.

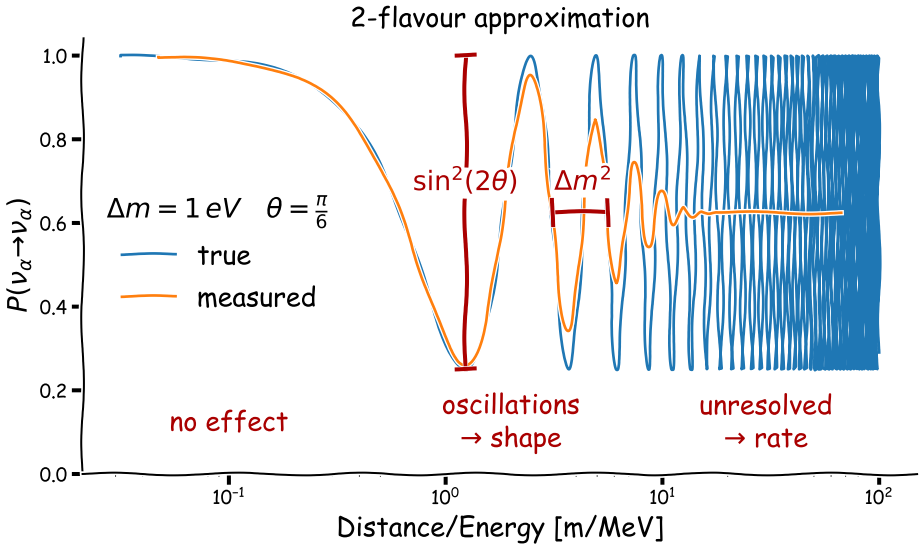

Figure 5.3: Survival probability as a function of the ratio distance L over energy E in a 2-flavour model (see equation 5.3). At intermediate baseline, the amplitude of the oscillations is governed by the mixing angle while the frequency is determined by the mass splitting. At higher values of L/E, the rapid oscillations can not be resolved experimentally [Böser et al., 2020].

In the framework of three flavours neutrino oscillations, the two mass splitting Δm^2_{3l} (l being the lightest neutrino depending on the mass ordering) and Δm^2_{21} can be investigated by 1-km-scale or 100-km-scale long baseline (LBL) reactor experiments respectively (see section 5.5).

The recent experimental anomalies initiated searches for sterile neutrino at much higher $\Delta m^2 \sim 1$ eV^2 with very short baseline (SBL) reactor experiments (see section 5.6). The most important results of these reactor experiments will be presented in sections 5.4 and 5.5.

5.3 Reactor anti-neutrino spectrum prediction

As discussed in the previous section, the neutrino oscillations could appear in rate of anti-neutrinos or in energy spectral shape distortion after oscillation. Therefore, in parallel of building new experiments, it is necessary to predict the reactor anti-neutrino flux and energy spectra with an increasing precision. There are two ways to build such prediction: the *summation* and the *conversion* methods.

5.3.1 The summation method

The summation method consists in summing all the β-decay spectra of all the fission fragments from the nuclear data. This requires very good knowledge of the four fissile isotopes ^{235}U, ^{239}Pu, ^{238}U and ^{241}Pu and their fission fragments: fission yields, half-lives, branching ratios, energy end-points and spectral shapes of all the β-branches, as well as the respective errors. The time evolution with fuel burn-up is also necessary to consider. Obviously, this method strongly depends on the knowledge of the nuclear data but has several advantages: it covers the full energy range and it can be computed for any type of fuel, at any irradiation time or conditions. This method was originally proposed in the 60's by [King and Perkins, 1958] later followed by [Avignone et al., 1968, Davis et al., 1979]. After the 80's, we can find the work of [Vogel et al., 1981, Klapdor and Metzinger, 1982a, Klapdor and Metzinger, 1982b, Tengblad et al., 1989, Rudstam et al., 1990, Kopeikin et al., 1997] adding newer data and using different ways to consider the unknown β-transitions.

We can illustrate the summation method with the work of [Sonzogni et al., 2015], which considers more than 800 individual fission fragments per fissile isotope and several thousand β-decay branches. This paper highlight that the high-energy part of the spectra are only due to 20 contributors, as shown on figure 5.4. These isotopes with large end-point values present larger uncertainties because of shorter half-lives and high-energy de-excitation γ's, which have lower tagging efficiency in germanium detectors investigating these isotopes.

During the preparation of the θ_{13} experiments (see section 5.5.2), the prediction of the reactor anti-neutrino spectra with the summation method, called *ab initio* in this paper, was improved by using all the available nuclear data, also including the forbidden β-transitions [Mueller et al., 2011]. The precision reached $\pm 10\%$ over the whole energy range, when comparing the prediction for the electron spectrum of ^{235}U (see figure 5.6 (left)) and ^{239}Pu to the ILL measurement [Von Feilitzsch et al., 1982]. This revision illustrated that the *pandemonium effect* affected some of the nuclear β-decay data, which are playing an important role in the calculation of the anti-neutrino energy spectrum. This effect is due to an inefficiency in the detection of the high-energy γ's emitted during the de-excitation of the high-energy levels in the measurements of the β-branches of nuclei [Hardy et al., 1984]. The branching ratios of these levels are then underestimated resulting in an overestimation of the high-energy part of the anti-neutrino energy spectra [Estienne et al., 2019]. This effect is said the major bias in the determination of the anti-neutrino spectra, specially at high-energy. Thus, the work of [Mueller et al., 2011] collected data from other measurements where β-spectra were recorded independently from the emitted γ's [Tengblad et al., 1989, Rudstam et al., 1990]. Another source of data to correct from the pandemonium effect comes from *Total Absorption Gamma-ray Spectroscopy* (TAGS) technique, like [Greenwood et al., 1992], which was used in this work. The

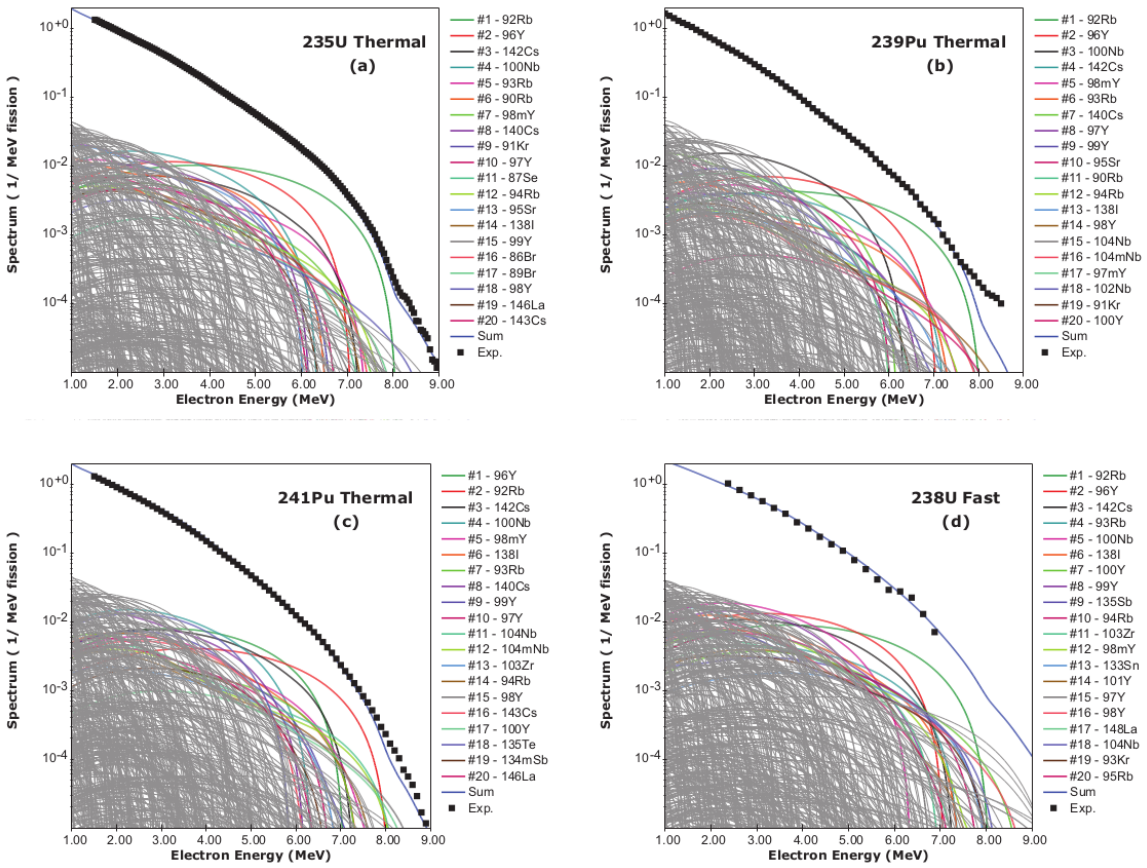

Figure 5.4: Calculated electron spectra [Sonzogni et al., 2015] following the thermal (fast) fission of ^{235}U, ^{239}Pu, and ^{241}Pu (^{238}U) compared to the high-resolution data from ILL, see section 5.3.2. The thin gray lines indicate the individual β-spectrum from each fission fragment and thick coloured lines highlight the 20 most important contributors above 6 MeV.

progress in the summation method allowed to identify a priority list to drive new measurements, for example ^{92}Rb and ^{96}Y [Sonzogni et al., 2015].

After a decade of new TAGS campaigns, the results of the updated summation model was published in 2019 [Estienne et al., 2019]. It demonstrated an improved agreement at 1.9% above the Daya Bay result without any renormalisation, as shown on figure 5.5. The slope of the average IBD yield σ_f as a function of the ^{239}Pu fission fraction F_{239} is also well reproduced.

5.3.2 The conversion method

The conversion method uses the measurements of the β-spectra of each fissile isotope after irradiation with neutrons. The electron spectra are then converted into anti-neutrino spectra, since the electron and the neutrino are sharing the same available energy, corresponding to the end-point of the β-branch. The β-spectra associated to the thermal fission of ^{235}U, ^{239}Pu, and ^{241}Pu have been measured in the 80's at the *Institut Laue-Langevin* (ILL) high neutron flux reactor in Grenoble by K. Schreckenbach et al. [Schreckenbach et al., 1981, Von Feilitzsch et al., 1982, Schreckenbach et al., 1985, Hahn et al., 1989]. The ^{238}U fissions only with fast neutrons but contributes to about 10% of the power in thermal reactors. This spectra was measured at the FRM II thermal and fast neutrons source in Garching and published in 2014 [Haag et al., 2014a]. Before that recent measurement, the ^{238}U contribution to the anti-neutrino spectra had to rely on the summation calculations.

The conversion procedure is described in the earliest publications of K. Schreckenbach et al. and of P. Vogel [Vogel, 2007]. In short, the measured β-spectrum is divided in slices that

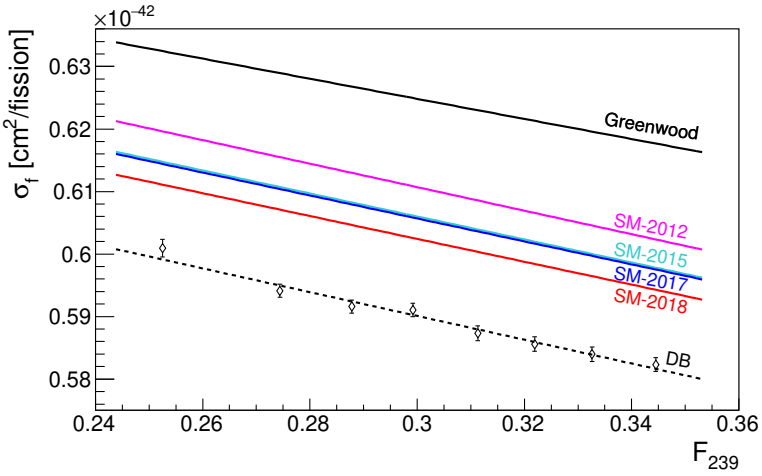

Figure 5.5: IBD yield as a function of the ^{239}Pu fission fractions for different versions of the summation model of Subatech group [Estienne et al., 2019] when adding over time more TAGS data. It is compared to the prediction of [Mueller et al., 2011] using only the TAGS data from [Greenwood et al., 1992].

are consecutively fitted with virtual β-shapes, to determine the end-point and the intensity of the branch, starting from the highest energy slice. At each slice, the previous contribution is subtracted over the whole energy range and the procedure continues till the lowest energy slice. The anti-neutrino energy spectra are then calculated by summing all the virtual β-branches converted to anti-neutrino branches. The initial work of K. Schreckenbach et al. was using about 30 allowed β-transitions.

This procedure can reach a 1% level precision, in the study of [Vogel, 2007] on a synthetic data set, for the smooth electron spectrum but is much larger for the jagged anti-neutrino spectrum, of the order of 10% or more [Vogel, 2007]. Indeed two problems appear. Firstly, since there is much lower β-branches compared to the thousands of real branches, the steps become more pronounced in the anti-neutrino spectrum. It is then recommended to use wider energy bins in the anti-neutrino spectrum than the β-spectrum slices used for the fit. The ILL measurements were originally published with quite large energy bins of 250 keV, while recorded in 50 keV bins. This has been corrected by re-publication in 2014 [Haag et al., 2014b]. Secondly, the nuclear charge Z, driving the shape of the β-branch, depends on the end-point energy. Thanks to nuclear data it can be determined as a function of the end-point energy, but only approximately because of missing nuclear data. Given these conditions, the errors on the conversion procedure should remain smaller than the statistical and systematic errors of the measured electron spectra (around 3% with a weak energy dependence). At this stage, the first (and higher orders) forbidden decays were neglected as well as the QED radiative corrections for the electrons and the weak magnetism corrections due to induced weak currents in the nucleon. They should be included.

In the work of [Mueller et al., 2011], it was realised that the improvements in the summation method could be combined to the conversion method. The determined distributions of the end-points and nuclear charges could be a precious information to control the conversion procedure. The improved conversion method consists in starting with the summation method and restrict the use of effective branches to fit only the missing few percent contribution of the difference with the reference ILL electron data. These data are still fitted but the contribution of unphysical virtual branches is reduced by an order of magnitude. In practice, the missing contribution to match the ILL electron spectrum is fitted using a set of 5 effective β-branches with a nuclear charge of Z=46, as represented on figure 5.6 (right). The relative comparison with the ILL β-spectrum agrees within 1% but the anti-neutrino spectra residues exhibit an upward shift

of 3.1%. This work also included the *off-equilibrium* effect due to longer half-lives isotopes produced in nuclear reactors compared to the few hours irradiation measurements performed at ILL.

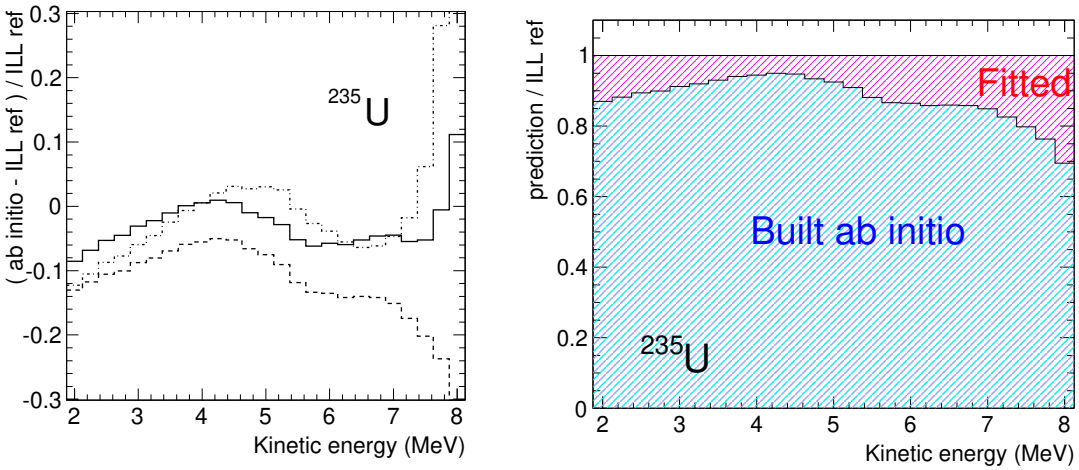

Figure 5.6: (left) Residues of the ^{235}U electron spectra (solid line) predicted by the ab initio calculations of [Mueller et al., 2011] compared to ILL data [Von Feilitzsch et al., 1982]. (right) The blue hatched area shows the same contribution and the magenta hatched area represents the contribution from unknown nuclei and remaining systematic effects of nuclear databases fitted using 5 effective β-branches [Mueller et al., 2011].

Few months after the publication of T. Mueller et al. work, P. Huber published an independent inversion of the ILL β-spectra for the ^{235}U, ^{239}Pu and ^{241}Pu [Huber, 2011]. This work precisely review all the various corrections to the allowed β-decay shapes (finite size, charge screening, radiative, weak magnetism) and estimate the associated theoretical errors. These corrections are applied at a branch-by-branch level to the allowed β-spectra. An effective nuclear charge $\bar{Z}$ including the missing nuclei is also computed. A comparison figure between the different conversion models for ^{235}U is shown in figure 5.7. The last cited two models agree and the upward shift of the anti-neutrino flux is confirmed.

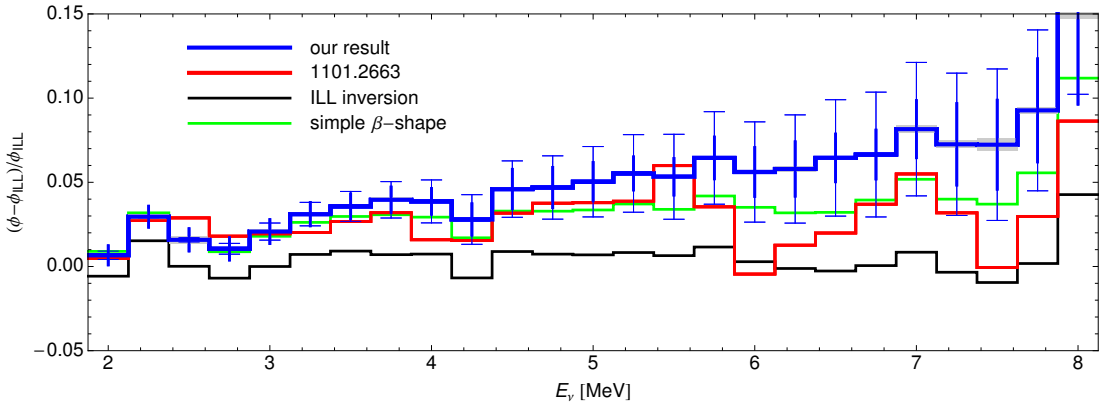

Figure 5.7: Comparison of the prediction of P. Huber [Huber, 2011] (in blue) with the T. Mueller et al. [Mueller et al., 2011] (in red), the ILL conversion [Schreckenbach et al., 1985] (in black) and a prediction without the corrections to the β-decay shapes (in green).

The combination of these two works, nowadays called the *Huber-Mueller model*, is used as the standard reference for the prediction of the reactor anti-neutrino spectrum of many modern experiments. We will see in section 5.6 that some discrepancies however persist between models and experimental data, specially for ^{235}U. This is also the case when comparing the ^{235}U

predictions between the summation and the Huber-Mueller model, as illustrated in figure 5.8. There is a good agreement in shape for all the fissile isotopes but a normalization issue appears for ^{235}U. We can highlight here a remark of P. Vogel in [Vogel, 2007], that fundamental input information of these methods are based on essentially unique, and so far not repeated, experiments performed in the 80's. At that time, measurements showed an excellent agreement in the β-shapes but the absolute normalization of these spectra differed by several percent.

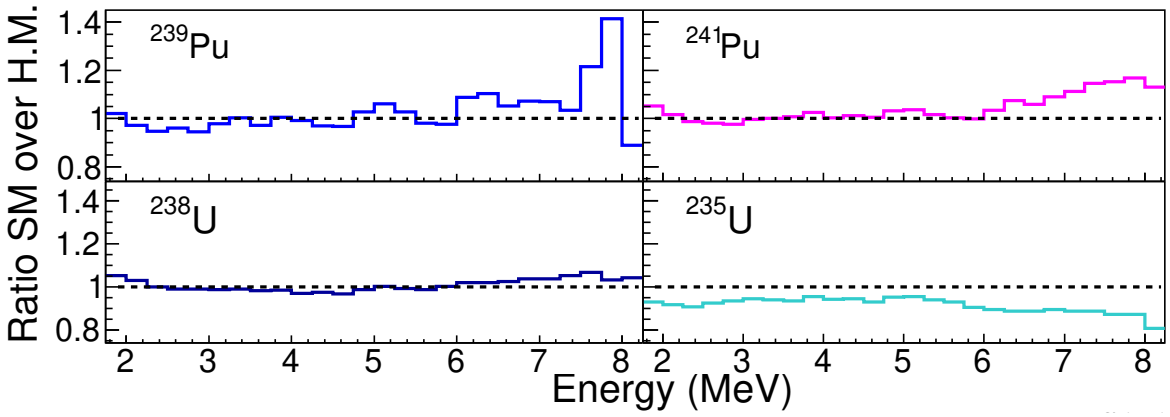

Figure 5.8: Ratios of the anti-neutrino energy spectra obtained with the SM-2018 [Estienne et al., 2019] model with the converted spectra for ^{239}Pu, ^{241}Pu, ^{235}U [Huber, 2011] and Mueller's prediction for ^{238}U [Mueller et al., 2011].

In the analysis of the anti-neutrino flux evolution in Daya Bay as a function of fuel burn-up [An et al., 2017a], A. C. Hayes et al. [Hayes et al., 2018] propose to investigate the ratio of the fission β-spectra ^{235}U/^{239}Pt. This work considers firstly the conversion method and includes different combinations of allowed and first forbidden (up to 40%) β-transitions to fit the ILL data. In all cases, the ratio of the anti-neutrino spectra and IBD yield ratio varies only slightly, with $\sigma_{235}/\sigma_{239}$ remaining close to 1.53, while individual spectra vary at few percent level. This ratio is found to be 6% higher than the Daya Bay result, it will be discussed in section 5.6.1. This work secondly considers the summation method and demonstrates that all the features seen in the evolution data of Daya Bay can be reproduced. However it predicts an average IBD yield 3.5% higher than observed. Finally, A. C. Hayes et al. conclude that a direct experimental measurement of the β-spectra ratio, free of normalization uncertainties, should be performed.

In 2021, V. Kopeikin et al. published the results of such experiment at the research reactor IR-8 in the NRC Kurchatov Institute (KI) [Kopeikin et al., 2021]. Relative measurements of the ratio $R_{235/239}$ between the cumulative fission β-spectra of ^{235}U and ^{239}Pu were carried out simultaneously with a systematic error of 0.5%. This result is compared to the ILL ratio, as shown on figure 5.7 (left). A clear excess of the ILL data is visible. It agrees in shape but not in normalisation. This excess has been fitted by a constant factor $k = 1.054 \pm 0.002$. This new result might be the conclusion of several decades of issues with the prediction of the ^{235}U anti-neutrino rate and of the reactor anti-neutrino anomaly, see section 5.6.1.

5.4 Short baseline reactor experiments

Many short baseline reactor experiments have be performed since the 80's. We cannot present all of them here, but we would like to focus on two experiments which have played an important role in the two reactor anomalies, see sections 5.6.1 and 5.6.2.

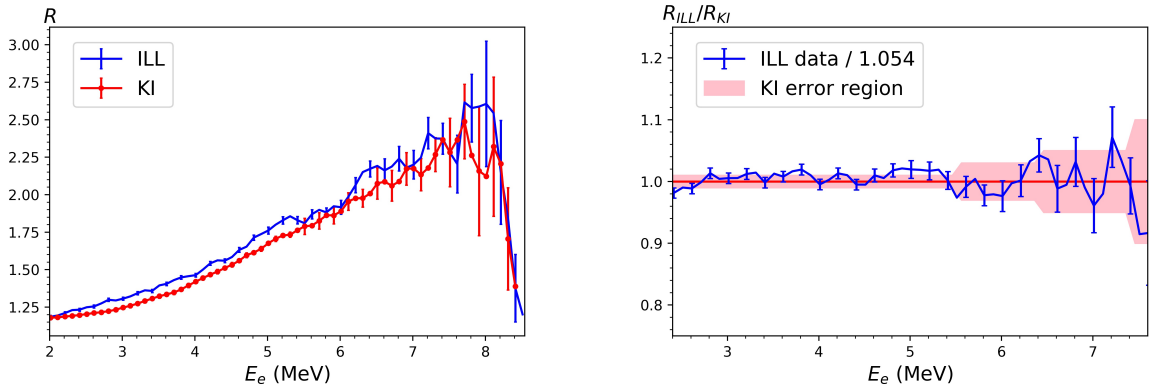

Figure 5.9: (left) Comparison of the ratios between β-spectra of ^{235}U and ^{239}Pu from the ILL data [Haag et al., 2014b] (in blue) and the KI data [Kopeikin et al., 2021] (in red). (right) Same ratios normalized to the KI data. The ILL data were divided by 1.054 and the coloured region shows the KI uncertainties.

5.4.1 The ILL neutrino experiment

The Institut Laue-Langevin (ILL) experiment was the first neutrino experiment designed to test oscillations [Kwon et al., 1981] in the 80's. The goal was to study the energy spectrum of neutrinos at 8.76 m from the point-like 57 MW core of the ILL reactor in Grenoble. The almost pure core composition of 93% in ^{235}U should give a well defined prediction of the $\overline{\nu}_e$ spectrum. The reactor operation consisted of about 40 days reactor ON for neutrino detection and 10 days reactor OFF for background measurements. The expected anti-neutrino spectrum has been determined by the conversion method from the measurement [Schreckenbach et al., 1981].

The detector was a multilayer sandwich of five liquid-scintillator planes and four ^{3}He-wire-counter planes installed in the basement of the reactor building. A total of 377 L of liquid scintillator (LS) and 80 L of pure ^{3}He gas constituted the active volumes. The positron was detected in one of the 30 vertical cells readout by two PMTs and its energy was measured. The neutron was detected after thermalisation, by capture on ^{3}He in the proportional counters. The detector was enclosed in a massive shielding of lead, polyethylene and LS muon veto. Thanks to this shielding no effect of reactor induced background was observed. The pulse shape discrimination along with the 2.5 m concrete overburden allowed a strong reduction of cosmic background. The signal-to-background ratio achieved was 1:1 at 2 MeV and better above that energy.

The experimental positron energy spectrum has been obtained by subtracting the reactor-off spectrum from the reactor-on spectrum. This spectrum is shown in figure 5.10 (left) with statistical errors only. In total, 4890 $\pm$ 180 neutrino-induced events have been detected. The total systematic error on the detection rate has been estimated to 11% and is energy independent. An uncertainty on the energy scale of 2% has also be taken into account. The ratio of the experimental to expected integral positron yield has then been determined to 0.955 $\pm$ 0.035 (stat) $\pm$ 0.110 (syst). To investigate an oscillation a χ^2 test on the experimental ratio over the non oscillated expected one is performed as function of Δm^2 and $\sin^2 2\theta$, see figure 5.10 (right). The experimental data are consistent with no oscillations or oscillations with a small mixing angle ($\sin^2 2\theta \lesssim 0.3$). At maximal mixing, an upper limit of $\Delta m^2 \leq 0.15$ eV^2 (90% CL) is found.

About 10 years later [Hoummada et al., 1995], it was announced that the operating power of the ILL reactor had been incorrectly reported since its earliest days of operation. The reactor was in fact operated at 1.095 times its full power. In addition, the prediction of the anti-neutrino spectrum was enhanced by nearly 5% after a new measurement of the ^{235}U beta

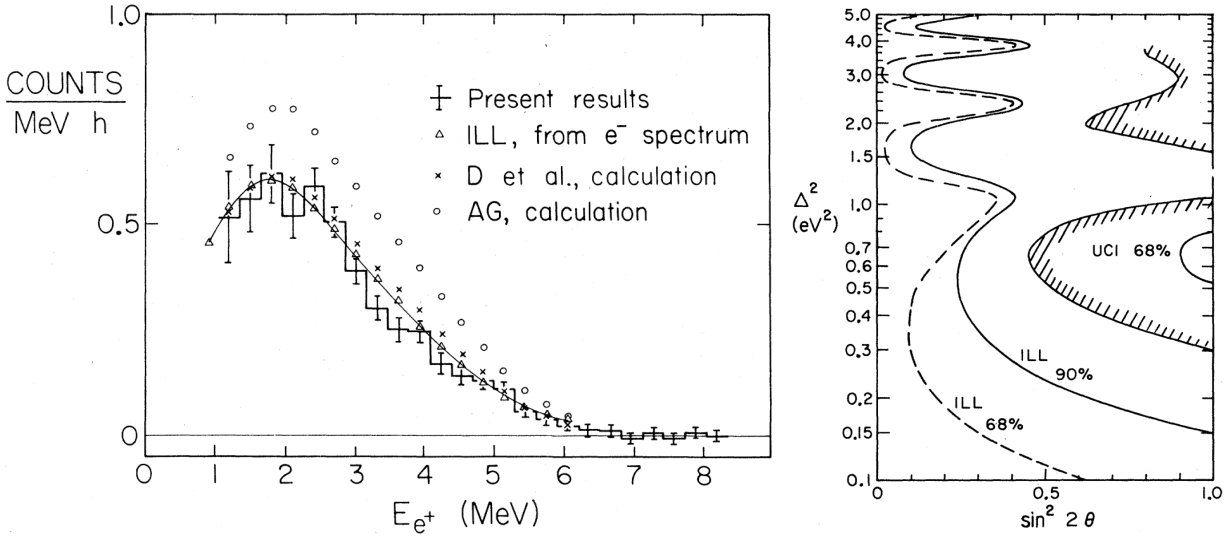

Figure 5.10: The ILL experiment results [Kwon et al., 1981]. (left) Measured positron energy spectrum compared the expected spectrum (solid curve) based on the ^{235}U beta-spectrum measurement [Schreckenbach et al., 1981]. (right) Limits on the neutrino-oscillation parameter Δm^2 versus $\sin^2 2\theta$ (right regions are excluded).

spectrum [Schreckenbach et al., 1985]. The neutron life-time has also been reduced from 926 s to 889 s, which boosts the IBD cross-section by 4%. Consequently, the ILL experiment data has been reanalysed in 1995, by some collaborators, taking into account this overall change of about 18% in the prediction. The expected rate became:

$$R_{ILL} = 0.832 \pm 0.029\ (stat) \pm 0.074\ (syst) \tag{5.5}$$

The statistical χ^2 analysis of this paper has been contested by B. K. Cogswell et al. [Cogswell et al., 2019], in terms of oscillation search but without bringing new understanding on the absolute normalisation. Nowadays, the ILL result remains unexplained and contributes to the global significance of the sterile neutrino hypothesis (section 5.6).

5.4.2 The Bugey-3 experiment

The Bugey-3 collaboration has carried out an oscillation search at the Bugey nuclear power plant in France, with four pressurized water reactors (PWR) with 2.8 GW_{th} each [Achkar et al., 1995]. Three identical detection modules have been used: one (module 1) located under the reactor building, at 15 meters from the core, and two outside the reactor building, inside a concrete bunker 40 meters away from the core. The data taken with module 1 were also used to extract the neutrino signal from another reactor located at 95 meters, when the nearest one was stopped. The statistical accuracy of Bugey-3 was significant, since about 150000 events have been recorded. In addition, about 40% of the whole data taking period was carried out simultaneously at the two locations. This has the advantage, when comparing data at two distances, of being less sensitive to the modification of the source spectrum due to the evolution with time of the fuel composition which is a source of systematic uncertainties.

The Bugey-3 detection modules consisted of 600 L stainless steal tanks with two acrylic windows to collect the scintillation light. These tanks are optically segmented in 98 (7×14) elementary cells (8.5×8.5×85.0 cm^3) readout by 3-inch photomultipliers. A light-yield of 150 photoelectrons (PE) per MeV has been reached with a determination of the interaction point along the cells. The modules are filled with ^{6}Li-loaded pseudocumene based LS. The detection principle uses the delayed coincidence of the IBD products and the neutron is detected by the

break-up reaction of the ^{6}Li nuclei: $n +^6 Li \rightarrow^4 He +^3 H$ releasing 4.8 MeV. Complete details about the detector design and performances, pulse-shape discrimination, background with its subtraction and signal extraction, that is all the ingredients of modern reactor experiments, can be found in [Achkar et al., 1995].

Comparing both the shapes and the rates of the positron spectra at 15 m, 40 m and 95 m distances, no neutrino oscillations have been observed, see figure 5.11 (left). The exclusion region in the plane of the oscillation parameters with respect to previous experiments has increased.

Another important result of the Bugey-3 experiment is the good agreement between the predicted and the measured positron spectra, see figure 5.11 (right). The anti-neutrino spectrum is calculated from the conversion method of [Schreckenbach et al., 1985] for the ^{235}U and [Hahn et al., 1989] for ^{241}Pu and ^{239}Pu. The spectra for ^{238}U, which is expected to contribute to less than 8% here, is calculated from the summation method [Klapdor and Metzinger, 1982a, Klapdor and Metzinger, 1982b]. With these predictions, all the ratios were compatible with one. This good agreement is confirmed with the second publication [Achkar and others., 1996], where two other prediction models are also tested. The best agreement still corresponds to the beta spectrum conversion from K. Schreckenbach et al.

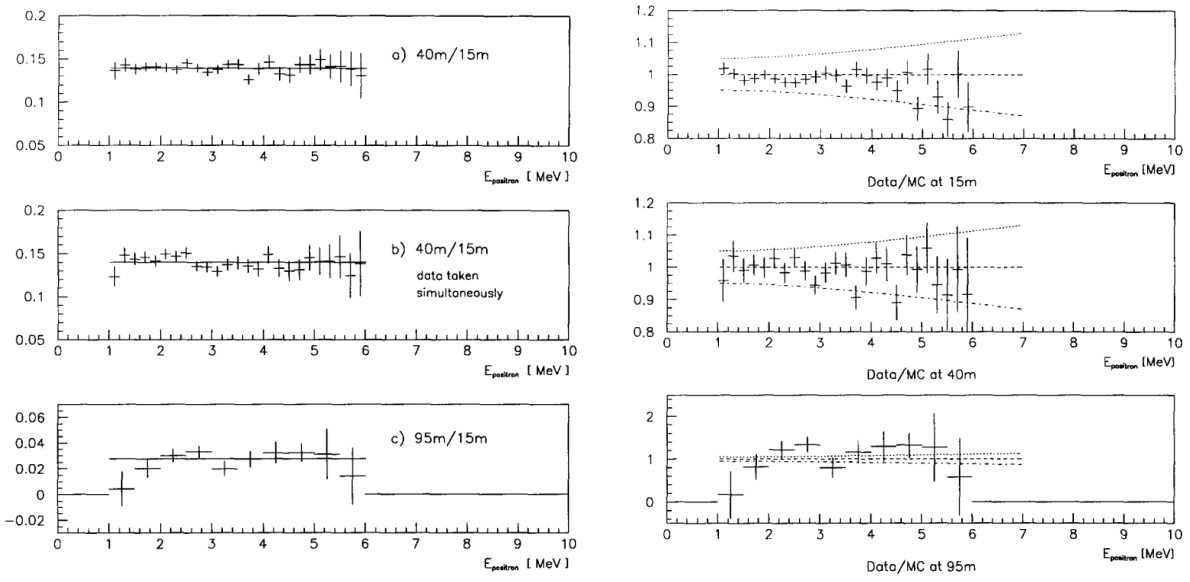

Figure 5.11: The Bugey-3 experiment results [Achkar et al., 1995]. (left) The ratio of the positron energy spectra at 40 / 15 m (upper), 40 / 15 m the part of the data taken simultaneously (middle) and 95 / 15 m (lower). (right) Ratio of the observed and predicted positron spectra.

5.5 Long baseline reactor experiments

In the late 90s, the phenomenon of neutrino oscillations started to be established with the atmospheric neutrinos in SuperKamiokande [Fukuda et al., 1998] and as the preferred solution to the solar neutrino problem [Vogel, 2019]. The large mixing angle suggested that long baseline reactor experiments could play a role. At distances greater than 100 km, with few MeV reactor neutrinos, it was possible to investigate the interpretation of the solar neutrino oscillation with a terrestrial experiment, without matter effects. At shorter distances of about 1 km, reactor experiments could try to determine the third mixing angle θ_{13}.

5.5.1 The KamLAND experiment

The KamLAND experiment was designed to validate the interpretation of the solar neutrino oscillations (mixing parameters θ_{12} and Δm^2_{21}) to solve the Solar neutrino problem. Compared to the first reactor experiments, the distance to reactors has to be much higher. The neutrino flux is then strongly reduced. To compensate the detector must be much larger and placed underground to suppress cosmic backgrounds. The radiopurity of the detector components and the detection medium must be well controlled.

The KamLAND detector consist of a 1 kt ultra-pure LS neutrino target contained in a transparent nylon-EVOH balloon (13 m diameter) surrounded by buffer oil to shield the radioactivity of the 1325 17-inch and 554 20-inch PMTs [Abe et al., 2010]. The vertex and energy resolutions at 1 MeV are respectively ∼12 cm and 6.4 %. The inner detector is shielded by 3.2 kton water-Cherenkov outer detector to absorb the radioactivity from the environment and serve as muon veto.

KamLAND dectector has been installed in the Kamioka mine (2700 m.w.e.) at the place of the first Kamiokande experiment. In the early 2000 years, there were 56 nuclear reactors operating in Japan but these number gradually decreased during the experiment. The flux-weighted average baseline to these reactors is ∼180 km. The absolute thermal power, used to normalize the fission rates, is measured to within 2% for each reactor. The $\overline{\nu}_e$ spectra per fission provided in [Vogel et al., 1981, Schreckenbach et al., 1985, Hahn et al., 1989] are used, and the uncertainties are further constrained from [Achkar and others., 1996]. In addition, the long-lived, out-of-equilibrium fission products ^{90}Sr, ^{106}Ru, and ^{144}Ce [Kopeikin et al., 2001] are evaluated from the history of fission rates for each isotope and are found to contribute only 0.6±0.3 %.

Electron anti-neutrinos are detected in KamLAND via the IBD reaction and the neutron delayed signal is selected in γ energy for capture on hydrogen or ^{12}C. The dominating background in KamLAND is produced by α decays of ^{210}Po long-lived daughter nucleus of ^{222}Rn. The (α, n) reaction on ^{13}C of the LS produces correlated p-recoil and n capture events. Delayed coincidences of $\beta - n$ ^{9}Li and ^{8}He, fast neutrons and atmospheric neutrinos are strongly reduced by muon veto cuts. They are nevertheless contributing to the backgrounds at a lower level. Finally, geo-neutrinos from the Earth ^{238}U and ^{232}Th decay chains are also fitted in the analysis. Using data collected from 2002 to 2009, the prompt energy spectrum is presented on figure 5.12. A total of 2106 events have been detected for 325.9 ± 26.1 background events expected. In the absence of $\overline{\nu}_e$ disappearance, 2879 ± 118 events from reactors would be expected.

A χ^2 scan of the $(\theta_{12}, \theta_{13}, \Delta m^2_{21})$ oscillation parameter space is carried out, minimizing χ^2 with respect to the backgrounds, the uncertainties on the reactor $\overline{\nu}_e$ spectra and energy scale, the event rate, and the energy dependent efficiencies [Gando et al., 2011]. Figure 5.13 compares the allowed regions in the $(\tan^2\theta_{12}, \Delta m^2_{21})$ plane from the two-flavor and three-flavour oscillation analyses. The allowed region from the solar data is in agreement with the KamLAND data. The oscillation frequency is much more constrained thanks to KamLAND data. For the three-flavour analysis combining the solar and KamLAND data, best-fit parameter values are found providing a first hint of non-zero θ_{13}: $\sin^2\theta_{13} = 0.020 \pm 0.016$. This result was compatible with other work combining CHOOZ, atmospheric, and accelerator experiments (see for example [Fogli et al., 2009]).

Figure 5.14 illustrates the $\overline{\nu}_e$ survival probability as a function of L/E in KamLAND. The data points are the ratio of the observed reactor $\overline{\nu}_e$ spectrum to that expected without oscillation. The oscillatory structure arising from the $\sin^2(1.267\ \frac{\Delta m^2_{21} L}{E})$ term is beautifully clear. The expected oscillation curves based on the best-fit parameters from the two- and three-flavour are also represented. Two full periods of oscillation are clearly visible for the first time, thanks to the KamLAND experiment.

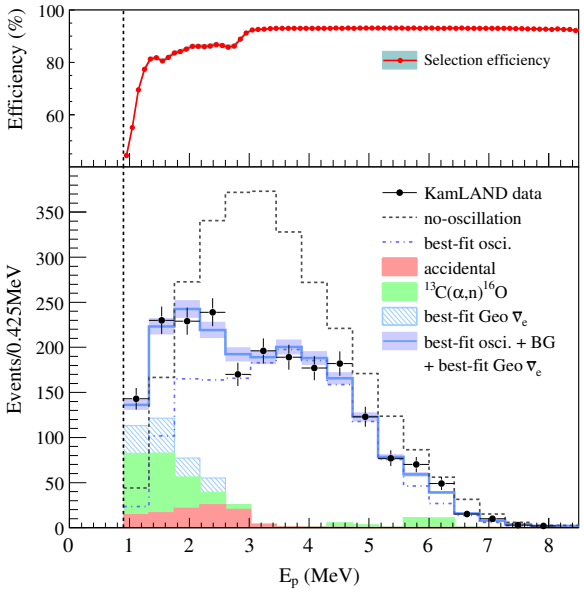

Figure 5.12: Prompt energy spectrum of the $\overline{\nu}_e$ candidates in KamLAND fitted from with a three-flavour oscillation analysis with the background and the reactor $\overline{\nu}_e$ contributions (shown on cumulative histogram) [Gando et al., 2011]. The top panel shows the energy-dependent selection efficiency.

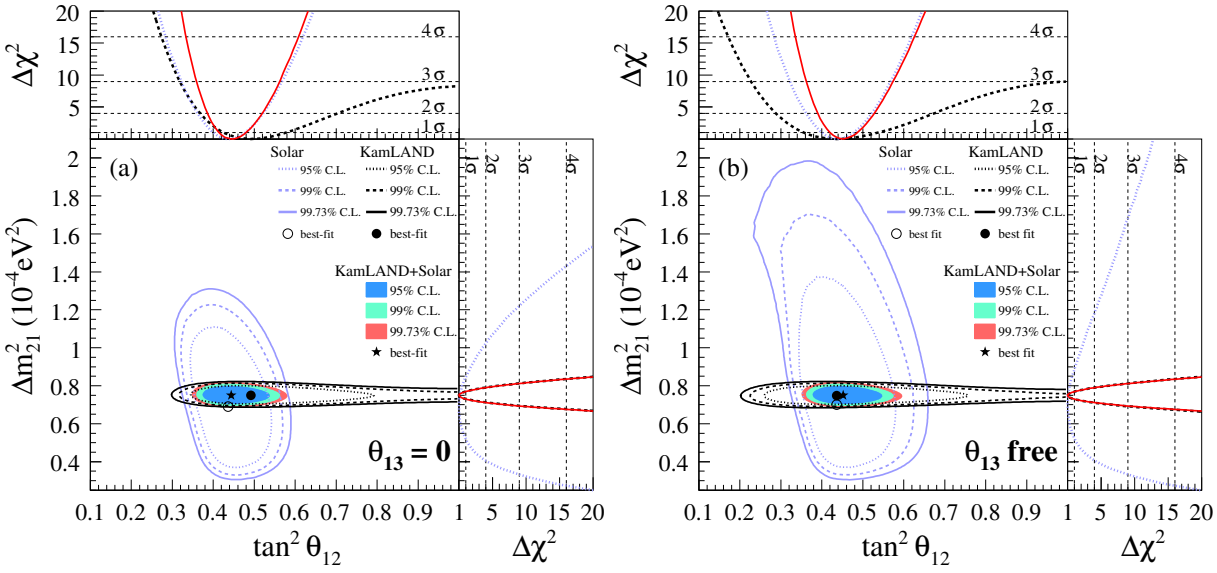

Figure 5.13: Allowed regions in the ($\tan^2\theta_{12}$, Δm^2_{21}) plane, for solar and KamLAND data from (left) the two-flavour oscillation analysis ($\theta_{13} = 0$) and (right) the three-flavour oscillation analysis (θ_{13} free). The coloured regions show the combined analysis [Gando et al., 2011].

5.5.2 The θ_{13} experiments

After the first measurements of the atmospheric (θ_{23}, Δm^2_{32}) and the solar oscillation parameters (θ_{12}, Δm^2_{21}) and the absence of reactor anti-neutrino disappearance in CHOOZ experiment [Apollonio et al., 2003], which put a limit at $\sin^2\theta_{13} \lesssim 0.15$ for the actual $\Delta m^2_{31} \approx 2.5 \times 10^{-3}$ eV^2, the quest for non-vanishing θ_{13} triggered three high precision experiments: Double-Chooz, Daya Bay and RENO. The principle of these experiments are the similar thus I will focus on the Double-Chooz experiment, since I've been involved in its construction. The key improvement of these experiments lies in having at least two identical detectors at different distances from the core. A near site to measure the un-oscillated anti-neutrino spectra, in order to cancel reactor prediction uncertainties, and a far site to measure the oscillated spectra.

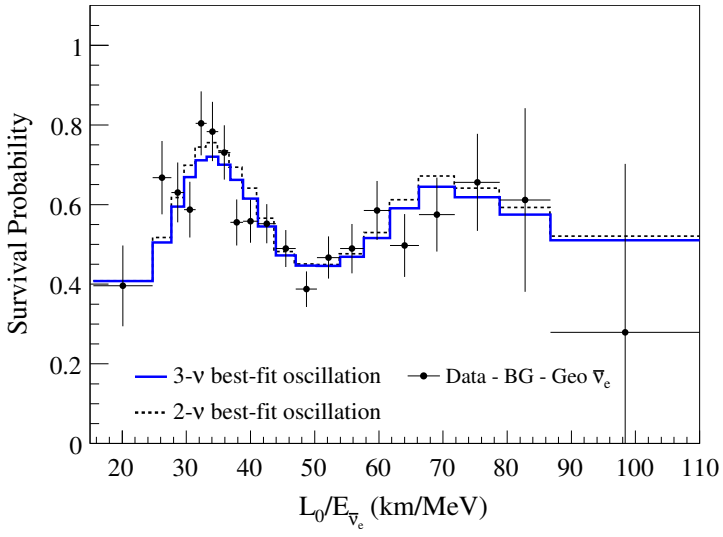

Figure 5.14: Ratio of the observed $\bar{\nu}_e$ spectrum to the no-oscillation case versus L_0/E for the KamLAND data. $L_0 \approx 180$ km is the flux-weighted average reactor baseline. The 2-ν and 3-ν histograms are expected from the best-fit parameters of the two- and three-flavour analyses [Gando et al., 2011].

The Double Chooz experiment

The Double Chooz (DC) experiment is located at the Chooz nuclear power plant in the French Ardennes. The electricity company (EDF) operates two of the most powerful pressurised water reactors with a full thermal power of 8.5 GW_{th}. As illustrated on figure 5.15 (left), the near detector (ND) and far detector (FD) are respectively located at the average distances of 400 m and 1050 m. There is almost an iso-flux geometry from the two reactors at these sites [Cucoanes et al., 2015]. The flux systematics reduce from 2.27% in the case of a single detector to $\leq 0.83\%$ using both detectors [de Kerret et al., 2020]. An external reactor $\bar{\nu}_e$ prediction model is used [Mueller et al., 2011, Huber, 2011] where ^{235}U, ^{239}Pu, ^{241}Pu fissile isotope contributions rely on ILL data [Von Feilitzsch et al., 1982, Schreckenbach et al., 1985, Hahn et al., 1989]. DC uses a measurement [Haag et al., 2014a] for the ^{238}U prediction, while Daya Bay and RENO use summation method.

The detectors exploits multi-layer LS design whose light is read out by many PMTs via a Flash-ADC deadtime-less electronics. The "Inner Detector" (ID) is subdivided, by transparent acrylic vessels, into 3 optically coupled volumes:

- the ν-Target (GdT) contains 10 m^3 of liquid scintillator, gadolinium-loaded at 1 g/L,
- the γ-Catcher (GC) contains 23 m^3 of liquid scintillator,
- a buffer of 100 m^3 filled with non-scintillating oil.

The "Inner Veto" (IV), 50 cm thick liquid scintillator, fully surrounds the ID while the "Outer Veto" (OV), made of tracking plastic scintillator strips, is placed on the top. The IV tags external rock γ's (anti-Compton veto), fast-neutrons and cosmic μ's while the OV only sees cosmic μ's. An external inert shield surrounds the IV: 15 cm steel (FD) and 1 m water (ND). The glove-box allows clean and safe deployment of the same calibration sources (^{252}Cf, ^{60}Co, ^{68}Ge, ^{137}Cs) in both the ND and FD. A complete description of the two detectors can be found in [de Kerret et al., 2022].

As a postdoc at the *Research Center for Neutrinos Science (RCNS)* in Sendai, I was in charge of coordinating the integration of the 390 low-background PMTs of the Double Chooz

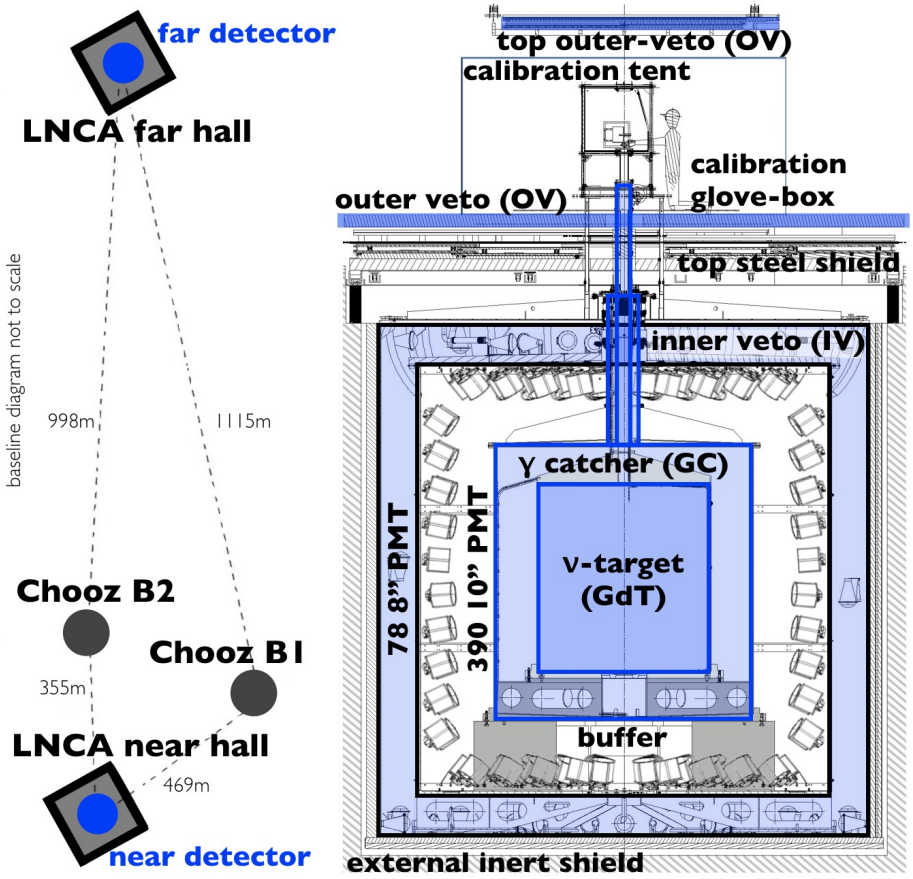

Figure 5.15: (left) Location of the near and far Double Chooz detectors with respect to the two Chooz reactors (B1 and B2). (right) Description of multi-layer (blue shaded) LS design of the two identical Double Chooz detectors [de Kerret et al., 2020].

far detector showed on figure 5.16. Beforehand, I participated to the evaluation of the 10-inch PMT performances on two test setups developed in Tokyo which provided, among all the key parameters, the efficiency maps of the active photo-cathode [Matsubara et al., 2012].

The anti-neutrinos are detected through IBD in the ν-Target and the neutron is quickly captured thanks to Gd ($\tau \sim 30$ µs) in the target. This capture produces a cascade of de-excitation gammas with a total energy of 8 MeV. These are detected in the GdT or in the GC to increase the target efficiency. Thanks to the excellent background rejection capabilities, visible on figure 5.17, another IBD detection approach revealed possible with Double Chooz. Not expected at the start of the experiment, the *Total neutron Capture (TnC)* exploits the selection of delayed γ's produced by all the nuclei available in the GdT and GC: H, C and Gd (shaded in red on figure 5.17). The TnC increased the efficiency by a factor 3 and conducted to an event rate of 816 (112) $\overline{\nu}_e$/day in the near (far) detector with signal-to-background ratio of 11.0 (20.2) [de Kerret et al., 2020]. After event selection and background rejection, the energy spectra of the anti-neutrino candidates are shown on figure 5.18 together with the background expectation and the no-oscillation expectation. The visible energy of the anti-neutrinos includes the annihilation γ's: $E_{\bar{\nu}_e} \approx E_{e^+} + 0.782$ MeV. The accuracy in the background determination has been demonstrated thanks to ~8 days of reactor off data [Abe et al., 2013], which was a unique opportunity among the θ_{13} experiments.

The θ_{13} measurement is obtained by fitting the ratio of the FD over the ND data, as presented in figure 5.19. The observed IBD spectral distortion (rate+shape) is applied corresponding to the neutrino oscillation model, as in equation 5.3, where θ_{13} is the unknown. Given the low frequency oscillation, it is not possible to measure the mass splitting with DC. Since the neutrino mass hierarchy is unknown, an average value of the mass splitting is taken from NuFIT-

Figure 5.16: Picture of the ID PMTs of the far detector of Double Chooz. The PMTs are encapsulated in cylindrical magnetic shields and acrylic supports. The ν-Target (GdT) and the γ-Catcher (GC) transparent acrylic vessels can also be seen. [Credits CEA-Saclay/IRFU]

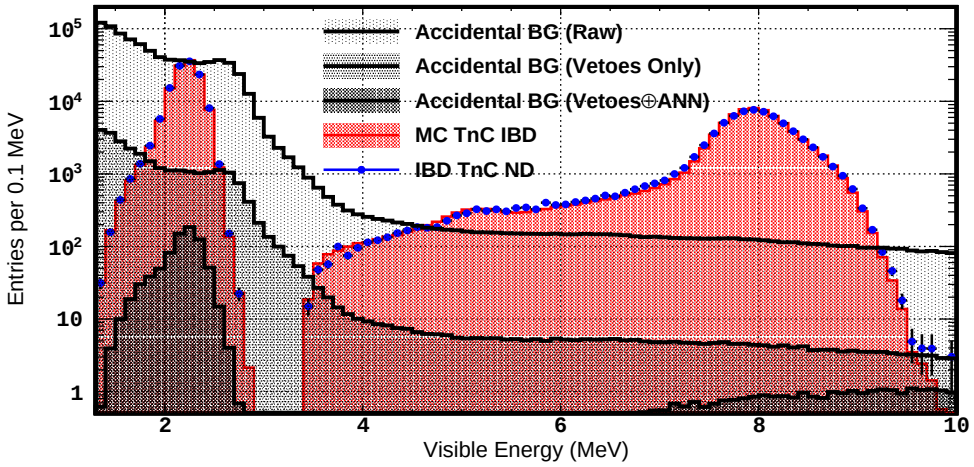

Figure 5.17: The TnC detection principle integrating the n-capture over all the capture-γ's: $\sim$2.2 MeV (H-n), $\sim$5.0 MeV (C-n) and $\sim$8 MeV (Gd-n). The overwhelming accidental BG (ND) is rejected over more than 4 orders of magnitude below 3.5 MeV using vetoes and the Artificial Neural Network (ANN) selection. Excellent data (blue points) to MC (red area) agreement is found in the delayed energy distribution after the rejection [de Kerret et al., 2020].

3.1 analysis: $\Delta m^2_{ee} = 2.484 \pm 0.036\ 10^{-3}$ eV^2. The best fit value is $\sin^2 2\theta_{13} = 0.105 \pm 0.014$. This corresponds to a 13.3% precision, dominated by the systematics since the statistical uncertainty represents only 0.005. The systematics are dominated by reactor flux (0.008) and detection (0.007), completed description in table 4 of [de Kerret et al., 2020].

The Double Chooz θ_{13} result exhibits an up to 48% higher central value, whose significance is $<2.0\sigma$ compared to the other measurements, as shown on figure 5.20.

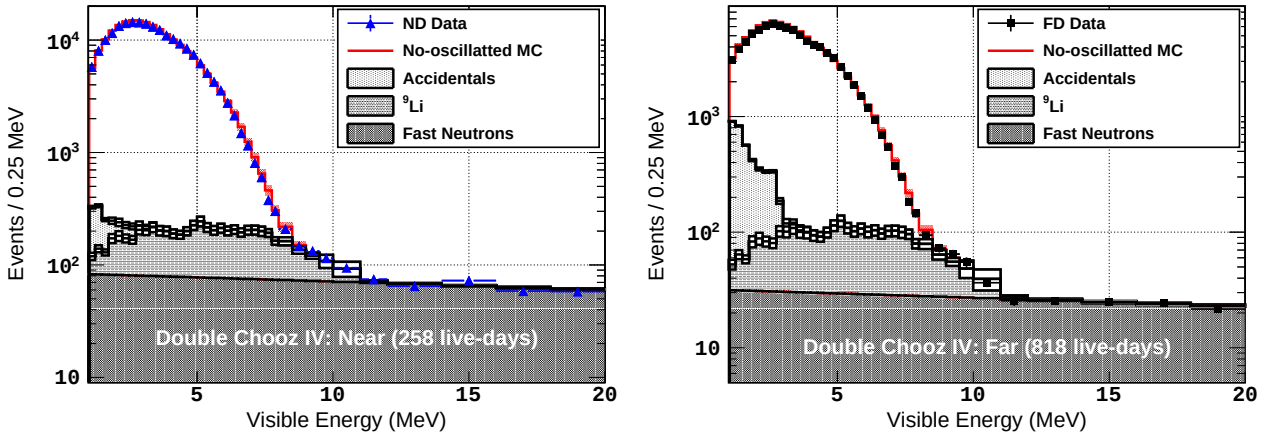

Figure 5.18: Prompt energy spectra of the IBD candidates for both ND (∼210k IBD's) and FD (∼90k IBD's) including the un-oscillated MC prediction (red) and the background model [de Kerret et al., 2020].

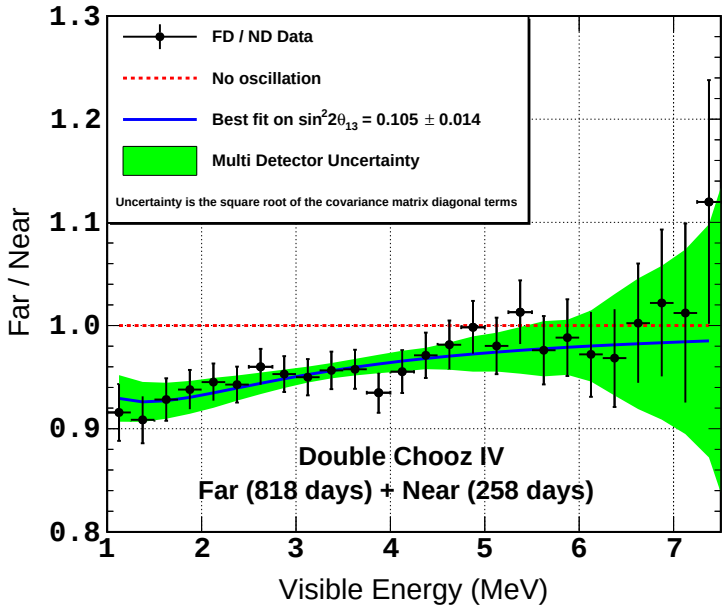

Figure 5.19: The FD to ND ratio (left) represents a clean θ_{13} rate+shape disappearance evidence used by the fit for parameter extraction. No traces of any remaining distortion are found, demonstrating the expected inter-detector cancellation to ensure the θ_{13} accuracy.

5.5.3 The JUNO experiment

The next long-baseline anti-neutrino is the Jiangmen Underground Neutrino Observatory (JUNO) experiment under construction in China. It has been designed to determine the neutrino mass ordering (MO) using an underground (700 m overburden) liquid scintillator detector. It is located 53 km away from both Yangjiang and Taishan Nuclear Power Plants in Guangdong. This distance has been precisely chosen to be sensitive to the two frequencies neutrino oscillations: a slow one driven by Δm^2_{21} and a fast one driven by Δm^2_{32}, as illustrated on figure 5.21. In six years of running, JUNO can resolve the neutrino mass hierarchy at a confidence level of 3-4σ [Djurcic et al., 2015]. The central detector, which contains 20,000 tons liquid scintillator, in an acrylic sphere of 35 m in diameter, and about 18,000 PMTs, is designed to have a very good energy resolution of 3% and a long lifetime of over 20 years. A second detection system of 25,600 3-inch photomultiplier tubes is also included in JUNO, forming a double calorimetry system, to improve the systematic uncertainty on the energy resolution. This unprecedented en-

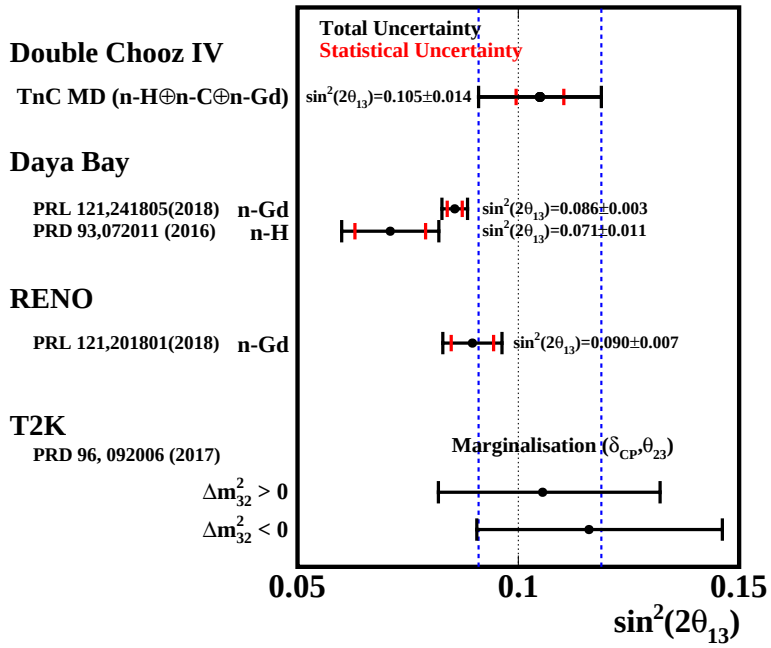

Figure 5.20: Published results of θ_{13} measurements as of 2020. References in figure 5 of [de Kerret et al., 2020]

ergy resolution for neutrino detection will lead to precise determination of the neutrino mixing parameters $\sin^2\theta_{12}$, Δm^2_{21} and $|\Delta m^2_{ee}|$ to an accuracy better than 1%. JUNO is also a multi-purpose experiment that will observe neutrinos from terrestrial and extra-terrestrial sources and investigate physics beyond the Standard Model.

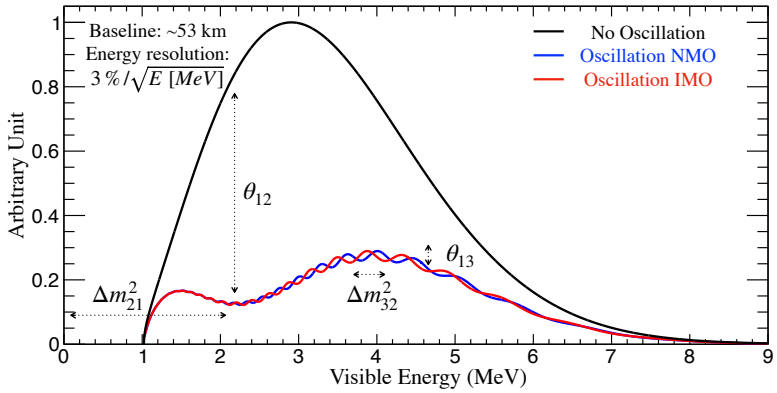

Figure 5.21: Effect of the two oscillations on the reactor anti-neutrinos detected in JUNO to measure the mass ordering (normal NMO or inverted IMO). The large amplitude and low frequency oscillation is driven by Δm^2_{21} and θ_{12} while the low amplitude and high frequency oscillation is driven by Δm^2_{32} and θ_{13} [Cabrera et al., 2022].

I have started to be involved in the JUNO experiment and collaborate with Subatech and IJCLab groups to work on the neutrino oscillation precision measurements. A recent study published in 2022 [Cabrera et al., 2022] from these groups and others, has investigated the possibility to reach an early resolution of the neutrino mass ordering ($\geq 5\sigma$ in 6 years) by combining JUNO and long-baseline neutrino beam experiments NOνA and T2K. The result is presented on figure 5.22.

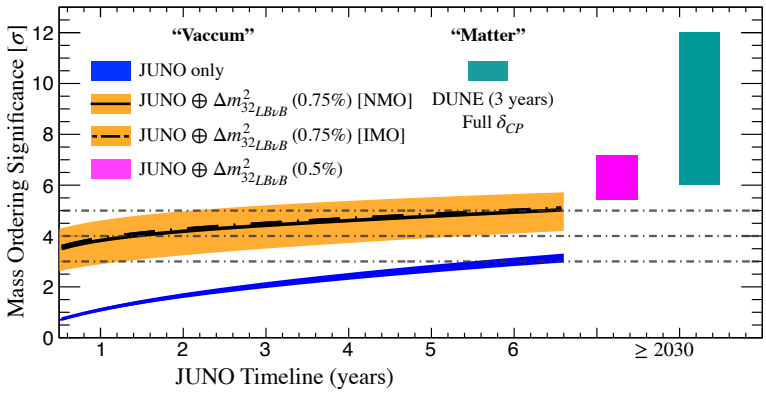

Figure 5.22: JUNO sensitivity on the MO determination illustrated as the difference between the JUNO alone (blue) and JUNO boosted by the combination with beam experiments (orange) curves. The Δm^2_{32} precision will be further enhanced up to $\sim 0.5\%$ by both DUNE and HK. At this moment, the JUNO data may exploit this precision to ensure a fully resolved vacuum only MO measurement (magenta), which can be compared to DUNE stand-alone measurement (green) [Cabrera et al., 2022].

5.6 Sterile neutrino search

5.6.1 The reactor anti-neutrino rate anomaly

We have presented in section 5.4 some results of short baseline reactor anti-neutrino experiments. More than 20 reactor experiments have been performed with baselines <100 m and their results are all consistent with each other. We have also presented the improved conversion model from Huber-Mueller (HM), in section 5.3.2, that predicted a neutrino flux increase of about 3.5% during the preparation of the θ_{13} experiments. This new prediction applies to all the reactor experiments and lead to an event rate deficit compared to the prediction, as shown on figure 5.23. This effect has been highlighted for the first time in a publication of G. Mention et al. [Mention et al., 2011]. Named the *reactor anti-neutrino anomaly* (RAA), this deficit has been computed to 0.943 ± 0.023, corresponding to a 2.5σ effect. This work investigated the compatibility of the RAA with short distance oscillation towards a sterile neutrino to explain the deficit. First mixing parameters were provided: $\Delta m^2 > 0.15$ eV^2 and $\sin^2 2\theta = 0.14 \pm 0.08$. The RAA has been re-evaluated, by a team including P. Vogel [Zhang et al., 2013], down to 1.4σ only after taking into account the recent results of the flux measurements of the θ_{13} experiments.

More complete investigations of the sterile neutrino hypothesis to explain the RAA where performed by several groups: J. Kopp et al., C. Giunti et al. or in the *light sterile neutrino white paper* [Abazajian et al., 2012]. The results were updated several times over the years also including new experimental results. On figure 5.24 (left), we present a plot J. Kopp et al. [Kopp et al., 2013] from 2013 that illustrates why the sterile neutrino could explain the deficit of the RRA. The dashed blue curve corresponds to the best fit of the SBL rates only, while the red curve corresponds to the global $\bar{\nu}_e$ disappearance fit. On figure 5.24 (right), is represented the $(\sin^2 2\theta, \Delta m^2)$ two-dimensional allowed region from C. Giunti et al. [Gariazzo et al., 2017]. The best fit point for these analyses is approximately at $\sin^2 2\theta \approx 0.1$ and $\Delta m^2 \approx 0.5$ eV^2.

In the sterile neutrino white paper [Abazajian et al., 2012], the authors highlight that ILL experiment might have seen a hint of oscillation in the energy spectrum, see section 5.4.1, but the Bugey-3 experiment did not show a spectral distortion, see section 5.4.2. The large core size of the Bugey reactor might have washed-out the oscillation pattern at 15 m. Combining the previously mentioned rate analyses to this shape analysis pushes the allowed region to higher values of $\Delta m^2 \gtrsim 1$ eV^2 with a best fit point around 2.4 eV^2.

We have previously mentioned the analysis by Daya Bay, published in 2017 [An et al., 2017a],

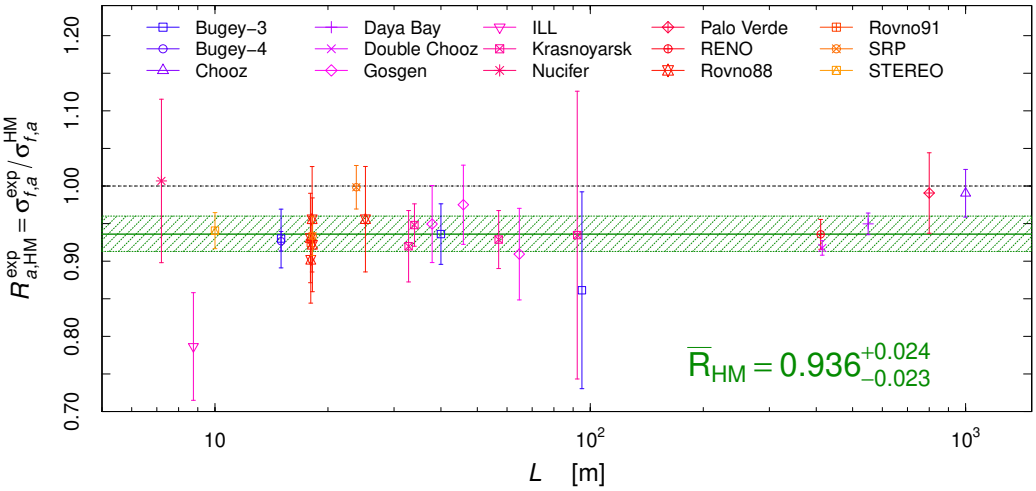

Figure 5.23: Ratio of the measured and expected IBD yields for the reactor experiments considered in the analysis of [Giunti et al., 2022] as a function of the reactor-detector distance L for the HM model. The error bars show the experimental uncertainties. The horizontal green band shows the average ratio $\overline{R}_{HM}$ and its uncertainty, that gives a 2.5σ RAA.

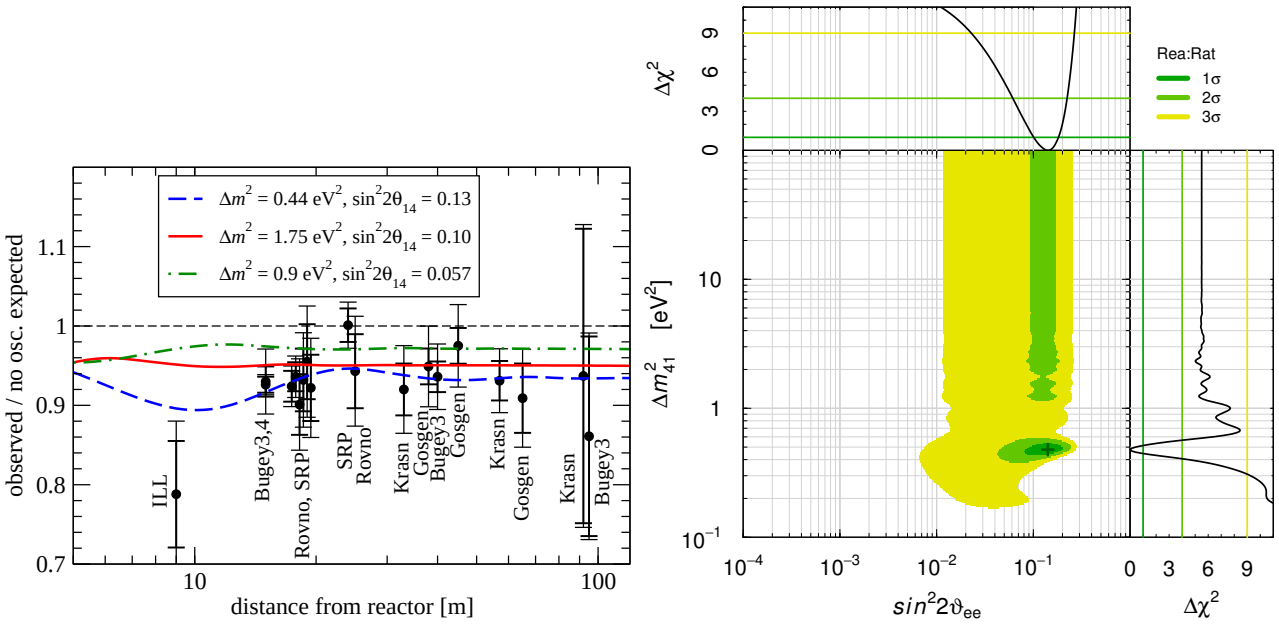

Figure 5.24: (left) Event rates in SBL reactor experiments compared to the predictions for three representative sets of oscillation parameters. The thick (thin) error bars correspond to uncorrelated (total) experimental errors. The neutrino flux uncertainty is not included in the error bars [Kopp et al., 2013]. (right) Allowed regions in the $(\sin^2 2\theta, \Delta m^2)$ plane from the combined fit of the rates of the SBL reactor neutrino experiments [Gariazzo et al., 2017].

about the evolution of the IBD yields and energy spectra using 2.2 millions IBD candidates over 1230 days data taking. This work allowed to disentangle the contribution of ^{235}U and ^{239}Pt using the evolution of the total IBD yield σ_f with the relative fission fraction F_{239} of ^{239}Pu. This is illustrated in figure 5.25 (left). The measured total IBD yield is in deficit of 5.1% compared to the HM prediction (1.7σ). Which is consistent with the global deficit of about 6% observed by past reactor experiments. Even after scaling by the HM prediction by this factor, a discrepancy of 3.1σ is still observed in the slope of the evolution $d\sigma_f/dF_{239}$. A χ^2 statistical analysis of the fission fractions of each isotope allows to extract the IBD yields σ_{235} for ^{235}U and σ_{239} ^{239}Pu. Allowed two-dimensional region and $\Delta\chi^2$ are shown on figure 5.25 (right). It reveals that the fission fraction σ_{235} is 7.8% lower than the HM prediction while the σ_{239} is in

good agreement. This deficit, not being equally distributed to all the fission isotopes, is not in favour of oscillations towards a sterile neutrino. This important result on the contrary indicates an incorrect prediction of the ^{235}U as the origin of the RAA.

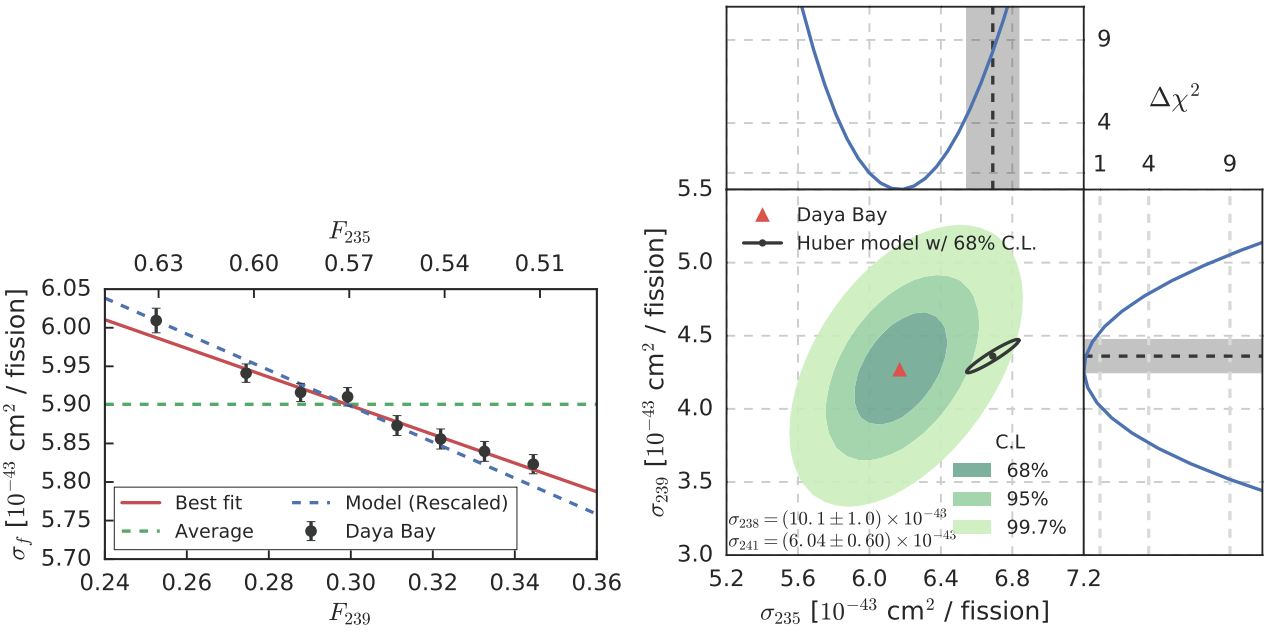

Figure 5.25: (left) Measurement of IBD yield per fission, σ_f, versus effective ^{239}Pu (lower axis) or ^{235}U (upper axis) fission fraction (black) with statistical error bars. Constant yield (dashed green line) and variable yield (red line) best fits are also pictured, as well as predicted yields from the Huber-Mueller model (dashed blue line), scaled to account for the difference in total yield $\bar{\sigma}_f$ between the data and prediction [An et al., 2017a]. (right) Combined measurement of ^{235}U and ^{239}Pu IBD yields per fission σ_{235} and σ_{239}. The red triangle indicates the best fit and green contours indicate two-dimensional 1σ, 2σ and 3σ allowed regions. Predicted values and 1σ allowed regions based on the Huber-Mueller model are also shown in black. The top and side panels show one-dimensional $\Delta\chi^2$ profiles for σ_{235} and σ_{239}, respectively [An et al., 2017a].

In a very recent publication of 2022, C. Giunti et al. revisited the reactor anti-neutrino anomaly in light of the recent reactor anti-neutrino flux calculations with the conversion and summation methods [Giunti et al., 2022]. This work compares the reactor IBD yields of 27 experiments with four prediction models: the Estienne-Fallot (EF) updated summation model [Estienne et al., 2019], the Kurchatov Institute (KI) conversion using the recent $R_{235/239}$ measurement [Kopeikin et al., 2021], the HKSS model using an improved conversion method considering first-forbidden transitions calculated with the nuclear shell model [Hayen et al., 2019] and a combination of the two last models. The addition of the fuel evolution data from Daya Bay [An et al., 2017a] also increases the discrimination between the models. In the end, the predictions of EF and KI provide the best agreements with the data at 0.8σ and 1.1σ respectively. The conclusion of this work is a *plausible robust demise of the reactor anti-neutrino anomaly* [Giunti et al., 2022]. This has also been reported in the Snowmass 2021 report on reactor anti-neutrinos opportunities [Akindele et al., 2022]. The figure 5.26 summarizes the situation on the reactor anti-neutrino rate anomaly presented in this report. It is clearly visible that all the experimental rates measurements are now well aligned with the recent predictions for ^{235}U and ^{239}Pu. The HM prediction used to compute the ratios r_{235} and r_{239} on this plot, clearly show the deficit for ^{235}U compared to one.

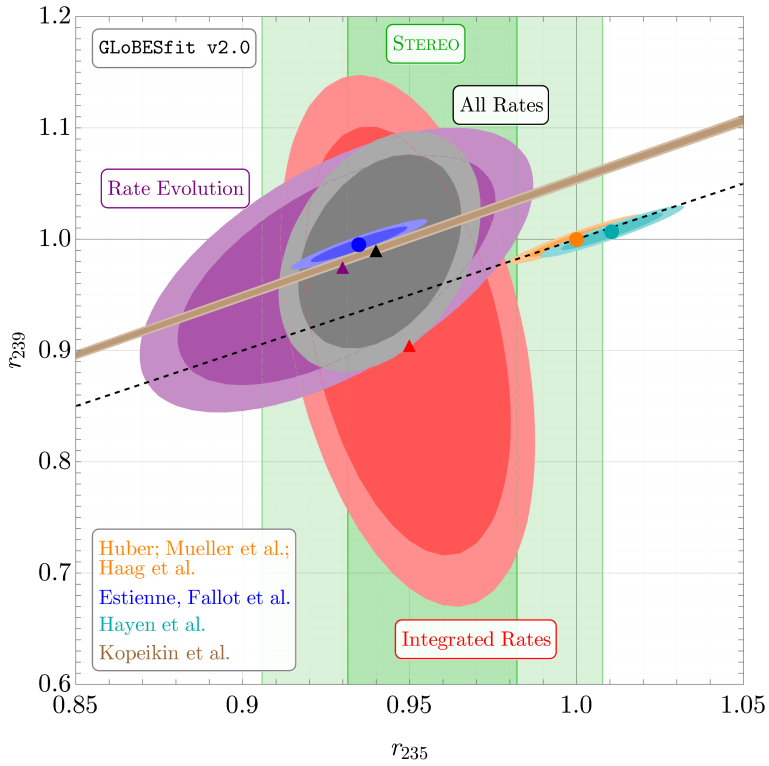

Figure 5.26: The 95% and 99% C.L. (dark / light) contours of the IBD yields ratios of the measured over HM prediction for ^{239}Pu versus ^{235}U for integrated rate (red), fuel evolution (purple) and all reactor experiments (gray/black) [Akindele et al., 2022]. The orange, blue and cyan ellipses represent the expectations from the HM, EF and HKSS flux models, 1σ and 2σ are shown in dark or light shades respectively. The brown bands represent the 1σ (dark) and 2σ (light) determination of the ^{239}Pu/^{235}U ratio from the KI. The black, dashed line represents the line along which $r_{235} = r_{239}$. The triangles represent the best-fit values for the three fits, and the circles show the central values for the flux models. Figure and caption adapted from [Berryman and Huber, 2021].

5.6.2 The reactor anti-neutrino shape anomaly

Since the Double Chooz experiment, presented in section 5.5.2, has started data taking first with the far detector only, the collaboration was relying on the neutrino energy spectrum prediction to measure θ_{13}. An unexpected spectral distortion, uncovered by the uncertainties, was then revealed by DC when comparing the measured spectra to the prediction. It was latter investigated with the near detector data as shown on figure 5.27 (left) [de Kerret et al., 2020]. This is called the 5 MeV excess/bump or the *reactor anti-neutrino shape anomaly*. An empirical structure is examined in DC by fitting with two models: one and two empirical Gaussian peaks with a common slope figure 5.27 (left). Both models reproduced data. This has been investigated also with a shape-only analysis, providing less reactor prediction uncertainties, and compared to other experiments, see figure 5.27 (right). A small deviation was already seen in the Chooz experiment [Apollonio et al., 2003]. The Bugey-3, see section 5.4.2, (not shown on the figure 5.27) is the only experiment not reproducing this structure.

In 2019, the Daya Bay collaboration published the extraction of the ^{235}U and ^{239}Pu with 1958 days of data gathering 3.5×10^6 IBD candidates from the four near detectors. The energy spectra have been extracted thanks to the evolution data, with similar method than presented in section 5.6.1, and are presented here on figure 5.28. The observed IBD yields have been used to normalize the HM prediction (to compensate for the RAA) by the factors 0.92 and 0.99 for ^{235}U and ^{239}Pu respectively. The shape anomaly is also observed by Daya Bay which is furthermore pointing to ^{235}U with a maximal local deviation of 4σ in the 4-6 MeV region

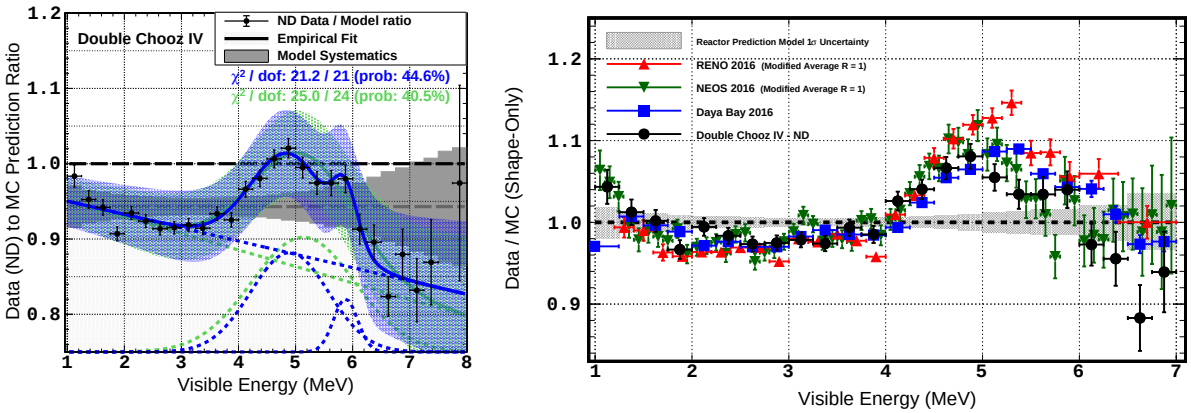

Figure 5.27: (left) ND data to the MC prediction ratio with the fit of two empirical models. (right) The data to prediction spectral ratio for several experiments exhibiting a common dominant pattern predominantly characterised by the 5 MeV excess.

(while it is only 1.2σ for ^{239}Pu). This effect cannot be explained by an hypothetical oscillation toward sterile neutrino but requires further studies.

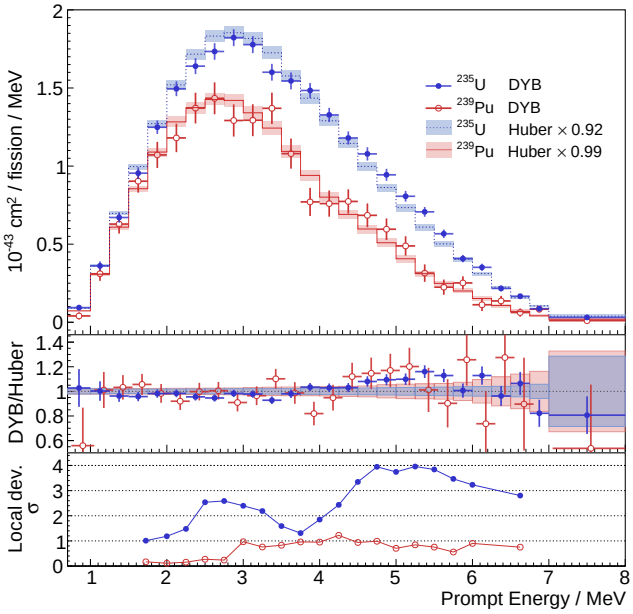

Figure 5.28: (top) Comparison of the extracted ^{235}U and ^{239}Pu spectra from Daya Bay and the corresponding Huber-Mueller model predictions with the normalization factors 0.92 and 0.99 [Adey et al., 2019]. The error bars in the data points are the square root of the diagonal terms of the covariance matrix of the extracted spectra. The error bands are the uncertainties from the HM model. (middle) Ratio of the extracted spectra to the predicted spectra. (bottom) Local significance of the shape deviations for the extracted ^{235}U and ^{239}Pu spectra compared to the model predictions.

The updated summation method [Estienne et al., 2019] as well is not able to explain this spectral distortion but the authors conclude that in this energy region the potential impact of remaining Pandemonium affected nuclei or unknown data remains important. L. Hayen et al. [Hayen et al., 2019], previously mentioned as the HKSS model, improved the conversion method in 2019 by calculating 36 dominant forbidden transitions above 4 MeV using the nuclear shell model. The HM was using strong approximations on their treatment and the studies from A.C. Hayes et al. were discussing their importance but not performing microscopic calculations. An increase of the order of 4-5% is observed in the anti-neutrino spectra in the region [4.5;7.5] MeV. It provides a partial explanation of the 5 MeV bump and demonstrates that a proper

understanding of the forbidden β-transition shapes is necessary. On the other end, this models predicts lager the anti-neutrino rates and would increase of the RAA.

5.6.3 Other neutrino anomalies

If the reactor anti-neutrinos anomalies would have been the only one seen in neutrino oscillations, we could have concluded that the issue was coming from the prediction of anti-neutrino rates and spectra. This would be fair given the complexity of the calculations we have tried to illustrate in the previous sections. However, persisting anomalies occurred in other neutrino oscillation experiments giving strength to the sterile neutrino hypothesis:

- The LSND experiment reported an evidence of $\bar{\nu}_\mu \rightarrow \bar{\nu}_e$ transitions because of an electron excess of events at 3.1σ, compatible with oscillation in the eV^2 region [Aguilar-Arevalo et al., 2001]. The experiment consisted in the detection of anti-neutrinos produced by the decay-at-rest of μ^+ at 30 m baseline with energies between 20 and 200 MeV in a LS detector.

- The MiniBooNE experiment was designed to investigate the excess seen by LSND with longer baseline and higher energy neutrino beam, irregardless providing similar L/E ratio. It also uses a LS detector but the neutrino beam is produced by decay-in-flight of mesons in magnetic focussing horns. A large and unexplained excess of 4.8σ at low energy (< 500 MeV) is reported both in neutrino and anti-neutrino mode [Aguilar-Arevalo et al., 2021]. The possible oscillation to sterile neutrino seen by LSND should manifest at higher energies but the combination of those data is still possible, as presented in [Dentler et al., 2018]. This low energy region is however excluded of some analyses in the search for oscillation to sterile neutrino [Giunti, 2016]. This excess could be due to a lack of background considerations. C. Ginuti et al. computed an higher production rate of $\Delta^{+/0}$ baryons, decaying into $p/n+\gamma$, by neutral current (NC) interactions on ^{12}C [Giunti et al., 2020]. The agreement with the data from this estimation is better and the significance in favour of oscillation decreases. The MicroBooNE experiment using a liquid argon TPC has been designed to test the MiniBooNE excess. Its excellent tracking capabilities allowed to probe $\Delta \rightarrow p\gamma$ and $\Delta \rightarrow n\gamma$ channels from neutrino NC interactions. The result published in 2022 rejects the MiniBooNE excess as ν_e's [Abratenko et al., 2022b].

- The calibration of the gallium solar neutrino experiments (SAGE and GALLEX) with radioactive sources obtained event rates lower than expected. These experiments used two electron-capture sources, ^{51}Cr and ^{37}Ar, providing mono-energetic ν_e (<1 MeV) to determine their efficiency to solar neutrinos detection through $^{71}\text{Ga}(\nu_e,e^-)^{71}\text{Ge}$ reaction. The observed deficit of about 16%, with a significance of about 3σ, is often refereed as the *gallium anomaly* (GA) [Giunti and Laveder, 2011b]. This anomaly has been revisited to lower significance (2.3σ) in 2019 [Kostensalo et al., 2019].

- Very recently, the gallium anomaly was confirmed by the Baksan Experiment on Sterile Transitions (BEST) specifically designed to investigate the ν_e deficit [Barinov et al., 2022]. The BEST experiment comprises two gallium volumes (133.5 cm diameter sphere and 234.5 cm high and 218 cm diameter cylinder) around the ν_e source in order to perform two-distances oscillation search. The ^{51}Cr has a well-understood spectrum relying on well-known nuclear and atomic physics parameters. The neutrinos interacting with ^{71}Ga produces ^{71}Ge, a radioactive isotope which is extracted and counted after a certain exposure. The ratios of the measured over the expected rates confirm the deficit since $R_{in} = 0.79 \pm 0.05$ and $R_{out} = 0.77 \pm 0.05$. But the ratio between the two volumes is compatible with one $R_{out/in} = 0.97 \pm 0.07$. Since the two measured ratios are similar at different distances, it pushes the allowed Δm^2 region to higher values and the $\sim$20%

deficit drives the mixing angle to larger values as well, see figure 5.29. The best fit for the BEST only data is $\Delta m^2 = 3.3$ eV^2 and $\sin^2 2\theta = 0.42$. For these large Δm^2 values, the BEST experiment is not sensitive to the high frequency oscillations but the observed ratios could be explained. The deficit of the GA is thus confirmed but BEST is not proving that it is due to oscillation effect, since no dependence on the length is observed. A second phase with ^{65}Zn source with higher energy and longer half-life compared to ^{51}Cr, is under investigation.

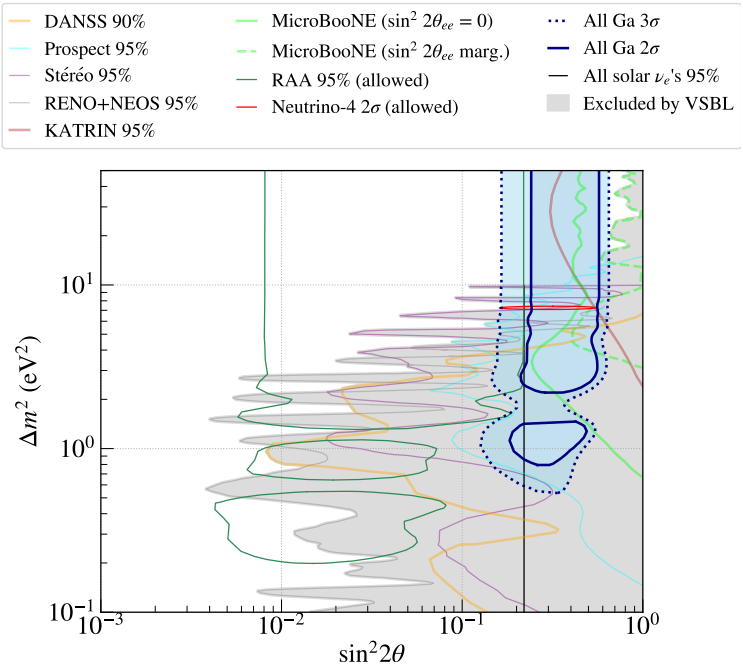

Figure 5.29: Exclusion contours of all Ga anomaly experiments: two GALLEX, two SAGE and two BEST results. The blue solid line and the blue dotted line shows the 2σ and 3σ confidence level respectively. The figure also presents the exclusion contours from [Barinov et al., 2022].

Before the recent exclusions of the very short baseline (VSBL) reactor experiments (see section 5.6.5), the GA was well overlapping with the RAA allowed region by oscillation to sterile neutrino above 1 eV^2, see figure 5.30 (left). This was a good motivation to start several new high precision experiments looking for oscillation. The next two sections will present the requirements for a search with VSBL reactor experiments and the recent results. Unfortunately, the recent result of the BEST experiment is putting more tension between the two allowed regions of the RAA and the GA. Indeed after the BEST result, the gallium anomaly looks more pronounced. In addition, and since the beginning, it is difficult to conciliate the anomalies coming from appearance (neutrino beams) and disappearance anomalies (RAA & GA) as can be seen on figure 5.30 (right). Invoking more neutrino species (3+2 scenario) seems to improve the agreement but it seems mainly statistical, since more parameters are introduced [Giunti and Laveder, 2011a].

5.6.4 Experimental parameters for sterile neutrino search at nuclear reactors

After the publication of the RAA in 2011, several very short baseline (<10 m) reactor experiments were triggered to search for an evidence of eV-scale active-to-sterile neutrino oscillation.

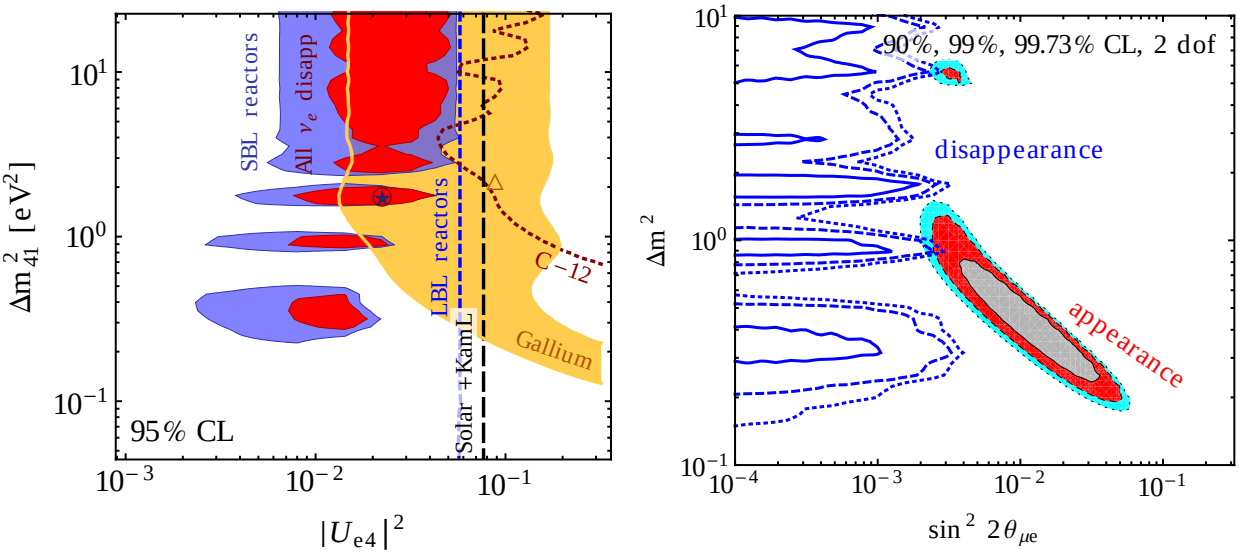

Figure 5.30: Results of the global fit in the 3+1 scenario, shown as exclusion limits and allowed regions for the effective mixing parameters and the mass squared difference Δm^2_{41} as of 2013 [Kopp et al., 2013]. (left) Allowed regions at 95% CL for SBL reactor data (blue shaded), gallium radioactive source data (orange shaded), disappearance constraints from ν_e-^{12}C scattering data from LSND and KARMEN (dark red dotted), long-baseline reactor data (blue short-dashed) and solar+KamLAND data (black long-dashed). The red shaded region is the combined region from all these ν_e and $\bar{\nu}_e$ disappearance data sets. (right) Comparison of the parameter region preferred by appearance data to the exclusion limit from disappearance data [Kopp et al., 2013].

These experiments were specifically designed to reveal an oscillation pattern, independently of the reactor predictions, either in distance along the detector or in neutrino energy. A publication of K.M. Heeger et al. [Heeger et al., 2013] in 2012 reviewed the key parameters to perform such experiments. With mass splitting of the order of $\sim$1 eV^2 an oscillation lengths of about 3 m is expected for few MeV reactor anti-neutrinos. The illustration of the oscillation pattern can be seen on figure 5.31.

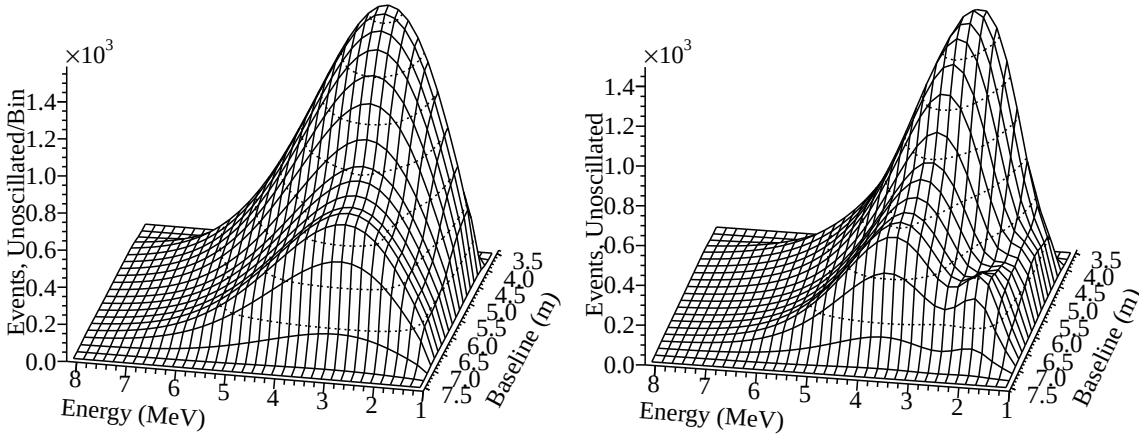

Figure 5.31: Un-oscillated (left) versus oscillated (right) detected $\bar{\nu}_e$ spectra with exaggerated oscillation parameters for illustration $\Delta m^2 = 1.8$ eV^2 and $\sin^2 2\theta = 0.5$ [Heeger et al., 2013].

In order to design or compare experiments we need to consider the sensitivity curves in the ($\sin^2 2\theta$, Δm^2) parameters space. These curves present an horizontal minimum at a given Δm^2

value while the sensitivity is driven by the mixing angle $\sin^2 2\theta$. Experiments target to reach as low as possible values of $\sin^2 2\theta$, since the RAA is an effect of few percent and cover the allowed region already presented in figure 5.24. We can summarize here the items considered by the study of K.M. Heeger et al. in the publication [Heeger et al., 2013]:

- **reactor core:** it can be either a commercial reactor with low ^{235}U enrichment (<6%) or a research reactor with high ^{235}U enrichment (>90%). Experiments at commercial reactors can quickly collect high statistics thanks to huge power (∼3 GW_{th}) and long reactor ON cycles (∼1.5 y). On the other end, the core dimension will spread the neutrino path lengths and push away the detector (∼20 m) decreasing the sensitivity to the higher Δm^2. Experiments close to research reactors collect lower statistics because of lower reactor power (<100 MW_{th}) but can get closer to the reactor core (<10 m). The almost pure ^{235}U fuel composition should simplify the comparison with predictions and provide valuable inputs to the models. In addition, these reactors alternate ON/OFF cycles of about 1.5 months. This slows down the collection of statistics but helps the background measurements.
- **detector parameters:** a large detector length enhances the ability to resolve oscillations with position (neutrino baseline) that is complementary to the researched spectral distortion in energy. It would increase the overall sensitivity but more specifically at lower values of Δm^2, where the detector length could reveal a full period of oscillation. Most of the detectors are segmented along the neutrino baseline and the size of the cells is determined by the interaction position resolution and statistics per position. Above several tens of cm, the sensitivity to higher values of Δm^2 quickly drops. This region is then strongly dependent on the energy resolution of the detector which is also of major importance to resolve the spectral distortion in energy caused by oscillation. Resolutions close to 10% that have been achieved by previous SBL neutrino experiments are recommanded.
- **detection and backgrounds:** the IBD detection efficiency directly scales the number of anti-neutrinos detected as the detector volume, the distance to reactor or the reactor power. The efficiency also reveals the capability to reject the backgrounds. The signal-over-background ratio (S/B) is crucial for the success of the experiment. At small S/B (∼0.1) it is difficult to resolve oscillation effects above statistical background fluctuations and uncorrelated background uncertainties. Precise knowledge of the backgrounds and their distribution in energy and position are critical for the experiment's sensitivity and for demonstrating the observation of neutrino oscillation. Very short baseline reactor experiments generally imply a small overburden of the detector (from a few to tens of meters). Therefore the cosmic-ray induced backgrounds are high and even dominant.

The impact on the sensitivity to the search for oscillation to sterile neutrino in the ($\sin^2 2\theta$, Δm^2) parameter space of all the aspects discussed above is qualitatively summarized in figure 5.32 of the K.M. Heeger et al. and precise numbers can be found in [Heeger et al., 2013].

5.6.5 Overview of recent results

During the last decade, many VSBL experiments provided results in the search for sterile neutrino. Results and updates with new exclusion contours were produced almost every year as well as global analyses. We can cite here the major VSBL experiments: NEOS [Ko et al., 2017], DANSS [Danilov, 2020], Neutrino-4 [Serebrov et al., 2019], STEREO [Almazán et al., 2020] and PROSPECT [Andriamirado et al., 2021]. We have explained in the previous section the key parameters these experiments have all tried to optimize. Here, I would like to try to focus on the major results at the time of writing these pages.

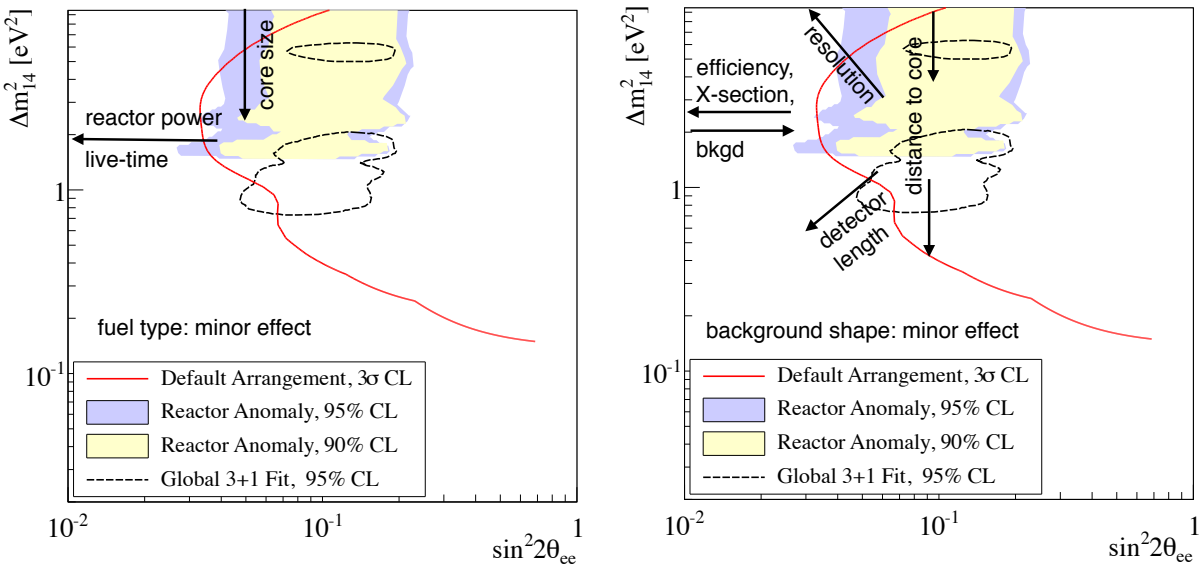

Figure 5.32: Summary plots of the reactor and detector parameters relevant for covering the suggested reactor anomaly in the ($\sin^2 2\theta$, Δm^2) parameter space. These graphs indicate the direction in which the sensitivity curve moved when reactor (left) and detector (right) parameters are improved or adjusted [Heeger et al., 2013]. Also pictured are the best-fit parameter spaces for the RAA [Mention et al., 2011] and for a 3+1 global fit of 2011 by C. Giunti et al. [Giunti and Laveder, 2011c].

The NEOS experiment

The NEOS experiment searching for light sterile neutrinos has been conducted at a nuclear reactor with a thermal power of 2.8 GW located at the Hanbit nuclear power complex in Korea. The NEOS detector consists of one ton of Gd-loaded LS in a vertical cylinder readout by PMTs. It is located in a tendon gallery approximately 24 m from the reactor core. This exact position at a commercial reactor provides a fantastic anti-neutrino rate of 1976 per day with a signal to background ratio S/B = 22, thanks to the 20 mwe overburden. After eight months data taking [Ko et al., 2017], no strong evidence of 3+1 neutrino oscillation is found in the energy shape analysis compared to the Daya Bay spectrum [An et al., 2017b], see figure 5.34 (left). The exclusion contour is presented on figure 5.33 (right). An excess around the 5 MeV prompt energy range is observed compared to HM prediction (weighted by the IBD cross sections estimated by Vogel and Beacom [Vogel and Beacom, 1999]) as seen in existing longer-baseline experiments (the bump is not seen on the comparison with Daya Bay on the figure 5.33 (left)).

In 2022, a similar study has been performed between RENO and NEOS [Atif et al., 2022]. Since both experiments are located at the Hanbit Nuclear Power Plant in Korea, it is expected to reduce significantly the systematic uncertainties. A nearly reactor model independent search for sterile neutrino oscillation, using 2509 days for RENO and 180 days for NEOS, on the prompt energy spectra has been performed. A large region of Δm^2 is excluded [0.1,7.0] eV^2 at 95% CL and an allowed region remains around a best fit point at $\Delta m^2_{14} = 2.41$ eV^2 and $\sin^2 2\theta_{14} = 0.08$.

The Neutrino-4 experiment

The Neutrino-4 experiment has published in 2018 the observation of an oscillation effect of 3.5σ [Serebrov et al., 2019] which has been reduced to 2.9σ in 2021 after taking into account systematics [Serebrov et al., 2021]. The Neutrino-4 detector consists of 1.8 m^3 gadolinium-loaded LS, divided into 5×10 vertical sections with squared sides of 22.5 cm and 85 cm high, readout by PMTs on the top. It is located at the SM-3 nuclear reactor in Dimitrovgrad,

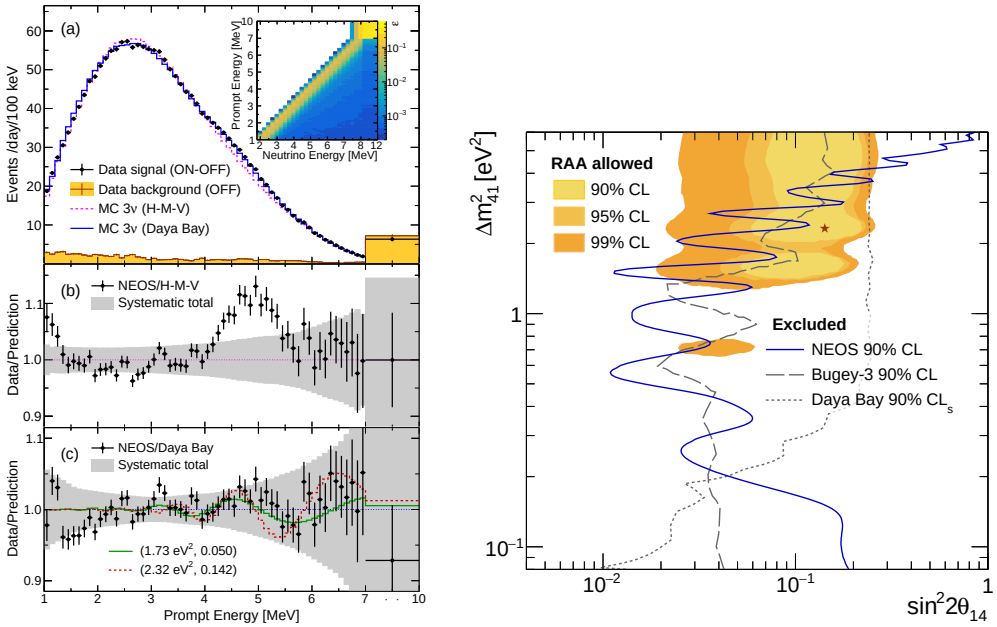

Figure 5.33: (left) (a) IBD prompt energy spectrum measured by NEOS [Ko et al., 2017]. The orange shaded histogram is the background spectrum measured during the reactor-off period. The detector response matrix in the inset shows the relation between the neutrino energy and the prompt energy. (b) Ratio of the observed prompt energy spectrum to the HM flux prediction with the 3ν hypothesis. The predicted spectrum is scaled to match the area of the data excluding the 3.4-6.3 MeV excess region. (c) Ratio of the data to the expected spectrum based on the Daya Bay result with the 3ν hypothesis, scaled to match the whole data area. The solid green line is the expected oscillation patterns for the best fit of the data to the 3+1 ν hypothesis. The dashed red line is the expected oscillation pattern for the RAA best fit. The gray error bands in (b) and (c) are estimated total systematic uncertainties, corresponding to the square roots of diagonal elements of the covariance matrices. (right) Exclusion curves for 3+1 neutrino oscillations in the $\sin^2 2\theta_{14} - \Delta m^2_{41}$ parameter space. The solid blue curve is the 90% C.L. exclusion contour based on the comparison with the Daya Bay spectrum, and the dashed gray curve is the Bugey-3 90% C.L. result [Achkar et al., 1995]. The dotted curve shows the Daya Bay 90% CL$_s$ result [An et al., 2016b]. The coloured area is the allowed region from the reactor anti-neutrino anomaly fit, and the star is its optimum point [Mention et al., 2011].

Russia. The reactor core is very compact ($35\times42\times42$ cm^3) and has a high reactor power of 90 MW. The detector sits on a movable platform which offers, with the detector segmentation, 24 measurement positions from 6.4 to 11.9 m. By summing the close L/E positions and binning with 500 keV energy bins, the number of anti-neutrinos detected over the average as a function of L/E is constructed. This is represented on figure 5.35 (left) where an oscillation signal is clearly seen. The most probable parameters of oscillation are determined with a fit to be $\Delta m^2_{14} = 7.30 \pm 1.17$ eV^2 and $\sin^2 2\theta_{14} = 0.36 \pm 0.12$, as presented on figure 5.35 (right). This result is controversial in the community and seems not favoured by other measurements.

The STEREO experiment

The STEREO experiment measures the anti-neutrino energy spectrum in six identical detector cells (369 mm thick, 892 mm wide and 918 mm high) filled with a total of 1.6 ton of gadolinium loaded LS readout by PMTs located on the top. The detector cells cover baselines between 9 and 11 m from the compact core of the ILL research reactor in Grenoble. The core uses highly enriched ^{235}U fuel. During STEREO live-time, the mean reactor power was about 52.8 MW, yielding to an average rate of detected antineutrinos after all the selection cuts of 394 per day. Massive shielding has been installed around the detector but also in the experiment hall

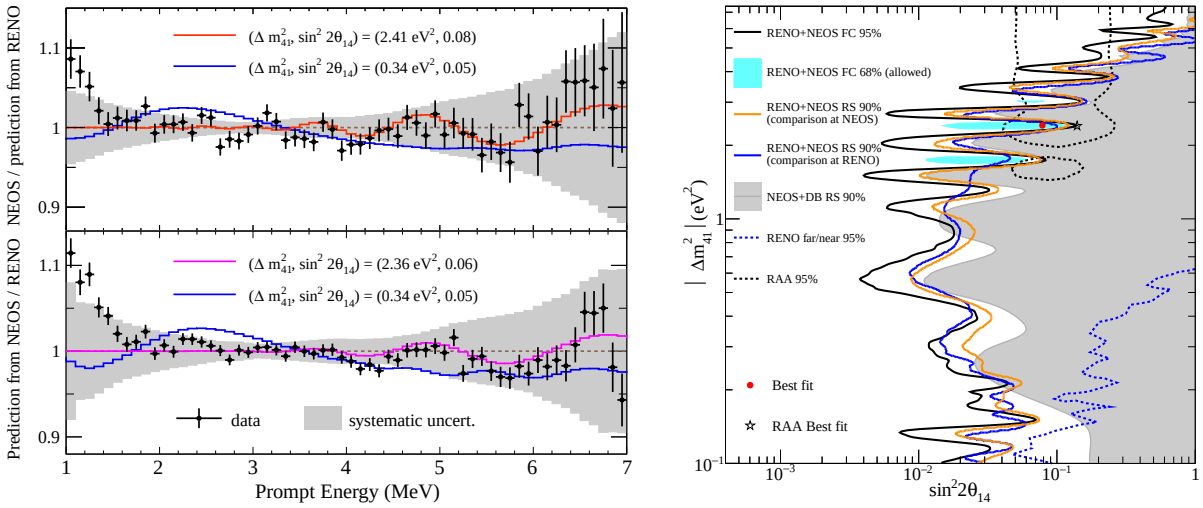

Figure 5.34: (left) Comparison of the normalised energy spectra of NEOS and RENO, on top NEOS relative to RENO, and the opposite for the bottom [Atif et al., 2022]. The red and magenta curves represent the best fits to the data. The blue curves represent ratios with one of sterile neutrino oscillation parameters excluded by this analysis. (right) Comparison of the exclusion limits on sterile neutrino oscillations and the allowed region from RENO and NEOS combined, using Feldman-Cousins (FC) or raster scan (RS) methods.

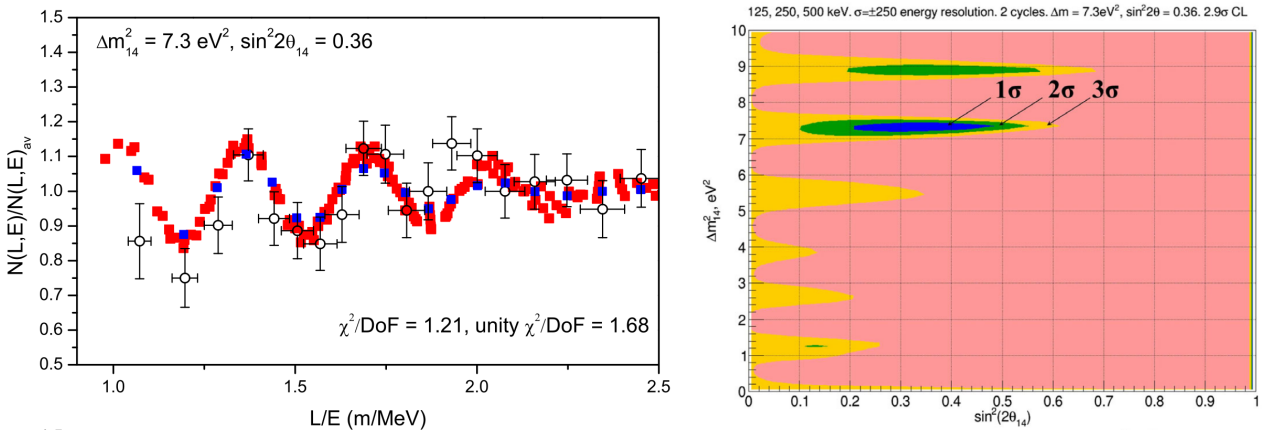

Figure 5.35: (left) Ratio of the number of anti-neutrinos detected over the average as a function of L/E parameter, relevant for oscillation search by the Neutrino-4 experiment [Serebrov et al., 2021]. The red points corresponds to the simulated rates from the best fit at 24 distances and the divisions of the energy spectrum. The white points with error bars correspond to the measurement, which is associated to the expected blue point (right) Allowed regions of the $(\Delta m^2, \sin^2 2\theta)$ parameter space of a 4^{th} sterile neutrino state, determined by the best fit of the L/E curve.

to protect from the surrounding experiments and neutron beams. The reactor transfer water channel is just above the detector, which benefits from 15 mwe overburden. The STEREO experiment has achieved a signal to background ratio of around 1, thanks to the surrounding unloaded LS crown, active muon-veto and *pulse shape discrimination* (PSD).

The latest results of STEREO, collecting 273 days of reactor on and 520 days of reactor off data over three years, has been published end of 2022 [Almazán et al., 2023]. No sign of neutrino oscillation has been reported by STEREO. As can be seen on figure 5.36, a large space of the RAA is excluded at 95% CL or greater. The oscillatory structure of the exclusion contour can be interpreted as statistical fluctuations. In addition, the best fit points of oscillation signals of Neutrino-4 and NEOS-RENO have been rejected at 3.3σ and 2.8σ respectively. The collaboration concludes that a few eV-scale sterile neutrino explanation to the RAA has been

ruled out by STEREO data.

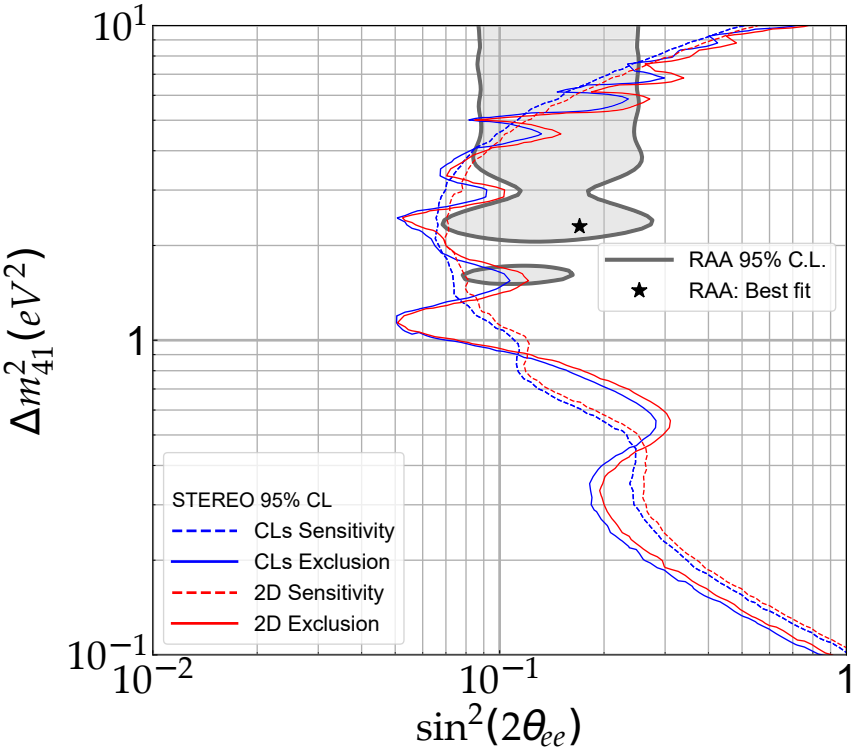

Figure 5.36: STEREO exclusion (solid) and sensitivity (dashed) contours at 95% CL (blue) produced by a χ^2 analysis using pseudo-experiments or by a 2D Feldman-Cousins framework (red) [Almazán et al., 2023]. The allowed regions of the RAA (grey) and its best-fit point (star) is also displayed [Abazajian et al., 2012].

Besides the search for sterile neutrino, the STEREO experiment measured the ^{235}U anti-neutrino energy spectrum [Almazán et al., 2023]. The total statistics of 107558 anti-neutrinos collected provides the largest sample of pure ^{235}U fission anti-neutrinos from a single experiment to date. As the six single-cell spectra are compatible with each other, the analysis of the anti-neutrino spectrum is performed by combining the selection of events in the six cells of the target volume. The resulting energy spectrum, presented on figure 5.37 (left), has been unfolded to provide a pure ^{235}U anti-neutrino energy spectrum. The spectral distortion around 5 MeV with respect to HM prediction is confirmed in the STEREO data (figure 5.37 (right)). A high energy deficit around 7 MeV is also observed. Double Chooz has fitted the energy spectrum with a negative slope component, which could account for this effect also seen by STEREO. The updated summation method [Estienne et al., 2019] provides a better agreement with the measured spectrum compared to HM model. The STEREO data have been compared to a new summation model where β^- transitions are simulated by a phenomenological Gamow-Teller β-decay strength model, and provides an excellent agreement with the data, both in normalisation and shape [Letourneau et al., 2023].

In the context of this HDR, I would like to indicate that I was examiners of 3 PhD theses in STEREO: Maxime Pequignot from Université Paris-Saclay [Pequignot, 2015], Aurélie Bonhomme from Université Paris-Saclay [Bonhomme, 2018] and Mathieu Vialat from Université Grenoble Alpes [Vialat, 2021].

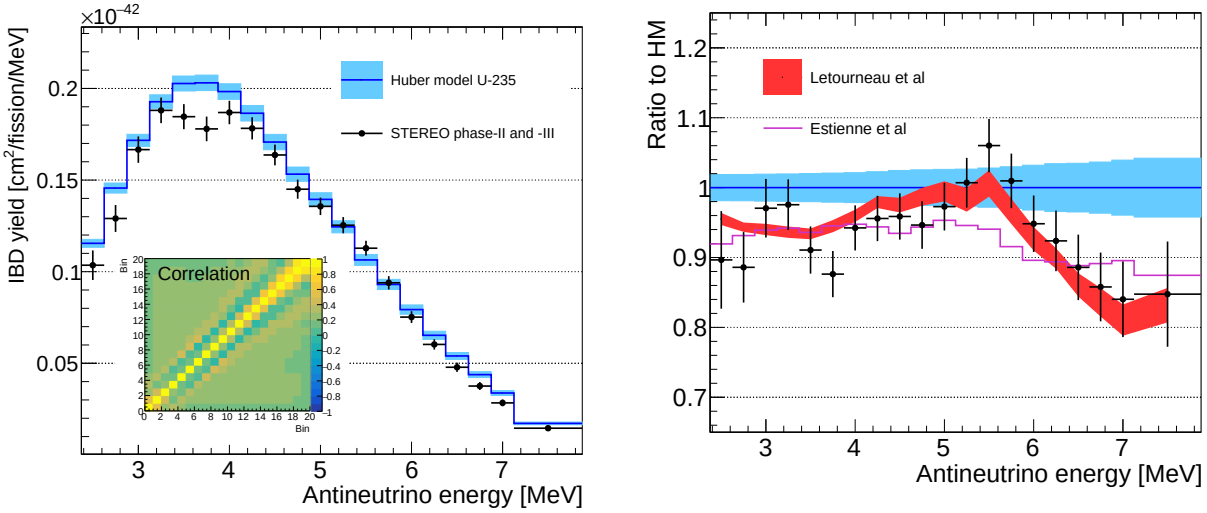

Figure 5.37: (left) Unfolded ^{235}U energy spectrum of STEREO [Almazán et al., 2023] along with the Huber-Mueller (HM) prediction (blue). The vertical bars and blue band represent the respective total uncertainties and the vertical axis provides the absolute IBD yield. The matrix illustrates the bin-to-bin correlations. (right) Relative deviations to the HM prediction (blue), exhibiting significant discrepancies in normalisation and in shape. However a better agreement is obtained with two recent summation models: the prediction of M. Estienne et al. (magenta) [Estienne et al., 2019] and a complementary approach from A. Letourneau et al. [Letourneau et al., 2023] (red).

The PROSPECT experiment

The PROSPECT experiment is also one of the major VSBL experiments searching for oscillations to a sterile neutrino. It is located at the 85 MW highly enriched High Flux Isotope Reactor (HFIR) at Oak Ridge. The four tons detector is segmented in 154 cells[3], with 14.5 cm squared sections and 118 cm length, filled with liquid scintillator loaded with ^{6}Li for neutron capture and closed by PMTs at each end. In addition to background rejection capabilities, this detector segmentation offers ten reactor-detector baselines between 6.7 and 9.2 m. The background rejection is of major importance since PROSPECT detector has a very low overburden of 0.5 mwe. A signal to background ratio of S/B = 1.4 has been achieved thanks to fiducialization, cosmic vetoing, position reconstruction and PSD. In 2020, the collaboration published the result of 96 days of reactor on data with more than 50000 anti-neutrino interactions [Andriamirado et al., 2021]. No statistically significant indication of oscillations to sterile neutrino has been observed. An exclusion contour similar to the one of STEREO (figure 5.36) has been produced. The RAA best-fit point is disfavoured at 2.5σ CL.

PROSPECT also published the measurement of a pure ^{235}U energy spectrum as displayed on figure 5.38 (left). The excess in the 5 MeV region is also observed by PROSPECT but seems less pronounced regarding the local deviation (bottom of the figure). The ^{235}U energy spectrum of PROSPECT has been compared to the unfolded Daya Bay spectrum [An et al., 2017b]. The Gaussian amplitude is varied and the best fit corresponds to 0.84±0.39 of the excess seen by Daya Bay, which is a bit lower but still compatible with one. To go further, the PROSPECT and STEREO collaborations presented a combined measurement of the pure ^{235}U anti-neutrino spectrum [Almazán et al., 2022]. The two measurements were found to be statistically compatible since $\chi^2/\text{ndf} = 24.1/21$. The comparison of the jointly unfolded ^{235}U spectrum to the area-normalized HM model is shown in figure 5.38 (right). The χ^2 comparison gives $\chi^2/\text{ndf} = 30.8/21$. A localized event excess is found in the 5-6 MeV region in anti-neutrino

[3]About 35% of the cells were inactive for this first measurement of PROSPECT.

energy. This excess with respect to the HM model can be described by a Gaussian with best-fit parameters $A = 0.099 \pm 0.033$, $\mu = 5.52 \pm 0.18$ MeV and $\sigma = 0.45 \pm 0.14$ MeV and provide a much better agreement to the joint data: $\chi^2/\text{ndf} = 18.8/18$. The deficit of events observed around 7 MeV is driven by a fluctuation in a single bin of STEREO prompt energy spectrum [Almazán et al., 2021].

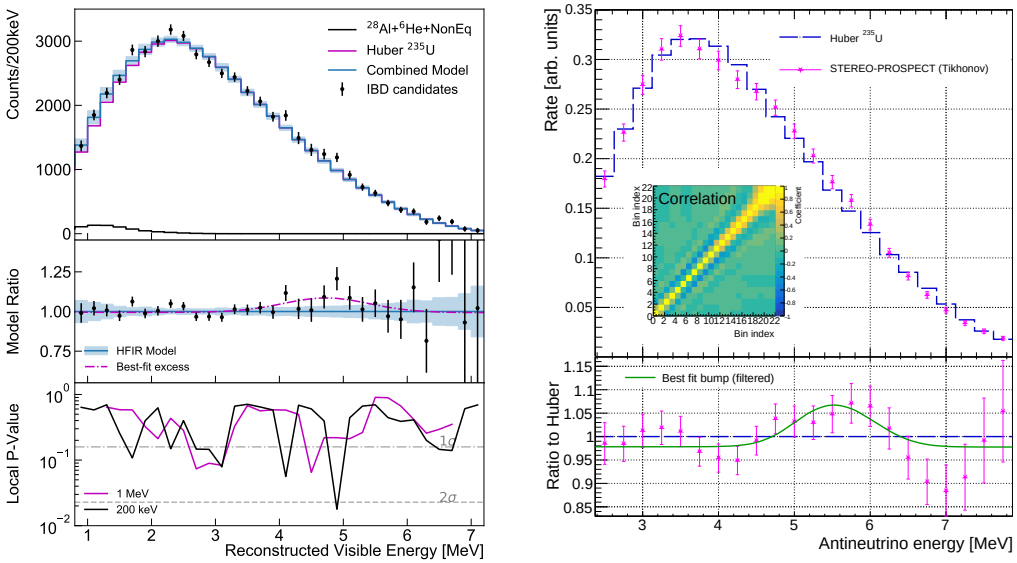

Figure 5.38: (left) Comparison of the measured PROSPECT energy spectrum to the ^{235}U model from HM model and to a combination with anti-neutrinos from surrounding HFIR reactor core and non-equilibrium isotopes. Ratio of the measurement to the prediction is plotted in the middle. The local p-value from 1 MeV- and 200 keV-wide sliding windows, quantifying any local deviations from the model prediction [Andriamirado et al., 2021]. (right) Jointly unfolded ^{235}U spectrum of STEREO and PROSPECT with diagonal errors and HM prediction normalized to unit area. Are also displayed the non-trivial correlation matrix and the ratio to Huber with the best-fit bump around 5 MeV [Almazán et al., 2022].

The KATRIN experiment

The KATRIN experiment, looking for the absolute neutrino mass in the energy spectrum of electrons produced in the β-decay of tritium with an unprecedented sensitivity, can investigate the presence of oscillation to sterile neutrino. The effective neutrino mass of the neutrino in the β-decay ($m_\nu^2 = \sum_i |U_{ei}|^2 m_i^2$) is manifesting in a slight spectral distortion of the electron energy spectra by reducing the maximal observed energy close to the end-point at 18.574 keV, as can be seen on figure 5.39 (left). This effect would be enhanced by the addition of an eV-scale sterile neutrino state to the mass term. After its second measurement campaign in 2019, the shape analysis of 3.76×10^6 electrons revealed no sign of sterile sterile neutrino. KATRIN is sensitive to much higher Δm^2 values but its great sensitivity pushes the low Δm^2 tail to the GA and RAA regions. This is presented on figure 5.39 (right).

Conclusion

In this chapter, we have presented an overview of the reactor anti-neutrino experiments which have played a major role in our understanding of neutrino production, flavour oscillations and detection. We have discussed the difficult task of predicting an energy spectrum of electron

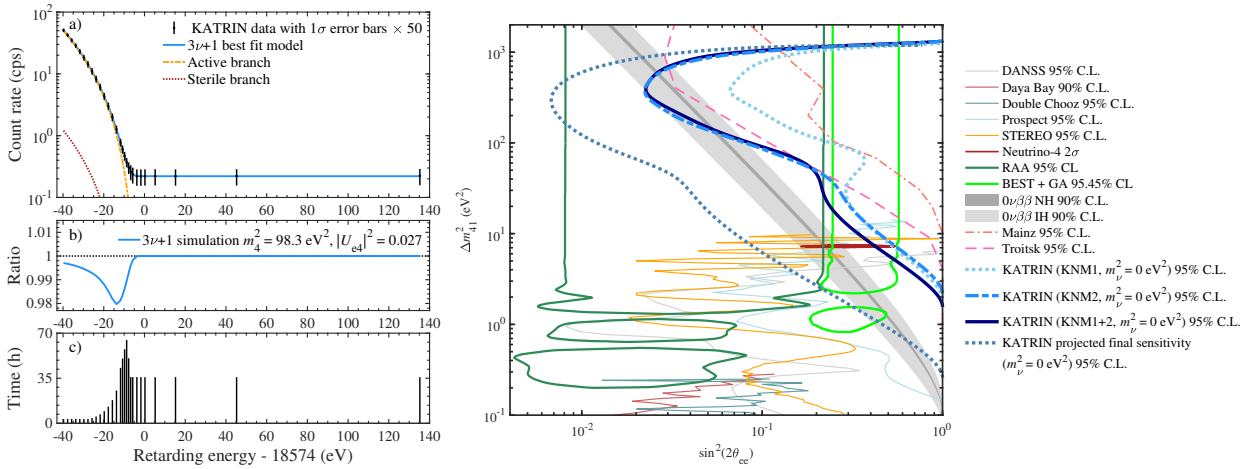

Figure 5.39: (left) KATRIN data and 3+1 best-fit model of the second measurement campaign with statistical uncertainties. The error bars are scaled by a factor 50 for visibility. The best-fit model in the 3+1 framework comprises signal contributions from both the active ($m_\nu^2 = 1.1\,\mathrm{eV}^2$) and sterile ($m_4^2 = 98.3\,\mathrm{eV}^2$, $|U_{e4}|^2 = 0.027$) branches. (right) The 95% C.L. KATRIN exclusion contours from the first two measurement campaigns with fixed $m_\nu^2 = 0\,\mathrm{eV}^2$, standalone and combined, are shown. The final sensitivity was computed following the first measurement campaign while assuming 1000 live days and a reduced background of 130 mcps [Aker et al., 2022b].

anti-neutrinos produced in a reactor given the huge number of β-decay branches involved. The summation and conversion method have made good progress in the last decade and the agreement with experimental data is getting close to high precision. We have also presented the last results on measuring the neutrino mixing parameters of the PMNS matrix, and the most recently measured θ_{13} angle. The neutrino mass ordering might also be discovered in a near future with the JUNO reactor experiment, under construction in China. Finally, this chapter focussed on the anomalies observed in several oscillation experiments already from the 80's. These anomalies could have been explained by oscillation towards a sterile neutrino. We have concluded that this hypothesis is now almost ruled-out by a new measurement of the ^{235}U β-spectrum at Kurchatov Institute and by the STEREO and PROSPECT neutrino oscillation experiments. However, anomalies in the neutrino calibration source experiments and in neutrino beam experiments still exit. The SoLid experiment was participating to the quest for the sterile neutrino at nuclear reactor. It will be the subject of the end of this document.

Chapter 6

The SoLid experiment

This chapter will present the main features of the SoLid experiment. To provide details on the innovative technology of the highly segmented SoLid detector, I will use the first publication of the collaboration [Abreu et al., 2017] and the publication of the SoLid Phase 1 detector [Abreu et al., 2021]. The performances of this technology have been illustrated by a large scale prototype, called SM1, which operated at the BR2 nuclear reactor in Mol, Belgium [Abreu et al., 2018b]. To prepare the next stage of the experiment, I was leading the light-yield optimisation campaign to improve the performances of the SoLid Phase 1 detector, this will be presented in chapter 7. The detector description in this chapter is taking into account the improvements obtained during this light-yield optimisation phase. A short presentation of the key features of the BR2 nuclear reactor and the main results of the SM1 prototype will continue this chapter, which finishes with the presentation of the backgrounds for SoLid experiment and the expected sensitivity.

Chapter contents

6.1 Goal of the SoLid experiment

As already presented in section 5.6, three anomalies persist in several neutrino experiments: the excess of electron neutrino appearance in beam experiments, deficit of electron neutrinos in the calibration of solar neutrino experiments and the 6.5% deficit of electron anti-neutrinos in the very short baseline reactor experiments. We have shown that it is difficult to combine all these data into a single solution but the hypothesis of oscillation towards a sterile neutrino could be an explanation and triggered a new generation of experiments. In addition to these anomalies, the reactor experiments looking for precision measurement of θ_{13} have reported a shape anomaly of the energy of the anti-neutrinos between 4 and 6 MeV, the so-called "5 MeV bump", compared to the model.

SoLid, or *Search for oscillations with a Lithium 6 detector*, is a very short baseline neutrino oscillation experiment, located near the BR2 reactor of the SCK•CEN in Belgium. Its main purpose is to perform a precise measurement of the electron anti-neutrino energy spectrum and flux as a function of the distance travelled by anti-neutrinos between the reactor core and their interaction in the detector. These measurements will be primarily used to search for the existence of one or more sterile neutrinos corresponding to mass eigenstates of order $\Delta m^2 \sim 1\,\mathrm{eV}^2$. Secondarily, the shape of the energy spectrum will serve as a reference measurement for electron anti-neutrinos originating from the fission of ^{235}U (the BR2 reactor uses 93.5 % of ^{235}U). In order to achieve these goals, the SoLid experiment aims to detect electron anti-neutrinos with a target efficiency of at least 10%, reconstruct their energy with a resolution of $14\%/\sqrt{E(\mathrm{MeV})}$, and obtain an overall signal to background ratio (S/B) of order unity, given that it operates with a minimal overburden of only 8 m water equivalent (mwe).

Operating very close to the reactor core and at sea level, where large cosmic and reactor backgrounds are produced, combined with small installation spaces, represents several challenges in terms of background rejection capabilities. Compared to the contemporary very-short baseline neutrino experiments near reactors, the SoLid detector has some unique features, which are described extensively in [Abreu et al., 2017]. It uses a finely 3D segmented plastic scintillator to detect electromagnetic energy deposits, combined with scintillation screens that contain ^{6}Li that provide distinct nuclear induced signals. The use of high segmentation and the dual scintillator, provides particle discrimination, and aims to identify and reduce backgrounds. Moreover, the materials used, the robustness and compactness are also attractive for future reactor monitoring applications.

6.2 SoLid detection principle

The SoLid detector is a highly 3D segmented detector ($8000\,\mathrm{voxels/m}^3$) based on a dual scintillation technology. Electron anti-neutrinos will interact primarily in the active detector volume via inverse beta decay (IBD) on hydrogen nuclei, producing a positron and a neutron in the final state: $\bar{\nu}_e + \mathrm{p} \rightarrow e^+ + \mathrm{n}$. Experimental approaches use the coincidence technique, which consists of detecting both the positron and the neutron, within a short time window, typically up to hundreds of microseconds. The neutron generally thermalizes via elastic collisions in the detector, after which it can be captured by nuclei with a high neutron capture cross section. As such, it typically induces a scintillation signal that is delayed in time with respect to the scintillation light caused by the positron and its corresponding annihilation gamma-ray photons. The time delay between the two signals can be tuned by the choice of neutron capture elements and their concentration and distribution in the detector.

SoLid opted for a combination of two scintillators. One is polyvinyltoluene (PVT), a relatively cheap plastic scintillator that is generally easy to machine in any desired shape or geometry, and the other is ZnS(Ag) used together with ^{6}LiF to capture thermal neutrons via the reaction:

$$^6_3\mathrm{Li} + \mathrm{n} \rightarrow {}^3_1\mathrm{H} + \alpha \ (4.78\,\mathrm{MeV}), \tag{6.1}$$

for which the decay products in turn induces scintillation in the ZnS(Ag) scintillator. The PVT-based scintillator is of the type EJ-200 produced by ELJEN Technology. It is a general purpose plastic scintillator that emits on average 10 000 photons per MeV of energy deposited by electrons in the blue-violet wavelength band with a peak emission wavelength of 425 nm. The choice of PVT is mainly motivated by its good light yield and its linear energy response over a wide range of energies ranging from 100 keV to several MeV. It combines a long optical attenuation length of about 380 cm, with a scintillation pulse decay time of 2.1 ns. The ^{6}LiF:ZnS(Ag) scintillator for neutron detection is produced by SCINTACOR, in the form of thin screens. These so-called neutron detection screens, emit photons at a peak emission wavelength of 450 nm. The nature of the neutron capture reaction and the longer scintillation decay time of 10 µs for the ^{6}LiF:ZnS(Ag) scintillator allows for a pulse shape discrimination between signals induced in the neutron detection screens via nuclear interaction, hereafter denoted as *NS*, and signals induced via electromagnetic processes in the PVT, denoted as *ES*. The anti-neutrino detection principle of SoLid is presented in figure 6.1.

The scintillation light produced by both ^{6}LiF:ZnS(Ag) and the PVT is captured in the cube due to internal reflection at the PVT-air interface. The cube, along with its ^{6}LiF:ZnS(Ag) layers, is wrapped in a reflective Tyvek sheet to further enhance light capture and to avoid leakage of light to neighbouring cells. The coupling between the neutron layer and the PVT cube, via a thin layer of air, also allows the photons produced in the ZnS(Ag) to be captured. Some of the scintillation light is subsequently trapped in wavelength shifting (WLS) fibres and re-emitted as green optical photons. The fibres are of the BCF-91A type from St Gobain with a square cross section of (3×3) mm^2 and lie within 5 mm grooves in the faces of each cube, crossing each detector plane in perpendicular directions. Placing the fibres onto two orthogonal faces of the cube enables the localisation of the scintillation signal.

The wavelength-shifted light travels via the fibres to a silicon photomultiplier (SiPM) from Hamamatsu called MPPC model S12572-050P, with a surface area matching that of the fibre. Each fibre has a SiPM which is optically coupled to one of the end of each fibre, with a mirror attached to the other end. The SiPM pulse amplitude spectrum has a quantised form, corresponding to an integer number of single pixel avalanches (PA) triggered by the incoming photons.

The components described above allow for a relatively inexpensive and modular tonne-scale detector system that provides adequate containment of the neutron capture scintillation signal – around a hundred times better than a LS + Gd detector, in terms of the volume needed to contain the scintillation signal – and a robust and precise three-dimensional positioning of both positrons and neutrons.

6.3 The BR2 nuclear reactor

The BR2 reactor (Belgian Reactor 2) is a materials testing reactor operated by the nuclear research center SCK • CEN in Mol (Belgium). Since its start-up in 1963, it is one of the most powerful research reactors in the world and thus plays an important role in nuclear material and fuel R&D. It is also widely used for production of medical isotopes and neutron transmutation doped silicon. The BR2 reactor is a pressurized "tank-in-pool" type reactor, cooled with water

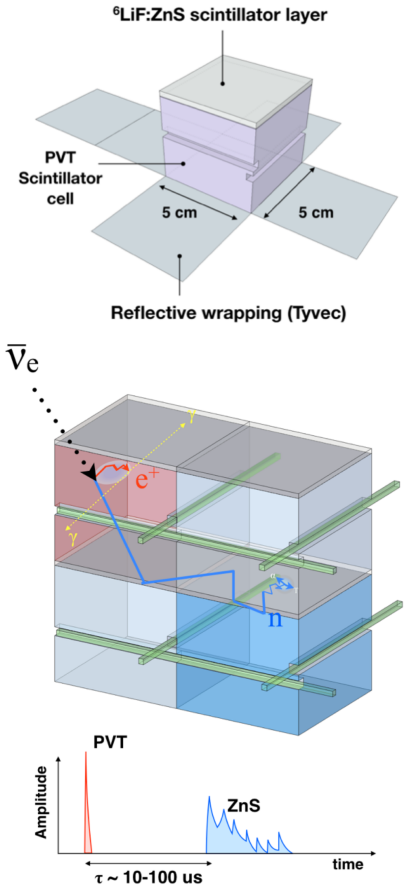

Figure 6.1: (top) The PVT cube is covered with a layer of ^{6}LiF:ZnS(Ag) and the assembly wrapped in a reflective material. (bottom) Principle of $\overline{\nu}_e$ detection in a volume made of separated voxels: wavelength shifting fibres placed in perpendicular orientations are used to collect the scintillation light from each cell of the array.

and moderated by its beryllium structure and water (see figure 6.2). It has a unique twisted design with inclined channels to obtain a compact core of about 50 cm in radius and 90 cm in height. The BR2 reactor uses highly enriched uranium fuel (HEU: 93.5% ^{235}U) at powers varying between 40 and 100 $\mathrm{MW_{th}}$. It thus produces a very high neutron flux, up to 10^{15} $\mathrm{n/cm^2/s}$, and provides an intense source of anti-neutrinos up to about $2{\times}10^{19}$ $\bar{\nu}_e$/s.

At the end of the SM1 prototype physics run, the BR2 reactor was shut down for a period of one year and a half, and has undergone a thorough overhaul. The BR2 operation was restarted in July 2016. In practice, the reactor operates at a nominal power of about 65 $\mathrm{MW_{th}}$, for 160 to 210 days per year, during cycles of about three to four weeks (ON periods). There are on average 6 cycles of reactor ON periods per year, that alternate with interim maintenance periods of the same duration (OFF periods). The Solid experiment takes advantage of the OFF periods to perform calibration campaigns and background measurements.

6.4 The SM1 prototype

The first full scale prototype submodule of SoLid, named SM1 with a fiducial mass of 288 kg was deployed near the BR2 reactor in winter 2014-2015, where it collected a small data sample during reactor operations at a nominal power of 60 $\mathrm{MW_{th}}$, followed by a longer background

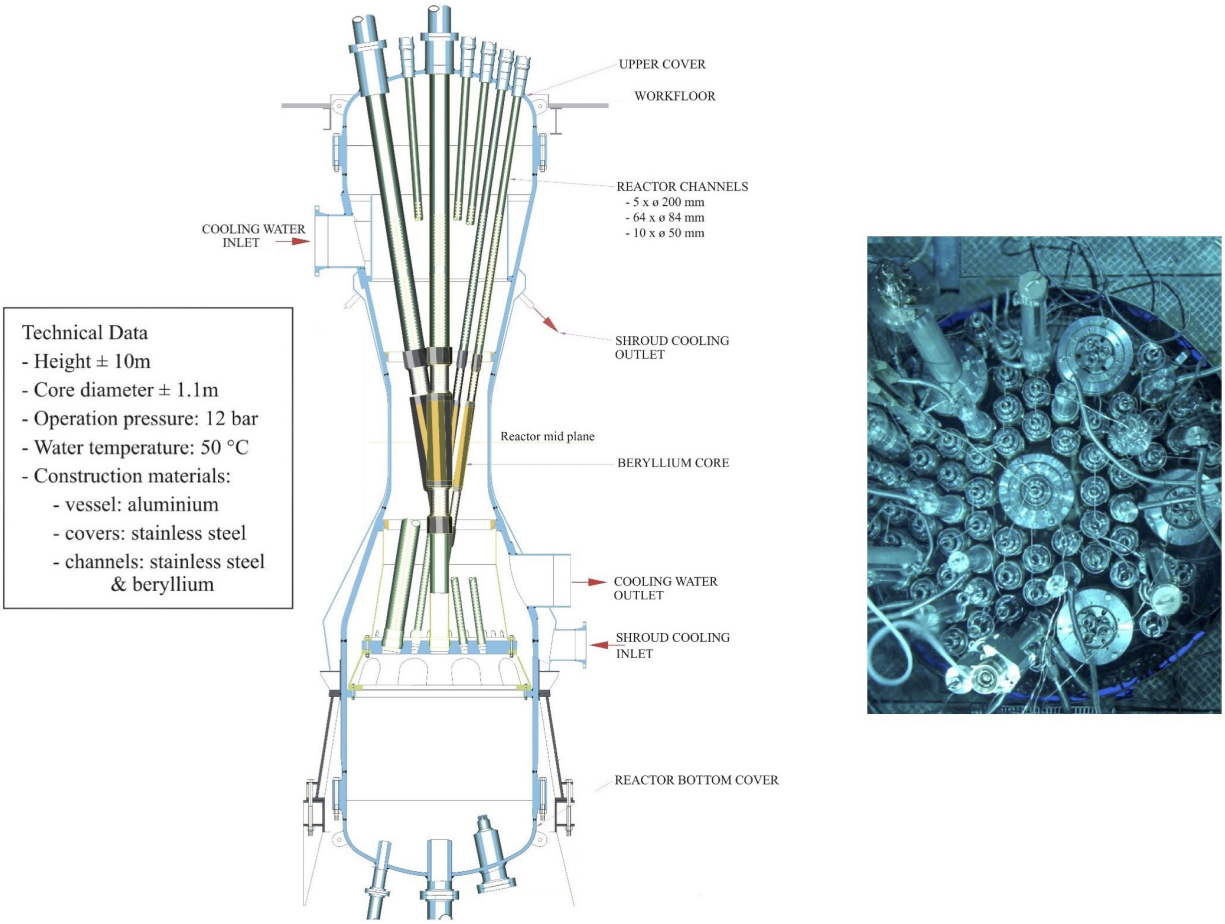

Figure 6.2: (left) Design and technical data of the BR2 reactor core. It consists of a beryllium matrix composed of 79 hexagonal channels containing the nuclear fuel elements, the control rods and the experimental channels. The beryllium core (yellow) is confined in an aluminium vessel (blue), that is completely under water. (right) Picture of the upper cover of the reactor vessel.

measurement campaign when the BR2 reactor was shut down in February 2015. During the latter period, several gamma and neutron sources were also used to investigate the detector response. The SM1 data tacking is illustrated in figure 6.3. After a description of the SM1 prototype detector this section will summarize the main physics results obtained as presented in [Abreu et al., 2018b].

The main purpose of the SM1 prototype was to demonstrate the scalability of the SoLid technology, the stability of operation at the reactor site, the capability to equalize the response of a large number of readout channels and to perform an initial analysis based on pulse shape discrimination, muon tracking and time correlation of signals. We participated to the data analysis of this campaign by studying accidental, cosmogenic and BiPo backgrounds. It was part of the early thesis work of Delphine Boursette.

6.4.1 The SM1 prototype detector

The fiducial mass of the detector is divided in cubical detection cells of dimension $5 \times 5 \times 5$ cm^3. The body of the cubes is made of ELJEN Technology EJ-200 polyvinyl toluene (PVT) based plastic scintillator, covered by a 225 μm thick ^{6}LiF:ZnS(Ag) neutron detection screen from SCINTACOR. Each cubic detection cell is optically isolated from its neighbours via a DuPont Tyvek wrapping with an average thickness of 75 g/m^2. The light produced either by the ZnS or the PVT scintillators is optically trapped in two wavelength shifting fibres of type BCF-

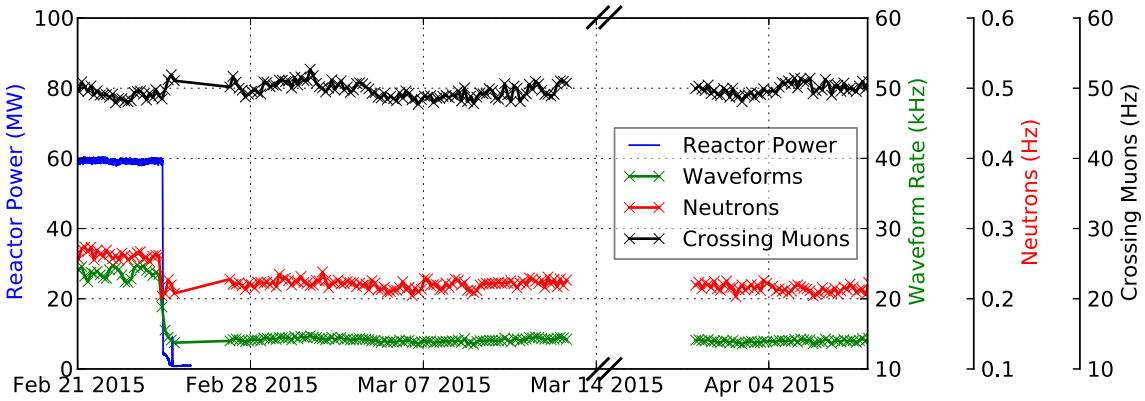

Figure 6.3: Data trends for the SM1 prototype data taking. The reconstructed muons (in black) are stable over time while the PVT (in green) and the ^{6}LiF:ZnS(Ag) (in red) signal rates are correlated with the reactor power.

91A from St. Gobain, consisting of a core surrounded by a single cladding. These fibres are 3×3 mm^2 in cross section and are aligned along two perpendicular faces of each cube, in a dedicated groove of 5×5 mm^2. All cubes are finally stacked in a 16×16 cube configuration, composing a detection plane. Each detection plane is lined on the inside with 2 cm thick black high density polyethylene (HDPE) to improve the moderation and reflection of neutrons created at the edges of the detector. The outer front and back surface of each detection plane is capped with a 2 mm thick black HDPE sheet. The optical fibres protrude from the edges of a detection plane into a hollow aluminium frame where they are coupled on one end to a multi-pixel photon counter (MPPC) from Hamamatsu type S12572-050P using optical grease. The other end of the fibre is mirrored with a thin aluminium tape. The position of the MPPC and mirror alternates between adjacent fibres to ensure a more uniform light response throughout the detector. The first full scale prototype submodule SM1 consists of nine collated planes to amount to a final configuration of $16 \times 16 \times 9 = 2304$ detection cubes, read out by a network of $32 \times 9 = 288$ fibres connected to one MPPC each. The whole module is surrounded by a passive shielding of 9 cm thick HDPE. A schematic view of the main components of SM1 is shown in figure 6.4.

Due to limited development and construction time for this prototype module, the readout electronics suffered a series of flaws that affected the data taking and trigger rates. The detail of the readout system and electronics can be found in the dedicated article [Abreu et al., 2018b]. These unexpected flaws in the readout electronics induced an overall lower neutron detection efficiency ($\mathcal{E}_n = 2.87 \pm 0.65\,\%$) and less performant pulse shape discrimination compared to expectations (as can be seen by the broad distributions and tails of the neutron signals in the high PID region of figure 6.5).

6.4.2 Time correlated cosmic ray events

Cosmic muons can produce several secondary events in the detector. Two classes of those are treated in this section: spallation neutrons and Michel electrons. A correct reconstruction of these events validates the time synchronisation of the detector readout as well as the particle identification based on the pulse shape discriminant discussed in the publication [Abreu et al., 2018b].

Michel electrons refer to muons that stop inside the detector and decay, $\mu^{\pm} \rightarrow e^{\pm} + \bar{\nu}_{\mu}(\nu_{\mu}) + \nu_e(\bar{\nu}_e)$, producing a high energy electron or positron. Due to the minimal overburden of the prototype, a large amount of Michel electrons is expected.

Stopped muons were selected searching for EM events with $E_{vis} > 3.5$ MeV in a time window of 1 - 26 µs after a tagged muon (on-time window). Additionally, a shifted window of 1001 -

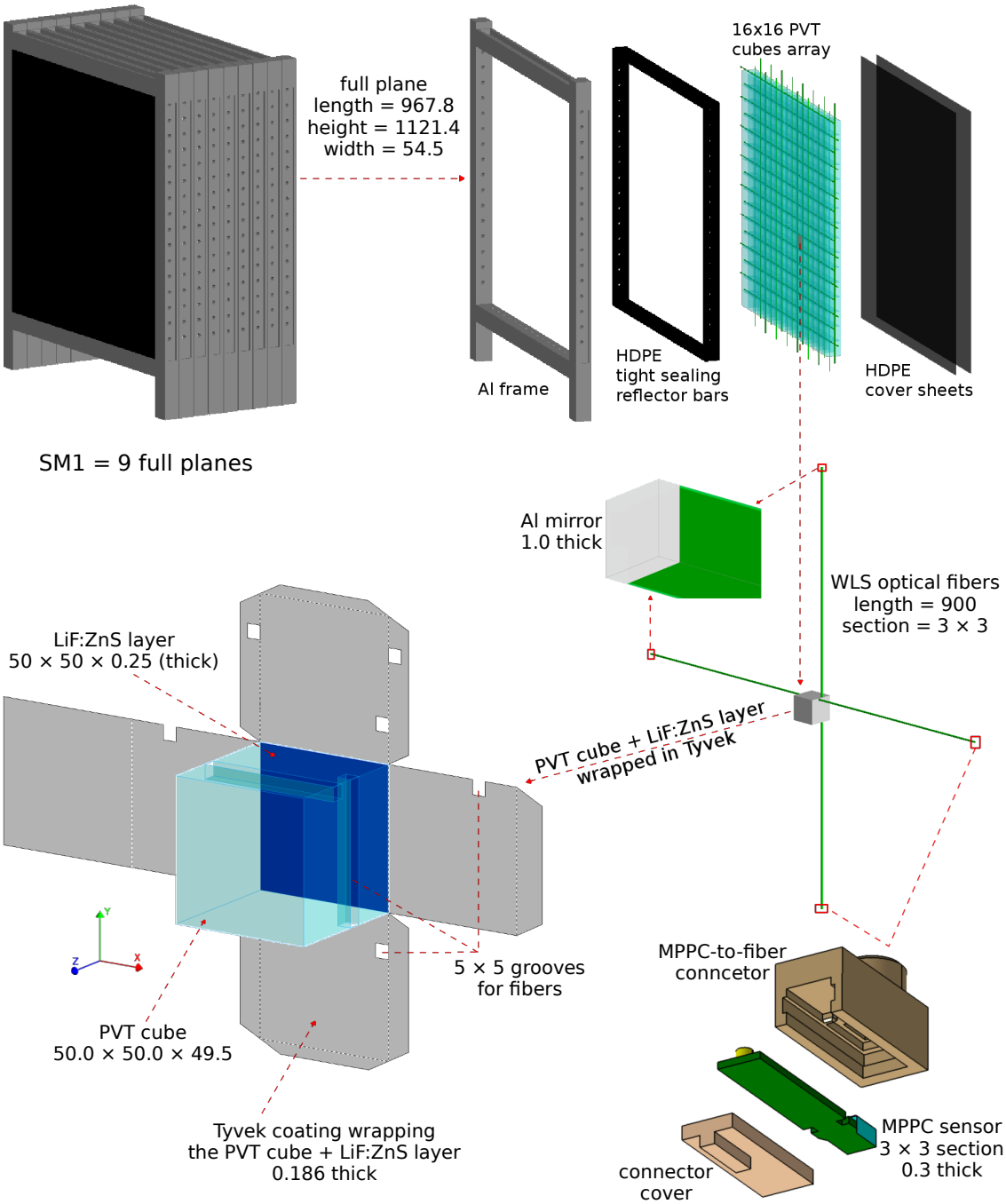

Figure 6.4: Diagram of the SM1 prototype detector, exploded frame, fibre readout and cube assembly. All indicated sizes are in mm.

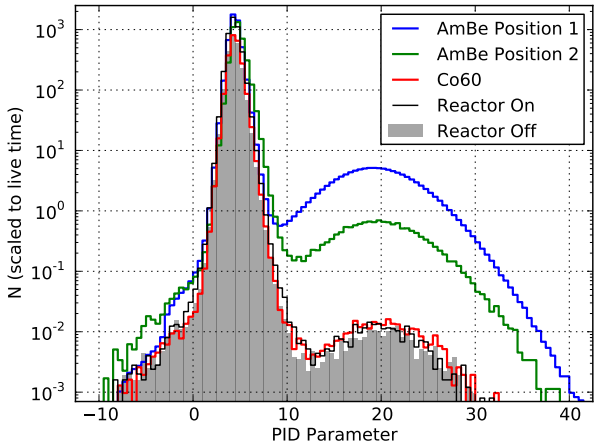

Figure 6.5: The neutron discriminant for several data sets that are either depleted in neutrons (grey filled, black and red line), or with an increased neutron rate (green and blue lines).

1026 µs was also used to estimate the expected background (off-time window). Figure 6.6 (left) shows the time-difference between a prompt muon and a Michel electron candidate ($\Delta t_{\mu-e}$) for both on- and off-time windows. The $\Delta t_{\mu-e}$ distribution in the off-time window is flat, as expected. Subtracting the two data sets and fitting the remaining points with an exponential function, one finds the muon life-time value of $\tau_\mu = 2.281 \pm 0.002\,(stat) \pm 0.052\,(syst)$ µs, figure 6.6 (right).

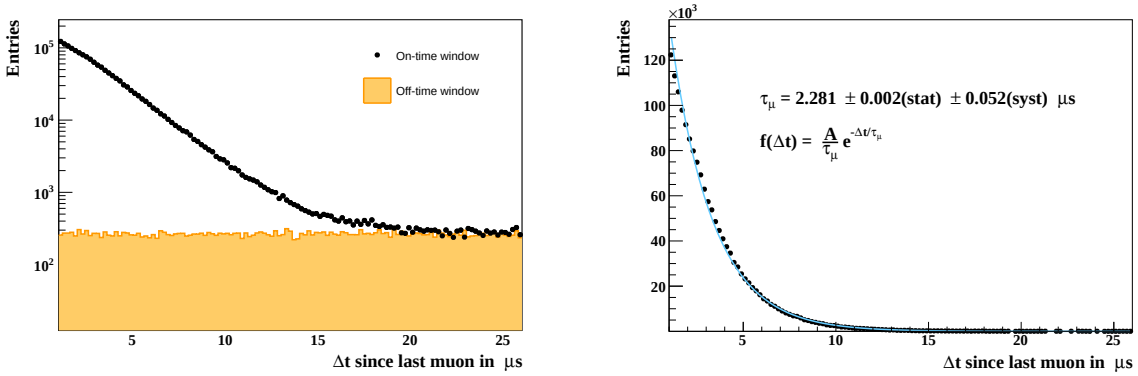

Figure 6.6: Δt distributions between a prompt muon and a Michel electron candidate for the on- and off-time windows (left) and the subtraction (right) fitted with an exponential to get the muon lifetime.

On the other hand, spallation neutrons were identified by searching for identified neutrons in a time window of 1 - 1001 µs after a tagged muon. Again, a time window shifted by 1 ms was employed for background estimation. The on- and off-time $\Delta t_{\mu-n}$ distributions are shown in figure 6.7 (left). A combined fit with an exponential function and a flat background (figure 6.7, right) yields the value of $\tau_n = 89.81 \pm 2.63\,(stat)\,\mu s$ for the neutron capture time on ^{6}LiF:ZnS(Ag).

Both measurements, combined with our knowledge on the decay properties of muons and the thermalisation of neutrons in PVT, confirm the purity of the particle identification and the validity of the timing of the detector electronics and readout. It gives confidence to investigate the IBD like signatures in the detector, characterized by a prompt EM signal, followed by a neutron induced signal in the ^{6}LiF:ZnS(Ag) in a time window in scale with the measured neutron capture time.

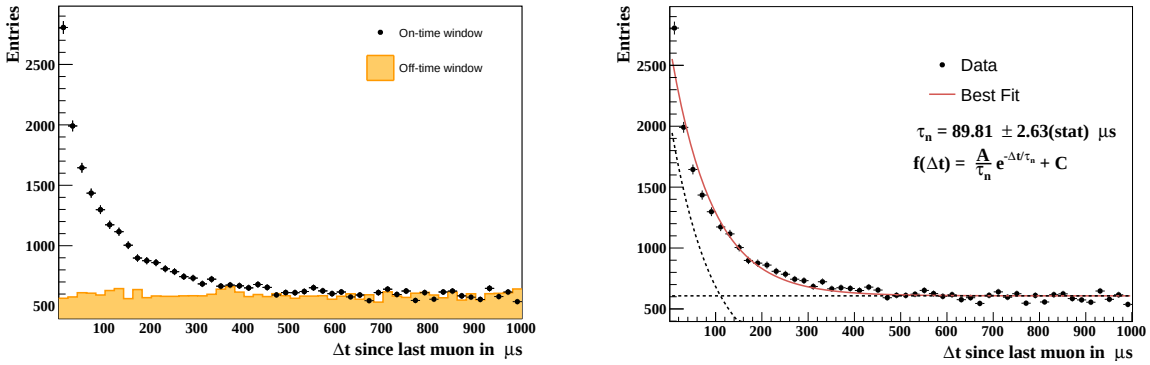

Figure 6.7: Δt distributions between a muon and neutron-like signal (left). The neutron capture time in LiF:ZnS(Ag) was deduced using an exponential with a flat background (right).

6.4.3 IBD analysis

IBD candidates are found by searching for time correlations between prompt EM and delayed neutron-like signals in the detector, using the same identification criteria as discussed before. The time difference between these coincidence pairs allows to characterize the time-correlated and uncorrelated background components from data. We will assume, in a simple background model, that the time-correlated background rate and its visible energy spectrum remains unchanged during reactor operations. This is justified when no fast neutron signals are induced by the reactor operating at full power. The accidental background rate and energy spectrum will receive an additional component during reactor operations, but we will demonstrate here that it can be reduced to a small contribution by exploiting the spatial segmentation of the detector. Note that due to its flat time structure the uncorrelated background can always be determined by an off-time search window in reactor ON and OFF conditions.

Based on the earlier measurements of the neutron thermalisation and capture time, IBD signatures are formed for cases where the time difference between an EM signal and tagged neutron is smaller than $\Delta t < 220\,\mu$s. It contains 91 % of all time-correlated background events. For each of these retained coincidence pairs, the radial separation in terms of cubes, $(\Delta r)^2 = (\Delta xy)^2 + (\Delta z)^2$, is determined. The cumulative distribution of Δr is shown in figure 6.8 for a simulated IBD signal and background components determined from the reactor-OFF data sample. It can be seen that the background populations extend to higher values of Δr, particularly for the accidental background, whereas the signal is mostly contained within a small number of cubes. We require further that the prompt EM and the delayed neutron-like signal are separated by at least one and maximally two cubes, which vastly reduces the accidental background component.

Since the prompt energy of background coincidence pairs is shifted towards low energies, the IBD candidates are required to have a visible energy associated with the prompt EM signal in the range of $1 < E_{Prompt} < 8$ MeV, where the upper bound serves as a muon veto. A multiplicity selection is also applied: the prompt candidate must be localised to maximally two cubes which share a cube face. This selection is effective at reducing muons or multiple proton recoils. Finally, a muon veto is applied, where IBD candidates cannot be formed within a time window of $250\,\mu$s after a muon candidate. A summary of the effect of these IBD selection criteria, applied in succession, for reducing the background components is shown in figure 6.9. Relative to forming coincidence pairs using timing information alone, referred to as pre-selection level, the accidental background has been reduced by more than a factor of 50, and the correlated background reduced by a factor of 10. The relative signal efficiency found for this selection from simulation, is 57 %, and is specific for this prototype module. The accidental

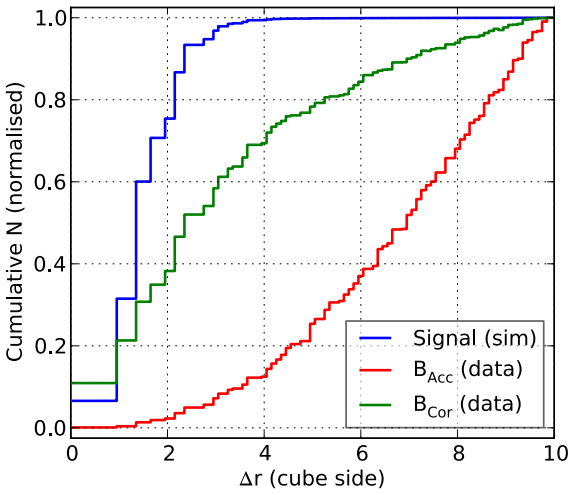

Figure 6.8: Cumulative distribution of the radial separation Δr between e^+ and n candidates, prior to other IBD selections. The accidental background is for reactor ON data.

background under reactor-on conditions, determined by a shifted off-time window, is shown to exhibit the same behaviour as the environmental accidental background.

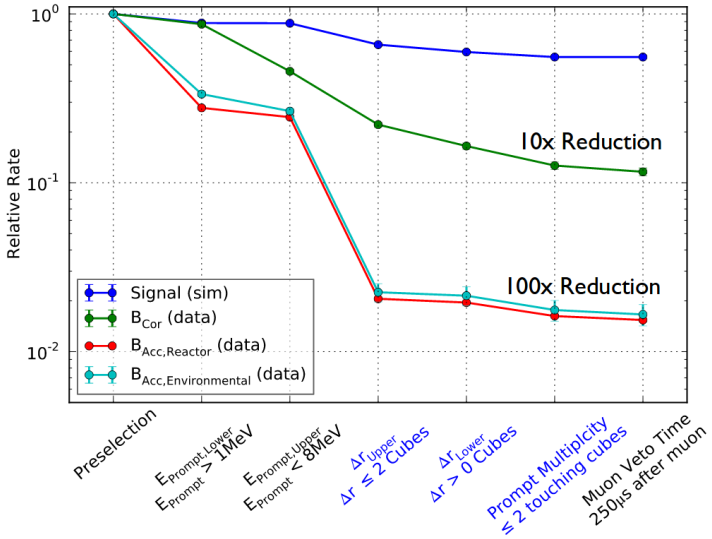

Figure 6.9: Signal and background relative rates for each selection cut applied sequentially. The relative rates are obtained by normalising to the number of prompt-delayed coincidences reconstructed (i.e. using a Δt cut only).

As mentioned earlier, the BR2 reactor overhaul and maintenance schedule coincided with the deployment of our submodule prototype. This allowed for only a small dataset to be collected of 50 hours under stable running conditions of the detector during reactor operations. Given the small neutron trigger and detection efficiency, the expected number of observed anti-neutrino events in the data run is $10 \pm 1(stat)$ which is unlikely to result in any statistically significant anti-neutrino excess in the data. The data can nevertheless be used to validate the assumptions made in the simple background model described above.

Figure 6.10 shows a comparison between the reactor-ON data and background model for the prompt visible energy distribution and the time difference, Δt, between the prompt signal and the delayed neutron candidate. The small signal expectation, from simulation, is also shown in the energy spectrum. The data agree with the background prediction, suggesting the background model is appropriate. Comparing the reactor on run to the expectation of the

background, a small excess is observed. Coincidentally, the excess is very near the expected signal yield, but given the errors, this is not statistically significant.

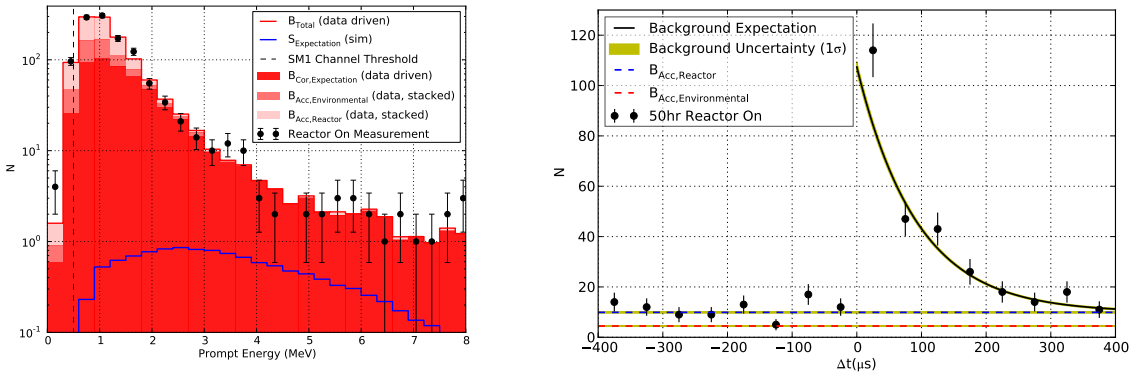

Figure 6.10: Comparison between data and background model for the prompt energy distribution of selected IBD candidates (left), and for the Δt distribution (right).

6.4.4 Conclusion on SM1 results and outlook

The commissioning of SM1 has demonstrated the equalisation and calibration of the individual channel energy response up to a level of 3 % and an energy resolution of 20 % for 1 MeV electrons interacting in the plastic scintillator. Calibration runs taken with gamma and neutron sources have demonstrated the possibility to exploit pulse shape discrimination for particle identification.

The prototype collected useful data during reactor operations, albeit with suboptimal trigger performance due to unexpected features in the readout electronics. Using this data, accidental and time-correlated backgrounds are measured in realistic conditions.

The spatial segmentation, a unique feature of the SoLid detector, is shown to be a powerful tool in reducing both accidental and time-correlated backgrounds. The background model, which is completely data driven, shows its applicability to the IBD analysis. The components of the time-correlated background are analysed using dedicated selections and are extrapolated to the IBD search region, indicating that fast neutron induced backgrounds dominate the experimental uncertainties in the current set-up.

6.5 The SoLid Phase 1 detector

Based on the observations made with the prototype module, the SoLid collaboration adapted a set of design changes for the full scale experiment. These include a new design of the front-end electronics with far superior noise-tolerances, and an improved light collection to achieve a better energy resolution (see chapter 7). In addition the final detector will contain twice the amount of ^{6}LiF:ZnS(Ag) screens to increase the neutron detection efficiency, and reduce the capture time. The detector will also be cooled to an ambient temperature of ∼10°C to reduce the dark count rate, in combination with a passive shielding to reduce the cosmic and reactor induced backgrounds. Finally, a dedicated neutron trigger based on pulse shape discrimination will be deployed. This section presents the main features of the SoLid detector extracted from [Abreu et al., 2021].

6.5.1 Mechanical design

Detection cell

The basic detection cell consists of a 5x5x5 cm^3 PVT cube, of which two faces are covered with neutron detection screens. Positrons with an energy of 10 MeV travel less than 48 mm in PVT, which implies that the majority of the IBD positrons will be stopped in the same cell as in which they are produced. In order to extract the scintillation photons produced in the PVT or in the neutron detection screens, 4 grooves with a $5\times5\,mm^2$ square cross section are machined in four different faces of each cube. Each groove accommodates an optical fibre with a square cross section of $3\times3\,mm^2$ that guides the light to an optical sensor at the edge of the detector. All detection cells are optically isolated via a DuPont Tyvek wrapping of type 1082D, whose thickness has been increased from 205 to 270 µm to reduce the optical transparency.

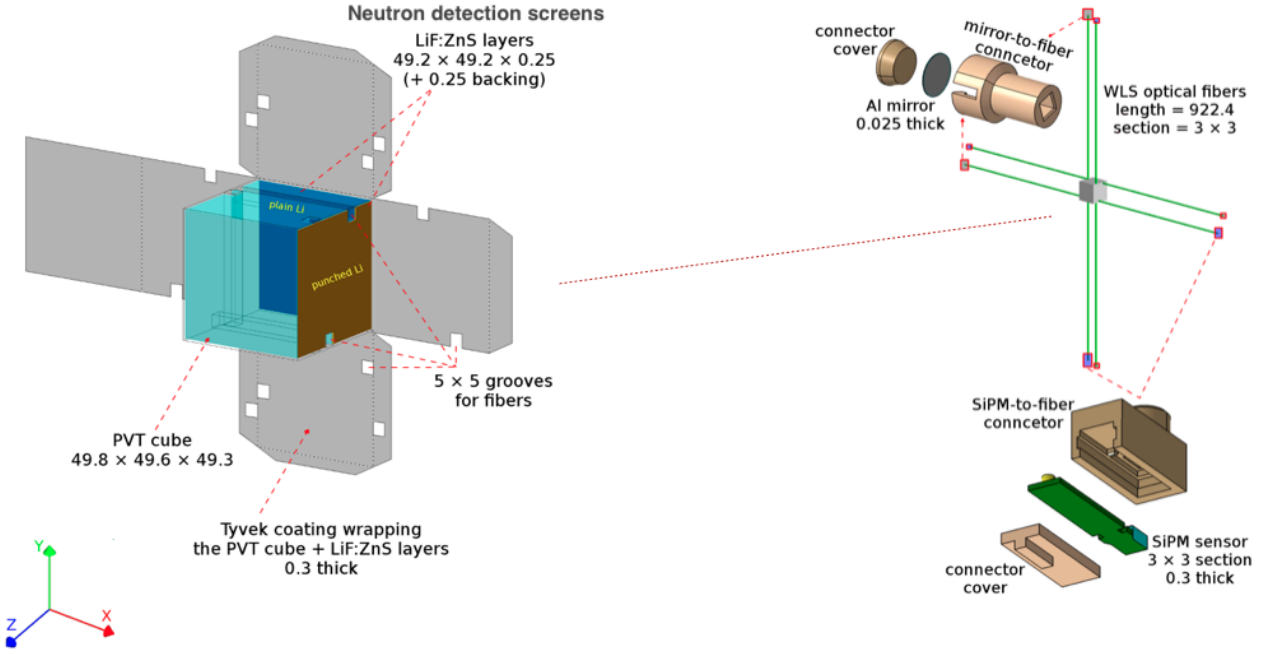

Figure 6.11: (left) A schematic view of the PVT detection cell, including the two neutron detection screens and its Tyvek wrapping. All cells are arranged such that the face "plain Li" (dark blue) faces the BR2 reactor. (right) Four wavelength shifting fibres cross each detection cell, with alternating positions of MPPCs and mirrors at the fibre ends. They are contained in plastic printed connectors. Dimensions are in mm.

The neutron detection screens are cut into squares of $5\times5\,cm^2$ and positioned, using no glues or optical gels, on two adjacent faces of the PVT cube. The two cube faces that are covered with neutron detection screens are the one that faces the reactor core, perpendicular to the Z-axis, and the one that is perpendicular to the X-axis, facing the electronic readout boxes that are mounted on one detector side. A schematic view of a detection cell together with the coordinate system and the position of the neutron detection screens is shown in figure 6.11. The bulk of the neutron detection screens have a 225 µm thick MELINEX-339 reflective backing. The addition of this backing on the neutron detection screens with respect to the prototype module, combined with the overall improved light detection in the cells increases the amplitude of the *NS* signals and improves the *NS-ES* waveform discrimination. By doubling the amount of neutron detection screens per cell, and due to the asymmetric placement around each cube, the capture efficiency for thermal neutrons in the SoLid detector was optimized and increased by 30%, compared to the SM1 prototype (see section 6.4). The capture time is also reduced

from about 90 to 65 µs, which decreases the background from random coincidences in the offline analyses.

The LiF component of the neutron detection screens is the dominant component in terms of radiopurity. Bulk amounts of this material were measured in the underground low background radiation facilities of Modane and Boulby. The most accurate measurement on the activity of the LiF yielded an activity of 69 ± 35 mBq/kg of pure LiF. The second largest contamination is ZnS, for which the upper limit on the rate is at least 5 times smaller. Our detector has a total of 8.9 kg of LiF, which yields a rate of 614 ± 311 mBq, which is also consistent with the measured intrinsic background rate by a dedicated analysis.

The scintillation photons produced in each detection cell are extracted and guided by 92 cm long double clad wavelength shifting fibres (494 nm), of type BCF-91A, produced by St.Gobain. One end of each optical fibre is covered by a Mylar foil with a reflective aluminium coating, and the other end is coupled to a Hamamatsu type S12572-050P MPPC, containing 3600 pixels, arranged in a 3×3 mm^2 matrix. For our current settings, the photon detection efficiency (PDE) is 32 %. The position of the MPPC and mirror alternates between the parallel fibres to mitigate the attenuation of light in the fibres and to ensure a more uniform light response throughout the detector (see figure 6.11).

Plane and module design

The detection cells are arranged into a detection plane of 16×16 cells (0.8×0.8 m^2), where each row and column of cells is read out by the same set of two optical fibres, accounting for a total of 64 optical fibres, and an equal number of readout channels, per detector plane, as shown in figure 6.12.

The detection planes are surrounded by a lining of white high-density polyethylene (HDPE) with a thickness of 46.0 and 46.8 mm, respectively in the vertical and horizontal directions. The HDPE bars act as reflectors for neutrons that would otherwise escape the detector. Each plane is structurally supported by a hollow frame of extruded aluminium that has been chrome coated to act as a Faraday cage for the MPPCs and their wirings. Each fibre protrudes through the HDPE lining and the frame where it is capped off on each end with two different plastic 3D printed caps. One cap holds an MPPC sensor, while the other end holds the aluminized Mylar mirror. Optical contact with both the mirror and the MPPC is ensured with a drop of optical gel. The MPPC bias voltage and signal is carried on twisted pair ribbon cables that are routed through the hollow frame and are terminated on one of the frame sides in four insulation displacement connectors (IDCs) each grouping 16 MPPC channels. The front-end electronics, which is described in section 6.5.5, is self-contained in an aluminium encasing mounted on one side of each detection plane. Each detection plane is finally covered with two square Tyvek sheets on each of its light sensitive faces to further ensure optical isolation from its neighbouring planes.

Frames and their attached readout electronics are grouped together by 10 units to form a detector module, mounted on a trolley (see figure 6.12). Each module can be operated as a standalone detector and has its own power supply and trigger electronics mounted on an overhead rail. The SoLid detector currently includes a total of five detector modules, accounting for a total of 50 detector planes and corresponding to a fiducial mass of 1.6 ton. The front and back planes of the detector are capped with a HDPE reflective shielding with a thickness of 9 cm. Under normal detector operations all modules are closely grouped together with an average spacing of 0.5 mm between two modules.

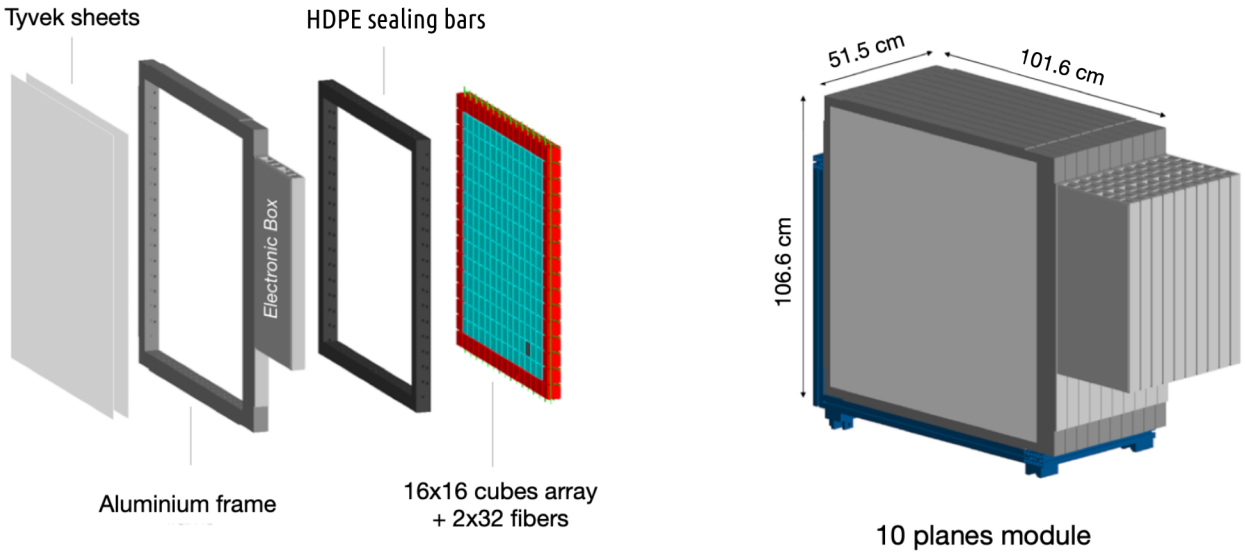

Figure 6.12: (left) Exploded view of a detection plane, showing the 16x16 detection cells (blue and red). The outer layer of active cells have neutron screens without a reflective backing (red). The active volume is surrounded by the HDPE neutron reflector (black),the aluminum frame for mechanical rigidity and attachment of the electronics, and two tyvek sheets for light isolation. (right) Sketch and dimensions of a 10 planes detector module mounted on its trolley (blue).

6.5.2 Container integration

The detector and its electronics are installed in a cooled cargo container with dimensions of $2.4 \times 2.6 \times 3.8\,\mathrm{m}^3$ as shown in figures 6.13 and 6.14. The container is further customized for thermal insulation and feed through of cooling lines. A dedicated patch panel, located on the side of the container, bundles all the connectors needed for the electronics (power supply, readout), the container instrumentation and the ethernet communication. The five detector modules are positioned off-center in the container in order to allow for access and service space. They are mounted on a rail system, that allows for an accurate and robust positioning and alignment. The electronics are cooled by a chiller system which is described later in section 6.5.5. Due to the dimensioning of the chiller system and its radiators it is possible to cool down and control the ambient air temperature in the container to a precision of 0.2°C. Under normal data taking circumstances, the ambient temperature of the SoLid detector is kept at a fixed value of 11°C. In order to keep the relative humidity of the air inside the detector at acceptable levels the container is permanently flushed with dry air that enters the container at a low flow rate of $5\,\mathrm{m}^3$/hour. This flushing also helps to remove possible traces of Rn gas inside the detector. Environmental parameters such as pressure, temperature and humidity in the container are constantly monitored by means of a custom sensor network that is controlled and read out by a Raspberry-Pi device. This specific readout is interfaced with the data acquisition of the experiment. During nominal data taking, the gamma background is monitored by a standard PMT coupled NaI scintillator, located inside the container. The airborne radon concentration is monitored by a radon detector, placed next to the NaI detector inside the container. The radon measurement is performed by sampling the air with a small pump and sending it to a pin-diode semiconductor detector based on the RADONLITE and RADONPIX technology, developed at CERN.

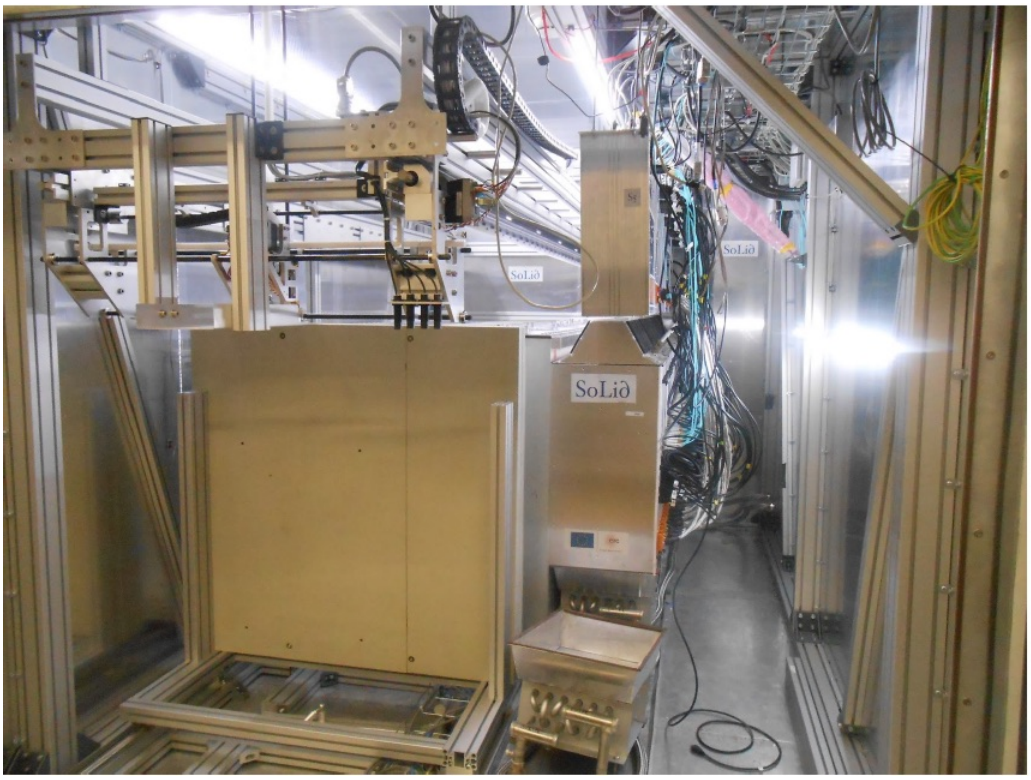

Figure 6.13: Picture of the SoLid detector in its cargo container prior to the installation of the last detection module. Environmental sensors are placed throughout the container, as well as radon and gamma background monitors, which are mounted on the inner wall of the container on the right hand side of the detector.

6.5.3 CROSS calibration system

In order to perform in-situ calibrations of the electromagnetic energy response and of the neutron capture efficiency, a calibration robot, CROSS, is mounted on top of the SoLid detector inside the container, as shown in figure 6.14. First, each of the modules is mounted on a trolley, which is itself mechanically connected by a pivot link to a linear actuator. This actuator allows to move the module carriage on the rails by a few centimetres, which is needed to insert small radioactive sources between modules during calibration. As such a total of six calibration air gaps of $30 \pm 5\,\text{mm}$ can be created sequentially on both sides of each module.

The calibration robot that straddles the whole detector along its longitudinal axis is equipped with a holder for radioactive calibration sources. Once the calibration robot is positioned between two modules, the source holder can further be moved along the X- and Y-axes. As such it can scan an area of 6 cells on the left and right sides of the plane center and 6 and 4 cells respectively above and below the plane center, covering nearly half of the detection plane's surface (see figure 6.14). The radioactive source are installed manually on the calibration arm from the outside of the container and the shielding, and are removed from the detector during normal data taking.

6.5.4 Detector integration on site

The SoLid detector is located at level 3 of the BR2 containment building in direct line-of-sight of the nominal reactor core center. This is the third detector installed at this location by the collaboration, after the two prototypes, NEMENIX [Abreu et al., 2017] and SM1 [Abreu et al., 2018b]. The 50 detector planes are oriented perpendicularly to the detector-reactor axis, and as close as possible to the reactor core. As such, the sensitive volume of the

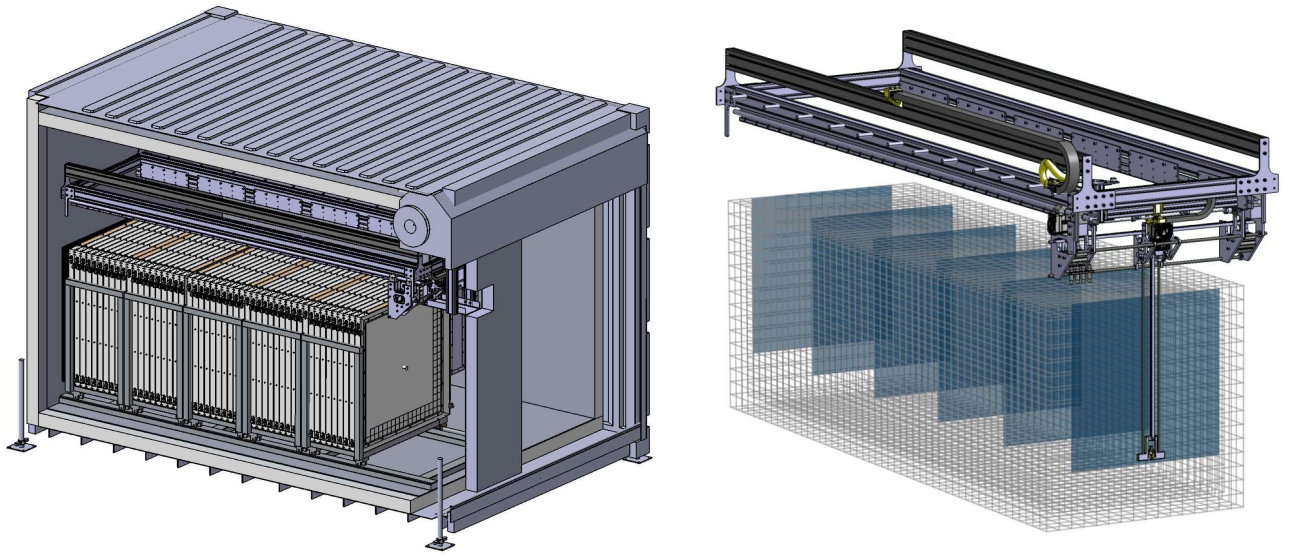

Figure 6.14: (left) Sketch of the CROSS calibration robot and its ground rail system inside the container. (right) Sketch of the radioactive source holder and the area it can access within an open gap indicated by the blue squares.

SoLid detector covers a baseline of [6300 mm − 8938 mm] away from the nominal center of the BR2 reactor core (see figures 6.15 and 6.16). As the aluminium reactor vessel is totally immersed in water, its radiation is properly shielded. Moreover, at this floor of the containment building, no other experiments surround the detector and all neighbouring beam ports have been shielded with 20 cm thickness of lead. It thus ensures stable and low reactor induced background.

The overburden above the detector is composed of 3 concrete floors and the steel roof of the containment building (see figure 6.15). It corresponds to 8 meters-water-equivalent. In order to mitigate the atmospheric and cosmic backgrounds, which were determined experimentally with SM1 and compared with a full-chain GEANT4-based Monte-Carlo simulation [Pinera-Hernandez, 2016b], a passive shielding surrounds the detector (see figure 6.16 and 6.17). It is maximized for cost, available space and floor load versus attenuation of cosmic neutrons. The top of the detector is shielded with a 50 cm PE layer made of 2.5 cm thick PE slabs that are staggered to avoid gaps. The PE slabs are supported by a steel scaffolding straddling the container and surrounded by a 50 cm thick water wall on the four sides of the container. The cosmic neutron flux in the energy range [1-20 MeV] is thus reduced by a factor of 10 and about 5% are converted to slow neutrons ($E_n < 10$ eV) that penetrate the wall. In order to capture these slow neutrons, thin cadmium sheets with a thickness of 2 mm are sandwiched between the passive shielding and the container housing of the detector. The capture efficiency of these cadmium sheets for slow neutron is about 88%. The cadmium sheets, cover the entire back side of the experiment container and most of its top and bottom surface, amounting to roughly 45% coverage of the experiment.

The environment of the BR2 containment building is continuously monitored and registered by the BR2 Integrated Data Acquisition System for Survey and Experiments (BIDASSE). During SoLid operation, environmental parameters, such as temperature, humidity and pressure, outside and inside the containment building, are constantly monitored. Also the background radiation is monitored using gamma and beta detectors placed in the vicinity of the SoLid container. So far, these variables are used as a cross check of the data coming from the container instrumentation, i.e. environmental sensors, NaI scintillator and radon detector.

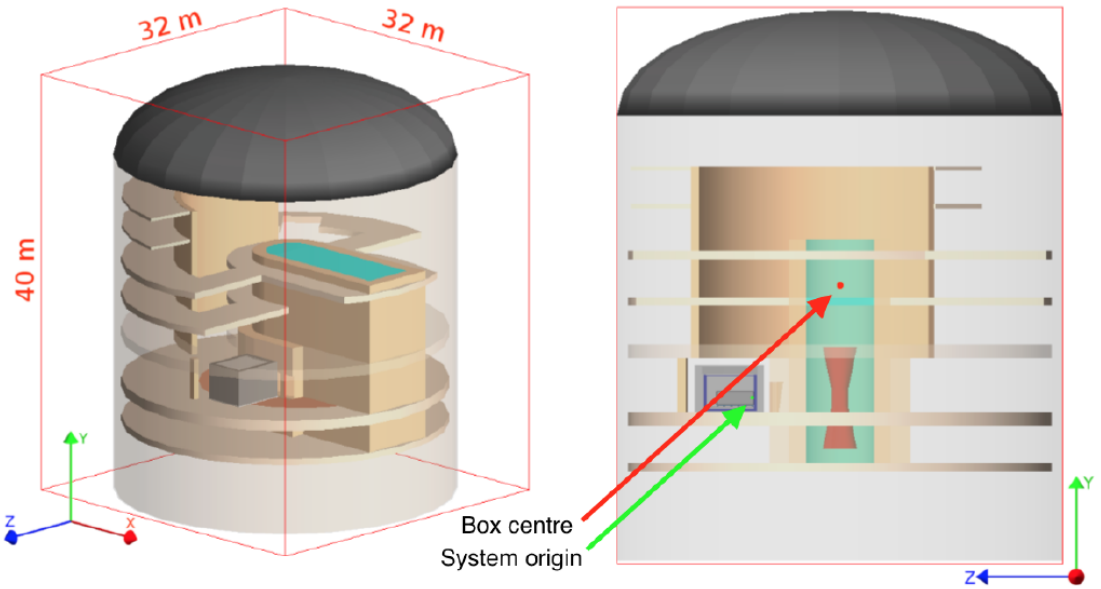

Figure 6.15: 3D representation of the BR2 geometry model and positioning of the SoLid detector as implemented in SoLidSim. The SoLid position system is based on three Cartesian coordinates along perpendicular axes in a right-handed system. The Z-axis is perpendicular to the detector planes and its direction points away from the nominal center of the BR2 reactor core. The Y-axis points upward towards the zenith, and the X-axis points to the right side of the detector, when facing the reactor.

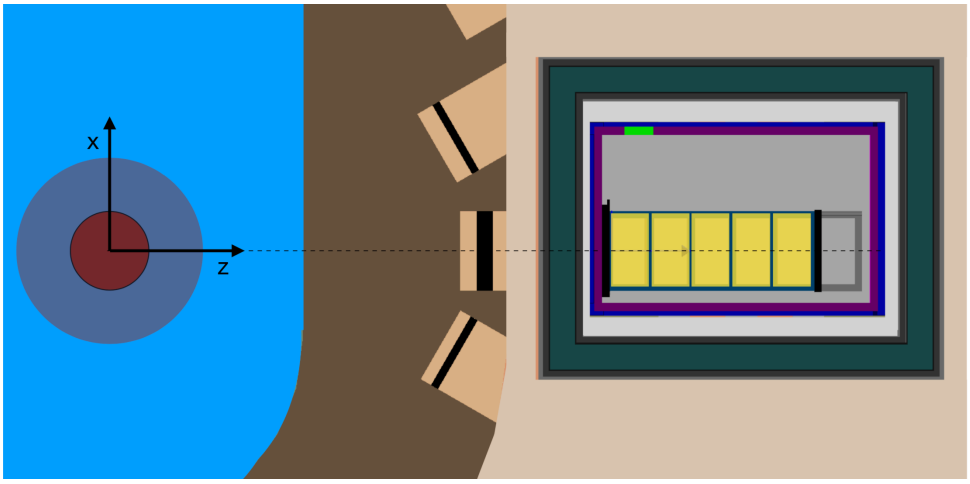

Figure 6.16: A vertical projection of the detector geometry and its positioning in the containment building (GEANT4 based). It shows the reactor core (red) submerged in water (blue) and the detector geometry including the detector module placement (yellow and blue rectangles) inside the cargo container, the rail system (dark grey rectangle), container insulation (purple) and passive water shielding (dark green).

6.5.5 Readout system design

The readout system is custom-made and based on a combination of analogue/digital front-end electronics and Field-Programmable Gate Array chips (FPGA). All MPPC signals are equalized, synchronized (< 1 ns) and continuously digitized at 40 MS/s. The use of zero suppression techniques (ZS), combined with pulse shape trigger algorithms, results in a data reduction factor of around 10 k, down to 20 Mb/s, with negligible dead time.

The readout system operates on three levels: plane, module and full detector. Each of

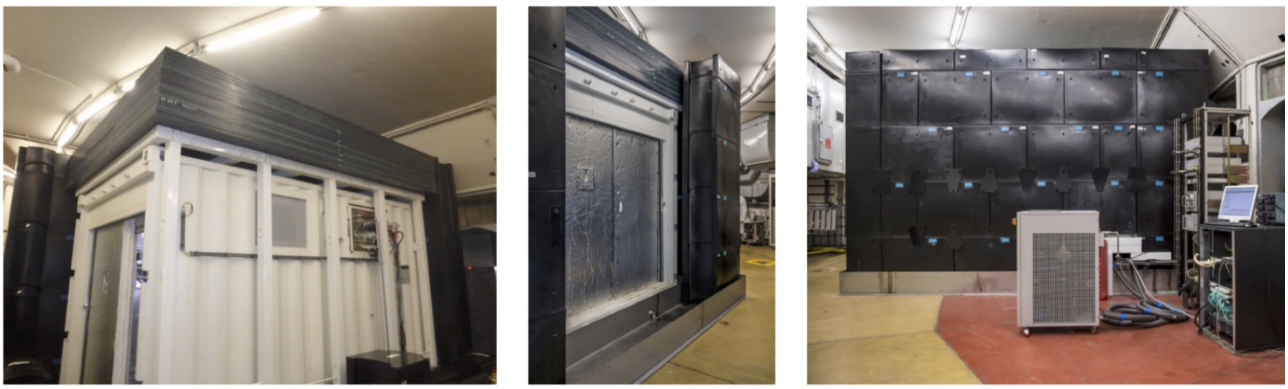

Figure 6.17: Pictures of the detector during its integration at BR2: cooled container (white) and passive shielding (black). The power supplies and DAQ system, together with the chiller used for the container cooling are visible on the side of the detector (front of picture).

the 50 single detection planes has its own readout system, mounted directly on its side within a dedicated aluminium enclosure (see figure 6.18). It contains all the front-end electronics to run in autonomous mode, as described below. Each detector module is equipped with a heat exchanger and a services box that contains a DC-DC voltage converter to power the module, clock and synchronization distribution board, network patch panel and Minnow JTAG programming system. The module clock board (master/slave mode) provides a common clock fan-out to synchronise the ten associated digital boards. A master clock-board allows to run the five detector modules synchronously.

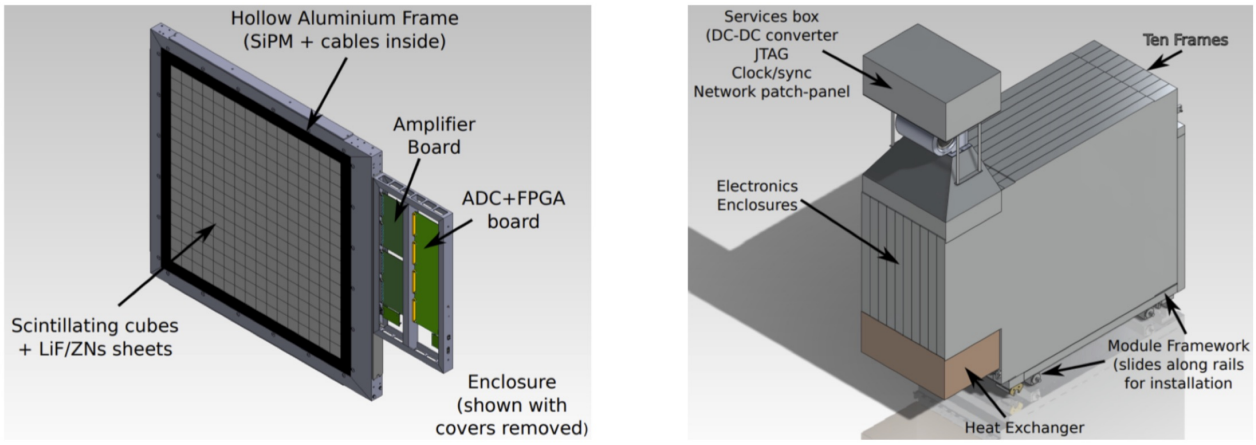

Figure 6.18: (left) CAD rendering of a detector plane and its aluminium electronics enclosure. The 64 MPPCs are connected via an interface place using twisted-pair ribbon cables that terminate into insulation displacement connectors. (right) Diagram of a ten planes detector module with its services box and its heat exchanger, placed below to take off heat generated by the electronics [Abreu et al., 2019a].

The front-end electronics of a single detection plane consists of two 32-channel analogue boards, a 64-channel digital board, together with a power distribution system and an Inter-Integrated Circuit module that reads out four environmental sensors mounted inside the hollow frame. These environmental sensors monitor temperature and humidity levels throughout the detector. The two analogue boards are connected to the cathodes of the 64 MPPCs of the plane. They provide a common 70 V power supply, as well as individual trim bias voltages (0-4 V) used to equalize the amplitude response of each MPPC individually. Before being sent to the digital boards and in order to perform more accurate time stamp and amplitude measurements, the fast MPPC pulses (a few ns) are read out in differential AC coupled mode, amplified, band-

pass filtered and shaped by a charge integrating operational amplifier to stretch the signal over several digital samples of 25 ns each.

The two analogue boards are connected to a 64-channel digital board for digitisation and trigger. Each digital board has eight 8-channel ADCs, operating at a rate of 40 MHz with 14 bit resolution. Digital boards are controlled and read out over a 1 Gbit/s optical Ethernet connection. A Phase-Locked Loop is included, which allows the digital boards to operate in stand-alone mode using an internally generated clock, or run synchronised to an external clock signal. Triggers and readout logic are implemented in a Xilinx Artix-7 (XC7A200) based FPGA device. JTAG connectors are included for remote firmware programming. Trigger signals from each digital board are propagated to all other detector planes by using two duplex 2.5 Gbit links. A complete description of the detector electronics is given in [Abreu et al., 2019a].

The entire readout electronics is coupled very close to the detector, within aluminium enclosures, inside the chilled container. Both act as a Faraday cage, providing shielding from outside electronics noise. The top and bottom sides of these enclosures have openings to allow air flow cooling. The electronics are cooled by six fans mounted between the services box and the plane electronics enclosures, pushing air downwards towards a heat exchanger which is capable of removing the 200 W of heat generated by each module (see figure 6.18). The radiator unit is based on circulating water containing 18% propylene glycol, connected to a chiller that operates nominally at a temperature of 5°C. It also acts as an overall cooling source to lower the ambient temperature inside the insulated detector container. As the environment temperature inside the container is maintained to 11°C, MPPC responses are stabilized at 1.4% level and the MPPC dark count rate is reduced by a factor of three compared to operation at room temperature.

6.5.6 Online triggers and data reduction

Multiple triggers and data reduction techniques have been implemented at the FPGA level. The trigger strategy for neutrinos relies solely on triggering on a scintillation signal generated in the neutron detection screens, further denotes as *NS*. As the *NS* scintillation process is characterized by a set of sporadic pulses emitted over several microseconds, the *NS* trigger algorithm involves tracking the time density of peaks in the waveform [Abreu et al., 2019a]. All algorithm parameters have been optimized during deployment: the amplitude threshold on waveform local maxima to be counted as a peak is set to 0.5 PA, the size of the rolling time window is fixed at 256 waveform samples (6.4 µs) and the number of peaks, required in the window, is set to 17 (see figure 6.19). These default values correspond to a trigger efficiency of 75% and a purity of 20% during nominal reactor ON periods. The offline neutron selection has demonstrated a purity of 99%. The 80% non-neutron triggers are mostly muon signals, which can be distinguished using an offline identification. For each *NS* trigger, a large space-time region is read out in order to encapsulate all signals from the IBD interaction. Three planes are read out on either side of the triggered plane, with a large time window of 500 µs before the trigger and 200 µs after the trigger. The *NS* trigger rate, which does not change significantly depending on reactor operation, fluctuates around 80 Hz.

Two additional triggers are also implemented to measure background and to survey the detector stability. A threshold trigger has been implemented to record high amplitude *ES* signals, such as muons. The default physics mode threshold is 2 MeV with a X-Y coincidence imposed. This gives a trigger rate of about 2.1 kHz during nominal reactor ON periods and decreases by around 10% during reactor OFF periods. A periodic trigger has also been implemented in order to monitor continuously the stability of the MPPCs, as well as any noise contributions. The entire detector is read out for a time window of 512 samples without zero suppression, with a default trigger rate of 1.2 Hz. The three triggers include storing MPPC waveforms for

offline analysis. A zero suppression value at 1.5 PA, respectively 0.5 PA in *NS* mode, allows to remove the pedestal contribution, whilst retaining all MPPC signals [Abreu et al., 2019a].

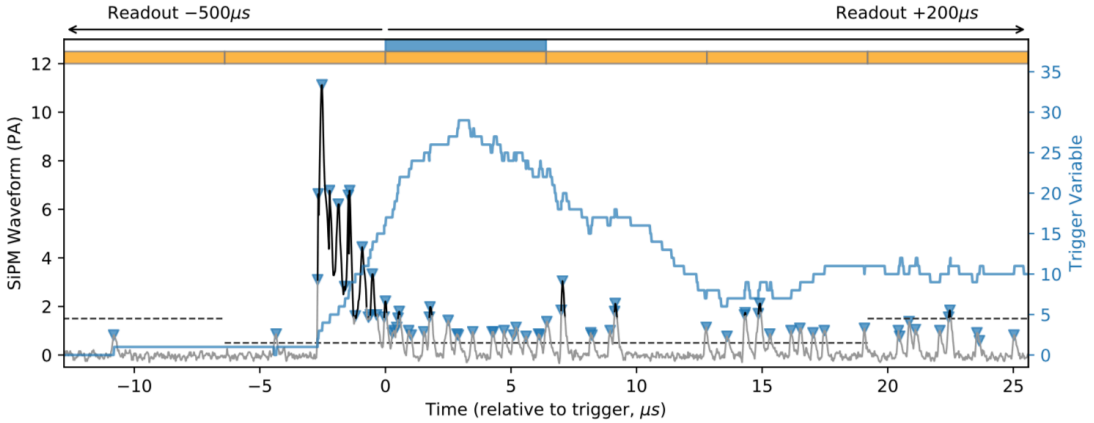

Figure 6.19: Example of a *NS* waveform (black). The dashed lines show the zero suppression threshold. The value of the *NS* trigger variable, i.e number of peaks in the rolling time window, is shown in blue [Abreu et al., 2019a].

The readout software runs on a disk server, located very close to the detector. It provides 50 TB of local storage, that is split into two data partitions, which are periodically swapped and cleared. All the data are first transferred to the Brussels HEP Tier 2 data centre, then subsequently backed up at CC-IN2P3 in France and at Imperial College in the UK using GRID tools, which are used for offline processing and simulation production.

6.6 Backgrounds in the SoLid experiment

The SoLid detector is also subjected to various background processes that contaminate the IBD samples for final analysis. Because the primary physics trigger is set to detect thermal neutrons interacting in the neutron detection screens, most backgrounds are related to either the production of neutrons via processes other than IBD interactions, or processes that excite the ZnS(Ag) scintillator embedded in the neutron detection screens. Some background processes exhibit a clear time structure between the triggered *NS* time and preceding *ES* signals and are called *correlated*. Others have a random time structure and are called *accidental*. Reactor independent backgrounds dominate our data sample and can be extracted from data collected during reactor OFF periods. We quantify our understanding of these background components by comparing background simulations with data in specific control regions that are enriched in one specific background component. Reactor dependent backgrounds are very scarce and are monitored using a dedicated NaI gamma ray detector and with dedicated control samples that are depleted of IBD events. It is mostly composed of gammas, and thus only populate accidental events, i.e. a random coincidence of a *NS* and *ES* signal within the IBD trigger window. In all cases we try to validate the background composition and the influence of selection criteria by using dedicated Monte Carlo simulations, wherever they are available. Below we summarize the main background processes and their origin, which are also schematized on figure 6.20.

A first source of neutrons to which the detector is constantly exposed is of atmospheric origin. These neutrons are produced by cosmic ray spallation when high energy primaries collide with atmospheric nuclei. Neutrons can penetrate much further into our atmosphere than the electromagnetic component and are shown to produce a complex energy spectrum [Gordon et al., 2004] ranging from sub-eV to multi-GeV. The flux contains slow and fast neutrons that induce a different response in the SoLid detector. Slow neutrons that enter our detector can, in combination

with an accidental coincidence of an *ES* signal such as those induced by gamma rays, produce signals similar to IBD events. The detector timing and spatial segmentation with corresponding topological selections can largely suppress this background. The passive water shield of 50 cm surrounding the experiment, combined with the Cd sheets placed on the outer walls of the container help to thermalize and capture some of the epithermal neutrons. The fast neutron component is able to penetrate the detector and can induce highly energetic proton recoils resulting in *ES* signals. If the neutron further thermalizes inside the detector it can be captured and induce a *NS* trigger. As such it introduces a time correlated background that dominates the selected IBD events samples for *ES* signals with energy above 5 MeV. This background is mainly suppressed by timing and *ES* signal multiplicity requirements.

Cosmic ray muons are also known to induce spallation reactions in materials near or inside the SoLid detector that produce neutrons or radioisotopes. The rate of neutron production increases with muon energy and with material density. The rate and spectrum is modelled using the CRY generator[1] by simulating cosmic ray showers on a surface that lies 30 m above the BR2 building and by tracking all shower components through the building and detector geometry. Roughly one third of the spallation neutrons are produced inside the detector, while the rest is created in surrounding structures. The techniques to mitigate the corresponding accidental and time correlated background are similar to those to reduce the atmospheric neutron background. Cosmic muons themselves are used as a calibration tool, as they generally leave a reconstructed track in the detector. In some cases, however, muons can clip the detector edges, leaving an isolated energy deposit that can contribute to the accidental backgrounds in the detector. Muons can also decay in the detector, resulting in the detection of the Michel electron or positron with a characteristic delay corresponding to the muon life time.

Intrinsic radioactivity of detector materials or airborne isotopes are another source of backgrounds. The airborne isotope of ^{222}Rn can produce several alpha and beta particles along its decay chain. Its presence inside the detector container is therefore monitored by a dedicated Rn detector, as described in section 6.5.2. Another source of intrinsic radioactivity are trace fractions of Bi isotopes contained in detector materials, in particular the neutron detection screens. The ^{214}Bi isotope is the most troublesome and is part of the long ^{238}U decay chain. It decays to ^{214}Po via β^- emission with a half-life of roughly 20 minutes and a Q_β value of 3.27 MeV. The resulting Po isotope has a half life of 164 µs and emits an energetic alpha particle that can cause a scintillation of the ZnS(Ag) scintillator of the neutron detection screens. The half-life of ^{214}Po is very similar to the thermalization and capture time of fast neutrons in the SoLid detector. This background, referred to as BiPo, dominates at prompt energies below 3 MeV and is difficult to mitigate. The use of cube and fibre topology information allows to localize the spatial origin of the alpha particle, while timing and energy can be used to tag the *ES* signal. In addition, also the integrated energy of the *NS* signal can be used to discriminate neutrons and alphas from the ^{214}Po decay.

Other backgrounds can be broadly categorized as accidentals and consist of random coincidences of *ES* signals that are typically induced by gamma rays and thermal neutrons in the surroundings of the detector. The accidental distribution can vary with reactor power, but can be easily extracted from data itself, using negative time differences between the *ES* and the *NS* signals. Accidentals contribute only marginally to the selected IBD events sample.

6.7 Simulations

The simulation of the SoLid detector is divided in two parts: one part models the particle interactions, energy losses and scattering, including neutrons, in the SoLid detector and the

[1] https://nuclear.llnl.gov/simulation/

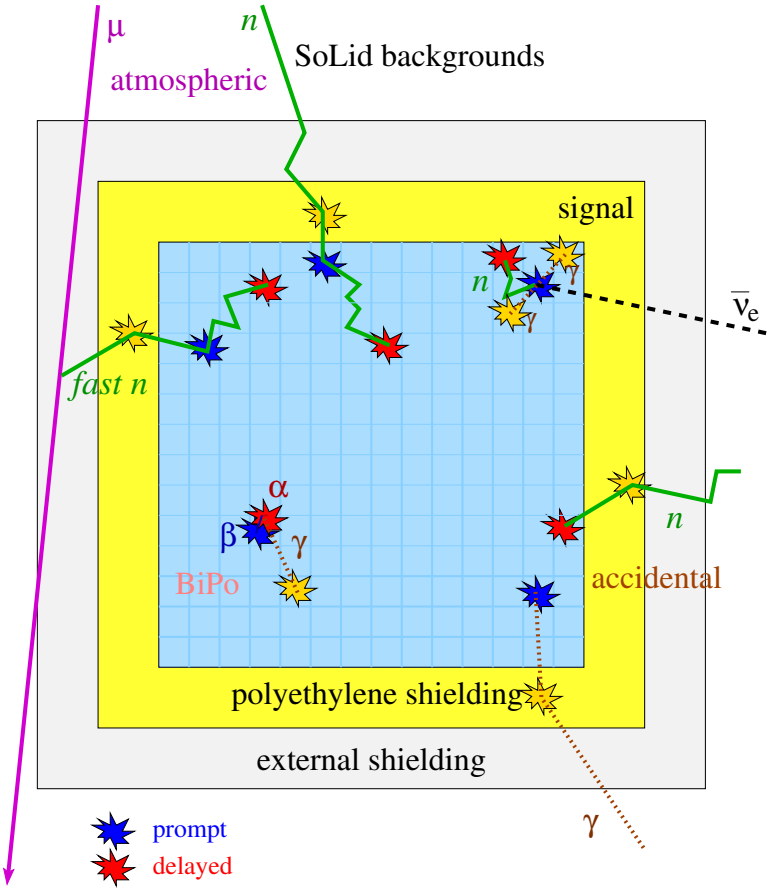

Figure 6.20: Schematic view of the main backgrounds in SoLid experiment.

BR2 reactor hall, while the second stage models the optical system of the detector, including the scintillator response, the optical transport, the photon collection by the MPPCs and the electronics response. This second part of the simulations will not be presented here but some details can be found in [Abreu et al., 2021, Pinera-Hernandez, 2016a, Verstraeten, 2021].

The first part, SoLidSim, is implemented using the GEANT4 simulation library [Agostinelli et al., 2003]. In order to accurately model the scattering of fast neutrons, the propagation of cosmic showers through the detector and the creation of spallation products in high-Z materials surrounding the detector, a detailed geometry model of the detector surroundings is made. This model, as graphically shown in figure 6.15, is based extensively on detailed blueprints of the reactor building and survey measurements performed prior to detector installation and includes as main features the majority of the concrete and steel structures of the BR2 containment building, including the cylindrical containment building inner and outer walls and dome cap, the concrete floors of level 3, where the detector is located, level 2 below the detector and levels 4 to 7 situated above the detector. Specific features such as staircases, elevator shafts, crane passways, and access holes are included as well. Special care is taken to model in detail the reactor fuel tank, the water pool and its concrete walls with beam ports including concrete and steel plugs, the 20 cm thick lead shielding wall in between the SoLid detector and the radial beam port facing the reactor core. The inclusion of these structures can be switched off in the tracking of particles through the detector to save time and computing power for simulations of IBD events or background processes occurring inside the detector.

On the detector side a precise description of the PVT cubes, the fibres, the Tyvek layers, the ZnS screens, the MPPCs, the aluminium frames, the HDPE neutron reflection screens has been used as described on figures 6.11 and 6.12. The geometry of the detector includes besides the sensitive volume of the detector, all HDPE neutron reflectors, all metal structures surrounding

the sensitive volume, including the electronics housing, the CROSS system, all mounting rails, the container insulation and steel walls, the passive water and PE shielding surrounding the detector and its support scaffolding.

6.8 Events reconstruction

6.8.1 Time clustering of waveforms

The first steps of the event reconstruction developed in SoLid has been the subject of the PhD thesis of Valentin Pestel at Caen University [Pestel, 2019]. As already said, the MPPC waveforms in the SoLid detection planes are digitized at 40 MHz and registered in blocks of 6.4 µs. The event reconstruction is performed by time windows, called *cycles*, where all the data blocks are readout until a time of 2.240 ms (350 blocks) after the last block is encountered. This time window has been optimized to limit memory consumption while preserving enough time to search for ES-NS coincidences and after muon events. The samples in the blocks of a cycle are then organised by channels to form *waveforms*.

Given the huge dark count rate of MPPCs, most of the recorded waveforms are due to thermal noise. The strategy to get rid of these bad pulses is to build *time clusters* of waveforms and to use an amplitude threshold of 2.5 PA. To further reduce the fake coincidences rate, the clustering is performed by detection planes where it is required to get at least one horizontal and one vertical channels. All the waveforms starting within seven samples (175 ns) of a given waveform are then clustered. The clusters built in the cycle can then be merged if they start within the same time limit, of seven samples, or if they share channels with another cluster. To keep the long trail of photons produced by ZnS, the clusters are extended with an additional time window. The duration of this time window depends on the length of the cluster and its number of channels. It can reach up to 25 µs.

The clusters are then categorized in three types for the analysis: muons, NS or ES clusters. Examples of ES and NS clusters are represented on figure 6.21. Muons are identified by short time clusters with a large number of channels and high amplitudes on the channels. The cube projection of a muon cluster are fitted with straight lines to get the interesting parameters for muon studies. The NS clusters are generally made of four channels forming a single cube. They are identified thanks to the duration of the cluster and the pulse shape analysis with a high integral over amplitude ratio. The remaining clusters are tagged as ES clusters and further treatment is needed to reconstruct the individual cube hits.

In order to avoid ambiguities in the reconstruction of the PVT cubes in the same detector planes and to get the best energy estimation in the individual cubes, the *CCube algorithm* has been developed by our colleagues from Clermont-Ferrand [Hervé Chanal, 2019]. It consists of an iterative process with Maximum Likelihood-Expectation Maximization (ML-EM) Bayesian approach [Dempster et al., 1977]. This method is extensively used in medical imaging and the NEXT experiment, for example. The principle is that the MPPC signals represent the four projection p_i of the energy deposited E_j in the cube j, which we want to reconstruct. The light sharing of the four MPPCs forming a cube are subject of the light collection effects: cubes light-yield variations, fibre attenuation, light leakages and fibre to MPPC optical coupling inhomogeneities. These optical effects are encoded in the *system matrix* A, such that $p_i = A_{ij}E_j$. To speed up the convergence of the iterative procedure, the algorithm is provided at the first step with the cubes which are at the crossing of the most energetic fibres. The algorithm then makes iteratively predictions E_j^{n+1} following this equation:

$$E_j^{n+1} = \frac{E_j^n}{\sum_i A_{ij}} \sum_i A_{ij} \frac{p_i}{\sum_{\hat{j}} A_{i\hat{j}} E_{\hat{j}}^n} \tag{6.2}$$

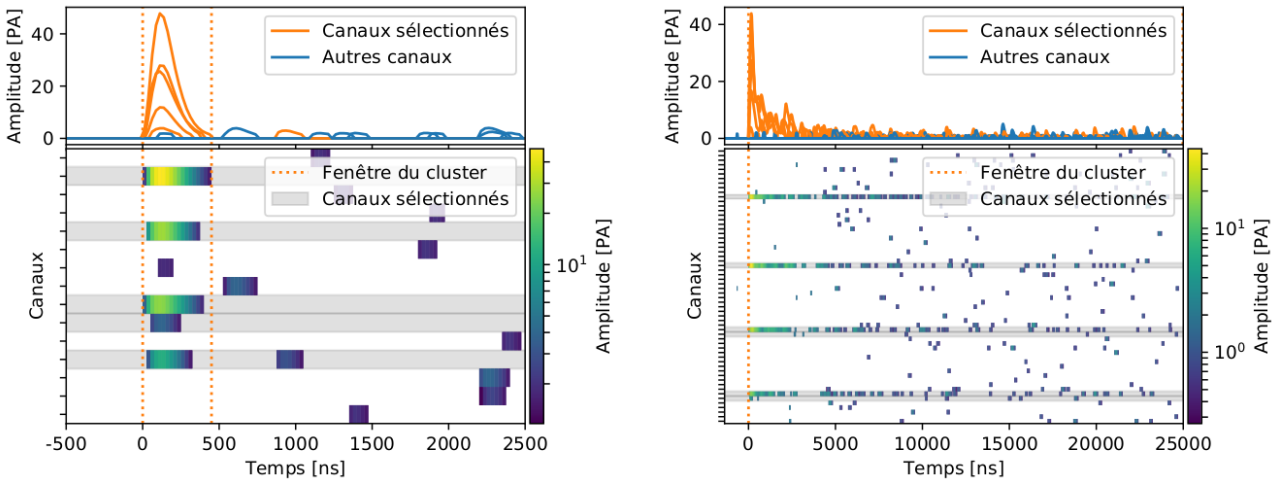

Figure 6.21: Examples of ES (left) and NS (right) clusters made with the reconstruction software of SoLid [Pestel, 2019]. On top are represented the digitized data samples and on the bottom the amplitude of the channels as a function of time.

where E_j^n is the energy of the cube j at the iteration n and $\hat{j}$ the index of the cubes in the same row or column as the cube j. The guessed projections are compared to the measurements and the difference is used to generate a new estimation, this is called back-projection. This algorithm has demonstrated on readout simulations an efficiency close to 80% to reconstruct real cubes with less than 7% of ghosts cubes [Hervé Chanal, 2019].

The first version of the CCube algorithm uses a flat system matrix where the light is equally shared among the four fibres (0.25 coefficients). A second version has latter been developed using horizontal muons to measure the light sharing pattern of each cube.

6.9 Expected sensitivity

The SoLid Phase 1 experiment sensitivity has been investigated in 2017 by L. N. Kalousis, from Vrije Universiteit Brussel, after the SM1 results and compiled in [Kalousis and Vercaemer, 2017]. These results are now outdated but allow me to illustrate the expected capabilities of SoLid experiment in the search for sterile neutrinos. More recent work is ongoing using the output of the phase 1 analyses (see chapter 9).

The anti-neutrino events are generated from the average number of anti-neutrino interactions in a given cube after an integral over the whole reactor core volume. The cross-section per fission for all the fissile isotopes can be derived from the anti-neutrino spectrum and flux. In SoLid, the prediction of the anti-neutrino flux is based on a detailed 3D model of the BR2 core, coupled to a Monte-Carlo based method, MCNPX/CINDER90, that produces the fission rates [Kalcheva et al., 2017]. The MURE code then used to track the burn-up of the fissile products in the reactor core [Méplan et al., 2005]. The energy spectrum is then computed with the Huber-Mueller model [Mueller et al., 2011, Huber, 2011] with off-equilibrium correction provided by the MURE code. On the figure 6.22 is represented an example of the evolution of the fissions and emitted anti-neutrino spectra as a function of burn-up or days for a given cycle. We can see that more than 99 % of the fissions are due to ^{235}U and that the anti-neutrino energy spectrum strongly evolves in time. The IBD cross-section in SoLid is computed following Vogel and Beacom [Vogel and Beacom, 1999].

To investigate the sensitivity to sterile neutrino search, the work presented here uses the so-called *SoLO*, for SoLid Oscillation framework. It generates the IBD interaction in the detector from the anti-neutrino spectrum model computed as explained before. *SoLO* computes the

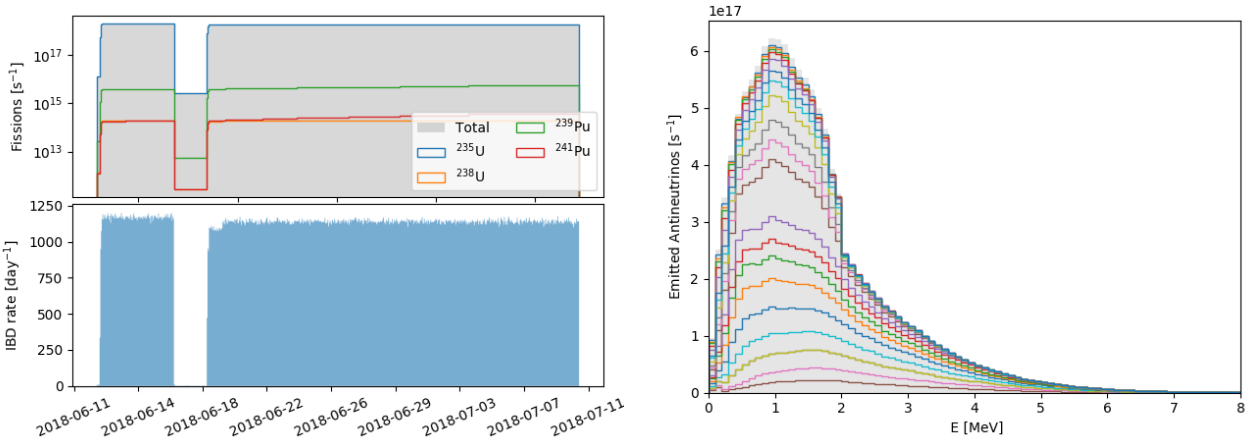

Figure 6.22: (left) Evolution of the fission rates (top) and the associated IBD interaction rate (bottom) during cycle 03/2018A. (right) Emitted anti-neutrino spectrum calculated using the summation method. The different colors correspond to different time steps before reaching equilibrium, from 0 to 28 days of irradiation time.[Kalcheva et al., 2017].

expected anti-neutrino interaction points inside the detector with their energies and momentum. The positron and the neutron created by the IBD interaction are also provided by the software, and SoLidSim will generate everything that happens after the IBD interaction. *SoLO* can also add a fake oscillation pattern to the anti-neutrino generated for further studies, as shown on figure 6.23.

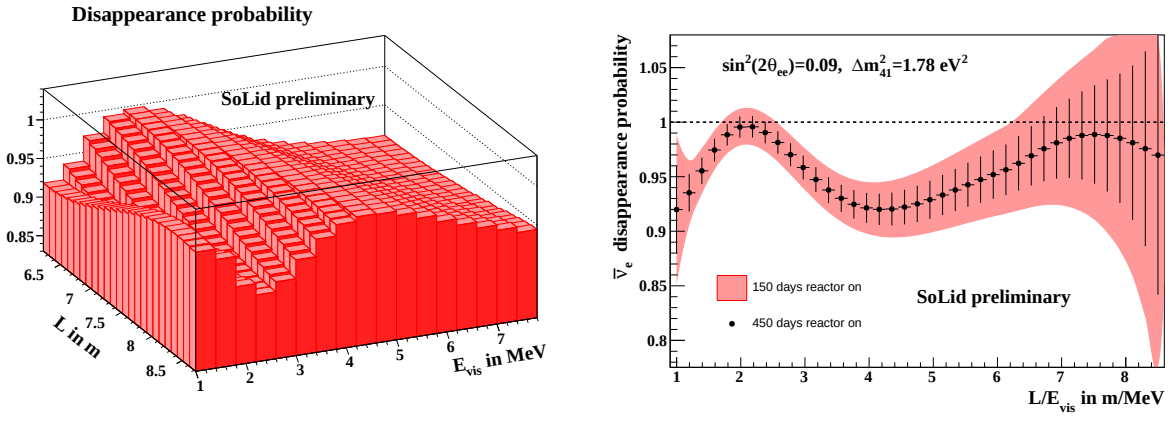

Figure 6.23: (left) Spectrum of the oscillated to the un-oscillated ratio of the visible energy E_{vis} versus the travel distance L for the J. Kopp et al. global best fit [Kopp et al., 2013]. (right) One dimensional spectrum of this ratio as a function of L/E_{vis}.

The oscillation sensitivity can then be estimated given some input parameters. The background is extrapolated from the SM1 data with a signal-over-background ratio of three[2]. The IBD efficiency is expected to be 30 %. The energy resolution is set at 14 %/$\sqrt{E(MeV)}$. The statistical test used in *SoLO* is then based on a gaussian χ^2, using pull terms for the correlated systematic uncertainties. The exclusion contours for 150 and 450 days of reactor ON are presented in figure 6.24. From this first study we could have expected a quick exclusion of the oscillation best-fit of the RAA from J. Kopp et al. [Kopp et al., 2013]. We will see that unfortunately the background encountered during phase 1 is much higher than expected.

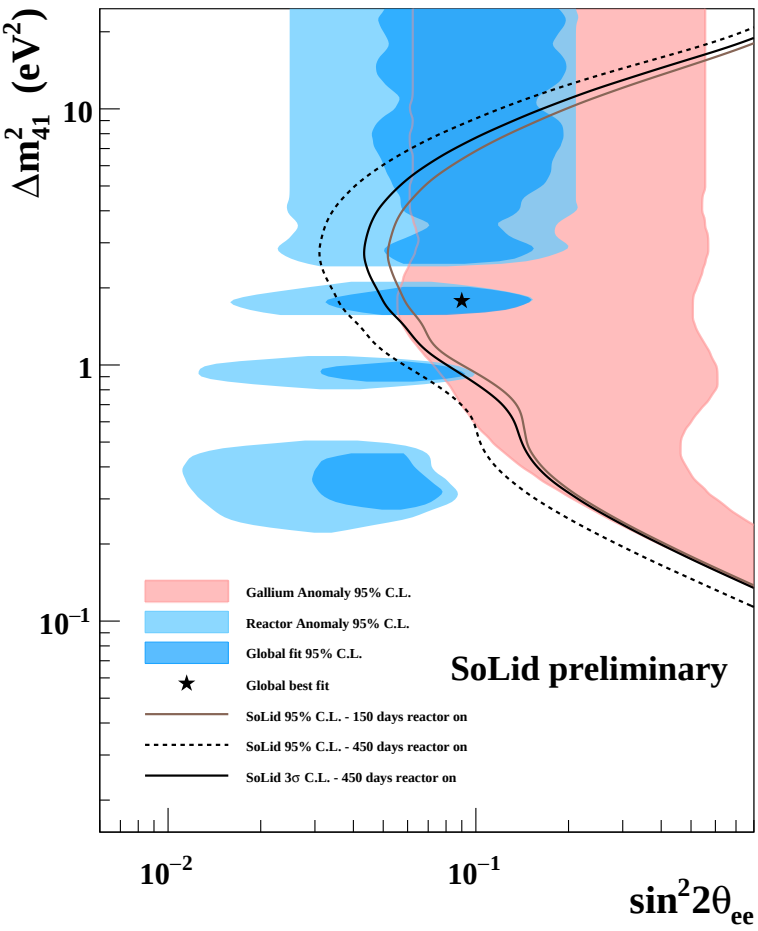

Figure 6.24: SoLid sensitivity contour as expected in 2017 after the SM1 prototype results.

[2]This value was very optimistic at that time and the target is now to try to get close to one.

Chapter 7

Light-yield optimization for SoLid

After the results of the SM1 prototype, the necessity to improve the light-collection for the SoLid detector clearly appeared. The cube readout for SM1 consisted of two single-clad optical fibres coupled to one MPPC at one end and a mirror at the other end. The first measurements of the light yield performed with SM1 resulted in 12 photo-avalanches (PA) per fibre corresponding to a stochastic energy resolution of 20 % at 1 MeV. In addition, because of attenuation along the fibres, the light collection was not uniform within the detection plane. Searching for oscillations to a sterile neutrino requires a good precision on the energy measurements and uniformity of the response in space, since the oscillation would manifest both in energy and travelled distance. Optimizing the light-collection would improve the energy resolution for the PVT signals, lower the detection threshold for the annihilation γ's and increase the neutron detection efficiency for the ZnS signals. Improve the light collection uniformity was also of major importance for an uniform detection efficiency.

The aim of SoLid Phase 1 is to reach a stochastic term of the energy resolution σ_E/E of at least 14 % at 1 MeV. This would require to collect more than 50 PA/MeV/cube summing the light yield from all the fibres in a cube, after correcting for effects such as cross-talk in the MPPCs. While joining SoLid collaboration, I proposed to take in charge the light-yield studies since we had experience in plastic scintillators, light collection and test benches at LAL. This work was realized with Delphine Boursette during her PhD thesis. We developed a dedicated scintillator cubes test bench and studied many aspects of the light collection of the SoLid technology. We obtained significative improvements that were implemented in the design of the SoLid Phase 1 detector. The studies performed over 1.5 years showed that large gains in light collection efficiency are possible compared to SM1 prototype. The light yield for the SoLid detector is expected to be at least 52 ± 2 photo-avalanches per MeV per cube, with a relative non-uniformity of 6 %, demonstrating that the required energy resolution of at least 14 % at 1 MeV can be achieved.

This work was compiled in the publication [Abreu et al., 2018a] and Delphine PhD thesis [Boursette, 2018]. In this chapter I will present the test bench and summarize the key results of this work we conducted.

Chapter contents

7.1 The test bench setup

The setup presented here has been inspired by the trigger system of an electron spectrometer [Marquet et al., 2015] used for the NEMO-3 and SuperNEMO experiments to qualify the plastic scintillators [Arnold et al., 2005, Arnold et al., 2010] and the regular deployment of ^{207}Bi sources in those detectors to produce the absolute energy calibrations. The principle of this setup is to use a ^{207}Bi calibration source and a trigger system to produce mono-energetic conversion electrons in order to compare different detector element configurations. Since the ^{207}Bi radioactive source is mainly emitting γ particles, it is necessary to use a triggering system to select only the conversion electrons entering the cubes. Otherwise, the signal would be dominated by Compton-scattering of γ-rays and the energy spectrum would give a lower precision on the light yield measurements than the peak from conversion electrons.

The setup aims at giving the absolute light-yield to determine the energy scale and energy resolution of the PVT detection elements in a certain configuration. It has been designed to be as flexible as possible in order to test various configurations for the SoLid scintillator cubes: wrapping, position and type of fibres, effect of the ^{6}LiF:ZnS(Ag) screen, machining and cleaning of the cubes, MPPCs and fibre reflectors. The test bench has been installed in a polyethylene black box ($120\times120\times20$ cm^3) sufficiently large to accommodate the full length of the SoLid fibres in both X and Y directions (see pictures 7.1). This setup has been designed and constructed by a mechanical team at LAL composed of Stéphane Jenzer, Alexandre Migayron and Aurélien Blot. The setup is installed in an air-conditioned room at a temperature of around 19 °C. The scintillator cubes and the triggering system are both mounted on a rail and can be moved with a light tight manual jack from outside the black box. This design allows for moving the full system along the fibre to be able to measure the light attenuation for different cube positions along the fibre. In the case of the SM1 prototype, the thickness of the Tyvek wrapping allowed for scintillation light to pass through the wrapping. However, the wrapping of neighbouring cubes allowed to recover a fraction of the light otherwise lost to the neighbouring environment. The rail allows then to perform measurements with a series of 16 cubes connected to a single fibre, which is closer to a realistic detector configuration.

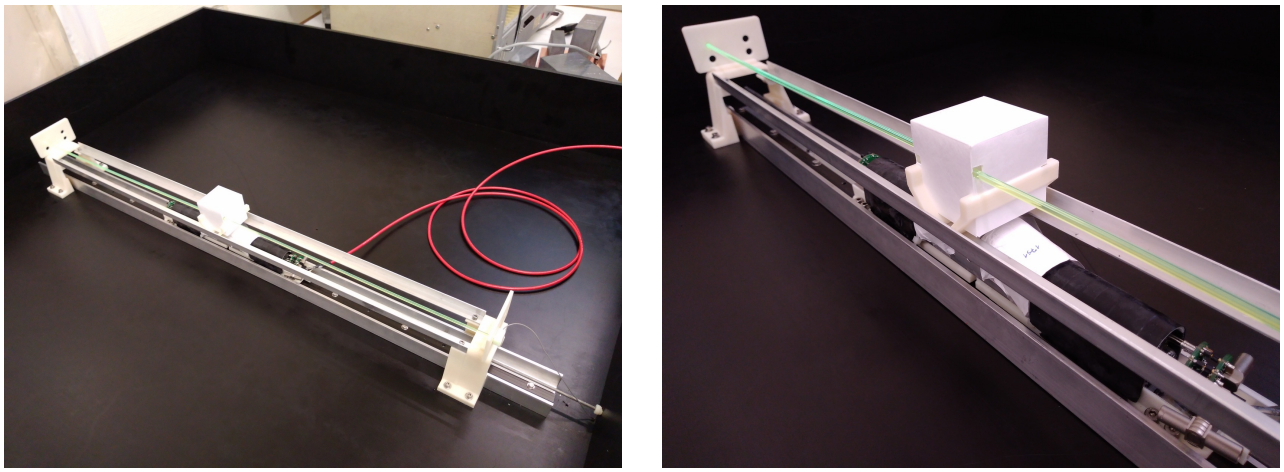

Figure 7.1: Pictures of the test bech setup in his black box without cover. We can see a scintillator cube in the middle wrapped in Tyvek, the triggering system under, the support rail and the 3D-printed pieces to support a fiber and the two MPPCs at the extremity.

In order to make comparisons between the different measurements and to simplify the operations a standard configuration has been defined for the main tests. This configuration is presented in figure 7.2. It consists of a single SoLid scintillator cube (almost always the same for this publication) with its Tyvek wrapping of thickness 270 µm and read out by a single fibre and one MPPC at each end. The MPPCs are supplied with an over-voltage of 1.5 V, which is the baseline voltage applied to operate the MPPCs in SoLid[1]. This setting balances gain and cross-talk for this generation of photo-detectors (Hamamatsu S12).

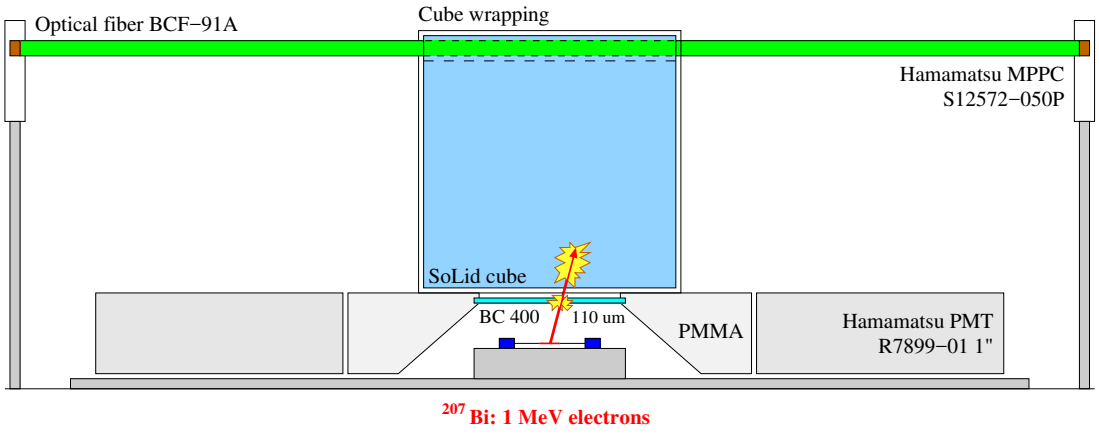

Figure 7.2: Schematic description of the scintillator test setup in the standard configuration used for most of the measurements (a single wrapped cube along one optical fibre with double end MPPC readout). The calibration source, the PMTs and the scintillator cube are mounted on a rail in order to allow moving the system along the fibre.

The ^{207}Bi isotope is well suited to test the SoLid scintillator performance in term of the energy scale and resolution since it produces mono-energetic electrons around 1 MeV. This is the same order of magnitude as the antineutrino energy determined from the positron energy deposit, which extands up to 8 MeV. As already mentioned the detected 1 MeV Gaussian peak allows accurate comparisons between different detector configurations.

[1]After the commissioning of Phase 1 detector, it was decided to increase to 1.8 V to increase the photon detection efficiency.

The ^{207}Bi isotope decays through electron capture almost exclusively to excited states of ^{207}Pb. The ^{207}Pb de-excitations occur through 3 main γ-ray emissions (570, 1064 and 1770 keV). These γ-ray emissions could be replaced by atomic K, L or M shell conversion electrons. The conversion electrons associated to the 1770 keV de-excitation are negligible and those associated to the 570 keV occur only in 1.5 % of the decays over an important γ background. Most of the useful conversion electrons are associated to the 1064 keV de-excitation and have an energy between 976 and 1060 keV with a total probability of 9.5 %. Given the finite energy resolution of the SoLid detector (14-20 %), only one main peak at an average energy of 995 keV, without losses in dead materials, has been determined by simulation (more details are presented in the publication).

The principle of the triggering system is to select only the mono-energetic conversion electrons by detecting them in the thin (110 µm) plastic scintillator (BC 400 - 2×1 cm^2) before they enter the SoLid scintillator cube. A detailed picture of this system can be seen on picture 7.3. It has be designed and constructed at LAL by Matthieu Brière. The light produced in the trigger scintillator is collected by two polymethyl methacrylate (PMMA) light guides which channel the light towards two 1" PMTs (Hamamatsu R7899-01) equipped with custom made dividers developed for PMT tests at LAL Orsay. Good optical coupling is ensured by optical grease (BC 630) between the thin scintillator and the light-guides and by an optical epoxy silicone rubber compound (RTV 615) between the light-guides and the PMTs. The light collection of this setup is not sufficient to reconstruct precisely the energy deposited by the crossing electrons but detailed GEANT4 based simulations show that it represents negligible energy loss. This thin scintillator provides a triggering signal to tag the charged particle entering the cube. The triggering system minimizes the distance between the source and the scintillator cube in order to reduce the solid angle and the energy loss of the electrons before they enter the cube.

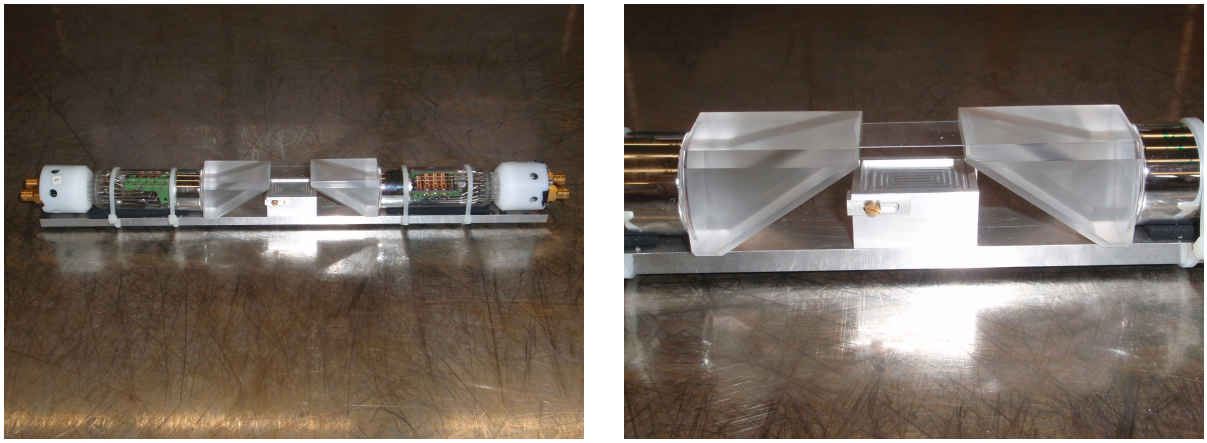

Figure 7.3: Detailed pictures of the triggering system of the test bech setup without the radioactive ^{207}Pb source insterted in the aluminium support.

7.1.1 Electronics and acquisition

The photo-detectors selected for SoLid are the Hamamatsu MPPCs S12572-050P 3×3 mm^2. These devices were not specifically studied in our setup. The measurements performed only concerned the cross-talk probability of the MPPCs that needs to be accounted for light yield determination. The MPPCs were soldered on custom made PCBs installed in 3D printed supports also used to hold the optical fibre, as in the SM1 prototype. The optical contact between the MPPC and the fibre is made by optical grease (BC 630).

To supply voltage, amplify, shape and extract the MPPC signals, a custom made three channels prototype board is used. This board has been developed to validate the analog electronic boards of the SM1 prototype. The voltage is provided by two external power supplies (EA-PSI 6150-01): one at 65 V for the MPPC supply and one at 5 V for the amplifiers. These power supplies have a very good resolution of 10 mV and a stability of better than 5 mV. With this setup the same voltage is provided to all the channels. The two MPPCs have been selected to have close operating voltages ($V_{OP} = 67.40$ and 67.46 V respectively). The two trigger PMTs are powered by an Ortec 556 power supply at -1400 V.

An eight channel waveform digitizer developed at LAL based on the WaveCatcher ASIC is capturing the signals from all photon detectors ([Breton et al., 2011, Breton et al., 2014]). This module is directly controlled by USB and a CVI software allowing to define the acquisition settings, perform analysis and store the digitized pulses. The trigger is set as a coincidence of the two negative PMT signals at -5 mV and the positive MPPC signals above 2 mV threshold. The sampling is made over 1024 points at 1.6 GS/s frequency to properly sample the waveforms over their whole pulse length. This corresponds to a 640 ns time window. More details on the reconstruction of the MPPC pulses and the energy are presented in section 7.2.

7.2 Measurements and data processing

7.2.1 Pulse reconstruction

When comparing the light yield performance for different configurations, the amplitude, the integral and the pedestal of the pulses are the main parameters to compute. This reconstruction is done off-line from the samplings registered by the acquisition. Figure 7.4 shows a cumulated view of all the pulses registered during one ^{207}Bi run. The individual photo-avalanches peaks cannot be distinguished well from the amplitude. In contrast, the integral spectrum of the photo-avalanche peaks shows a good resolution.

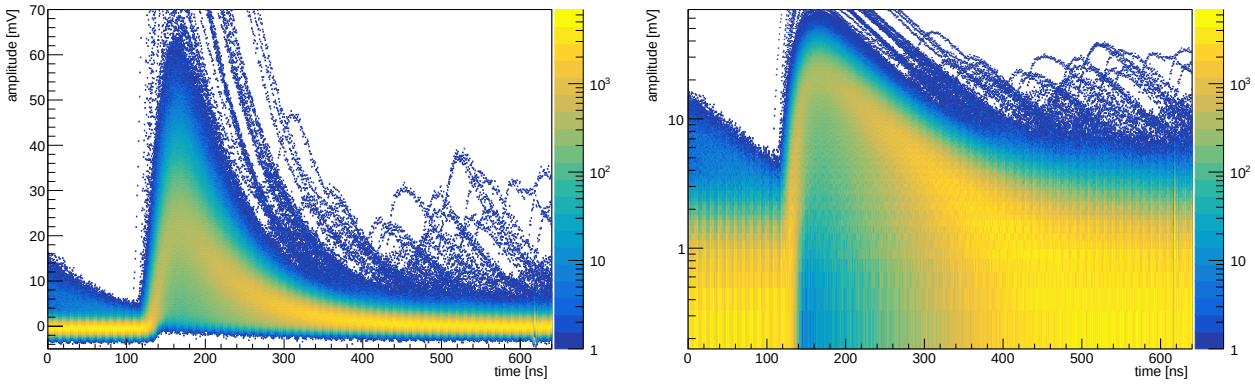

Figure 7.4: Persistence view of MPPC pulses registered from a SoLid scintillator cube during a ^{207}Bi measurement in linear (left) and log (right) scales. The few delayed pulses could be due to random coincidences or after-pulses.

To calculate the pedestal, the pulse position in the 640 ns acquisition window is set to buffer samples in a period of 100 ns before the rise of the pulse. This method has been compared to a pedestal measurement with random triggers over the full sampling window and the results are similar. The pedestal value is typically around 0.1 V×ns (integration of amplitude pulses in V over time in ns) while the ^{207}Bi peak is around 2.5 V×ns in a single channel. After determining the pedestal, the MPPC pulses are identified by the maximal amplitude value. The integral is obtained by integrating the voltage amplitudes from 50 ns before the maximum value to around

190 ns after the maximum value. This integral is expressed in V×ns as for the pedestal. The integration end value of the range is not exactly at the end of the pulse for high amplitude pulses but it avoids fluctuations due to the noise. Variable integration windows as a function of the pulse amplitude have also been tested but no improvements were observed.

7.2.2 MPPC cross-talk correction

Optical cross-talk occurs in MPPCs when during the primary avalanche multiplication some photons are emitted and start secondary avalanches in one or more neighbouring cells. Since a few tens of photons are emitted by a single avalanche, the cross-talk probability is high when no optical barrier (metallic trench) is implemented. This is the case for the generation of MPPCs used in the SoLid experiment, resulting in cross-talk probability of 10 to 30 % depending on the over-voltage setting. From our measurements presented in the publication, we obtain on average 17.7 ± 1.0 (stat) % for the two MPPCs at 1.5 V over-voltage. This value is subtracted to all the light-yield results presented in this chapter.

7.2.3 Procedure to calculate the light yield

The MPPC pulses are reconstructed and calibrated using the individual PA peaks in order to produce calibrated spectra expressed in PAs of the two MPPCs as presented in figure 7.5 (the calibration procedure is presented in the published article). We can also look at the sum of the charges of both channels and the correlation between the signals. The integral spectra for the individual MPPCs give a similar peak position (here 19.1 and 20.0 PAs) and the linear correlation is over 60 %. The summed integral spectrum is used to give the final result of the measurement with the 1 MeV peak fitted by a Gaussian function. In this example $N_{PA} = 40.5$ PA has been measured without taking into account the cross-talk. Subtracting the cross-talk results in a light yield of $N_{PA} = 33.3$ PA at ∼910 keV corresponding to 36.6 PA/MeV. The stochastic term of the detector energy resolution could then be estimated by the formula $1/\sqrt{N_{PA}}$, which corresponds to 16.5 % at 1 MeV for this cube with only 1 fibre and a double MPPC readout. This example illustrates the procedure to get the light yield for a given configuration.

The statistical uncertainty for a light-yield measurement is around 0.2 % (given by the fit error). The systematic uncertainties have been measured by 32 tests presented in the publication and are estimated to be 5 %.

7.3 Scintillator light collection studies

This section presents the studies of the light collection for a single SoLid cube. The influence of the scintillator material, the cube wrapping, the optical fibres and the ^{6}LiF:ZnS(Ag) screen on the light collection is studied.

7.3.1 Plastic scintillator material, production and cleaning

Plastic scintillator cubes in the SoLid experiment primarily serve as the antineutrino target since they contain a large number of free protons in the form of hydrogen nuclei. At the same time, it allows the measurement of the positron energy deposition, which in turn is related to the neutrino energy. The SoLid experiment uses ELJEN Technology EJ-200 PVT scintillator, one of the most efficient plastic scintillators with a light yield of around 10,000 photons per MeV. Light around 425 nm wavelength is produced with a decay time of 2.1 ns. Its refractive index is 1.58.

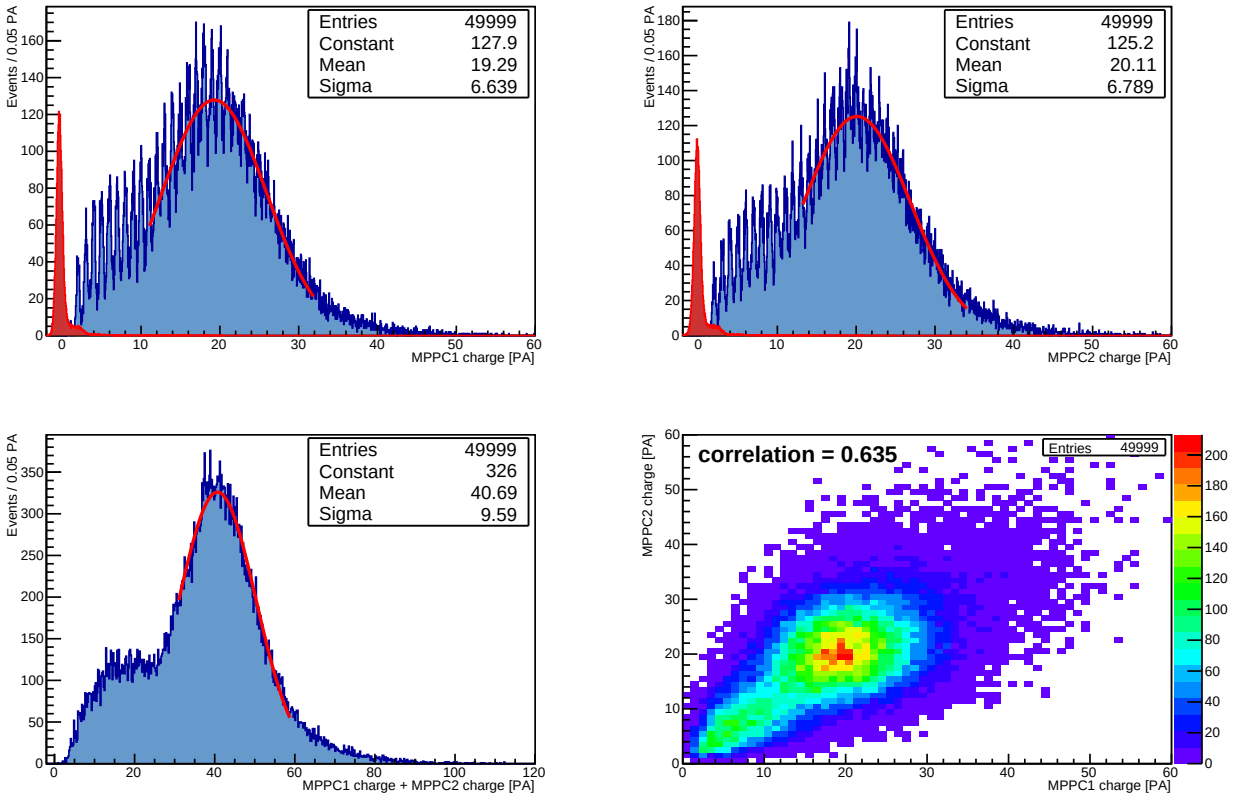

Figure 7.5: The top panel shows the calibrated PA spectra for the two MPPCs with the Gaussian fit. The red distribution is the calibrated pedestal spectrum. The bottom left represents the sum of the two MPPC integrals and right shows the correlation between the integrals of the two MPPCs.

For the SoLid Phase 1 detector, the scintillator cube machining has been improved to obtain a better cube surface quality. Polishing the 12800 cubes needed for the experiment would improve the light yield further, but this was not cost effective. Therefore we focussed on optimizing surface quality after machining. In order to estimate the quality of the machining we measured with a roughness meter the surface roughness average (R_a). For SM1 cubes it was around 0.45 µm compared to 0.04 µm for the new cubes. This increased the light yield by 10 %.

In order to prevent the scintillator from heating, a lubricant is used during the machining. This leaves a grease film on the surface of all the cubes. As a reference measurement, the light yield of a cube was measured directly after machining, hence before cleaning. This gave a light yield of 35 PA/MeV. The cubes were then cleaned by hand in a soap solution at room temperature, rinsed with demineralised water and left to dry in the air or with tissues. The increase in light-yield is then 25 % after cleaning. Two other cleaning methods have been tested and provide similar results.

7.3.2 Cube wrapping material

The primary role of the cube wrapping is to optically isolate each scintillator cube in order to be able to locate the position of the IBD interaction. Additionally, the wrapping also acts as a reflector, increasing the light collected by the fibres.

Teflon (or PTFE) is known to be one of the best reflective materials for scintillation light. A SoLid cube was wrapped with 0.2 mm thick Teflon tape (80 $g\,m^{-2}$) and tested. The result of the measurement with Teflon leads to the best light yield measured in this configuration,

giving 44 PA/MeV. However, the wrapping of cubes with Teflon tape, leaving a hole for the fibre and avoiding extra layers for electron energy loss is time consuming and error prone. Since the SoLid Phase 1 contains 12800 cubes, Teflon tape was excluded for practical reasons. Nevertheless, this test provides a good reference to select appropriate wrapping material.

Tyvek is another very good candidate for reflecting scintillation light. It is also much more convenient to use as wrapping for the cubes since it is possible to cut and pre-fold a pattern using press techniques. This is shown in figure 7.6 where the Tyvek wrapping is unfolded around a cube. This material was already used for the SM1 detector but the Tyvek used at that time was not the thickest possible. Indeed for cubes assembled in the detector plane, the surrounding Tyvek layers from other cubes contributed to an increase of the light yield compared to a single cube. To quantify this effect, up to four layers of Tyvek wrapping have been added successively around a PVT cube. The second layer improved the light yield by about 20 %, the third one gave an extra 10 % with respect to two layers while the fourth one had no additional effect. For the construction of the SoLid Phase 1 detector it is not convenient to use several layers of wrapping around each cube so we have selected the thickest Tyvek from DuPont™ (1082D). A light yield of 36.7 PA/MeV was measured for this Tyvek compared to 33.6 PA/MeV for the Tyvek used in the SM1 detector. This is an improvement of 10 % for a single cube. Although this is a 15 % lower light yield than Teflon, it was the best material found taking into account construction constraints.

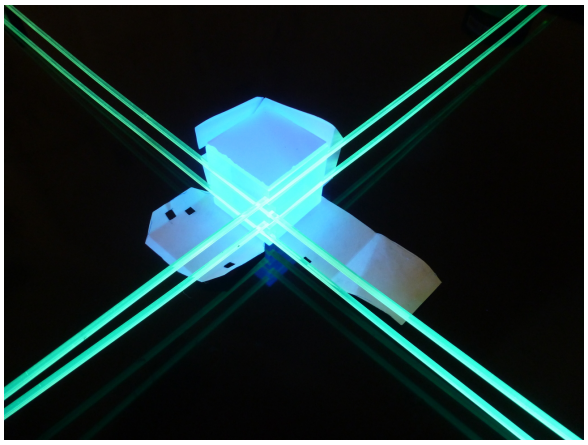

Figure 7.6: Picture of a SoLid cube with its Tyvek wrapping opened, a ^{6}LiF:ZnS(Ag) sheet on top of the cube and four optical fibres. The cube is enlighted with UV light to highlight the detector components. On this prototype cube, the fibres were going along two faces of the cube instead of four faces in the final design.

7.3.3 Optical fibres

SoLid optical fibres are 3×3 mm^2 squared fibres produced by Saint-Gobain under the reference BCF-91A. The shape and dimensions of these fibres are well adapted to the Hamamatsu MPPCs S12572-050P 3×3 mm^2. They have a polystyrene core, an acrylic cladding and a fluor-acrylic cladding in the case of double clad fibres. The refractive indexes of these parts are respectively 1.60, 1.49 and 1.42. The BCF-91A optical fibres have been selected because they match both the PVT emission spectrum as well as the MPPC spectral response. These fibres shift blue light to green with absorption at 420 nm and emission peaking around 494 nm. The MPPC photon detection efficiency is maximal with 35 % at 450 nm but it is almost the same at 500 nm. The decay time constant of the emitted light of 12 ns is much shorter than the time difference between positron and neutron signals in the SoLid detector. This time difference is

dominated by the thermalisation and capture of the IBD neutron, which takes several tens of micro seconds [Abreu et al., 2017, Abreu et al., 2018b].

When the SM1 detector was constructed only single-clad fibres were available. However for the Phase 1 detector, Saint-Gobain was able to produce double-clad fibres. The test bench has been prepared with one single-clad fibre used in the SM1 detector and one double-clad fibre used for the Phase 1 detector going through the same cube at the same time to be able to compare both. The two MPPCs are each connected to one of the fibres and the other extremity is left free to avoid reflections. The assembly is mounted on the rail to allow cube translation along the fibres. The result of 12 measurements along the fibres at different cube positions is presented in figure 7.7.

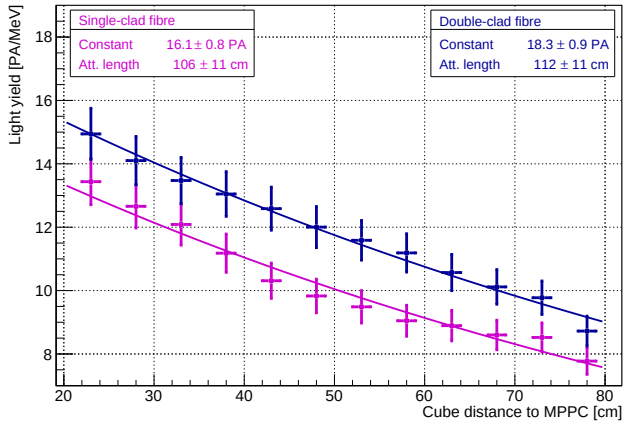

Figure 7.7: Comparison of single-clad and double-clad BCF-91A optical fibre from Saint-Gobain used in the SM1 prototype and SoLid Phase 1 detector. The measurements were performed at the same time with a single cube and a single MPPC readout per fibre. The uncertainties corresponds to a 5 % systematic uncertainty on the Y-axis and a 1 cm positioning precision on the X-axis.

The exponential decay fit of the light yield as a function of the distance shows that about 15 % more light is trapped by the double-clad fibre ('Constant' parameter of the fit). The attenuation length for single and double-clad fibres are respectively measured to 106±11 and 112±11 cm. Thus we don't observe difference in the attenuation lengths for both fibres with this measurement method. Varying the fit range on the data shown in figure 7.7 gives a systematic uncertainty for this measurement, resulting in a change in light yield by 10 % and the attenuation length by 20 %. These results show that double-clad fibres give an improvement in term of light yield compared to single-clad fibres. Therefore, the double-clad fibres are used for the SoLid Phase 1 experiment.

7.3.4 ^{6}LiF:ZnS(Ag) neutron screens

The SoLid neutron screen (NS) is a ^{6}LiF:ZnS(Ag) scintillator from Scintacor. The neutron capture on ^{6}Li produces two nuclei ^{3}H and ^{4}He sharing a kinetic energy of 4.78 MeV. This energy is converted into scintillation light which enters in the PVT cube and is subsequently collected by the optical fibres. The ^{6}LiF:ZnS(Ag) scintillator emits light with a maximum emission at 450 nm, close to the PVT emission, so the collection will be similar as for the plastic scintillator. It is a slower scintillator with a decay time of about 80 µs. This time difference makes it easy to distinguish between light produced in the PVT and in the NS scintillators. The NS has a thickness of about 250 µm and a molecular LiF to ZnS ratio of 1:2. Three types of NS produced at different times are used for the construction of the SoLid

Phase 1 detector. The first two generations were fragile so a third generation was produced with a less fragile substrate as backing.

PVT scintillator light yield measurements with the different types of NS have been performed. Two NS per PVT cube were used, similar to the SoLid Phase 1 detector design. A light yield of 27.2 PA/MeV for the oldest generation of NS, 29.9 PA/MeV for the second generation and 29.8 PA/MeV for the NS with a less fragile backing have been measured. The oldest generation results in about 10 % lower light yield. The three types of screens had to be used for the construction of the SoLid Phase 1 detector. Because of this lower light yield and greater fragility, the oldest ^{6}LiF:ZnS(Ag) scintillators are used in the external layer of the detector planes where neutron detection efficiency is lower because of edge effects.

When neutrons interact in the NS the emitted light will have to go through the plastic scintillator before being trapped in the fibre. Since the sensitivity of the light yield to the wrapping material is large, an important impact of having a NS between the cube and its wrapping is expected. For the SM1 prototype only one NS per cube was used. For the SoLid Phase 1 detector, two NS will be used since simulation studies have shown that neutron detection efficiency could significantly increase, reducing at the same time the neutron capture time. One of the screens will be oriented perpendicular to the antineutrino direction to increase efficiency. The second NS will pass along a fibre between the PVT scintillator and the Tyvek (section 7.4).

To check this hypothesis, the light yield measurements were performed for a cube wrapped with SoLid Phase 1 Tyvek and either one fibre without NS, or with one NS sheet on a face without fibre, or with the same NS on a face where the fibre is going through the cube. For these three configurations respectively 33.6, 30.6 and 29.7 PA/MeV were measured. The first drop of about 9 % confirms that adding ^{6}LiF ZnS:Ag decreases the PVT light yield. The loss is then only $\sim$3 % when the surface of one NS is parallel to the fibre. This effect is close to our systematic error but is significant.

In conclusion for the SoLid Phase 1 detector, the plastic scintillator light loss due to the NS will be limited to about 12 % thanks to the fact that one of the two NS sheets will be placed along an optical fibre between the PVT scintillator and the Tyvek instead of covering a face of the cube where no fibre is going through.

7.4 Detector configuration studies

In this section the detector design and configuration will be studied for what concerns the light yield of individual scintillator cubes.

7.4.1 Position of the fibres in the scintillator cube

For the SM1 cubes, squared 5×5 mm^2 grooves at the surface of the cube were holding the 3×3 mm^2 fibres (figure 7.8 left). This design was relatively easy to machine and allowed for easy detector assembly. For the SoLid Phase 1 cubes a design was considered with the fibre going through the core of the cube to have more scintillating material surrounding the fibre. Cubes with circular holes drilled through the scintillator were tested and resulted in a 10 % increase in light yield. However, when considering the machining time, the cost and a possible heating damage to the scintillator during drilling, this design solution was not selected. Several positions for the surface grooves where then considered, but the actual position of the grooves turned out not to be important for the light yield. Hence the position of the grooves was driven by the detector mechanical design. The scintillator cube design has been optimized with four grooves on four faces with 2.5 mm spacing as shown in figure 7.8 right. The four fibres remain in the 16×16 cubes plane to allow the stacking of the detector planes along the neutrino direction.

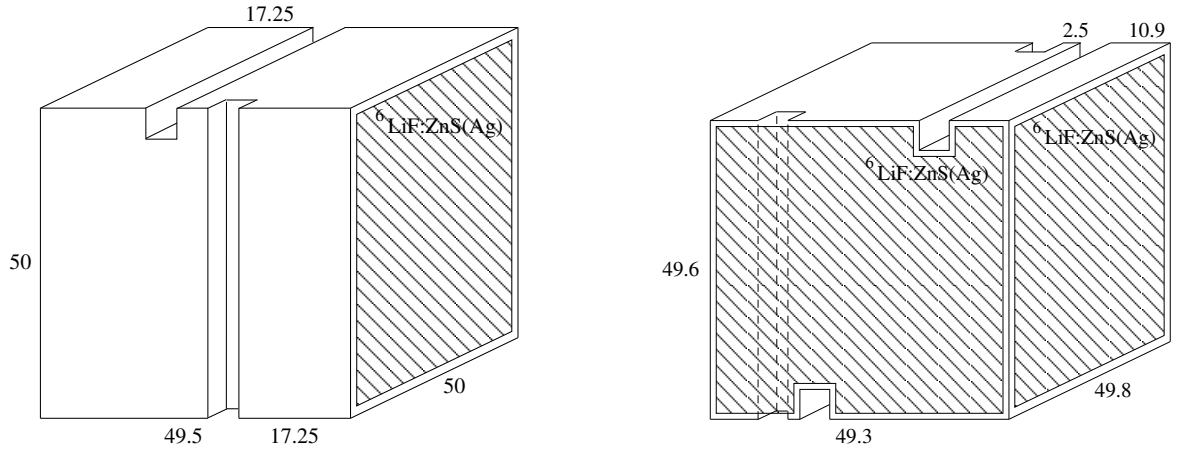

Figure 7.8: Design of the SM1 (left) and the SoLid Phase 1 (right) PVT scintillator cubes with two and four 5×5 mm^2 fibre grooves respectively. The position of the ^{6}LiF:ZnS(Ag) screens is indicated. Lengths are given in mm.

The SM1 detector was limited to two fibres per cube with a single readout. One potential optimisation would be to have a double readout per fibre. Another option would be to have 4 fibres with a single readout. Both options result in a higher light yield. To decide which option is best a comparison was performed between single and double readout of a fibre. The test bench does not allow for reading out four fibres. Therefore, the measurement consisted of measuring the light yield of one fibre read out by one MPPC on one end and with or without a mirror at the other end of the fibre. The materials used were selected based on the studies in section 7.4. With mirror we measured 25.3 PA/MeV and without mirror 15.9 PA/MeV, which is an improvement of 60 %. For a double readout, the light yield of a fibre without mirror would be doubled. For two such fibres, we would therefore obtain 63.6 PA/MeV. For four fibres with single readout and a mirror, the light yield would become 101.2 PA/MeV. Based on this estimation, the latter configuration would be preferred. However, putting more fibres in the cube will reduce the amount of light collected per fibre. To quantify the reduction of the light yield due to the presence of other fibres an additional measurement is performed. A reference fibre is inserted in the cube with a double readout. Additional fibres are then inserted one by one into the cube and the light yield for the first fibre is measured. Since the cube is already machined with four grooves this measurement cannot take into account a possible light reduction produced by the grooves themselves. The result is presented in table 7.1. Each new fibre that is introduced takes on average ∼15 % of the light from the first one. The third row in the table 7.1 shows that ∼16 % less light is collected per fibre with the two fibres design and 40 % less light per fibre in the four fibres design. With this reduction, the estimated light yield for the two fibres with double readout is 53.4 PA/MeV compared to 60.7 PA/MeV for the four fibres with single readout and a mirror. Hence, the configuration with four fibres with single readout performs 15 % better in terms of light yield. The stochastic term of the energy resolution is also improved from 14 % to less than 13 % at 1 MeV. Moreover, the four fibres configuration with single readout and mirror also improves the detector uniformity, as discussed in section 7.5. Based on these studies, the four fibres configuration with single readout was adopted for the SoLid Phase 1 detector.

To verify whether the four fibres are collecting the same amount of light, we have measured the light yield four times, moving the same fibre each time in a different groove. These four measurements give a light yield that is consistent within 4 %, which is smaller than the systematic uncertainty. Hence the location of the fibre does not matter in terms of light yield. We also rotated the cube along the fibre direction to check different faces of the scintillator cube. We do not observe differences in all these measurements either. These tens of measurements

Table 7.1: Impact of the number of double-clad optical fibres inserted in the plastic scintillator grooves on the light yield of the first fibre with double readout. Adding other fibres decrease the light-yield per fibre but increases the total light-yield.

Number of fibres	**1**	**2**	**3**	**4**
light yield for the first fibre [PA/MeV]	33.1	27.6	24.1	19.8
Variation to previous [%]	-	-16.4	-12.9	-17.6
Variation to 1 fibre [%]	-	-16.4	-27.2	-40.0
Total light yield [PA/MeV]	33.1	55.2	72.3	79.2

indicate that the scintillation light is uniformly distributed in the scintillator volume, confirming the results in section 7.1 where the response for localized electron interactions and gamma interactions in the whole scintillator volume are compared.

7.4.2 Reflector at the end of the optical fibre

The impact of using a mirror at one end of the fibres has been shown. Therefore we investigated the impact of the type of mirror. For the SM1 fibres, an aluminium sticker mirror was used. We have explored different other options and tested aluminised mylar film. The aluminium has a standard thickness of ∼200 nm. Several thicknesses for the mylar were possible, but showed no differences in light yield. A mylar thickness of 70 µm was selected for its rigidity, which is more convenient when inserting the end of the fibre in the 3D printed connectors. We compared the mirror used in SM1 and the aluminised mylar mirror using the same cube and the same fibre with a single MPPC readout. We measured the light yield for six distances along the fibre in both cases. The result is presented in figure 7.9. The function used for the fit is given by equation 7.1, which is taking into account the reflection at the end of the fibre with the mirror.

$$f(x) = C\ (e^{-x/L_{att}} + R\ e^{-(2\times L_{fibre}\ -\ x)/L_{att}}) \tag{7.1}$$

where C is a normalisation coefficient, L_{att} is the attenuation length in cm, R the light reflection coefficient of the mirror and L_{fibre} is the total length of the fibre, which is 92.2 cm.

In order to compare only the reflection coefficient, the normalisation coefficient and the attenuation length are fixed to 24.7 PA/MeV and 112 cm, respectively, as determined from previous measurements. We find that the SM1 mirror has a reflection coefficient of 73 ± 6 % while it is 98 ± 6 % for the other mirror. Consequently the aluminised mylar mirrors have been selected for the SoLid Phase 1 detector. The effect on the total light yield per cube depends on its position along the fibre because of attenuation. For example this mirror would produce an increase of light yield per fibre of 5 % for the cube farthest to the mirror, 7 % for a cube at the centre and 11 % for the cube closest to the mirror.

7.4.3 Impact of neighbouring cubes

In the SoLid Phase 1 detector the cube and fibre environment is different than that in the test bench. Indeed the fibres will be surrounded by scintillator cubes along their full length. This could have an impact on the light yield for a single cube or on the attenuation length. We performed a test with 16 cubes positioned along one double clad fibre, which is read out by two MPPCs. Considering the central cube, we observe an increase of the light yield of 12 % compared to the same measurement where only one cube was positioned along the fibre (figure 7.7). Since the ^{207}Bi source and the trigger system are free to move along the fibre the light yield of each of the 16 cubes was measured. The measurements are normalised to the sum of the two MPPC signals for each cube to cancel the potential effect of a different response for

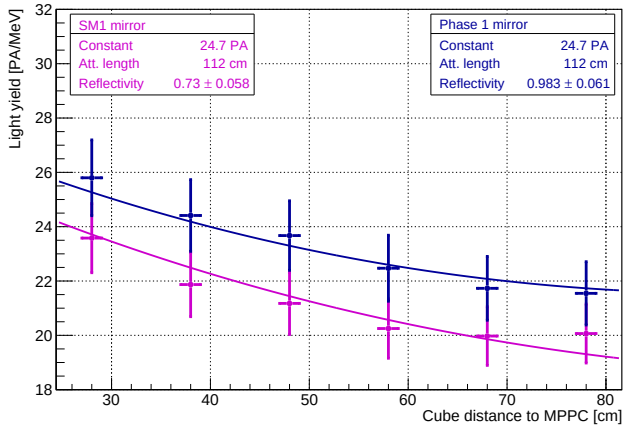

Figure 7.9: Comparison of the aluminium sticker mirror used for the SM1 fibres and the 70 µm aluminised mylar film mirrors used for the fibres in the SoLid Phase 1 detector. The cube and fibre used for the measurement is the same in both cases.

the cubes. The result of the attenuation measurement for the individual MPPC signals after correction is presented in figure 7.10. The attenuation length seems to increase a bit although the uncertainty is quite large. The difference between the two MPPCs is partially due to the difference in breakdown voltages. This measurement implies that the light yield will be better in the real detector where 16×16 cubes are assembled in planes compared to our test bench studies.

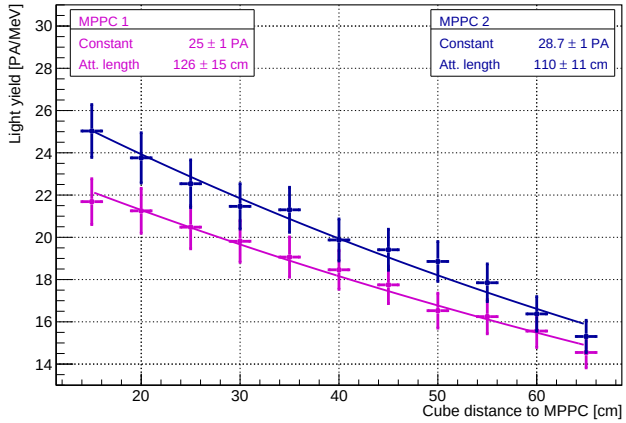

Figure 7.10: Attenuation along a double clad fibre going through 16 cubes with double readout. The MPPC light yield is corrected for the individual cube light yield that is different for each cube along the fibre.

A second effect we measure in this test, is the light escaping to neighbouring cubes. This optical cross-talk could for instance come from light going through the Tyvek, but is more likely to come from leaks through the holes in the Tyvek where the fibres pass. A second cube is placed next to the one interfaced with the calibration source. Two fibres were put through these two cubes perpendicularly to the fibre going through the 16 cubes. Some light has been observed in the neighbouring cube with a peak in the integral spectrum between 1 and 2 PA. After calibrating the light collected by this cube with the ^{207}Bi source, we conclude that in 90 % of the cases we record less than 10 % ($<$ 100 keV) of the light in the cube next to the source. The correlation with the integral spectrum of the cube with the source is weak (< 0.2) but this might be due to the low number of PA measured. Optical cross-talk should not affect

the energy reconstruction for the SoLid experiment since it is very low and the four channel readout per cube will allow for distinguishing the different light origins. We have performed the same test with the next to next cube but no light excess was visible.

7.5 Summary of the light yield improvements for the SoLid Phase 1

Table 7.2 summarizes all the improvements for the light yield of the Phase 1 detector based on the studies presented in this article. For improvements of the light yield quantified per fibre, one has to take into account that each cube in the SoLid Phase 1 detector will be read out by four fibres. The overall light yield improvement is expected to be around 150 %.

Table 7.2: Summary of all the light yield effects for the SoLid Phase 1 detector compared to the SM1 detector.

Detector component	**SM1**	**SoLid Phase 1**	**Relative effect**
Cube machining	$R_a = 0.45$ µm	$R_a = 0.04$ µm	+ 10 % per cube
Cube wrapping	75 g m^{-2}	105 g m^{-2}	+ 10 % per cube
Optical fibre	single-clad	double-clad	+ 15 % per fibre
Number of neutron screens	1 screen	2 screens	- 3 % per cube
Number of fibres	2 per cube	4 per cube	+ 40 % per cube
Mirror	aluminium	aluminised mylar	+ 7 % per fibre
Overall expected gain			+ 145 % per cube

In order to validate all these improvements for the SoLid Phase 1 detector design together, we performed two more measurements in a configuration as close as possible to either the SM1 or Phase 1 design. For the SM1 configuration we have used an SM1 cube with one SM1 neutron screen, SM1 Tyvek, two single clad fibres with each an MPPC on one end and an SM1 mirror at the other end. For the SoLid Phase 1 configuration, we have used a Phase 1 cube with two Phase 1 NS, Phase 1 Tyvek, four double-clad fibres with each an MPPC on one end and an aluminised mylar mirrors on the other end. Since the prototype amplifier board has only three channels, the measurement was repeated for the four fibres case changing only position of the MPPC for the two measurements.

For the SM1 configuration we obtain a total cube light yield of 18.6 PA/MeV and for the SoLid Phase 1 configuration 51.6 PA/MeV. This is an improvement of almost a factor 2.8, or 180 %, in the light yield for one cube of the new detector. This is better than the prediction computed in Table 7.2 which was a simple summation and was not taking into account all possible effects and the inter-dependence of effects. With this light yield the energy resolution target of $\sigma_E/E = 14$ % at 1 MeV has been achieved for the SoLid experiment.

The measured light yield for the SM1 configuration is almost 30 % lower than the observed value for the real SM1 detector, which was 24 PA/MeV [Abreu et al., 2018b]. This difference is certainly dominated by the impact of neighbouring cubes in the real SM1 detector. To lesser extent, it could be due to the different set-up or electronics. The result for the Phase 1 cube is in agreement with the calculation presented in section 7.4 where 60.7 PA/MeV was expected for four fibres in the same cube but without the two neutron screens. Adding two NS would reduce the light yield to 53.6 PA/MeV, which is in agreement with 51.6 PA/MeV measured in this last test given the systematic uncertainty of 5 %.

From this last measurement for a single cube at the central position of the 16×16 cubes detector plane and the attenuation length measurements (section 7.4) we can build the 2D

light yield maps for the SM1 and SoLid Phase 1 16×16 cubes planes. These are shown in figure 7.11. For the SM1 configuration the average light yield of a plane is 19.0 PA/MeV, with values ranging between 16.1 to 23.1 PA/MeV. The difference between these two extreme values is 43 %. For the Phase 1 configuration we observe a much more uniform light yield in the plane with only 6 % difference between the most extreme light yields (51.6 and 54.5 PA/MeV). The average value over the plane is 52.3 PA/MeV. This illustrates the strong improvement in light yield and uniformity expected for the SoLid Phase 1 detector.

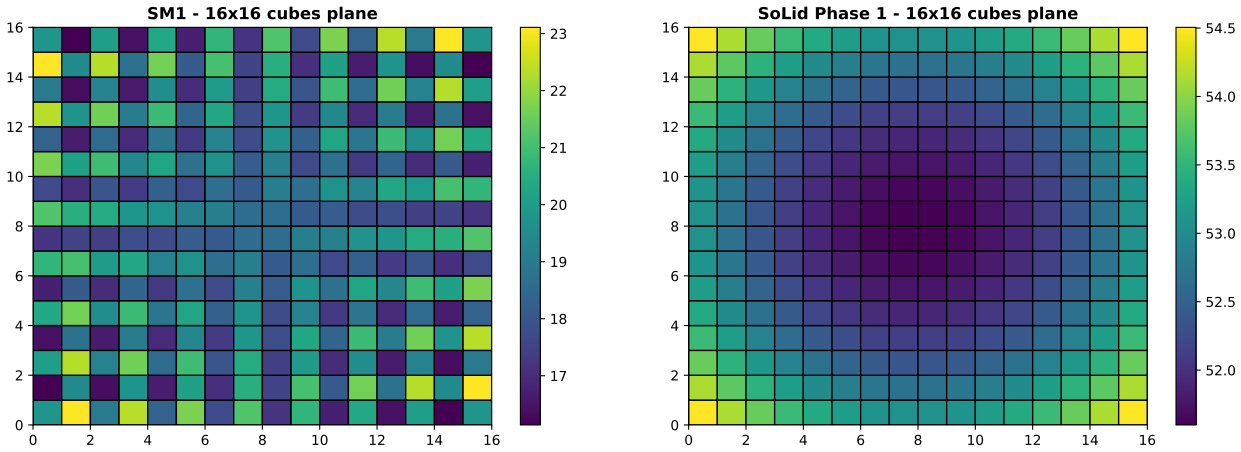

Figure 7.11: 16×16 cubes detector plane light yield maps for SM1 (left) and SoLid Phase 1 (right) extrapolated from the light yield measurements presented in this article. The average light yield is 18.9 and 52.3 PA/MeV for SM1 and SoLid Phase 1, respectively. The maximal difference, is only 6 % for the Phase 1 compared to 43 % for SM1.

Chapter 8

Energy calibration of the SoLid detector

The construction of the SoLid detector was realised by planes in Gent University involving all the members of the collaboration (some details can be found in [Abreu et al., 2021]). After assembly, each detection plane was tested on the so-called Calipso test bench that will be presented in this chapter. The LAL group with the major involvement of Luis Manzanillas, postdoc that I recruited thanks to the SoLid ANR funding, was in charge of testing the PVT response thanks to gamma calibration sources. We formed a team with Subatech and the PhD student David Henaff developed an analytical fit method for gamma spectra while we developed a numerical method based of GEANT4 simulations. This method was taken from the one I originally developed to calibrate the BiPo detector [Loaiza et al., 2017]. This work, called *quality assurance (QA)*, also including calibration with neutron sources in charge of LPC Caen, was compiled in the publication written by Luis Manzanillas [Abreu et al., 2019b].

At the start of the Phase 1 data taking, we continued and refined this work still in collaboration with Subatech. The contract of Luis Manzanillas ended in September 2019 and the task was then pursued by David Henaff [Henaff, 2021], Subatech PhD student, and Noë Roy [Roy, 2021], PhD student at LAL/IJCLab. I was the supervisor of the thesis of Noë Roy even after my change of affectation from LAL/IJCLab to Subatech in Summer 2020. The working group was convened by Benoit Viaud from Subatech.

This chapter will focus on the gamma calibration of PVT scintillator to which I participated and I supervised the work of LAL group. For more informations about the calibration of SoLid with neutron sources, to determine the anti-neutrino detection efficiency, please refer to the PhD thesis of Valentin Pestel from LPC Caen [Pestel, 2019].

Chapter contents

8.1 Quality assurance process

8.1.1 Calipso design

The Calipso system was designed at LPC Caen to perform a time efficient and accurate quality assurance process while constructing the SoLid detector [Abreu et al., 2019b]. The system is driven by a dedicated data acquisition system, which provides simultaneous control of the robots movement and data taking. Calipso has sub-millimetre precision $\mathcal{O}(0.5)$ mm in the XY axes (parallel to the detection plane) with adjustment in the Z axis. In neutron mode the planes are placed between plates of polyethylene (brown plates in the figure 8.1) and a neutron source is placed inside a polyethylene collimator (see details in [Abreu et al., 2019b]). In gamma mode, these PE plates are removed and a system for an external trigger is used, as shown on figure 8.2. This setup was proposed and designed by the LAL group.

A dedicated Monte-Carlo model (GEANT4 based), including Calipso and its direct environment was developed, in order to optimise the setup and the QA procedure. The ^{22}Na radioactive gamma source was simulated using the radioactive decay class.

8.1.2 Light-yield measurement

In order to assess the light-yield (LY) of each SoLid cube, a ^{22}Na gamma source was used, in conjunction with an external trigger. The external trigger consists of a PVT cube, readout by a short wavelength shifting fibre, coupled to an MPPC at each end. The system is contained within a 3D printed, externally mounting head; designed to combine the external trigger components, together with the ^{22}Na source as shown in figure 8.2.

^{22}Na decays via β^+ (90.3 %) and via electronic capture (9.6 %) into ^{22}Ne. In almost all cases, ^{22}Na decays into the first excited state of ^{22}Ne, which in turn decays to its ground state via the emission of a 1.27 MeV gamma. Hence, in 90% of the ^{22}Na decays the emission of a positron in conjunction with a 1.27 MeV gamma occurs; however, the e^+ annihilates inside the source capsule, emitting two back-to-back 511 keV gammas. These gammas are then used for the external trigger as illustrated in figure 8.2 (right). If one of these gammas interacts in the

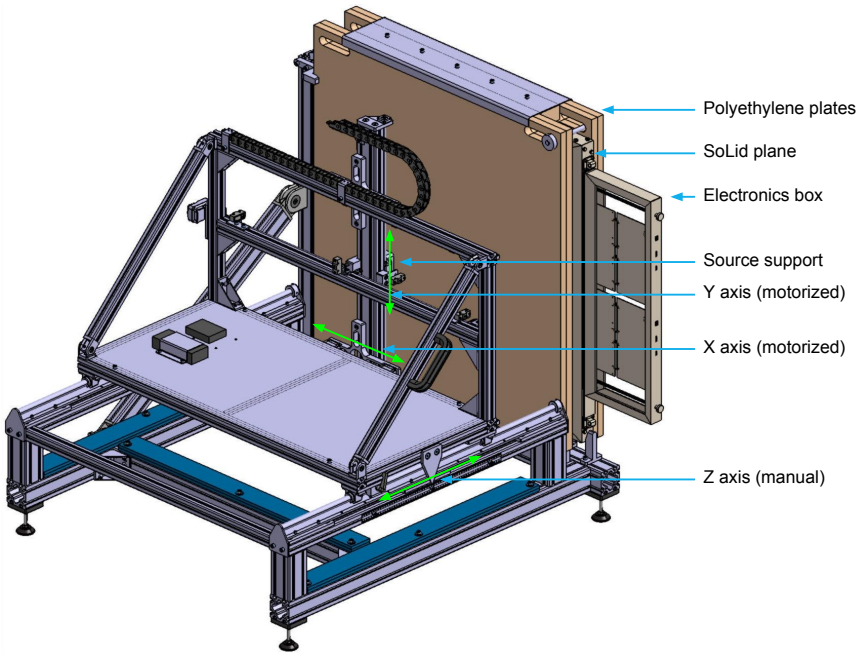

Figure 8.1: Illustration of the Calipso system for calibration of the SoLid planes. The Calipso robot provides sub-millimetre precision for accurate and consistent placement of the radioactive sources at any point in the XY plane.

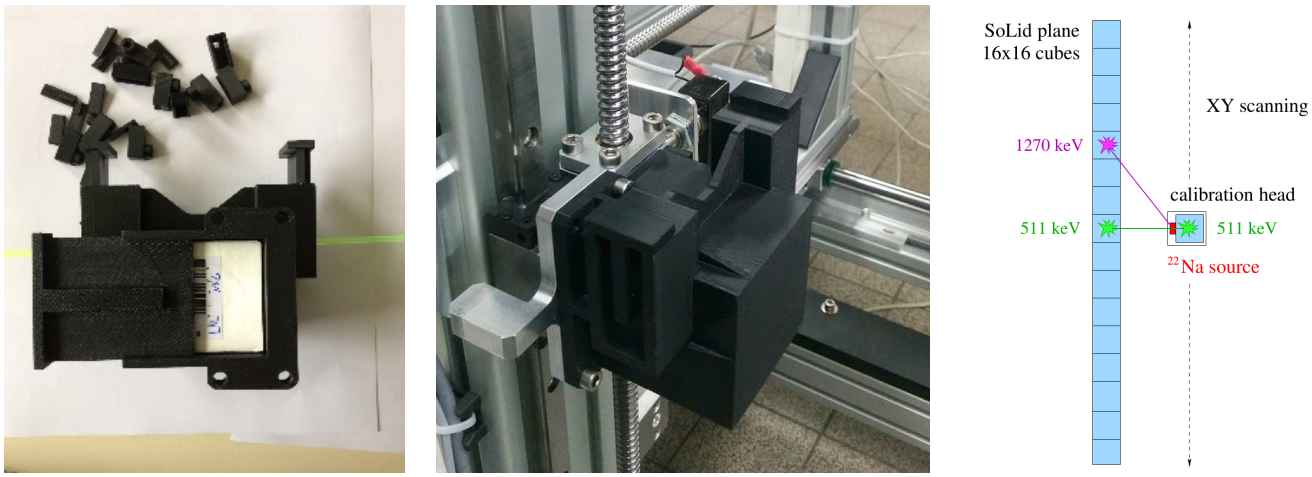

Figure 8.2: 3D printed external head for gamma calibration with the ^{22}Na source (splitted on the left showing the PVT cube and fixed to Calipso in the middle). (right) Principle of the external head triggering in coincidence with the 511 keV of the ^{22}Na source and cube calibration with the 511 keV and 1.27 MeV gammas.

external cube, we deem this a triggered event, and the full SoLid plane is readout. In this way, calibration samples with almost zero background can be collected. This allows an accurate calibration using the 1.27 MeV gamma, in conjunction with the 511 keV gammas. Accounting for the ^{22}Na source activity, the exposure time per cube was set to 30 seconds, in order to guarantee at least 15000 γ interactions in each PVT cube.

8.1.3 Determining the MPPC operating voltage

Before taking calibration data, the correct operation of all 64 MPPCs, within each frame, must be verified. The validation process began with an initial non-equalised over-voltage data

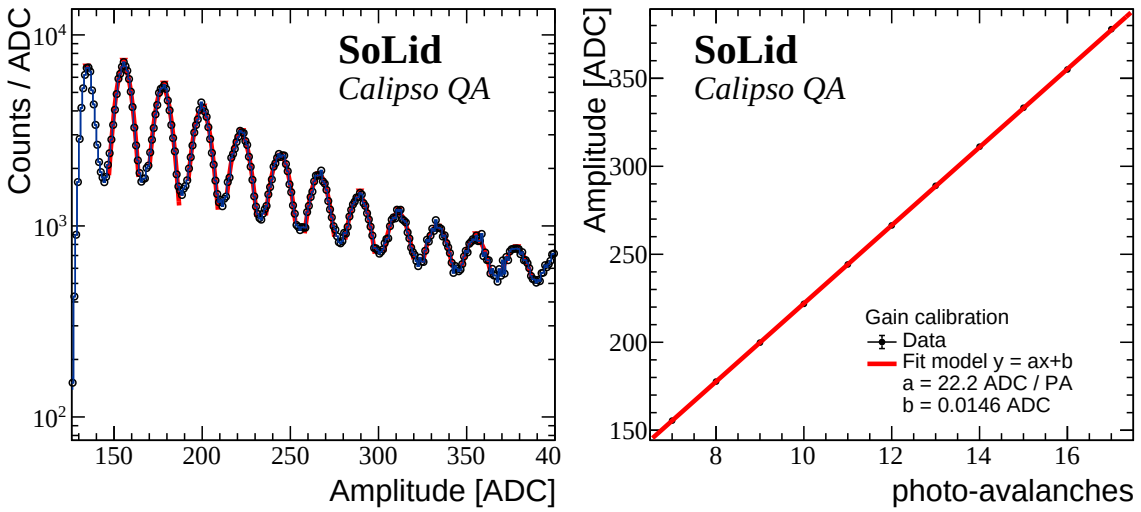

Figure 8.3: (left) Low amplitude part of the detected spectrum in an MPPC using the ^{22}Na source showing the individual PA peaks. (right) Linear fit of the PA peaks, where the slope corresponds to the gain.

run. In a few cases the initial run identified unresponsive MPPCs which were replaced before continuing with the process. As the operating breakdown voltage for each MPPC is different, and requiring all the MPPCs to operate with an over-voltage (OV) of 1.5 V, a voltage scan is required to determine the individual breakdown values. The voltage scan consisted of 25 runs using a fixed high voltage, close to the manufacturers nominal value in conjunction with a variable low voltage input. In these runs the gain of each MPPC was measured, which increased linearly with the OV. The individual breakdown voltages were identified by fitting the resulting gain values as a function of the varying voltage, and extrapolating to a gain of zero. For an OV of 1.5 V, a gain of about 22 Analogue-to-Digital Conversion units (ADC) per pixel avalanche was determined. Uncertainties in the estimation of the breakdown voltage, and the variation in gain response with voltage between the MPPCs, translated into the operational gains varying from channel to channel by about 3%. This methodology was further refined during calibration runs after installation at BR2 and achieved an equalisation variance at the 1% level.

8.1.4 Cube light-yield and signal reconstruction

The energy spectra of each cube can be computed by summing the total amount of light collected by the four MPPCs associated with the cube. Variations in gain from channel to channel need to be taken into account before summing the signals of the four sensors, as each MPPC has a slightly different breakdown response. Gains for the individual cubes are recalculated by identifying the PA values in the ^{22}Na energy spectra. Each PA peak position is fitted with a Gaussian function as shown in figure 8.3. A linear fit of the PA peaks amplitudes has a slope corresponding to the gain of the channel. The first peak in figure 8.3 (left) corresponds to the 6^{th} PA peak, and not the first one. This "shift" is caused by a zero suppression (ZS) threshold set to 5 PA used during the Calipso data taking in order to reduce the data rate. This reduction is needed since the QA is performed at standard room temperature ($\sim$25°), at which the dark rate of peaks below 5 PA is unacceptably high and would dominate the data taking. In this example, the gain is calculated to be 22.2 $\pm$ 0.01 ADC per PA. The intersection of the curve for 0 PA is 0.01 $\pm$ 0.07 ADC, in very good agreement with a linear response.

Once the MPPC gains aligned, the total ^{22}Na spectrum per cube can be computed to give the total amount of light collected in a given cube. To effect this, coincidences are sought between

the two vertical and the two horizontal sensors, coupled to the four fibres going through each cube. Thus, the total amplitude per cube A_{ij} in PA is defined as the sum of the four MPPC amplitudes divided by their respective gains.

Gammas from the ^{22}Na source (511 keV and 1270 keV) interact in the PVT mostly through Compton scattering. In addition, given the granularity of the detector planes, only a fraction of the total gamma energy is deposited within each PVT cube. Consequently no narrow photo-peak can be reconstructed within individual cubes. The light-yield must therefore be derived from a more complicated distribution, and two approaches were employed to this end. The first method consists in fitting the Compton edge profile of the spectrum by an analytical function and to compare the result with the predicted value. The second method compares the measured energy spectrum to a GEANT4 simulated sample varying the light-yield and the energy resolution. In the next two sections these methods are discussed in more detail.

8.1.5 Compton edge analytical fit

For a given cube undergoing calibration, we assume that a 1.27 MeV gamma interacts within the cube only via Compton scattering and, that the gamma only scatters once per cube. In this instance, the distribution of the true energy deposits of scattered electrons is defined according to the Klein-Nishina cross-section, σ_c [Siciliano et al., 2008, KLEIN et al., 2008]:

$$\frac{d\sigma_c}{dT} = \frac{\pi r_e^2}{m_e c^2 \alpha^2}\left(2 + \left(\frac{T}{E_0 - T}\right)^2\left(\frac{1}{\alpha^2} + \frac{E_0 - T}{E_0} - \frac{2}{\alpha}\left(\frac{E_0 - T}{T}\right)\right)\right) \tag{8.1}$$

where T represents the kinetic energy of scattered electrons, $\alpha = E_0/m_e c^2$, m_e the electron mass and E_0 the initial energy of the incident photon. This cross-section is peaked for energies approaching the kinematical limit for the energy transferred to the scattered electron, and displays an abrupt fall to zero above this energy. This *Compton Edge (CE)* is the strongest feature of this distribution and is used to determine the light-yield. Determining the CE position in the distribution of PAs, can be translated into a light-yield since the theoretical CE is well known since corresponding to an angle of deflection, θ, of the incident gamma of 180 degrees. This leads to the following equation:

$$E_C = T_{max} = E_0\left(1 - \frac{1}{1 + \frac{2E_0}{m_e c^2}}\right) \tag{8.2}$$

wich only depends of the initial gamma energy E_0 and the electron mass m_e. For gammas of 511 keV and 1270 keV the Compton edges are 341 keV and 1057 keV respectively.

Experimentally the Compton edge shape is smeared according to the energy resolution σ_0 of the detector. The CE value can be identified by fitting the energy spectrum profile according to equation 8.1, convoluted with a Gaussian function, in order to account for a stochastic energy resolution. The resulting *probability density function (pdf)* depending on the cube amplitude x in PA, can be written as:

$$f(x) = \left(\int_0^{E_C} \frac{d\sigma_c}{dT}(T)\ \frac{1}{\sqrt{2\pi}\sigma_0\sqrt{T}}\ \exp\left(-\frac{(x/ly - T)^2}{2\sigma_0^2\ T}\right) dT\right) \Big/ \int_0^{E_{CE}} \frac{d\sigma_c}{dT}\ dT \tag{8.3}$$

where ly and σ_0 are the cube light-yield and the energy resolution to determine.

Figure 8.4 shows the energy spectrum for a calibration sample in a SoLid cube with the ^{22}Na source. The Compton edge profile has been fitted using the *pdf* defined in equation 8.3. It is estimated at 85.8 PA, which can be translated in a light-yield of 81.2 PA/MeV for this cube. The energy resolution is estimated at 14.3 %, inline with the SoLid physics requirements. The accuracy of this fit has been evaluated with the Monte-Carlo. It was found that in the case of

the 1.27 MeV gamma from the ^{22}Na source, the estimation of the CE is biased by about +3.5%. This bias can be explained by cases of multiple scattering in the same cube, rather than the assumed single scattering, leaving a deposited energy per cube higher than E_{CE}.

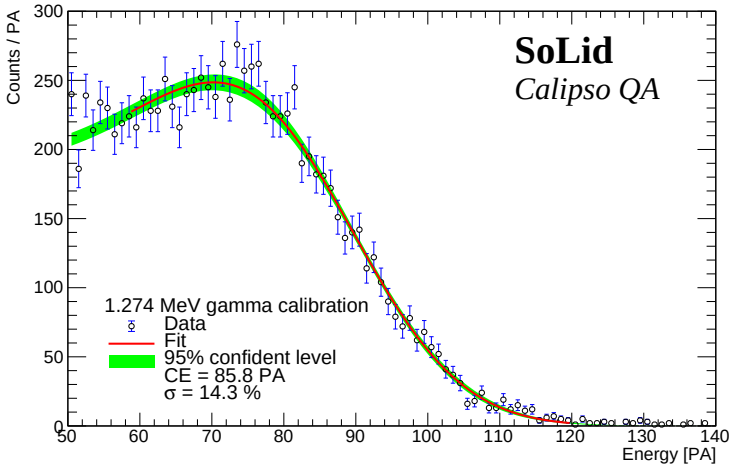

Figure 8.4: Compton edge profile of the 1.27 MeV gamma for a calibration sample in a SoLid cube using a ^{22}Na gamma source. The Compton edge is obtained by fitting the distribution with the *pdf* defined in equation 8.3.

8.1.6 Kolmogorov-Smirnov test

A second light-yield estimation is obtained by comparing a GEANT4 simulated ^{22}Na energy spectrum with the observed sample using a Kolmogorov-Smirnov (K-S) test [Karson, 1968]. The true deposited energy in each cube is used to build a set of spectra with different energy resolutions, varying from 5% to 20%. Each spectrum is then compared to the calibration sample for each cube, varying the light-yield from 50 to 120 PA. The light-yield is taken from the point of best agreement between the spectra of the calibration sample and the prediction. At this point the K-S test maximises its score.

Figure 8.5 shows the K-S test result for a specific cube giving a LY of 83 PA/MeV. For values where the data and the Monte-Carlo are not compatible, the K-S test returns zeroed values. Varying the section of the spectrum, the binning, and the number of steps used to maximise the K-S test, a systematic error of about 2% was estimated for this method.

Finally the two methods of CE analytical fit and K-S test were compared in order to validate the procedure and provide an estimation of the systematic uncertainties. Both approaches assume that the convolution product is correct, which means a Gaussian behaviour of the energy resolution at 1 MeV, and that the reconstruction efficiency is flat in E. Since only the region around 1 MeV is used, no sizeable effect for introduced errors has been found when using the MC. All other sources of systematic uncertainties are reasonably assumed to be measured by the difference between the two approaches because they are based on completely different assumptions; the analytical fit supposes that there is only one single scattering per cube per event, while the K-S test assumes that the GEANT4 simulation is correct.

A very good agreement was found between the values of LY obtained using the K-S test and the method of fitting with an analytical Compton *pdf* after bias correction as shown in figure 8.6. The difference between both methods remains at less than 2%. The tails on the sides of figure 8.6 corresponds to cubes with one problematic channel, where the accuracy of the analytical fit is less good.

The K-S test method was deemed more rigorous when looking to automate the procedure for the 12800 cubes, and so this test was used during the QA process prior to the detector

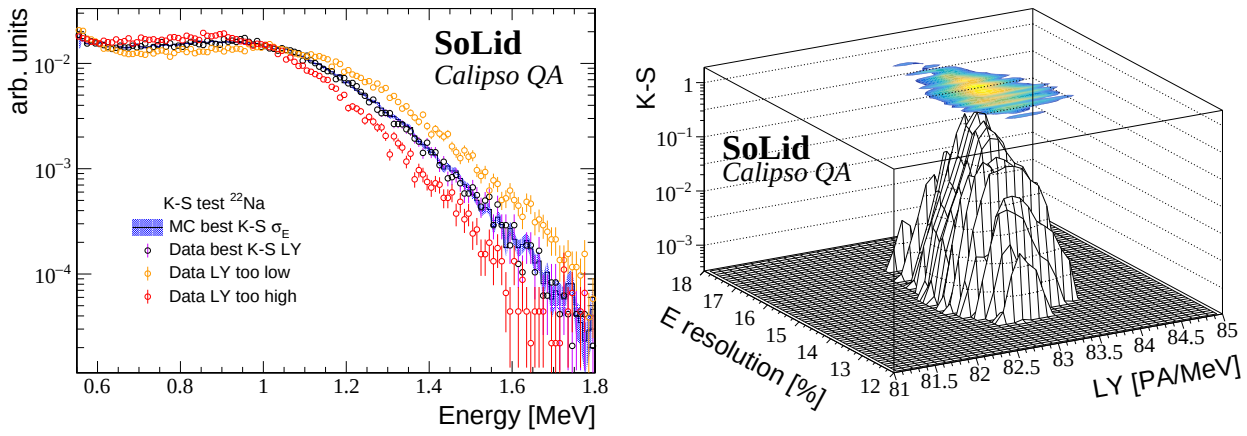

Figure 8.5: (left) Data compared to MC for different values of LY. Violet corresponds to a LY value where the K-S test is maximised, while the red and yellow show two cases where the LY is found to be too high and too low respectively. (right) Distribution of the K-S test values in the parameter space of energy resolution from MC and light-yield from the data. The K-S test takes values of 0 when the data is not compatible with the predicted spectrum, and take positive values when agreement is found.

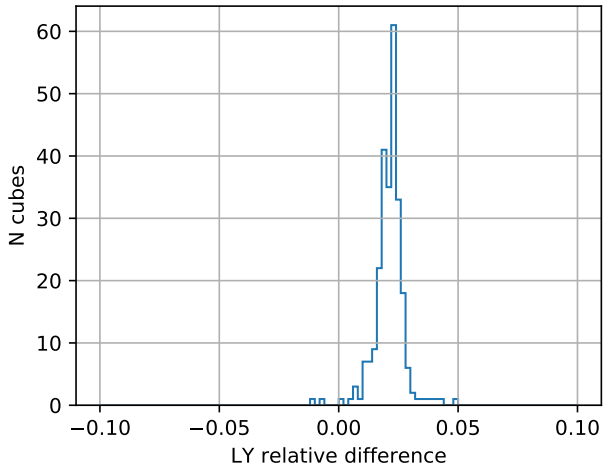

Figure 8.6: Relative difference in the light-yield results for frame number 10 using the analytical fit and K-S test methods. A relative difference of about 2% can be observed, which can be due to the cuts used for the sample selection for the analytical fit.

construction. The evaluation of the light-yield thanks to this QA process allowed an early identification of possible defects of the detector assembly like MPPC of mirror bad optical coupling to the fibre. In these cases, a manual intervention allowed to recover good performances and to prepare the best possible detector before integration at BR2.

Calibration samples for all 50 frames were collected; as such the LY of each SoLid cube was evaluated prior to detector assembly. For the in-situ calibrations at BR2, a combination of the two approaches are continually being used, providing a good control of systematic uncertainties.

8.1.7 Light-yield results

This initial calibration with Calipso served not only for quality assurance purposes, but also to obtain a first estimation of the light-yield. An average light-yield of 83 PA/MeV before

MPPC cross-talk subtraction was measured, as can be observed in figure 8.7. Because of time constraints it was not possible to take dedicated cross-talk measurements with the Calipso system. However, the MPPC cross-talk has been estimated through other means at 17% for an OV of 1.5 V [Abreu et al., 2018a]. Nevertheless, assuming a MPPC crosstalk of 17%, the final light-yield is expected to be larger than 70 PA/MeV, inline with the SoLid physics requirements.

A light-yield of about 70 PA/MeV should allow to reach an energy resolution of around 12%, that is better than the original requirements of SoLid. Moreover it could be improved, since the Calipso calibration data was taken at 1.5 V overvoltage, while the full detector will operate at BR2 at 1.8 V overvoltage thanks to detector cooling. The photon detection efficiency would increase by about 15 %, going from 24 to 27.5 %.

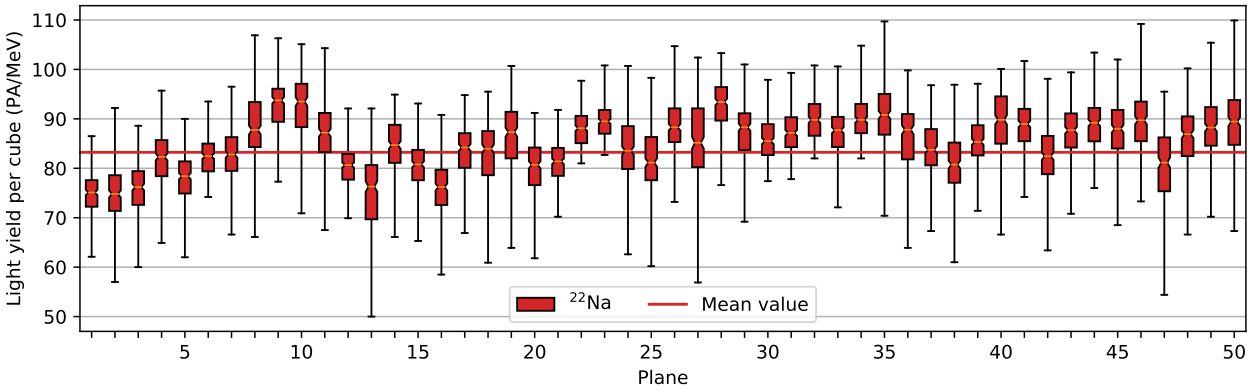

Figure 8.7: Candle plot for the light-yield of the 50 planes of the SoLid detector obtained with ^{22}Na gamma source. An average of 83 PA/MeV/Cube was found without MPPC cross-talk subtraction, which is estimated to be around 17 %. Orange line represents the mean value of each plane, while filled boxes represent cubes between the first and the third quartiles (50% of the data points). Black lines represent cubes below and above respectively the first and third quartiles.

8.2 Energy calibration of the SoLid detector

This section will now present the methods and results of the energy calibration of the SoLid detector at BR2. As already mentioned in the introduction, the energy calibration of the SoLid detector was the thesis work of David Henaff [Henaff, 2021] and Noë Roy [Roy, 2021]. It was initiated by the work done with Calipso, but it was highly improved in precision and robustness during calibrations at BR2. Over the two years data taking of the Phase 1, ten energy calibration campaigns were realized with different sources and tests. As the detector response can vary over time, the energy calibration work consisted in providing the best calibration parameters, for a given time period, for each of the 12800 cubes of the SoLid detector.

Most of the numbers and plots presented here corresponds to the September 2018 calibration campaign.

8.2.1 Channel equalisation

Prior to the energy calibration itself, it was necessary to survey the stability of the electronics over time. At the start of the SoLid Phase 1, all the 3200 MPPC channels were equalized in gain at 1 % to 31.5 ADC/PA [Abreu et al., 2019a]. Because of environmental variations, like temperature or humidity changes, the gains are expected to slightly vary over time. This has been studied by Noë Roy as presented in his thesis [Roy, 2021]. He has computed all the gain

corrections and set databases for the data processing. This was performed using a small sample of data that were automatically processed, approximately every 8 min by the DAQ. Combining these data over 6 hours time range, the gains were computed from the individual PA peaks for each channel (with the same procedure similar as in section 8.1.4). The electronics revealed to be very stable since the gain variations remain within 2 % over the whole Phase 1 data taking period.

Lower variations of the channels pedestal have also been observed over time and corrected in the same way. The pedestal drift is computed from the intercept of the linear fit of the signal amplitudes versus the photo-avalanche number from the same data as for gain corrections. The pedestal drifts over the whole Phase 1 data taking period remained well below 1 %.

At this stage, we can synthesise the extraction of the number of photo-avalanches detected A_i from the measured signal amplitude a_i for a channel i, with the gain g_i and pedestal drift p_i corrections, by this formula:

$$A_i \text{ [PA]} = (a_i \text{ [ADC]} - p_i \text{ [ADC]}) \ / \ g_i \text{ [ADC/PA]} \tag{8.4}$$

The first reconstruction of the number of photo-avalanches detected A_c in a SoLid cube c is then a sum of the amplitudes A_i of the four MPPC signals related to this cube:

$$A_c \text{ [PA]} = \sum_{i=1}^{4} A_i \text{ [PA]} \tag{8.5}$$

where the index i corresponds to the position of the MPPC in the SoLid detector plane: *top*, *bottom*, *left* and *right*. At the cube level, the energy deposited is expected to be shared equally in the four fibres. This was seen on the test bench data where no difference was observed between the four grooves of the tested cube, see section 7.4.

8.2.2 Fibre attenuation length and optical coupling

As expected from the test bench measurements and confirmed in the Calipso campaign, light losses occur from the collection in the scintillator cubes to the MPPCs. This can produce non-uniformities between the cubes of SoLid detector and needs to be corrected. The first cause is due to the attenuation of light during transport in the optical fibre because of scattering or absorption. This has been reduced to few percent by having two fibres in the same direction with alternated MPPC positions but it still needed to be considered. The second cause is due to optical coupling of the fibre to the MPPC at one end and to the mirror at the other end. It revealed too complicated to address these two parameters separately so the reflection at the mirror side has been fixed and inhomogeneities where only attributed to the coupling at the MPPC side.

At the start of the calibration process, a preliminary energy calibration is done using the numerical method in order to select the 1.27 MeV gamma from the ^{22}Na source. This allows to apply some quality cuts on the reconstructed cube to calibrate and to select events where this cube is isolated in the detection plane.

The first method developed to measure the attenuation lengths and the optical couplings, called the *sequential method*, is measuring the parameters one after the other.

Fibre attenuation length

To measure the attenuation of light along the fibre, we need to consider, for a given cube c, the fraction of light $f_{i,c}$ seen by each channel i:

$$f_{i,c} = A_{i,c} \ / \ \sum_{j=1}^{4} A_{j,c} \tag{8.6}$$

in order to avoid the light-yield variation from one cube to another along the fibre. This light fraction seen in the cubes along the fibre should follow a double exponential law:

$$f_{i,c} = C \times \left(\frac{1}{2} \exp(-\frac{d_{i,c}}{\lambda_i}) + \frac{1}{2} R_{mirror} \times \exp(-\frac{2L_{fibre} - d_{i,c}}{\lambda_i}) \right) \tag{8.7}$$

where $f_{i,c}$ represents the light fraction of the channel i in the cube c, $d_{i,c}$ is the cube c distance to the MPPC i, λ_i attenuation length of the fibre i, L_{fibre} the length of the fibres (92 cm), R_{mirror} the mirror reflectivity and C an arbitrary constant. The first exponential represents the attenuation of half of the light (factor 1/2 in the equation) that goes directly to the MPPC. The second exponential is the attenuation of the other half of the light that travels to the reflector at the other end of the fibre before going back to the MPPC. The coefficient R_{mirror} was fixed arbitrarily at 0.8 because of difficulties in fitting the attenuation lengths with too many free parameters. The value of 0.8 was chosen after measurements on test bench on several types of mirrors [Abreu et al., 2018a]. The same value was used in the simulation of the attenuation effect in order to have equivalent models in simulation and data.

The attenuation pattern was then fitted for every fibre of the planes such as presented on figure 8.8 with the data points for one channel and the exponential fits for all the channels of the detection plane. There is a very good agreement between this model and the data point since Noë Roy demonstrated that the residuals are centred at zero better than 1 % with a spread of $\sigma = 5$ %.

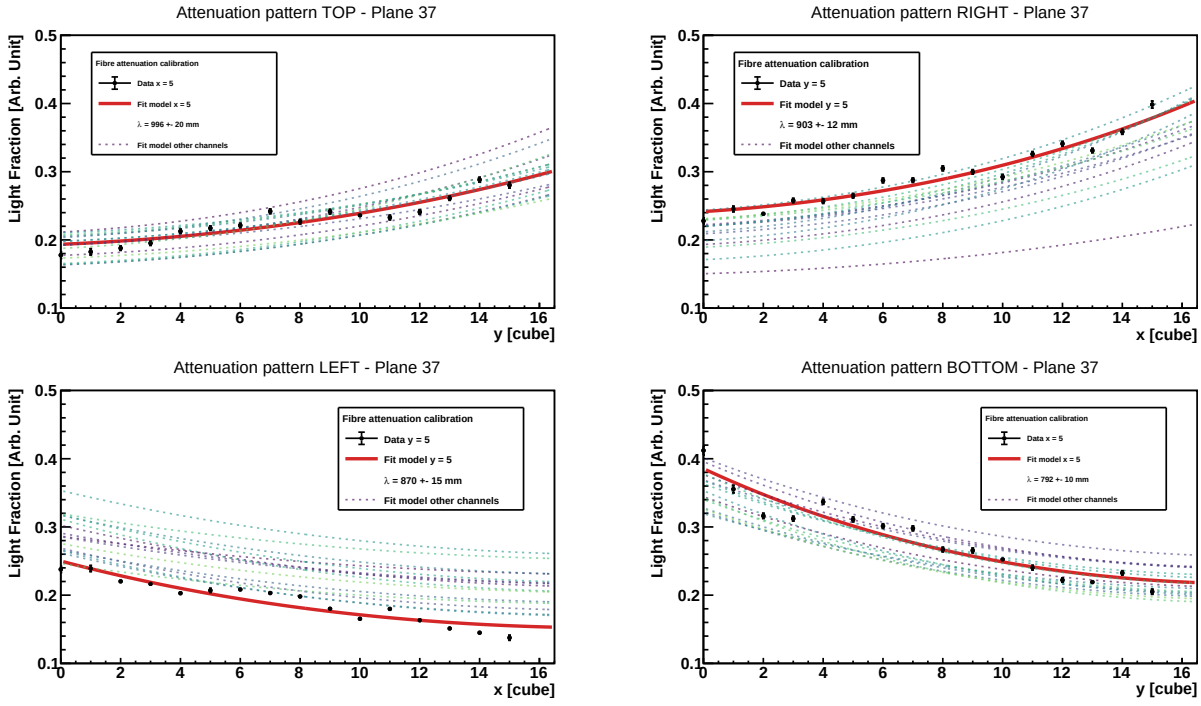

Figure 8.8: Fitted attenuation curves for the plane 37 using the equation 8.7. The black points are the data for the four channels of a cube. The red line is the attenuation fit of these channel. The dotted lines are the other fits of the plane for illustration.

The attenuation length distribution of all the SoLid optical fibres can be seen on figure 8.9. The average value is 97 ± 17 cm.

The number of photo-avalanches detected by the cube, previously calculated with equation 8.5, can now be corrected from the fibre attenuation with:

$$A_c \text{ [PA]} = \sum_{i=1}^{4} A_i \text{ [PA]} \times f_{i,c} \tag{8.8}$$

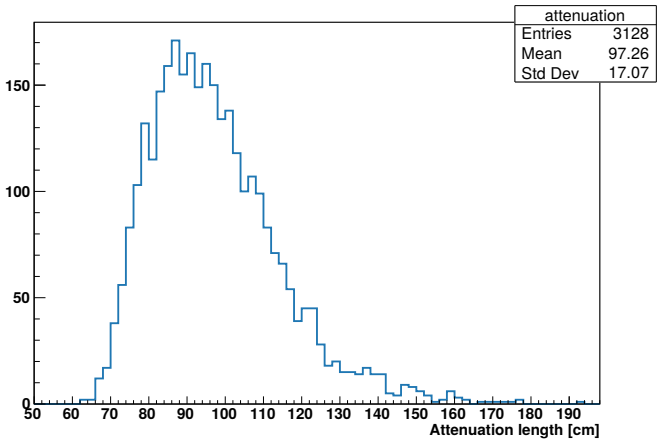

Figure 8.9: Attenuation lengths distribution for all the active channels determined by the sequential method.

Optical coupling

On figure 8.10 can be seen the amplitudes readout by the channels in the four sides of a plane after attenuation correction. The difference observed in amplitudes between the row and columns is due to the optical coupling of the MPPC with the fibre. To measure this coupling parameter $\epsilon_i^{coupling}$ for channel i, we compute the ratio of the average amplitude of a channel $\langle A_i \rangle$ respectively to the average amplitude $\langle A_j \rangle$ of all the 16 channels[1] in the same position of a plane:

$$\epsilon_i^{coupling} = \langle A_i \rangle \; / \; \frac{1}{16} \times \sum_{j=1}^{16} \langle A_j \rangle \tag{8.9}$$

The distribution of the measured coupling parameters is shown in figure 8.11. It has a Gaussian shape, centred at one by construction, with a spread of around 15 %.

The number of photo-avalanches detected by the cube, previously calculated with equation 8.8, can now be corrected from the fibre attenuation with:

$$A_c \; [\text{PA}] = \sum_{i=1}^{4} A_i \; [\text{PA}] \times f_{i,c} \times \epsilon_i^{coupling} \tag{8.10}$$

Asymmetry method

Even if the results are quite good with the sequential method, we can suspect interdependence between the measured attenuation lengths and optical couplings. In order to avoid this, a second method, named the *asymmetry method*, has been developed in Subatech. It consists in a simultaneous fit of the 128 parameters of a plane at once. This method is based on computing three asymmetries: *horizontal-vertical*, *left-right* and *top-bottom* for a given cube to cancel possible cube to cube light-yield dependence. This method also allows to take into account all the attenuation lengths and couplings of all the channels of the plane that could have affected the individual measurements in the sequential method. A global χ^2 is defined by summing the χ^2 of each asymmetry to perform the fit. Given the complexity of this fit, the initialization of the parameters comes from the results of the sequential method. A comparison of the two methods is presented in figure 8.12. The asymmetry method has been preferred

[1] this ratio is not computed over all the channels of a plane since we have observed systematic differences between the different positions: *top*, *bottom*, *left*, *right*, certainly due to mechanical construction effects.

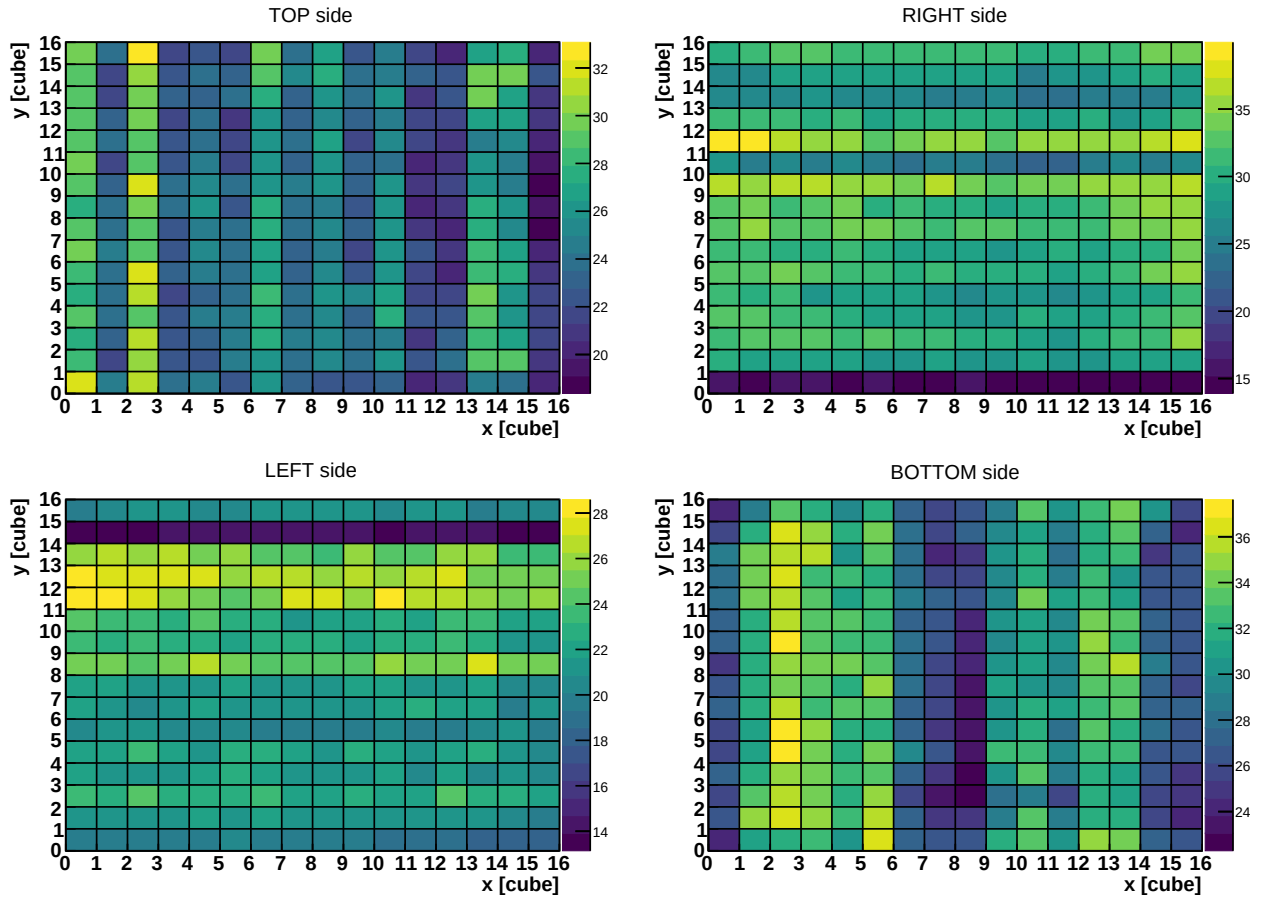

Figure 8.10: Amplitudes measured by the channels in the 4 sides of a plane after attenuation correction.

because it provides lower bias with a lower spread when comparing inputs to fit results on a ^{22}Na simulation.

The asymmetry method is presented in detail in David Henaff thesis [Henaff, 2021] and was maintained by Noë Roy who provided the parameters for data processing of Phase 1.

8.2.3 Cube energy calibration

After the determination of the fibre attenuation lengths and the optical couplings to MPPCs, only remains the individual cube light-yields to determine.

The two methods developed for the Calipso campaigns (see sections 8.1.5 and 8.1.6) have also been used here for the energy calibration of the SoLid cubes. Therefore we will only present here the improvements and the results of the calibration of SoLid Phase 1. Having two methods developed in parallel was a chance to find issues, improve the precision of both methods and finally determine the systematic uncertainties related to the energy scale and resolution. In order to perform a precision measurement of the anti-neutrino energy spectrum and a sensitive search for sterile neutrino, the target was to reach an understanding of 2 % or better on the energy scale.

Analytical fit

The main improvement in the analytical fit method compared to section 8.1.5 lies in taking into account the detector efficiency. Indeed the shape of the ^{22}Na energy spectra in calibrations with the full detector is impacted by selection cuts and reconstruction effects. The efficiency corrections are computed with a GEANT4 simulation. The detector effects are then applied to

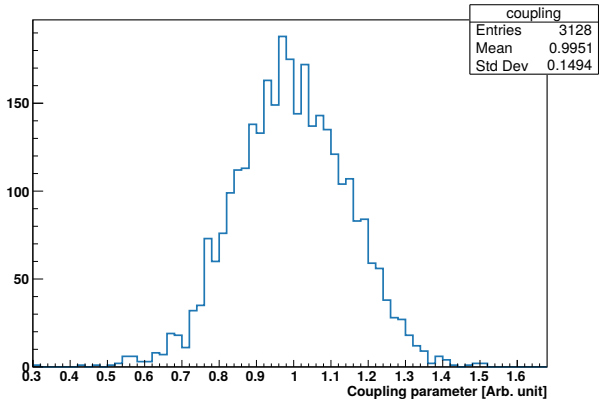

Figure 8.11: Coupling parameters distribution for all the active channels determined by the sequential method.

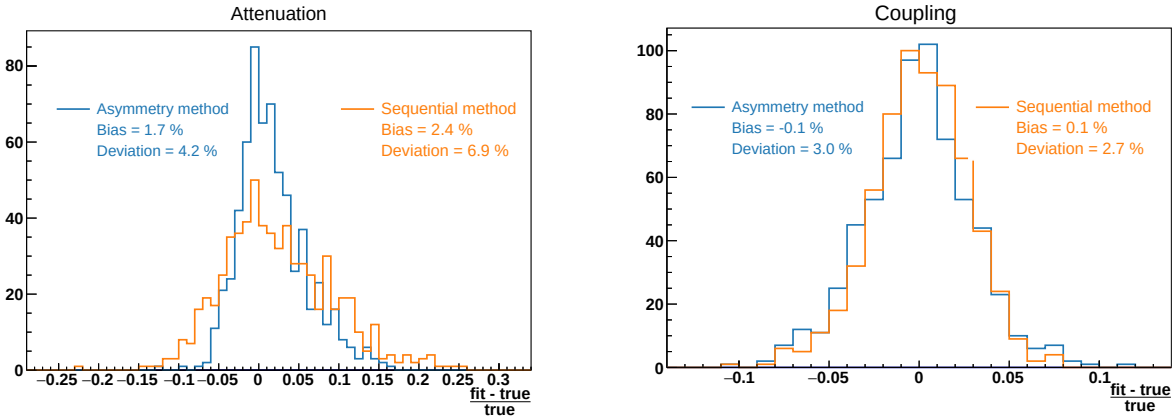

Figure 8.12: Comparison of the input parameters of a dedicated ^{22}Na simulation with the fit results of both calibration methods for attenuation length (left) and coupling (right).

the simulated events with the readout simulation and the events are reconstructed the same way as real data. For each cube, the ratio between the true energy spectrum of the reconstructed and selected events over the true energy spectrum of all the events is computed to correct the *pdf* (see equation 8.3). This is illustrated on figure 8.13. At low energy the drop in efficiency is due to the requirement to have signal in the four MPPCs to build a cube while one or more could be below the trigger threshold. At higher energies the inefficiency comes from the selection cuts and the interactions of the gammas in the same plane or in the detector. This effect results in a multiplicative correction factor ϵ_{reco}, depending on the energy, applied at the cube reconstruction. The factor is computed from a polynomial fit of the efficiency ratio seen on the bottom of figure 8.13.

The CROSS system (section 6.5.3) allows only to place the calibration sources in front or between the five SoLid detector modules, that is every ten planes. We therefore have to calibrate cubes up to five planes after the source and the ^{22}Na gammas might interact in the detector before reaching the cube to calibrate. The Compton edge region for these cubes is depleted compared to the cubes close to the source. In the numerical method based on GEANT4 this effect is already included but it was necessary to apply a correction for the analytical method. The multiplicative correction factor ϵ_{int}, depending on the detected energy T, is computed for each energy bin, $i = 0, ..., i_{E_C}$ of energy T_i up to the Compton edge E_C, by the ratio between the true energy deposited in the cube to calibrate and the energy deposited in the cube in front of the source. The final *pdf* as a function of the cube amplitude x in PA, compared to equation

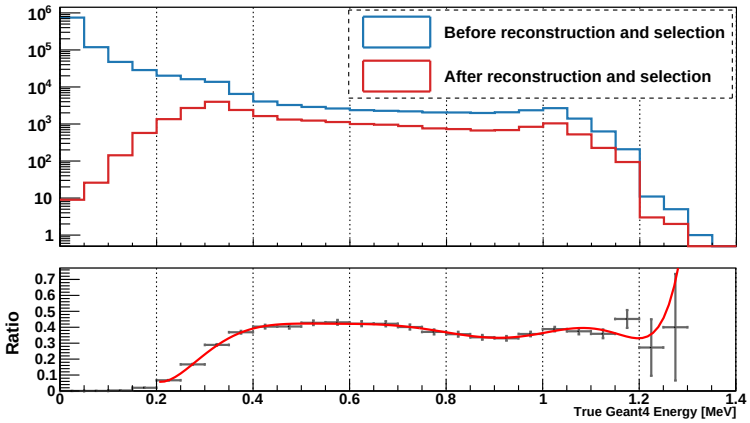

Figure 8.13: GEANT4 energy distribution of the gamma energy deposits in the ^{22}Na events. In blue is represented the distribution of all the simulated events and in red the energy distribution of only the selected and reconstructed events. The ratio between the two energy distributions is shown in the bottom with its polynomial fit.

8.3, where we want to determine the cube light-yield ly and energy resolution σ_0 becomes:

$$f_{conv}(x) = \left(\sum_{i=0}^{i_{E_C}} \epsilon_{reco}(T)\ \epsilon_{int}(T)\ \frac{d\sigma_c}{dT}(T_i)\ \frac{1}{\sqrt{2\pi}\sigma_0\sqrt{T_i}} \exp\left(-\frac{(x/ly - T_i)^2}{2\sigma_0^2\ T_i} \right) \right) \Bigg/ \left(\sum_{i=0}^{i_{E_C}} \epsilon_{reco}(T)\ \epsilon_{int}(T)\ \frac{d\sigma_c}{dT}(T_i) \right) \quad (8.11)$$

An example of calibration of a cube two planes away from the source with the analytical fit, without and with these efficiency corrections applied, is presented in figure 8.14. The impact on the spectrum shape is quite important, especially at low energy, but it only affects the determined light-yield by 1 % while it reduces the energy resolution of about 5 % in relative.

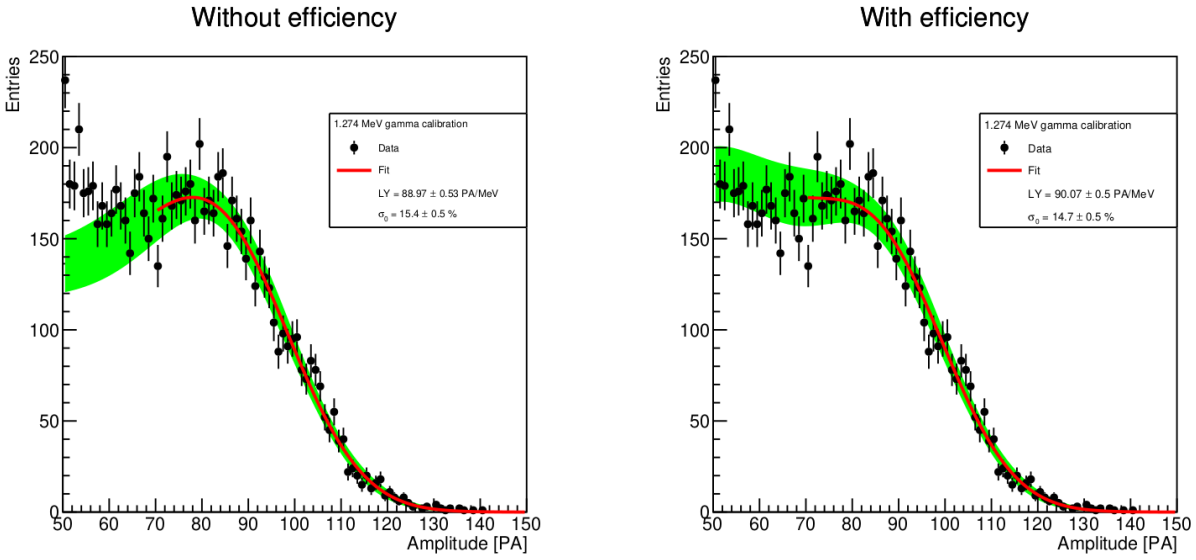

Figure 8.14: Analytical fit of a cube spectra from ^{22}Na calibration without and with efficiencies taken into account [Henaff, 2021]. The red line is the best fit and the green band corresponds to the 95 % CL interval.

Numerical method

The second calibration method, called the Kolmogorov-Smirnov test in section 8.1.6, is now called the *numerical method* to better correspond to the full process. It was a major part the thesis work of Noë Roy, under my supervision. The complete detector geometry at BR2 is simulated with the ^{22}Na source positions and the simulated energy spectra of each cube is convoluted with a Gaussian energy resolution. This resolution takes into account only a statistical term in the form of $\sigma_E = \sigma_0\sqrt{E}$. The data spectra is shifted in light-yield, ly in PA/MeV, and a statistical test is performed between the data and the simulation to find the best couple (ly, σ_0). An isolation of the cube in the plane is requested and the reconstruction efficiency as a function of energy compared to the true GEANT4 energy deposit is used, like in the analytical method. This time, the possibility that the gammas interact before reaching the cube is already taken into account by the full detector simulation. An example of fit of the 1.27 MeV gamma of ^{22}Na is presented in figure 8.15.

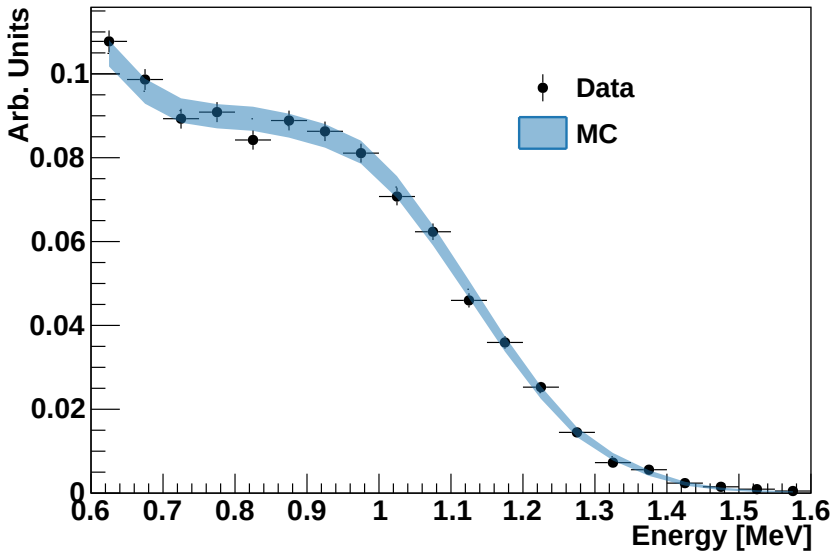

Figure 8.15: Numerical fit of a cube with the 1.27 MeV gamma of ^{22}Na [Roy, 2021]. The blue envelope represents the best convoluted GEANT4 energy spectra with the 1σ statistical uncertainty and the black points represent the data.

The original statistical test used a K-S approach but a chi-square χ^2 test was also used. The first test was expected to behave better in case of low statistics but thanks to the improvements on the energy calibration data taking, the χ^2 test behaved well. Both tests give similar results (ratio of 0.998 with a spread $\sigma = 0.013$ [Roy, 2021]) but the second one allowed to perform a $\Delta\chi^2$ analysis and derive an uncertainty on the calibration parameters used.

In the end, both methods were compared from dedicated simulations and with the calibration data. Applying the same selections criteria to the data conducted to a perfect agreement between the results of both methods, in terms of light-yield and energy resolution determination. The relative difference between numerical and analytical method on the light-yield show a Gaussian shape centred in zero with a spread of about 2 %.

In the end of the calibration process, from the individual equalized amplitudes A_i in PA of the MPPC signals of a cube c given by equation 8.5, the energy detected E_c in a cube c can be determined with:

$$E_c \text{ [MeV]} = \left(\sum_{i=1}^{4} A_i \times f_{i,c} \times \epsilon_i^{coupling}\right) \Big/ ly_c \text{ [PA/MeV]} \tag{8.12}$$

8.2.4 Cube light-yield uniformity

After a measurement of the individual visible cube light-yields, the homogeneity of the detector has been measured with a spread of 7% of light-yields. This is in very good agreement with the expectations from the test bench results presented in section 7.5. On figure 8.16 (left), is shown a map of the light-yield in the planes, averaged over all the planes of the detector. Since the light attenuation in fibres is only applied to the SoLid simulations, the attenuation pattern, with lower light-yield in the centre of the planes, is visible on this map. On the figure 8.16 (right) is plotted the distribution of the cube light-yields in the detector, the average light-yield is 96.3 ± 6.8 PA/MeV. The approximately 20 % MPPC cross-talk is not subtracted to this value since it is directly added to the readout simulations to reproduce the data. Taking into account the different settings of the MPPCs, this result is much higher than the light-yield expectations presented in section 7.5. We believe this is due to the presence of cubes all along the four optical fibres and the presence of extra Tyvek sheets due to neighbouring cubes and between the planes compared to the measurements with a single cube on the test bench, even though we have tried to quantify these effects during the test bench studies.

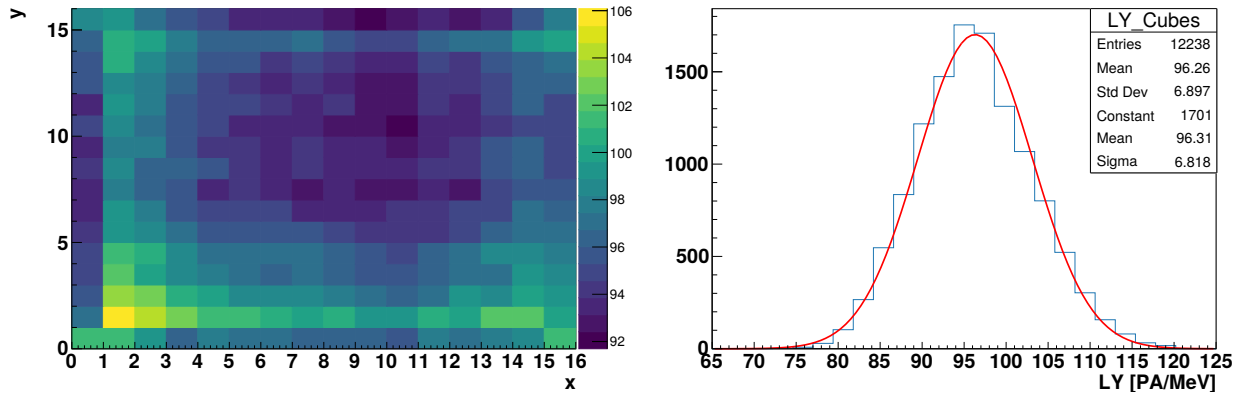

Figure 8.16: Left: light-yield by cube positions, averaged in z position. Right: light-yield distribution on the cubes with 4 active channels.

The variation of light-yield from one plane to another is represented on figure 8.17 (top) in the form of a candle plot. Almost 80 % of the planes are within ± 5 % interval around the mean value. Those variations are applied in the simulations to correspond to the data. For the current anti-neutrino analyses of SoLid, the detection planes are gathered in five modules to search for an oscillation signal. The average light-yield difference is lower than 5 % between the modules, as can be seen on figure 8.17 (bottom). This shows a good uniformity of the SoLid detector over its baseline.

To ensure that all the possible calibration effects have been taken into account in each plane, the intrinsic light-yield variations within each plane of the detector is computed. The intrinsic light-yield dispersion within each plane is the ratio between the corrected light-yield of each cube and the average light-yield of the plane. As shown on figure 8.18, the dispersion obtained for the whole detector has a 3 % spread, which shows a very good uniformity of the energy response within the planes. This 3 % effect will be treated as a systematic uncertainty for the antineutrino analysis.

8.2.5 Time evolution of the energy response

To survey the energy response of the detector over time, several calibration campaigns were taken during the Phase 1 of SoLid. For all those periods, the couplings, attenuation lengths

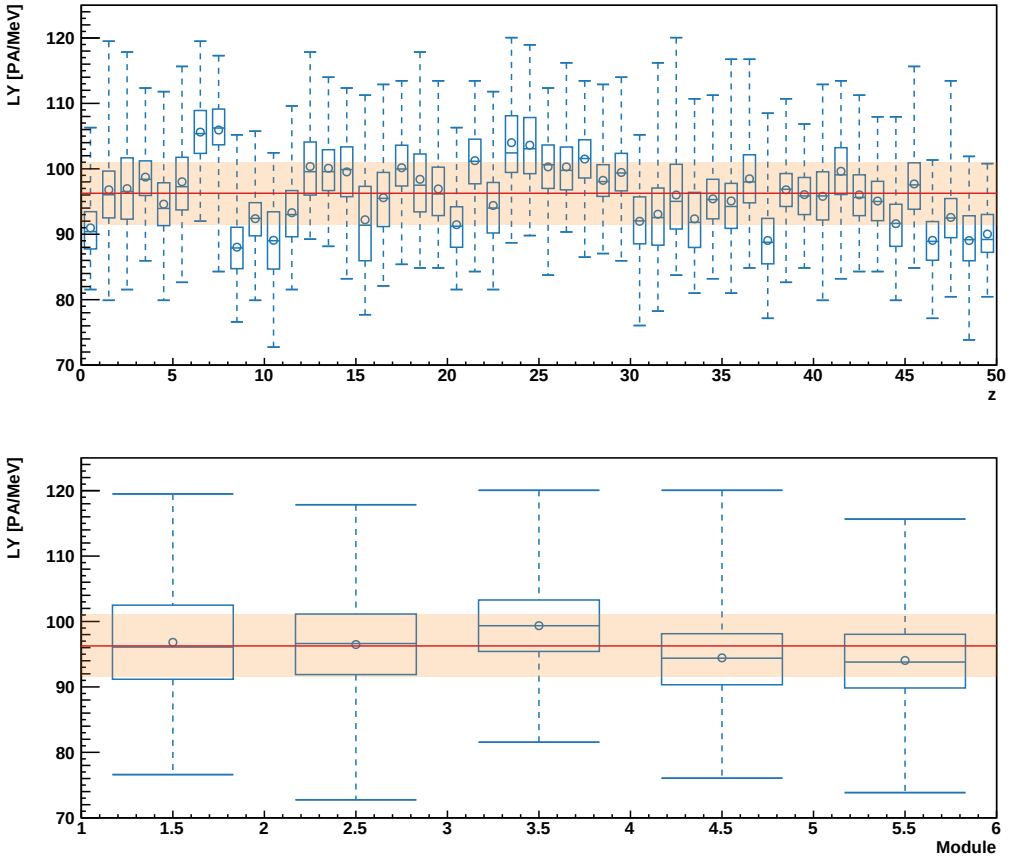

Figure 8.17: Top: light-yield dispersion per plane. Bottom light-yield dispersion per module. The red lines represent the average light-yield of the detector and the orange bands a 5 % variation.

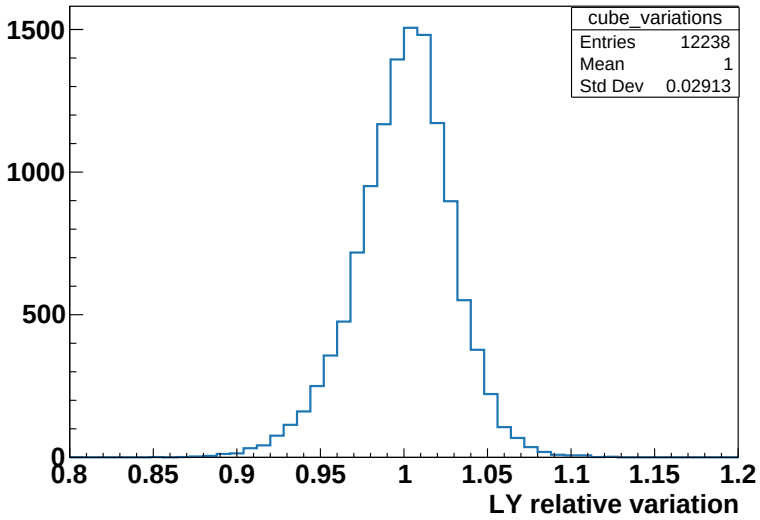

Figure 8.18: Relative light-yield variation with respect to the average light-yield of each plane. The light-yields here are corrected of the attenuation and coupling effects.

and light-yields have been measured with the methods presented in the previous sections. The light-yield evolution, through the two years of data of the SoLid Phase 1, can be seen on figure 8.19. The effect of the PVT ageing can be seen with a global decrease of the average light-yield through time. Two periods can be identified before and after May 2019, where the average light-yield dropped suddenly of few percent. This drop happened just after a chiller failure in

the detector container and an issue in the monitoring procedure during a maintenance of the detector. This leads to an increase of the temperature up to 50 °C at the detector level, instead of the usual 11 °C. It is believed that this heating caused a direct degradation of the PVT light-yield and could have accelerated the ageing from -1.2 % to -3.3 % per year. This would need to be confirmed by looking at some candle events, crossing muons or BiPo background, during physics data taking mode in a more regular time stepping. The total light-yield loss between the first and last calibration is -5.6 % in average over the whole detector.

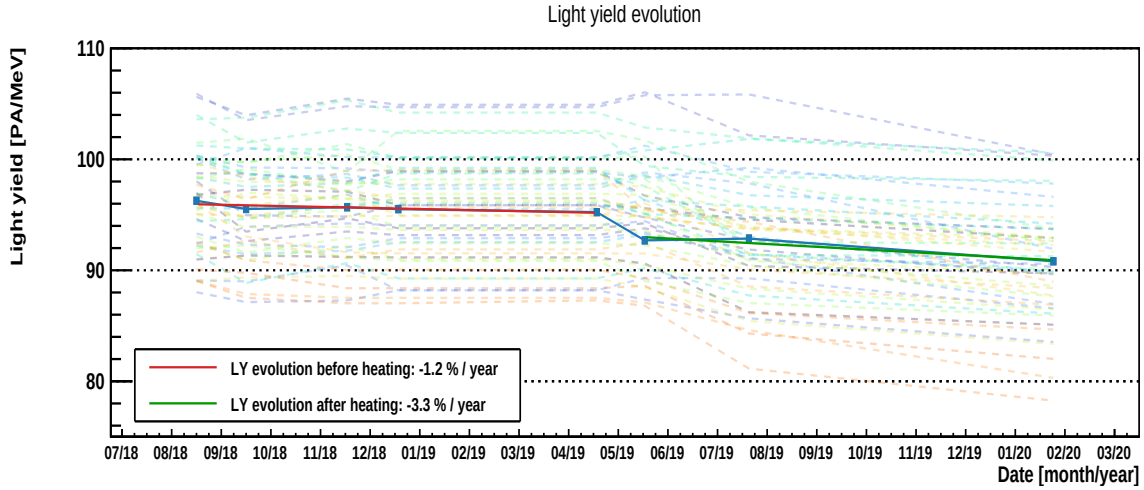

Figure 8.19: Time evolution of the average light-yield in the detector. Each plane is represented by a doted line and the average variation is represented by the blue dots and solid line fits. An effect of the heating of the detector can be seen around May 2019 with a sudden drop of the light-yield.

The other energy losses due to attenuation length and optical couplings have also been tested over time with these calibrations but no degradation has been observed. This was also in favour of PVT ageing.

8.2.6 Energy response linearity

The PVT scintillator was selected in SoLid because of his good energy response linearity compared to liquid scintillators. A dedicated calibration campaign with other sources than ^{22}Na was realised in order to test this linearity. The detail of the sources and the gamma lines used are presented in table 8.1.

Calibration source	Gamma energies [keV]	Compton edges [keV]
^{22}Na	1274	1061
^{207}Bi	569 - 1063 - 1770	393 - 857 - 1547
AmBe	4438	4196

Table 8.1: List of the calibration sources used in SoLid with gamma energies and the respective Compton edges to test the energy response linearity

To avoid a bias on the energy measurement of low-energy deposits, a periodic trigger has been used for ^{207}Bi and ^{22}Na gamma energy calibrations and a threshold trigger was used for the higher energy of the AmBe to gather more statistics in the region of interest. Due to limited time for the calibration campaign, the sources were only put at 2 positions in the detector: at the middle and at the top corner (electronic box side) of gap 5. A total of 239 cubes, about 2 % of the detector, was used for this linearity test. For the ^{22}Na and ^{207}Bi calibrations the

same selections than regular calibrations have been used. For the AmBe calibration, there is an important proton-recoil background caused by the emitted neutrons due to the source activity and the thermalisation time of neutrons[2]. To purify the calibration sample, events with a neutron capture within 500 µs at the other side of the source compared to the gamma interaction were selected.

Each cube light-yield was measured for the different gammas with the numerical method. Examples of the fits for the ^{207}Bi and AmBe can be seen on figure 8.20. Those values were then averaged over the cubes per gamma energy to get an averaged linearity measurement on the tested cubes, see figure 8.21. As shown by the bottom ratio, the fitted light-yields at each point are in agreement within 2 %, which confirms the good linearity of the energy response of the PVT. The linearity curve for each cube were also fitted and the slopes show a Gaussian shape with a spread of about 5 % in light-yield. This is a major success of the calibration work performed and an asset for energy measurements with SoLid technology.

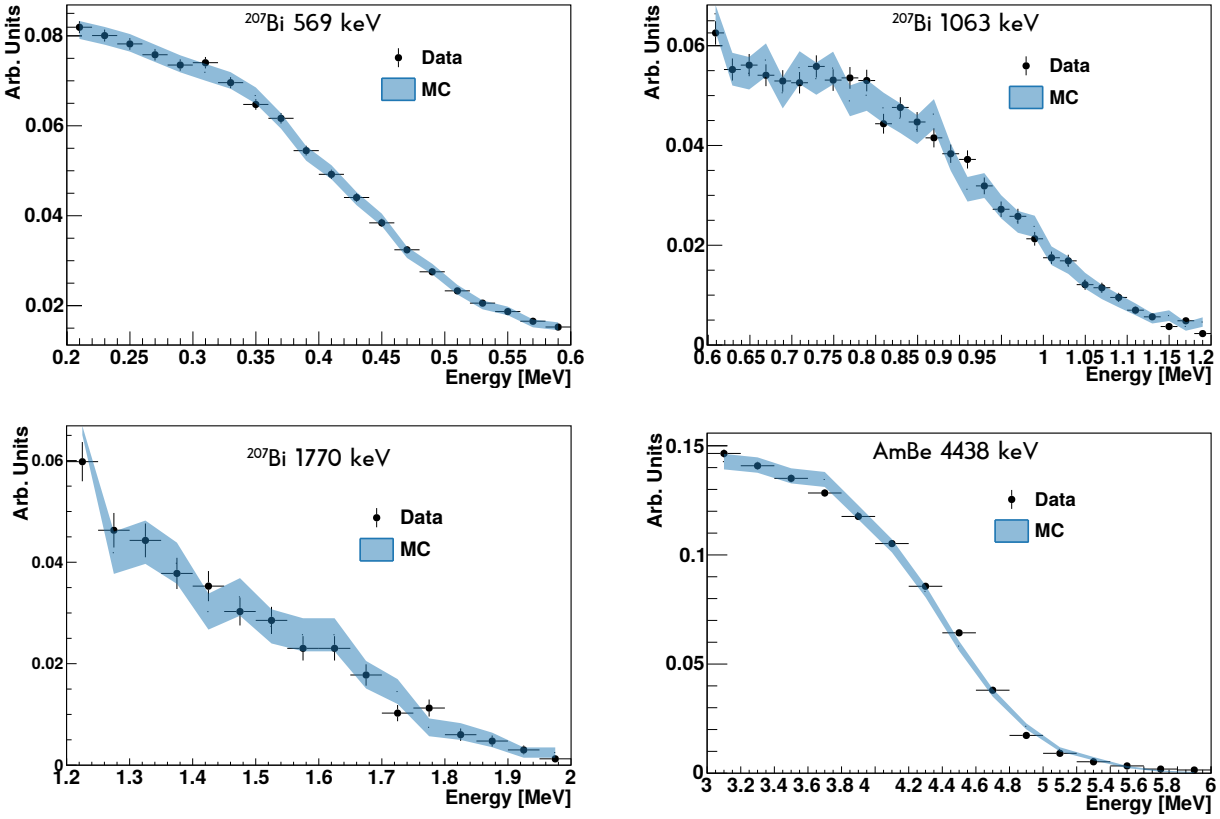

Figure 8.20: Fit for a given cube for ^{207}Bi (top, and bottom left), and AmBe (bottom right). The blue envelope represents the best convoluted GEANT4 with a 1 σ statistical uncertainty on the Monte-Carlo.

This calibration campaign was also used to test the energy resolution as a function of the energy with an *abc model*. The values of the *abc* constants were determined with a good statistical precision of 1 %. But since no improvement was observed on the comparison between GEANT4 and calibration spectra (see section 8.3) there were no need to complex more the calibration.

[2]The AmBe is mostly used in SoLid as a neutron source to calibrate the anti-neutrino detection efficiency but provides a high-energy gamma of 4.438 MeV in coincidence with a neutron in 57.5 % of the cases [Liu et al., 2007].

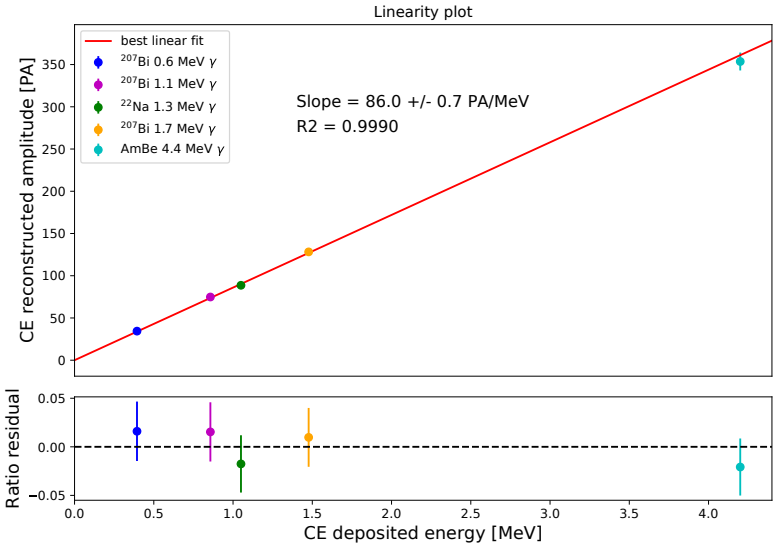

Figure 8.21: Average light-yields measured on Gap 5 with two source positions at different gamma energies with its linear fit and ratio [Roy, 2021].

8.3 Data - Monte Carlo comparison

After the meticulous work performed on the calibration of the 12800 cubes of the SoLid detector and in sight of preparing the anti-neutrino analysis, it was decided to investigate data - Monte Carlo agreement. The calibration ^{22}Na data are well suited to this work since, in addition to the 1.27 MeV gamma, the source also produces two annihilation gamma at 511 keV, like a positron after anti-neutrino interaction. Some low energies discrepancies have been observed and reported in [Henaff, 2021] and [Roy, 2021]. These are dues to the threshold trigger used to take the calibration data and will not be discussed here. Instead we will focus on the periodic trigger data taken during calibrations that show the real potential to detect the annihilation gammas in the SoLid experiment. This detection is of major importance in order to boost the background rejection of SoLid.

The result of this test is presented on figure 8.22 with a single cube on the left and for several cubes on the right. An agreement within ± 5 % is found in the energy range [15-130] PA, corresponding approximately to [150-1350] keV. This demonstrates the good reconstruction of the low-energy part of the spectra attributed to the 511 keV gammas. This channel has been intensively studied by David Henaff in his thesis [Henaff, 2021], in chapter 4. Many physics variables of interest for the anti-neutrino analysis: like different energy estimators, energies of the annihilation gammas, events categories or topological variables have been tested and validated in term of agreement between data and Monte Carlo (of the order of 10 % or better). This provides good confidence for the anti-neutrino analysis.

8.4 Summary of the calibration of the SoLid detector

The Calipso campaign of quality assurance was a decisive work to start data taking at BR2 with the best possible detector without complicated, or sometime impossible, interventions inside the detector container. After corrections of the possible defects, the calibrations data permitted to develop the first analysis methods and to have a first idea of the detector performances. This also provided the first inputs to the readout simulation of the experiment.

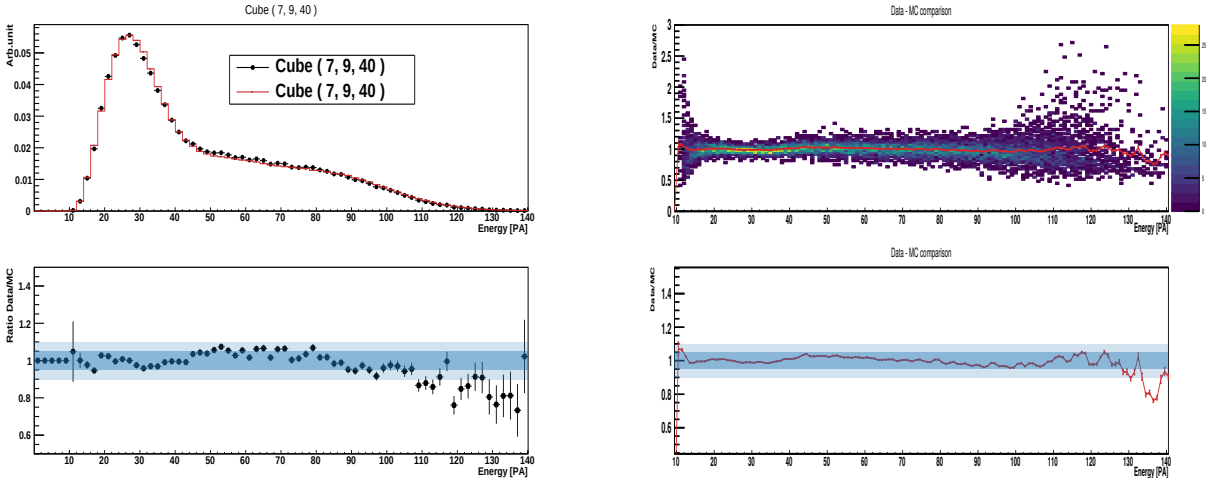

Figure 8.22: [left] Comparison between ^{22}Na periodic trigger data and simulation for one cube. (right) Same comparison for several cubes. Each bin in the top histogram represents a bin on the left histogram for each cube. The average per energy bin is plotted in red.

This chapter followed by explaining the state-of-the-art energy calibration of the SoLid detector. The gain and the pedestal variations are computed on 6 h time intervals and corrected during data reconstruction. They show respectively less than 3 % and less than 1 % variation (before correction) over the whole Phase 1 data taking period.

The attenuation lengths of all the fibres with an active MPPC have been measured to an average value of 97 ± 17 cm. The optical coupling of the fibre with the MPPCs have also been measured with a central value at one by construction and a spread of around 15 %. These parameters were then measured with an asymmetry method to avoid correlations and reduced the dispersion of the values.

After correction of these light losses, the individual cube light-yields were computed with two methods : the analytical and the numerical methods. They provide compatible results and confronting the two methods helped to improve the understanding of the SoLid detector and to quantify the precision on the energy scale determination, which is quantified at 3 %. The average light-yield is 96.3 ± 6.8 PA/MeV, which should lead to a stochastic energy resolution of better than 12 % at 1 MeV, after cross-talk subtraction. But the determination of the energy resolution by the calibration methods give results closer to 14 % at 1 MeV, thus being the sign of other contributions to the energy resolution.

Several calibration data taking occurred over the Phase 1 of the SoLid experiment. The calibrations studies were realized on all these data and demonstrated and ageing of the PVT scintillators resulting in a light-yield reduction of 5.6 % averaged over the whole detector cubes. A punctual temperature accident also affected the PVT response.

Finally, the linearity of the energy response of the PVT scintillator cubes used in SoLid has been demonstrated with calibration at different energies using ^{22}Na, ^{207}Bi and AmBe sources. The dependence on the energy resolution as a function of the energy was investigated as well with these data. No evidence to use this more complex description was found in the data - Monte Carlo so far.

The work on calibration is concluded by data - Monte Carlo agreement specially at the low energy region of the 511 keV of the annihilation gammas that are or particular interest for the identification of an anti-neutrino interaction from the positron detection.

Chapter 9

Anti-neutrino analysis in SoLid

This chapter presents the results of the data analysis of the SoLid experiment performed by the two PhD students I have supervised. The first one is the thesis of Delphine Boursette defended in 2018 [Boursette, 2018]. The technical work about the light-yield optimization she accomplished has already been presented in chapter 7. During, her last year of PhD she was among the first physicists to try to identify the anti-neutrino interactions in the SoLid detector and to investigate the backgrounds. I will summarize here these preliminary results.

The second thesis I supervised is the one of Noë Roy [Roy, 2021], defended in 2021. The SoLid phase 1 detector was already taking data at the start of his thesis. Noë took a major role in the energy calibration of the detector, as already presented in chapter 8. The second part of his work was dedicated to improving the anti-neutrino analysis on the data of SoLid Phase 1. Given the importance of the search for a sterile neutrino, the collaboration adopted a blind analysis strategy with only one reactor on and two reactor off datasets opened for analysis. As we will see in this chapter, the SoLid experiment is facing a very high background because of low overburden and higher radioactivity background than expected in the neutron screens. Intense efforts have been conducted in the collaboration to reject these backgrounds. Noë developed a multi-variate analysis based on *boosted decision tree* to reach the best performances possible. He also performed dedicated studies on the atmospheric background and investigate its behaviour in an original study of the subtraction of the reactor off periods between them, which allowed an unblinding of all the reactor off data. The thesis could have been concluded by opening the full reactor on dataset of SoLid but anomalies in these reactor off-off subtraction prevented to do so. This work will be summarized in this chapter before giving perspectives on the ongoing work in SoLid.

Chapter contents

9.1 Analysis of the first physics dataset

As already said in chapter 6, the SoLid phase 1 detector construction ended early 2018. Commissioning data with the full detector[1] started in February with reactor ON and OFF cycles but the optimal detector settings and operation conditions were reached at the end of April 2018. The thesis of Delphine Boursette [Boursette, 2018] thus consisted in the analysis of the reactor ON cycle from 25/04 to 22/05 (18 days - cycle 2) and the reactor OFF cycle from 23/05 to 11/06 (7 days used for background measurements because of detector calibrations on the other days - inter-cycle 2-3). This dataset was defined as *the first physics dataset*.

The reconstruction in SoLid was rather simple at that time. The first objects reconstructed were *neutron signals* (NS), muons tracks or clipping[2] and *electromagnetic* cubes (EM). Looking for anti-neutrino interactions consisted in building coincidences between a NS, that has triggered the detector, and the EMs stored in the buffer window at $[-500\,;\,+200]$ µs of the NS. The muons were rejected as prompt signal candidate or as veto prior to an IBD-like coincidence. The EM reconstruction was quite problematic when having several cubes in the same detector plane. For example two cubes in a plane correspond to signals in four horizontal and four vertical fibres that point to four possible cubes, two cubes are real and two are ghosts. The complexity increases with even more cubes hit in the plane. Delphine overcame this difficulty by using an asymmetry cut to reject the ghost cubes, for which the sum of the horizontal and the sum of the vertical amplitudes of the signals should differ. The analysis of Delphine was validated with IBD simulations and on AmBe calibration data. In this data the prompt EM signal is produced by a 4.4 MeV gamma and the neutron signal, which is delayed because of the thermalisation time of the neutron. The AmBe coincidences were well identified and the two exponential decay time-constants corresponding to the thermalisation were in very good in agreement with previous studies and simulations. The use of the negative time window, looking for an uncorrelated EM after the NS instead of before as for IBD-candidates, to measure the accidental background was also validated with these AmBe data. The analysis work continued by investigating the two main backgrounds: the BiPo contamination of the ^{6}LiF:ZnS screens and the atmospheric events induced by muons.

The BiPo background was first studied on reactor OFF data by selecting an enhanced sample, requiring the EM and the ES to be in the same cube ($\Delta R = 0$) and an energy cut on the EM, selecting the [1;3] MeV region. The decay time of ^{214}Po was well describing the delay time distribution (Δt), which confirms the purity of this BiPo sample. This first test showed a good performance of the analysis but unfortunately revealed the very high level of the BiPo background, at an even higher level than in SM1 prototype. The comparison to BiPo simulations was not well advanced at that time and we could not extract the precise contamination levels. Also we thought that removing the correlated events constricted to the same cube would remove almost all the BiPo background for a loss of only 15% of the IBD events. Latter, with the refinement of the analysis and of the simulations, it turned out that the ^{214}Bi decays into excited states of ^{214}Po was also source of background. The de-excitation γ's thus increased in volume the influence of BiPo.

To investigate the atmospheric background, after muon events were used by Delphine. The principle was to apply the IBD selection studied on IBD simulations, to the reactor OFF data but requiring explicitly to have detected a muon before the IBD-candidate. Varying the veto time between the muon and the IBD-candidate, we observed a quick drop of the correlated background before 200 µs. Vetoing these events helps removing 95% of the atmospheric back-

[1] Four of the five detector modules under an incomplete shielding were already operating in December 2017. Delphine participated to the analysis of these preliminary data. It allowed to prepare the first reconstruction tools on real data and to have a first look to the backgrounds.

[2] A clipping muon is identified by a high-energy deposit on a corner cube of the detector.

ground for a modest dead-time loss of 5%. Similar time cut between two consecutive NS has also been applied to the IBD selection to reduce the nucleonic component of the atmospheric background. Indeed several neutrons could be produced by an atmospheric event.

The IBD analysis in SoLid was at its early ages at the time of PhD thesis of Delphine and stable detector conditions were just met for one reactor ON/OFF cycle. The approach was thus to use a sequence of rectangular cuts in order to have a first estimation of the backgrounds and of the reactor ON excess compared to the reactor OFF, which would be due to anti-neutrino interactions. In figure 9.1 are presented three representative distributions: the NS-EM distance ΔR, the prompt EM energy and the time delay Δt of the IBD-candidates in the reactor ON and OFF periods. We can see a small excess of events in the reactor ON over a very large background illustrated by reactor OFF data. The excess seemed consistent with IBD simulations, but the limited statistics of this sample and the large background level encountered prevented to perform a precise comparison.

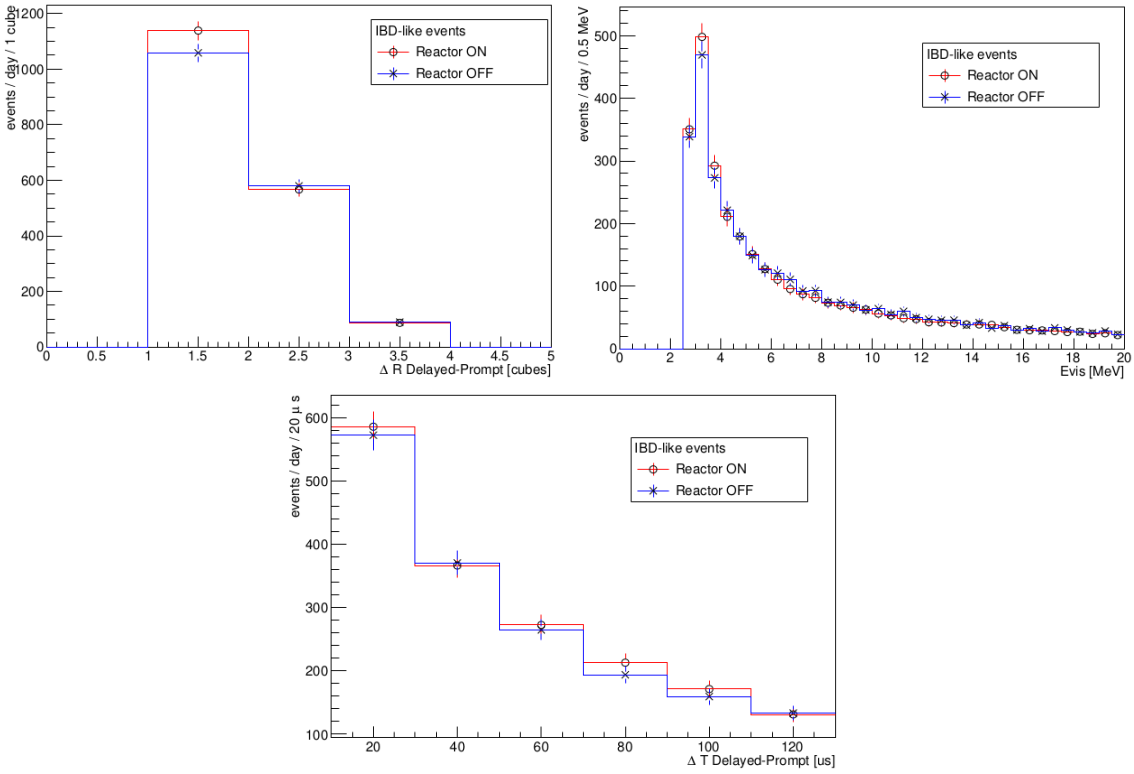

Figure 9.1: Distributions of the variables of interest for the IBD-candidates in reactor on and off periods [Boursette, 2018]. (left) Distance ΔR between the delayed NS cube and the prompt EM cube. (right) Prompt energy of the EM cube E_{vis}. (bottom) Distribution of the time delay Δt.

The excess and the backgrounds were further investigated by looking at the IBD-candidates rate per day, as presented on figure 9.2 (top). An event rate of 1918 was found in reactor OFF and a rate of 2078 per day in reactor ON. An average excess of around 160 ± 2 $(stat)$ events per day appeared between reactor ON and reactor OFF data[3]. This would lead to a signal over background ratio of $S/B = 0.08$. This is really too low and far from the target to get of the order of one. The accidental background, also presented on figure 9.2 (bottom), on the other end turned out to be small enough. The increase of accidentals during the reactor on period is due to the neutron activation on airborne ^{40}Ar in the reactor building, producing ^{41}Ar which is a β^- emitter with $Q_\beta = 2.49$ MeV accompanied by a 1.29 MeV γ in 99% of the β-decays. These γ's are then interacting in the detector. As already said, the BiPo background

[3]The numbers quoted here differ a little from the thesis, because they were recalculated from the plot.

was assumed to be negligible after the set of cuts used for this first IBD selection. In addition, the delay time distribution seemed to be in good agreement despite a tiny difference between reactor ON and OFF, as can be seen on figure 9.1 (bottom). The atmospheric background on its side depends on the atmospheric pressure which is varying over the data taking periods. It should then differ between reactor ON and OFF periods. The pressure is constantly monitored by the reactor survey system and we could average the pressure for each day, as shown on figure 9.2 (middle). A slight anti-correlation can be seen and both the background estimation and subtraction should take this into account before extracting the IBD signal. This was not done at the time of Delphine's analysis but the main challenge of SoLid after this first result consisted in strongly reducing further the backgrounds.

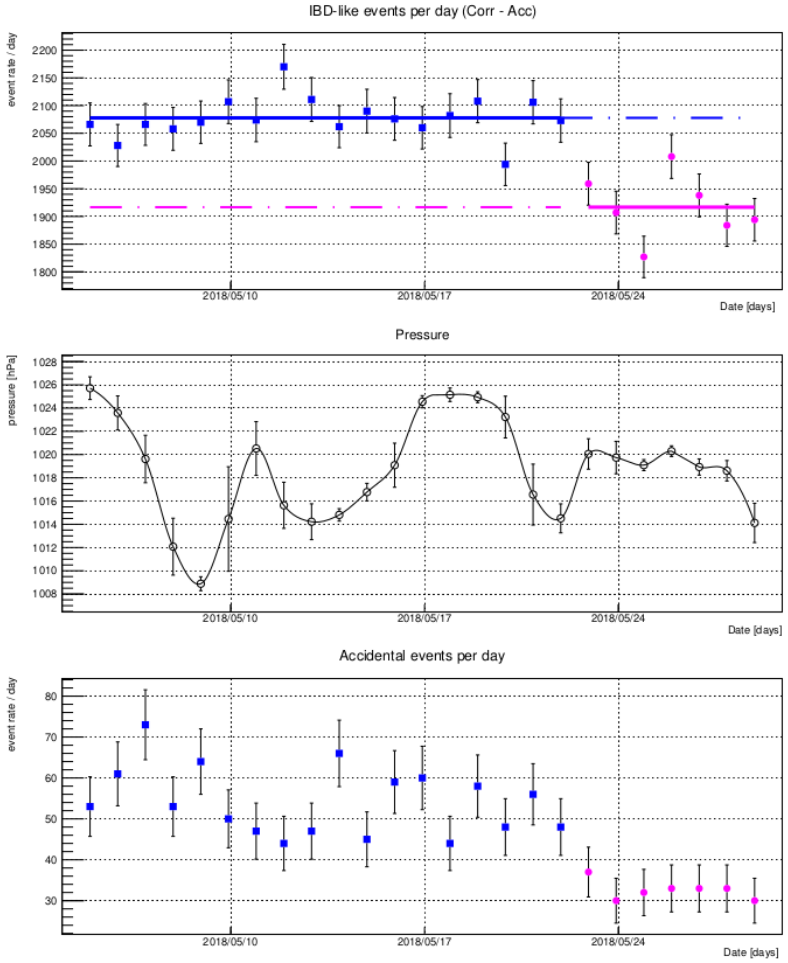

Figure 9.2: (top) Distribution of the IBD-candidates rate per day after accidentals subtraction. (middle) Distribution of the environmental average pressure per day. (bottom) Rate of the accidental background per day [Boursette, 2018].

The first analysis of physics data in the thesis of Delphine Boursette, that I supervised, was a very good boost for the collaboration of SoLid. The detection of anti-neutrinos was demonstrated over the huge background close to the BR2 reactor at very low overburden. Unfortunately, this background turned out to be so high that the preliminary reconstruction and analysis tools would not be sufficient to produce a competitive search for sterile neutrino or a measurement of the ^{235}U energy spectrum. The PhD thesis of Noë Roy inherited this situation after Delphine Boursette. The SoLid collaboration gained in expertise over the years and more sophisticated tools were used.

9.2 Analysis of the open dataset

Given the rigour required to search for a sterile neutrino in VSBL experiments, the SoLid collaboration adopted a blind analysis strategy from the very beginning of the data analysis. This should prevent to introduce an unintended bias in the final result. It was decided to use only a part of the second physics dataset of the phase 1, corresponding to 21 days of reactor ON (19/06 to 09/07/2018 - BR2 cycle 3) and 19 days of reactor OFF data (12 to 31/07/2018 - BR2 inter-cycle 3-4). This is called the *open dataset* that was not blinded to the collaboration. The work mostly focused on the reactor OFF data to measure the backgrounds and to reduce them with the help of precise IBD simulations, in order to maximise the sensitivity to detect anti-neutrinos. The reactor ON data are used to train the background subtraction and estimate the IBD excess rate. But the opened statistics is too low to investigate possible oscillations. The BR2 reactor simulations combined to the detector acceptance calculations have predicted a rate of 1088 IBDs per day for the reactor cycle 3, see section 6.9. Once the analysis selection and methods would be frozen and the systematics estimated, the collaboration would be allowed to open new cycles of data step by step. The analysis work of Noë first concentrated on the open dataset and was latter extended to all the reactor OFF periods of the phase 1 data taking.

The event reconstruction was strongly improved with the CCubes algorithms, presented in section 6.8, compared to the time of Delphine's thesis. The IBD-candidates are now formed of a cluster of *electromagnetic signals* (ES) and a cluster of *nuclear signals* (NS) in time and space coincidence. The buffer time window, $[-200\,;\,+500]$ µs, is still fixed by the trigger as well as the spatial coincidence of three planes around the NS-triggered plane, see section 6.5.6. The more sophisticated reconstruction allowed to build many discriminative variables: the time (Δt) and space ($\Delta R, X, Y, Z$) differences between the NS and the ES, the number of cubes in the ES cluster ($promptNCCube$) and its volume ($promptVolume$). Some of these variables are similar to the ones presented in section 9.1, but they are more robust and not restricted to only certain types of events (single cube events for example). The comparison of these variables between IBD simulations and reactor OFF data, presented on figure 9.3, illustrates the power of the hybrid scintillator and segmented technology of SoLid to scrutinise the topology of the events and reject the backgrounds.

From this preliminary study, Noë Roy also investigated several energy estimators and decided to use the *crown energy*, which is summing the energy of the *annihilation cube* and the $3 \times 3 \times 3$ volume of cubes around it. This estimator allows to contain the energy of an escaping positron to a neighbouring cube and the optical light leakages but might contain some annihilation γ's energy deposits.

9.2.1 Background measurements

As well as the reconstruction tools, the understanding of the backgrounds seriously improved in SoLid over the years. As already said, the experiment is concerned by three types of backgrounds: accidental, BiPo and atmospheric. The study of the different background properties were taken as much as possible from data-driven measurements to avoid any possible mismatch with background simulations.

Accidental background

During the study of the accidental background, it turned out that the negative Δt window presented a non-negligible slope, as can be seen on figure 9.4. This effects sheds doubts about the extrapolation to the positive time window and thus to the correct estimation of this background. A new method emerged in the collaboration with the use of the *false positive neutron triggers* (FPNTs). This kind of events occurs with the peak counting algorithm of the neutron trigger

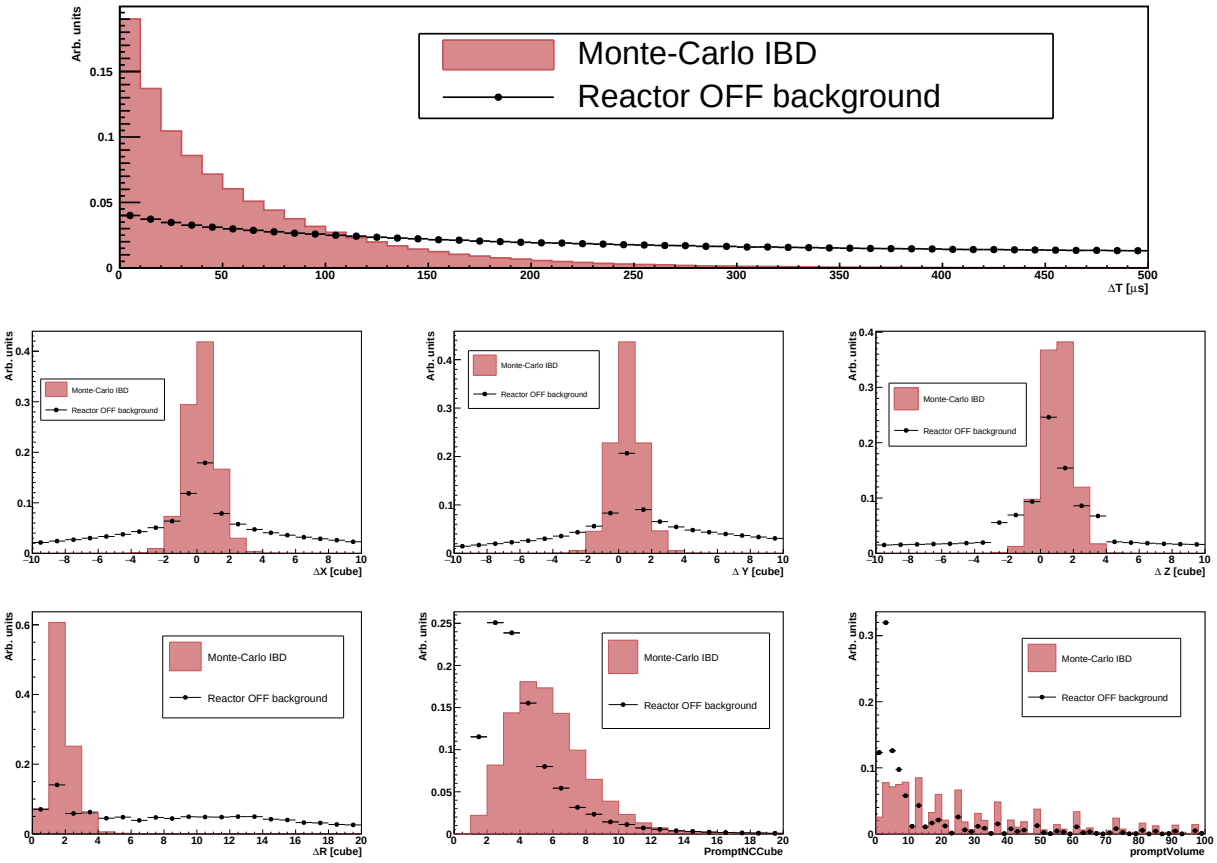

Figure 9.3: Distribution of the low-level discriminative variables with areas normalized to one using four days of reactor OFF background (back points) and IBD simulations (red) [Roy, 2021].

accepts high-energy muon signals because of bounces in the tail of the high amplitude pulses. This is not an issue for the IBD analysis since it can be easily rejected offline. Building ES-NS coincidences with FPNTs provides high-statistics for this background determination and revealed to be very accurate.

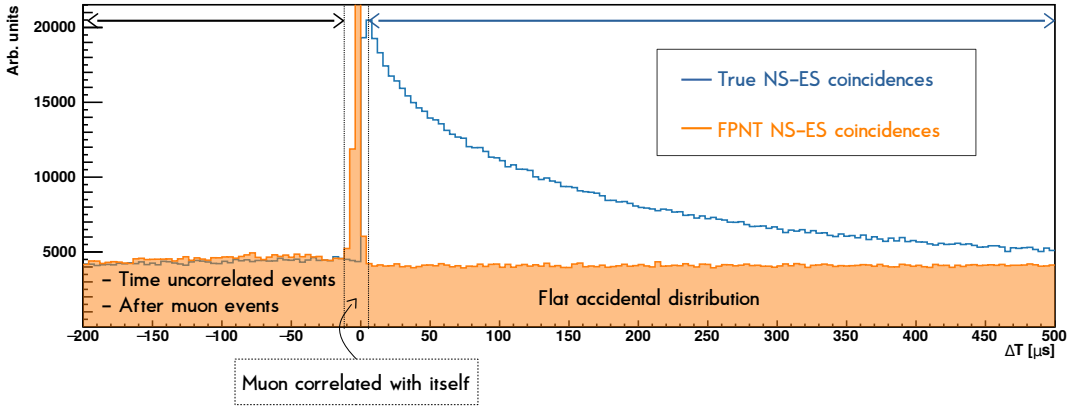

Figure 9.4: Delay time of the true and the FPNT's ES-NS coincidences in four days of reactor OFF to illustrate the accidental background determination [Roy, 2021].

BiPo background

The BiPo background can be easily identified thanks to the close spatial coincidence between the alpha decay detected in the ZnS and the β-decay detected in the PVT at the two sides of the neutron screen ($\Delta X = 0, -1$ and $\Delta Z = 0, 1$), see figure 6.11. Compared to Delphine's analysis, the reconstruction tools now allow to fully exploit the BiPo events extended in space by the γ interactions. This can be seen on the ΔR distance distribution on figure 9.5 (left) where up to nine cubes distance can be observed. This confirms that the previous selection ($\Delta R = 0$) was missing the major part of the BiPo background. The strategy to reduce the BiPo background first focussed on the analysis of the NS. The ^{6}Li break-up reaction is releasing 4.8 MeV while the ^{214}Po α-decay is releasing 7.7 MeV. It implies different pulse shapes in the inorganic scintillator. This was firstly exploited in the thesis of Valentin Pestel [Pestel, 2019], with a variable called *BiPonisher*. It was recently improved by a one-dimensional convolutional neural network (CNN) providing a better discriminative variable called *BiPonator*. The discrimination power is illustrated on figure 9.5 (right), where AmBe neutron calibration and BiPo enhanced data samples are compared. The BiPo events can be reduced by a factor 3 for an untouched neutron detection efficiency. The second handle on the BiPo background is the longer decay time of ^{214}Po of $\tau_{214} = 237$ µs compared to the long-component neutron thermalisation time $\tau_n \approx 64$ µs.

Besides the background discrimination, the usage of these two variables provided a very valuable tool to the collaboration to precisely study the BiPo background and extract the corresponding data driven variables. Two-dimensional sidebands have been determined, as explained on figure 9.6, one for the signal region and one for the BiPo region. The latter is used to scale expected BiPo background in the signal region. A third intermediate BiPo sideband ($\Delta t \in [200; 500]$µs and *BiPonator* $\in [0.22; 0.65]$) has also been extensively used in the collaboration to perform data to Monte-Carlo comparison and thus to validate our simulations [Danny Galbinski, 2021]. This is of major importance to trust our IBD simulations used to optimize the events selection.

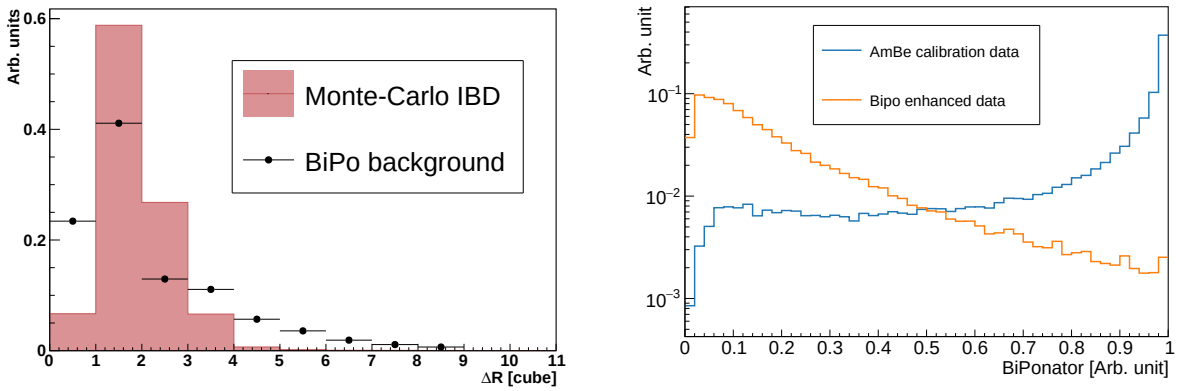

Figure 9.5: (left) Distribution ΔR of the ES-NS coincidences for a BiPo enhanced reactor OFF sample in black points and for Monte-Carlo IBD in red [Roy, 2021]. (right) Distribution of the *BiPonator* discrimination variable for AmBe calibration and BiPo enhanced data.

Atmospheric background

As already introduced, the atmospheric background depends on the atmospheric pressure. It can be studied in reactor OFF only data but we need to validate the extrapolation to reactor ON data without compromising the blinding of the IBD events. Like for the BiPo sideband, the atmospheric background of the open dataset was studied in the thesis of Noë with a minimal energy cut of 7 MeV to exclude BiPo and IBD events. Other cuts were added to reduce

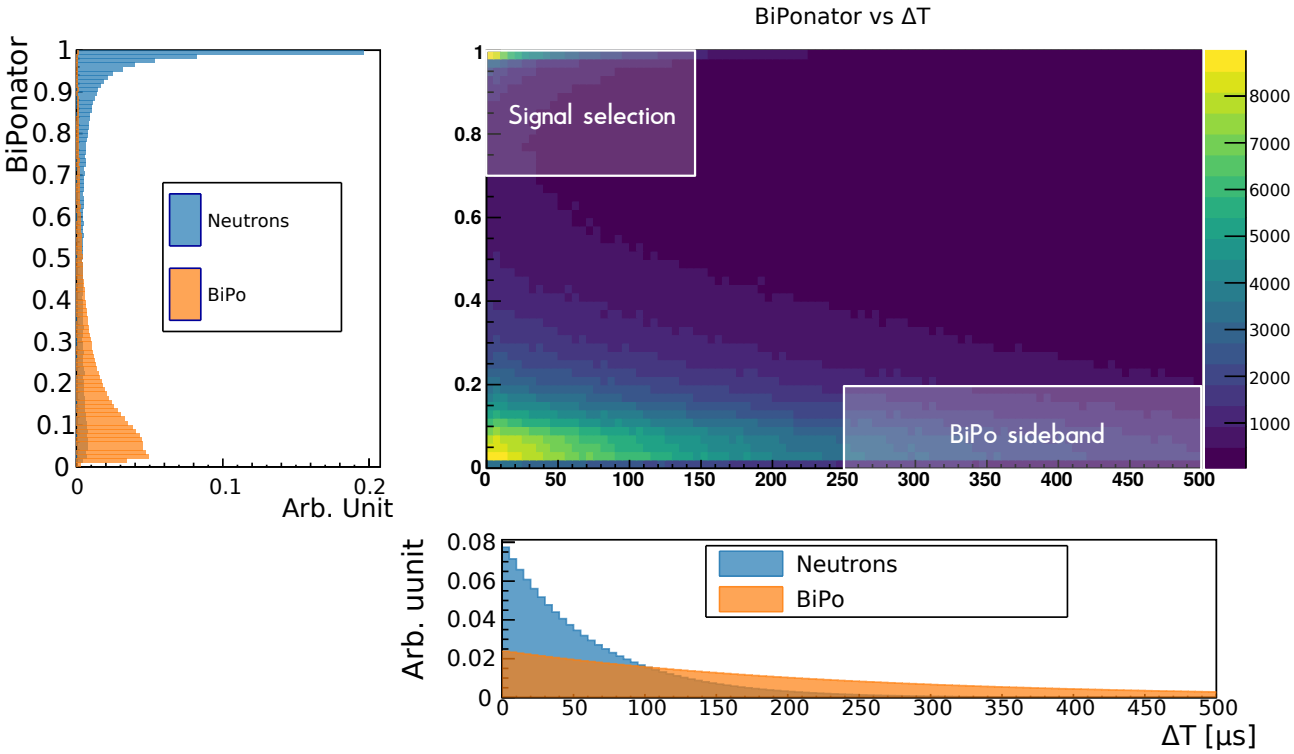

Figure 9.6: The two-dimensional histogram of Δt versus *BiPonator* and the one-dimensional distributions of both Δt and *BiPonator* are represented normalized to one for both neutron induced (blue) and BiPo induced (orange) events in reactor OFF data. The two white rectangles on the 2D histogram represent the Δt and *BiPonator* selection used for the antineutrino analysis and for the BiPo sideband [Roy, 2021].

the accidental background as well, in order to obtain a pure atmospheric sample. The pressure variation and the relative atmospheric background rate, called ΔR_{atm}, are computed daily with respect to the average in both reactor ON and OFF of the open dataset. They are represented on figure 9.7. The anti-correlation can be seen and negative slope allows to fit the relative event rates as a function of the pressure variation. This seems to indicate the background extrapolation should be well under control but the pressure variation in this dataset is rather limited.

In order to test the pressure model and in the process of going further in the unblinding strategy before going to reactor ON data, Noë was authorized to look at all the reactor OFF data with this specific atmospheric selection. The distribution is represented on figure 9.8. We can see that the slope has slightly increased compared to figure 9.7. But most important, we also notice a wider dispersion and some accumulation of points in a region between 0 and 5 hPa, which seems not corresponding to the global fit. We can suspect that the atmospheric background in these periods might not be well estimated by the pressure model with the global linear fit.

Noë then scrutinized individually all the BR2 reactor OFF inter-cycles to see if there are deviations to the global fit, as presented on figure 9.9. The rates and pressures are averaged only on each inter-cycle periods to make these figures. We can see that inter-cycle 2-3, that is the first physics dataset studied in Delphine's thesis, was problematic and thus discarded from the analysis. It is suspected to be due to unstable running conditions with humidity issues before dry air flushing of the experiment. Gathering again all the reactor OFF data of phase 1, the daily rates ΔR_{atm} are better aligned with the global fit compared to figure 9.8, with a χ^2/ndf falling to 1.21 (instead of 2.80). This model was tested by Noë in sampling the periods and checking the residues, which are aligned to zero and have standard deviation around 2.5%.

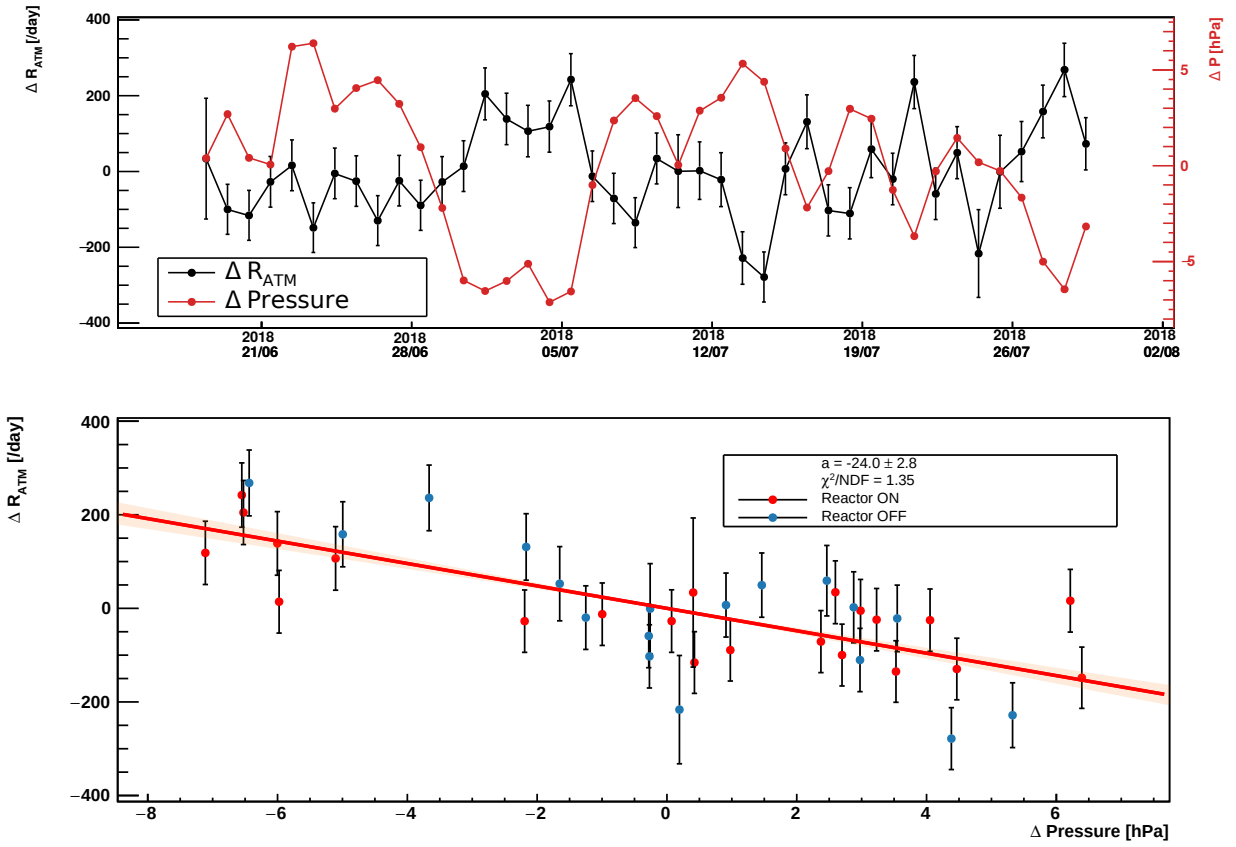

Figure 9.7: (top) Time evolution of the relative atmospheric pressure (in red) and the relative atmospheric background rate. (bottom) Pressure model fit (red line and 1σ orange band) of the open dataset on both reactor ON (red points) and OFF (blue points) data [Roy, 2021].

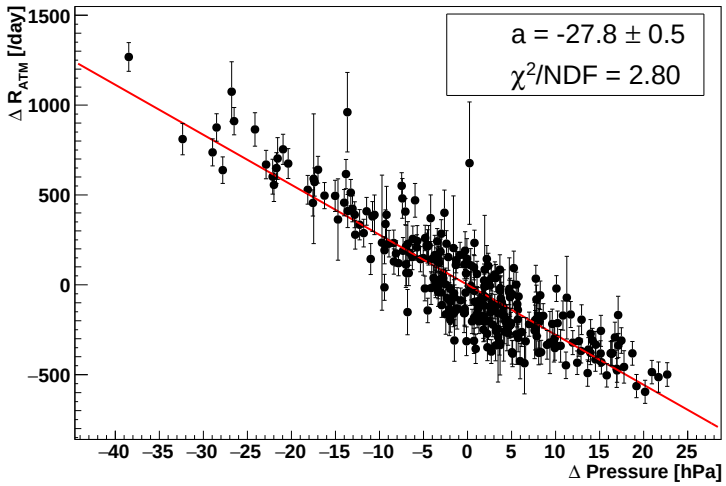

Figure 9.8: Relative daily rates of the atmospheric background as a function of the pressure variation with its linear fit [Roy, 2021].

We should thus be able to rely on atmospheric subtraction with the pressure model correction.

9.2.2 IBD analysis

The IBD analysis of Noë started with a classical analysis with cuts on the low-level discrimination variables. This was a preliminary step to get an idea of the initial situation and to prepare

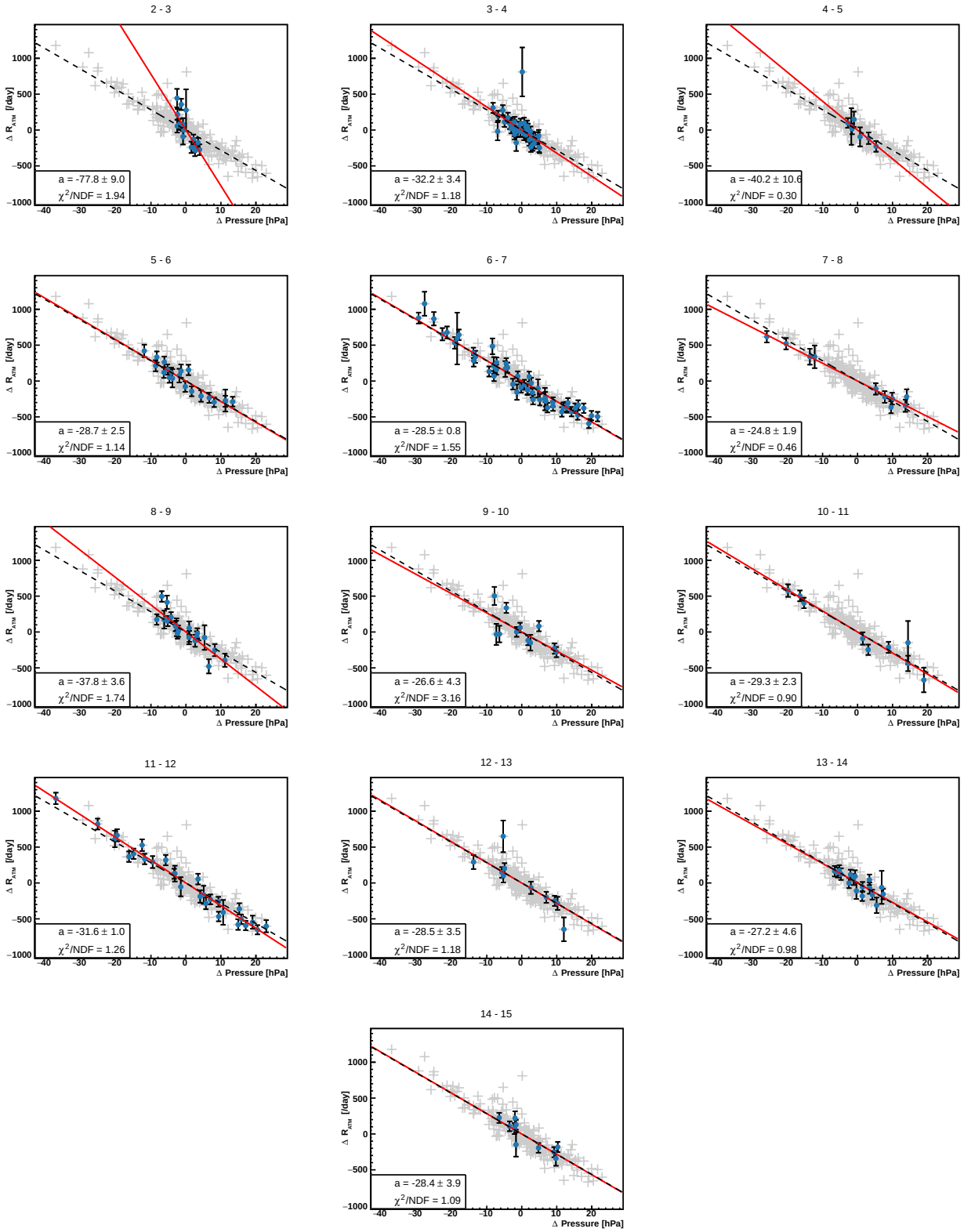

Figure 9.9: Relative daily rates of the atmospheric background as a function of the pressure variation with its linear fit for each reactor OFF inter-cycle periods. The grey points and the dashed black line corresponds to the whole reactor OFF phase 1 dataset [Roy, 2021].

the samples for the multi-variates analysis. On the open dataset and without real optimisation, the signal rate was estimated to 149 per day (42% IBD efficiency) for a background rate of 4892 per day. It corresponds to a signal over background ratio of $S/B = 0.03$, which is obviously too low to perform a sterile neutrino search.

To go beyond this situation, we need to exploit the fine segmentation of SoLid to better identify the anti-neutrino interactions. The key is to detect, as much as possible, the two back-to-back γ's produced by the annihilation of the positron with an electron. This should be very efficient since the prompt events of the backgrounds don't have this signature. The BiPo background has a β^- (accompanied with γ's or not) and the atmospheric background comes from a proton recoil (produced by neutron scattering) or a clipping muon. This strategy was first implemented in David Henaff's thesis [Henaff, 2021] and continued by Noë. This work was benefiting from the developments of the analytical fit for the gamma calibration of the detector (section 8.1.5). The anti-neutrino interaction cube is identified because it has the higher energy in the ES cluster. The annihilation gammas are then searched by the *gamma tracking* algorithm using the travel distance probability, from Klein-Nishina cross-section, and the energy deposits. The cubes are investigated one after the other and the gamma tracks are built iteratively from the best likelihood scores. The total energy of the gamma track is also computed by summing the energy of the cubes associated to each track. The process ends-up with an event classification with three possible categories: zero, one or two gammas reconstructed. For illustration purpose, an example of event with two gammas reconstructed is presented on figure 9.10. To estimate the algorithm performances, the proportion of tracks reconstructed as a function of the number of real tracks has been represented on figure 9.11. Overhaul good performance has been reached with almost 60% efficiency to detect the true tracks (diagonal terms). The limitation of this algorithm is due to the low energy deposits of the 511 keV γ's $\mathcal{O}$(100 keV), which are difficult to detect given the detector light-yield and the cube reconstruction threshold.

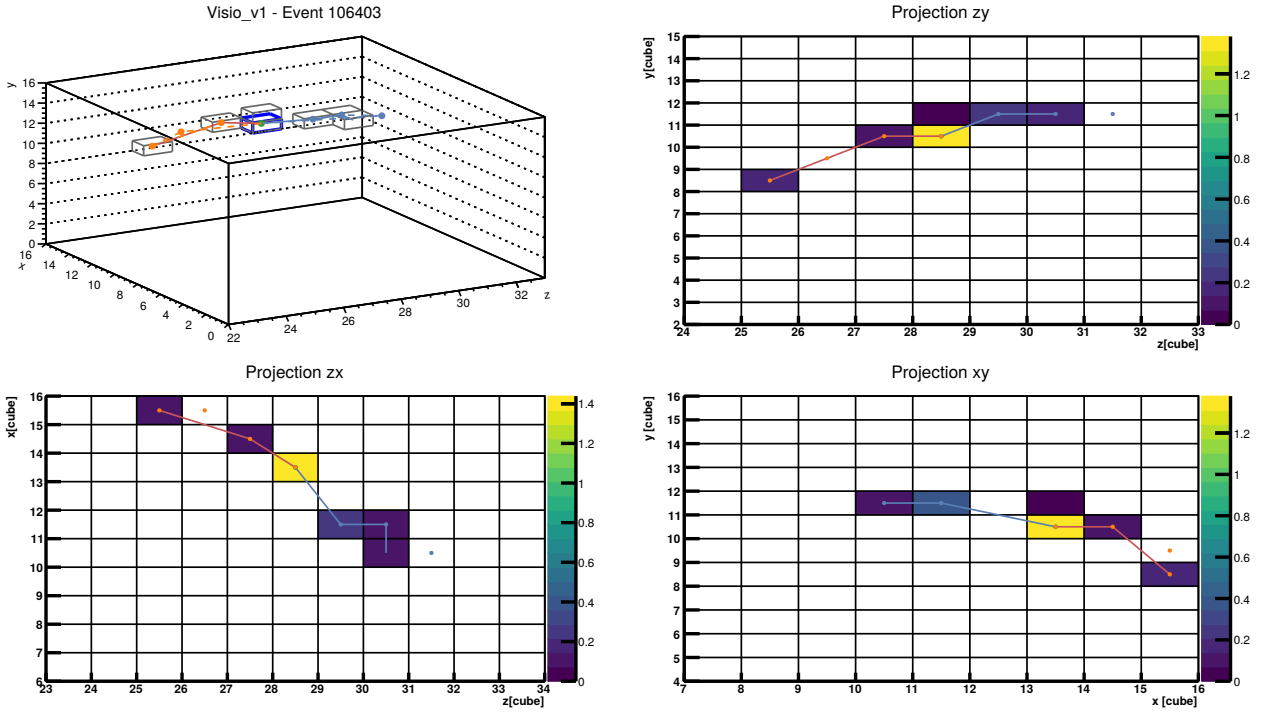

Figure 9.10: Representation of a Monte-Carlo IBD two gammas event with a three-dimensional view and the three projections. The two plain lines (orange and blue) represent the tracks reconstructed with the *gamma tracking* algorithm, the rectangles represent the reconstructed cubes and the dots the true interactions before reconstruction, with two colours for the two different gammas. On the projections, the annihilation cube is represented in yellow [Roy, 2021].

The analysis strategy has to be adapted to the three reconstructed categories. Several variables have been built for each category in order to reach the best discrimination power in each topology. Detail can be found in the PhD thesis [Roy, 2021]. To fully exploit these

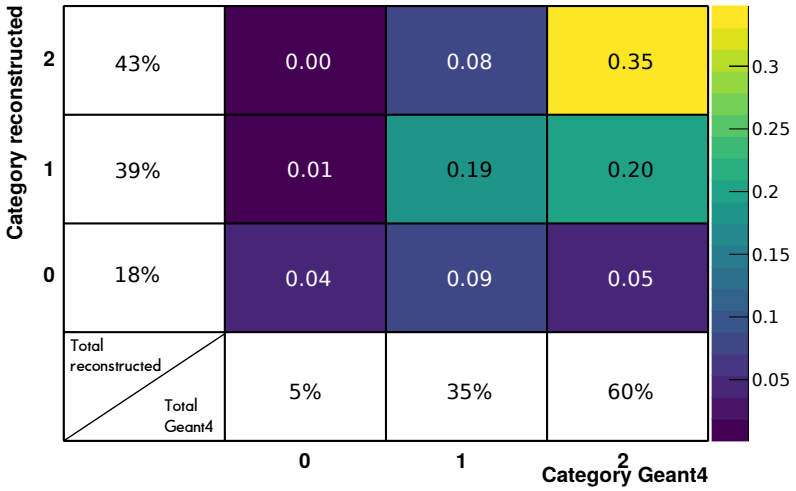

Figure 9.11: Proportion of reconstructed gammas as a function of the number of real gammas that deposited energy in the detector from GEANT 4 before any event selection [Roy, 2021].

variables, a multivariate analysis using a *gradient boosted decision tree* (gBDT), from TMVA package of ROOT, was chosen by Noë. One gBDT for each reconstructed category in order to fit with the corresponding variables. The gBDTs were provided two pure datasets: the signal sample from IBD simulations and the background sample from 20 days of reactor OFF data of the open dataset. Half of these datasets have been used from training and half for test. The final cuts on the BDT scores have been optimized at the same time for the three BDTs with the statistical significance figure of merit $S/\sqrt{S+B}$, where S is computed from the selection efficiency to the expected 1088 IBDs per day. The no gamma category has been completely rejected by the BDT. The one gamma category selects 24 signal event for 104 background events ($S/B_{1\gamma} = 0.23$). The two gammas category selects 41 signal event for 138 background events ($S/B_{2\gamma} = 0.30$). The total expectation rates are thus 65 signal events for 243 background events per day. The signal over background ratio is boosted by almost a factor 10 compared to the very basic analysis, since $S/B_{gBDT} = 0.27$. This performance is getting closer to the original objective of $S/B \sim 1$ but comes with a strong efficiency reduction, which becomes only $\mathcal{E}_{IBD} \approx 6\%$.

9.2.3 Reactor data subtraction

Now the best performances on background rejection have been determined on the reactor OFF data, the goal is to extract the measured IBD events from the reactor ON data. This is done step by step on both data samples. Firstly, the accidentals are removed thanks to the FPNTs. The BiPo background is then subtracted after scaling from the BiPo side-band (also after accidental subtraction in the side-band). In the reactor OFF data remains only the atmospheric background which is used to estimate the atmospheric background level after pressure model correction in the reactor ON data. The total event rate with the individual contribution of each background is presented on figure 9.12. We observe a negligible accidental background and an almost equal proportion of BiPo and atmospheric backgrounds. The atmospheric background is lower in the reactor OFF period because of higher atmospheric pressure, as can be seen on figure 9.7. The final excess of events in the reactor ON data represents the anti-neutrinos detected.

The reactor ON excess is further investigated after the background subtraction presented on figure 9.13. The reactor OFF subtraction is well compatible with zero which is a good proof

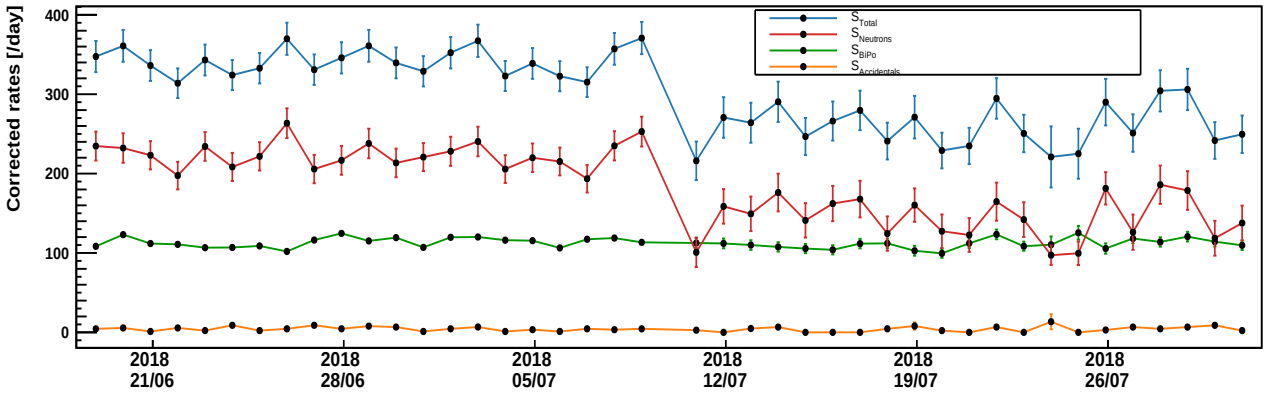

Figure 9.12: Total event rate (in blue) for the open dataset with the individual contribution of each background: accidental (in orange), BiPo (in green) and atmospheric (in red) [Roy, 2021]. The reactor ON→OFF transition occurred on the 10/07/2018.

of the correct backgrounds estimations. The excess in reactor ON data is stable over time with an average of 71±4 events per day. It is a little bit larger than the expectation of 65 events per day, but this is only a 1.5σ deviation. Given the limited statistics of the open data this is nevertheless a good achievement.

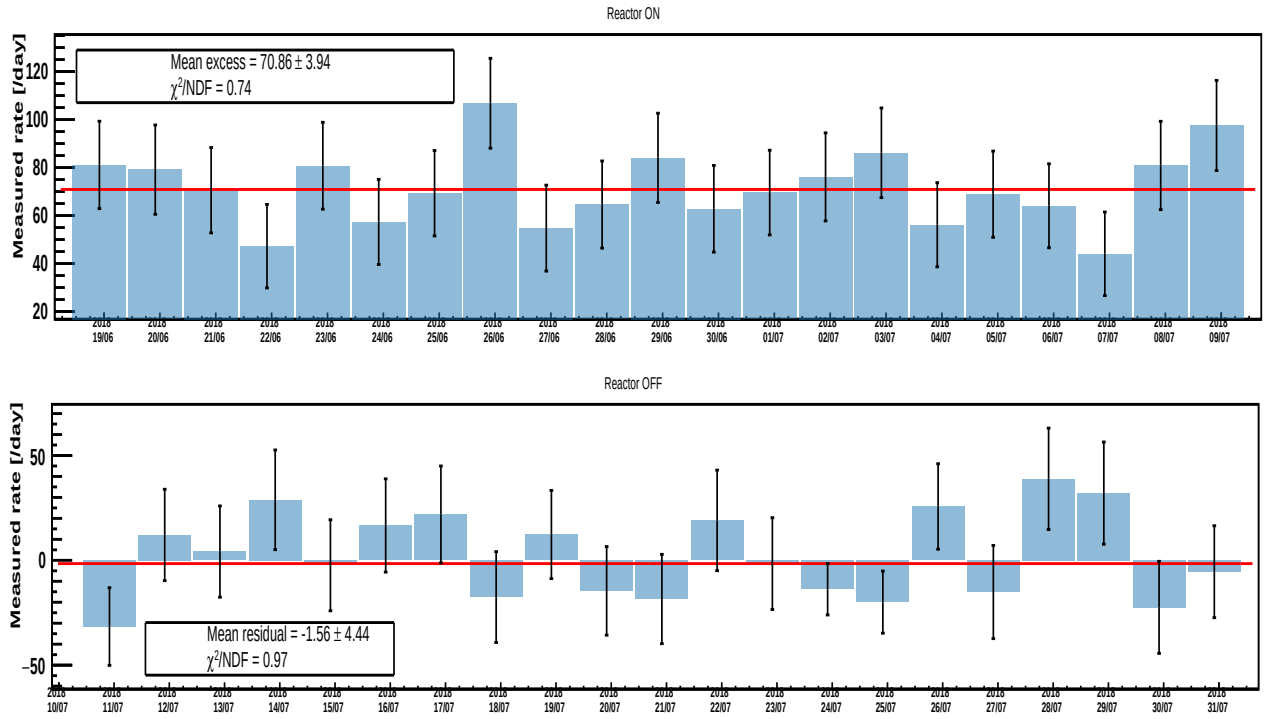

Figure 9.13: Measured event rate after subtraction of the backgrounds for reactor ON (top) and reactor OFF (bottom) open data with the zero degree polynomial fits (red line) [Roy, 2021].

We can then look at the two most interesting distributions for the search of sterile neutrino: the oscillation baseline and the positron energy. These two distributions are presented on figure 9.14 and 9.15 with the breakdown of the backgrounds and after subtraction. As already said the energy estimator is the crown energy. The anti-neutrino interaction positions (along Z-axis) have been merged into detector modules, ten planes, given the limited statistics of the open dataset. The last bin suffers a lower efficiency because of many dead channels in the last planes constructed. As far as we can tell, the agreement with the simulation is good given the

limited statistics. This comparison with the IBD simulations will be the key to unveil a possible oscillation signal in dedicated analyses that were not the subject of the thesis of Noë Roy.

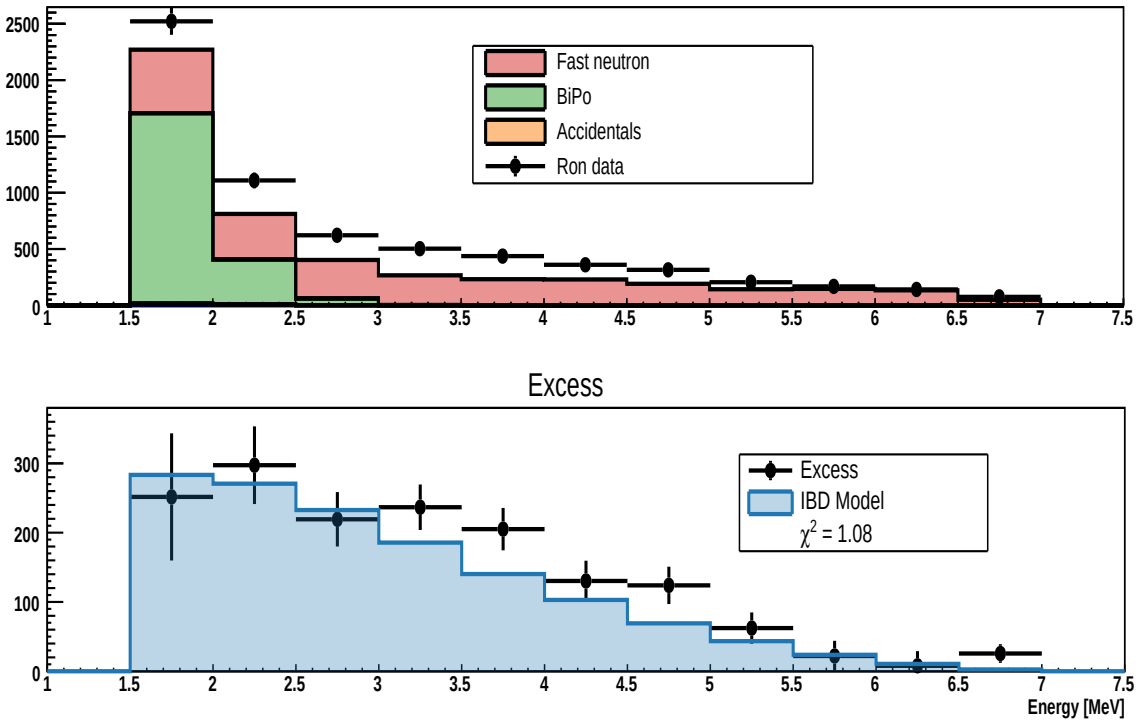

Figure 9.14: Energy distribution of the selected IBD-candidates for the reactor ON open dataset after gBDT selection with the background breakdown on top and compared to the IBD simulations after subtraction on the bottom [Roy, 2021].

At this stage of Noë's analysis we were very optimistic about unblinding more data and provide for the first time an analysis on the two years of reactor ON data. In total, 326 days of reactor ON and 187 of reactor OFF are available for the phase 1 data taking of SoLid. Before doing so, we wanted to check the stability of the background estimation and subtraction over all the inter-cycles reactor OFF data. This is presented on figure 9.16 except for the periods $8-9$ and $9-10$ impacted by the high temperature incident that occurred on the detector. Unfortunately, we can spot several periods where the subtraction is not behaving correctly (periods 4-5, 7-8 and 14-15) in the first energy bins. These energy bins are dominated by the BiPo background and Noë quickly pointed to variations in the *BiPonator* variable, used in the side-band scaling, over time.

This test was very instructive but unfortunately stopped the unblinding procedure and the PhD thesis of Noë ended. The *BiPonator* issue was quickly resolved by the colleagues in Caen and interesting new developments were implemented. The work of Noë have to be continued in the collaboration but it is important to highlight the great achievement it was to push the analysis so far. This was well recognized by the collaboration and by the jury of the PhD examination.

9.3 Conclusion and perspectives of SoLid analysis

The PhD thesis of Delphine on the very first physics data of SoLid has revealed the high challenge it would be to reject the backgrounds in the experiment. The IBD analysis of Noë, presented in the previous section 9.2, has demonstrated relatively good performances given the

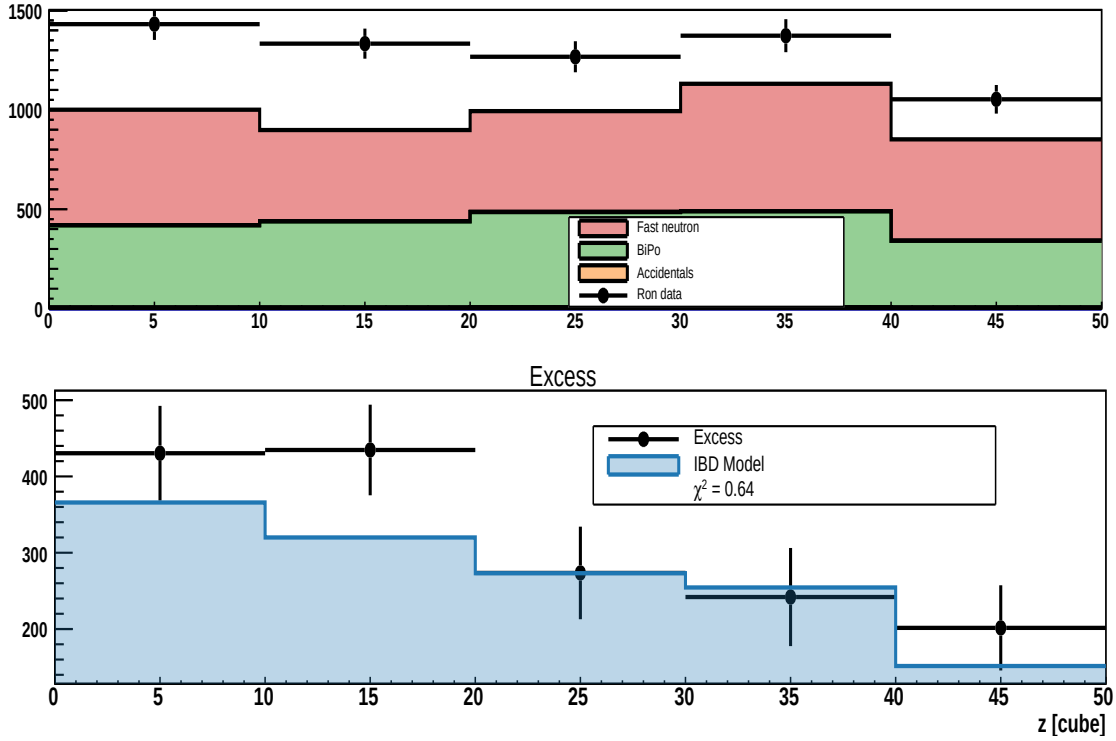

Figure 9.15: Interaction position distribution of the selected IBD-candidates for the reactor ON open dataset after gBDT selection with the background breakdown on top and compared to the IBD simulations after subtraction on the bottom [Roy, 2021].

huge background level faced by SoLid. Another analysis using *uniform BDT* (uBDT) from our UK colleagues has shown similar results. This is illustrated on figure 9.17 (left) where the S/B ratio as a function of the event excess per day, which depends on the BDT score cut, is represented for both analyses. The gBDT analysis is in good agreement with the prediction while the uBDT analysis is more fluctuating around the prediction. These results have been used for an oscillation search and preliminary sensitivity contours have been produced as shown on figure 9.17 (right). Unfortunately, the background rejection is not sufficient to reach a good performance on the search for a sterile neutrino with SoLid data. These results have been presented in 2021 at the summer conferences, like NuFact for example.

With one year shift compared to the thesis of Noë, another approach was developed by our colleagues in Clermont-Ferrand with the thesis of Mike Yeresko, defended in 2022 [Yeresko, 2022]. The analysis focussed on the two gammas topology to increase the signal purity at its best. The events topologies are constructed from a cluster approach [Hervé Chanal, 2020], instead of the gamma tracking algorithm. Event sub-categories are also constructed and the best ones are selected for the IBD analysis. The background rejection is also performed with BDTs and new interesting variables were introduced. The second difference of this analysis is also to avoid using the pressure model for atmospheric background that might not be reliable enough. The strategy consists of using a multi-dimensional fit of Δt and ΔR variables simultaneously. Using a fine binning, the ΔR variable offers the discrimination between IBD and atmospheric background events that are degenerate in Δt. A signal to background ratio better than one has been achieved on the two gamma channel for event excesses below 25 per day. This is almost a factor two increase compared to Noë's analysis. The reduction of statistics seems to be balanced by the strong background reduction in terms of oscillation sensitivity.

After the defence of Noë's thesis, several improvements in the events reconstruction were implemented in SoLid software. The first implementation concerned an hardware issue occurring

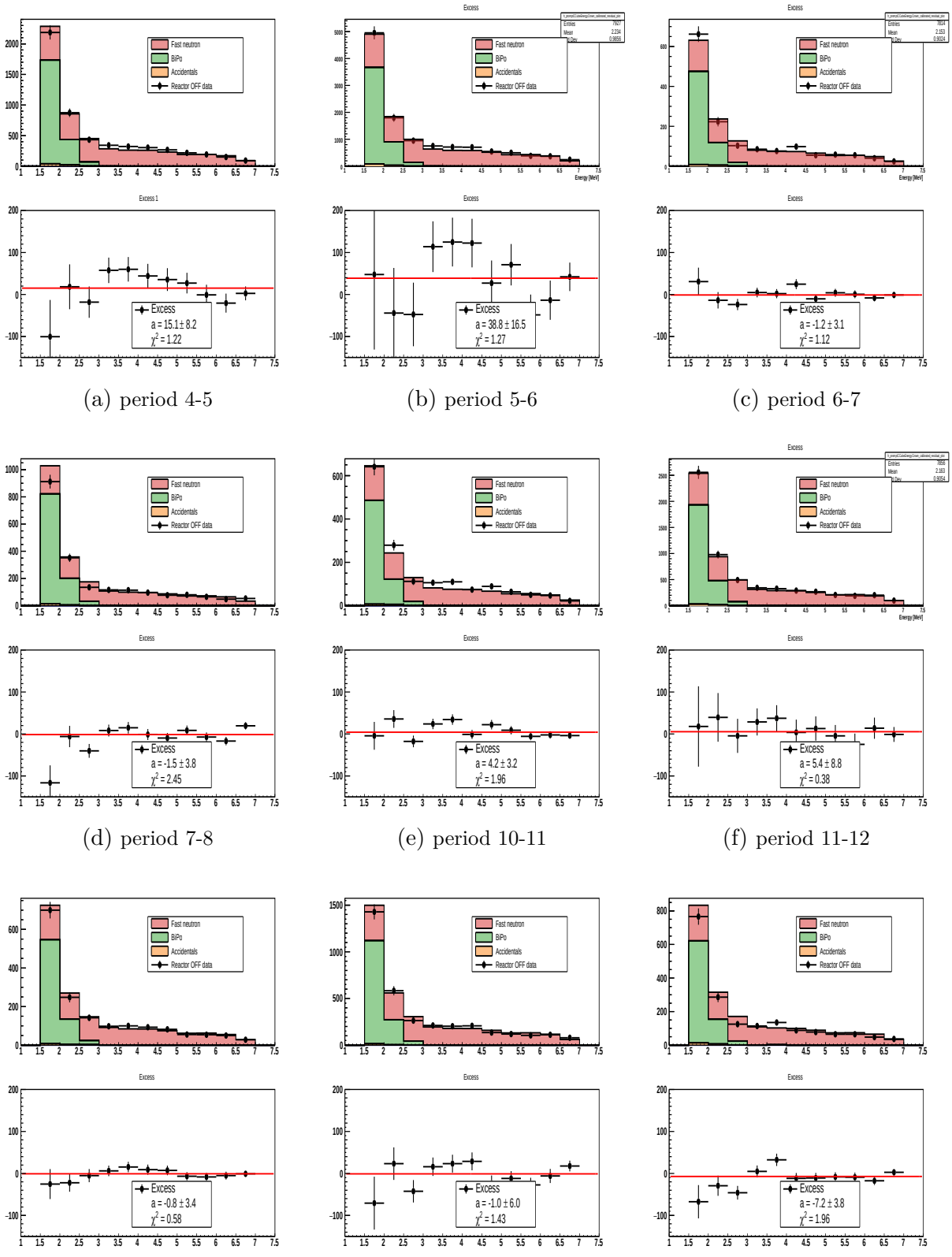

(a) period 4-5 (b) period 5-6 (c) period 6-7

(d) period 7-8 (e) period 10-11 (f) period 11-12

(g) period 12-13 (h) period 13-14 (i) period 14-15

Figure 9.16: Energy distributions and subtraction of the reactor OFF periods $4-5$ to $14-15$ (without the problematic periods $8-9$ and $9-10$) with the reactor OFF open dataset [Roy, 2021].

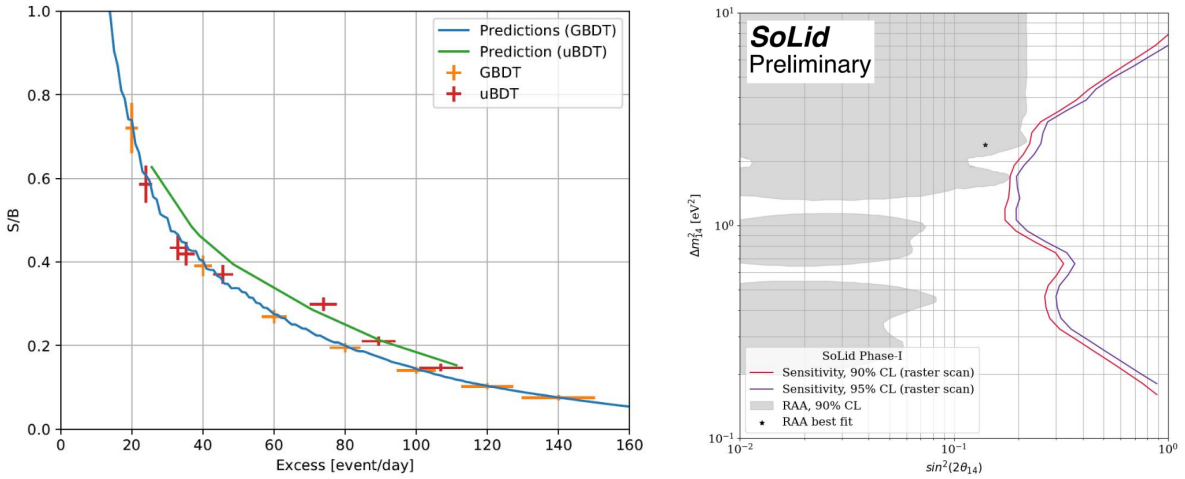

Figure 9.17: SoLid preliminary results presented at NuFact 2021 conference. (left) Evolution curve of the signal to background ratio as a function of the event excess selected by the two BDT analyses for data (error bar points) and predictions (solid lines). (right) Preliminary sensitivity contour on the search for sterile neutrino with gBDT on the phase 1 data with the RAA allowed region and best-fit.

during the data taking, where some channels randomly shuts-down because of an overflow of the FPGA buffers [Danny Galbinski, 2021]. This impacts the reconstruction of cubes because the overflow causes a 20% decrease of cubes with four channels, transferred to three channel cubes, during the 480 s runs. The second major change concerns the CCubes reconstruction (presented in section 6.8) which was using the flat system matrix with the scintillation light supposed to be equally shared among the four channels. The new implementation, called the *muon system matrix*, uses the measured light sharing and leaks from horizontal muons passing through single cubes in SoLid planes. These major changes required to reprocess all the phase 1 data and to redo the work performed by Noë and David on the calibration and IBD analysis. This is still ongoing at the time of writing these pages and two theses should include these new results.

Beyond the ongoing improvements on the analysis, an hardware upgrade of the SoLid detector occurred at summer 2020. All the 12$^{\text{th}}$ generation Hamamatsu MPPCs have been replaced by the generation 14$^{\text{th}}$ for which the cost reduction made possible its funding. These SiPMs offer better photon detection efficiency and a lower cross-talk. An increase of the cube light-yield of more than 40% has been demonstrated by the first ^{22}Na calibration analysed by Noë. Indeed the average LY of the detector increased from 91 PA/MeV in February 2020 to 129 PA/MeV in November 2020. This light increase should boost the discrimination power thanks to a better identification of the two annihilation γ's around the positron. An upgrade of the DAQ firmware should also reduce the channel overflowing issue that increase with the increase of PDE. The phase 2 data taking of SoLid ended-up at BR2 after Summer 2022. The decline of the manpower in the SoLid collaboration might be an issue to perform this final analysis.

Conclusion and outlook

In the first part of this document, we have tried to illustrate how important it would be to prove the Majorana nature of the neutrino. First, it would open the path to matter creation processes and a possible explanation of the matter-antimatter asymmetry of the Universe. Secondly, it could explain the smallness of neutrino masses thanks to the introduction of the Majorana mass terms in the Standard Model Lagrangian. New physics beyond Standard Model could participate to this mass term. The only experimental way to test the nature of the neutrino is the search for neutrinoless double beta decay, a lepton number violating process. In case of discovery, the $0\nu\beta\beta$ decay rate could bring important constraint on the effective neutrino mass of the neutrino $m_{\beta\beta}$. In combination with the measurements from flavour oscillations, direct mass in β-decay and cosmology, we might be able to finally determine the neutrino masses.

We have presented that the experimental search for neutrinoless double beta decay is a very active field of research, driving very innovative technologies always pushing the limits of the extremely low background levels. The experimental sensitivity is now investigating the inverted mass ordering region of the effective neutrino mass, and might completely cover this region in a near future, down to around 18 meV. I believe that the neutrinoless double beta decay is about to be discovered. In parallel to the experimental search, very important progresses are being made in nuclear physics theory to compute the nuclear matrix elements for double beta decay. These are mandatory to determine the effective neutrino mass $m_{\beta\beta}$.

Among the experimental search for $0\nu\beta\beta$, I was involved in the SuperNEMO experiment. The combination of a gaseous tracker and a segmented calorimeter provides SuperNEMO the unique feature of detecting individually the two electrons, measure their single energies and the angular distribution. This is very effective to reject the backgrounds but most importantly, it is of particular importance if we want to understand the underlying mechanism of the decay. These parameters can also provide very important insights to the nuclear models. The collaboration is about to achieve the construction of the demonstrator studying more than 6 kg of ^{82}Se and should provide the best sensitivity for this isotope in the next three years.

In the case of discovery in other experiments, we could envisage to build more SuperNEMO detectors to reach the corresponding sensitivity and investigate the decay mechanism. We have learned a lot from the difficult construction of the SuperNEMO demonstrator and we already have ideas for improvements. In the mean time technologies of scintillation and photo-detection have made important progresses. For example, I think the use of SiPMs and optical fibres could really improve the compactness, reduce the backgrounds and solve the magnetic field and gas tightness issues of SuperNEMO. I believe this could certainly happen without loosing performances on detection efficiency, energy resolution and timing performances of the experiment. In the near future, I would like to keep an eye on the progress of the analysis of the SuperNEMO demonstrator data. At longer term, in parallel to the pure calorimetric search, I have the conviction we should keep aiming at detecting the two electrons individually. I would be happy to participate to reflections on this subject with the French collaboration of SuperNEMO, if they are willing to.

The second part of this document concerned neutrino oscillations. The last two decades

were extremely fruitful in determining the three neutrino mixing paradigm and in measuring most of the mixing parameters to a few percent precision. Decisive results are about to come in the next decade with the determination of the θ_{23} octant, the neutrino mass ordering and the CP-violating phase δ_{CP}. The confrontation and combination of several major experiments, like JUNO, NOνA, T2K, Hyper-K, DUNE and ORCA, will be very exciting. I hope to contribute on JUNO side to these future neutrino oscillation measurements. In the last decade, several persisting anomalies in neutrino oscillations data have triggered an important experimental effort to answer the question of a possible existence of a sterile neutrino. Among them the reactor anti-neutrino anomaly could have been explained by very short baseline active-to-sterile neutrino oscillations. The recent experimental results on the ^{235}U β-spectrum and neutrino oscillations search at reactors seem to rule-out this hypothesis. From the theoretical point of view, the sterile neutrino is however still needed to provide mass to the neutrinos. The reactor anti-neutrino shape anomaly on its side cannot be explained invoking a sterile neutrino.

The SoLid experiment was one of the very innovative neutrino experiments which tried to investigate oscillation at around 10 m of a reactor core, in a difficult environment of radioactive and atmospheric background. The technology was aiming to reach an unprecedented localisation precision on the anti-neutrino interaction and detect the annihilation γ's accompanying the positron signal, before the delayed neutron capture. For these purposes, the detector design consisted in combining two types of scintillators and collect the light through optical fibres to SiPMs. Unfortunately, the background levels in SoLid experiment were too high. This forced the collaboration to implement very sophisticated multi-variates analyses. As such, it was a great opportunity to train the physicist, and specially the PhD students and postdocs. We were also aiming at providing insights to nuclear physics, thanks to the measurement of the pure ^{235}U spectrum.

Like for double beta decay, this illustrates the need for improvements in understanding nuclear physics, both from theoretical and experimental point of view. This is a real concern for neutrino physics and the communities would gain in collaborating more. The understanding of nuclear reactors as a neutrino source will still be important in the near future. This is of interest for the measurement of the mass ordering with JUNO. Satellites experiments are specifically dedicated to this task, like the TAO detector or the AM-OTech project in France. The other neutrino oscillation anomalies still persist and will need to be answered.

The ongoing R&D with LiquidO might improve what we were aiming at with SoLid technology. The first two prototypes (μ-liquido and mini-liquido) have given already good evidences of the scintillation light confinement, but the full capabilities of LiquidO are still to be demonstrated. This should be done in the near future thanks to the next prototype under construction (mini-γ) and the AM-OTech demonstrator, which will be installed at 30 m from one core of the Chooz power plant, in France. This research could be the path to future reactor projects, like SuperChooz, aiming at improving the precision on θ_{13} angle and test the unitarity of the PMNS matrix. This could happen after JUNO experiment, at horizon of 2030.

List of Figures

Bibliography

[Aalbers et al., 2023] Aalbers, J. et al. (2023). A next-generation liquid xenon observatory for dark matter and neutrino physics. *J. Phys. G*, 50(1):013001. (page 37)

[Abazajian et al., 2012] Abazajian, K. N. et al. (2012). Light Sterile Neutrinos: A White Paper. (page 142, 154, 255)

[Abe et al., 2010] Abe, S., Enomoto, S., Furuno, K., Gando, Y., Ikeda, H., Inoue, K., Kibe, Y., Kishimoto, Y., Koga, M., Minekawa, Y., and et al. (2010). Production of radioactive isotopes through cosmic muon spallation in kamland. *Physical Review C*, 81(2). (page 135)

[Abe et al., 2023] Abe, S. et al. (2023). Search for the Majorana Nature of Neutrinos in the Inverted Mass Ordering Region with KamLAND-Zen. *Phys. Rev. Lett.*, 130(5):051801. (page 14, 35, 36, 244)

[Abe et al., 2013] Abe, Y. et al. (2013). Direct Measurement of Backgrounds using Reactor-Off Data in Double Chooz. *Phys. Rev. D*, 87(1):011102. (page 138)

[Abgrall et al., 2021] Abgrall, N. et al. (2021). The Large Enriched Germanium Experiment for Neutrinoless $\beta\beta$ Decay: LEGEND-1000 Preconceptual Design Report. (page 30, 39, 244)

[Abratenko et al., 2022a] Abratenko, P. et al. (2022a). First constraints on light sterile neutrino oscillations from combined appearance and disappearance searches with the MicroBooNE detector.

[Abratenko et al., 2022b] Abratenko, P. et al. (2022b). Search for Neutrino-Induced Neutral-Current Δ Radiative Decay in MicroBooNE and a First Test of the MiniBooNE Low Energy Excess under a Single-Photon Hypothesis. *Phys. Rev. Lett.*, 128:111801. (page 147)

[Abreu et al., 2017] Abreu, Y. et al. (2017). A novel segmented-scintillator antineutrino detector. *JINST*, 12(04):P04024. (page 159, 160, 173, 193)

[Abreu et al., 2018a] Abreu, Y. et al. (2018a). Optimisation of the scintillation light collection and uniformity for the SoLid experiment. *JINST*, 13(09):P09005. (page 185, 208, 210)

[Abreu et al., 2018b] Abreu, Y. et al. (2018b). Performance of a full scale prototype detector at the BR2 reactor for the SoLid experiment. *JINST*, 13(05):P05005. (page 159, 163, 164, 173, 193, 198)

[Abreu et al., 2019a] Abreu, Y. et al. (2019a). Commissioning and Operation of the Readout System for the SoLid Neutrino Detector. *JINST*, 14(11):P11003. (page 176, 177, 178, 208, 257)

[Abreu et al., 2019b] Abreu, Y. et al. (2019b). Development of a Quality Assurance Process for the SoLid Experiment. *JINST*, 14(02):P02014. (page 201, 202)

[Abreu et al., 2021] Abreu, Y. et al. (2021). SoLid: a short baseline reactor neutrino experiment. *JINST*, 16(02):P02025. (page 159, 169, 180, 201)

[Achkar et al., 1995] Achkar, B., Aleksan, R., Avenier, M., Bagieu, G., Bouchez, J., Brissot, R., Cavaignac, J.-F., Collot, J., Cousinou, M.-C., Cussonneau, J., Declais, Y., Dufour, Y., Favier, J., Garciaz, F., Kajfasz, E., de Kerret, H., Koang, D., Lefièvre, B., Lesquoy, E., Mallet, J., Metref, A., Nagy, E., Pessard, H., Pierre, F., Obolensky, M., Stutz, A., and Wuthrick, J. (1995). Search for neutrino oscillations at 15, 40 and 95 meters from a nuclear power reactor at bugey. *Nuclear Physics B*, 434(3):503 – 532. (page 133, 134, 152, 251, 254)

[Achkar and others., 1996] Achkar, B. and others. (1996). Comparison of anti-neutrino reactor spectrum models with the bugey 3 measurements. *Physics Letters B*, 374(1):243–248. (page 134, 135)

[Adey et al., 2019] Adey, D. et al. (2019). Extraction of the ^{235}U and ^{239}Pu Antineutrino Spectra at Daya Bay. *Phys. Rev. Lett.*, 123(11):111801. (page 146, 253)

[Adhikari et al., 2022] Adhikari, G. et al. (2022). nEXO: neutrinoless double beta decay search beyond 10^{28} year half-life sensitivity. *J. Phys. G*, 49(1):015104. (page 37)

[Aghanim et al., 2020] Aghanim, N. et al. (2020). Planck 2018 results. VI. Cosmological parameters. *Astron. Astrophys.*, 641:A6. [Erratum: Astron.Astrophys. 652, C4 (2021)]. (page 20)

[Agostinelli et al., 2003] Agostinelli, S. et al. (2003). GEANT4: A Simulation toolkit. *Nucl. Instrum. Meth.*, A506:250–303. (page 180)

[Agostini et al., 2017] Agostini, M., Benato, G., and Detwiler, J. A. (2017). Discovery probability of next-generation neutrinoless double-β decay experiments. *Phys. Rev. D*, 96:053001. (page 44)

[Agostini et al., 2021] Agostini, M., Benato, G., Detwiler, J. A., Menéndez, J., and Vissani, F. (2021). Testing the inverted neutrino mass ordering with neutrinoless double-β decay. *Phys. Rev. C*, 104(4):L042501. (page 43, 44, 45, 245)

[Agostini et al., 2023] Agostini, M., Benato, G., Detwiler, J. A., Menéndez, J., and Vissani, F. (2023). Toward the discovery of matter creation with neutrinoless $\beta\beta$ decay. *Rev. Mod. Phys.*, 95(2):025002. (page 14, 17, 19, 22, 23, 42, 43, 44, 243, 245)

[Agostini et al., 2020] Agostini, M. et al. (2020). Final results of gerda on the search for neutrinoless double-β decay. *Phys. Rev. Lett.*, 125:252502. (page 38, 39, 244)

[Aguerre, 2023] Aguerre, X. (2023). *Recherche de la décroissance double beta sans émission de neutrinos du 82Se avec l'expérience SuperNEMO : reconstruction de l'énergie mesurée avec le calorimètre et analyse des premières données du démonstrateur.* Theses, Université de Bordeaux. (page 93, 99, 106, 113, 114, 115, 116, 250)

[Aguilar-Arevalo et al., 2001] Aguilar-Arevalo, A. et al. (2001). Evidence for neutrino oscillations from the observation of $\bar{\nu}_e$ appearance in a $\bar{\nu}_\mu$ beam. *Phys. Rev. D*, 64:112007. (page 147)

[Aguilar-Arevalo et al., 2021] Aguilar-Arevalo, A. A. et al. (2021). Updated MiniBooNE neutrino oscillation results with increased data and new background studies. *Phys. Rev. D*, 103(5):052002. (page 147)

[Aker et al., 2022a] Aker, M. et al. (2022a). Direct neutrino-mass measurement with sub-electronvolt sensitivity. *Nature Phys.*, 18(2):160–166. (page 19)

[Aker et al., 2022b] Aker, M. et al. (2022b). Improved eV-scale sterile-neutrino constraints from the second KATRIN measurement campaign. *Phys. Rev. D*, 105(7):072004. (page 157, 255)

[Akimov et al., 2017] Akimov, D. et al. (2017). Observation of Coherent Elastic Neutrino-Nucleus Scattering. *Science*, 357(6356):1123–1126. (page 126)

[Akindele et al., 2022] Akindele, O. A. et al. (2022). High Energy Physics Opportunities Using Reactor Antineutrinos. In *2022 Snowmass Summer Study*. (page 144, 145, 253)

[Alamos, 1997] Alamos, L. (1997). The Reines-Cowan Experiments. *Los Alamos Science*, 3(25). (page 125)

[Albanese et al., 2021] Albanese, V. et al. (2021). The SNO+ experiment. *JINST*, 16(08):P08059. (page 40)

[Alfonso et al., 2023] Alfonso, K. et al. (2023). Cupid: The next-generation neutrinoless double beta decay experiment. *Journal of Low Temperature Physics*, 211(5):375–383. (page 41, 244)

[Allega et al., 2022] Allega, A. et al. (2022). Improved search for invisible modes of nucleon decay in water with the SNO+detector. *Phys. Rev. D*, 105(11):112012. (page 14)

[Almazán et al., 2020] Almazán, H. et al. (2020). Improved sterile neutrino constraints from the STEREO experiment with 179 days of reactor-on data. *Phys. Rev. D*, 102(5):052002. (page 150)

[Almazán et al., 2021] Almazán, H. et al. (2021). First antineutrino energy spectrum from ^{235}U fissions with the STEREO detector at ILL. *J. Phys. G*, 48(7):075107. (page 156)

[Almazán et al., 2022] Almazán, H. et al. (2022). Joint Measurement of the ^{235}U Antineutrino Spectrum by Prospect and Stereo. *Phys. Rev. Lett.*, 128(8):081802. (page 155, 156, 255)

[Almazán et al., 2023] Almazán, H. et al. (2023). STEREO neutrino spectrum of ^{235}U fission rejects sterile neutrino hypothesis. *Nature*, 613(7943):257–261. (page 153, 154, 155, 255)

[Alvis et al., 2019] Alvis, S. I. et al. (2019). A Search for Neutrinoless Double-Beta Decay in ^{76}Ge with 26 kg-yr of Exposure from the MAJORANA DEMONSTRATOR. *Phys. Rev. C*, 100(2):025501. (page 39)

[An et al., 2016a] An, F. et al. (2016a). Neutrino Physics with JUNO. *J. Phys. G*, 43(3):030401. (page 43)

[An et al., 2016b] An, F. P. et al. (2016b). Improved search for a light sterile neutrino with the full configuration of the daya bay experiment. *Phys. Rev. Lett.*, 117:151802. (page 152, 254)

[An et al., 2017a] An, F. P. et al. (2017a). Evolution of the Reactor Antineutrino Flux and Spectrum at Daya Bay. *Phys. Rev. Lett.*, 118(25):251801. (page 131, 142, 144, 253)

[An et al., 2017b] An, F. P. et al. (2017b). Improved Measurement of the Reactor Antineutrino Flux and Spectrum at Daya Bay. *Chin. Phys. C*, 41(1):013002. (page 151, 155)

[Andriamirado et al., 2021] Andriamirado, M. et al. (2021). Improved short-baseline neutrino oscillation search and energy spectrum measurement with the PROSPECT experiment at HFIR. *Phys. Rev. D*, 103(3):032001. (page 150, 155, 156, 255)

[Anton and others", 2019] Anton, G. and others" (2019). Search for neutrinoless double-β decay with the complete exo-200 dataset. *Phys. Rev. Lett.*, 123:161802. (page 37, 244)

[Apollonio et al., 2003] Apollonio, M. et al. (2003). Search for neutrino oscillations on a long baseline at the CHOOZ nuclear power station. *Eur. Phys. J. C*, 27:331–374. (page 136, 145)

[Aprile et al., 2019] Aprile, E. et al. (2019). Observation of two-neutrino double electron capture in ^{124}Xe with XENON1T. *Nature*, 568(7753):532–535. (page 17)

[Argyriades et al., 2009] Argyriades, J. et al. (2009). Measurement of the background in the NEMO 3 double beta decay experiment. *Nucl. Instrum. Meth. A*, 606:449–465. (page 51, 53, 70)

[Argyriades et al., 2010] Argyriades, J. et al. (2010). Results of the BiPo-1 prototype for radiopurity measurements for the SuperNEMO double beta decay source foils. *Nucl. Instrum. Meth. A*, 622:120–128. (page 54, 55, 56)

[Armengaud et al., 2020] Armengaud, E. et al. (2020). The cupid-mo experiment for neutrinoless double-beta decay: performance and prospects. *The European Physical Journal C*, 80(1):44. (page 42, 245)

[Armengaud et al., 2021] Armengaud, E. et al. (2021). New limit for neutrinoless double-beta decay of ^{100}Mo from the cupid-mo experiment. *Phys. Rev. Lett.*, 126:181802. (page 42, 245)

[Arnold et al., 2005] Arnold, R. et al. (2005). Technical design and performance of the NEMO 3 detector. *Nucl. Instrum. Meth.*, A536:79–122. (page 48, 68, 76, 186)

[Arnold et al., 2010] Arnold, R. et al. (2010). Probing New Physics Models of Neutrinoless Double Beta Decay with SuperNEMO. *Eur. Phys. J.*, C70:927–943. (page 29, 65, 186)

[Arnold et al., 2014a] Arnold, R. et al. (2014a). Investigation of double beta decay of ^{100}Mo to excited states of ^{100}Ru. *Nucl. Phys. A*, 925:25–36. (page 17)

[Arnold et al., 2014b] Arnold, R. et al. (2014b). Search for neutrinoless double-beta decay of ^{100}Mo with the NEMO-3 detector. *Phys. Rev. D*, 89(11):111101. (page 49, 52, 245)

[Arnold et al., 2018] Arnold, R. et al. (2018). Final results on ^{82}Se double beta decay to the ground state of ^{82}Kr from the NEMO-3 experiment. *Eur. Phys. J. C*, 78(10):821. (page 53)

[Arnold et al., 2019] Arnold, R. et al. (2019). Detailed studies of ^{100}Mo two-neutrino double beta decay in NEMO-3. *Eur. Phys. J. C*, 79(5):440. (page 21, 50, 245)

[Arnold et al., 2020] Arnold, R. et al. (2020). Search for the double-beta decay of ^{82}Se to the excited states of ^{82}Kr with NEMO-3. *Nucl. Phys. A*, 996:121701. (page 17)

[Arnold et al., 2021] Arnold, R. et al. (2021). Measurement of the distribution of ^{207}Bi depositions on calibration sources for SuperNEMO. *JINST*, 16(07):T07012. (page 92, 112, 249)

[Arnold et al., 2023] Arnold, R. et al. (2023). Measurement of double beta decay of ^{150}Nd to the 0_1^+ excited state of ^{150}Sm in NEMO-3. *The European Physical Journal C*, 83(12):1117. (page 17)

[Atif et al., 2022] Atif, Z., Choi, J. H., Han, B. Y., Jang, C. H., Jang, H. I., Jang, J. S., Jeon, E. J., Jeon, S. H., Joo, K. K., Ju, K., Jung, D. E., Kim, B. R., Kim, H. J., Kim, H. S., Kim, J. G., Kim, J. H., Kim, J. Y., Kim, J. Y., Kim, S. B., Kim, S. Y., Kim, W., Kim, Y. D., Ko, Y. J., Kwon, E., Lee, D. H., Lee, H. G., Lee, J., Lee, J. Y., Lee, M. H., Lim, I. T., Moon, D. H., Oh, Y. M., Pac, M. Y., Park, H. K., Park, H. S., Park, J. S., Park, K. S., Park, R. G., Seo, H., Seo, J. W., Seo, K. M., Shin, C. D., Siyeon, K., Sun, G. M., Yang, B. S., Yeo, I. S., Yoo, J., Yoon, S. G., and Yu, I. (2022). Search for sterile neutrino oscillations using reno and neos data. *Phys. Rev. D*, 105:L111101. (page 151, 153, 254)

[Augier, 2005] Augier, C. (2005). *Expérience NEMO 3 - Avantages et limitations. Prospective pour la physique double bêta.* Habilitation à diriger des recherches, Université Paris Sud - Paris XI. (page 48, 76, 78)

[Avignone et al., 1968] Avignone, F. T., Blakenship, S. M., and Darden, C. W. (1968). Theoretical fission-antineutrino spectrum and cross section of the reaction ^{3}He$(\overline{\nu}_e, e^+)^3$H. *Phys. Rev.*, 170:931–934. (page 127)

[Azzolini et al., 2019a] Azzolini, O. et al. (2019a). Background model of the cupid-0 experiment. *The European Physical Journal C*, 79(7):583. (page 41, 244)

[Azzolini et al., 2019b] Azzolini, O. et al. (2019b). Background Model of the CUPID-0 Experiment. *Eur. Phys. J. C*, 79(7):583. (page 41)

[Azzolini et al., 2019c] Azzolini, O. et al. (2019c). Evidence of single state dominance in the two-neutrino double-β decay of ^{82}Se with cupid-0. *Phys. Rev. Lett.*, 123:262501. (page 21)

[Azzolini et al., 2019d] Azzolini, O. et al. (2019d). Final result of cupid-0 phase-i in the search for the ^{82}Se neutrinoless double-β decay. *Phys. Rev. Lett.*, 123:032501. (page 41, 95)

[Balantekin and Kayser, 2018] Balantekin, A. B. and Kayser, B. (2018). On the properties of neutrinos. *Annual Review of Nuclear and Particle Science*, 68(1):313–338. (page 14, 15, 243)

[Balysh et al., 1996] Balysh, A., De Silva, A., Lebedev, V. I., Lou, K., Moe, M. K., Nelson, M. A., Piepke, A., Pronskiy, A., Vient, M. A., and Vogel, P. (1996). Double beta decay of ^{48}Ca. *Phys. Rev. Lett.*, 77:5186–5189. (page 23)

[Barabash et al., 2017a] Barabash, A. et al. (2017a). Calorimeter development for the SuperNEMO double beta decay experiment. *Nucl. Instrum. Meth. A*, 868:98–108. (page 78)

[Barabash et al., 2017b] Barabash, A. S. et al. (2017b). The BiPo-3 detector for the measurement of ultra low natural radioactivities of thin materials. *JINST*, 12(06):P06002. (page 57, 59, 60, 61, 246)

[Baranger, 1960] Baranger, M. (1960). Extension of the shell model for heavy spherical nuclei. *Phys. Rev.*, 120:957–968. (page 24)

[Barea et al., 2015] Barea, J., Kotila, J., and Iachello, F. (2015). $0\nu\beta\beta$ and $2\nu\beta\beta$ nuclear matrix elements in the interacting boson model with isospin restoration. *Phys. Rev. C*, 91(3):034304. (page 24)

[Barinov et al., 2022] Barinov, V. V. et al. (2022). Results from the Baksan Experiment on Sterile Transitions (BEST). *Phys. Rev. Lett.*, 128(23):232501. (page 147, 148, 253)

[Bé et al., 2006] Bé, M.-M., Chisté, V., Dulieu, C., Browne, E., Baglin, C., Chechev, V., Kuzmenko, N., Helmer, R., Kondev, F., MacMahon, D., and Lee, K. (2006). *Table of Radionuclides*, volume 3 of *Monographie BIPM-5*. Bureau International des Poids et Mesures, Pavillon de Breteuil, F-92310 Sèvres, France. (page 108, 250)

[Bé et al., 2010] Bé, M.-M., Chisté, V., Dulieu, C., Mougeot, X., Browne, E., Chechev, V., Kuzmenko, N., Kondev, F., Luca, A., Galán, M., Nichols, A., Arinc, A., and Huang, X. (2010). *Table of Radionuclides*, volume 5 of *Monographie BIPM-5*. Bureau International des Poids et Mesures, Pavillon de Breteuil, F-92310 Sèvres, France. (page 92, 112, 250)

[Berryman and Huber, 2021] Berryman, J. M. and Huber, P. (2021). Sterile Neutrinos and the Global Reactor Antineutrino Dataset. *JHEP*, 01:167. (page 145, 253)

[Bilenky and Pontecorvo, 1978] Bilenky, S. and Pontecorvo, B. (1978). Lepton mixing and neutrino oscillations. *Physics Reports*, 41(4):225–261. (page 126)

[Bilenky and Petcov, 1987] Bilenky, S. M. and Petcov, S. T. (1987). Massive neutrinos and neutrino oscillations. *Rev. Mod. Phys.*, 59:671–754. (page 15)

[Bongrand, 2008] Bongrand, M. (2008). *Mesure de processus de double désintégration bêta du ^{130}Te dans l'expérience NEMO 3. RetD du projet SuperNEMO : étude d'un détecteur BiPo.* Theses, Université Paris Sud - Paris XI. (page 47, 55)

[Bonhomme, 2018] Bonhomme, A. (2018). *Anomalie des antineutrinos de réacteurs : recherche d'un état stérile avec l'expérience STEREO.* Theses, Université Paris Saclay (COmUE). (page 154)

[Böser et al., 2020] Böser, S., Buck, C., Giunti, C., Lesgourgues, J., Ludhova, L., Mertens, S., Schukraft, A., and Wurm, M. (2020). Status of Light Sterile Neutrino Searches. *Prog. Part. Nucl. Phys.*, 111:103736. (page 126, 251)

[Boursette, 2018] Boursette, D. (2018). *Neutrino physics with SoLid and SuperNEMO experiments.* Theses, Université Paris-Saclay. (page 63, 70, 102, 110, 185, 223, 224, 225, 226, 247, 260)

[Breton et al., 2005] Breton, D., Delagnes, E., and Houry, M. (2005). Very high dynamic range and high sampling rate vme digitizing boards for physics experiments. *IEEE Transactions on Nuclear Science*, 52(6):2853 – 2860. Cited by: 35; All Open Access, Green Open Access. (page 55)

[Breton et al., 2011] Breton, D., Delagnes, E., Maalmi, J., Nishimura, K., Ruckman, L. L., Varner, G., and Va'vra, J. (2011). High resolution photon timing with MCP-PMTs: a comparison of commercial constant fraction discriminator (CFD) with ASIC-based waveform digitizers TARGET and WaveCatcher. *Nucl. Instrum. Meth.*, A629:123–132. (page 83, 189)

[Breton et al., 2014] Breton, D., Delagnes, E., Maalmi, J., and Rusquart, P. (2014). The wavecatcher family of sca-based 12-bit 3.2-gs/s fast digitizers. In *2014 19th IEEE-NPSS Real Time Conference*, pages 1–8. (page 189)

[Brown and Bolsterli, 1959] Brown, G. E. and Bolsterli, M. (1959). Dipole state in nuclei. *Phys. Rev. Lett.*, 3:472–476. (page 24)

[Cabrera et al., 2019] Cabrera, A. et al. (2019). Neutrino Physics with an Opaque Detector.

[Cabrera et al., 2022] Cabrera, A. et al. (2022). Synergies and prospects for early resolution of the neutrino mass ordering. *Sci. Rep.*, 12(1):5393. (page 141, 142, 252)

[Calvez, 2017] Calvez, S. (2017). *Development of reconstruction tools and sensitivity of the SuperNEMO demonstrator*. Theses, Université Paris-Saclay. (page 63, 78, 79, 81, 90, 91, 95, 96, 97, 248, 249)

[Cappuzzello et al., 2018] Cappuzzello, F. et al. (2018). The NUMEN project: NUclear Matrix Elements for Neutrinoless double beta decay. *Eur. Phys. J. A*, 54(5):72. (page 26)

[Caurier et al., 2005] Caurier, E., Martínez-Pinedo, G., Nowacki, F., Poves, A., and Zuker, A. P. (2005). The shell model as a unified view of nuclear structure. *Rev. Mod. Phys.*, 77:427–488. (page 23)

[Caurier et al., 2012] Caurier, E., Nowacki, F., and Poves, A. (2012). Shell Model description of the beta beta decay of 136Xe. *Phys. Lett. B*, 711:62–64. (page 23)

[Caurier et al., 1990] Caurier, E., Poves, A., and Zuker, A. (1990). A full $0\hbar w$ description of the $2\nu\beta\beta$ decay of ^{48}ca. *Physics Letters B*, 252(1):13–17. (page 23)

[Chapon, 2011] Chapon, A. (2011). *Mesure des processus de double désintégration bêta du ^{100}Mo vers l'état excité 0+1 du 100Ru dans l'expérience Nemo3 - Programme de R&D SuperNEMO : mise au point d'un détecteur BiPo pour la mesure de très faibles contaminations de feuilles sources*. Theses, Université de Caen. (page 56)

[Cogswell et al., 2019] Cogswell, B. K., Ernst, D. J., Ufheil, K. T. L., Gaglione, J. T., and Malave, J. M. (2019). Neutrino oscillations: The ILL experiment revisited. *Phys. Rev. D*, 99(5):053003. (page 133)

[Collaboration, 2022] Collaboration, T. C. (2022). Search for majorana neutrinos exploiting millikelvin cryogenics with CUORE. *Nature*, 604(7904):53–58. (page 40, 244)

[Cucoanes et al., 2015] Cucoanes, A., Novella, P., Cabrera, A., Fallot, M., Onillon, A., Obolensky, M., and Yermia, F. (2015). Reactor Neutrino Flux Uncertainty Suppression on Multiple Detector Experiments. (page 137)

[Danilov, 2020] Danilov, M. (2020). Recent results of the DANSS experiment. *PoS*, EPS-HEP2019:401. (page 150)

[Danny Galbinski, 2021] Danny Galbinski, Savitri Gallego, S. V. M. B. (2021). A note on quality assurance of phase-i data and stability studies conducted using bipo background. *SoLid TechNote*, 2021-09:DocDb–1768. (page 229, 239)

[Davis et al., 1979] Davis, B. R., Vogel, P., Mann, F. M., and Schenter, R. E. (1979). Reactor antineutrino spectra and their application to antineutrino-induced reactions. *Phys. Rev. C*, 19:2259–2266. (page 127)

[de Kerret et al., 2020] de Kerret, H. et al. (2020). Double chooz θ_{13} measurement via total neutron capture detection. *Nature Physics*, 16(5):558–564. (page 137, 138, 139, 140, 141, 145, 252)

[de Kerret et al., 2022] de Kerret, H. et al. (2022). The Double Chooz antineutrino detectors. *Eur. Phys. J. C*, 82(9):804. (page 137)

[Declais et al., 1994] Declais, Y. et al. (1994). Study of reactor anti-neutrino interaction with proton at Bugey nuclear power plant. *Phys. Lett. B*, 338:383–389.

[Dempster et al., 1977] Dempster, A. P., Laird, N. M., and Rubin, D. B. (1977). Maximum likelihood from incomplete data via the em algorithm. *Journal of the Royal Statistical Society: Series B (Methodological)*, 39(1):1–22. (page 181)

[Dentler et al., 2018] Dentler, M., Hernández-Cabezudo, A., Kopp, J., Machado, P. A. N., Maltoni, M., Martinez-Soler, I., and Schwetz, T. (2018). Updated Global Analysis of Neutrino Oscillations in the Presence of eV-Scale Sterile Neutrinos. *JHEP*, 08:010. (page 147)

[Djurcic et al., 2015] Djurcic, Z. et al. (2015). JUNO Conceptual Design Report. (page 140)

[Dolinski et al., 2019] Dolinski, M. J., Poon, A. W., and Rodejohann, W. (2019). Neutrinoless double-beta decay: Status and prospects. *Annual Review of Nuclear and Particle Science*, 69(1):219–251. (page 20, 24, 25, 243)

[Elliott et al., 1987] Elliott, S. R., Hahn, A. A., and Moe, M. K. (1987). Direct evidence for two-neutrino double-beta decay in ^{82}Se. *Phys. Rev. Lett.*, 59:2020–2023. (page 34)

[Engel and Menéndez, 2017] Engel, J. and Menéndez, J. (2017). Status and Future of Nuclear Matrix Elements for Neutrinoless Double-Beta Decay: A Review. *Rept. Prog. Phys.*, 80(4):046301. (page 22)

[Engel et al., 1988] Engel, J., Vogel, P., and Zirnbauer, M. R. (1988). Nuclear structure effects in double-beta decay. *Phys. Rev. C*, 37:731–746. (page 23)

[Esteban et al., 2020] Esteban, I., Gonzalez-Garcia, M. C., Maltoni, M., Schwetz, T., and Zhou, A. (2020). The fate of hints: updated global analysis of three-flavor neutrino oscillations. *JHEP*, 09:178. (page 124, 251)

[Estienne et al., 2019] Estienne, M. et al. (2019). Updated Summation Model: An Improved Agreement with the Daya Bay Antineutrino Fluxes. *Phys. Rev. Lett.*, 123(2):022502. (page 127, 128, 129, 131, 144, 146, 154, 155, 251, 255)

[Eurin, 2015] Eurin, G. (2015). *Search for the double-beta decay of 96Zr with the NEMO-3 detector and ultra-low radioactivity measurements for the SuperNEMO experiment using the BiPo-3 detector / Guillaume Eurin.* PhD thesis. (page 47, 56, 57, 63)

[Fiorini et al., 1967] Fiorini, E., Pullia, A., Bertolini, G., Cappellani, F., and Restelli, G. (1967). A search for lepton non-conservation in double beta decay with a germanium detector. *Physics Letters B*, 25(10):602–603. (page 34)

[Fireman, 1948] Fireman, E. L. (1948). *Physical Review*, 74(9):1238. (page 34)

[Fireman, 1949] Fireman, E. L. (1949). A measurement of the half-life of double beta-decay from $^{124}_{50}$Sn. *Physical Review*, 75(2):323. (page 34)

[Fogli et al., 2009] Fogli, G. L., Lisi, E., Marrone, A., Palazzo, A., and Rotunno, A. M. (2009). Neutrino oscillations, global analysis and theta(13). (page 135)

[Fukuda et al., 1998] Fukuda, Y. et al. (1998). Evidence for oscillation of atmospheric neutrinos. *Phys. Rev. Lett.*, 81:1562–1567. (page 134)

[Furry, 1939] Furry, W. H. (1939). On transition probabilities in double beta-disintegration. *Phys. Rev.*, 56:1184–1193. (page 17)

[Gando et al., 2011] Gando, A. et al. (2011). Constraints on θ_{13} from A Three-Flavor Oscillation Analysis of Reactor Antineutrinos at KamLAND. *Phys. Rev. D*, 83:052002. (page 135, 136, 137, 252)

[Gando et al., 2016] Gando, A. et al. (2016). Search for Majorana Neutrinos near the Inverted Mass Hierarchy Region with KamLAND-Zen. *Phys. Rev. Lett.*, 117(8):082503. [Addendum: Phys.Rev.Lett. 117, 109903 (2016)]. (page 35)

[Gando et al., 2019] Gando, A. et al. (2019). Precision measurement of the ^{136}Xe two-neutrino $\beta\beta$ spectrum in KamLAND-Zen and its impact on the quenching of nuclear matrix elements. *Phys. Rev. Lett.*, 122(19):192501. (page 27, 28, 243)

[Gariazzo et al., 2017] Gariazzo, S., Giunti, C., Laveder, M., and Li, Y. F. (2017). Updated Global 3+1 Analysis of Short-BaseLine Neutrino Oscillations. *JHEP*, 06:135. (page 142, 143, 253)

[Gavrilyuk et al., 2013] Gavrilyuk, Y. M., Gangapshev, A. M., Kazalov, V. V., Kuzminov, V. V., Panasenko, S. I., and Ratkevich, S. S. (2013). Indications of $2\nu2k$ capture in ^{78}kr. *Phys. Rev. C*, 87:035501. (page 17)

[Girard-Carillo, 2020] Girard-Carillo, C. (2020). *Study of ^{208}Tl background rejection influence on the $0\nu\beta\beta$ decay sensitivity, characterisation of SuperNEMO demonstrator calorimeter timing performance*. Theses, Université Paris-Saclay. (page 63, 99, 103, 104, 105, 108, 109, 112, 250)

[Giunti, 2016] Giunti, C. (2016). Light Sterile Neutrinos: Status and Perspectives. *Nucl. Phys. B*, 908:336–353. (page 147)

[Giunti, 2017] Giunti, C. (2017). Improved Determination of the ^{235}U and ^{239}Pu Reactor Antineutrino Cross Sections per Fission. *Phys. Rev.*, D96(3):033005.

[Giunti et al., 2020] Giunti, C., Ioannisian, A., and Ranucci, G. (2020). A new analysis of the MiniBooNE low-energy excess. *JHEP*, 11:146. [Erratum: JHEP 02, 078 (2021)]. (page 147)

[Giunti and Kim, 2007] Giunti, C. and Kim, C. W. (2007). *Fundamentals of Neutrino Physics and Astrophysics*. Oxford University Press. (page 15)

[Giunti and Laveder, 2011a] Giunti, C. and Laveder, M. (2011a). 3+1 and 3+2 Sterile Neutrino Fits. *Phys. Rev. D*, 84:073008. (page 148)

[Giunti and Laveder, 2011b] Giunti, C. and Laveder, M. (2011b). Statistical Significance of the Gallium Anomaly. *Phys. Rev. C*, 83:065504. (page 147)

[Giunti and Laveder, 2011c] Giunti, C. and Laveder, M. (2011c). Status of 3+1 Neutrino Mixing. *Phys. Rev.*, D84:093006. (page 151, 254)

[Giunti et al., 2022] Giunti, C., Li, Y., Ternes, C., and Xin, Z. (2022). Reactor antineutrino anomaly in light of recent flux model refinements. *Physics Letters B*, 829:137054. (page 143, 144, 252)

[Goeppert-Mayer, 1935] Goeppert-Mayer, M. (1935). Double beta-disintegration. *Phys. Rev.*, 48:512–516. (page 16, 17)

[Gordon et al., 2004] Gordon, M., Goldhagen, P., Rodbell, K., Zabel, T., Tang, H., Clem, J., and Bailey, P. (2004). Measurement of the flux and energy spectrum of cosmic-ray induced neutrons on the ground. *IEEE Transactions on Nuclear Science*, 51(6):3427–3434. (page 178)

[Greenwood et al., 1992] Greenwood, R., Helmer, R., Lee, M., Putnam, M., Oates, M., Struttmann, D., and Watts, K. (1992). Total absorption gamma-ray spectrometer for measurement of beta-decay intensity distributions for fission product radionuclides. *Nuclear Instruments and Methods in Physics Research Section A: Accelerators, Spectrometers, Detectors and Associated Equipment*, 314(3):514–540. (page 127, 129, 251)

[Gysbers et al., 2019] Gysbers, P. et al. (2019). Discrepancy between experimental and theoretical β-decay rates resolved from first principles. *Nature Phys.*, 15(5):428–431. (page 24, 26, 27, 243)

[Haag et al., 2014a] Haag, N., Gütlein, A., Hofmann, M., Oberauer, L., Potzel, W., Schreckenbach, K., and Wagner, F. M. (2014a). Experimental Determination of the Antineutrino Spectrum of the Fission Products of ^{238}U. *Phys. Rev. Lett.*, 112(12):122501. (page 128, 137)

[Haag et al., 2014b] Haag, N., von Feilitzsch, F., Oberauer, L., Potzel, W., Schreckenbach, K., and Sonzogni, A. A. (2014b). Re-publication of the data from the BILL magnetic spectrometer: The cumulative β spectra of the fission products of ^{235}U, ^{239}Pu, and ^{241}Pu. (page 129, 132, 251)

[Hahn et al., 1989] Hahn, A., Schreckenbach, K., Gelletly, W., von Feilitzsch, F., Colvin, G., and Krusche, B. (1989). Antineutrino spectra from 241pu and 239pu thermal neutron fission products. *Physics Letters B*, 218(3):365–368. (page 128, 134, 135, 137)

[Hardy et al., 1984] Hardy, J., Jonson, B., and Hansen, P. (1984). A comment on pandemonium. *Physics Letters B*, 136(5):331–333. (page 127)

[Haxton and Stephenson, 1984] Haxton, W. C. and Stephenson, G. J. (1984). Double beta Decay. *Prog. Part. Nucl. Phys.*, 12:409–479. (page 20, 21)

[Hayen et al., 2019] Hayen, L., Kostensalo, J., Severijns, N., and Suhonen, J. (2019). First-forbidden transitions in the reactor anomaly. *Phys. Rev. C*, 100(5):054323. (page 144, 146)

[Hayes et al., 2018] Hayes, A. C., Jungman, G., McCutchan, E. A., Sonzogni, A. A., Garvey, G. T., and Wang, X. (2018). Analysis of the Daya Bay Reactor Antineutrino Flux Changes with Fuel Burnup. *Phys. Rev. Lett.*, 120(2):022503. (page 131)

[Heeger et al., 2013] Heeger, K. M., Littlejohn, B. R., Mumm, H. P., and Tobin, M. N. (2013). Experimental Parameters for a Reactor Antineutrino Experiment at Very Short Baselines. *Phys. Rev.*, D87:073008. (page 149, 150, 151, 254)

[Henaff, 2021] Henaff, D. (2021). *Toward the search of a sterile neutrino with the SoLid experiment at the SCK-CEN BR2 reactor : detector calibration and design of a multivariate topological selection of antineutrino events*. Theses, Ecole nationale supérieure Mines-Télécom Atlantique. (page 201, 208, 212, 214, 220, 233, 259)

[Herrero-Gómez et al., 2022] Herrero-Gómez, P. et al. (2022). Ba^{+2} ion trapping using organic submonolayer for ultra-low background neutrinoless double beta detector. *Nature Commun.*, 13(1):7741. (page 38)

[Hervé Chanal, 2019] Hervé Chanal, Stephane Monteil, P. C. (2019). The ccube algorithmt. *SoLid TechNote*, 2019-02. (page 181, 182)

[Hervé Chanal, 2020] Hervé Chanal, Stephane Monteil, P. C. M. Y. (2020). Topological reconstruction of ibd candidates. *SoLid TechNote*, 2020-07. (page 237)

[Hoballah, 2022] Hoballah, M. (2022). *Characterization of the Timing Properties of the SuperNEMO Demonstrator. Extraction of the SuperNEMO Sensitivity to the Axial-Vector Coupling Constant*. Theses, Université Paris-Saclay. (page 27, 99, 104, 107, 109, 111, 250)

[Hodák et al., 2019] Hodák, R. et al. (2019). Characterization and long-term performance of the Radon Trapping Facility operating at the Modane Underground Laboratory. *J. Phys. G*, 46(11):115105. (page 60, 66, 90)

[Hoummada et al., 1995] Hoummada, A., Lazrak Mikou, S., Avenier, M., Bagieu, G., Cavaignac, J., and Holm Koang, D. (1995). Neutrino oscillations i.l.l. experiment reanalysis. *Applied Radiation and Isotopes*, 46(6):449–450. (page 132)

[Huber, 2017] Huber, A. (2017). *Recherche de la nature du neutrino avec le détecteur SuperNEMO : simulations optiques pour l'optimisation du calorimètre et performances attendues pour le 82Se*. Theses, Université de Bordeaux. (page 106, 113)

[Huber, 2011] Huber, P. (2011). Determination of antineutrino spectra from nuclear reactors. *Phys. Rev. C*, 84:024617. (page 130, 131, 137, 182, 251)

[Ianni, 2016] Ianni, A. (2016). Canfranc underground laboratory. *Journal of Physics: Conference Series*, 718(4):042030. (page 60)

[Šimkovic et al., 2018] Šimkovic, F., Dvornický, R., Štefánik, D. c. v., and Faessler, A. (2018). Improved description of the $2\nu\beta\beta$-decay and a possibility to determine the effective axial-vector coupling constant. *Phys. Rev. C*, 97:034315. (page 26, 28, 243)

[Šimkovic et al., 1999] Šimkovic, F., Pantis, G., Vergados, J. D., and Faessler, A. (1999). Additional nucleon current contributions to neutrinoless double β decay. *Phys. Rev. C*, 60:055502. (page 22)

[Inghram and Reynolds, 1950] Inghram, M. G. and Reynolds, J. H. (1950). Double beta-decay of ^{130}Te. *Phys. Rev.*, 78:822–823.

[Jeremie et al., 2022] Jeremie, A. et al. (2022). Classical and Novel recipes for more than 6 kilograms of enriched Selenium foils for the SuperNEMO double beta decay demonstrator. *NEMO DocDB*, 5626. (page 68, 69)

[Kalcheva et al., 2017] Kalcheva, S., van den Branden, G., Koonen, E., Giot, L., and Fallot, M. (2017). Reactor Core Simulations for Determination of the Antineutrino Spectrum for the SoLid Experiment at BR2 Reactor. In *M&C 2017 - International Conference on Mathematics & Computational Methods Applied to Nuclear Science & Engineering*, Proceeding Meeting International Conference on Mathematics & Computational Methods Applied to Nuclear Science & Engineering, Jeju, Korea, April 16-20, 2017„ Jeju, South Korea. (page 182, 183, 257)

[Kalousis and Vercaemer, 2017] Kalousis, L. N. and Vercaemer, S. (2017). Solid sensitivity contours. *SoLid TechNote*, 2017-01. (page 182)

[Karson, 1968] Karson, M. (1968). Handbook of methods of applied statistics. volume i: Techniques of computation descriptive methods, and statistical inference. volume ii: Planning of surveys and experiments. i. m. chakravarti, r. g. laha, and j. roy, new york, john wiley; 1967, $9.00. *Journal of the American Statistical Association*, 63(323):1047–1049. (page 206)

[Katayama et al., 1962] Katayama, Y., Matumoto, K., Tanaka, S., and Yamada, E. (1962). Possible unified models of elementary particles with two neutrinos. *Prog. Theor. Phys.*, 28:675. (page 122)

[King and Perkins, 1958] King, R. W. and Perkins, J. F. (1958). Inverse beta decay and the two-component neutrino. *Phys. Rev.*, 112:963–966. (page 127)

[Kirsten and Müller, 1969] Kirsten, T. and Müller, H. (1969). Observation of 82se double-beta decay in selenium ores. *Earth and Planetary Science Letters*, 6(4):271–274. (page 34)

[Klapdor and Metzinger, 1982a] Klapdor, H. and Metzinger, J. (1982a). Calculation of the antineutrino spectrum from thermal fission of 235u. *Physics Letters B*, 112(1):22–26. (page 127, 134)

[Klapdor and Metzinger, 1982b] Klapdor, H. V. and Metzinger, J. (1982b). Antineutrino spectrum from the fission products of ^{239}Pu. *Phys. Rev. Lett.*, 48:127–131. (page 127, 134)

[Klapdor-Kleingrothaus et al., 2001] Klapdor-Kleingrothaus, H. V., Dietz, A., Harney, H. L., and Krivosheina, I. V. (2001). Evidence for neutrinoless double beta decay. *Mod. Phys. Lett. A*, 16:2409–2420. (page 34)

[Klapdor-Kleingrothaus and Krivosheina, 2006] Klapdor-Kleingrothaus, H. V. and Krivosheina, I. V. (2006). The evidence for the observation of 0nu beta beta decay: The identification of 0nu beta beta events from the full spectra. *Mod. Phys. Lett. A*, 21:1547–1566. (page 34)

[KLEIN et al., 2008] KLEIN, O. et al. (2008). Über die Streuung von Strahlung durch freie Elektronen nach der neuen relativistischen Quantendynamik von Dirac. *Nuclear Instruments and Methods in Physics Research Section A: Accelerators, Spectrometers, Detectors and Associated Equipment*, 594(2):232 – 243. (page 205)

[Ko et al., 2017] Ko, Y. J. et al. (2017). Sterile Neutrino Search at the NEOS Experiment. *Phys. Rev. Lett.*, 118(12):121802. (page 150, 151, 152, 254)

[Kopeikin et al., 1997] Kopeikin, V., Mikaelyan, L., and Sinev, V. (1997). Spectrum of electronic reactor antineutrinos. *Physics of Atomic Nuclei*, 60(2):172–176. (page 127)

[Kopeikin et al., 2021] Kopeikin, V., Skorokhvatov, M., and Titov, O. (2021). Reevaluating reactor antineutrino spectra with new measurements of the ratio between U235 and Pu239 β spectra. *Phys. Rev. D*, 104(7):L071301. (page 131, 132, 144, 251)

[Kopeikin et al., 2001] Kopeikin, V. I., Mikaelyan, L. A., and Sinev, V. V. (2001). Inverse beta decay in a nonequilibrium anti-neutrino flux from a nuclear reactor. *Phys. Atom. Nucl.*, 64:849–854. (page 135)

[Kopp et al., 2013] Kopp, J., Machado, P. A. N., Maltoni, M., and Schwetz, T. (2013). Sterile Neutrino Oscillations: The Global Picture. *JHEP*, 05:050. (page 142, 143, 149, 183, 253, 254, 257)

[Kostensalo et al., 2019] Kostensalo, J., Suhonen, J., Giunti, C., and Srivastava, P. C. (2019). The gallium anomaly revisited. *Phys. Lett. B*, 795:542–547. (page 147)

[Kotila and Iachello, 2012] Kotila, J. and Iachello, F. (2012). Phase-space factors for double-β decay. *Phys. Rev. C*, 85:034316. (page 16, 17, 243)

[Kwon et al., 1981] Kwon, H., Boehm, F., Hahn, A. A., Henrikson, H. E., Vuilleumier, J. L., Cavaignac, J. F., Koang, D. H., Vignon, B., Feilitzsch, F. v., and Mössbauer, R. L. (1981). Search for neutrino oscillations at a fission reactor. *Phys. Rev. D*, 24:1097–1111. (page 132, 133, 251)

[Lemiere et al., 2014] Lemiere, Y. et al. (2014). SuperNEMO Collaboration Component Labelling Strategy. *NEMO DocDB*, 3414. (page 77, 247)

[Letourneau et al., 2023] Letourneau, A., Savu, V., Lhuillier, D., Lasserre, T., Materna, T., Mention, G., Mougeot, X., Onillon, A., Perisse, L., and Vivier, M. (2023). Origin of the Reactor Antineutrino Anomalies in Light of a New Summation Model with Parametrized β-Transitions. *Phys. Rev. Lett.*, 130(2):021801. (page 154, 155, 255)

[Liu et al., 2007] Liu, Z., Chen, J., Zhu, P., Li, Y., and Zhang, G. (2007). The 4.438mev gamma to neutron ratio for the am–be neutron source. *Applied Radiation and Isotopes*, 65(12):1318–1321. (page 219)

[Loaiza et al., 2017] Loaiza, P. et al. (2017). The BiPo-3 detector. *Appl. Radiat. Isot.*, 123:54–59. (page 69, 201)

[Majorana, 1937] Majorana, E. (1937). Teoria simmetrica dell'elettrone e del positrone. *Nuovo Cim.*, 14:171–184. (page 14, 17)

[Maki et al., 1962] Maki, Z., Nakagawa, M., and Sakata, S. (1962). Remarks on the unified model of elementary particles. *Prog. Theor. Phys.*, 28:870–880. (page 122)

[Marquet et al., 2015] Marquet, C. et al. (2015). High energy resolution electron beam spectrometer in the MeV range. *JINST*, 10(09):P09008. (page 53, 186)

[Matsubara et al., 2012] Matsubara, T. et al. (2012). Evaluation of 400 low background 10-in. photo-multiplier tubes for the Double Chooz experiment. *Nucl. Instrum. Meth. A*, 661:16–25. (page 138)

[Mention et al., 2011] Mention, G., Fechner, M., Lasserre, T., Mueller, T. A., Lhuillier, D., Cribier, M., and Letourneau, A. (2011). The Reactor Antineutrino Anomaly. *Phys. Rev.*, D83:073006. (page 142, 151, 152, 254)

[Méplan et al., 2005] Méplan, O., Nuttin, A., Laulan, O., David, S., Michel-Sendis, F., and Wilson, J. (2005). MURE : MCNP Utility for Reactor Evolution - Description of the methods, first applications and results. ENC 2005 - European Nuclear Conference. Nuclear Power for the XXIst Century : From basic research to high-tech industry. Poster - PACS. (page 182)

[Minkowski, 1977] Minkowski, P. (1977). $\mu \to e\gamma$ at a rate of one out of 109 muon decays? *Physics Letters B*, 67(4):421–428. (page 15)

[Mirea et al., 2015] Mirea, M., Pahomi, T., and Stoica, S. (2015). Values of the phase space factors involved in double beta decay. *Rom. Rep. Phys.*, 67(3):872. (page 16)

[Moe, 2014] Moe, M. (2014). The first direct observation of double-beta decay. *Annual Review of Nuclear and Particle Science*, 64(1):247–267.

[Mueller et al., 2011] Mueller, T. A. et al. (2011). Improved Predictions of Reactor Antineutrino Spectra. *Phys. Rev.*, C83:054615. (page 125, 127, 129, 130, 131, 137, 182, 251)

[Oliviero, 2018] Oliviero, G. (2018). *SuperNEMO experiment for the search of neutrinoless double beta decay : design and implementation of the trigger system for the demonstrator module*. Theses, Université Caen Normandie. (page 95, 104)

[Pastore et al., 2018] Pastore, S., Carlson, J., Cirigliano, V., Dekens, W., Mereghetti, E., and Wiringa, R. B. (2018). Neutrinoless double-β decay matrix elements in light nuclei. *Phys. Rev. C*, 97:014606. (page 24)

[PDG, 2022] PDG (2022). Review of Particle Physics. *Progress of Theoretical and Experimental Physics*, 2022(8):083C01. (page 14, 122)

[Pequignot, 2015] Pequignot, M. (2015). *Les expériences Nucifer et Stéréo : étude des antineutrinos de réacteurs à courte distance*. Theses, Université Paris Sud - Paris XI. (page 154)

[Perrot et al., 2020] Perrot, F. et al. (2020). SuperNEMO Anti-Radon Tent (ART) requirements and status. *NEMO DocDB*, 5196. (page 90)

[Pestel, 2019] Pestel, V. (2019). *Détection de neutrinos auprès du réacteur BR2 : analyse des premières données de l'expérience SoLid*. Theses, Normandie Université. (page 181, 182, 201, 229, 257)

[Pin, 2020] Pin, A. (2020). *Recherche de la nature du neutrino via la décroissance double bêta sans émission de neutrinos : Caractérisation et optimisation du calorimètre SuperNEMO et impact sur la recherche de la décroissance du 82Se : Développement du premier prototype LiquidO*. Theses, Université de Bordeaux. (page 99, 113)

[Pinera-Hernandez, 2016a] Pinera-Hernandez, I. (2016a). Br2 building geometry & model for solid geant4 simulations. *SoLid TechNote*, 2016-03. (page 180)

[Pinera-Hernandez, 2016b] Pinera-Hernandez, I. (2016b). Identification of background components with the SoLid anti-neutrino detector. In *Proceedings, 2016 IEEE Nuclear Science Symposium and Medical Imaging Conference: NSS/MIC 2016: Strasbourg, France*, page 8069849. (page 174)

[Pontecorvo, 1967] Pontecorvo, B. (1967). Neutrino Experiments and the Problem of Conservation of Leptonic Charge. *Zh. Eksp. Teor. Fiz.*, 53:1717–1725. (page 122)

[Pujol et al., 2009] Pujol, M., Marty, B., Burnard, P., and Philippot, P. (2009). Xenon in archean barite: Weak decay of 130ba, mass-dependent isotopic fractionation and implication for barite formation. *Geochimica et Cosmochimica Acta*, 73(22):6834–6846. (page 17)

[Quinn, 5 28] Quinn, W. (2023-05-28). *The sensitivity of the NEMO technique to neutrinoless double beta decay and the commissioning of the SuperNEMO demonstrator module*. PhD thesis. (page 106, 111)

[Rakhimov et al., 2020] Rakhimov, A. V. et al. (2020). Development of methods for the preparation of radiopure ^{82}se sources for the supernemo neutrinoless double-beta decay experiment. *Radiochimica Acta*, 108(2):87–97. (page 68)

[Rath et al., 2010] Rath, P. K., Chandra, R., Chaturvedi, K., Raina, P. K., and Hirsch, J. G. (2010). Uncertainties in nuclear transition matrix elements for neutrinoless $\beta\beta$ decay within the PHFB model. *Phys. Rev. C*, 82:064310. (page 24)

[Rodin et al., 2003] Rodin, V. A., Faessler, A., Šimkovic, F., and Vogel, P. (2003). Uncertainty in the $0\nu\beta\beta$ decay nuclear matrix elements. *Phys. Rev. C*, 68:044302. (page 24, 25, 243)

[Rodriguez and Martinez-Pinedo, 2010] Rodriguez, T. R. and Martinez-Pinedo, G. (2010). Energy density functional study of nuclear matrix elements for neutrinoless $\beta\beta$ decay. *Phys. Rev. Lett.*, 105:252503. (page 24)

[Roy, 2021] Roy, N. (2021). *Search for sterile neutrino oscillations with the SoLid experiment at BR2 reactor : Energy calibration of the detector and antineutrino signal extraction.* Theses, Université Paris-Saclay. (page 99, 201, 208, 215, 220, 223, 228, 229, 230, 231, 232, 233, 234, 235, 236, 237, 238, 259, 260, 261)

[Rudstam et al., 1990] Rudstam, G., Johansson, P., Tengblad, O., Aagaard, P., and Eriksen, J. (1990). Beta and gama spectra of short-lived fission products. *Atomic Data and Nuclear Data Tables*, 45(2):239–320. (page 127)

[Saakyan, 2013] Saakyan, R. (2013). Two-neutrino double-beta decay. *Annual Review of Nuclear and Particle Science*, 63(1):503–529. (page 16, 18, 21, 24, 29, 33, 243, 244)

[Schechter and Valle, 1982] Schechter, J. and Valle, J. W. F. (1982). Neutrinoless double-β decay in su(2)×u(1) theories. *Phys. Rev. D*, 25:2951–2954. (page 20)

[Schreckenbach et al., 1985] Schreckenbach, K., Colvin, G., Gelletly, W., and Von Feilitzsch, F. (1985). Determination of the antineutrino spectrum from 235u thermal neutron fission products up to 9.5 mev. *Physics Letters B*, 160(4):325–330. (page 128, 130, 133, 134, 135, 137, 251)

[Schreckenbach et al., 1981] Schreckenbach, K., Faust, H., von Feilitzsch, F., Hahn, A., Hawerkamp, K., and Vuilleumier, J. (1981). Absolute measurement of the beta spectrum from 235U fission as a basis for reactor antineutrino experiments. *Phys. Lett. B*, 99:251–256. (page 128, 132, 133, 251)

[Serebrov et al., 2019] Serebrov, A. P. et al. (2019). First Observation of the Oscillation Effect in the Neutrino-4 Experiment on the Search for the Sterile Neutrino. *Pisma Zh. Eksp. Teor. Fiz.*, 109(4):209–218. (page 150, 151)

[Serebrov and Samoilov, 2020] Serebrov, A. P. and Samoilov, R. M. (2020). Analysis of the Results of the Neutrino-4 Experiment on the Search for the Sterile Neutrino and Comparison with Results of Other Experiments. *JETP Lett.*, 112(4):199–212.

[Serebrov et al., 2021] Serebrov, A. P., Samoilov, R. M., Ivochkin, V. G., Fomin, A. K., Zinoviev, V. G., Neustroev, P. V., Golovtsov, V. L., Volkov, S. S., Chernyj, A. V., Zherebtsov, O. M., Chaikovskii, M. E., Petelin, A. L., Izhutov, A. L., Tuzov, A. A., Sazontov, S. A., Gromov, M. O., Afanasiev, V. V., Zaytsev, M. E., Gerasimov, A. A., and Fedorov, V. V. (2021). Search for sterile neutrinos with the neutrino-4 experiment and measurement results. *Phys. Rev. D*, 104:032003. (page 151, 153, 255)

[Siciliano et al., 2008] Siciliano, E., Ely, J., Kouzes, R., Schweppe, J., Strachan, D., and Yokuda, S. (2008). Energy calibration of gamma spectra in plastic scintillators using compton kinematics. *Nuclear Instruments and Methods in Physics Research Section A: Accelerators, Spectrometers, Detectors and Associated Equipment*, 594(2):232 – 243. (page 205)

[Simón et al., 2021] Simón, A. et al. (2021). Boosting background suppression in the NEXT experiment through Richardson-Lucy deconvolution. *JHEP*, 07:146. (page 37)

[Sinatkas et al., 1992] Sinatkas, J., Skouras, L. D., Strottman, D., and Vergados, J. D. (1992). Shell-model calculations in the a=80-100 mass region: I. a study of the n=50 nuclei. *Journal of Physics G: Nuclear and Particle Physics*, 18(8):1377. (page 23)

[Sonzogni et al., 2015] Sonzogni, A. A., Johnson, T. D., and McCutchan, E. A. (2015). Nuclear structure insights into reactor antineutrino spectra. *Phys. Rev. C*, 91:011301. (page 127, 128, 251)

[Takenaka et al., 2020] Takenaka, A. et al. (2020). Search for proton decay via $p \to e^+\pi^0$ and $p \to \mu^+\pi^0$ with an enlarged fiducial volume in Super-Kamiokande I-IV. *Phys. Rev. D*, 102(11):112011. (page 14)

[Tedjditi, 2021] Tedjditi, H. (2021). *Optimisation de la reconstruction gamma de l'expérience SuperNEMO en vue de l'étude du bruit de fond : développement d'un détecteur sphérique proportionnel pour l'étude du radon dans l'expérience SuperNEMO*. PhD thesis. Thèse de doctorat dirigée par Busto, José Physique des particules et astroparticules Aix-Marseille 2021. (page 99, 105)

[Tengblad et al., 1989] Tengblad, O., Aleklett, K., Von Dincklage, R., Lund, E., Nyman, G., and Rudstam, G. (1989). Integral $\bar{\nu}$-spectra derived from experimental β-spectra of individual fission products. *Nuclear Physics A*, 503(1):136–160. (page 127)

[Tretyak, 2011] Tretyak, V. I. (2011). False starts in history of searches for 2β decay, or Discoverless double beta decay. *AIP Conf. Proc.*, 1417(1):129–133. (page 34)

[Vergados et al., 2016] Vergados, J. D., Ejiri, H., and Šimkovic, F. (2016). Neutrinoless double beta decay and neutrino mass. *Int. J. Mod. Phys. E*, 25(11):1630007. (page 24)

[Verstraeten, 2021] Verstraeten, M. (2021). *Search for sterile neutrinos in the eV and MeV mass range with the SoLid detector*. PhD thesis, University of Antwerp. (page 180)

[Vialat, 2021] Vialat, M. (2021). *Détection des neutrinos stériles auprès de l'ILL, l'expérience Stéréo*. Theses, Université Grenoble Alpes [2020-....]. (page 154)

[Vissani, 1999] Vissani, F. (1999). Signal of neutrinoless double beta decay, neutrino spectrum and oscillation scenarios. *JHEP*, 06:022. (page 19, 243)

[Vogel, 2007] Vogel, P. (2007). Conversion of electron spectrum associated with fission into the antineutrino spectrum. *Phys. Rev. C*, 76:025504. (page 128, 129, 131)

[Vogel, 2012] Vogel, P. (2012). Nuclear structure and double beta decay. *J. Phys. G*, 39:124002. (page 22)

[Vogel, 2019] Vogel, P. (2019). Reactor neutrinos: towards oscillation. In *International Conference on History of the Neutrino: 1930-2018*. (page 123, 125, 134)

[Vogel and Beacom, 1999] Vogel, P. and Beacom, J. F. (1999). Angular distribution of neutron inverse beta decay, $\overline{\nu}_e + \vec{p} \; e^+ + n$. *Phys. Rev. D*, 60:053003. (page 151, 182)

[Vogel et al., 1981] Vogel, P., Schenter, G. K., Mann, F. M., and Schenter, R. E. (1981). Reactor antineutrino spectra and their application to antineutrino-induced reactions. ii. *Phys. Rev. C*, 24:1543–1553. (page 127, 135)

[Vogel and Zirnbauer, 1986] Vogel, P. and Zirnbauer, M. R. (1986). Suppression of the Two Neutrino Double beta Decay by Nuclear Structure Effects. *Phys. Rev. Lett.*, 57:3148–3151. (page 23)

[Von Feilitzsch et al., 1982] Von Feilitzsch, F., Hahn, A. A., and Schreckenbach, K. (1982). Experimental beta spectra from Pu-239 and U-235 thermal neutron fission products and their correlated anti-neutrinos spectra. *Phys. Lett. B*, 118:162–166. (page 127, 128, 130, 137, 251)

[Weinberg, 1979] Weinberg, S. (1979). Baryon- and lepton-nonconserving processes. *Phys. Rev. Lett.*, 43:1566–1570. (page 14)

[Yao et al., 2018] Yao, J. M., Engel, J., Wang, L. J., Jiao, C. F., and Hergert, H. (2018). Generator-coordinate reference states for spectra and $0\nu\beta\beta$ decay in the in-medium similarity renormalization group. *Phys. Rev. C*, 98:054311. (page 24)

[Yao et al., 2015] Yao, J. M., Song, L. S., Hagino, K., Ring, P., and Meng, J. (2015). Systematic study of nuclear matrix elements in neutrinoless double-β decay with a beyond-mean-field covariant density functional theory. *Phys. Rev. C*, 91(2):024316. (page 24)

[Yeresko, 2022] Yeresko, M. (2022). *Search for antineutrino disappearance with the SoLiϑ detector : novel reconstruction, calibration and selection.* Theses, Université Clermont Auvergne. (page 237)

[Zhang et al., 2013] Zhang, C., Qian, X., and Vogel, P. (2013). Reactor antineutrino anomaly with known θ_{13}. *Phys. Rev. D*, 87:073018. (page 142)

Titre: Physique des neutrinos avec les expériences SuperNEMO et SoLid.
Mots clés: Neutrino, double désintégration bêta, neutrino de Majorana, oscillations, neutrino stérile.

Résumé: Le Modèle Standard de la physique des particules décrit avec une précision remarquable les particules élémentaires et leurs interactions. Parmi celles-ci, on trouve les neutrinos, des leptons qui existent sous trois saveurs : électron, muon et tau. Ne possédant pas de charge électrique, les neutrinos n'interagissent qu'à travers l'interaction faible, ce qui les rend très difficiles à étudier. Certaines propriétés des neutrinos, comme leur faible masse ou la possible indistinction entre neutrinos et antineutrinos selon la théorie de Majorana, défient le Modèle Standard. Les oscillations de saveurs, où un neutrino change de type durant sa propagation, ne sont pas entièrement expliquées dans ce modèle. Il est aussi possible qu'un neutrino stérile, insensible à toutes les interactions du modèle, existe.

Les recherches présentées dans cette *Habilitation à diriger des recherches* concernent d'abord la nature Majorana du neutrino, avec l'étude de la double désintégration bêta sans émission de neutrinos. L'expérience SuperNEMO analyse les désintégrations de l'isotope ^{82}Se au Laboratoire Souterrain de Modane. Un détecteur de traces permet de reconstruire les électrons émis, et un calorimètre segmenté mesure leurs énergies. Nous présenterons les caractéristiques du démonstrateur SuperNEMO, sa construction et les premières performances de son calorimètre.

Deuxièmement, cette habilitation aborde la recherche du neutrino stérile à courte distance d'un réacteur nucléaire, pouvant expliquer le déficit d'anti-neutrinos observé par rapport au prédictions. L'expérience SoLid, menée près du réacteur BR2 à Mol, en Belgique, cherche un signal d'oscillation d'anti-neutrinos. Grâce à sa fine segmentation et à l'utilisation hybride de scintillateurs, elle lutte contre les bruits de fond atmosphériques et radioactifs. Nous présenterons les motivations de SoLid, son principe expérimental, la calibration en énergie et ses premiers résultats.

Title: Neutrino physics with SuperNEMO and SoLid experiments.
Keywords: Neutrino, double beta decay, Majorana neutrino, oscillations, sterile neutrino.

Abstract: The Standard Model of particle physics describes elementary particles and their interactions with remarkable precision. Among these are neutrinos, leptons that exist in three flavors: electron, muon, and tau. Lacking an electric charge, neutrinos interact only through the weak interaction, making them very difficult to study. Certain properties of neutrinos, such as their extremely low mass or the possible indistinction between neutrinos and antineutrinos according to Majorana's theory, challenge the Standard Model. Flavor oscillations, where a neutrino changes type during its propagation, are also not fully explained by this model. It is also possible that a sterile neutrino, insensitive to all interactions described by the model, exists.

The research presented in this *Habilitation à Diriger des Recherches* first focuses on the Majorana nature of the neutrino, with the study of neutrinoless double beta decay. The SuperNEMO experiment analyzes the decays of the ^{82}Se isotope at the Modane Underground Laboratory. A tracking detector reconstructs the emitted electrons, and a segmented calorimeter measures their energies. We will present the characteristics of the SuperNEMO demonstrator, its construction, and the initial performances of its calorimeter.

Secondly, this habilitation addresses the search for a sterile neutrino at short range from a nuclear reactor, which could explain the observed anti-neutrino deficit compared to predictions. The SoLid experiment, conducted near the BR2 reactor in Mol, Belgium, seeks a signal of anti-neutrino oscillation. Thanks to its fine segmentation and hybrid use of scintillators, it actively mitigates background noise from atmospheric and natural radioactivity. We will present the motivations behind SoLid, its experimental principle, energy calibration, and its initial results.

Maison du doctorat de Université Paris-Saclay
2^{e} étage, aile ouest, École normale supérieure Paris-Saclay
4 avenue des Sciencs
91190 Gif-sur-Yvette, France